PROGRESS IN BIOMEDICAL OPTICS

Proceedings of

Surgical Applications of Energy

Thomas P. Ryan
Chair/Editor

Abraham Katzir
Biomedical Optics Series Editor

25–26 January 1998
San Jose, California

Sponsored by
AFOSR—U.S. Air Force Office of Scientific Research
SPIE—The International Society for Optical Engineering
IBOS—International Biomedical Optics Society

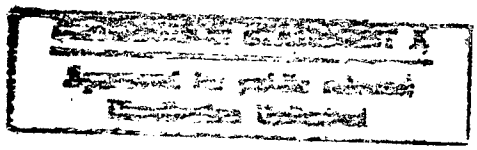

19980828 037

DTIC QUALITY INSPECTED 1

Volume 3249

PROGRESS IN BIOMEDICAL OPTICS

Proceedings of

Surgical Applications of Energy

Thomas P. Ryan
Chair/Editor

Abraham Katzir
Biomedical Optics Series Editor

25–26 January 1998
San Jose, California

Sponsored by
AFOSR—U.S. Air Force Office of Scientific Research
SPIE—The International Society for Optical Engineering
IBOS—International Biomedical Optics Society

Published by
SPIE—The International Society for Optical Engineering

Volume 3249

SPIE is an international technical society dedicated to advancing engineering and scientific applications of optical, photonic, imaging, electronic, and optoelectronic technologies.

DTIC QUALITY INSPECTED 1

The papers appearing in this book comprise the proceedings of the meeting mentioned on the cover and title page. They reflect the authors' opinions and are published as presented and without change, in the interests of timely dissemination. Their inclusion in this publication does not necessarily constitute endorsement by the editors or by SPIE.

Please use the following format to cite material from this book:
Author(s), "Title of paper," in *Surgical Applications of Energy*, Thomas P. Ryan, Editor, Proceedings of SPIE Vol. 3249, page numbers (1998).

ISSN 0277-786X
ISBN 0-8194-2688-1

Published by
SPIE—The International Society for Optical Engineering
P.O. Box 10, Bellingham, Washington 98227-0010 USA
Telephone 360/676-3290 (Pacific Time) • Fax 360/647-1445

Copyright ©1998, The Society of Photo-Optical Instrumentation Engineers.

Copying of material in this book for internal or personal use, or for the internal or personal use of specific clients, beyond the fair use provisions granted by the U.S. Copyright Law is authorized by SPIE subject to payment of copying fees. The Transactional Reporting Service base fee for this volume is $10.00 per article (or portion thereof), which should be paid directly to the Copyright Clearance Center (CCC), 222 Rosewood Drive, Danvers, MA 01923. Payment may also be made electronically through CCC Online at http://www.directory.net/copyright/. Other copying for republication, resale, advertising or promotion, or any form of systematic or multiple reproduction of any material in this book is prohibited except with permission in writing from the publisher. The CCC fee code is 0277-786X/97/$10.00.

Printed in the United States of America.

Contents

vii *Conference Committee*
ix *Introduction*

SESSION 1 THERAPEUTIC MINIATURE ULTRASOUND APPLICATORS

2 **Prostate thermal therapy with interstitial and transurethral ultrasound applicators: a feasibility study** [3249-02]
C. J. Diederich, W. H. Nau, D. L. Deardorff, I. S. Khalil-Bustany, Univ. of California/San Francisco; E. C. Burdette, Acoustic MedSystems; P. R. Stauffer, M. Wu, Univ. of California/San Francisco

13 **Directional interstitial ultrasound applicators for thermal coagulation of tissue** [3249-03]
W. H. Nau, C. J. Diederich, P. R. Stauffer, D. L. Deardorff, Univ. of California/San Francisco

20 **Feasibility of interstitial thermotherapy with ultrasound waveguide applicator arrays** [3249-04]
B. J. Jarosz, Carleton Univ. (Canada)

31 **Catheter application of cryogenic temperatures inside the heart** [3249-05]
J. W. Lewis, CryoCath Technologies Inc. (Canada); M. Dubuc, Institut de Cardiologie de Montréal (Canada)

SESSION 2 THERAPEUTIC MICROWAVE DEVICES

38 **Implantable microwave antennas for thermal therapy** [3249-06]
P. R. Stauffer, Univ. of California/San Francisco

50 **Microwave occlusion of the rabbit uterine horn** [3249-07]
B. Trembly, Dartmouth College; P. D. Manganiello, P. J. Hoopes, Dartmouth-Hitchcock Medical Ctr.

61 **Microwave catheter ablation for the treatment of atrial flutter** [3249-08]
D. Bérubé, L. B. Liem, Fidus Medical Technology

SESSION 3 THERAPEUTIC LASER AND ARGON DEVICES

68 **Tissue effects of argon gas flow during electrosurgery** [3249-09]
C. F. P. van Swol, Univ. Hospital Utrecht (Netherlands); R. J. van Vliet, Univ. Hospital Utrecht (Netherlands) and Dr. Daniel den Hoed Cancer Ctr. (Netherlands); M. G. M. Grimbergen, R. M. Verdaasdonk, Univ. Hospital Utrecht (Netherlands)

72 **High-speed and thermal imaging of the mechanism of action of the cavitron ultrasonic surgical aspirator (CUSA)** [3249-10]
R. M. Verdaasdonk, C. F. P. van Swol, M. G. M. Grimbergen, Univ. Hospital Utrecht (Netherlands); G. Priem, Valleylab Benelux (Netherlands)

85 **Experimental study and first clinical results with a cooled applicator system for interstitial laser coagulation (LITT)** [3249-32]
A. Roggan, Institut für Medizinische/Technische Physik und Lasermedizin/Freie Univ. Berlin (FRG); V. Knappe, Laser- und Medizin-Technologie gGmbH (FRG); M. G. Mack, T. J. Vogl, Universitätsklinikum Rudolf Virchow/Humboldt-Univ. zu Berlin (FRG); D. Albrecht, C. T. Germer, J.-P. Ritz, Universitätsklinikum Benjamin Franklin der Freien Univ. Berlin (FRG); F. Kniep, Somatex (FRG); G. J. Müller, Institut für Medizinische/Technische Physik und Lasermedizin/Freie Univ. Berlin (FRG) and Laser- und Medizin-Technologie gGmbH (FRG)

94 **New application system for simultaneous laser and ultrasonic transmission in endoscopic surgery (LUST)** [3249-34]
K. Desinger, Laser- und Medizin-Technologie gGmbH (FRG); J. Helfmann, T. Stein, Institut für Medizinische/Technische Physik und Lasermedizin/Freie Univ. Berlin (FRG); K. Liebold, Laser- und Medizin-Technologie gGmbH (FRG); G. J. Müller, Laser- und Medizin-Technologie gGmbh (FRG) and Institut für Medizinische/Technische Physik und Lasermedizin/Freie Univ. Berlin (FRG)

SESSION 4 THERAPEUTIC RF DEVICES AND TECHNIQUES

104 **Advances in radio frequency tumor ablation therapy: technical considerations, strategies for increasing coagulation necrosis volume, and preliminary clinical results** [3249-12]
S. N. Goldberg, G. S. Gazelle, Massachusetts General Hospital

115 **Quantitative and qualitative histopathological comparisons of multielectrode balloon and thermal balloon endometrial ablation** [3249-13]
S. L. Thomsen, Univ. of Texas M.D. Anderson Cancer Ctr.; T. P. Ryan, K. Kuk-Nagle, Valleylab Inc.; C. Soto, Univ. of Texas M.D. Anderson Cancer Ctr.; T. G. Vancaillie, Univ. of Texas Health Science Ctr.; J. Garza-Leal, Univ. Hospital/Monterrey (Mexico)

125 **Controlled radio frequency vessel sealing system for surgical applications** [3249-14]
J. S. Kennedy, S. Buysse, J. Chandler, J. Eggleston, K. D. Taylor, Valleylab Inc.; S. L. Thomsen, Univ. of Texas M.D. Anderson Cancer Ctr.

130 **Heating stents with radio frequency energy to prevent tumor ingrowth: modeling and experimental results** [3249-15]
T. P. Ryan, K. Lawes, Valleylab Inc.; S. N. Goldberg, Massachusetts General Hospital

142 **New electrosurgical ball electrode with nonstick properties** [3249-16]
J. Rondinone, Fusion Medical Technologies, Inc.; J. Brassell, S. A. Miller III, J. O. Thorne, Battelle Product Development Group; D. M. Rondinone, Berkeley Engineering and Research; J. Safabash, F. Vega, Fusion Medical Technologies, Inc.

147 **Interstitial bipolar rf-thermotherapy (RFITT): therapy planning by computer simulation and MRI monitoring—a new concept for minimally invasive procedures** [3249-33]
K. Desinger, Laser- und Medizin-Technologie gGmbH (FRG); T. Stein, Institut für Medizinische/Technische Physik und Lasermedizin/Freie Univ. Berlin (FRG); G. J. Müller, Laser- und Medizin-Technologie gGmbH (FRG) and Institut für Medizinische/Technische Physik und Lasermedizin (FRG); M. G. Mack, T. J. Vogl, Universitätsklinikum Rudolf Virchow/Humboldt-Univ. zu Berlin (FRG)

SESSION 5 IMAGE GUIDANCE AND THERMAL IMAGING

162 **MR imaging guidance for minimally invasive procedures** [3249-17]
T. Z. Wong, J. Kettenbach, S. G. Silverman, R. B. Schwartz, P. R. Morrison, D. F. Kacher, F. A. Jolesz, Brigham and Women's Hospital/Harvard Medical School

171 **Toward a clinical implementation of a noninvasive microwave imaging system for temperature monitoring** [3249-18]
P. M. Meaney, Dartmouth College; K. D. Paulsen, Dartmouth College and Norris Cotton Cancer Ctr.; J. T. Chang, M. Fanning, Dartmouth College

182 **Motion compensation algorithm for noninvasive two-dimensional temperature estimation using diagnostic pulse-echo ultrasound** [3249-19]
C. Simon, P. D. VanBaren, E. S. Ebbini, Univ. of Michigan

193 **Electrical impedance imaging for tissue monitoring and assessment during thermal therapy** [3249-20]
K. D. Paulsen, Dartmouth College and Norris Cotton Cancer Ctr.; A. Hartov, Dartmouth College and Dartmouth Hitchcock Medical Ctr.; K. S. Osterman, R. Mazzarese, Dartmouth College; T. Kerner, Dartmouth College and Dartmouth Hitchcock Medical Ctr.

SESSION 6 MODELING OF THERAPEUTIC DEVICES

206 **Finite-element model for endometrial ablation systems** [3249-22]
T. P. Ryan, R. C. Platt, Valleylab Inc.; S. Humphries, Field Precision

217 **Effect of vessel architecture on fusion by radio frequency current** [3249-23]
J. A. Pearce, Univ. of Texas at Austin; S. L. Thomsen, Univ. of Texas M.D. Anderson Cancer Ctr.

SESSION 7 FOCUSED ULTRASOUND FOR TISSUE THERAPY I

230 **Image-guided noninvasive surgery with ultrasound phased arrays** [3249-24]
E. S. Ebbini, P. D. VanBaren, C. Simon, Univ. of Michigan

SESSION 8 FOCUSED ULTRASOUND FOR TISSUE THERAPY II

242 **Influence of acoustic power on parietal thermometry during extracorporeal high-intensity focused ultrasound treatments** [3249-26]
F. Lacoste, Edap-Technomed (France); B. Feuillu, J. Schlosser, Ctr. Hospitalier Universitaire de Nancy-Brabois (France); G. Vallancien, CERA/Institut Montsouris (France)

246 **Intensity dependence of focused ultrasound lesion position** [3249-27]
P. M. Meaney, Dartmouth College; M. D. Cahill, St. Thomas' Hospital (UK); G. R. ter Haar, Royal Marsden Hospital (UK)

257 **Treatment of in-vivo bladder tissue with electronically scanned high-intensity focused ultrasound** [3249-28]
B. Feuillu, Ctr. Hospitalier Universitaire de Nancy-Brabois (France); F. Lacoste, Edap-Technomed (France); J. Schlosser, Ctr. Hospitalier Universitaire de Nancy-Brabois (France); G. Vallancien, CERA/Institut Montsouris (France)

260 **Focused ultrasound surgery-induced vascular occlusion in fetal medicine** [3249-29]
I. H. Rivens, I. Rowland, Royal Marsden Hospital (UK); M. Denbow, N. M. Fisk, Queen Charlotte's Hospital (UK); M. O. Leach, G. R. ter Haar, Royal Marsden Hospital (UK)

267 **Focused ultrasound surgery on the kidney** [3249-30]
J. Schlosser, B. Feuillu, Ctr. Hospitalier Universitaire de Nancy-Brabois (France); F. Lacoste, Edap-Technomed (France); J. André-Bougaran, G. Vallancien, CERA/Institut Montsouris (France)

270 **Phase one clinical trial of the use of focused ultrasound surgery for the treatment of soft-tissue tumors** [3249-31]
G. R. ter Haar, I. H. Rivens, E. Moskovic, R. Huddart, A. G. Visioli, Royal Marsden Hospital (UK)

277 *Addendum*
278 *Author Index*

Conference Committee

Conference Chair

Thomas P. Ryan, Valleylab Inc.

Program Committee

Emad S. Ebbini, University of Michigan
S. Nahum Goldberg, M.D., Massachusetts General Hospital and Harvard Medical School
Keith D. Paulsen, Dartmouth College and Norris Cotton Cancer Center
Sharon L. Thomsen, M.D., University of Texas M.D. Anderson Cancer Center

Session Chairs

1 Therapeutic Miniature Ultrasound Applicators
Emad S. Ebbini, University of Michigan

2 Therapeutic Microwave Devices
S. Nahum Goldberg, M.D., Massachusetts General Hospital and Harvard Medical School

3 Therapeutic Laser and Argon Devices
Rudolf M. Verdaasdonk, University Hospital Utrecht (Netherlands)

4 Therapeutic rf Devices and Techniques
Sharon L. Thomsen, M.D., University of Texas M.D. Anderson Cancer Center

5 Image Guidance and Thermal Imaging
Thomas P. Ryan, Valleylab Inc.

6 Modeling of Therapeutic Devices
Keith D. Paulsen, Dartmouth College and Norris Cotton Cancer Center

7 Focused Ultrasound for Tissue Therapy I
Terence Z. Wong, M.D., Brigham & Women's Hospital/Harvard Medical School

8 Focused Ultrasound for Tissue Therapy II
Chris J. Diederich, University of California/San Francisco

Introduction

This conference addresses rapidly changing medical technology regarding energy applied to tissue for treatment or controlled ablation. There are many factors driving the changes in medical procedures. Four of the important factors are listed below:

1) **Managed Care.** A strong drive to reduce patient care costs is causing a push for minimal hospital stays, minimal procedure costs, and minimal recovery time. Obviously, the minimal hospital stay is zero days, so office-based procedures are beginning to replace surgical procedures.

2) **Media.** The media announce new procedures as they occur, with the result being nearly instant publicity around the world. This fast dissemination of information has patients inquiring about a new breakthrough procedure the same day that it is performed.

3) **Patients.** Patients have become very savvy and up-to-date on medical therapy and new procedures and treatments. They get much information from the Internet. Any treatments that replace surgery and are office-based will create immense patient interest.

4) **Advancement of Technology.** The plethora of new procedures and therapies stems in part from innovative thinking on the part of engineers and physicians, and also advances in technology that include robotics, computer-controlled treatment, and thermal therapy.

Surgical procedures have also rapidly advanced in the last few years. Many surgeries have converted to laparoscopic procedures that, instead of a 15-cm incision, utilize small 5- to 10-mm incisions as entries or ports for long, slender instruments, all guided by an endoscope. Some of these procedures are moving from 5- to 10-mm ports to 2- to 3-mm ports. Even less invasive are the percutaneous procedures that are performed by interventional radiologists. These are guided by fluoroscopy, CT, MR, or ultrasound to achieve localization in an organ or disease site. Once access is achieved, some kind of treatment procedure can be performed, such as ablation, inserting a stent where there is blockage or obstruction, or doing a balloon procedure.

The following are the three key factors driving the advanced procedures:

1) **Access.** With the advent of steerable scopes that can be navigated deep into the body, new types of access are evolving. These scopes carry operating channels that allow instruments such as forceps, snares, probes, or needles to be used once the scopes are in place.

2) **Imaging.** The scopes mentioned above allow visualization and guidance deep into organ structures. Other procedures are guided by external imaging, such as CT,

ultrasound, or MR, that allow deep-tissue visualization in any plane. Imaging and visualization of a probe or device inserted percutaneously provide the clinician with a powerful combination to access and perform a medical procedure deep in the body.

3) **Treatment.** Once imaging and access bring the clinician to the disease or target site in the body, the next logical step is to provide a treatment that will obviate the need for surgery. In this regard, current techniques involve thermal treatment utilizing microwaves, ultrasound, rf, cryoablation, or lasers. However, to fully utilize the treatment access and treatment, a noninvasive imaging technique for temperature and an assessment of the treatment site for extent of coagulation necrosis are necessary.

Medical science has certain future directions that are already being embarked upon. One of these is less organ removal, choosing to treat rather than remove. Many surgical procedures have now become office-based, with some patients coming forward for treatment who previously did not want a surgical procedure. These patients will often suffer with discomfort until a minimally invasive procedure comes along. Some of these advanced procedures are computer controlled and rely increasingly less on operator skill. In addition, they assess how the treatment is progressing. Real-time diagnostics will be a real boon to endoscopic procedures that will allow the three-prong attack on disease: endoscopic guidance to the target site, optical diagnosis for tissue characterization, and therapy to ablate the suspicious areas.

The conference covers many of the advanced topics listed above, including treatment of the prostate and endometrium layer of the uterus with nonsurgical thermal treatment using rf, ultrasound, and microwaves; minimally invasive catheter access treatment of the heart using cryotherapy and microwaves; and several clinical applications of extra-corporeal focused ultrasound. An interesting batch of presentations utilizes modeling to design instruments by simulating tissue effects with a certain instrument geometric configuration. Image-guided therapy is examined, as well as image-guided tissue characterization following ablation treatment. Ultrasound and MR are presented as viable, noninvasive, temperature evaluation modalities in real time.

These advances capture the state of the art of current applications using the most advanced imaging techniques.

Thomas P. Ryan

SESSION 1

Therapeutic Miniature Ultrasound Applicators

Prostate Thermal Therapy With Interstitial And Transurethral Ultrasound Applicators: A Feasibility Study

Chris J. Diederich [a], Will H. Nau [a], Dana L. Deardorff [a], Ismail S. Khalil-Bustany [a], Everette C. Burdette [b], Paul R. Stauffer [a] and Max Wu [a]

[a] University of California at San Francisco, Radiation Oncology Department
San Francisco, CA 94143-0226
[b] Acoustic MedSystems, Champaign, IL 61820

ABSTRACT

The purpose of this study was to determine the feasibility of using a transurethral ultrasound applicator in combination with implantable ultrasound applicators for inducing thermal coagulation and necrosis of localized cancer lesions or BPH within the prostate gland. The concept being evaluated is the potential to treat target zones in the anterior and lateral portions of the prostate with the transurethral applicator, while simultaneously treating regions of extracapsular extension and zones in the posterior prostate with the directive implantable applicators in combination with a rectal cooling bolus. Biothermal computer simulations, acoustic characterizations, and *in vivo* thermal dosimetry experiments were used to evaluate the performance of each applicator type and combinations thereof. The preliminary results of this investigation demonstrate that implantable ultrasound applicators, in combination with a transurethral ultrasound applicator, have the potential to provide thermal coagulation and necrosis of small or large regions within the prostate gland, while sparing thermally sensitive rectal tissue.

Keywords: Ultrasound, Transurethral, Interstitial, Thermal Therapy, Prostate, Hyperthermia

1. INTRODUCTION

Benign prostatic hyperplasia (BPH) [1, 2] is a common affliction in males which often requires surgical intervention (transurethral resection) to reduce symptoms such as urinary outflow obstruction. Adenocarcinoma of the prostate is the most commonly diagnosed cancer in the U.S. male population, and is typically treated by radiotherapy, surgery, androgen ablation, and/or chemotherapy. Due to the older age and often serious coexisting medical problems in many of these patients, alternative forms of minimally invasive therapy are being investigated which have lower risks and complication rates than current standard therapies. Thermal therapy with intracavitary, interstitial, and external heating methods is currently being investigated for use as a minimally invasive alternative for surgery in the treatment of benign and cancerous disease. Some of the most prolific developments of this technology have been in the treatment of benign prostatic hyperplasia. Transurethral, transrectal, and transperineal interstitial applications of energy have been implemented to thermally destroy tissue regions surrounding the urethra as an alternative to surgical transurethral resection. Heating modalities commonly used for prostate thermal therapy include microwaves[3, 4], lasers[5], RF currents[6] and ultrasound[7]. Some other examples of minimally invasive thermal therapy in lieu of surgical resection include treatment of liver metastases with laser fibers [8] and MW antenna[9]; brain tumors with interstitial laser[10, 11] , microwave antenna [12], and RF needles[13]; prostate cancer with focused ultrasound[14, 15]; breast fibromas with MR-guided focused ultrasound [16] and breast cancer with interstitial lasers [17].

The objective of this study was to determine the feasibility of combining a multielement transurethral ultrasound applicator [18] with a small number (2-3) of miniature multielement implantable ultrasound applicators [19-21] for the application of thermal therapy in treating prostate cancer and BPH. Computer simulations, laboratory measurements, and thermal dosimetry measurements with *in vivo* canine prostate models were employed to evaluate the performance and establish the feasibility of this combination approach.

Further Author Information-
C.J.D. (correspondence): Email: diederic@radonc17.ucsf.edu; Tel: (415) 476-6132; Fax: (415) 502-5175

SPIE Vol. 3249 • 0277-786X/98/$10.00

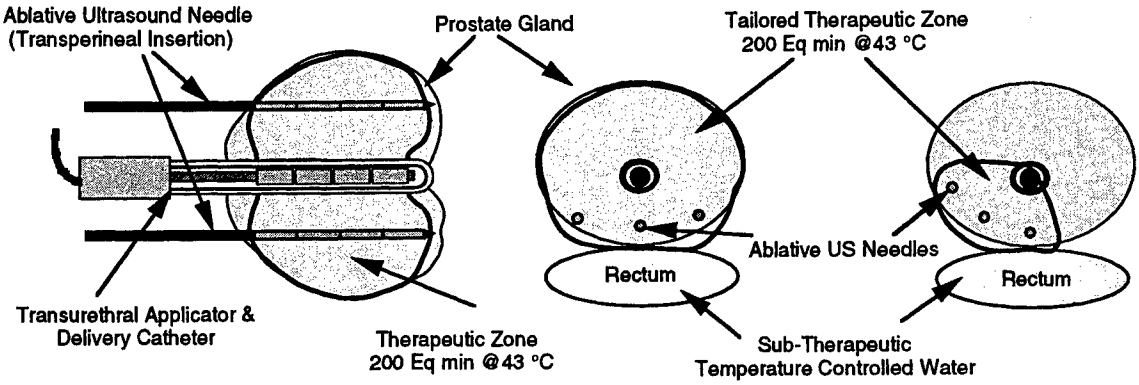

Fig. 1. Generalized schema of combined transurethral plus interstitial ultrasound applicators for prostate thermal therapy.

2. DESCRIPTION OF COMBINATION THERAPY

The transurethral multielement ultrasound applicator consists of tubular sections of piezoceramic radiators, each with independent connections to accommodate separate power control, which generate acoustic or heating energy which is emitted radially from the length of each segment. The power deposition along the length of the applicator is adjustable, to tailor the heating distribution to fit the prescription within the intended target region. The beam distributions from tubular radiators are modified to minimize overheating and damage to rectal tissue compared to current microwave technologies. The ultrasound applicator is inserted within a multi-lumen catheter delivery system, which allows circulation of temperature regulated water to control the urethra/catheter interface temperature. This design was initially developed for treating BPH via urethral heating alone[18].

The basic design schema for implantable ultrasound applicators follows that determined from earlier work developing direct-coupled interstitial ultrasound applicators designed for simultaneous delivery of hyperthermia (41-45°C) and radiation cancer therapy [20]for brain tumors, and more recently adapted for thermal therapy [21]. The applicators consist of an array of tubular ultrasound transducers, with miniature thermocouple sensors placed on the surface to monitor the applicator/tissue interface temperature during therapy. The outer surface of the transducers are coated with a biocompatible layer of electrical isolation along the entire length of the applicator. The number, lengths and frequency of the transducer elements are dictated by the clinical situation (intended target size and prescriptions) and can be fabricated accordingly.

A generalized schematic of this combination "transurethral plus interstitial thermal therapy" heating scheme is illustrated in Fig. 1. The multiple heating elements along each implanted applicator (ultrasound needles) and transurethral applicator, each modified to be angularly directive, may be independently power controlled to localize and dynamically control thermal dose distributions within the target volume. The treatment goal is to deliver thermal doses greater than 250 EM43°C and temperatures greater than 48-50°C to generate coagulation and thermal necrosis of the target tissue [22, 23]. This combination approach should permit highly controlled spatial and temporal treatment delivery, permitting maximization of thermal dose to the target tissue while simultaneously minimizing interaction with sensitive normal tissue (bladder, rectal mucosa, sphincters).

3. BIOTHERMAL SIMULATIONS

An existing treatment planning program developed for interstitial thermal therapy [32,33] was modified for the thermal dosimetric evaluation and design feedback of these two types of multielement ultrasound applicators. This program uses CT, MR, or TRUS images to generate acoustic and biothermal models based upon the anatomy of the target region. A minimax-based optimization sequence is used to automatically determine applicator placements and power levels which produce optimal heating distributions (i.e., those that conform the tightest to prescribed thermal distributions within the target region and surrounding normal tissue). This program was modified for our specific case of prostate thermal therapy to include *(i)* new acoustic models to account for the angular or directive beam distributions for both transurethral and implantable

applicators, *(ii)* optimization of transurethral power levels and position and power for interstitial ablative needles at higher temperature thresholds, *(iii)* temperature regulation/control of the rectal tissue via the rectal obturator. Accordingly, an anatomically correct two-dimensional finite element model was constructed from a transverse MR image at mid-gland of the prostate to become our "standard" model. A series of forward-planning biothermal computer simulations, based upon the bio-heat transfer equation [24], were used to establish performance characteristics of various configurations of the implantable and transurethral ultrasound applicators, either alone or in combination.

Fig. 2 a-b is a comparison of the 180° and 270° sectored transurethral applicators, each with 35 °C urethral cooling and 37°C rectal cooling via a rectal obturator. Transurethral applicators with 180° sectoring are more effective for heating the anterior portion of the prostate to therapeutic temperatures (>48°C), and applicators with 270° sectoring can effectively extend heating into the lateral regions as well. Fig. 2c-d are thermal distributions for the 180° and 270° transurethral applicators, respectively, in combination with three 180° sectored implantable applicators placed in the posterior portion of the gland with the active sectors directed away from the rectal wall. The directive implants and rectal cooling allow effective heating of the posterior portion of the gland to within 3-5 mm of the rectal wall. In addition, these simulations (Fig. 2.e) have demonstrated that effective isolation of the heating patterns to the posterior portion of the gland can also be obtained using three directive 180° sectored implantable applicators and transurethral cooling (35°C) only. The optimization portion of the planning program was used to determine applicator positions and initial power levels required to best attain a given thermal prescription (i.e., target >48°C and rectal <43°C), as shown in Fig. 2f, for an implant with seven implantable applicators (360° active sectoring).

4. APPLICATOR CONSTRUCTION & ACOUSTIC PERFORMANCE MEASUREMENTS

Transurethral applicators were fabricated, using three tubular transducers (each 6 mm long, 2.5 mm OD) attached to form a segmented array, following the design initially developed for treating BPH via urethral heating alone [18]. Each transducer was modified for an 180° active sector. Measurements of the acoustic output power from these tubular transducers has demonstrated acoustic efficiencies typically between 50-60% and that sufficient acoustic power levels are attainable (>15 acoustic W per tube). Furthermore, acoustic beam measurements have verified that the energy deposition is collimated to the axial dimensions of each transducer segment, and that the angular energy pattern follows what is expected for a 180° active sector (Fig. 3.a).

Direct-coupled interstitial applicators specific for this combination ablative therapy [20, 21] were constructed using 1.8 mm piezoceramic (PZT-4) tubular transducers. The outer diameter of 1.8 mm was selected to maintain applicator dimensions similar in size to 14-gauge needles. The tubes were sectored to form a 180° electrically active portion. Single junction constantan-manganin thermocouple sensors were placed over the center of each transducer, and the applicator coated with a thin layer of biocompatible epoxy and tubing. A family of applicators was constructed, consisting of single-element devices with 10 mm or 6 mm long transducers, and two-element devices using 10 mm long transducers. Acoustic output power measurements demonstrated these sectored 1.8 mm OD direct coupled applicators were 45-50% efficient at approximately 7 MHz, and were able to sustain performance with 10 W applied electrical power and approximately 4.5 W acoustic power output without self-destruction. The rotational beam plots have demonstrated that the acoustic fields emitted by each transducer segment are collimated and confined within the axial transducer boundaries, are fairly uniform in the circumferential direction, and the fields can be shaped (Fig. 3.b).

5. *IN VIVO* THERMAL DOSIMETRY

Experiments were conducted in the prostate glands of three large dogs (25-30 kg) to examine temperature distributions and corresponding thermal damage attainable with the final applicator designs. In general, animals were anesthetized with intravenous administration of Ketamine (5 mg/kg) plus valium (0.25 mg/kg) and maintained at a surgical state of anesthesia throughout all procedures with isoflourane and oxygen. The prostate gland and bladder were exposed via a suprapubic incision. A plastic thermometry template was placed over the anterior surface of the prostate, and 20 G thermometry needles were placed laterally and/or anterior-posterior in a mid-gland transverse plane, depending on the specific set-up. Two types of custom thermometry probes, consisting of six-junction constantan-manganin thermocouple sensors (0.025 mm wire) spaced 4 mm apart and encased within fused silica tubing (FS sensors) or four-junction thermocouple sensors spaced 3 mm

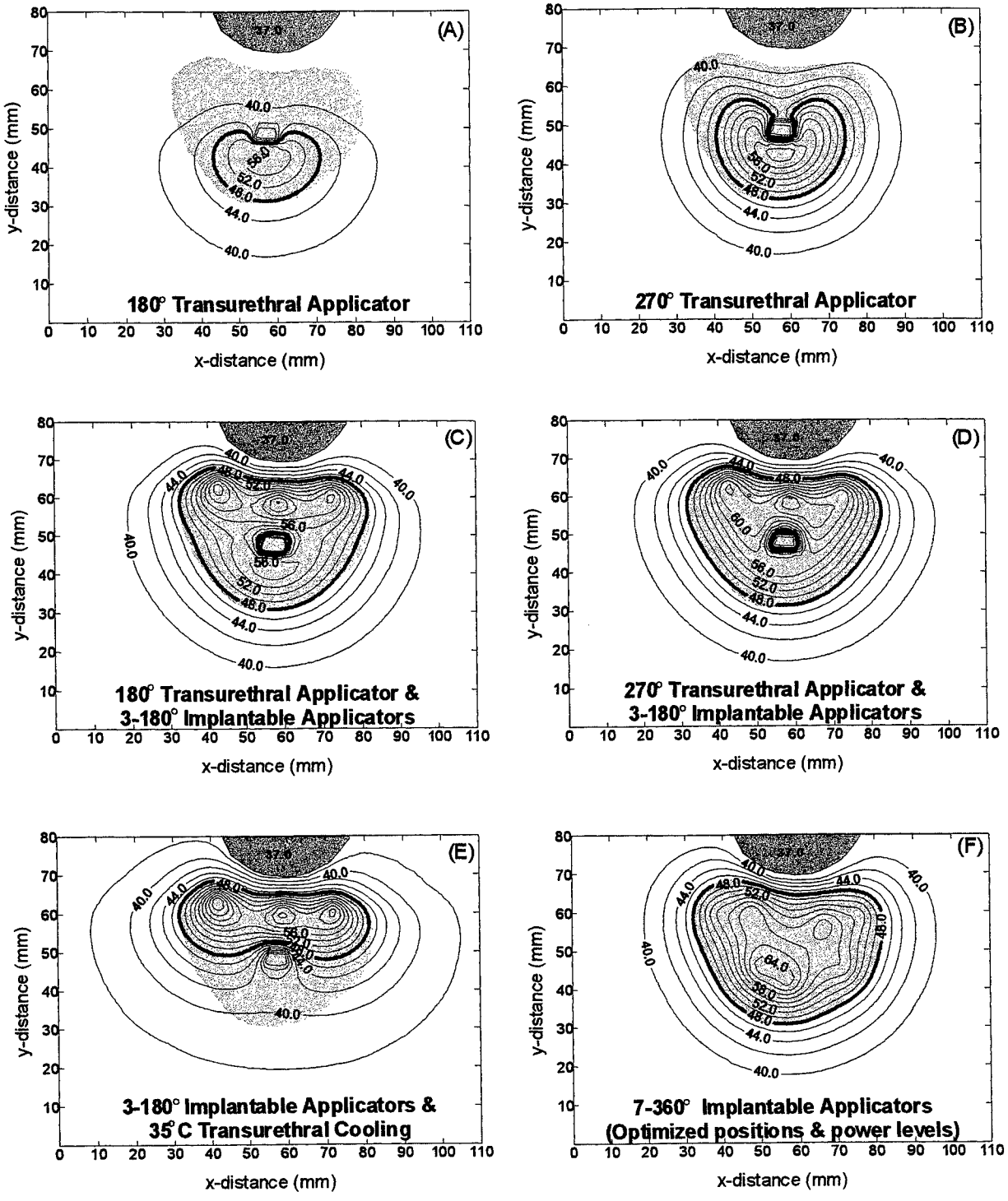

Fig. 2. Thermal dosimetry characterizations of transurethral and implantable ultrasound applicators, either in combination or alone, using biothermal simulations and minmax based optimization of power and position.

(A) Transurethral Applicator, 3 Element, 180 deg. Sectors
Element #1 Rotational Beam Plot at 8 mm Radial Depth

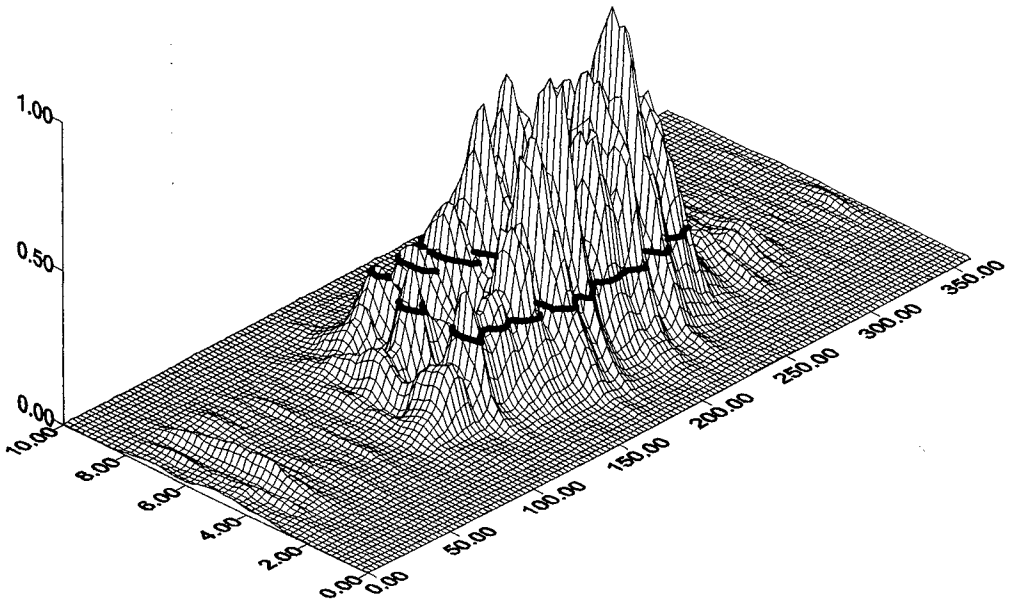

(B) Implantable Ultrasound Applicator
1.8 mm OD x 10 mm long, 180 deg. Active Sector

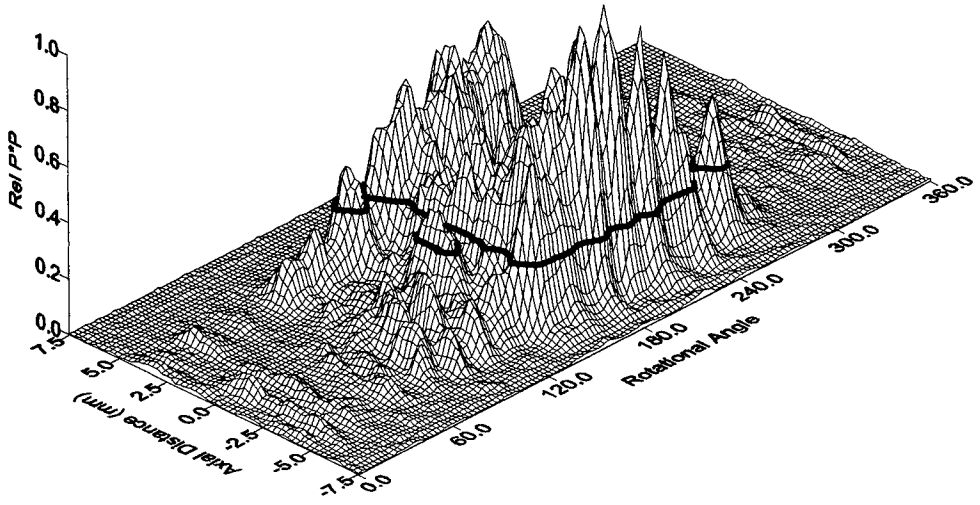

Fig. 3. Rotational beam plots in degassed water measured at a radial distance of 8 mm for (a) a single element of a 3-element transurethral applicator and (b) an implantable applicator.

apart and encased within polyethylene tubing (PE sensors), were placed within these thin-walled 20G spinal needles. This arrangement reduces the temperature measurement error due to ultrasound absorption artifact [44] and thermal conduction [45] errors. The transurethral applicator within the water-cooled delivery catheter was placed through an incision in the bladder into the prostate gland, while the implantable ultrasound needles were placed posterior to the urethra from base to apex. Placement of heating applicators with respect to the tissue thermometry catheters was verified with localization scans using a transrectal ultrasound imaging system. Additional thermometry needles were placed within the surrounding rectal tissue. Temperatures were monitored using a 56 channel thermocouple system, which was calibrated immediately prior to each procedure. The ultrasound applicators were connected to a 32 channel RF amplifier system (Advanced Surgical Systems, Boston) which automatically monitors forward and reflected power levels to each channel. Following the series of dosimetry experiments, the animals were euthanized via intravenous injection of sodium pentobarbital (200 mg/kg) without waking from anesthesia. These procedures have been approved by the Committee on Animal Research at UCSF (UCSF Protocol Approval #A1143-02006-07 on 9/96), which is an IUAUC approved institution. The following series of specific experiments were performed using these general procedures.

Study 1: The goal of this experiment was to directionally heat in the right lobe and anterior regions of the prostate. The transurethral applicator (3 elements, 180° active sectors, @6.4 MHz) plus delivery catheter was positioned within the prostatic urethra so that the active portion was centered mid-gland (thermometry plane) and aimed anteriorly. The circulating degassed water was set to 35°C with a flow rate of 200 ml/min. A multiple element implantable applicator (2 elements, 180° active sectors, @ 7.0 MHz) was placed freehand in the right lobe of the prostate, with the active portion of the tip transducer directed anteriorly and to the midline, and lined up with thermometry sensors. Thermometry probes (20 G needles + thermocouple sensors) were placed through the template, anterior to posteriorly. The experimental setup is illustrated in Fig. 4a,b. The approximate dimensions of the gland were 3 cm apex to base, 2.5 cm x 2.5 cm in the transverse plane at mid-gland. The transrectal imaging probe, modified for rectal cooling at 35 °C, was kept in place during the experiment. The RF power was applied for 15 minutes to the applicator combination: Approximately 2.5 W was applied to the interstitial element, and 7 W to each transurethral element for the first ten minutes, then power was raised to 12 W per transurethral element for the remainder of the heating. At 15 minutes heating time, the PE temperature probes (4 sensor, 3 mm spacing) were mapped within the needles to sample a total length of approximately 18 mm. The resulting temperature profiles along each needle track are shown in Fig. 4b. After the procedure the prostate gland was removed, fixed in formalin, and prepared and stained for histological mounting with Hemotoxylin and Eosin (H&E) standard staining techniques. The histological cross-section of the central heating plane is shown in Fig. 4c. Post experiment the applicators were inspected for damage and found to be operating normal without damage. Results clearly demonstrate that each component (applicator) contributes to heating, combination is effective, necrosing and coagulating temperature rises are achieved quickly, and that applicators can produce enough power. Note the preferential heating to the anterior and right lobe of the prostate as evidenced from mapping data.

Study 2: The purpose of this experiment was to determine the heating characteristics of the directive interstitial applicators when used alone. The prostate was isolated as above, and measured 3.5 cm wide x 2.5 cm apex to base. Six thermometry probes (20 G needles + FS sensors with six junctions spaced 4 mm apart) were placed in the prostate using a plastic template: two probes were placed laterally through the heating zone, and four were placed anterior to posterior. Two single element interstitial applicators (1.8 mm OD x 10 mm long, 180 ° active sector) were placed in the posterior portion of the prostate gland, one in each lobe, and aligned with the mid-gland. The 180° active regions were directed midline. The experimental setup is demonstrated in Fig. 5a,b. For trial 1, 2 W RF power was applied to the applicator in the left posterior region of the prostate for a total of 10 minutes. After 20 minutes to allow the temperatures to return to baseline, 2.5-3.0 W of RF power was applied to the second applicator in the right posterior portion of the prostate for a total of 15 minutes. The peak temperatures are shown in Fig. 5b. The histological cross-section and whole mount corresponding to the central plane are shown in Fig. 5c. These results clearly demonstrate the directive nature of single implantable applicators, which produce an acute thermal damage zone extending up to 8 mm in the center of the active zone, with little extension behind the applicator. Both the 10 and 15 minute sequences produced effective heating patterns.

Study 3: The purpose of this experiment was to determine the extent of thermal damage from the combination of two implantable needles in combination with the transurethral applicator. The prostate was surgically isolated as above, and measured 2.5 cm x 2 cm. The prostate was lifted while two implantable applicators were placed in the posterior portion of the gland, one on each side. Each of these applicators consist of a single 1 cm long x 1.8 mm OD transducer with a 180° active sector and operated at 7.2 MHz. The transducer portion of the applicators were aligned with the mid-gland transverse plane, with the 180° active regions directed midline. The transurethral applicator and delivery catheter were inserted through

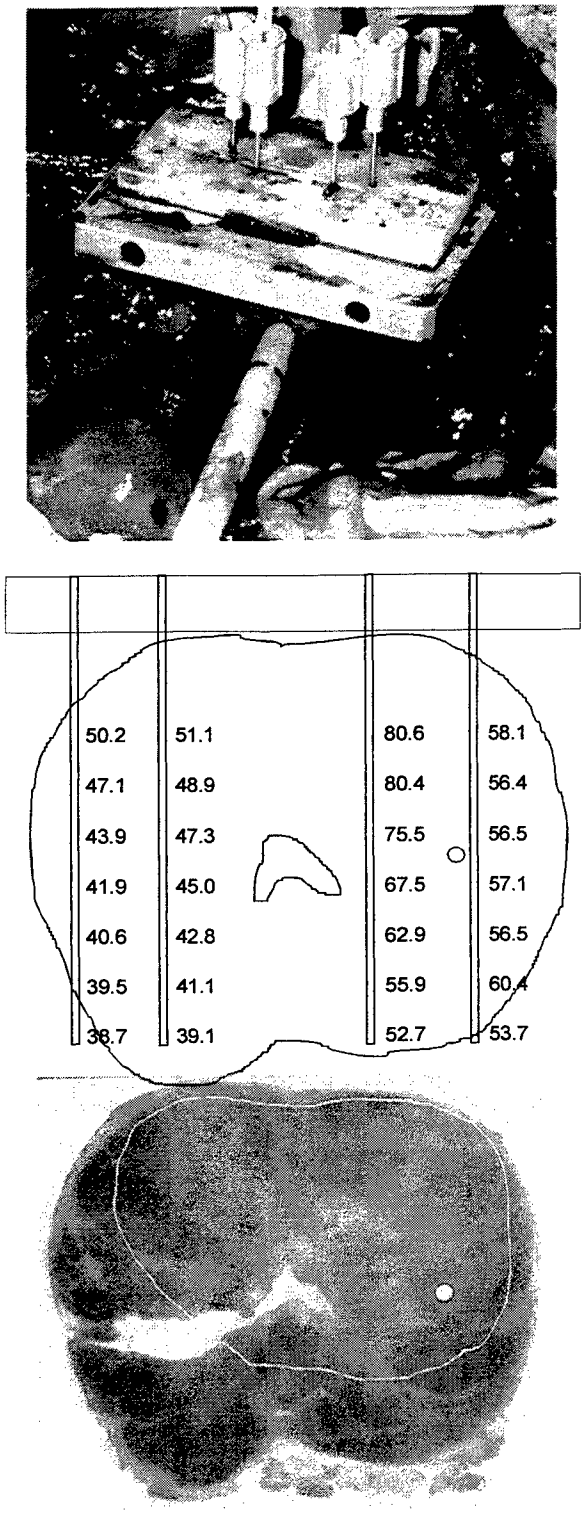

Fig. 4. *In Vivo* canine prostate study 1, evaluating a transurethral applicator aimed anteriorly combined with an implantable applicator in the right lateral zone directed toward the anterior midline: (a) picture of experimental setup; (b) maximum temperatures and their approximate positions as measured during heating trial; and (c) histological cross-section of the prostate with approximate zone of coagulation outlined.

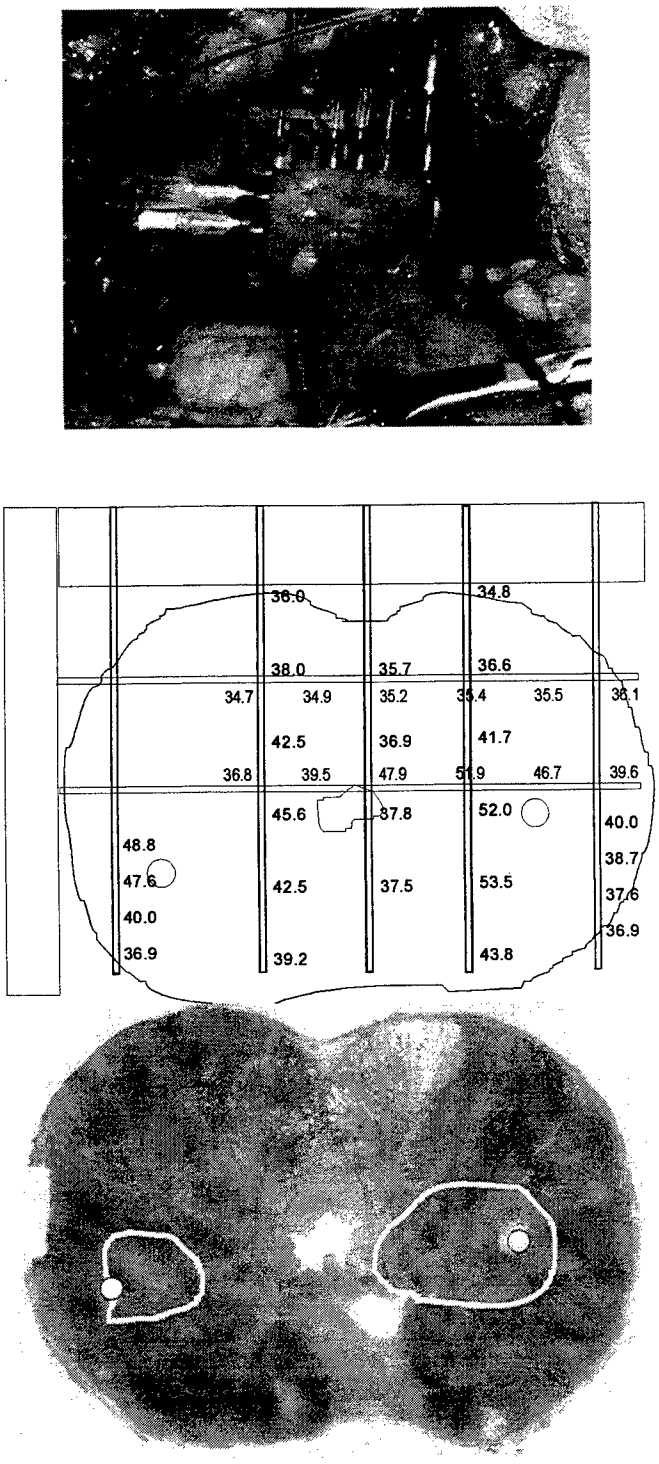

Fig. 5. *In Vivo* canine prostate study 2, evaluating two implantable applicators, each directed toward the midline, operated at different power levels and heating times: (a) picture of experimental setup; (b) maximum temperatures and their approximate positions as measured during both heating trials; and (c) histological cross-section of the prostate with approximate zones of coagulation outlined.

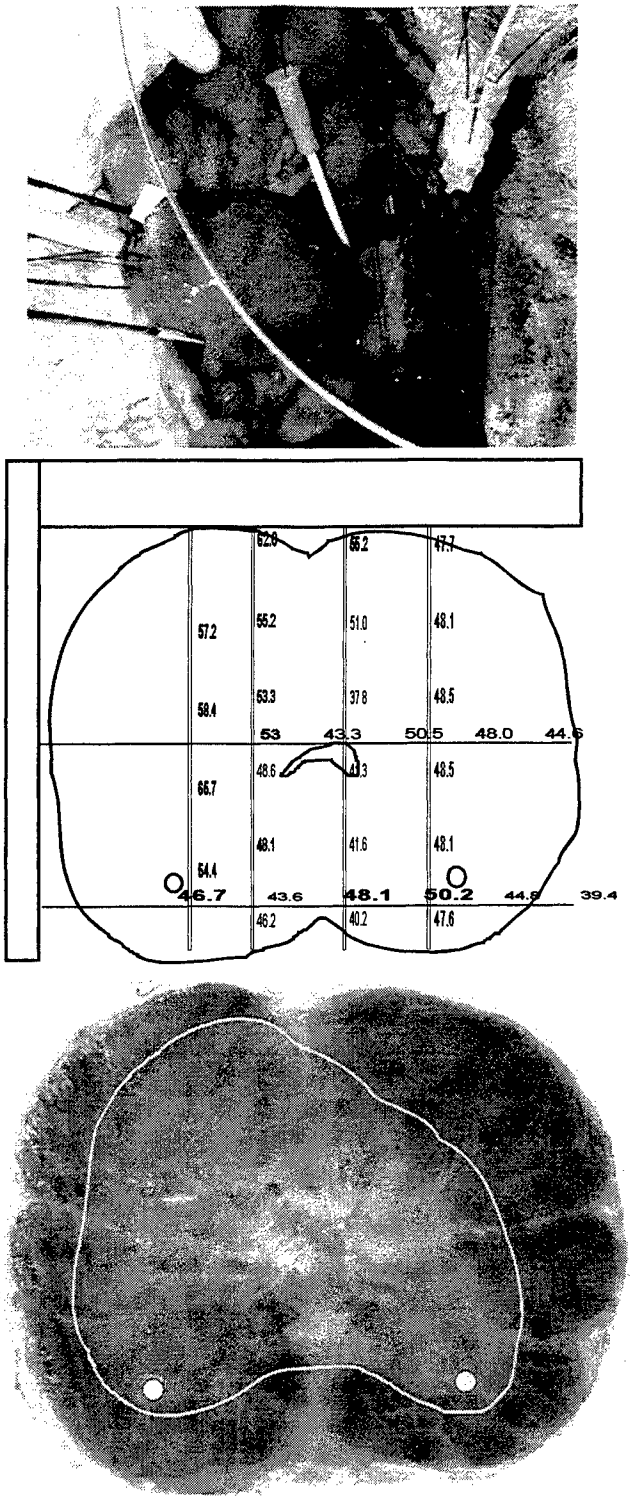

Fig. 6. *In Vivo* canine prostate study 3, evaluating a transurethral applicator aimed anteriorly combined with two implantable applicators in the posterior zone directed anteriorly: (a) picture of experimental setup; (b) maximum temperatures and their approximate positions as measured during heating trial; and (c) histological cross-section of the prostate with approximate zone of coagulation outlined.

the bladder neck into the prostatic urethra, and the active heating portion (20 mm) was aligned with mid-gland. The thermometry template and thermometry needles/sensors were placed through this transverse plane similar to procedures used in Trial 2 study. A picture of the experimental setup is shown in Fig. 6a. The implantable applicators were driven with 3 W RF power, and each of the three elements of the transurethral applicator were driven with 12 W, for a total therapy time of 20 minutes. The temperature distribution after 20 minutes of heating and the resulting histology is shown in Fig. 6b-c. The results of this study reaffirmed that this combination of therapy applicators is a feasible technique for controlled directional thermal therapy to effectively ablate large regions of the prostate.

6. SUMMARY

This preliminary study has demonstrated that using implantable ultrasound applicators in combination with a transurethral ultrasound applicator provides directive thermal coagulation and necrosis of small regions within the prostate gland or the entire gland, while sparing thermally sensitive rectal tissue. The transurethral applicator can effectively treat target zones in the anterior and lateral portions of the prostate, while the directive implantable applicators in combination with a rectal cooling bolus can simultaneously treat regions of extracapsular extension and zones in the posterior prostate. These initial findings are positive, and provide the rationale for continuing investigations into the combination of these devices for thermal therapy in the treatment of benign and cancerous disease.

7. ACKNOWLEDGMENTS

This work was supported by NIH Grants CA68421, DK51939, and CA09215.

8. REFERENCES

1. T. Hald,"Review of current treatment of benign prostatic hyperplasia," *Eur. Urol.*, vol. 25, no. Suppl. 1, pp. 15-19, 1994.
2. F. A. Madsen, R. C. Bruskewitz,"Clinical manifestations of benign prostatic hyperplasia," *Urol. Clin. North Am.*, vol. 22, no. 2, pp. 291-298, 1995.
3. Z. Petrovich, F. Ameye, L. Baert, K. H. Bichler, S. D. Boyd, L. W. Brady, R. C. Bruskewitz, C. Dixon, P. Perrin, G. M. Watson,"New trends in the treatment of benign prostatic hyperplasia and carcinoma of the prostate," *Am. J. Clin. Oncol.*, vol. 16, no. 3, pp. 187-200, 1993.
4. B. Goldfarb, T. Bartkiw, J. Trachtenberg,"Microwave therapy of benign prostatic hyperplasia," *Urol. Clin. North Am.*, vol. 22, no. 2, pp. 431-439, 1995.
5. C. M. Dixon,"Lasers for the treatment of benign prostatic hyperplasia," *Urol. Clin. North Am.*, vol. 22, no. 2, pp. 413-422, 1995.
6. C. M. Dixon,"Transurethral needle ablation for the treatment of benign prostatic hyperplasia," *Urol. Clin. North Am.*, vol. 22, no. 2, pp. 441-444, 1995.
7. S. Madersbacher, M. Susani, M. Marberger,"Thermal ablation of BPH with transrectal high-intensity focused ultrasound," *Prog Clin Biol Res*, vol. 386, no. pp. 473-8, 1994.
8. C. P. Nolsoe, S. Torp-Pedersen, F. Burcharth, T. Horn, S. Pedersen, N. E. Christensen, E. S. Olldag, P. H. Andersen, S. Karstrup, T. Lorentzen, et al.,"Interstitial hyperthermia of colorectal liver metastases with a US-guided Nd-YAG laser with a diffuser tip: a pilot clinical study," *Radiology*, vol. 187, no. 2, pp. 333-7, 1993.
9. R. Murakami, S. Yoshimatsu, Y. Yamashita, T. Matsukawa, M. Takahashi, K. Sagara,"Treatment of hepatocellular carcinoma: value of percutaneous microwave coagulation [see comments]," *AJR Am J Roentgenol*, vol. 164, no. 5, pp. 1159-64, 1995.
10. T. Menovsky, J. F. Beek, M. J. van Gemert, F. X. Roux, S. G. Bown,"Interstitial laser thermotherapy in neurosurgery: a review," *Acta Neurochir (Wien)*, vol. 138, no. 9, pp. 1019-26, 1996.
11. B. C. Devaux, F. X. Roux,"Experimental and clinical standards, and evolution of lasers in neurosurgery," *Acta Neurochir (Wien)*, vol. 138, no. 10, pp. 1135-47, 1996.
12. X. P. Zhou, Q. L. Xie, J. M. Liu, Z. J. Yue, K. H. Cai,"Resection of meningiomas with implantable microwave coagulation," *Bioelectromagnetics*, vol. 17, no. 2, pp. 85-8, 1996.

13. Y. Anzai, R. Lufkin, A. DeSalles, D. R. Hamilton, K. Farahani, K. L. Black,"Preliminary experience with MR-guided thermal ablation of brain tumors," *AJNR Am J Neuroradiol*, vol. 16, no. 1, pp. 39-48; discussion 49-52, 1995.
14. A. Gelet, J. Y. Chapelon, R. Bouvier, R. Souchon, C. Pangaud, A. F. Abdelrahim, D. Cathignol, J. M. Dubernard,"Treatment of prostate cancer with transrectal focused ultrasound: early clinical experience," *Eur Urol*, vol. 29, no. 2, pp. 174-83, 1996.
15. S. Madersbacher, M. Pedevilla, L. Vingers, M. Susani, M. Marberger,"Effect of high-intensity focused ultrasound on human prostate cancer in vivo," *Cancer Res.*, vol. 55, no. 15, pp. 3346-51, 1995.
16. K. Hynynen, W. Freund, H. E. Chung, R. Watkins, J. Vetro, F. A. Jolesz,"A clinical noninvasive MRI monitored ultrasound surgery method," *Radiographics*, vol. 16, no. pp. 185-195, 1996.
17. D. S. Robinson, J. M. Parel, D. B. Denham, F. Manns, X. Gonzalez, R. Schachner, A. Herron, E. C. Burdette,"Stereotactic uses beyond core biopsy: model development for minimally invasive treatment of breast cancer through interstitial laser hyperthermia," *Am Surg*, vol. 62, no. 2, pp. 117-8, 1996.
18. C. J. Diederich, E. C. Burdette,"Transurethral ultrasound array for prostate thermal therapy: initial studies," *IEEE Trans. Ultrason., Ferroelect., Freq. Contr.*, vol. 43, no. 6, pp. 1011-1022, 1996.
19. C. J. Diederich,"Ultrasound applicators with integrated catheter-cooling for interstitial hyperthermia: theory and preliminary experiments," *Int. J. Hyperthermia*, vol. 12, no. 2, pp. 279-297, 1996.
20. C. J. Diederich, I. S. Khalil, P. R. Stauffer, P. K. Sneed, T. L. Phillips,"Direct-coupled interstitial ultrasound applicators for simultaneous thermobrachytherapy: a feasibility study," *Int. J. Hyperthermia*, vol. 12, no. 3, pp. 401-419, 1996.
21. C. J. Diederich, W. H. Nau, P. R. Stauffer, E. C. Burdette, I. S. Khalil,"Interstitial ultrasound applicators for localized thermal coagulation of tissue," *IEEE Ultrasonics Symposium Proceedings*, vol. 2, no. pp. 1303-1307, 1996.
22. W. C. Dewey,"Arrhenius relationships from the molecule and cell to the clinic," *Int. J. Hyperthermia*, vol. 10, no. 4, pp. 457-483, 1994.
23. J. Pearce, S. Thomsen, "Rate process analysis of thermal damage," In: A. J. Welch, M. J. C. Van Gemert (eds) *Optical-Thermal Response of Laser-Irradiated Tissue*. Plenum, London, pp. 561-606, 1995
24. H. H. Pennes,"Analysis of tissue and aterial blood temperatures in the resting human forearm," *J. Appl. Physiol.*, vol. 1, no. pp. 93-122, 1948.

Investigation of directional interstitial ultrasound applicators for thermal coagulation of tissue

William H. Nau, Chris J. Diederich, Paul R. Stauffer, Dana L. Deardorff

Department of Radiation Oncology
University of California, San Francisco 94143-0226

ABSTRACT

Direct-coupled and catheter-cooled interstitial ultrasound applicators have been evaluated for thermal necrosis of small, localized tumors. Emphasis of the design criteria has been on directionality of power deposition and the corresponding tissue heating. Ultrasound applicators have been fabricated using piezoceramic tubes operating at approximately 7 MHz. The applicators have full 360° active acoustic zones, or are sectored to provide different angular heating patterns. The applicators were characterized through acoustic power output measurements, beam profile distributions in water, thermal distribution measurements in an *in vitro* perfused kidney model, and *in vivo* thermal dosimetry in porcine thigh muscle. Bench tests demonstrated that high power output levels could be sustained in both the direct-coupled and catheter-cooled devices without degradation of the ultrasound transducer. The angular power depositions obtained in water were closely correlated to the resultant temperature distributions measured both in the *in vitro* kidney and *in vivo* experiments, thus demonstrating the ability to shape the beam profiles for controlled, directional ablation of tissue.

Keywords: Ultrasound, hyperthermia, thermal ablation, interstitial, prostate, tumor

1. INTRODUCTION

Over the last decade, advances in heating technology have stimulated research in the field of hyperthermia, and thermal therapy for treatment of localized, deep-seated tumors. One method of tissue heating is through the use of implantable energy sources. Although more invasive than external heating methods, interstitial techniques localize the heating to the targeted volume, providing greater control over tumor heating, and sparing the surrounding healthy tissue[1]. Interstitial devices have been developed using rf, laser, microwave, or ultrasound energy to heat tissue for either hyperthermia treatment in conjunction with radiotherapy or chemotherapy, or for thermal ablation[2]. Of these devices, ultrasound devices offer several advantages over the other modalities. Some of these include the ability to heat larger volumes of tissue due to penetration of ultrasound energy in tissue, and control of heating along the length of the applicator by controlling the power to individual transducers in multi-element configurations[1].

Recently, interstitial ultrasound applicators have been described for simultaneous thermobrachytherapy[3]. These devices consist of a segmented array of tubular piezoceramic transducers that can be implanted directly into the tissue, and were able to heat a 1-1.5 cm region radially surrounding the applicator. These applicators were also designed to accommodate radiation seed implants. Interstitial ultrasound applicators with integrated water-cooling have also been evaluated for hyperthermia applications[4]. An advantage of the catheter-cooled applicators is that the peak temperature is displaced radially, away from transducer surface, thus increasing the depth of thermal penetration.

The feasibility of using both direct-coupled and catheter-cooled interstitial ultrasound applicators for tissue ablation has also been established[5]. These applicators were able to generate therapeutic temperatures at radial distances greater than 1 cm away in perfused tissues within 5 minutes of heating.

In this study, modified versions of the direct-coupled and catheter-cooled interstitial ultrasound applicators were investigated to ascertain the capabilities of directional power deposition, and the resultant tissue heating. Prototypes of both types of applicators were fabricated with directional power deposition patterns and evaluated through bench tests, and *in vitro*

and *in vivo* experiments. Results revealed that beam profiles could be shaped to provide angular control of tissue ablation which may be beneficial for preferential treatment of small, localized lesions in the prostate.

2. APPLICATOR FABRICATION & PERFORMANCE CHARACTERIZATION

Direct-coupled applicators were fabricated using 1 cm long cylindrical piezo-ceramic crystals with a 2.2 mm outer diameter. These were mounted on stainless steel tubes to provide structural support, and a bio-inert plastic outer layer was applied for electrical and biological insulation (Figure 1). A single-sensor constantan-manganin thermocouple was embedded in the coating on the transducer surface to monitor the transducer-tissue interface temperature. This allowed feedback control of the power supplied to the transducer element.

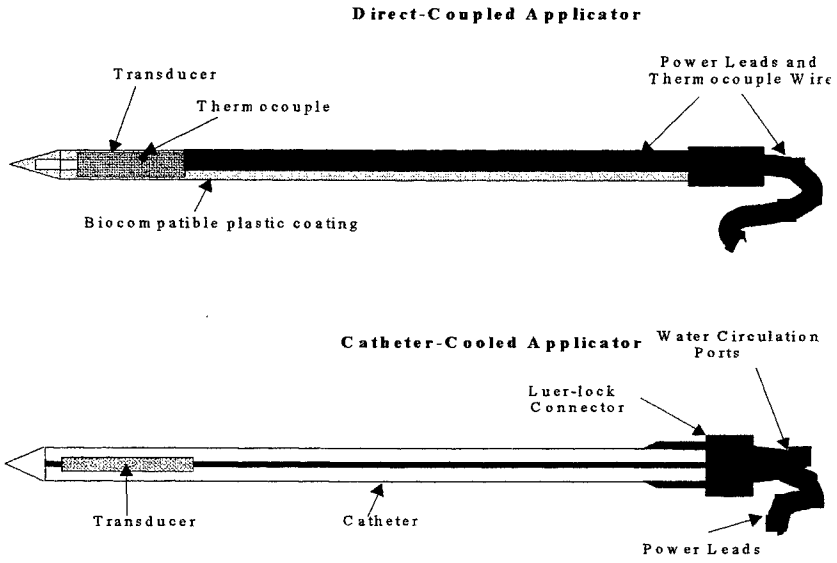

Figure 1. Schematic of interstitial ultrasound applicators.

Catheter-cooled applicators were fabricated in the same manner as the direct-coupled applicators. However, the transducer elements were 1 cm long × 1.5 mm outer diameter to allow for insertion of the applicator into a 13 gage nylon catheter. A mating Luer-lock fitting was tightened around the stainless steel needle tubing at the distal end of the applicator which was then inserted into a nylon catheter and locked in place. A closed-circuit circulation system pumped degassed water through the lumen of the needle support, and collected return flow from the catheter. A bubble trap placed in line before the applicator removed any air bubbles. The temperature of the cooling system was controlled by a waterbath and heat exchanger.

Directionality and shaping of the beam profile was achieved by making two longitudinal notches in the outer electrode surface. Power lead wires were soldered to the inner and outer surfaces of one of the regions (acoustic active zone). The region that did not receive power was effectively an acoustic dead zone.

Applicators were evaluated in three ways. The first was a measure of the electrical impedance as a function of frequency to locate the peak resonance frequency. The transducer portion of the applicator was suspended in a tank of degassed water, and the power leads connected to a network analyzer (Hewlett Packard Model #3577A). The magnitude and phase of the electrical impedance were measured over a range from 5 to 10 MHz. Peak resonant frequencies and total electrical impedances were measured at 7.3 to 7.5 MHz and 69 to 79 Ω for the 2.2 mm O.D. transducers, and 7.1 to 7.4 MHz and 82 to 138 Ω for the 1.5 mm O.D. transducers.

The acoustic efficiencies (ratio of acoustic output power to the applied electrical power) were measured as a function of frequency using the force balance technique[6,7] with a computer-controlled system. Measurements of the acoustic output power were made over the 6.5 to 7.5 MHz frequency range in increments of 100 kHz while maintaining the net applied electrical power at 2 W. The net applied electrical power was measured using a high power directional coupler (Werlatone, Inc. Model #C2625), and a two-channel power meter (Hewlett Packard Model #438A). Acoustic efficiencies ranged from 32-57% for the direct-coupled applicators, and from 36-55% for the catheter-cooled applicators. No correlation between the measured acoustic efficiencies and sectoring angles were observed. The acoustic output power was then measured as a function of the applied electrical input power at the frequency exhibiting the highest acoustic efficiency up to 10 W forward power to determine whether the applicators would begin to fail at high power output levels. All applicators were able to sustain these high power levels with degradation to performance.

Rotational scans of the acoustic pressure squared distributions emitted from the transducer were obtained in an acoustic scanning tank filled with degassed, de-ionized water with a calibrated needle hydrophone[8]. The voltages measured by the hyodrophone were squared and normalized to the maximum value. The hydrophone was scanned longitudinally in 0.25 mm increments with a computer-controlled stepper motor at a radial distance of 8 mm from the transducer surface. The applicator was then rotated 2.5° using another computer-controlled stepper motor, and scanned again. This was continued through full 360° rotation of the applicator thus producing a longitudinal-angular map of the acoustic pressure distribution (Figure 2).

These beam plots indicate that the acoustic energy emitted from the transducers is collimated, and confined axially to the transducer boundaries. They also demonstrate the ability to shape the beam profile such that directional power deposition may be achieved. For the 360° transducers, the circumferential beam profile remains relatively uniform. The beam profile emitted from the 90° sectored transducers is also uniform across the acoustic active zone. For the 180° and 270° sectored transducers, a region of low energy output is seen. This could be due to near field diffraction, or to the vibrational behavior of the sectored regions.

3. TEMPERATURE MEASUREMENTS IN AN *IN VITRO* KIDNEY

Porcine kidneys were previously prepared using the alcohol fixation technique[9]. The kidney was placed in a water bath and maintained at 26 °C. A heat exchanger ensured that the water being pumped through the kidney was at ambient temperature. The applicator was inserted into the cortex of the kidney, and a four- sensor thermocouple (junctions spaced at 0, 3, 6, and 9 mm) placed parallel to the applicator at a radial distance of 8 mm. With a setting of 0.5 W forward power, steady-state temperature was achieved in approximately 5 minutes. After temperatures were recorded, the applicator was turned 20°, and the system allowed to reach steady-state again. The process was continued until the applicator had completed one full rotation.

Temperature changes from baseline were normalized to peak temperatures and plotted versus relative acoustic pressure squared values averaged along the longitudinal length of the transducer at each angle of rotation (see Figures 3 and 4). Regions of low acoustic pressure in the active zone did not produce low temperature changes, but rather thermal conduction and convection allowed for a more uniform temperature distribution at depth.

4. MEASUREMENT OF *IN VIVO* TEMPERATURE DISTRIBUTIONS

A 100-lb. female pig was used to evaluate the performance of the applicators *in vivo*. Anesthesia was induced using a mixture of Ketamine HCl (30 mg/Kg) and Xylazine (2 mg/Kg), then maintained with 1.5% Isoflourane after the animal was intubated and connected to a respirator. A 13 mm thick plexi-glass template was fixed in place on the inner thigh using 10 gage stainless steel needles to ensure alignment of the thermometry probes and the applicator. Eight 20 gage needles were spaced at 45° intervals at a radial distance of 8 mm from the applicator surface. Thermocouple probes consisting of 4 sensors at 3 mm spacing were inserted into the spinal needles for thermal mapping[10,11]

A computer controlled 32 channel amplifier with independent frequency, modulation sweep, and power control (Advanced Surgical Systems, Inc.) was used to drive the applicators with a net electrical power of approximately 2.5-3.0 W. Temperature data were recorded every 5 seconds using a data acquisition system. The applicators were on for 15 minutes until steady-state was achieved. Temperature was then monitored for 5 minutes after power was discontinued, as it decayed

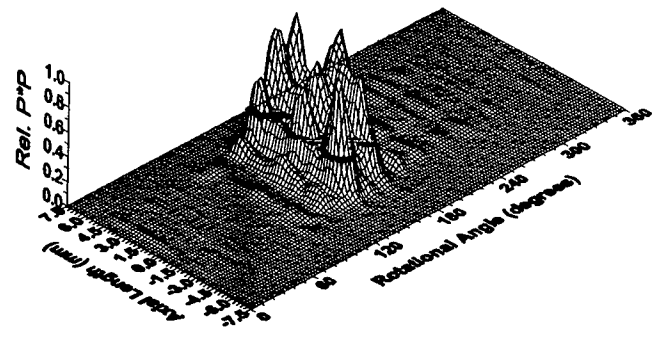

90 Degree Active Sector
Direct-coupled Applicator

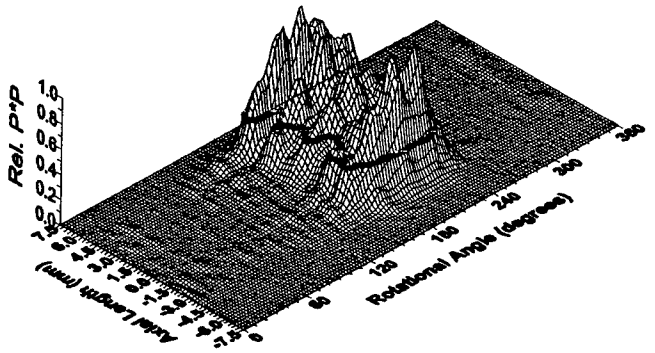

180 Degree Active Sector
Catheter-cooled Applicator

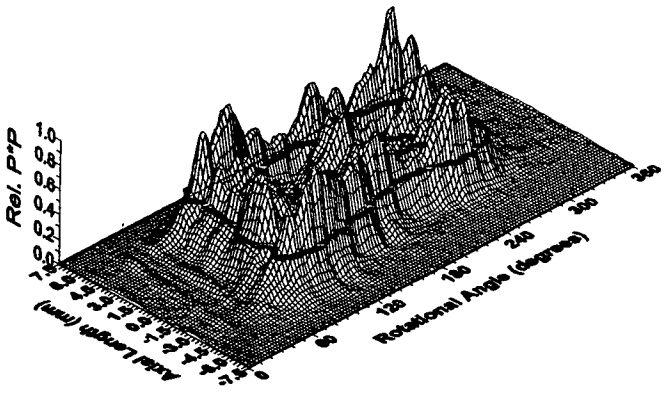

270 Degree Active Sector
Direct-coupled Applicator

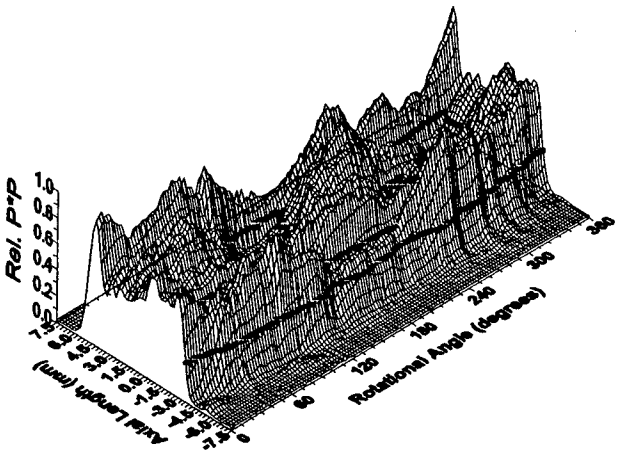

360 Degree Active Sector
Catheter-cooled Applicator

Figure 2. Rotational beam plots from direct-coupled applicators (90 and 270 degree acoustic zones) and catheter-cooled applicators (180 and 360 degree acoustic zones).

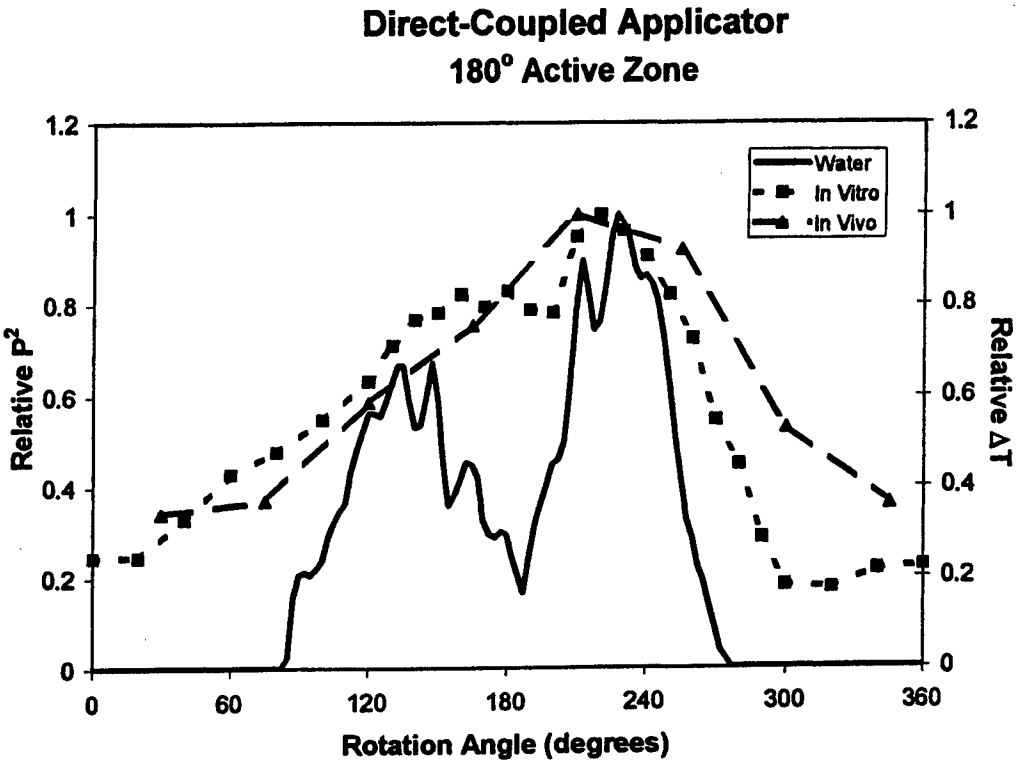

Figure 3. Superimposed average beam distribution, in vitro temperature distribution, and in vivo temperature distribution for 180° direct-coupled applicator.

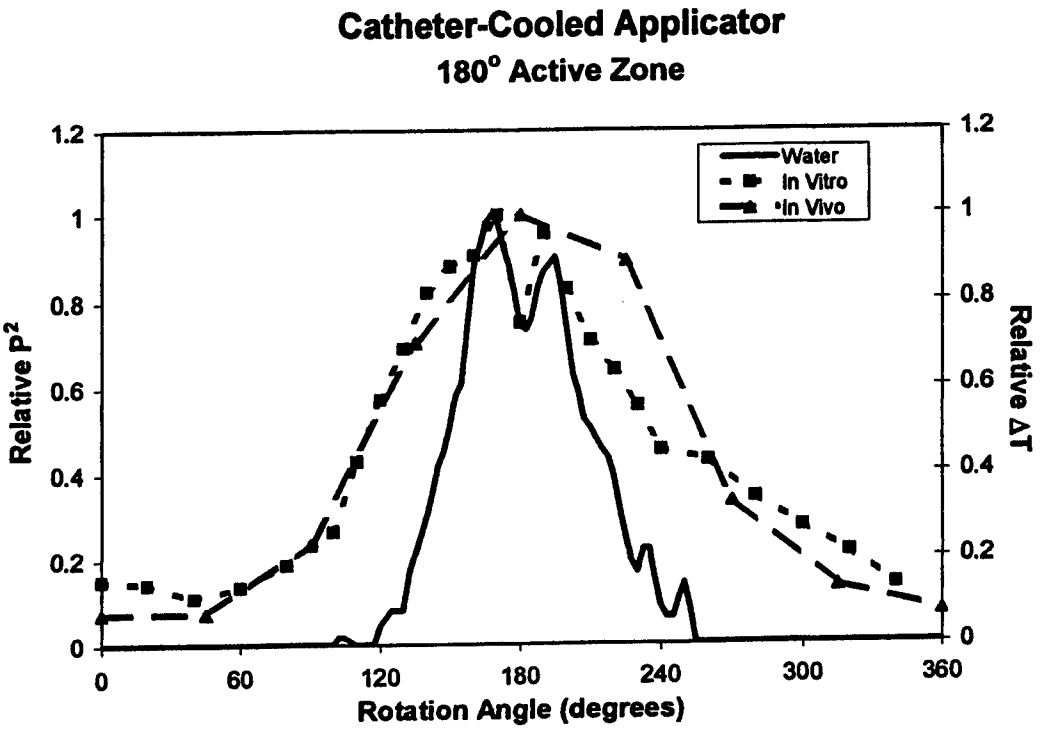

Figure 4. Superimposed average beam distribution, in vitro temperature distribution, and in vivo temperature distribution for 180° direct-coupled applicator.

back to baseline values. The template was then moved to a fresh location and another applicator was tested. Two applicators were evaluated in only two animals.

Steady-state temperatures recorded by the middle two sensors on each thermocouple probe (centered along the axis of the transducer) were averaged and normalized to their peak temperatures. These were then plotted and compared to the in vitro temperature measurements, and the beam distribution measurements (Figures 3 and 4). The resulting heating pattern was again closely correlated to the beam distribution, and also to the heating pattern measured *in vitro*.

In vivo temperature measurements in the porcine thigh muscle confirmed the measurements collected in the *in vitro* experiments. Again, an angular heating pattern was achieved, and was closely correlated to the emitted beam profile measured in water. Regions of low power output from the transducer were not evident in the measured temperature distributions, indicating that thermal conduction and thermal convection act to smooth out the peaks and valleys seen in the beam plots thus providing a more uniform temperature distribution in the targeted region.

Although no power is emitted from the acoustic dead zone of the transducers, tissue heating in that region still occurred due to thermal conduction from the transducer. Poor acoustic efficiency of the transducer results in the conversion of electrical power to heat, which is then dissipated away from the applicator via thermal conduction. This effect was more noticable with the direct-coupled applicators, although the temperature rise in tissue adjacent to the dead zone was insufficient to cause unwanted necrosis. An advantage of the catheter-cooled devices is that the circulating water carries heat away from the transducer surface. This reduces tissue heating in the dead zone, thus further acting to protect non-targeted tissues. Thus catheter-cooled applicators may be inserted between a tumor and adjacent healthy tissue to selectively heat the tumor, while simultaneously protecting the healthy tissue from thermal damage. Additional investigations on the parameters that affect the heating characteristics of the catheter-cooled devices are currently underway.

5. SUMMARY

A family of interstitial ultrasound applicators was fabricated in both direct-coupled, and catheter-cooled configurations with sectored transducers to provide controlled angular heating. Applicators with 90°, 180°, 270°, and 360° active acoustic zones were constructed and evaluated based on acoustic efficiency, acoustic power output, and angular heating characteristics through bench, *in vitro*, and *in vivo* experiments. The results of this study demonstrate the ability to shape the beam profile by notching the piezoceramic tubes to produce an acoustic dead zone. The resulting angular deposition of acoustic energy permits directional heating of targeted tissue. Possible uses for these directional devices would be in the treatment of tumors residing in the posterior portion of the prostate. These applicators would allow for selective ablation of tumor tissue while protecting the rectum from thermal damage.

6. ACKNOWLEDGMENTS

This work was supported by NIH Grant CA-68421 and NIH Grant CA-9215.

7. REFERENCES

1. Diederich, C.J. & Hynynen, K.H., "Ultrasound technology for interstitial hyperthermia" in *Medical Radiology Interstitial and Intracavitary Thermoradiotherapy* (eds. Seegenschmiedt, M.H. & Sauer, R.) 55-61 Springer-Verlag, Berlin, 1993.
2. Stauffer, P.R., "Techniques for Interstitial Hyperthermia" in *An Introduction to the PracticalAspects of Clinical Hyperthermia* (eds. Field, S.B. & Hand, J.W.) 344-370 Taylor & Francis, London, 1990.
3. Diederich, C.J., Khalil, I.S., Stauffer, P.R., Sneed, P.K. & Phillips, T.L., "Direct-coupled interstitial ultrasound applicators for simultaneous thermobrachytherapy: a feasibilty study", *International Journal of Hyperthermia* **12**, 401-419 1996.
4. Diederich, C.J., "Ultrasound applicators with integrated catheter-cooling for interstitial hyperthermia: theory and preliminary experiments", *International Journal of Hyperthermia* **12**, 279-297 1996.
5. Diederich, C.J., Nau, W.H., Stauffer, P.R., Burdette, E.C. & Khalil, I.S., Interstitial ultrasound applicators for localized thermal coagulation of tissue in *IEEE Ultrasonics Symposium* 1303-1307 1996.

6. Stewart, H.F., "Ultrasonic measurement techniques and equipment output levels" in *Essentials of Medical Ultrasound: A Practical Introduction to the Principles, Techniques, and Biomedical Applications* (eds. Repacholi, M.H. & Benwell, D.A.) 77-116 Humana Press, Inc., Clifton, 1982.
7. Hynynen, K., "Acoustic power calibrations of cylindrical intracavitary ultrasound hyperthermia applicators", *Medical Physics* **20**, 129-134 1993.
8. Hynynen, K., "Biophysics and Technology of Ultrasound Hyperthermia" in *Method of External Hyperthermic Heating* (ed. Gautherie, M.) 61-116 Springer-Verlag, Berlin, 1990.
9. Holmes, K.R., Ryan, W., Weinstein, P. & Chen, M.M., A fixation technique for organs to be used as perfused tissue phantoms in bioheat transfer studies in *ASME Advances in Bioengineering* (ed. Spiker, R.L.) 9-10 New York, 1984.
10. Hynynen, K. & Edwards, D.K., "Temperature measurements during ultrasound hyperthermia", *Medical Physics* **16**, 618-626 1989.
11. Dickinson, R.J., "Thermal conduction errors of manganin-constantin thermocouple arrays", *Physics in Medicine and Biology* **30**, 445-453 1985.

Further Author Information-
WHN (correspondence): E-mail: nau@itsa.ucsf.edu; Tel: (415) 502-5177; Fax: (415) 502-5175

Feasibility of interstitial thermotherapy with ultrasound waveguide applicator arrays

B. J. Jarosz

Carleton University, Ottawa-Carleton Institute for Physics
1125 Colonel By Drive, Ottawa, Canada K1S 5B6

ABSTRACT

We discuss potential of ultrasound waveguide applicator arrays for interstitial heating of brain tissue. First we describe specific absorption rate and show the importance of attenuation term at higher frequencies for cylindrical applicators. Ultrasound propagation characteristic to the applicator results in a shear component in the tissue. The component is significant over a small distance from the applicator. We obtain 3-D temperature distribution using finite element analysis simulations for four-applicator array. The simulations show that the array is capable of heating the tissue to 56°C. This high temperature leads to an undesired effect of heat toxicity in the adjacent tissue. The following simulations demonstrate how to optimize energy deposition, especially for asymmetries in boundary temperature. We investigate effects of effective thermal conductivity and antenna's length on the temperature pattern. We find that the array can be used for thermotherapy in clinically relevant volumes with the transducers operated at higher frequencies.

Keywords: ultrasound, thermotherapy, waveguide applicator, interstitial heating, applicator arrays.

1. INTRODUCTION

Interstitial application of heat in thermal treatment of cancer has a clear advantage in cases of deep lying tumors with a need to spare surrounding tissue[1-2]. We have shown before[3] that a single waveguide applicator operated at 1 MHz can generate temperatures required for hyperthermia treatments within 1-cm diameter. This diameter has been observed in porcine brain *in vivo* and *ex vivo* as well as in tissues *in vitro* and in tissue phantoms. Our analytical calculations also resulted in similar value for the diameter. Since the length of radiating part, the antenna, is typically in the 1.0 - 2.5-cm range, this implies the treatment volume of about 0.8 - 2.0 cm^3.

In clinical applications this volume must be substantially more, on the order of tens of cm^3. We investigated efficiency of multiapplicator arrays in heating larger volumes[4]. Temperature distributions were determined for three- and four-applicator arrays in a brain tissue phantom. The temperature was measured with microthermistors at ten discrete locations. Finite Element Analysis (FEA) simulations followed the measurements. After we verified the validity of the FEA model we proceeded with FEA simulation of heating effects with the arrays. The number of applicators in the array varied from three to six. The volume with temperature in hyperthermic range was 16 - 65 cm^3.

Recent discussions[5] of role of cancer thermal therapy point to treatments at a higher temperature, 45 - 70°C that could result in killing the diseased tissue. At these temperatures, tissue coagulation occurs. These treatments, unlike hyperthermia, would be a stand-alone procedure. We have discussed possibility of interstitial thermal therapy in the higher temperature range with the two-applicator array in brain tissue[6]. Our FEA simulations presented there gave 0.64 W/cm^3 as the volume specific absorption rate (SAR) needed for the thermal therapy. The above SAR value exceeds power output capabilities of our applicators operated at 1 MHz. We suggested then that the applicators be operated at higher frequencies. Also, as shown before[4], with more applicators in the array the power required at each antenna is less.

Correspondence: B. J. Jarosz. Other author information: Email: jarosz@carleton.physics.ca; Telephone: 613-520-2600 x 4318; Fax: 613-520-4061; Supported by NSERC grant.

SPIE Vol. 3249 • 0277-786X/98/$10.00

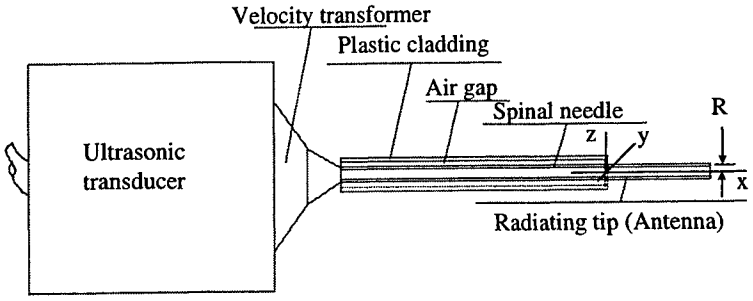

Figure 1. Cross-section of the applicator

This presentation addresses the issue of thermal therapy with a four-applicator array in brain tissue. Using FEA simulations, we discuss 3-D temperature distribution produced by the array placed close to the base of the brain's frontal lobe. We consider heating with the applicators operated in the 1 - 10 MHz frequency range. To see the effects of frequency, we look first at the relative SAR at various frequencies for an applicator. We show that for the highest frequency the SAR pattern is significantly different from the others. Our discussion includes also shear mode effects in immediate proximity of the antenna. The array is intentionally located to the side of the brain's middle line. This results in asymmetry in heat flux and we intend to show how the temperature distribution is affected. We show also how the simulations enable a choice of SAR set that guarantee a required distribution or, in other words, that simulations of this type must precede the thermal treatment.

2. THERMOTHERAPY MODELING

Heating with our applicators requires that they be placed far from significant blood vessels. In presence of microvasculature only we can use effective thermal conductivity equation (ECTE) in modeling. Before we present the ECTE, we briefly describe geometry of the applicator and volume SAR patterns.

2.1. Applicator geometry

Details of the applicator's construction have been given elsewhere[3]. Here we list its major components and we define coordinate system used in the paper. Fig. 1 shows cross-section of the applicator. The transducer uses thickness oscillations of the PZT disk to generate ultrasound (US) in the 1 - 10 MHz frequency range. The US travels to the applicator's spinal needle via a stainless steel conical velocity transformer glued to the transducer. The needle is in a plastic cladding except at the tip. Heat generation occurs by conversion of the US energy deposited from the tip. The tip serves then as the antenna. In the figure, R represents the antenna's radius. For the G19 needles used in measurements, it was 1.1 mm.

Cartesian coordinate system used in the paper has its x-axes pointing along the symmetry axis of the needle. We chose the origin to be at the termination of the cladding on the antenna side. Each applicator is cylindrically symmetrical. This symmetry does not apply to the four-applicator array we will discuss below. However, close to each applicator this symmetry still does exist. These facts have been used in building our FEA mesh.

2.2. Volume SAR

The ECTE requires amount of heat deposited in unit time per unit volume. This is known as the volume SAR, $g(y,z)$. In our case the heat results from conversion of US energy. The acoustic pressure along the antenna was of a standing wave form. Its

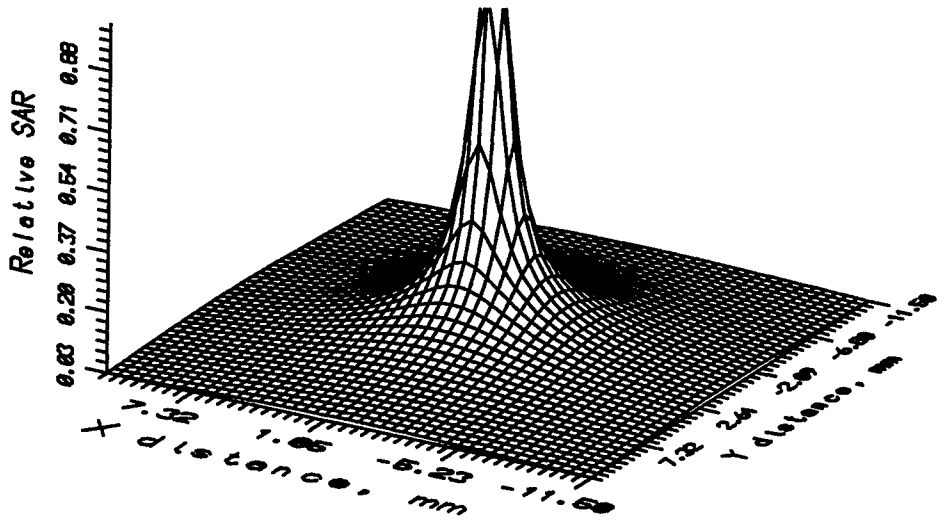

Figure 2. Relative SAR for 1.1 mm diameter antenna

spatial periodicity was 2.4 mm. This periodicity will not show in the SAR because of tissue smoothing effects. We can use x averaged volume SAR, $<g(y,z)>_x$ written as

$$< g(y,z)>_x \;=\; a\; I_o\; \frac{R}{r} e^{-\mu(r-R)}\;, r = \sqrt{y^2+z^2}. \quad (1)$$

In the above equation, a and μ represent US power absorption and attenuation coefficients and I_o is the initial US intensity. Fig. 2 presents relative SAR as a function of distance from the antenna for μ = 0.1 Np/cm. The graph illustrates how fast the SAR drops for distant points. In the four-applicator array, the antennas' axis separation was 24 mm. The maximum 11.50 mm corresponds approximately to the distance to the middle points between the antennas.

It has been discussed before[4] that for 1 MHz US the SAR is mainly defined by the divergence term, R/r. One has to be careful in immediate extension of this statement to other frequencies. The variation of attenuation coefficient for tissues with frequency is of the form $\mu = \mu_o f^{\alpha}$, where $\alpha = 1.14$ for brain tissue[7]. Fig. 3 illustrates the calculated relative SAR variation for the 1 - 10 MHz frequency range. The figure demonstrates that up to 3 mm radial distance from the antenna the SAR decreases almost identically for all the frequencies. Past that distance the relative SAR for 10 MHz US starts to drop off faster reaching almost zero at 1.8 cm. This different behavior at frequencies over 5 MHz results in different pattern of power deposition in the space between antennas. To maintain therapeutic temperature within the required volume at higher frequencies, the temperature at the antenna's surface will have to be higher, too.

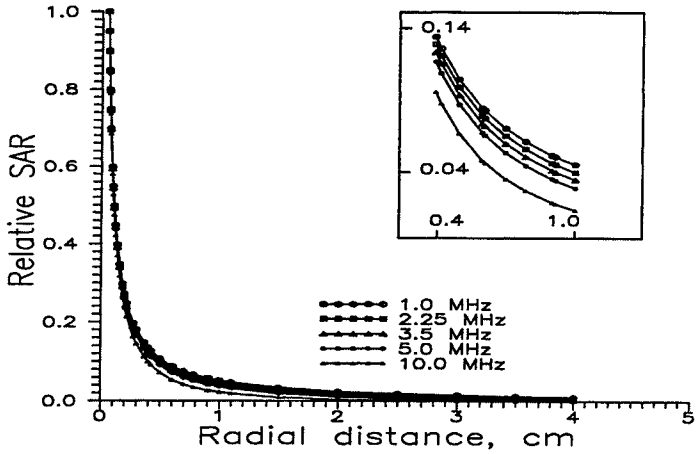

Figure 3. Relative SAR vs. radial distance from the 1.1 mm dia. antenna for 1.0, 2.25, 3.5, 5 and 10 MHz US

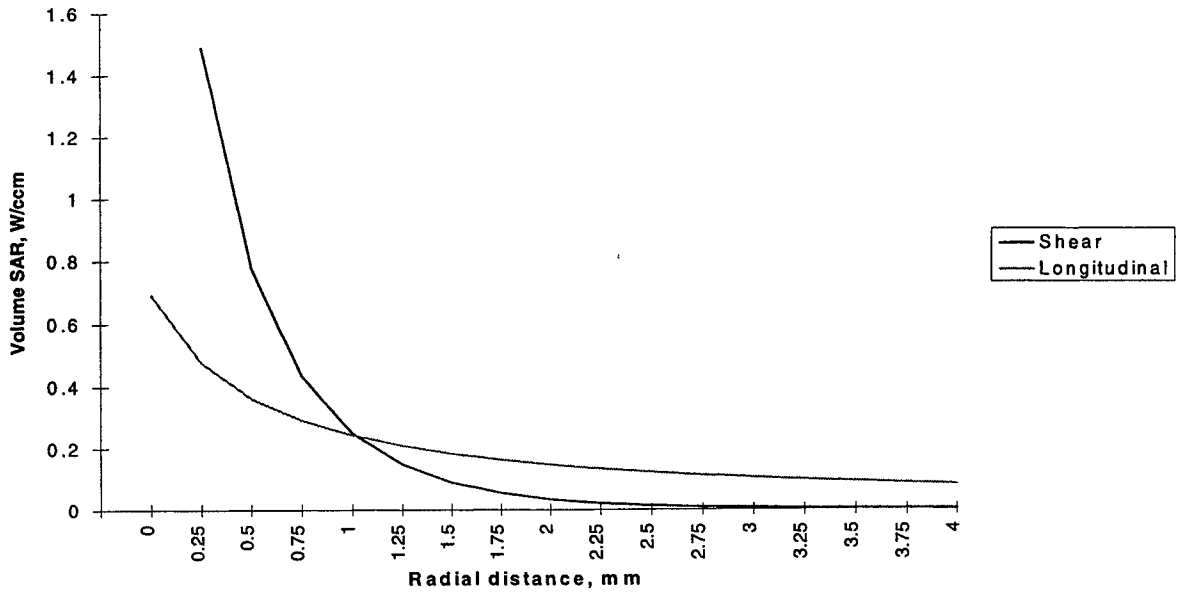

Figure 4. Longitudinal and shear wave contribution to volume SAR vs. radial distance

In comments on equation (1) and illustrating it fig. 2, we did not include a contribution of shear wave component to heating. Our previous results[4] suggested a presence of such component near the antennas. We have no direct means of evaluation of the component contribution. The antenna's acoustic output was measured in water. A needle hydrophone used for measurements sensed only the radial component. The following is proposed as a plausible estimate. US propagates along the antenna as a Rayleigh type surface wave[8]. Particle motion in the wave has in- and out-of-plane components[9]. The out-of-plane displacement amplitude, in radial direction in the tissue, is one and half of the other one. As the components contribute to the SAR proportionally to the displacement squared, we estimate the in-plane (shear for the tissue) component contributes about 31% to the total US energy deposited from the antenna.

The role of the shear component in tissue has been questioned because of its two features. One of them requires a non-vanishing shear modulus. The other pertains to its rapid attenuation with the coefficient up to 150 of that for longitudinal wave[10]. Recent studies[11,12] of stress waves in tissues imply a need to include shear components in thermal effects. We have included the shear component in our simulations when testing experimentally our FEA model. That led to a substantial improvement of the simulation quality factor (root-mean-square deviation between measured and simulation temperature). It dropped from 0.54°C to 0.11°C. The above indicates that the shear component plays a role in US heating. Fig. 4 compares the volume SAR for longitudinal and shear components. The calculations were done assuming 150 as the ratio of the shear and longitudinal attenuation coefficients. One can see that the shear component contributes significantly up to a distance of about 2 mm where its volume SAR is a little less than 20% of the total SAR. It decreases fast with the distance and past 2.75 mm from the antenna its contribution is less than 1%. As expected, the shear wave contribution is very localized and it does not affect heating patterns at large distances.

2.3. Analytical basis of the simulations

The knowledge of the volume SAR for an applicator leads to an analytical formulation that will be used in the FEA simulations. In general, the volume SAR for each of the four-applicator array will have to be different if we want to maintain more symmetric temperature distribution. The ECTE can be written in the form

$$\nabla^2 \tau + \frac{\sum_{i=1}^{4} < g_i(y,z) >_x}{k_{eff}} = \frac{1}{\alpha_{eff}} \frac{\partial \tau}{\partial t}, \quad (2)$$

where $\tau = T - T_o$ is the temperature elevation above basal, T_o temperature; k_{eff} represents tissue effective thermal conductivity which defines effective thermal diffusivity, $\alpha_{eff} = k_{eff}/(\rho\, c)$. The two symbols in the denominator correspond to tissue density

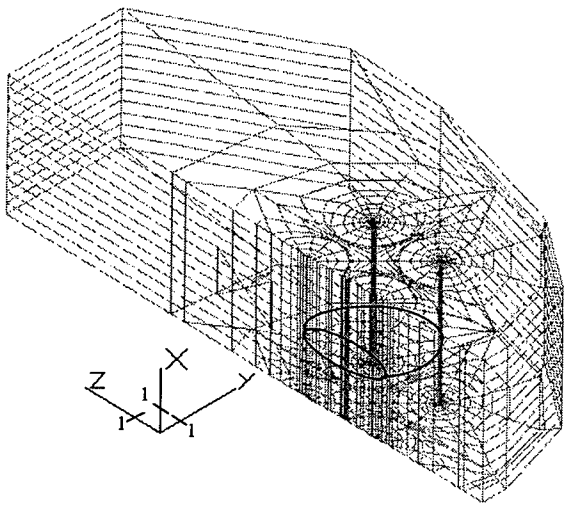

Figure 5. FEA mesh of the 3-D model

and specific heat capacity. Majority of our simulations were carried out for steady state. That implies equation (2) assuming homogeneous form.

2.4. FEA simulation model.

Our 3-D simulation model of heating in brain tissue assumed the tumor to be close to the base of the frontal lobe. This is the largest area of the brain cross-section. Fig. 5 presents the model's 3-D mesh. To show details of the model, it has been cut with a plane perpendicular to y axes at 2 mm distance from the two antennas with lowest y coordinate. The ticks on the coordinate axis indicate a unit of 1 cm. The model had three layers. The middle layer was the one in which heating occurred. Treatment volume is delineated by a dark line. It is pancake shaped with 1.5 cm maximum height and of 2.5 cm diameter. In the simulations, the height was varied up to 2.5 cm. The other two layers 2 and 2.5 cm thick were below and above thermally treated layer. The FEA mesh of all the layers was in the form of bricks of rectangular walls and quadrilateral bases. All the bricks had a constant 5-mm height in x direction.

Fig. 5 shows that the heated volume is to the right of the middle line in the frontal lobe. We have chosen this location to explore influence of asymmetrical boundary condition on heating effect. In the simulations, the external boundary temperature was maintained at basal, 37°C. To minimize number of bricks forming the 3-D mesh, we modified sides of quadrilaterals relative to expected temperature gradients. Their sizes varied substantially from about 0.14 and 0.25 mm in vicinity of the antennas and interconnecting regions through about 0.8 cm at the basal temperature boundary proximal to the heated region to about 7 cm at the boundary distal from that region. The FEA mesh of the full model had 25,544 lines and 8801 nodes.

3. RESULTS AND DISCUSSION

We have carried out simulations for effective thermal conductivity in the 0.006 - 0.030 W/cm/K range. The range covers typical k_{eff} values. This was ascertained from equation relating k_{eff} and blood flow[13] for typical values of the latter[14]. The maximum tissue temperature was in the 45 - 56°C range. To achieve these temperatures, we adjusted the volume SAR. We begin presentation of the results with discussion of asymmetry in temperature pattern.

3.1. Effects of asymmetric boundary conditions

The simulations we have presented before[4] dealt with the treatment volume positioned centrally within the overall volume. The temperature of the whole volume boundary remained fixed during heating. As expected, with the volume SAR maintained the same at all the antennas, the temperature pattern reflected geometry of the array. For example, for four-applicator array with the applicators' tips at the corners of a rectangle, the outline therapeutic temperature range was a rectangle with rounded corners.

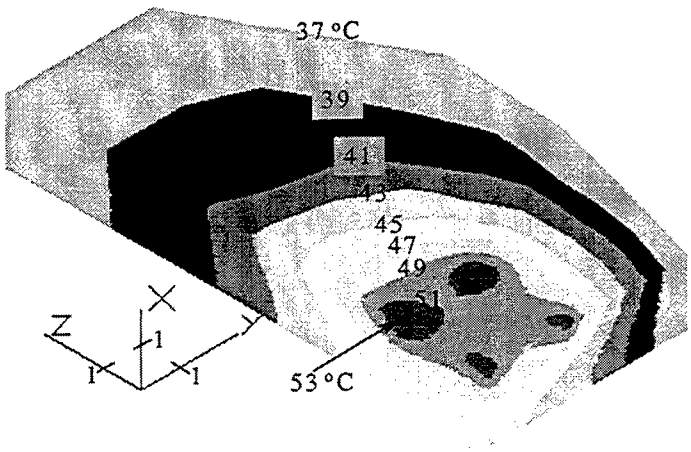

Figure 6. 3-D temperature distribution at 0.69 W/cc volume SAR

The shape of this range was also a function of effective thermal conductivity. For low k_{eff} the range resembled a circle while high values of k_{eff} resulted in the 'rectangle' sides indented towards the center of the treatment volume.

Fig. 6 demonstrates the effect of asymmetric boundary condition in the temperature distribution. The four applicators had the same volume SAR, 0.69 W/cm^3 at the antennas. As discussed in Section 2.2, we have included shear component in the SAR. In the figure, the bands of different shade of grey represent temperature of the tissue in °C. The labels indicate temperature intervals within the band. For clarity, we labeled only one of four bands with temperature above 51°C and only one of two with temperature above 53°C. As in fig. 5, the ticks on coordinate axis represent a unit of 1 cm. We have assumed k_{eff} = 0.01 W/cm/K in this and the next two figures. The 3-D model was cut with three planes to reveal relevant temperature distribution. To reveal the top pattern, the plane perpendicular to x-axes bisecting the antennas was used. The other planes were perpendicular to the y and z axis and they were just past the antennas towards the center of the heated region. We have fixed maximum allowable temperature at 55°C in this simulation. It was reached at only one, top left (low y, high z coordinates) antenna. The pattern exhibits substantial asymmetry. The temperature at both the lower left (low y, low z coordinates) and right (high y, low z coordinates) antennas barely reaches 51°C. More importantly, there is a significant dip in the 47 and 49°C contours. The region

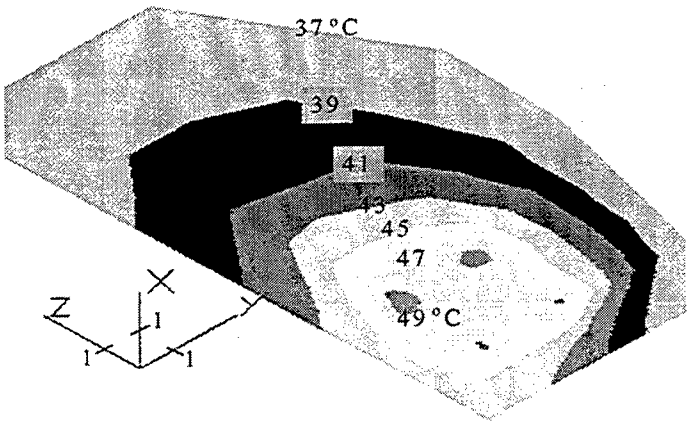

Figure 7. 3-D temperature pattern at 0.53 W/cc volume SAR

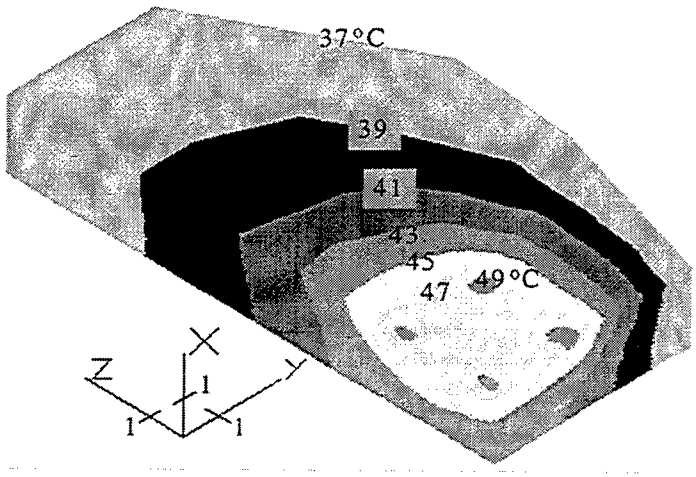

Figure 8. 3-D temperature pattern with distinct SAR values at each antenna

with temperatures above 45°C needs to be examined, too. As seen from fig. 6, the latter extends to the "healthy" layer below and also, not shown in the figure, above.

This intrusion of the above 45°C region into a healthy layer is not acceptable from clinical standpoint. Heat toxicity would result in radical healthy cell kill. We looked then at lowering the maximum allowable temperature to 51°C. The resultant temperature pattern is shown in fig. 7. We used similar convention as in the previous figure. Once again, the maximum allowable temperature was only at the upper left antenna. We can see that the above 45°C range does not extend substantially beyond the treatment volume. On the other hand, it becomes very shallow at the lower right (high y, low z coordinates) antenna and a concern arises that there the treatment volume may not be entirely covered.

We complete the above discussion with the results obtained for the four antennas run at individual SARs. First we looked for a method that enables a correction of asymmetry in temperature pattern by appropriate SAR choice. Observations led us to a following procedure. In the temperature pattern of initial simulation we measured the extent of last disconnected isotherms around antennas. The inverse of ratio of their sizes served as an indicator how to increase SAR at the antennas.

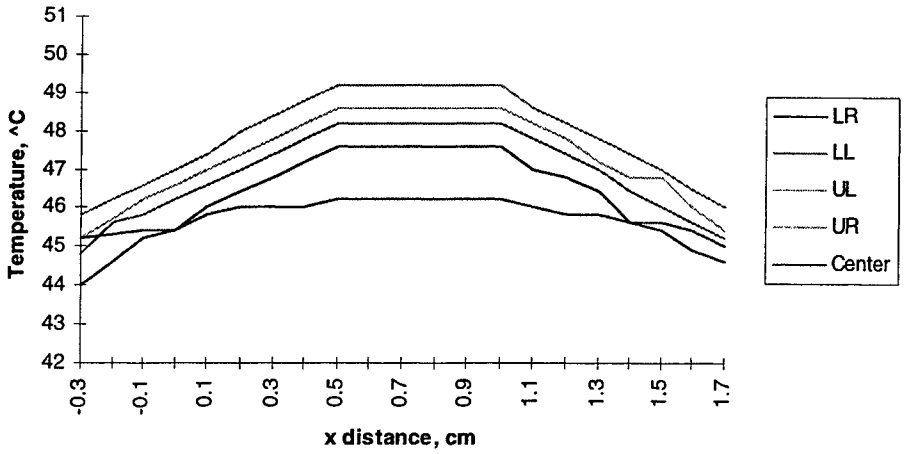

Figure 9. Temperature distribution along the x axes with volume SAR of 0.53 W/cc at all the antennas

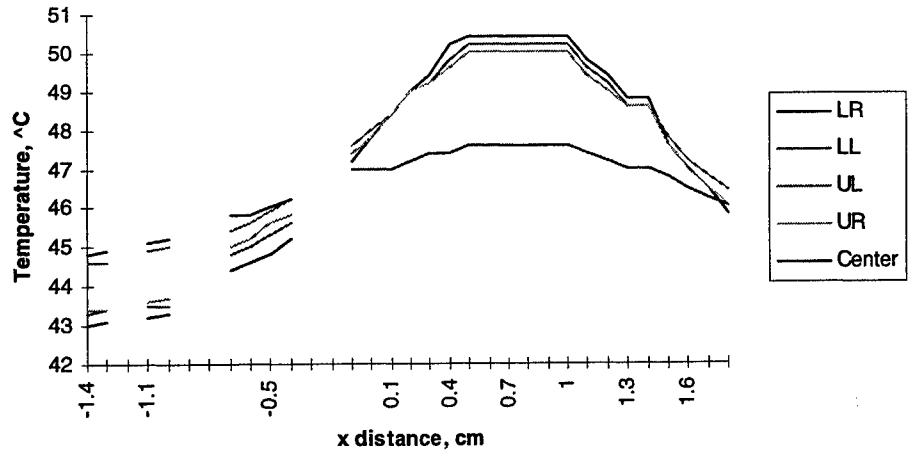

Figure 10. Temperature distribution along the x axes with individual SAR at each antenna

Assume the 0.53 W/cm^3 volume SAR at the upper left antenna as a reference. Fig. 8 presents temperature pattern with the SAR at the antennas in clockwise direction of 110, 135, and 120% of the reference. The pattern around each antenna is almost identical. More importantly, the range with temperature above 45°C is more symmetrical, it covers well the volume at the lower right antenna. The range extends farther into the volume around the upper right antenna, too.

Figs. 9 and 10 show details of temperature pattern along the x axes. We registered the therapeutic temperature, above 45°C. The labels LR, LL, UL and UR in these two figures stand for lower right, lower left, upper left and upper right antenna, respectively, as seen in figs. 7 and 8. The center corresponds to the points directly above the center of the square formed by the antennas' tips. Fig. 9 demonstrates clearly rapid decrease in temperature around lower right antenna, close to the brain periphery. The figure's plot is a bit misleading as it suggests that the therapeutic temperature is maintained in the volume defined by the antennas. Fig. 7 gives better information on that. Therapeutic range around lower right antenna connects with the ranges of other antennas only along 0.8 cm of its central part. Past that length and also 0.1 cm over its total length, the therapeutic temperature around it is disconnected from the others.

Fig. 10 indicates that the individual adjustment of SAR resulted in substantial improvement in temperature uniformity. There is slight, on the order of 0.3°C temperature deviation for the four antennas over their whole, 1.5 cm length. The temperature at the center remains above 45°C 1.1 cm below and (not shown in the figure) 2.5 cm above the origin (see fig. 1). This temperature protrudes to that extent into the under- and overlaying layers only at the center. As one can see, the temperature at the antennas drops below the therapeutic value at 0.5 - 0.7 cm beyond the antennas. The latter values are direct result of keeping the same volume SAR at the upper left applicator. We did this to have better comparison of the SAR adjustment effects. In practice one would adjust the SAR simultaneously, i.e., the factors used in the increment would be as before but the SAR at the upper left antenna would be reduced.

3.2. Effects of other parameters.

In our simulations, we have used a range of k_{eff}. The lowest, 0.006 W/m/K is typical for the non-perfused tissue. Results for this thermal conductivity are meaningful in the thermotherapy case since its final goal is to coagulate the tissue. The beginning of the preceding section describes effects of low k_{eff} on the shape of therapeutic volume. The other observation is that the asymmetric boundary conditions influence the temperature pattern less. At this low k_{eff} there is no need to individualize SAR to obtain therapeutic temperatures within the volume defined by the antennas' length.

Results for the highest k_{eff} = 0.03 W/cm/K are presented in fig. 11. The plane set used to reveal the temperature pattern was the same as described above. We used individual SAR values for the array's antennas. We calculated them in similar fashion as those to get fig. 8. This time we selected 48°C as the maximum temperature. The volume SAR at the reference, upper left antenna was 1.12 W/cm^3. The figure demonstrates that the therapeutic temperature volume is reasonably

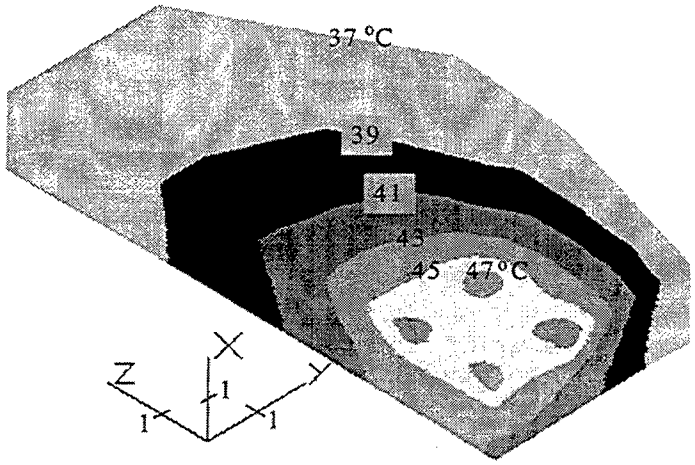

Figure 11. 3-D temperature distribution at k_{eff} = 0.03 W/cm/K. Individual SAR values used.

symmetrical with the maximum temperature in similar volumes around each antenna. Closer inspection of the results show that the volume with the therapeutic temperature starts as expected at the termination of the cladding (x = 0) and continues until 0.05 cm above the antennas' tips. At x = 1.5 cm, tip of the antennas, the therapeutic range of both the upper antennas are still connected. Past that point the therapeutic temperature exists still around all the antennas for about 0.25 cm. These were small, disconnected volumes. The pattern is asymmetric at these locations.

We looked also at effects of the antenna's length. The results for the 2.5 cm length at k_{eff} = 0.01 W/cm/K were very similar to the ones described in discussion of fig. 8. In this simulation we used individual SAR values. The factors used in calculations were the same as described above. The layers above and below the treatment volume were 2.5 and 2.0 cm thick as before. The fact that the overall volume of the tissue has increased by about 17% had no substantial impact on temperature pattern. We conclude that for active heating, properties of adjacent layers have the largest impact.

3.3. Feasibility of thermal therapy

In our simulations, we typically set the maximum temperature of the tissue and adjusted the volume SAR to achieve it. We will evaluate now if our applicators can supply the required energy. Radiation balance measurements showed that the maximum acoustic output of our transducers is about 4 W. Efficiency of our applicators was 30 - 40%. If we add shear component that can exist in tissues but not in water, the total power from the antenna can be in the 1.6 - 2.1 W range. In our evaluations we have used volume averaged temperature elevation, $< \tau >$ defined as

$$< \tau > = \frac{\int_V \tau \, dV}{V} \qquad (3)$$

where V represents the total volume. Fig. 12 shows shape of various temperature ranges as seen in the plane bisecting the antennas perpendicular to the x axes of the previous figures. Only every other band is labeled for clarity. The range above 47°C is indicated by the arrows. The shapes are very irregular and in effect we had to carry out approximate integration. It gave $< \tau >$ = 1.9°C. We evaluate that US has to be applied for 18 - 23 min. It compares reasonably with experiments in which 7 - 25 min US heating resulted in the steady state.

The other question that remains to be addressed is the SAR values. Fit of our 1-MHz data with the simulations shows that the antennas provide up to 0.5 W/cm^3 volume SAR. The values reported in the previous sections start at 0.53 W/cm^3 and go up to 1.51 W/cm^3. We could generate higher acoustic outputs by cooling the 1-MHz applicators or replacing formerly used 12.7-mm diameter piezoelectric disks with 25.4-mm disks. We have tried both and we have observed an expected increase. Both the modifications enlarge substantially the size of the array. Also, the transducer holders that provide efficient

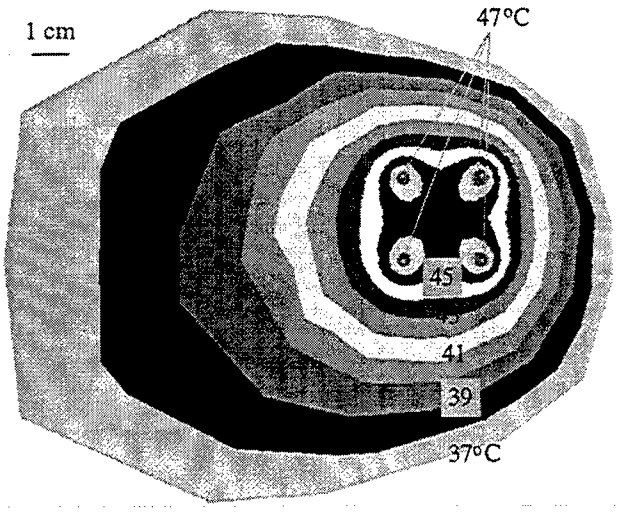

Figure 12. Temperature distribution in the plane perpendicular to the x axes bisecting the antenna

cooling suffer enlargement. Instead we propose replacement of 1-MHz piezoelectric elements with either 3.5- or 5-MHz elements. Results of these simulations done for 1-MHz applicators apply up to those frequencies (compare fig. 3) within about 2%. The discussion in Section 2.2 indicates clearly that the 3.5-MHz transducer can provide the required volume SAR even for the highest k_{eff} reported here. There are some atypically high blood flow[14] values. Even then the waveguide applicator array can heat the tissue to the therapeutic level but then 10-MHz transducers must be used. Separate simulations have to be carried for this high frequency. We have reported such simulations[6] for the two-applicator array and we found that the array can render satisfactory temperature distribution.

4. CONCLUSIONS

Volume SAR for US waveguide applicators depends mostly on the divergence term for low frequencies. At higher (above 5 MHz) frequencies the attenuation term becomes significant at large compared to the antenna's radius distances. This leads to serious reduction of US penetration depth. Shear component in tissue characteristic to the applicator plays a role in heating over a small distance. At high acoustic power this distance is less than 3 mm.

The 3-D simulations provide details of temperature distribution that can hardly be obtained from direct measurements. Placement of the applicators defines the 3-D temperature distribution shape in the middle part of the antennas. The shape there does not depend on the antenna's length or the layers of tissue below and above. The extent of this part is mainly defined by effective thermal conductivity. If the array volume SAR is high enough (0.69 W/cm^3 for the discussed here four-applicator array), in the case of low k_{eff} (low blood flow) the maximum temperature reaches 56°C. In this case the temperature above 45°C extends to the adjacent layers. This is due to high US penetration. It is an undesired effect since it results in heat toxicity in healthy layers. The SAR values in the array should be optimized to minimize this effect.

The array operated at 1 MHz can supply satisfactory SAR if the heated volume of low k_{eff} is placed centrally in the overall volume (symmetric boundary conditions). If the treatment volume suffers asymmetrical cooling, individual volume SAR at each applicator has to be used. The simulations give the information on how to modify power deposition. For the four-applicator array, the required three applicators SARs were beyond capability of the 1-MHz applicator. We conclude that 3.5- or 5-MHz transducers will have to be used in typical cases. Special cases of very high blood flow may require 10-MHz transducers.

ACKNOWLEDGMENT

This research has been supported in part by the NSERC grant.

REFERENCES

1. M. H. Seegenschmiedt and R. Sauer, Eds., *Interstitial and intracavitary thermoradiography*, Heidelberg: Springer-Verlag, 1993.
2. L. Handl-Zeller, Ed., *Interstitial hyperthermia*, Wien: Springer-Verlag, 1992.
3. B. J. Jarosz, "Feasibility of ultrasound hyperthermia with an interstitial waveguide applicator", *IEEE Trans. Biomed. Eng.*, **43**, 1106-1115, 1996.
4. B. J. Jarosz, D. Kaytar, "Ultrasonic waveguide applicator arrays for interstitial heating: a model study", *IEEE Trans. UFFC*, accepted for publication, 1997.
5. M. R. Gertner, B. C. Wilson, A. E. Worthington, M. D. Sherar, Ultrasound properties and images of *ex-vivo* liver during thermal therapy", *Proceedings*, 1997 IEEE Int. Ultrasonics Symp., October 5-8, 1997, Toronto, ON.
6. B. J. Jarosz, "Feasibility of ultrasound thermal therapy with interstitial waveguide applicator array", *Proceedings*, COMP/CCPM Ann. Meet., Charlottetown, PEI, July 10-12, 1997.
7. S. A. Goss, R. L. Johnston, F. Dunn, "Ultrasonic absorption and attenuation in mammalian tissues", *Ultrasound Med. Biol.*, **5**, 181-186, 1979.
8. B. J. Jarosz, R. L. Clarke, "Ultrasound propagation in thin rods in water", *Can. J. Phys.*, **64**, 671-676, 1986.
9. I. A. Viktorov, *Rayleigh and Lamb waves*, New York: Plenum Press, 1967, pp. 4-5.
10. A. P. Sarvazyan, "Acoustic properties of tissues relevant to therapeutic applications", *Br. J. Cancer*, **45**, Suppl. V, 52-54, 1982.
11. D. Albagli, M. Dark, C. v. Rosenberg, L. Perelman, I. Itzkan, M. S. Feld, "Laser-induced thermoelastic deformation: A three-dimensional solution and its application to the ablation of biological tissue", *Med. Phys.*, **21**, 1323-1331, 1994.
12. A. G. Doukas, T. J. Flotte, "Physical characteristics and biological effects of laser-induced stress waves", *Ultrasound Med. Biol.*, **22**, 151-164, 1996.
13. J. Creeze, J. J. W. Langendijk, "Temperature uniformity during hyperthermia: the impact of large blood vessels", *Phys. Med. Biol.*, **37**, 1321-1337, 1992.
14. A. Toglia, J. M. Kittelson, R. B. Roemer, J. A. Hodak, L. P. Carter, "Cerebral bloodflow in and around spontaneous malignant gliomas", *Int. J. Hyperthermia*, **12**, 461-476, 1996.

Catheter application of cryogenic temperatures inside the heart

James W Lewis[a] and Marc Dubuc[b]

[a]CryoCath Technologies Inc, Saint Laurent, Quebec, Canada H4T 2B5
[b]Institut de Cardiologie de Montréal, Montreal, Quebec, Canada H1T 1C8

ABSTRACT

A new catheter-based cryosurgery system is proving its potential as a valuable tool for electrophysiologic (EP) applications inside the heart. The long, narrow, flexible catheter evaporates room-temperature liquid refrigerant within its tip to produce localized cryogenic temperatures. The catheter provides a "less invasive" percutaneous approach to the inner walls of the heart to confirm and ablate arrhythmogenic sites with cryosurgical benefits—preservation of tissue integrity, absence of thrombus formation. The system's primary engineering challenges are safe refrigerant handling and catheter temperature performance. Surgical results in the animal model demonstrate the system has sufficient cooling power and temperature range to alter EP response, both temporarily and permanently. With tip temperatures between –20°C and –35°C at the atrioventricular (AV) junction, reversible conduction block is produced in the AV node with minimal damage to heart structures. Taking the tip below –50°C creates permanent block in the AV node through formation of a necrotic lesion. Summing these results leads to the conclusion that the technology has the potential to identify arrhythmogenic sites without damage, to verify the site, and to ablate it—within the same procedure, without moving the catheter.

Keywords: catheter, cryoablation, ablation, cryosurgery, endocardial

. . . . .

1. CRYOSURGERY

Treating disease or injury through the application of cold has a long history, dating back to studies first recorded in 1824. By the nineteen sixties, with new technologies to lower and to control the level of cold and to more effectively apply it to the body, cold came into its own as a legitimate and valuable surgical tool. Surgery by cold, especially the use of extreme cold to bring about the destruction or elimination of abnormal cells, is called cryosurgery. Today, cryosurgery is applied almost everywhere on or within the body. It treats a variety of conditions from abnormal heartbeats to enlarged prostates to warts.

Cryosurgical tools combine *cryogenics,* meaning the production of icy cold, with the natural effects cold has on tissue to create their effect. In the physical sciences, the field of cryogenics is considered to deal with temperatures below –150°C; temperatures below what can typically be reached by refrigerants. However in physiology, cryogenic temperatures are any temperatures below which tissue functions, reactions, or viability are altered by cold. This monograph is particularly interested in the cryosurgical aspect of cold on heart tissue, namely, the catheter application of cryogenic temperatures inside the heart to eliminate its electrical properties in interventional cardiac electrophysiology.

2. CARDIAC CRYOABLATION

The medical term for cryosurgical removal or elimination of a body part or the destruction of its function is *cryoablation.* In interventional cardiac electrophysiology, cryoablation is primarily used for removing the electrical properties of heart tissues that interfere with the proper beating of the heart. Cryoablation involves temperatures below which significant destruction of tissue takes place; temperatures below about –35°C.

In the heart, cryoablation is not the only use for cold: cold at all levels has many clinically desirable effects. Temperatures near the freezing point of water can disrupt electrical activity in tissue without causing permanent destruction; this effect is called reversible block [Camm et al. 1979; Camm et al. 1980]. Ice formation in bodily fluids and tissue can cause instruments to stick to bodily structures to "anchor" the cryosurgical tool, particularly useful for maintaining contact with the walls of a beating heart. Extreme cold can cause cell death without compromising the structural integrity of the tissue [Ott et al. 1987; Markovitz et al. 1988]. Heart muscle killed by cold is replaced naturally by fibrous tissue that is electrically inactive

[Jensen et al. 1987; Murray et al. 1994]. Freezing of blood and tissue has negligible tendency to create thrombi during application and leaves the site of application relatively undisturbed and smooth.

A primary use of cardiac cryoablation in electrophysiology has been the treatment of arrhythmia that were unresponsive to drug therapy. It was particularly well suited for treating the atrioventricular (AV) junction [Bredikis 1985; Harrison et al. 1977; Klein et al. 1980]. Typically, arrhythmia cryoablation was a multiple-step process. First, the focus of the arrhythmia (called the arrhythmogenic site) would be identified using standard electrophysiological procedures. Then, the chest would be opened. The surgeon would proceed to confirm the ablation site by creating a reversible block while under cardioplegia. Finally, cryoprobes on the outer and inner surfaces of the heart would be used to ablate the pacing or conducting function of cells at the arrhythmogenic site.

Beginning in the early nineties, however, the number of cardiac cryoablation procedures performed for arrhythmia declined sharply. This drop was due largely to the advent of refined electrosurgical ablation catheters. These long, flexible, steerable catheters could be introduced through a simple puncture in the skin and threaded through the vascular system into the heart. There, they could deliver radio-frequency electrical energy to the inner walls of the heart, using heat instead of cold to ablate the arrhythmogenic site without having to open the chest or stop the heart. Although electrosurgical procedures were limited to only certain types of arrhythmia, the advantages of catheter-based energy systems were clear: the systems greatly decreased invasiveness of the procedure. Introduction of these catheters all but ended the use of open procedures, including cryoablation, for the indications where catheter ablation applied.

3. CATHETER CRYOABLATION SYSTEM

Now, a new cryosurgery system, where freezing temperatures are delivered to the end of a long, flexible, steerable catheter, is again bringing the advantages of cryoablation to interventional electrophysiology, only in a less invasive form. The new system is being developed by CryoCath Technologies in the Montreal metropolitan area. It has demonstrated already that sufficiently low temperatures can be sustained in a beating heart to cryoablate the AV node or to create transmural lesions in any chamber of the heart in dogs.

The catheter cryoablation system has three major elements: cryocatheter, umbilical, and console. The cryocatheter is the component that is introduced into the body and placed in position at the arrhythmogenic site. Then, room-temperature liquid refrigerant is delivered and evaporated in its tip to produce the localized cold needed. The umbilical system connects the refrigerant and electrical systems of the catheter to the console and to an ECG monitor for interpretation and control of the procedure. The console is the main control unit where electronics control and display the procedure variables; the refrigerant is stored, delivered, and recovered; and the electronic safety and alarm systems reside.

The primary technology of the system is the use of a room-temperature liquid refrigeration system. The simple evaporative liquid system provides several advantages over competing technologies: flexibility, lower pressures, and higher cooling power. Until recently, most cryoablation systems used cryogens, liquefied permanent gases, to create the needed temperatures, the most popular of these being liquid nitrogen. Obviously, systems moving cryogens are large and stiff, these systems are not compatible with flexible catheters. Other cryoablation systems meant for use in catheters use adiabatic expansion of gases, the Joule-Thompson or Kelvin-Thompson effect, to reach the low temperatures. These systems often require system pressures in the neighborhood of 800 to 2000 psi compared to the liquid system that operates between 250 and 500 psi. Although the Joule-Thompson systems can attain quite low temperatures, they do not have the cooling power obtained by taking a liquid through to its vapor state.

Figure 1 is a schematic representation of the catheter illustrating one embodiment of the liquid refrigerant system. Liquid refrigerant is delivered down the center of the catheter in a micro injection tube. The small size of the tube helps keep the refrigerant liquid until it reaches the tip of the catheter. The main lumen of the catheter is maintained under vacuum ensuring that the evaporation chamber in the tip is under vacuum for complete evaporation of the refrigerant as the liquid exits the injection tube. The vacuum in the lumen also provides for evacuation of the spent refrigerant vapor. The schematic shows the current "spot" catheter that uses an impinging-jet flow configuration for efficient transfer of heat in the small tip. This tip forms a relatively spherical ice ball, thus the spot name. This type of system gives a relatively stable temperature-versus-

flow relationship allowing reasonable temperature control over a wide temperature range, more than 30°C, by simple injection-pressure control.

The system's main engineering challenges are obtaining the necessary catheter temperature performance, injecting and recovering refrigerant safely, assuring proper catheter positioning in the heart, and providing an easy to use user interface.

Temperature performance of the system relates to the absolute temperatures it can reach and to the stability at those temperatures. To receive full benefit from the use of cold in electrophysiology, each aspect of cold needs to be available through the system. That means that the system must not only be able to reach cryoablation temperatures, but it must be capable of making reversible block at warmer temperatures. Reversible block is used to confirm that the catheter is positioned correctly before ablation is undertaken. To obtain reversible block, the catheter must be controllable at temperatures above –30°C range. To assure deep and permanent ablation of heart tissue, the catheter must reach temperatures lower than –50°C. The exact stability necessary to control confirmation or ablation processes is not known, but several clinicians have expressed they would like to see better than ±5°C. By creating proper restrictions in the refrigerant injection system and using a PID control system of the injection pressure keying off the tip temperature, the current system has been shown to create controlled temperatures in the dog heart from –25°C to –55°C within ±2°C.

The purpose of most of the active safety systems is to address the safe movement of refrigerant in and out of the catheter; vacuum inside the main lumen of the catheter being the main safety attribute. Since the catheter is under vacuum, a leak in any part of the catheter results in blood ingress into the catheter lumen, rather than refrigerant release into the body. A pull wire, which runs the length of the catheter and is used to deflect the catheter tip, serves as the leak sensor. Blood entering the catheter creates an electrical short with the pull wire, the short is detected by the console. Once the leak detection is activated, injection of refrigerant is disabled, but vacuum is maintained to insure that the refrigerant is removed from the catheter. When the blood reaches the optical fluid sensor in the catheter handle, the vacuum is turned off. The console hardware monitors the vacuum connection as well as the state of vacuum throughout the console at all times. If loss of vacuum, catheter leak, or injection tube blockage is detected, the console disables refrigerant injection as well as provides an audible alarm.

Properly positioning the catheter is accomplished through mechanisms and sensors internal and external to the catheter. To allow the physician to manipulate the catheter and position it, a single-axis deflection mechanism is built into the catheter. Curvature of the tip is activated by a pull wire attached to a lever on the handle of the catheter. Using ECG signals coming from quadrapolar electrodes on the catheter (the tip and three electrode rings arrayed down the shaft) and fluoroscopic visualization of the catheter in the heart, the clinician can manipulate the catheter into position and then begin the procedure.

The user can preset procedure variables—application mode, temperature, and (if desired) time—through a menu-driven user interface on a computer touch screen on the console. The interface records and displays all information about the procedure, including settings, tip temperature, application time, cautions, and warnings. Initiation and termination of the procedure is done through manual buttons on the console. These buttons are not dependent on software operation. A separate hardware display of tip temperature and procedure time are also on the console to insure safe shut-down should there be a problem with the software controls.

4. ENDOCARDIAL CRYOABLATION

The catheter cryoablation system described has been used in more than 20 animal studies to examine the effects and limitations of catheter cryoapplication on the inside of the heart with respect to reversible electrophysiologic effects and to the system's capacity to create chronic electrical block of the AV node.

Eight dogs were studied to demonstrate that AV node conduction could be transiently interrupted by cooling the AV node area with complete recovery after passive warming. Cold confirmation by creating a reversible conduction block by cryoapplication was termed ice mapping by the researchers. At the AV node, cryoapplication with progressive lowering of the temperature was done. As soon as high degree AV block or lengthening of the PR interval greater than 50% was obtained, cryoapplication was stopped with subsequent passive rewarming. Recovery of 1:1 conduction occurred several seconds after cryoapplication was stopped in all animals. When tip temperatures remained between –20 C and -35 C at the AV node, reversible conduction block was produced in the AV node with minimal damage to heart structures. The researchers concluded that reversi-

ble ice mapping is feasible using catheter cryoablation technology and that this technique may allow for identification of successful ablation site (cold confirmation).

Twelve dogs were studied to demonstrate that AV node conduction could be permanently blocked by cooling the AV node area. At the AV node, two cryoapplications of five minutes each were done at the lowest temperature attainable. Taking the tip below –50°C created permanent block in eight out of nine animals; the ninth had an anatomical defect that prevented successful blockage. The conclusion of these studies was that the catheter cryoablation technology has the cooling capacity to successfully cryoablate the AV node in dogs.

Taking these results together leads to the conclusion that the technology has the potential to identify and position the cryoablation catheter at the arrhythmogenic site, to reversibly confirm the site with minimal damage to heart structures, and to ablate it—within the same procedure, without moving the catheter.

The catheter cryoablation system provides a "less invasive" percutaneous approach to the inner walls of the heart to confirm and ablate arrhythmogenic sites with cryosurgical benefits—preservation of tissue integrity, absence of thrombus formation. The safety, effectiveness, and confidence of cryoablation should soon be available in a catheter system.

REFERENCES

Barron RF 1985. *Cryogenic Systems* (second edition). New York: Oxford Univ Press.

Bredikis J 1985. Cryosurgical ablation of atrioventricular junction without extracorporeal circulation. *J Thorac Cardiovasc Surg* 90: 61-7.

Camm J, Ward DE, Cory-Pearce R, Rees GM, Spurrell RAJ 1979. The successful cryosurgical treatment of paroxysmal ventricular tachycardia. *Chest* 75(5):621-4.

Camm J, Ward DE, Spurrell RAJ, Rees GM 1980. Cryothermal mapping and cryoablation in the treatment of refractory cardiac arrhythmias. *Circulation* 62(1):67-74.

Harrison L, Gallagher JJ, Kasell J, Anderson RH, Mikat E, Hackel DB 1977. Cryosurgical ablation of the A-V node-His bundle: a new method for producing A-V block. *Circulation* 55(3): 463-70.

Jensen JA, Kosek JC, Hunt TK, Goodson WH, Miller DC 1987. Cardiac cryolesions as an experimental model of myocardial wound healing. *Annals of Surgery* 206(6):798-803.

Klein GJ, Sealy WC, Pritchett ELC, Harrison L, Hackel DB, Davis D 1980. Cryosurgical ablation of the atrioventricular node-His bundle: long-term follow-up and properties of the junctional pacemaker. *Circulation* 61(1): 8-15.

Markovitz LJ, Frame LH, Josephson ME, hargrove WC 1988. Cardiac cryolesions: factors affecting their size and a means of monitoring their formation. *Ann Thorac Surg* 46:531-5.

Murry CE, Giachelli CM, Schwartz SM, Vracko R 1994. Macrophages express osteopontin during repair of myocardial necrosis. *American Journal of Pathology* 145(6):1450-1462.

Ott DA, Garson A, Cooley DA, Smith RT, Moak J 1987. Cryoablative techniques in the treatment of cardiac tachyarrhythmias. *Ann Thorac Surg* 43:138-143.

FIGURE 1

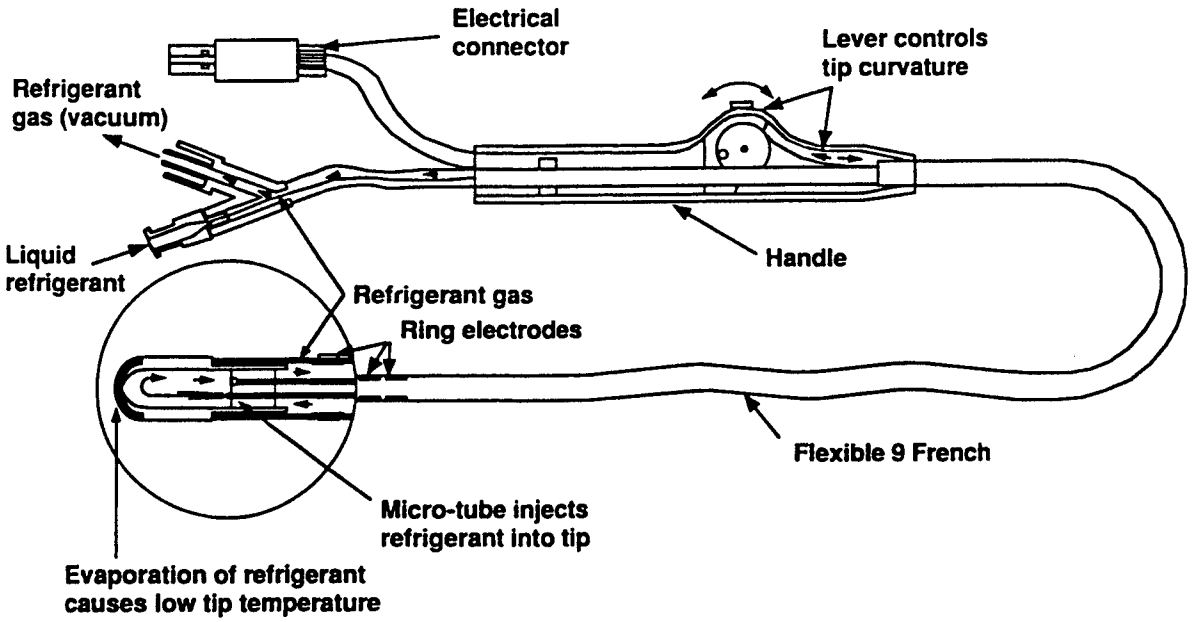
Electrical connector
Lever controls tip curvature
Refrigerant gas (vacuum)
Liquid refrigerant
Handle
Refrigerant gas
Ring electrodes
Flexible 9 French
Micro-tube injects refrigerant into tip
Evaporation of refrigerant causes low tip temperature

SESSION 2

Therapeutic Microwave Devices

Implantable Microwave Antennas for Thermal Therapy

Paul R. Stauffer

[a] University of California, Radiation Oncology Dept., San Francisco CA, 94143

ABSTRACT

The purpose of this article is to review the physical construction and power deposition characteristics of interstitial microwave antennas that may be used for highly localized heating of tissue at depth in the human body. Several different antenna designs are described and matched with potential clinical applications that range from moderate temperature Hyperthermia therapy to tissue-necrosing Thermal Ablation therapy. Typical clinical procedures are outlined for thermal treatment of target sites such as brain, prostate, heart, and gynecologic region tissues. Associated methods of implanting the antennas and coupling microwave energy into the surrounding tissue are also described, including the use of single or multi-chamber stiff, flexible or inflatable balloon type catheters, with or without circulating air or water cooling. With numerous references to the primary literature, this material should provide a framework for analyzing potential new applications for interstitial microwave antennas, as derived from the physical capabilities and limitations of the available hardware and techniques.

Keywords: Interstitial, microwave, antenna, array, implants, Thermal Therapy, Hyperthermia, prostate, brain, cancer

1. INTRODUCTION

Invasive heating techniques offer a number of advantages over external heating approaches for localizing heat in small tissue volumes at depth in the body. Over the past two decades, nine distinctly different interstitial heating modalities have emerged in response to changes in clinical treatment procedures and implant hardware. They consist of: 1) implantable microwave antennas operating between 0.4 and 2.5 GHz [1-3], 2) resistively-coupled radiofrequency (RF) electrodes driven at 0.3-3 MHz for local current field (LCF) heating between paired electrodes [4-7], 3) single-ended RF electrodes (CC-RF) driven at 8-27 MHz to couple current capacitively into surrounding tissue [8-10], 4) internal LCF type electrodes coupled inductively to external 6-13 MHz power sources via receiving loop antennas implanted just under the skin (IC-RF) [11], 5) 5-12 MHz tubular ultrasound (US) radiators [12-14], 6) laser illuminated, fiberoptic coupled crystal diffusers [15, 16], and three 'Hot Source' techniques: 7) hot water tubes [17-19], 8) DC voltage driven resistance wires [20-22], and 9) inductively coupled, thermoregulating ferromagnetic implants (Ferroseeds) [23]. These heating techniques have been described in numerous review articles [24-32] as well as the associated primary literature. Along with the rapid development of physical devices, there has been a parallel evolution of associated diagnostic tools and clinical treatment protocols. Thus despite innovative development efforts that have produced many quite functional interstitial heating techniques, technical challenges remain to optimize the application of interstitial heat to meet the clinical requirements.

This article presents an overview of microwave antenna technology that is available for thermal therapy of human tissues. A brief description of the design evolution of implantable microwave antennas is presented as an aid to understanding the current state of the art as well as future potential of the technology. Heating performance characteristics are summarized for representative microwave antenna designs and highlights of key investigations are referenced for more in depth study. Issues of appropriate thermometry and quality assurance procedures are covered elsewhere [26, 33-37]. The article ends with a summary of potential applications for interstitial microwave antennas, as derived from the physical capabilities and limitations of current designs.

2. IMPLANTABLE MICROWAVE APPLICATOR DESIGN

At frequencies above approximately 300 MHz, tissue acts as a lossy dielectric and the predominant mode of propagation for electromagnetic waves is radiative rather than conductive. In order to localize microwave radiation within a small tissue volume underlying normal tissues that must be protected, several miniature antenna designs have evolved based on 1-2 mm diameter flexible coaxial cable feedlines implanted in tissue inside insulating plastic catheters. Minor modifications to the tip portion of the implanted cables cause significant variations in the radiation patterns of single antennas as well as in the interaction of antenna arrays. These are discussed below.

SPIE Vol. 3249 • 0277-786X/98/$10.00

2.1 Dipole Antennas

The simplest antenna structure useful for interstitial implantation is a length of semi-rigid coaxial cable with a section of outer conductor removed to expose a length of inner conductor at the distal tip (Fig. 1a). This open-ended coaxial cable radiates most efficiently if implanted a distance of about $\lambda/4$ for use as a monopole above the skin surface ground plane [38], or if implanted to a depth of approximately $\lambda/2$ or twice the exposed conductor length. In this case, the structure operates as a half-wave dipole with current minimums at the tip and tissue entrance points, and a current maximum near mid-depth at the "junction" of inner and outer conductor sections. This produces a circularly symmetric gaussian (football) shaped heating pattern in tissue around the dipole. At the most commonly used microwave frequencies of 433, 915 and 2450 MHz, the wavelength in tissue is about 10, 4.5, and 1.7 cm respectively. Since the antennas are often implanted within catheters ($\varepsilon_r<3$) surrounded by a variable amount of air, the effective wavelength of radiation into the catheter-air-tissue load is somewhat longer than that of a bare antenna in tissue. In typical use, the resonant $\lambda/2$ length of an insulated dipole antenna in human soft tissue is about 6-8 cm at 915 MHz. Effects of catheter thickness, diameter and material on the radiation pattern, input impedance, and efficiency of dipole antennas have been studied extensively [39-45]. Because the clinical application of this technique requires adapting antenna heating patterns to fit different size tumors, many have also studied the effects of variable insertion depth. The literature documents significant changes in dipole antenna radiation patterns for different insertion depths, for both single antennas and antenna arrays [3, 46-49]. Mechling and Strohbehn [50] related the effects of these SAR pattern changes on the ability to heat several realistic deep seated tumor cases.

Power deposition in tissues surrounding the antennas is determined from $P_D = \sigma |E_T|^2/2\rho$ where σ and ρ are the tissue electrical conductivity and density and $E_T = \sum E_i$ is the total electric field summed from all antennas. For a single insulated dipole in a dissipative medium, E_T has a significant radially oriented field component along much of the antenna length in addition to the axially directed field that dominates in the junction plane [1, 56]. This complex field produces unavoidable variation of E_T (and thus SAR) along the dipole length in addition to the rapid falloff of SAR radially from the peak near the junction. The point receiving 50% of maximum SAR occurs within 2-3 mm of the antenna junction for a single antenna at 915 MHz [1, 57]. Methods of extending the radial penetration of heating 2-3 mm deeper into tissue have been identified, including the use of air [58-60] or water [61, 62] cooling of the antenna-tissue interface.

Since the target volume is often too large to heat with one antenna alone, antennas may be placed in an array configuration and driven either non-coherently to avoid interactions, or with phase-adjusted (coherent) signals to obtain enhanced heating between antennas where the individual fields add constructively. Because power deposition increases with E_T^2, SAR can be increased significantly near mid-depth in the array center where the electric fields are all directed predominantly parallel to the antenna axes. While this configuration produces good central array heating with larger antenna spacing, there is progressively less enhancement of SAR at increasing axial distance from the junction plane due to the increasing proportion of radial field components that cancel rather than add constructively. SAR patterns possible with phased arrays of dipole antennas have been studied by numerous investigators [43, 50, 51, 63-66] though their use in heterogeneous tissue requires extra care in order to obtain the theoretically expected phase coherence. For example, [67] reported significant perturbations of array heating patterns when one antenna of a four antenna array was shifted axially just 1 cm from perfect alignment. Additionally, HPC site visit tests identified a variation of up to 35% in efficiency for supposedly "identical" commercially supplied antennas [68]. This implies that equal power application to "in-phase" antenna arrays will not necessarily produce the theoretically expected central hot spot and suggests that independent dynamically controlled power and phase control of each antenna is essential.

As a means of reducing fixed phase errors from unmatched hardware and heterogeneous tissue loads while at the same time improving the uniformity of SAR within the implant volume, several investigators have demonstrated the advantages of using phase modulation to sequentially rotate in-phase "hot spots" around the array [69-73]. In fact, [74] reported a 300% increase in tissue volume heated above 41.5°C for an optimized phase rotation sequence. This technique has been successfully incorporated into a clinical system that combines power variation by computer-planned, time modulated phase delays to four-antenna arrays with automatic temperature control by multi-frequency radiometry [75-77]. Continuing one step further - since varying the insertion depth of one antenna was found to produce a phase shift in that source, an alternative method of producing controllable phase modulation by time sequencing of dipole insertion depth changes has been proposed [67]. While increasing system complexity, appropriately controlled cyclic scanning of antennas should be expected to provide further improvement in array heating uniformity due to controllable variation of SAR along each catheter as well as phase modulation shifting of the array focal hot spot.

Other efforts to improve control of SAR along the antenna length have produced several alternatives to the basic dipole structure as seen in Fig. 1. Modifications include the use of multiple active sections to extend the heating pattern [53], partial

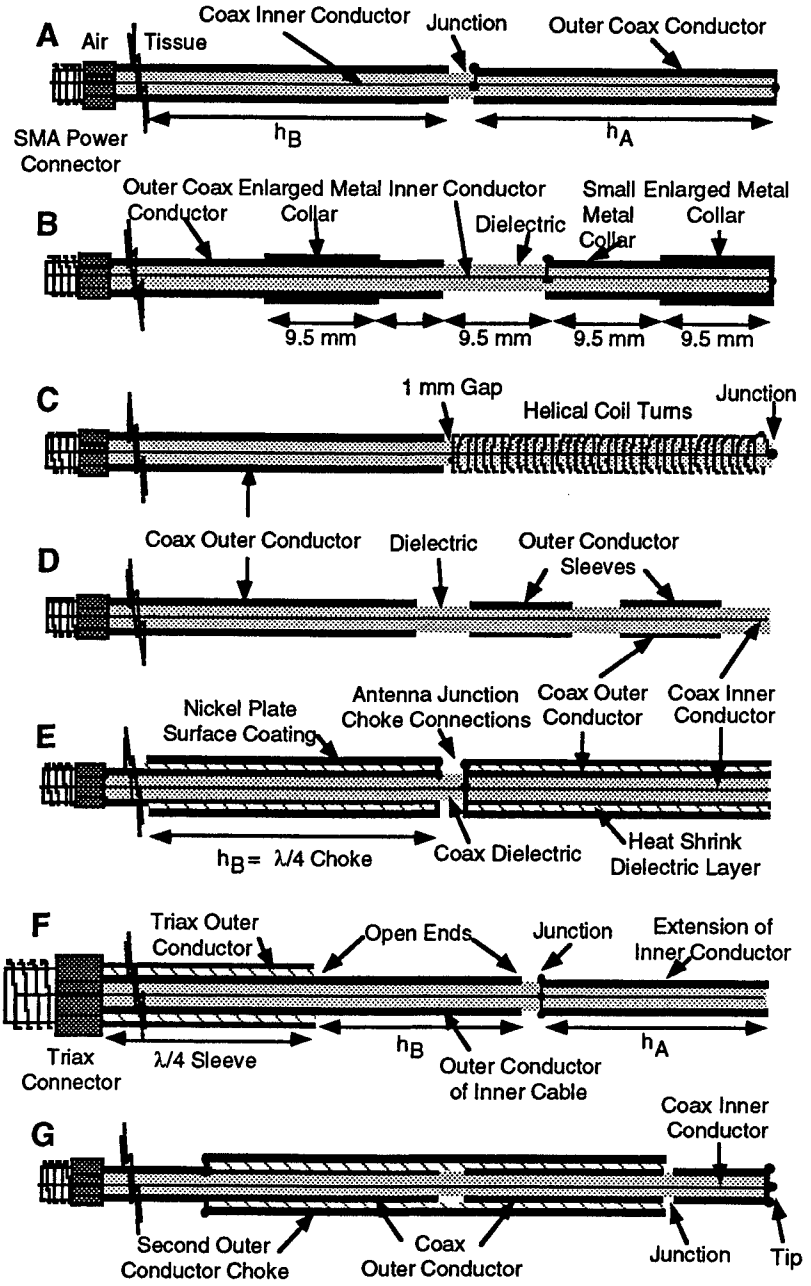

Fig. 1 - Schematic drawings of miniature coax cable interstitial microwave antennas intended for insertion within insulating catheters in lossy tissue: A) Dipole antenna showing extension of the coax inner conductor (h_A), and implanted length of outer conductor (h_B), separated at the 'junction' [1]. B) Dipole with enlarged diameter collars for increased capacitive coupling through the catheter wall which helps extend the heating pattern axially [51]. C) Helical Coil antenna with fine wire coil approximately 1 turn per mm axial length. The coil attaches to the inner conductor at the tip and has a 1 mm separation gap from the outer conductor [52]. D) Multi-node antenna with short sections of outer conductor removed to expose inner conductor 'nodes' [53] for extending the heating pattern axially. E) Dipole antenna with λ/4 chokes made from a metallic coating on the outer dielectric surface over both the h_A and h_B antenna sections [3]. F) Sleeve dipole antenna with λ/4 sleeve and transformed open end [54]. G) Sleeved coaxial slot radiator formed with second outer conductor choke and short tip portion shorted to the inner conductor at the tip [55].

wavelength chokes to restrict radiation back along the feedline [45, 54, 55], and enlarged diameter sleeves for preferential (capacitive) coupling of current through selected portions of the catheter insulation [51, 78, 79]. Although these efforts have produced stepwise improvements in tip heating and/or reduced feedline heating, most dipole-based arrays still demonstrate variable heating patterns for different insertion depths and little ability to adjust the effective heating length outside a limited range. Current 915 MHz dipole-type antennas appear useful for heating regions up to 3-5 cm long and approximately 1 cm in diameter per single antenna, or for larger regions that can be implanted with an array of antennas spaced up to 2.0 cm apart. For the larger tissue regions, the dipole-type arrays appear most appropriate for situations that can benefit from phase addition of fields near the array center (or peripherally between antennas with dynamic phase rotation) at the expense of heating towards the proximal and distal ends of the array (i.e. cases where the spacing of parallel antennas must be maximized but the antennas can be inserted 1-2 cm past the deep margin of the target [50, 80].

2.2 Helical Coil Antennas

One alternative antenna design merits separate consideration. The basic implantable Helical Coil antenna is constructed simply by stripping away a section of outer conductor from the distal end of a miniature (1-2 mm diameter) coaxial cable and winding a high density coil of fine wire (e.g. 29 ga Cu) tightly over the insulated inner conductor (Fig. 1C). With minor variations in radiated field, the coil may be connected to the coaxial cable feedline at the tip [2, 52, 81] or at both ends of the coil [82, 83]. Using an appropriate combination of coil length, diameter, and winding pitch for the given operating frequency, efficient coil radiators that restrict heating to a cylindrical region immediately surrounding the coil are easily constructed. For typical winding densities of approximately 1 turn per mm axial length, the spacing between turns is small compared to the wavelength at 915 MHz, but is still adequate to induce a predominantly circularly polarized electric field in tissue surrounding the coil. Numerous theoretical [84, 85] and experimental [2, 52, 81, 86-88] studies of Helical Coil antennas have demonstrated both independence of heating pattern on insertion depth in tissue and an improved extension of heating out to the antenna tip as compared to dipole type radiators. Fig. 2 shows SAR profiles along the antenna length at a radial distance of r=5 mm in tissue equivalent phantom. Note the close correspondence of SAR to the length and position of the coils (ranging from 1.1-3.0 cm long) which results from improved heating at the antenna tip and lack of overheating near the tissue surface even for coils implanted just 5 mm into the surface. Despite the advantages of improved heat localization around variable length coils located at any depth in tissue, helical coil antennas are not optimum for all applications. The antennas are normally driven with non-coherent microwave sources to limit interaction of the complex circularly polarized fields so the peak SAR occurs adjacent to each coil rather than in the tissue centrally between antennas. Several independent studies have reported comparative evaluations of heating patterns from the above antennas [2, 86-90]. In general, the data suggest that Helical Coil antennas may be preferable for heating smaller target volumes (1-4 cm diameter) in critical tissues where factors such as heating out to the antenna tip and a steep falloff of SAR proximal to the coil section are more important than maximizing the separation of antennas.

2.3 Implant catheters

Interstitial microwave antennas are normally placed inside <2 mm diameter plastic catheters in order to insulate the metal conductors from the lossy tissue load. Most catheter materials are soft and thin walled to minimize implant diameter and subsequent trauma and discomfort for the patient. Thus catheters are generally quite flexible by themselves and are implanted with the aid of a removable stiff inner stylet to obtain straight parallel arrays. Commonly used materials include thin walled Teflon, polyurethane, and similar plastics with low dielectric loss and high melting temperatures. The wide range of clinical applications for implantable microwave antennas necessitates an equally wide range of special purpose catheters. Our institution has a long and successful experience heating brain tumors using thick walled silicone catheters having slightly larger diameter (2.5 mm OD) and blunt, closed tips for insertion of Helical Coil antennas through burr holes in the skull [91, 92]. For this application, the silicone material provides the required high degree of flexibility to minimize trauma to sensitive brain tissues which may shift slightly relative to the skull during the multiple-day implant period. Recently, more sophisticated multi-channel catheters are becoming available to provide access for inflow and outflow of air or water cooling around the antenna. Although such designs are generally larger in diameter, they may be quite acceptable for use in natural body cavities such as the urethra. Astrahan [83] describes a modified silicone urological catheter with multiple lumens for microwave power cable, urine drainage, and temperature measurement cannulas within the same catheter as a helically wound copper ribbon antenna. Other multi-lumen silicone catheters have been reported [93] for use in implanting multiple microwave antennas and temperature monitoring probes in transurethral and esophageal heating applications. More recently, multi-lumen catheters have become available made with lightweight very thin wall materials to provide more effective temperature control of the applicator surface via water cooling of the catheter mounted antenna. For cavities that allow insertion of even larger diameter implants (e.g. rectum, vagina, esophagus), additional features may be added such as inflatable balloons to aid in positioning the antenna [94] and extra channels for filling, draining or insertion of multiple heat sources and probes. Valdagni [95] describes a large custom fitted vaginal applicator that allows placement of two microwave antennas and a water cooling system for heating cervical recurrences near the vaginal apex.

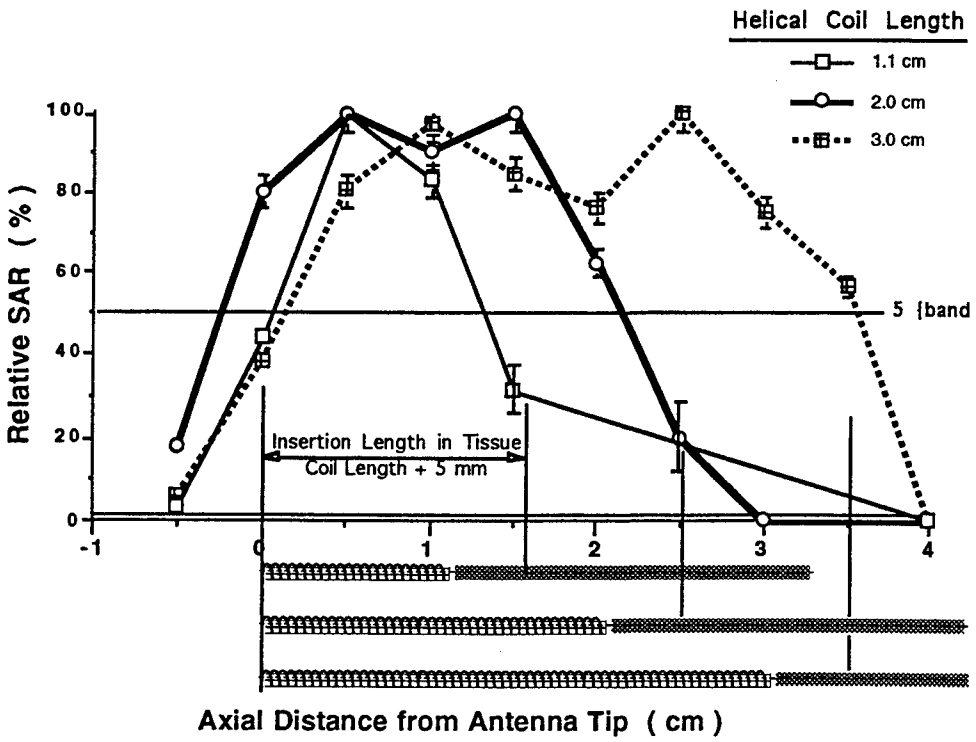

Fig. 2 - Measured relative SAR at a distance of 5 mm from three different length Helical Coil antennas in 915 MHz muscle tissue equivalent phantom. Insertion depth for each antenna was the coil length plus 5 mm. Standard deviations are for three independent trials. Similar curve shapes were measured for helical coil antennas with 1.3, 1.5, and 2.5, and 3.5 cm long coils (data not shown for clarity) and for antennas inserted deeper in tissue.

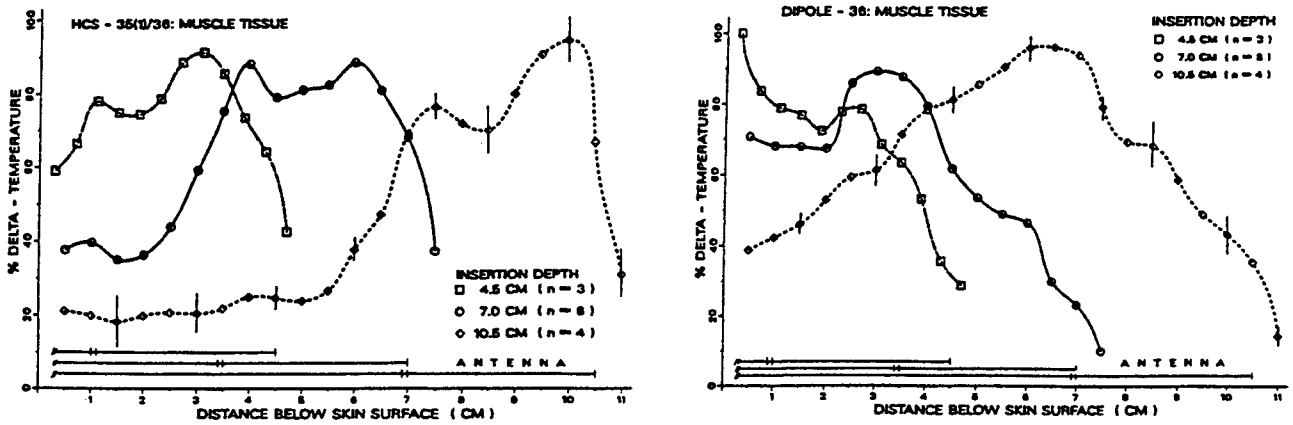

Fig. 3 - Normalized steady state temperature rise in dog thigh muscle in vivo at a distance of 5 mm from a simple dipole antenna (left) with 3.5 cm tip-junction length and implanted 4.5, 7, or 10 cm. Corresponding temperature distributions for a 3.5 cm long Helical Coil antenna (right) implanted to the same depths in the same implant sites. The standard error bars were calculated from independent measurements of %Temperature Rise in 3-8 different implant sites for each matched pair of heat trials. The maximum steady state temperature attained in each trial was approximately 43 °C.

3. POWER DEPOSITION CHARACTERISTICS

Numerous experimental studies of microwave antenna heating patterns clearly demonstrate that circularly-polarized Helical Coil type antennas provide superior independence of heating pattern from insertion depth changes and improved

extension of heating out to the antenna tips as compared to predominantly linearly-polarized dipole type antennas which produce less reproducible centrally peaked "football" shaped patterns [2, 48, 52, 83, 86, 87]. While exhibiting irregularities inherent with heterogeneous *in vivo* tissue measurements, Fig. 3 shows the basic differences between 915 MHz dipole (no $\lambda/4$ choke) and Helical Coil antenna radiation patterns as measured in canine muscle *in vivo*. While the Helical Coil antenna produces nearly identical heating patterns for insertion depths of 4.5, 7, and 10 cm, the dipole antenna unavoidably overheats skin and superficial tissues near the feedline entrance site for shallow insertion depth tests and changes to a much broader heating pattern when implanted deeper below the surface. For all insertion depths, the dipole leaves >1 cm of tissue near the tip below 50% of maximum temperature rise, in contrast to the Helical Coil which heats effectively (>50% of maximum temperature rise) out past the coil tip in all three trials.

For multi-antenna arrays of Helical Coil antennas driven non-coherently to minimize interaction between antennas, a similar close correspondence of heating pattern to the implanted coil lengths is obtained. Fig. 4 shows the steady state temperature profiles along two thermal dosimetry catheters implanted within an array of four Helical Coil antennas in a 3x3x2.5 cm human brain tumor that was located under 2.3 cm of normal brain tissue and with the antennas inserted through small burr holes in the skull. Two antennas had 2.0 cm long coils and two had 2.5 cm long coils in order to fit the irregular shaped tumor geometry. One mapping catheter was placed near the tumor periphery in the smaller lobe and the other catheter through tumor center. Note the close conformance of heating to the tumor extent as marked by vertical dashed lines along the two catheters.

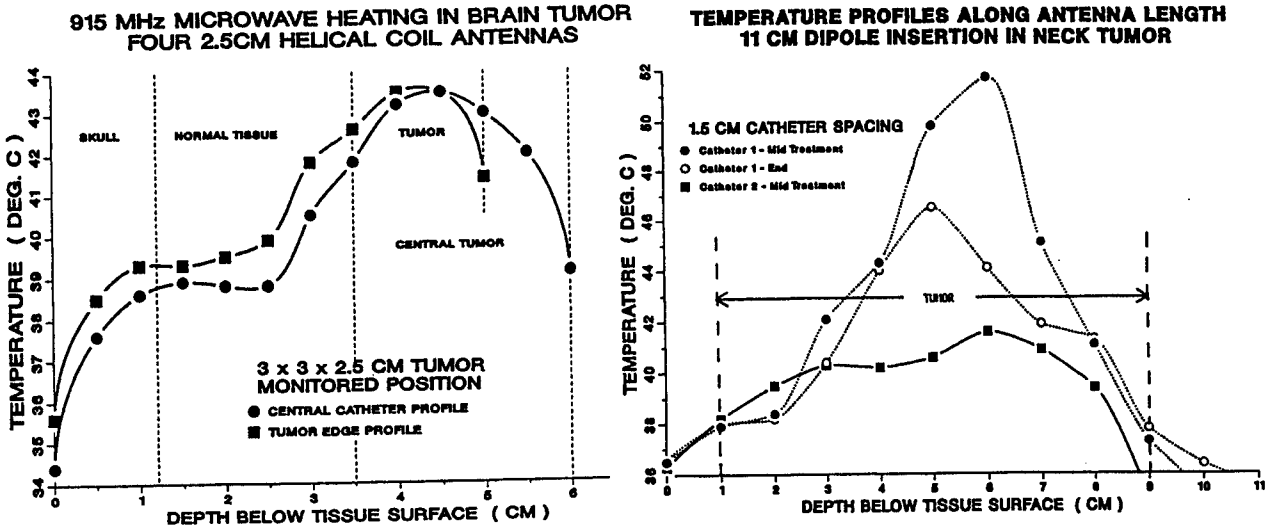

Fig. 4 - Steady state temperature profiles along two catheters in a 2 cm square array of Helical Coil antennas implanted in brain tumor. Note the excellent localization of heating in tumor and sparing of overlying normal brain, skull and scalp tissues. From Stauffer [26].

Fig. 5 - Steady state temperature profiles along two catheters inside an array of 12 dipole antennas with h_A = 3.5 cm junction-tip length and implanted 11 cm deep in an 8x8x5 cm neck tumor. Note the centrally peaked pattern which contributes to relatively poor coverage of the tumor with therapeutic temperatures.

4. CLINICAL APPLICATIONS

Potential clinical applications for implantable microwave antennas are extremely diverse. Regardless of tissue site, delivery of therapeutic heat from implanted microwave antennas may be considered either Hyperthermia Therapy (subtle heating generally <45°C for more than one 60 min treatment used as an adjuvant to radiation and/or chemotherapy for cancer) or Thermal Therapy (consisting of intentional tissue destruction from much higher temperatures for a single shorter heat session as sole therapeutic agent). Much of the early clinical experience with implanted microwave antennas was in the field of Hyperthermia for cancer therapy. For this purpose, it was generally required to implant an array of catheters at 1.5 - 2 cm spacing throughout the tumor target in an attempt to produce uniform moderate temperatures between 42.5 and 45 and maintain the temperature for one hour or longer. This procedure requires very uniform temperatures to avoid unacceptable pain in the awake patients while bringing minimum tumor temperatures up to a therapeutic level. For use in brain tumors where there is no pain response from heat, some investigators have allowed temperatures as high as 50°C during Hyperthermia if it is known to be in tumor rather than in surrounding normal tissues [92, 96]. Due to the critical nature of treating brain, implant catheters are placed stereotactically by the neurosurgeon following accurate CT-based treatment

planning and are normally within 1-2 mm of the desired position. Because brain tumors that are candidates for implant therapy generally range from 1 - 3.5 cm in diameter, they tend to fall on the small side for 915 MHz dipoles which require 6-8 cm insertion in tissue beneath the skull, and a bit too large for typical 2450 MHz dipole antennas [97]. The UCSF experience has found 915 MHz Helical Coil antennas to be ideally suited to heating brain tumors since they are easily constructed with coils in the 1-3.5 cm range that effectively restrict power deposition to deep lying targets of corresponding size without overheating normal dura, skull, and scalp tissues. Numerous investigators have used implanted microwave antennas for successful heat treatments of small targets (< 3-4 cm diameter) in sites such as brain, liver [98], bile duct [99], base of tongue, esophagus [93], cervix [100] and perhaps most frequently of all sites - prostate [101, 102]. Attempts to treat larger volumes in the neck, breast, bronchus, esophagus, and extremities with 915 or 433 MHz microwaves have been problematic due to the lack of adjustability of heating pattern along the antenna length. Longer helical coil antennas have been fabricated to heat the larger regions but they do not typically produce as uniform a heating pattern along the coil length [103, 104]. Fig. 5 shows thermal dosimetry results obtained during treatment of an 8x8x5 cm neck mass treated with a 12 implant array of dipole antennas placed freehand at about 1.5 cm spacing throughout the tumor mass. As discussed elsewhere [32], there are generally better techniques available than implanted microwave antennas for treating targets larger than about 60-100 cm^3 due to the lack of adjustability of wavelength dependent SAR variations along the antenna length.

In recent years, there has been increasing attention on the use of microwave antennas for non-oncologic applications such as treatment of benign prostatic hyperplasia (BPH) [105], intra-arterial thermal angioplasty [106], and cardiac ablation of arrhythmias [107-109]. These applications generally require a highly focused therapy with the intent to coagulate, ablate or in some way completely necrose the target tissue within a single heat session, often with the antennas inserted via natural body cavities for minimum trauma to the patient. For these higher power ablative procedures, the microwave antennas provide advantages over radiofrequency electrodes in that desiccation of tissue near the antenna surface does not interfere with power deposition at distance, but rather increases the effective penetration due to reduced attenuation of the electromagnetic field in desiccated tissue and reduced blood perfusion cooling near the source. When the antennas are located in or near critical normal tissues such as rectum however, the microwave antennas are normally mounted in surface temperature controlled catheters to protect tissues within 2-3 mm of the antenna surface.

The largest variables in determining optimum treatment configurations for a particular application are the target volume size, location relative to surrounding critical tissues, and heterogeneity of tissue properties. The targets may vary from small <2 cm^3 lesions [92] to large >200 cm^3 masses [6, 110] located either superficially or deep within the body. Tissue temperature distributions vary not only from non-uniform power deposition in heterogeneous tissue but also from dynamic changes in blood perfusion during heating. Treatment of larger volumes >60-100 cm^3 is probably best left to external heating techniques or to one of the alternative interstitial modalities discussed elsewhere [31, 32]. Because of power deposition directly in tissue at distance from the source, interstitial microwave antennas appear best suited for small to moderate size target volumes located near critical normal tissues where there is a need to minimize the number of implants. In addition to applications in easily reached superficial sites, microwave antennas have worked well for localized heat treatment of deep tissue targets in brain and prostate. The relative performance characteristics of dipole-based phase-modulated antenna arrays are compared with helical coil antenna arrays in Table 1. An expanded comparison of capabilities relative to alternative interstitial heating technologies is given in Stauffer [32].

5. SUMMARY

Over the past two decades, development of implantable microwave antenna technology has produced a number of special purpose antennas which address a large variety of clinical requirements. Key developments in this evolution are listed below with reference to representative papers for more in depth study. Early work on clinical interstitial microwave hyperthermia systems was reported separately for frequencies of 915 MHz [39], 2450 MHz [111], and 433 MHz [64]. Clinically practical implantable antenna designs were developed, including dipole [38, 40], multinode [53], $\lambda/4$ choke [45, 54, 55], variable diameter [51, 78], and helical coil [52, 82, 83, 85, 103] styles. Methods of improving the axial homogeneity and radial penetration of heat along the antenna, and/or protecting tissue immediately adjacent to the antenna were investigated, such as antenna surface cooling with circulating air [59] or water [61, 62]. Improved uniformity of SAR within an implant array volume by cyclic modulation of phase differences between adjacent dipoles has been studied [70, 72, 75] as well as tissue temperature monitoring and feedback control by multi-frequency radiometry from inside the interstitial antenna sources [76, 112].

While providing overlapping capabilities, the present armamentarium of interstitial microwave antennas provides extremely useful flexibility of heating patterns for the wide range of clinical treatment requirements. Commercial implementation of developments such as computer control of individual antenna amplitude and phase adjustment, air or water surface cooling, and concurrent interstitial multi-frequency microwave radiometry feedback control should produce

significant gains in volume heating effectiveness of microwave dipole arrays. In the meantime, localization of heat into small tissue volumes at depth is readily accomplished with variable length Helical Coil antennas that effectively restrict heating to a cylindrical region around each implanted coil. While engineering developments continue, existing microwave systems are already capable of producing relatively uniform, well-localized hyperthermia of many deep tissue sites. In short, interstitial microwave technology appears primed and ready to begin new protocols aimed at maximizing the therapeutic potential of heat alone or heat combined with radiation and/or chemotherapy for treatment of well-localized non-superficial disease.

Table 1. Comparative Evaluation of Heating Performance Characteristics

Performance Characteristic	Phase Modulated Dipoles	Helical Coil Antennas
Implant Spacing Requirements	++	+
Need for Parallel Alignment of Implant Catheters	-	++
Insertion Depth Independence	--	+
Knowledge of Tissue T_{max} within Array	--	--
Knowledge of Tissue T_{min} within Array	--	--
Current Accuracy of 3D Treatment Planning	+	--
Potential Accuracy of 3D Treatment Planning	+	+
Flexibility of Possible Heating Lengths	--	+
Tip Heating, Axial Uniformity	--	+
Heating Outside Implant Array Boundaries	++	+
Complexity and Expense of System	--	-
Treatment Setup including Planning and Connections	-	+
Thermometry Requirements	-	-
Adjustability of Lateral SAR (Temp) Uniformity	++	+
Adjustability of Axial SAR (Temp) Uniformity	--	+a
Ease of Realtime Control of Array Heating Uniformity	--	+a

KEY

++ Strong advantage of technique
+ Advantage of technique
- Disadvantage of technique
-- Strong disadvantage of technique
a By replacing with a source of different heating length during treatment.

6. REFERENCES

1. King, R.W.P., B.S. Trembly, and J.W. Strohbehn, "The electromagnetic field of an insulated antenna in a conducting or dielectric medium.". IEEE Transactions on Microwave Theory and Techniques, **31**: p. 574-583, 1983.
2. Satoh, T., P.R. Stauffer, and J.R. Fike, "Thermal dosimetry studies of helical coil microwave antennas for interstitial hyperthermia". International Journal of Radiation Oncology, Biology and Physics, **15**: p. 1209-1218, 1988.
3. Ryan, T.P., J.A. Mechling, and J.W. Strohbehn, "Absorbed power deposition for various insertion depths for 915 MHz interstitial dipole antenna arrays: experimental vs. theory". International Journal of Radiation Oncology, Biology and Physics, **19**: p. 377-387, 1990.
4. Doss, J.D. and C.W. McCabe, "A technique for localized heating in tissue: An adjunct to tumor therapy". Medical Instrumentation, **10**(16-21): p. 16-21, 1976.

5. Astrahan, M.A. and A. Norman, "A localized current field hyperthermia system for use with 192-iridium interstitial implants.". Medical Physics, **9**(3): p. 419-424, 1982.
6. Vora, N., *et al.*, "Interstitial implant with interstitial hyperthermia". Cancer, **50**(11): p. 2518-2523, 1982.
7. Corry, P.M., *et al.*, "Simultaneous hyperthermia and brachytherapy with remote afterloading", in *Brachytherapy HDR and LDR*, A.A. Martinez, C.G. Orton, and R.F. Mould, Editors, 193-204, Nucletron, Dearborn, MI. 1989.
8. Marchal, C., *et al.*, "Practical interstitial method of heating operating at 27.12 MHz.". Int. J. Hyperthermia, **5**: p. 451-466, 1989.
9. Lagendijk, J.J.W., "A microwave-like LCF interstitial hyperthemia system". Strahlenther Onkol, **166**: p. 521, 1990.
10. Deurloo, I.K.K., *et al.*, "Application of a capacitive-coupling interstitial hyperthermia system at 27 MHz: study of different applicator configurations". Physics in Medicine and Biology, **36**(1): p. 119-132, 1991.
11. Doss, J.D. and C.W. McCabe, "Total implants for hyperthermia application and thermometry". International Journal of Hyperthermia, **4**(6): p. 617-625, 1988.
12. Hynynen, K. and K.L. Davis, "Small cylindrical ultrasound sources for induction of hyperthermia via body cavities". International Journal of Hyperthermia, **9**(2): p. 263-274, 1993.
13. Diederich, C.J., "Ultrasound applicators with integrated catheter-cooling for interstitial hyperthermia: theory and preliminary experiments". International Journal of Hyperthermia, **12**(2): p. 279-97, 1996.
14. Diederich, C.J., *et al.*, "Direct coupled interstitial ultrasound applicators for simultaneous thermobrachytherapy: a feasibility study". International Journal of Hyperthermia, **12**(3): p. 401-19, 1996.
15. Bown, S.G., "Tumour therapy with the Nd:YAG laser.", in *Neodymium-YAG Lasers in Medicine and Surgery*, S. Joffe, M. Muckerheide, and L. Goldman, Editors, 51-59, Elsevier, New York. 1983.
16. Panjehpour, M., *et al.*, "Nd:YAG laser induced interstitial hyperthermia using a long frosted contact probe". Lasers in Surgery and Medicine, **10**: p. 16-24, 1990.
17. Schreier, K., *et al.*, "Preliminary studies of interstitial hyperthermia using hot water.". International Journal of Hyperthermia, **6**: p. 431-444, 1990.
18. Handl-Zeller, L. and O. Handl, "Simultaneous application of combined interstitial high- or low-dose rate irradiation with hot water hyperthermia", in *Interstitial Hyperthermia*, L. Handl-Zeller, Editor, 165-170, Springer-Verlag, Wien New York. 1992.
19. Brezovich, I., *et al. Hyperthermia with water-perfused catheters.* in *5th Intl. Symposium on Hyperthermic Oncology, 1988.* 1988. Kyoto: Taylor and Francis.
20. Marchosky, J.A., *et al.*, "Conductive, interstitial hyperthermia: A new modality for treatment of intracranial tumors", in *Consensus on Hyperthermia for the 1990's*, H.I. Bicher and e. al., Editors, 129-143, Plenum Press, New York. 1990.
21. DeFord, J.A., *et al.*, "Accuracy and precision of computer-simulated tissue temperatures in individual human intracranial tumors treated with interstitial hyperthermia". International Journal of Hyperthermia, **6**(4): p. 755-770, 1990.
22. Patel, U.H., J.A. DeFord, and C.F. Babbs, "Computer-aided design and evaluation of novel catheters for conductive interstitial hyperthermia". Medical & Biological Engineering & Computing, **29**: p. 25-33, 1991.
23. Stauffer, P.R., T.C. Cetas, and R.C. Jones, "Magnetic induction heating of ferromagnetic implants for inducing localized hyperthermia in deep seated tumors.". IEEE Transactions on Biomedical Engineering, **31**: p. 235-251, 1984.
24. Strohbehn, J.W., "Interstitial techniques for hyperthermia.", in *Physics and Technology of Hyperthermia*, S.B. Field and C. Franconi, Editors, 211-240, Martinus Nijhoff Publishers, Dordrecht,Boston,Lancaster. 1987.
25. Strohbehn, J.W. and J.A. Mechling, "Interstitial techniques for clinical hyperthermia", in *Physical techniques in clinical hyperthermia*, J. Hand and J. James, Editors, 210-287, Research Studies Press, Letchworth. 1986.
26. Stauffer, P.R., "Techniques for interstitial hyperthermia.", in *An introduction to the practical aspects of clinical hyperthermia*, S.B. Field and J.W. Hand, Editors, 344-370, Taylor & Francis, London, New York. 1990.
27. Trembly, B.S., T.P. Ryan, and J.W. Strohbehn, "Physics of microwave hyperthermia", in *Hyperthermia and oncology, Vol 3, Interstitial hyperthermia*, M. Urano and E.B. Douple, Editors, , VSP BV, Utrecht. 1992.
28. Hand, J.W., "Physical aspects of interstitial hyperthermia", in *Interstitial Hyperthermia*, L. Handl-Zeller, Editor, , Springer-Verlag, Wien, New York. 1992.
29. Handl-Zeller, L., ed. *Interstitial Hyperthermia.* , , Springer-Verlag, Wien, New York, 1992.
30. Seegenschmiedt, M.H. and R. Sauer, eds. *Interstitial and intracavitary thermoradiotherapy.* , , Springer Verlag, Berlin, Heidelberg, New York, 1993.
31. Seegenschmiedt, M.H., *et al.*, "Clinical practice of interstitial thermoradiotherapy", in *Thermoradiotherapy and Thermochemotherapy Vol. 2: Clinical Applications*, M.H. Seegenschmiedt, P. Fessenden, and C.C. Vernon, Editors, 207-262, Springer-Verlag, Berlin, Heidelberg. 1996.
32. Stauffer, P.R., C.J. Diederich, and M.H. Seegenschmiedt, "Interstitial heating technologies", in *Thermoradiotherapy and Thermochemotherapy Vol. 1: Biology, Physiology, and Physics*, M.H. Seegenschmiedt, P. Fessenden, and C.C. Vernon, Editors, 279-320, Springer Verlag, Berlin, New York. 1995.
33. Hand, J.W., "Invasive thermometry practice for interstitial hyperthermia", in *Interstitial and intracavitary thermoradiotherapy*, M. Seegenschmiedt and R. Sauer, Editors, 83-87, Springer Verlag, Berlin, Heidelberg, New York.

1993.
34. Emami, B., *et al.*, "RTOG quality assurance guidelines for interstitial hyperthermia". International Journal of Radiation Oncology, Biology and Physics, **20**(5): p. 1117-1124, 1991.
35. Shrivastava, P., *et al.*, "Hyperthermia quality assurance guidelines". International Journal of Radiation Oncology, Biology and Physics, **16**: p. 571-587, 1989.
36. Ibbott, G.S., *et al.*, *Performance evaluation of hyperthermia equipment*, ed. A.R. #26American Institute of Physics, New York, 1989.
37. ESHO, *Interstitial and intracavitary hyperthermia: a task group report of the European Society for Hyperthermia Oncology*. Ter Vergata Medical Physics Monograph Series. Vol. 4 Univ. Rome Tor Vergata, Rome, 1993.
38. Taylor, L., "Electromagnetic syringe". IEEE Transactions on Biomedical Engineering, **25**: p. 303-304, 1978.
39. Strohbehn, J.W., *et al.*, "An invasive antenna for locally induced hyperthermia for cancer therapy.". Journal of Microwave Power, **14**: p. 339-350, 1979.
40. de Sieyes, D.C., *et al.*, "Some aspects of optimization of an invasive microwave antenna for local hyperthermia treatment of cancer.". Medical Physics, **8**: p. 174-183, 1981.
41. Casey, J.P. and R. Bansal, "The near field of an insulated dipole in a dissipative dielectric medium". IEEE Transactions on Microwave Theory and Techniques, **34**: p. 459-463, 1986.
42. Jones, K.M., *et al.*, "SAR distributions for 915 MHz interstitial microwave antennas used in hyperthermia for cancer therapy.". IEEE Trans. Biomed. Engng. BME, **35**: p. 851-857, 1988.
43. Zhang, Y., *et al.*, "The determination of the electromagnetic field and SAR pattern of an interstitial applicator in a dissipative dielectric medium.". IEEE Transactions on Microwave Theory and Techniques, **36**(10): p. 1438-1444, 1988.
44. Iskander, M.F. and A.M. Tumeh, "Design optimization of interstitial antennas". IEEE Transactions on Biomedical Engineering, **36**(2): p. 238-246, 1989.
45. Wong, T. and B. Trembly, "A theoretical model for input impedance of interstitial microwave antennas with choke". International Journal of Radiation Oncology, Biology and Physics, **28**(3): p. 673-682, 1994.
46. Denman, D.L., *et al.*, "The distribution of power and heat produced by interstitial microwave antenna arrays: II. The role of antenna spacing and insertion depth.". International Journal of Radiation Oncology, Biology and Physics, **14**(30): p. 537-545, 1988.
47. James, B.J., *et al.*, "The effect of insertion depth on the theoretical SAR patterns of 915 MHz dipole antenna arrays for hyperthermia.". Int. J. Hyperthermia, **5**: p. 733-747, 1989.
48. Chan, K.W., *et al.*, "Changes in heating pattern of interstitial microwave antenna arrays at different insertion depths". International Journal of Hyperthermia, **5**(4): p. 499-507, 1989.
49. Zhang, Y., W.T. Joines, and J.R. Oleson, "Prediction of heating patterns of a microwave interstitial antenna array at various insertion depths". International Journal of Hyperthermia, **7**(1): p. 197-207, 1991.
50. Mechling, J.A., J.W. Strohbehn, and T.P. Ryan, "Three-dimensional theoretical temperature distributions produced by 915 MHz dipole antenna arrays with varying insertion depths in muscle tissue". International Journal of Radiation Oncology, Biology and Physics, **22**: p. 131-138, 1992.
51. Turner, P.F., "Interstitial equal-phased arrays for EM hyperthermia". IEEE Transactions on Microwave Theory and Techniques, **34**(5): p. 572-577, 1986.
52. Satoh, T. and P.R. Stauffer, "Implantable helical coil microwave antenna for interstitial hyperthermia.". International Journal of Hyperthermia, **4**(5): p. 497-512, 1988.
53. Lee, D., *et al.*, "A new design of microwave interstitial applicator for hyperthermia with improved treatment volume.". International Journal of Radiation Oncology, Biology and Physics, **12**: p. 2003-2008, 1986.
54. Hurter, W., F. Reinbold, and W.J. Lorenz, "A dipole antenna for interstitial microwave hyperthermia". IEEE Transactions on Microwave Theory and Techniques, **39**(6): p. 1048-1054, 1991.
55. Lin, J.C. and Y.J. Wang, "Interstitial microwave antennas for thermal therapy.". Int. J. Hyperthermia, **3**: p. 37-47, 1987.
56. King, R.W.P. and K. Iizuka, "Field of a half-wave dipole in a dissipative medium". IEEE Transactions on Antennas and Propagation, **11**: p. 275-285, 1963.
57. Babij, T.M., *et al.*, "Evaluation of heating patterns of microwave interstitial applicators using miniature electric field and fluoroptic temperature probes". International Journal of Hyperthermia, **7**(3): p. 485-492, 1991.
58. Eppert, V., B.S. Trembly, and H.J. Richter, "Air cooling for an interstitial microwave hyperthermia antenna: theory and experiment". IEEE Transactions on Biomedical Engineering, **38**(5): p. 450-460, 1991.
59. Trembly, B.S., E.B. Douple, and P.J. Hoopes, "The effect of air cooling on the radial temperature distribution of a single microwave hyperthermia antenna in vivo". International Journal of Hyperthermia, **7**(2): p. 343-354, 1991.
60. Yeh, M.M., *et al.*, "Theoretical and experimental analysis of air cooling for intracavitary microwave hyperthermia applicators". IEEE Transactions on Biomedical Engineering, **41**(9): p. 874-82, 1994.
61. Gentili, G.B., *et al.*, "A water-cooled EM applicator radiating in a phantom equivalent tissue-experiments and numerical analysis". IEEE Transactions on Biomedical Engineering, **38**(9): p. 924-928, 1991.
62. Moriyama, E., *et al.*, "Hyperthermia for brain tumors: improved delivery with a new cooling system.". Neurosurgery, **23**:

p. 189-195, 1988.
63. Strohbehn, J.W., B.S. Trembly, and E.B. Douple, "Blood flow effects on the temperature distributions from an invasive microwave antenna array used in cancer therapy.". IEEE Transactions on Biomedical Engineering, **29**: p. 649-666, 1982.
64. Trembly, B.S., "The effects of driving frequency and antenna length on power deposition within a microwave antenna array used for hyperthermia.". IEEE Transactions on Microwave Theory and Techniques, **32**: p. 152-157, 1985.
65. Wong, T.Z., *et al.*, "SAR patterns from an interstitial microwave antenna array hyperthermia system.". IEEE Transactions on Microwave Theory and Techniques, **34**: p. 560-567, 1986.
66. Jones, K.M., *et al.*, "Theoretical and experimental SAR distributions for interstitial dipole antenna arrays used in hyperthermia.". IEEE Transactions on Microwave Theory and Techniques, **37**: p. 1200-1209, 1989.
67. Clibbon, K.L., A. McCowen, and J.W. Hand, "SAR distributions in interstitial microwave antenna arrays with a single dipole displacement". IEEE Transactions on Biomedical Engineering, **40**(9): p. 925-932, 1993.
68. Wilkinson, D.A., *et al.*, "Calorimetric evaluation of antennas used for microwave interstitial hyperthermia". International Journal of Hyperthermia, **6**(3): p. 655-663, 1990.
69. Trembly, B.S., *et al.*, "Control of SAR pattern with an interstitial microwave antenna array through variation of antenna driving phase.". IEEE Transactions on Microwave Theory and Techniques, **34**(5): p. 568-571, 1986.
70. Trembly, B.S., *et al.*, "Comparison of power deposition by in phase 433 and phase-modulated 915 MHz interstitial antenna array hyperthermia systems.". IEEE Transactions on Microwave Theory and Techniques, **36**(5): p. 908-916, 1988.
71. Zhang, Y., W.T. Joines, and J.R. Oleson, "Microwave hyperthermia induced by a phased interstitial antenna array". IEEE Transactions on Microwave Theory and Techniques, **38**(2): p. 217-221, 1990.
72. Zhang, Y., W.T. Joines, and J.R. Oleson, "Heating patterns generated by phase modulation of a hexagonal array of interstitial antennas". IEEE Transactions on Biomedical Engineering, **38**(1): p. 92-96, 1991.
73. Trembly, B.S., *et al.*, "The effect of phase modulation on the temperature distribution of a microwave hyperthermia antenna array *in vivo*". International Journal of Hyperthermia, **10**(5): p. 691-705, 1994.
74. Camart, J.C., *et al.*, "Coaxial antenna array for 915 MHz interstitial hyperthermia: design and modelization - power deposition and heating pattern - phased array". IEEE Transactions on Microwave Theory and Techniques, **40**(12): p. 2243-2249, 1992.
75. Camart, J.C., *et al.*, "915 MHz microwave interstitial hyperthermia. Part II: Array of phase-monitored antennas". International Journal of Hyperthermia, **9**(3): p. 445-454, 1993.
76. Fabre, J.J., *et al.*, "915 MHz microwave interstitial hyperthermia. Part I: Theoretical and experimental aspects with temperature control by multifrequency radiometry". International Journal of Hyperthermia, **9**(3): p. 433-444, 1993.
77. Prevost, B., *et al.*, "915 MHz microwave interstitial hyperthermia. Part III: Phase II clinical results". International Journal of Hyperthermia, **9**(3): p. 455-462, 1993.
78. Roos, D. and A. Hugander, "Microwave interstitial applicators with improved longitudinal heating patterns". International Journal of Hyperthermia, **4**: p. 609-615, 1988.
79. Cerri, G., R. DeLeo, and V.M. Primiani, ""Thermic End-Fire" interstitial applicator for microwave hyperthermia". IEEE Transactions on Microwave Theory and Techniques, **41**(6/7): p. 1135, 1993.
80. Mechling, J.A., J.W. Strohbehn, and L.J. France, "A theoretical evaluation of the performance of the Dartmouth IMAAH system to heat cylindrical and ellipsoidal tumour models". International Journal of Hyperthermia, **7**(3): p. 465-483, 1991.
81. Stauffer, P.R., *et al. Thermal dosimetry characterization of implantable helical coil microwave antennas.* in *Ninth Annual Conference of the IEEE Engineering in Medicine and Biology Society.* 1987. Boston, MA: IEEE Press.
82. Wu, A., *et al.*, "Performance characteristics of a helical microwave interstitial antenna for local hyperthermia.". Medical Physics, **14**(2): p. 235-237, 1987.
83. Astrahan, M.A., *et al.*, "Heating characteristics of a helical coil microwave applicator for transurethral hyperthermia of benign prostatic hyperplasia". International Journal of Hyperthermia, **7**: p. 141-155, 1991.
84. Casey, J. and R. Bansal, "Finite length helical sheath antenna in a general homogeneous medium". Radio Science, **23**(6): p. 1141-1151, 1988.
85. Mirotznik, M.S., N. Engheta, and K.R. Foster, "Heating characteristics of thin helical antennas with conducting cores in a lossy medium - I. Noninsulated antennas". IEEE Transactions on Microwave Theory and Techniques, **41**(11): p. 1878-1886, 1993.
86. Ryan, T.P., "Comparison of six microwave antennas for hyperthermia treatment of cancer: SAR results for single antennas and arrays". International Journal of Radiation Oncology, Biology and Physics, **21**: p. 403-413, 1991.
87. Sathiaseelan, V., *et al.*, "Characteristics of improved microwave interstitial antennas for local hyperthermia". International Journal of Radiation Oncology, Biology and Physics, **20**: p. 531-539, 1991.
88. Ryan, T.P., *et al.*, "Experimental brain hyperthermia: techniques for heat delivery and thermometry". International Journal of Radiation Oncology, Biology and Physics, **20**: p. 739-750, 1991.
89. Tumeh, A. and M.F. Iskander, "Perfomance comparison of available interstitial antennas for microwave hyperthermia". IEEE Transactions on Microwave Theory and Techniques, **37**(7): p. 1126-1133, 1989.

90. Ryan, T.P., *et al.*, "Interstitial microwave hyperthermia and brachytherapy for malignancies of the vulva and vagina I: design and testing of a modified intracavitary obturator". International Journal of Radiation Oncology, Biology and Physics, **23**(1): p. 189-199, 1992.
91. Sneed, P.K., *et al.*, "Interstitial irradiation and hyperthermia for the treatment of recurrent malignant brain tumors". Neurosurgery, **28**: p. 206-215, 1991.
92. Sneed, P.K., *et al.*, "Thermoradiotherapy of recurrent malignant brain tumors". International Journal of Radiation Oncology, Biology and Physics, **23**(4): p. 853-861, 1992.
93. Astrahan, M.A., *et al.*, "A technique for combining microwave hyperthermia with intraluminal brachytherapy of the oesophagus". International Journal of Hyperthermia, **5**(1): p. 37-51, 1989.
94. Kitamura, K. and K. Sugimachi, "Thermoradiotherapy combined with chemotherapy for esophageal tumors", in *Thermoradiotherapy and Thermochemotherapy Vol. 2: Clinical Applications*, M.H. Seegenschmiedt, P. Fessenden, and C.C. Vernon, Editors, 85-94, Springer-Verlag, Berlin, Heidelberg. 1996.
95. Valdagni, R., M. Amichetti, and L. Cristoforetti, "Intracavitary hyperthermia: construction and heat patterns of individualized vaginal prototype applicators". International Journal of Hyperthermia, **4**(5): p. 457-66, 1988.
96. Sneed, P.K., *et al.*, "Survival Benefit of Hyperthermia in a Prospective Randomized Trial Of Brachytherapy Boost ± Hyperthermia For Glioblastoma Multiforme". International Journal of Radiation Oncology, Biology and Physics, **40**(2)1998.
97. Sneed, P.K., *et al.*, "Interstitial microwave hyperthermia in a canine brain model". International Journal of Radiation Oncology Biology Physics, **12**: p. 1887-97, 1986.
98. Murakami, R., *et al.*, "Treatment of hepatocellular carcinoma: value of percutaneous microwave coagulation". AJR Am J Roentgenol, **164**(1159-64)1995.
99. Wong, J.Y.C., *et al.*, "Intracatheter hyperthermia and iridium-192 radiotherapy in the treatment of bile duct carcinoma". International Journal of Radiation Oncology Biology Physics, **14**: p. 353-359, 1988.
100. Li, D.J., *et al.*, "Design of intracavitary microwave applicators for the treatment of uterine cervix carcinoma". International Journal of Hyperthermia, **7**(5): p. 693-701, 1991.
101. Petrovich, Z., *et al.*, "New trends in the treatmetn of benigh prostatic hyperplasia and carcinoma of the prostate". American Journal of Clinical Oncology, **16**(187-200)1993.
102. Goldfarb, B., T. Bartkiw, and J. Trachtenberg, "Microwave therapy of benign prostatic hyperplasia". Urologic Clinics of North America, **22**(2): p. 431-439, 1995.
103. Li, K.J., *et al.*, "Design and thermometry of an intracavitary microwave applicator suitable for treatment of some vaginal and rectal cancers". International Journal of Radiation Oncology, Biology and Physics, **10**(11): p. 2155-2162, 1984.
104. Liu, R.L., *et al.*, "Heating pattern of helical microwave intracavitary oesophageal applicator". International Journal of Hyperthermia, **7**(4): p. 577-86, 1991.
105. Kaplan, S.A. and C.A. Olsson, "State of the art: microwave therapy in the management of men with benign prostatic hyperplasia: current status". Journal of Urology, **150**: p. 1597-1602, 1993.
106. Landau, C., *et al.*, "Microwave balloon angioplasty effectively seals arterial dissections in an atherosclerotic rabbit model". Journal of the American College of Cardiology, **23**(7): p. 1700-7, 1994.
107. Langberg, J.J., *et al.*, "Catheter Ablation of the Atrioventricular Junction Using a Helical Microwave Antenna: A Novel Means of Coupling Energy to the Endocardium". Pacing and Clinical Electrophysiology, **14**(12): p. 2105-2113, 1991.
108. Wonnell, T.L., P.R. Stauffer, and J.J. Langberg, "Evaluation of microwave and radio frequency catheter ablation in a myocardium-equivalent phantom model". IEEE Transactions on Biomedical Engineering, **39**(10): p. 1086-95, 1992.
109. Liem, L.B., *et al.*, "In vitro and in vivo results of transcatheter microwave ablation using forward-firing tip antenna design". Pacing and Clinical Electrophysiology, **19**(11 Pt 2): p. 2004-8, 1996.
110. Stea, B., *et al.*, "Interstitial hyperthermia with ferromagnetic seed Implants: preliminary results of a Phase I clinical trial", in *Interstitial Hyperthermia*, L. Handl-Zeller, Editor, 183-193, Springer-Verlag, Wien, New York. 1992.
111. Samaras, G.M., "Intracranial microwave hyperthermia: heat induction and temperature control". IEEE Transactions on Biomedical Engineering, **31**(1): p. 63-69, 1984.
112. Mizushina, S., T. Shimizou, and T. Sugiura. *Precision of non-invasive temperature profile measurement using a multi-frequency microwave radiometric technique.* in *6th Intl. Conference on Hyperthermic Oncology.* 1992. Tucson, AZ.

Further Author Information -
P.R.S. Email: stauffer@radonc17.ucsf.edu; Phone: 415-476-4877; Fax: 415-502-5175

Microwave Occlusion Of The Rabbit Uterine Horn

Stuart Trembly[a], Ph.D., Paul Manganiello[b], M.D., and Jack Hoopes[b], D.V.M., Ph.D.

[a]Thayer School of Engineering, Dartmouth College, Hanover, New Hampshire 03755.[1]
[b]Dartmouth-Hitchcock Medical Center, Lebanon, New Hampshire 03756

ABSTRACT

A microwave applicator was developed and tested in a rabbit model, with the goal of developing a system to sterilize a human female through a transvaginal-transcervical-transuterine retrograde technique. The clinical procedure would create an occluding lesion in the isthmic portion of the human fallopian tube in an out-patient procedure. The microwave applicator consisted of a flexible coaxial cable from which the inner conductor was extended to form a resonant monopole antenna. The coaxial cable and monopole were placed within a sealed teflon catheter of 3 mm diameter. A second parallel catheter of 1 mm diameter was secured to the first to provide guidance for a microwave-immune thermometry probe. Following laparotomy exposure, the applicator was placed with a transvaginal-transcervical retrograde technique in each uterine horn in succession. The temperature was elevated to 65 °C for 5 minutes. Thirty days following treatment, there was marked constriction and discoloration of the treated site as well as significant architectural effacement of the tissue composing the uterine wall. In some cases, the uterine lumen was completely occluded. Future experiments will assess the tissue response to smaller thermal doses.

Keywords: fallopian tube, occlusion, microwave, sterilization

1. INTRODUCTION

Medical Significance

Historically, sterilization has been the most widely used contraceptive method among married women, being used by approximately 17%. Approximately 400,000 non-pregnancy-associated tubal sterilizations have been performed annually[1]. At Dartmouth-Hitchcock Medical Center, approximately 200 tubal sterilization's are performed annually, with over half of these being non-pregnancy-associated tubal sterilizations. Assuming reliable contraception could be attained, it would be desirable to develop techniques of female sterilization as an alternative to laparoscopic/laparotomy tubal ligation. Possible advantages could be: 1) elimination of general anesthesia; 2) use of an outpatient setting; 3) reduced cost; 4) increased simplicity and safety. For comparison, laparoscopic tubal ligation with cautery in general results in a failure rate of approximately two to six per thousand women.

Investigators have been trying to occlude the fallopian tube transcervically since as early as 1849 (Froriep method, silver nitrate solution).[2,3] The transcervical techniques can be reduced to either: 1) destructive techniques; and 2) mechanical obstruction. Recently, Shuber described his attempts at tubal closure with methyl 2-cyanoacrylate (MCA) in the delivery system FEMCEPT in 35 women.[4] On the fifth day of the woman's menstrual cycle, 0.6 cc of MCA was delivered without anesthesia in an outpatient setting. The balloon device, FEMCEPT, pushes the MCA from the uterine cavity and, ideally through both fallopian tubes. The procedure took less than five minutes to perform. Follow-up with continued

[1] Further author information-
email: b.stuart.trembly@dartmouth.edu; telephone: 603-646-2118; fax: 603-646-3856

SPIE Vol. 3249 • 0277-786X/98/$10.00

observation for 48 months has occurred in 15 patients, 42% of the total. Hysterosalpingography at 4 months revealed that 88% of the patients had complete obstruction with no pregnancies reported in these patients. In this small group of patients no complications were noted.

Although this procedure was easy, required no anesthesia, was performed in the outpatient department and was less costly than laparoscopic tubal ligation (LTL), there are some drawbacks. Its inability to cause bilateral obstruction in 12% of women in this series and 20% in other clinical trials brings to question its efficacy. In injecting the MCA, one is uncertain as to whether or not both tubes have been treated. Finally, although no complications have been reported to date, it is unclear what effect an accidental direct injection of MCA intravascularly would have. Other agents have been used, such as Quinacrine, which have a poor closure rate, requiring multiple applications. Hysteroscopy has been utilized to obstruct the fallopian tubes with either silastic plugs or intratubal devices. Although the pregnancy rates have been extremely low in those that are successfully occluded, 5-10% of the patients cannot have the device inserted or at least one device is expelled. As stated by one reviewer, the ideal hysteroscopic method has yet to be developed.[5,6,7,8]

Apparently, Kocks in 1878 attempted the first transuterine tubal cauterization with the intent of sterilization. Most recently this has been attempted hysteroscopically, with electrocautery or with neodymiun, yttrium, aluminum garnet (Nd:YAG) laser, bipolar radio-frequency, and a combined approach with photodynamic therapy (PDT), and argon laser. This has not gained acceptance due to failure to occlude the tubes bilaterally in 33% of the patients as well as such complications as uterine perforation, ectopic pregnancies, bowel damage, peritonitis and even death. This method at present requires general or regional anesthesia, is "blinded" past the take-off of the tubal ostea; is comparable LTL in cost and not comparable to LTL in efficacy or safety. It also requires an experienced hysteroscopist.[5]

Coaxially directed fluoroscopy[9] and new fiberoptic technology (Linear Everting Catheter, LEC)[10] now allow retrograde access to the human fallopian tube. The LEC provides a minimally invasive method to directly view the fallopian tube lumen without surgery, via a distensile membrane. This allows the safe passage of the fiberoptic viewing system through the uterus and into the fallopian tube. An energy delivery catheter could be placed in the fallopian tube via the same catheter used for visualization of the tube via the falloposcope. Alternatively, a catheter could be delivered coaxially over a guide wire which has been inserted through the fallopian tube under fluoroscopic direction. These procedures can be performed in a nonsurgical setting.[9,10] In 1985, Platia and Krudy reported the first successful transcervical catheterization of one obstructed fallopian tube in a woman with bilateral tubal obstruction.[9] This resulted in a subsequent pregnancy. They utilized the 3 French (0.99mm hole polyethylene catheter with a 0.018" pediatric guide wire). Today it is possible to hysterosopically access the Fallopian tube in a retrograde fashion[10,11,12]. We have investigated two means of energy delivery that could be used in a catheter placed by these techniques. Our experience with radio-frequency (RF) delivery is summarized below, and our study with microwave energy is described in detail in this paper.

Anatomy

The first two of the four segments that make up the human fallopian tube are the intramural and isthmic regions. The intramural segment, which enters the uterus, has a mean length of approximately 10 mm (range 9 to 17 mm). Its course is variable and can be straight, curved or tortuous[13]. The next segment, the isthmic segment, usually receives the occlusive treatment at the time of laparoscopic tubal ligation; it is approximately 20 to 30 mm long and contains the narrowest lumen of the fallopian tube. The average inside diameter is 0.4 mm (range 0.1 to 2.0 mm). This portion also has the thickest musculature of the extra-uterine tube[13]. Measurements of the thickness of the wall of the isthmic portion of the human tube have not been published. However, an unpublished study of hysterectomy specimens in parous females states that the isthmic portion of the tube is approximately 3 mm to 4 mm in diameter, measured from serosa to serosa in the freshly excised state After stenting the tube with a 3-French catheter, the mucosa-to-serosa distance was found to be approximately 1.2 mm to 1.5 mm[14].

Merchant, *et al.*[15], performed an anatomical study of the uterotubal junction, the intramural segment of the human fallopian tube[10]. The study consisted of 75 women who had undergone a hysterectomy because of uterine prolapse or dysfunctional uterine bleeding. They subjected the uteri to hysteroscopic visualization, hysterosalphingography, as well as gross dissection. Hysteroscopic visualization of the endometrial funnel, or pit, yielded measurements from 0.5 to 1.5 mm. Hysterosalphingography showed the tube was straight in 26-30% of the cases, curved in 30% of the cases, or convoluted in 40-44% of the cases, and its length varied from 4 to 14 mm. Histologically, as the intramural portion approaches the isthmus the longitudinal layer gets thinner while the outer circular layer thickens. The uterine musculature thins out markedly as the isthmic portion of the tube approaches. This could explain the bowel burns resulting from attempts at hysteroscopic tubal cauterization, since the bowel is in closer proximity. Merchant also hypothesized from his studies why caustic substances have not resulted in lower failure rates: 1) The wide endometrial funnel does not become completely obliterated. 2) In animal experiments, regeneration occurs in the endometrial funnel within one month. 3) Chemicals are not in contact with tubal epithelium long enough to result in permanent blockage. Rocca, *et al*, injected Latex into ten human hysterectomy specimens to examine the course of the intramural segment of the fallopian tube[15]. It appeared to have an "S-shaped course, neither identical in length and size, and with great variability in the degree of tortuosity." The length of the intramural segment varied from 9 to 17 mm, with a mean of approximately 10 mm.

At our institution we found from a sample of hysterectomy patients that the isthmic portion of the fallopian tube is approximately 2 to 3 cm in length and contains the narrowest lumen of any segment of the tube. The range is from 100 microns to 2 mm with an average width of 400 microns. It also has the heaviest musculature of the extrauterine tube. The average thickness of the entire isthmic portion of the fallopian tube is yet to be reported, however.

Previous Study

In 1988, we began to develop a bipolar radio-frequency (RF) catheter which could be passed retrograde into the fallopian tube, either under fluoroscopic guidance, or under direct visualization hysteroscopically. Our ultimate goal was to produce an obstructing lesion in the isthmic portion of the human fallopian tube. To investigate the technique, we sought first to occlude the uterine horn of a cat using the bipolar RF catheters. The feline uterine horn closely resembles the human Fallopian tube. By creating an RF lesion, we attempted to destroy the epithelial surface and a specific depth of underlying submucosa-muscularis which would then result in the collapse, coalescence, fibrosis, stricture and occlusion of the uterine horn[16].

Our results indicated that the RF heating may have been self-limiting, in that charring on the surface of the applicator may have blocked the flow of RF current from the electrodes of the applicator and thus prevented further heating at a desirable depth. The result could be shallow damage to the uterine wall that would not result in occlusion or that would permit recanalization. Consequently, we have sought to develop a system that will not be self-limited in this way. A microwave applicator heats tissue through a physical mechanism that does not depend on the flow of current from a metallic conductor in direct contact with tissue. In fact, the energy may pass through an insulating outer layer of the applicator, which furthermore is biocompatible, for example, teflon. The mechanism of microwave heating of tissue is described in the following section.

Mechanism of Microwave Heating

The system we have developed elevates the temperature of living tissue through absorption of microwave energy. The energy is delivered by an applicator inserted into proximity with the tissue to be heated. The applicator contains a coaxial cable for transferring microwave energy from a generator outside the body to the site of heating without significant deposition of energy in overlying tissue. At the site of intended heating, the applicator contains a monopole antenna for coupling microwave energy to the

surrounding tissue without direct contact of a metal conductor with tissue. The monopole is embedded in a cylinder of insulating, biocompatible material, such as polytetraflouroethylene (teflon).

At the site of intended heating, the oscillating current and charge on the monopole conductor produce oscillating electric and magnetic fields in the surrounding tissue. The oscillating electric field causes polar molecules in tissue, such as water, to rotate in place, generating frictional heating. The presence of an overlying layer of insulating material does not prevent the formation of electric and magnetic fields in tissue, because the length of the monopole is chosen to form a resonant or approximately resonant structure. Such a structure ensures coordination of the electric and magnetic fields such that they sustain themselves outside the applicator and thus radiate energy away from the applicator. The length of a resonant structure is inversely proportional to the microwave frequency and is inversely proportional to the square root of a weighted average of the permittivity (dielectric constant) of the insulating layer and the surrounding tissue. At 915 MHz or 2450 MHz (MHz = 10^6 cycles/second), the length of an insulated monopole at or near resonance in tissue is one centimeter to several centimeters. These values of microwave frequency are those permitted by the FCC for use in industrial, scientific, or medical applications (ISM frequencies). At frequencies less than microwave frequencies, say less than 100 MHz, the length of a resonant structure would be impractically long for use in the human body. Consequently, a low-frequency system, such as a radio-frequency applicator, must instead incorporate a metallic conductor in direct contact with tissue to permit the flow of a conduction current. This heats tissue through the translational motion of dissolved ions in tissue, not through the rotation of polar molecules. We found in our earlier study described above that the intense conduction currents produced at the surface of a metal conductor in contact with tissue may cause charring of tissue and hence poor control of the heating process. We have developed a system based on a different physical principle to avoid this problem.

2. METHODS

Design and Construction of Microwave Applicator

The microwave applicator is depicted in Fig. 1. In its simplest form, it consists of a 1.6 mm diameter, flexible, coaxial cable with an extension of the inner conductor to form a monopole at the location of intended energy deposition. The point at which the inner conductor emerges from the feedline is called the driving point, or junction. The coaxial cable is placed within one lumen of a custom catheter described below; a second lumen is available for a thermometry probe with which to measure tissue temperature. The theory of an insulated microwave antenna surrounded by tissue is described in King, *et al.*[17]. With this theory, the resonance length of the antenna can be computed as an inverse function of frequency. At the resonance length, the antenna deposits energy most efficiently. Preliminary calculations show this length to be approximately 3 cm at 915 MHz. In order to fit the anatomy of our subjects, it would be desirable to use a shorter monopole, as would be possible at a higher frequency, such as the next-highest ISM frequency of 2450 MHz. However, the 50 watt microwave generator available to us operates at 915 MHz, and we investigated our technique at this frequency for practical reasons.

We constructed the antenna from standard flexible coaxial cable (1.6 mm OD, 50 ohms), from which the outer braid was removed at the tip to form the monopole of resonance length. At the proximal end of the cable, we installed a standard, miniature microwave connector (SMA type) for connection to the microwave generator. The antenna was placed within a catheter of 2.2 mm outer diameter. We measured the impedance of the antenna over the frequency range 700 MHz to 1100 MHz with a Hewlett Packard Network Analyzer Model 8753C. The length of the distal section of the prototype antenna was trimmed or lengthened, as appropriate, to make the impedance purely real at 915 MHz. The voltage reflection coefficient was less than 0.1.

To characterize the heating pattern of the applicator, we immersed it in tissue-equivalent phantom, a semi-transparent, viscous liquid mixture with the same conductivity and dielectric constant as soft tissue at microwave frequencies[18]. The applicator was secured to a sheet of liquid crystal, which indicates temperature over a 5 °C range with a calibrated color change (Edmund Scientific, Barrington, NJ). The liquid crystal sheet had a rectangular cutout to accommodate the applicator in a plane parallel to its long

axis. We photographed the liquid crystal sheet at 2 minutes after application of 30 watts of microwave power in order to visualize the heating pattern of the applicator. We found the length heated above 40 °C at 2 minutes was a 3 cm zone extending 2 cm proximal to the junction.

After the first heating of a rabbit, we constructed a second applicator in the form of a choked dipole in order to prevent significant energy deposition on the feedline. The choke consists of a new cylindrical conductor insulated from the feedline by a dielectric layer (Fig. 2). The new conductor is connected electrically to the feedline only at the antenna junction. The gap between the feedline and new conductor has a length of approximately a quarterwavelength; consequently, an approximate choke, or open circuit, is formed on the feedline, according to transmission line theory[19]. This approximate choke tends to block the microwave current that otherwise would flow on the feedline and heat tissue proximal to the target zone[20]. We refer to this applicator below as the choked dipole. This antenna was inserted in a catheter of 3 mm OD. As noted above, the length of this heating zone may be greater than required ultimately in a clinical system and is a practical consequence of our use of 915 MHz in this study. The microwave applicator we designed allowed us to perform a pilot study of microwave heating in vivo.

Other components in the heating system are the microwave generator itself, the microwave-immune thermometry system, and hardware associated with measuring and controlling microwave power (Fig. 3). The microwave generator (AMT Model 1120) produces 50 watts of microwave power in each of its eight channels. We used only one channel. The power is controlled manually by adjusting a dc voltage applied to the back panel of the generator. The dual directional coupler diverts one-hundredth of the power applied to the applicator to allow measurement of it by a power meter; this is referred to as forward power. It also diverts one-hundredth of any power reflected from the applicator for the same purpose. This serves to confirm normal operation of the applicator during a procedure, since reflected power is negligible when the applicator is functioning normally. A critical component is the microwave-immune thermometry system (Luxtron, Mountain View, CA). The fiber optic probe of this system is 0.5 mm in diameter, and it fits within the second lumen of our custom catheter. With it we can measure the temperature of tissue adjacent to the applicator during a treatment to confirm conformance to our treatment protocols described below.

Animals

We chose anestrus rabbits as the animal model for the following reasons: the uterine horn of the anestrus rabbit is similar in size and shape to the isthmic segment of the human fallopian tube; the animal can be maintained easily in anestrus; experimental manipulation is technically easy and morbidity tends to be extremely low; and the animals are colony bred, can thus allowing selection for age and weight uniformity. This study was approved by the Dartmouth College Institutional Animal Care and Use Committee (IACUC) .

Pre-estrous female rabbits (3.5 to 5 kg) were purchased from Milbrook Farms (Amherst, MA). All treatments were performed under general anesthesia, which consisted of ketamine/xylazine (2.0/0.2 mg/kg IM) induction followed by intubation and maintenance anesthesia (1.5% halothane/100% oxygen). All rabbits were prepared for laparotomy using standard aseptic techniques. A midline incision was made, then the bladder was elevated out of the incision and separated from the lower uterine segment. The uterus was isolated, and connective tissue was dissected away to allow a nearly straight insertion into one uterine horn with a transvaginal-transcervical approach. The microwave catheter was then inserted. The uterine horn was isolated thermally from adjacent bowel and bladder by saline-filled balloons packed around the horn. After the microwave heat treatment, an ovariectomy was performed.

All animals survived the experimental treatments without serious morbidity, and were sacrificed with intravenous KCl, following deep anesthesia, at 31 (± 4) days after treatment. Immediately following euthanasia, each uterus was removed *en bloc* and hysterosalpingographic guidance was performed *ex vivo*. The tissue was placed in neutral 4% neutral buffered formaldehyde and submitted for histologic processing. Five tissue sections were taken from the lesioned or control segment in each horn. Representative histologic sections were taken through the treated region, as well as proximal and distal to the treated area.

Treatment Protocol

Rabbit I was treated with the unchoked monopole (Fig. 1) in both uterine horns. In the left horn, a maximum temperature of 65 °C was maintained for 10 minutes by applying 7 watts of forward microwave power at 915 MHz. In the right horn, a maximum temperature of 70 °C was maintained for 5 minutes by applying 10 watts of forward microwave power. The reflected power was approximately 10%.

Rabbits II through IV were treated with the choked dipole (Fig. 2) in both uterine horns. The target temperature, time at target temperature, and microwave power for each horn in each subject are shown in Table 1. Reflected power was approximately 10%. In five of the six treatments in Rabbits II through IV, the temperature distribution adjacent and parallel to the microwave catheter was measured in the steady-state.

Table 1.
Summary of Rabbit Treatments

Rabbit	Applicator	Horn	Target	Time	Power
I	Unchoked	left	65 °C	10 min	7 W
		right	70 °C	5 min	10 W
II	Choked	left	65 °C	5 min	33 W
		right	75 °C	8 min	50 W
III	Choked	left	65 °C	6 min	40 W
		right	55 °C	5 min	20 W
IV	Choked	left	70 °C	5 min	30 W
		right	70 °C	5 min	30 W

3. RESULTS

The longitudinal temperature distribution measured in the steady-state at the surface of the microwave catheter had a maximum value located approximately at the antenna junction; temperature values decreased distal and proximal to the junction. To quantify the length of the temperature distribution, the value of body temperature was subtracted from the maximum temperature, and this value was divided by two to yield a quantity defined as ΔT_{50}. The length along the applicator surface at which temperatures above ΔT_{50} were measured was defined as L_{50}. For five treatments with the choked dipole, the average value of L_{50} was 5.3 cm ± 0.8 cm.

Lesions were observed on the serosa of the uterine horn immediately after treatment. The average length of lesion was 3.8 cm ± 1.5 cm, and the location of the lesion center was on average 1.6 cm ± 0.5 cm proximal to the applicator junction (Fig. 2). The lesions did not extend around the entire circumference of the horn, but instead involved a quarter or half arc of a circle. No charring of tissue was observed at any location in any of the treatments.

After sacrifice, gross assessment of the treated uteruses showed pale discoloration and a markedly reduced circumference of the treated segment of uterus horn. The normal uterine anatomy, which contains numerous folds and villi covered by specialized columnar epithelium on the surface and numerous glands in the submucosa (Figure 4). By contrast, the 30-day post-treatment uterine horns showed very marked edema and vascular dilatation resulting in significant thickening of the submucosa, near complete loss of the submucosal glands and the covering epithelium and the influx of a mixed inflammatory infiltrate. These pathologic changes generally resulted extensive architectural effacement of the inner portion of the uterine wall anatomy and occlusion of all or part of the lumen space (Figures 5 & 6). In some cases, the tissue damage and resultant healing were significant enough to cause complete occlusion of the lumen. In these instances, the lumen and adjacent tissues were completely replaced by fibrosis and inflammation.

4. DISCUSSION

In the first rabbit, acute blanching of the overlying bowel was observed, indicating significant thermal damage beyond the target tissue. In subsequent experiments, the uterine horn was isolated thermally to allow us to study the target tissue only. In later studies we must reduce the thermal dose, while still producing blockage of the horn, or devise a modified technique to avoid thermal damage to overlying bowel. In contrast to the effects of RF heating, no charring of tissue was observed. The length of the heated zone we observed was suitable for a study of tissue effects, but it may be too long for tubal occlusion in a human patient. In future studies, we plan to use a generator operating at 2450 MHz, since the resonance dipole length and hence value of L_{50} will decrease in inverse proportion. External lesion formation appears to be sensitive to the degree of contact of the applicator within the horn, since lesions did not form around the entire circumference. However, this did not seem to affect effacement or internal occlusion of the horn.

We believe that highly-controlled microwave hyperthermia may be used to safely and effectively occlude the human fallopian tube in an out-patient setting. While indicating the need for further refinement and extensive testing, the results presented here suggest not only that the anestrous rabbit uterus is an appropriate and useful animal model for studying human fallopian tube occlusion, but that complete tubal occlusion can be produced accurately and effectively with the appropriate microwave applicator. Our initial experimental treatments were not without complications, including acute blanching of the bowel overlying the treated portion of uterus. This effect demonstrated the potential for significant thermal damage beyond the target tissue if an inappropriate thermal dose was used. In subsequent experiments, the uterine horn was isolated from the bowel to allow for a more intense study of the microwave hyperthermia effects in the target tissue (uterus), without the risk of damaging a critical organ.

The pathologic changes resulting from our treatment are similar to changes seen with other types of energy (laser , PDT, cryotherapy, caustic substances etc). However, we believe microwave hyperthermia treatment can be more precisely controlled in this setting than other currently available energy sources can be. This is especially important in an environment which contains a number of cell types with different thermal sensitivities, and, potentially, very sensitive bowel tissue immediately adjacent to the structure being treated, the fallopian tube.

It now seem clear that for this treatment to be effectively tested in a clinical setting, we must continue to temporally reduce and refine the thermal dose and pathology , while improving on the uniformity and degree of the tubal blockage. The occlusion must have sufficient length and mass to prevent recanalization of the occlusive scar (fibrosis) and produce absolute, permanent blockage of sperm and egg migration along the tube. Our current studies are designed to modify and optimize device placement and the safety and efficacy of the heating technique.

5. CONCLUSIONS

A microwave applicator within a 3 mm OD catheter has been developed for inducing thermal blockage of the uterine horn of a rabbit. When a maximum temperature of 70 °C was maintained for 5 minutes, the architecture of the uterine horn was completely effaced four weeks after treatment. During the treatment, no charring of tissue occurred and no associated self-limiting of heating occurred, as has been observed with radio-frequency applicators. Overlying bowel was damaged during one treatment, in which the uterine horn was not thermally isolated. In future studies, smaller thermal doses delivered by a 2450 MHz generator will be studied with the aims of attaining blockage of the horn without effacement of the tissue and the aim of avoiding damage to overlying bowel tissue.

6. REFERENCES

1. Greenspan JR, Phillips JM, Rubin GL, Rhodenhiser EP, Ory HW. "Tubal sterilizations performed in freestanding, ambulatory-care surgical facilities in the United States in 1980." *J Reproductive Med* 1984; 29(4):237-241.
2. Siegler AM, Valle RF. "Therapeutic hysteroscopic procedures (Modern trends)." *Fertil Steril* 1988; 50(5):685.
3. Zipper JA, Stachetti E, Medel M. "Human fertility control by transvaginal application of Quinacrine on the fallopian tube." *Fertil Steril* 1970; 21(8):581.
4. Shuber J. "Transcervical sterilization with the use of methyl 2-cyanoacrylate and a newer delivery system (the FEMCEPT device)." *Am J Obstet Gynecol* 1989; 160:887-889.
5. Donnez J, Malvaux V, Nisolle M, Casanas-Roux F. Hysteroscopic sterilization: An atlas of laser operative laparoscopy and hysteroscopy. Pearl River, NY: Parthenon Publishing, 1994, 337-342.
6. Zatuchini G. "Contraceptive technologies for the future." *Curr Prob Obstet Gynecol* 1984; 7(11):14-37.
7. Neuwirth RS. Hysteroscopy: Major problems in obstetrics and gynecology. Philadelphia: Saunders, 1975:59-71.
8. Eddy CA, Pauerstein CJ. "Tubal reproductive function and the development of reversible sterilization techniques." In: Sciarra J, Zatuchni G, Speidel J, editors. Reversal of sterilization. New York: Harper and Row, 1978.
9. Platia MP, Krudy AG. "Transvaginal fluoroscopic recanalization of a proximally occluded oviduct." *Fertil Steril* 1985; 44(4):704.
10. Dunphy B, Taenzer P, Bultz B, Ingleson B, Hartman D, Dodd C. "A comparison of pain experienced during hysterosalpingography and in-office falloposcopy." *Fertil Steril* 1994; 62(1):67-70.
11. Kerin J, Daykhovsky L, Grundfest W, Surrey E. "Falloposcopy: A microendoscopic transvaginal technique for diagnosing and treating endotubal disease incorporating guide wire cannulation and direct balloon tuboplasty." *J Reproductive Med* 1990; 35(6):602-612.
12. Pearlstone A, Surrey E, Kerin J. "The linear everting catheter: A non-hysteroscopic, transvaginal technique for access and microendoscopy of the fallopian tube." *Fertil Steril* 1992; 56(4):854-857.
13. Rocca M, el Habashy M, Nayel S, Madwar A. "The intramural segment and the uterotubal junction, an anatomic and histologic study." *Int J Gynecol Obstet* 1989; 28:343-349.
14. Manganiello, PD, unpublished study.
15. Merchant RN, Prabhu SR, Chougale A. "Uterotubal junction - morphology and clinical aspects." *Int J Fertil* 1983; 28(4):199-205.
16. Manganiello PD, Hoopes PJ, Sueoka BL, Valentine DR, "Radiofrequency Lesioning Of The Feline Uterine Horn: A Model For Fallopian Tube Occlusion In Women," submitted to *The Journal of the American Association of Gynecologic Laparoscopists*, June , 1997.
17. King, RWP, Shen, LC, Wu, TT, "Embedded insulated antennas for communication and heating," *Electromagnetics 1:51-72, 1981.*
18. Hartesgrove, G, Kraszewski A, and Surowiec A, "Simulated biological materials for electromagnetic radiation absorption studies," *Bioelectromagnetics* 8:29-36, 1987.
19. Jordan EC and Balmain KG, Electromagnetic Waves and Radiating Systems (Englewood Cliffs, NJ: Prentice-Hall), 1968.
20. Jones, K.M., J.A. Mechling, B.S. Trembly, and J.W. Strohbehn, "SAR Distributions for 915 MHz Interstitial Microwave Antennas Used in Hyperthermia for Cancer Therapy" *IEEE Transactions on Biomedical Engineering* 35(10):851-857, October 1988.
21. Colby E, "Suppression/induction of estrus in cats: Current therapy in theriogenology." In: David A. Morrow, editor. Current therapy in theriogenology: diagnosis, treatment and prevention of reproductive diseases in animals. Philadelphia: Saunders 861-865, 1980.

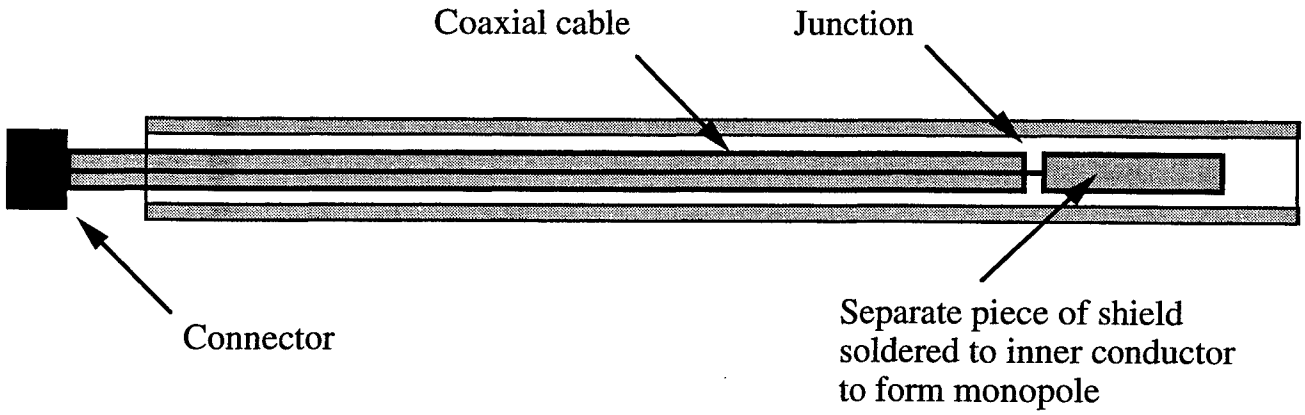

Fig. 1. Unchoked Monopole

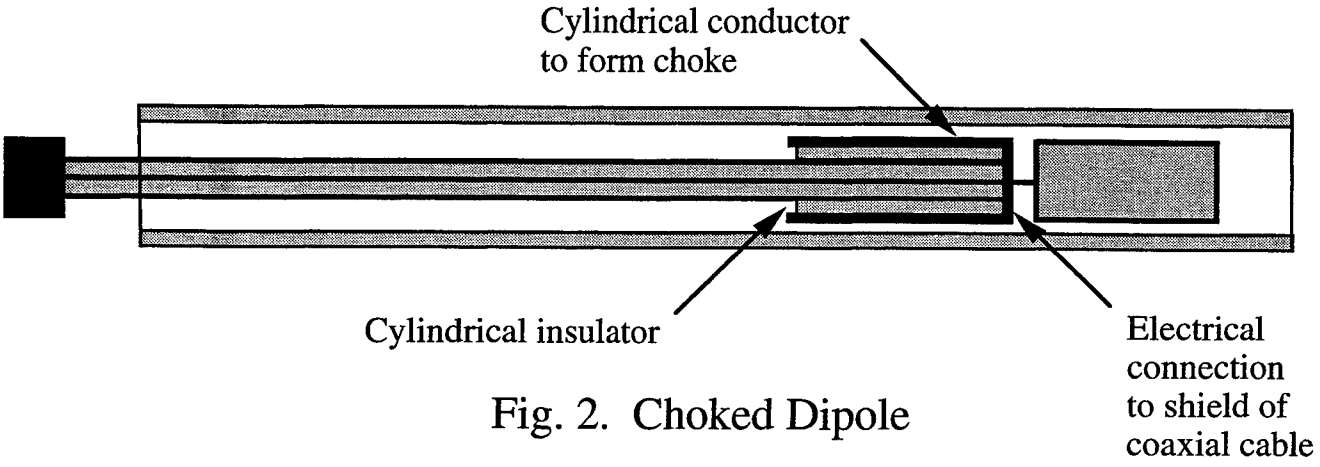

Fig. 2. Choked Dipole

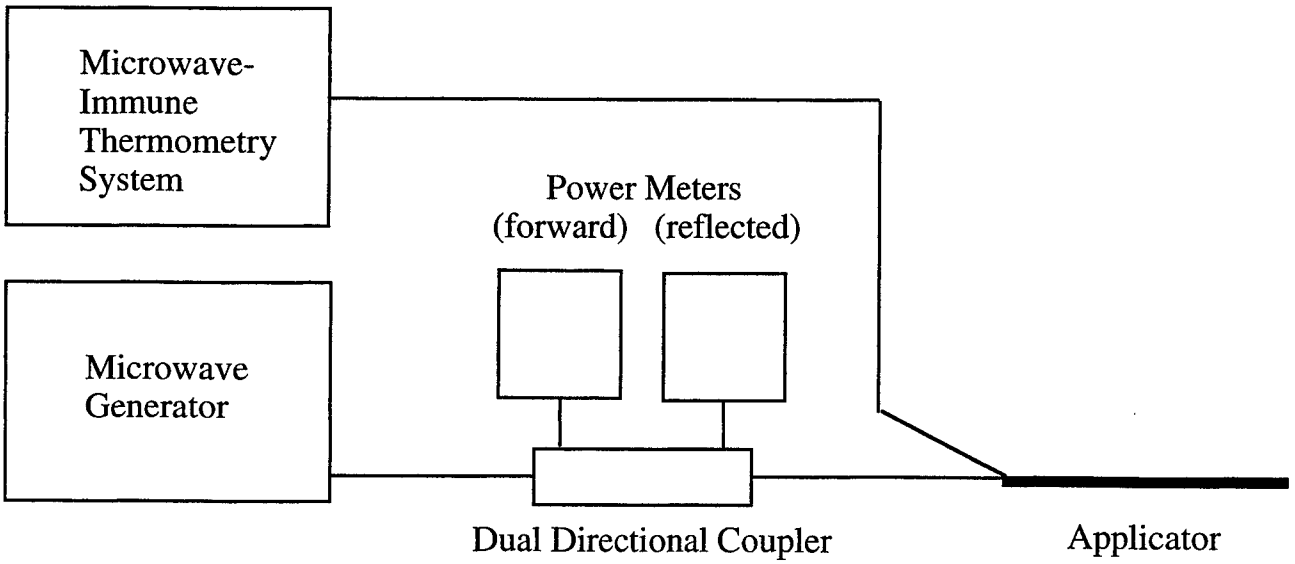

Fig. 3. System Diagram

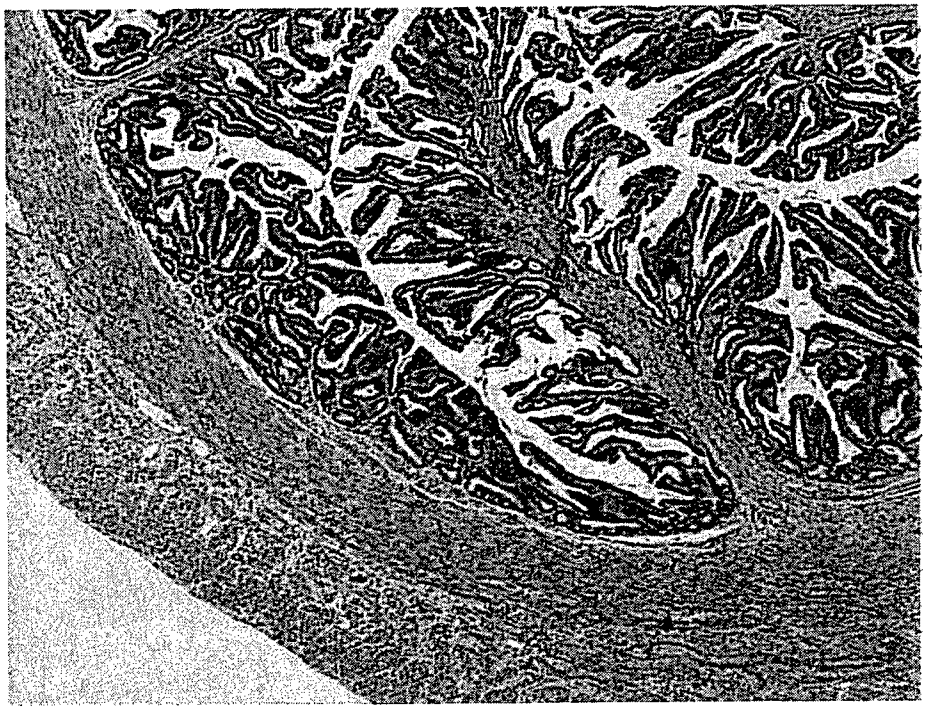

Fig. 4. Normal Uterus

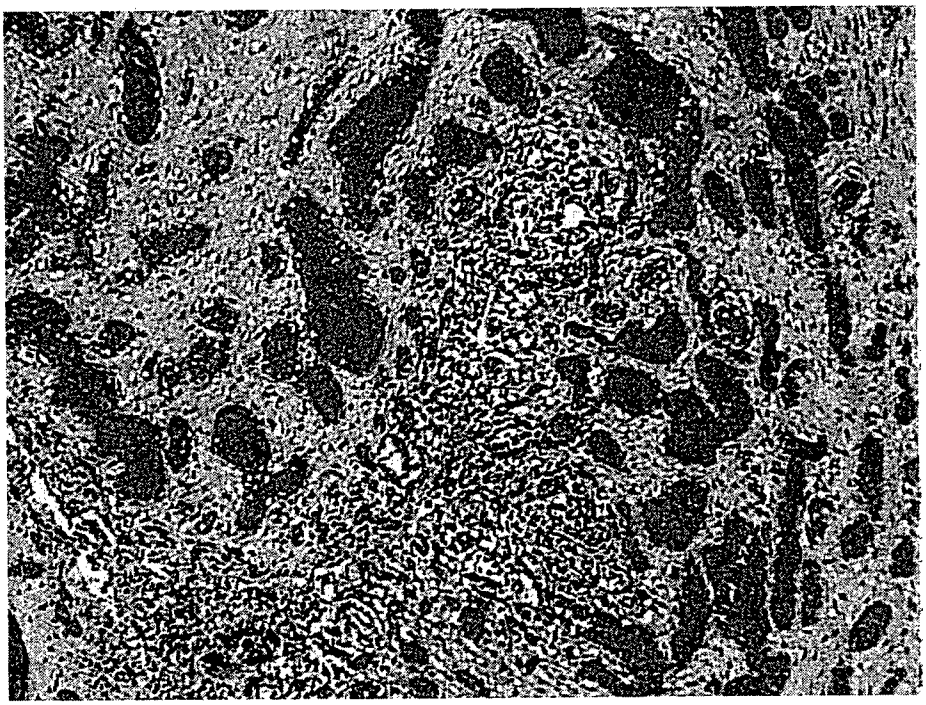

Fig. 5. Occluded Uterus

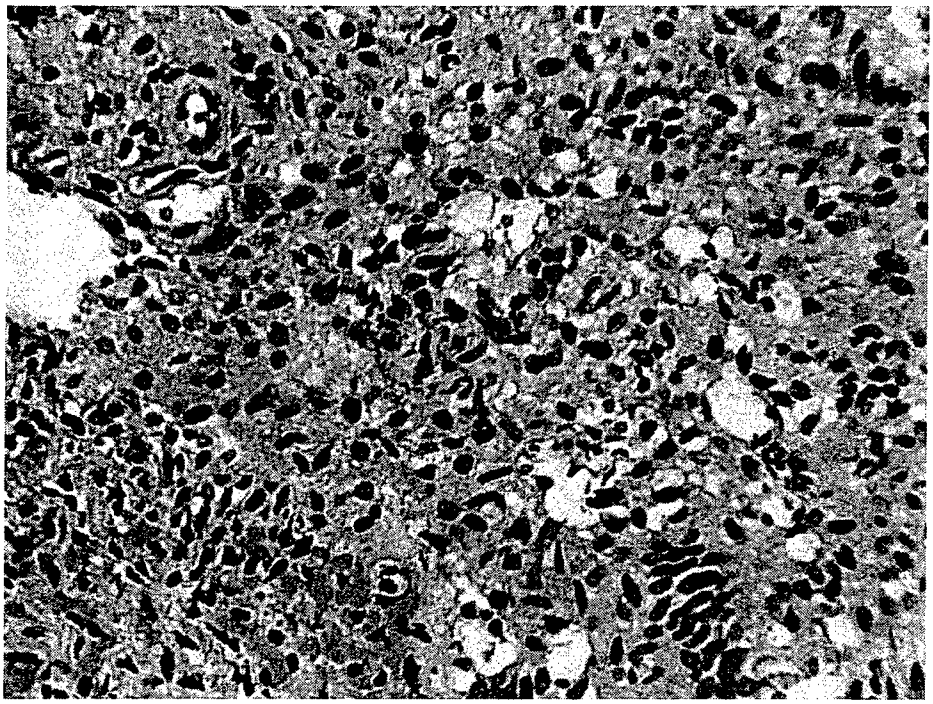

Fig. 6. Occluded Uterus (High magnification)

Microwave Catheter Ablation for the Treatment of Atrial Flutter

Dany Bérubé and L. Bing Liem

Fidus Medical Technology, 47929 Fremont Blvd, Fremont, CA 94538; (510) 651-7430

1. INTRODUCTION

In the past several years, there has been an increasing interest in the use of advanced energy modalities such as microwave for ablation of more complex cardiac arrhythmia including atrial flutter, atrial fibrillation and ventricular tachycardia. It has been demonstrated that microwave energy can produce larger and deeper lesions than radio-frequency (RF) energy and therefore clinicians worldwide are interested in using microwave ablation. Thus, the development of efficient microwave generators, catheters and applicators that are well adapted for cardiac tissue ablation is essential. This paper pertains to the physical properties of tissue at microwave frequencies, the theoretical background of microwave ablation and the initial clinical results obtained with the Fidus's microwave ablation system.

2. THEORETICAL BACKGROUND

In the last decade, the treatment of cardiac arrhythmias has been revolutionized by the success of catheter ablation. The technique consists of positioning the tip of the catheter on the arrhythmogenic substrate at the endocardial surface and delivering RF current at 500 kHz between the electrode at the tip and a large ground electrode on the skin. The flow of RF current causes an increase in tissue temperature by means of conduction losses, resulting in irreversible damage to the myocardial cells. The success rate obtained with this technique is very good for simple arrhythmias such as the Wolff-Parkinson-White syndrome where the target for ablation is small and superficial. However, for the treatment of more complex arrhythmias such as atrial fibrillation or ventricular tachycardia, which require larger and deeper lesions, the results obtained with RF ablation are disappointing. Even for atrial flutter, where RF ablation is reasonably successful, the recurrence rate is still quite high, reportedly at 30% and 45% [1, 2, 3]. Furthermore, the procedure time using RF ablation can be relatively long, up to2 to 4 hours.

McRury et Haines [4] provides a good synthesis of the thermal and electrical phenomena with RF and other modalities. Since power deposition decreases by $1/r^4$ where "r" is the radial distance from the RF electrode, it would be difficult to reach a deep substrate with RF ablation. Kaouk *et Al.* [5] has demonstrated that using the same power output and applicator geometry, lesions obtained with microwave energy are larger than those obtained with RF energy. Such differential results are consistent with the physical processes involved with the respective ablation techniques. In RF, the electrical resistance to the conducted current causes tissue heating. With microwave, which uses a much higher frequency, heating is caused by dielectric losses that are typically higher than resistive losses. These dielectric losses are caused by the oscillation or the rotation of water molecules when they are exposed to electromagnetic (EM) radiation emitted by the energy applicator of the catheter. The energy is thus carried by two different entities: conductive current for RF ablation and EM radiation for microwave ablation. The energy coupling to the tissue is different when comparing conductive current and EM radiation, which explains why lesions produced by microwave are larger and deeper than the lesions created by RF energy for the same output power. Another advantage of the microwave applicator is the antenna. Its structure can be designed to radiate in a manner that produces lesions shaped as required for the treatment of a specific arrhythmia. The production of long and deep lesions using only one (or few) energy applications would reduce the procedure time and improve the practicality of arrhythmia treatment.

In order to help understand and model the deposition of microwave energy inside the myocardium, the complex permitivity ($\varepsilon^* = \varepsilon' - j \cdot \varepsilon''$) has been measured within the frequency range of 915 MHz and 6.44 GHz and a temperature range between 37°C and 60°C by using a reflectometry technique. The virtual line model [6] has been used to calculate θ^* from the complex reflection coefficient ($\tilde{g}^*$) obtained at the end of an open-ended coaxial cable and a sample of myocardium by a six-port reflectometer. Bérubé *et Al.* [7] has demonstrated that this model is the most accurate for the measurements of θ^* when

the sample under test has high dielectric losses. The measured permitivity of healthy myocardium was $\varepsilon^* = 57 - 14 \cdot j$ at 2.45 GHz, while for the blood was $\varepsilon^* = 58 - 16 \cdot j$. Those values remained constant with changes of temperature at 2.45 GHz. Therefore, in a real application, the efficiency of the energy deposition in the myocardium does not change with time as the temperature of the tissue increases. At lower and higher frequencies, variations of the complex permitivity with temperature have been observed. These measurements have been used to describe the dielectric properties of the surrounding medium of the antenna during the design process of the applicator.

3. MICROWAVE APPLICATOR

The microwave applicators used by Fidus Medical Technology are made with helical antennas as shown in Figure 1.

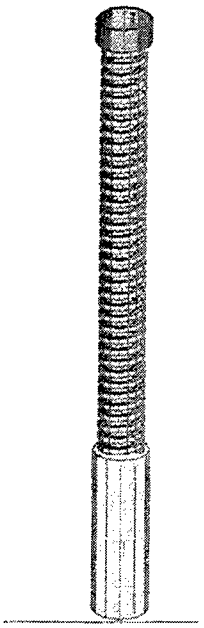

Figure 1: A sketch of the helical antenna

The antenna consists of a coaxial cable where the outer conductor has been removed in order to add the helical antenna. This antenna is soldered to the inner conductor of the coaxial cable at the distal end and to the outer conductor at the proximal end. An electrode ring is positioned at the end of the applicator for myocardial recording and pacing. All components are covered with a biocompatible dielectric.

In order to maximize the efficiency of the applicator, view the EM field, and understand the potential penetration depth of the microwave energy, the HFSS[a] (High Frequency Structure Simulator) has been used. This software uses a finite element method to solve Maxwell's equations for the defined geometry. Five steps are required to solve these equations. The first step is to draw all of the physical elements of the applicator, as well as the surrounding medium. The second step is to define the physical properties of these elements. The metallic parts have been defined as perfect metallic conductors and the complex permitivity of all the dielectric components has been specified in the simulator. The complex permitivity of the blood was obtained by the method described in [6]. The third step is to define the boundary conditions and the input port. The input port is defined at the entrance of the coaxial cable, specifying the use of the TEM mode. The antenna is drawn in a rectangular box, which is defined as having the dielectric properties of blood. The box dimensions are 0.5" x 0.5" x 1.25".

[a] Made by Ansoft.

Its boundaries are defined as radiative, meaning that none of the incident EM radiation reaching the boundary is reflected back. This condition is used to simulate the propagation of EM radiation in an infinite medium of blood. Because of the size of the rectangular box and the high losses in the blood at microwave frequencies, the incident energy at the boundary is very low. The fourth step is to define the frequency band where the problem is to be solved (2.45 GHz for this case), the kind of mesh needed for solving, and the convergence criterion. The last step is to solve the problem itself, using an adaptive process to arrive at the solution. The simulator divides each part of the model into small elements: the meshing process. It then solves Maxwell's equations and calculates the S_{11} parameter at the defined port. In regions where the electrical field gradient is determined to be significant, the mesh is refined and the software solves the problem a second time, this time determining the electrical and magnetic field as well as the S_{11} parameter. If the difference between the S_{11} parameter obtained during this pass and the previous pass is less than the convergence criterion, the software stops the process and the solution is retained. If not, this process continues until the convergence criterion is met.

The EM field and the adaptation of the applicator shown in figure 2 have been obtained using this technique. The active length of the applicator and the number of turns of the helix have been modified in order to obtain a resonant frequency of 2.45 GHz when the structure is surrounded by blood. The simulated S_{11} parameter of the final configuration is -13 dB, which means that $1/20^{th}$ of the power is reflected at the interface between the coaxial cable and the antenna. This result is in agreement with the values measured on prototypes using the network analyzer. The magnitude of the electric field, shown in gray scale in figure 2 and in relief in figure 3, is based on an incident power at the input port of 1 Watt. The energy is concentrated all along the antenna, which has a physical length equal to two times the wavelength. The energy is also present at the unipolar electrocardiogram electrode, allowing the catheter to produce an ablation at the same location where electrocardiogram recording takes place. Figure 3 shows that the energy can penetrate up to 5 mm inside the myocardium when the output power is 1 Watt. The energy deposition of the catheter is higher at the four hot spots, but the lesions produced by the catheter will be more continuous than the radiation pattern because of thermal flow within the myocardial tissue. The figures show that it is possible to produce a deep lesion of 20 mm in only one energy application when the contact between the endocardium and the energy applicator is adequate.

4. PRELIMINARY CLINICAL RESULTS

Because microwave technology has shown promising characteristics, a microwave system was developed by Fidus, and clinical tests were conducted with the system for the treatment of simple and complex arrhythmias. For the treatment of atrial flutter, helical antennas 18-mm in length were positioned across the isthmus between the inferior vena cava and the tricuspid annulus resulting in lesions of adequate length and depth to terminate the arrhythmia.[8] To efficiently eliminate isthmus conduction, which is the cause of atrial flutter, lesions must be on the order of 1½ to 3 cm in length. Because lesions produced by RF are smaller and shallower, many more are required to ablate an equivalent volume of tissue, and thus procedures can take many hours. Initial results using microwave have shown promising results, with several patients cured in less than one hour. The ablation process created effective lesions using only a few applications of microwave energy, resulting in improved procedure times.

If indeed microwave ablations can create deeper and longer lesions in the myocardium, the technology can greatly enhance the success rates for other complex cardiac arrhythmia treatments. For example, atrial fibrillation is a very common arrhythmia associated with significant morbidity that remains difficult to treat with drugs and current technologies. Because with microwave ablation linear lesions can potentially be accomplished within a reasonable amount of time, catheter-based maze procedures for atrial fibrillation would be feasible.

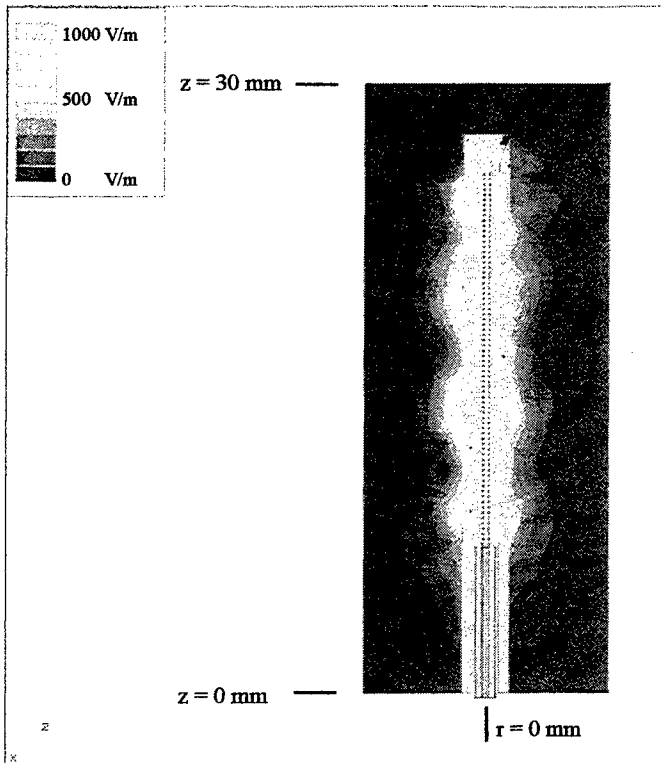

Figure 2: Magnitude of the electrical field (P = 1 W)

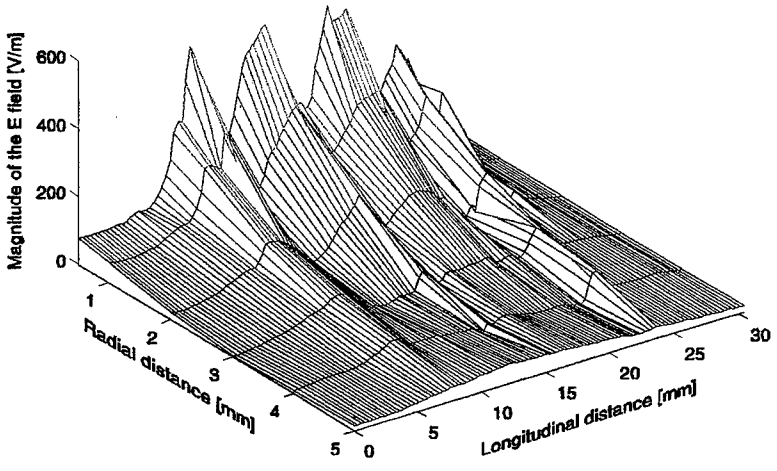

Figure 3: Magnitude in relief of the electrical field (P_{in} = 1 W)

[1] Gregory K. Feld *et Al.*; "Radiofrequency Catheter Ablation for the treatment of human type 1 atrial flutter (Identification of a critical zone in the reentrant circuit by endocardial mapping techniques)", Circulation, Vol. 86, No. 4, October 1992, pp.1233-1240.

[2] Francisco G. Cosio et Al.; "Radiofrequency ablation of the inferior vena cava-tricuspid valve isthmus in common atrial flutter", The American Journal of Cardiology, Vol. 71, March 1993, pp.705-709.

[3] Michael D. Lesh, George F. Van Hare et Al., "Radiofrequency Catheter Ablation of Atrial Arrhythmias, Results and Mechanisms", Circulation, Vol. 89, No. 3, March 1994; pp. 1074-1089.

[4] I. D. McRury, D. E. Haines, "Ablation for the treatment of arrhythmias", Proceedings of the IEEE, vol. 84, No. 3, pp. 404-416, March 1996.

[5] Z. Kaouk, A. Kheber, P. Savard, "A finite element model of a microwave catheter for cardiac ablation", IEEE Transactions on Microwave Theory and Techniques, vol. 44, no. 10, pp. 1848-1854, 1996.

[6] Fadhel M. Ghannouchi, Renato G. Bosisio, "Measurement of microwave permitivity using a six-port reflectometer with an open-ended coaxial line", IEEE transactions on instrumentation and measurement, Vol.38, No.2, pp. 505-508 April 1989.

[7] D. Bérubé, F.M. Ghannouchi, P. Savard, "A comparative study of four open-ended coaxial probe models for permitivity measurements of lossy dielectric/biological materials at microwave frequencies", IEEE Transactions on Microwave Theory and Techniques, vol. 44, no. 10, pp. 1928-1934, 1996.

[8] Liem L. B. et al, "Microwave ablation facilitates bidirectional block at the inferior vena cava - tricuspid annulus Isthmus" Circulation, 1997: 96: I-258.

SESSION 3

Therapeutic Laser and Argon Devices

Tissue Effects of Argon Gas Flow During Electrosurgery

Christiaan F.P. van Swol[1,2], Remco J. van Vliet[2,3], Matthijs G.M. Grimbergen[2] and Rudolf M. Verdaasdonk[2]

[1]Dept. of Urology and [2]Dept. of Clinical Physics, University Hospital Utrecht, The Netherlands, and
[3]Dept. of Clinical Physics, Dr. Daniel den Hoed Cancer Center, Rotterdam, The Netherlands

ABSTRACT

Argon gas-enhanced electrosurgery has recently been introduced for its potential beneficial effects on hemostasis during electrical cutting. In this study, the influence of argon gas on electrosurgery on tissue was investigated.

A standard electrosurgery unit was used extended with a gas unit (GSU) and accommodated handset, which enabled a flow of argon blown along the electrode in contact with tissue. The temperature distribution was visualized in polyacrylamide gel using a color-Schlieren technique. Bovine tissue was used to evaluate the macroscopic effect of the lesions. The electrode was moved over the tissue surface with different settings for speed, gas flow, gas-outlet positioning and depth of the electrode in the tissue.

During cutting, coagulation was significantly increased using argon gas; coagulation on both sides of the track ranging from 1.0 mm without argon flow up to 4.5 mm with argon flow could be obtained. Changing the gas flow from laminar to affected neither the coagulation nor the cutting. The extent of the coagulation depended on the combination of power and distance of the gas-outlet to the tissue. The coagulation depth beyond the bottom of the tracks was not influenced by argon and remained less then 1 mm.

Argon gas-enhanced electrode surgery is especially effective when just touching the tissue thus obtaining a superficial coagulation (and hemostasis) of the surrounding tissue.

1. INTRODUCTION

Electrosurgery equipment is used to control bleeding during surgical procedures by coagulation of tissue. A high-frequency electrical current is generated inside tissue resulting in heat dissipation. The local temperatures on and inside the tissue depend mainly on the pathways of lowest resistance. Argon gas enhanced electrosurgery is becoming increasingly popular as it may have beneficial effects on hemostasis during cutting. The working mechanism is still not clear but the effect might be ascribed to argon gas influencing the electrical resistance between electrode and tissue.

2. MATERIAL AND METHODS

2.1 Argon-Enhanced Electrosurgery

For argon-enhanced electrosurgery a standard electrosurgery unit is extended with an accommodated handset and a gas unit (GSU). The electrode in the electrosurgery handset could be set in eight different positions towards the end of the gas-outlet, three were compared: 6, 13 and 21 mm. The argon flow from the GSU was set at 0, 5 and 9 l/min. The experiments were performed at 25 and 40 W output power of the electrical generator and for both needle and blade electrodes.

2.2 The Schlieren set-up

The set-up of the Schlieren technique has been described before[1,2] and will be discussed briefly. Using the Schlieren technique a parallel beam of light transits an object plane where a temperature gradient is present. Rays are deflected due to very small changes in the refractive index caused by this gradient. The deflected rays are color coded and are presented in real-time 'thermal' images. By blocking the non-deflected rays only deflected rays will

SPIE Vol. 3249 • 0277-786X/98/$10.00

contribute to the image at the image plane. This results in a contrast enhancement of the image due to subtraction of the background light. The rays are color coded by a filter consisting of concentric rings colored in rainbow order. The Schlieren set-up was calibrated using a known heat source with geometry similar to the electrosurgery sources. A 10% PAA-gel (PolyAcrylAmide) was used as phantom tissue. This gel is highly transparent (essential for Schlieren techniques) and is assumed to have thermal and electrical characteristics similar to "real" tissue. In these experiments the GSU handset was translated in contact with the phantom tissue in the object plane and real time Schlieren images of the heat distribution were obtained. The experiments were performed at four different speeds: 1, 2, 3 and 4 mm/s.

2.3 Tissue experiments

Bovine tissue was exposed under similar conditions and settings as the experiments for the thermal imaging. The translation speed was set at 4 mm/s because it was most comparable to the clinical situation. After tracks in the tissue had been formed with the needle or blade, photographs were taken of each track so the extent of the coagulation zone around it could be measured.

3. RESULTS

3.1 Schlieren images

The Schlieren images of the needle and the blade on the phantom tissue show the extent of the heat distribution in a range of 1.9 to 3.2 mm measured from the tip of the electrode into the tissue. The depth of the heat distribution around the electrode varied depending on the position of the electrode in the handset, the argon flow and the depth of the electrode into the tissue. When the distance between the tip of the electrode and the gas-outlet decreases, the heat distribution around the electrode becomes larger (not only superficial but also in depth). The extent of the heat distribution decreases when the argon gas flow increases from 5 to 9 l/min. When the electrode is placed on the tissue and the depth of the electrode increases during cutting the effect of the argon flow decreases. When the depth of the electrode exceeds 2.5 mm the argon flow has minimal effect and the heat distribution is similar as in the no argon flow case. The different electrodes ,the needle and the blade, show a similar heat distribution in depth. The superficial heat distribution is larger for the needle when argon is used.

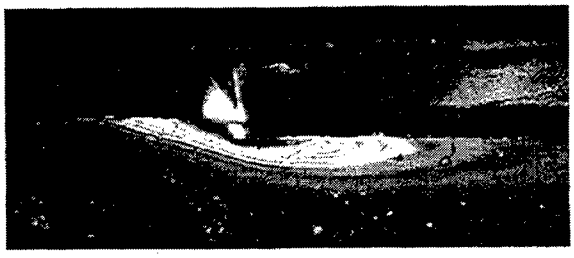

Figure 1: Schlieren image of needle in contact with tissue (moved from left to right, 40 W. translation speed 2 mm/s, argon flow 5 l/min. and gas-outlet is positioned at 13 mm above tissue)

3.2 Tissue experiments

The coagulated area around the lesions of "real" tissue are classified in two zones: coagulation depth and coagulation width of the track. In all measurements the largest coagulation zone is taken and the average of these measurements is presented in figure 2.

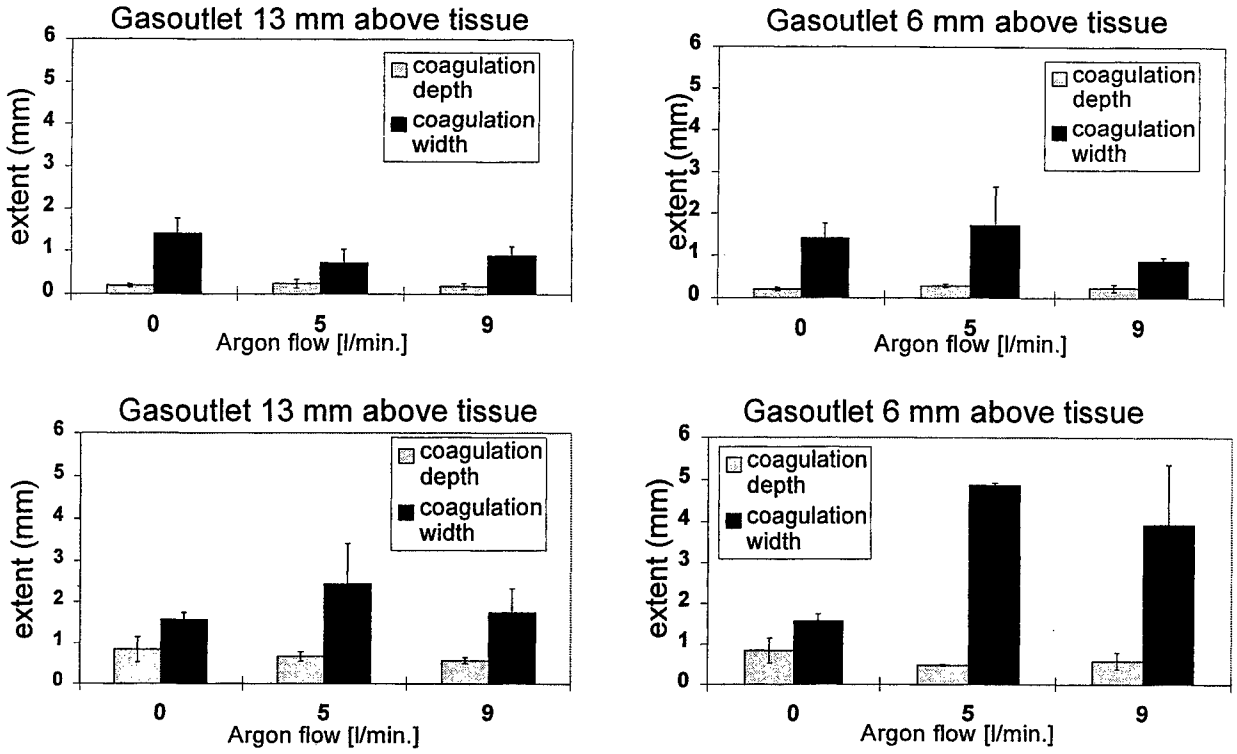

Figure 2: Extent of coagulation zone with 25 W (top) and 40 W output power (bottom)

The coagulation depth at the bottom of the track seems to be independent of the presence and flow rate of the argon flow. However, the coagulation width next to the track varied significantly. The coagulation zone tend to increase with argon flow. However when argon is used, a flow of 5 l/min. produces a larger coagulation zone then a flow of 9 l/min. Comparing the different handset positions the difference showed to be negligible when no argon was used. When argon was used positioning of the gas-outlet at 6 mm above the tissue produced the largest coagulation zone. The depth of the track seemed to have no significant influence on the total coagulation (depth and width).

4. DISCUSSION

4.1 In-vitro effects of Argon gas on tissue

The effect of argon is in general a larger superficial coagulation zone, however the effect depends on various parameters:

Power: without argon gas flow, the coagulation zone for power settings of 25 and 40 W are almost similar. However, in presence of an argon flow, the extent of the coagulation zone at 40 W is almost two times larger compared to 25 W. At the higher power, the sparks reach further away from the electrode contributing to the coagulation width.

Gas flow rate: The coagulation zone created using an argon flow of 9 l/min. is approximately 1 mm smaller compared to the coagulation zone using a flow of 5 l/min. This might be attributed to the transition from a laminar to a turbulent gas flow. Due to the turbulence, the argon gas concentration along the electrode might have decreased and change the mechanism of sparking between electrode and tissue[3].

Depth of the track: Studying the effect of argon in the Schlieren set-up, the thermal distribution proves to be dependent on the depth of the electrode into the tissue. However, this observation was not supported by the extent of the coagulation zone in real tissue. Probably, the imaging is more sensitive and will show a larger area of tissue that is effected by heat but not till the point of coagulation. Polarization microscopy is a method to enable visualization of thermal damage in tissue resulting in tissue necrosis.

Distance of gas outlet: The influence of the distance from the gas-outlet to the tissue was consistent in the Schlieren set-up and the tissue experiments. The coagulation decreases when the outlet is moved away from the tissue. This can again be ascribed to the dilution of the argon gas concentration around the electrode.

4.2 Extrapolation to the clinical situation

Clinical experience shows a large superficial coagulation when argon gas is applied, enhancing fulguration effects This phenomenon was less prominent in the in-vitro experiments presented. There are two possible explanations:

- The in-vitro experiments were performed with the electrode in contact with the tissue while in the clinical situation fulguration is achieved in 'minimal' contact to obtain a large superficial coagulation zone.
- There was no working micro-vascular structure or blood present in the in-vitro tissues. In the in-vivo situation, the blood in the micro-vascular structure attract the sparks due to a lower impedance. However, at the higher power settings, this vascular structure will be shut down almost immediately, coming closer to the in-vitro situation

5. CONCLUSION

The extent of the coagulation zone depended on gas flow rate in combination with power and the distance of the gasoutlet to the tissue. The color Schlieren technique was effective to visualize the influence of gas flow, position of the gas-outlet, output power and depth of electrode in the tissue. Argon gas-enhanced electrodes showed to be especially effective just touching the tissue to obtain a superficial coagulation of the surrounding tissue

6 REFERENCES

1 W.L. Howes. Rainbow schlieren and its applications, Applied Optics, 23: 2449-2459, 1984.

2 R.M. Verdaasdonk. Imaging laser induced thermal fields and effects, in Jacques(Ed.): Laser-Tissue interaction VI. Bellingham. SPIE proc. vol. 2391,1995.

3 R.C.Platt. Effects of Argon flow on Arc Performance in the E2520 Handset and the Clip-on Accessory, Valleylab, Boulder (CO), 1995.

High-speed and Thermal Imaging of the Mechanism of Action of the Cavitron Ultrasonic Surgical Aspirator (CUSA)

Rudolf Verdaasdonk, Christiaan van Swol
*Matthijs Grimbergen and *Gert Priem*

Dept. Clinical Physics & Biomedical Engineering #
University Hospital, Utrecht, and *Valleylab Benelux The Netherlands

ABSTRACT

The Cavitron Ultrasonic Surgical Aspirator (CUSA) is being used, especially in neuro- and liver surgery, to resect selectively soft and hard tissue in favor of elastic tissues like blood vessels, enabling the removal of tumors with minimal loss of blood. In this study the phenomena associated with CUSA were visualized to expand the understanding of the mechanism of action of the CUSA. Real-time high-speed imaging techniques were applied to capture cavitation phenomena during application of the CUSA under physiological settings: in water, at tissue surfaces and inside artificial tissue. Close-up photography using a 1 μs flashlight showed the expanding and imploding cavitation bubbles around the rim of the ultrasonic vibrating hollow tip. Shock waves generated by imploding cavitation bubbles were observed using Schlieren techniques with a temporal resolution of 10 ns and synchronized with the duty cycle of the vibrating tip. In addition, thermal effects associated with friction between the vibrating tip and tissue were visualised using a thermal imaging technique. The CUSA mechanism has proven to be a combined effect of cavitation induced fragmentation, mechanical cutting and thermal deterioration of tissue depending on the irrigation/aspiration flow, intermittent vibration regime and degree of tissue contact. The impact of the shock waves observed is undetermined yet. These real-time imaging techniques will contribute to expand the understanding of the working mechanism of CUSA and to show the characteristics of probe designs and influence of driving frequency.

Keywords: CUSA, cavitation, ultrasonic therapy, ultrasonic surgery, ultrasonic aspirator, shock wave, high speed imaging techniques, thermal imaging techniques

1. INTRODUCTION

1.1 Ultrasonic Surgery

Beside its diagnostic capabilities, ultrasound is also being used for therapeutic purposes. High energetic ultrasonic waves can be focussed from outside the body onto specific targets within the body with high accuracy. The mechanical forces induced at the focal area are strong enough to break stones as it is being used for lithotripsy in the kidney. In contrast with these usually big medical devices, ultrasonic forces can also be generated at much smaller scales. Ultrasonic cavitation surgical instruments are small handheld devices with specific characteristics for precise tissue resection. They are mostly applied in neuro surgery [1 2] and liver surgery [3 4] for selective resection of soft and hard tissue in favor of elastic tissues like blood vessels. This enables the removal of tumors with minimal loss of blood since the vasculature remains intact while removing the surrounding tissue. There are several systems on the market based on this principle with similar characteristics. One of pioneering systems in this type of surgery is called the Cavitron Ultrasonic Surgical Aspirator or abbreviated CUSA.

Further author information: R.V. (correspondence): email R.M.Verdaasdonk@id.azu.nl, website http://www.urolog.nl/lasercenter, tel: 31-30-2507302, fax: 31-30-2542002

SPIE Vol. 3249 • 0277-786X/98/$10.00

2. DESCRIPTION CUSA SYSTEM

The system consists of a console containing the power supply, control panel, fluid irrigation and suction unit with reservoirs connected to the surgical handpiece. In the handpiece, a transducer is activated by electrical energy, which induces laminated metal strips to expand and contract under influence of a magnetic field (magnetoconstriction). By alternating the electrical current in a coil surrounding the metal sheets, the transducer is generating vibration waves with a typical frequency of 23 kHz. These waves are passed to a 100 mm long conical titanium needle which is hollow. Due to its shape the original longitudinal vibration amplitude of around 10 µm is amplified to 350 µm expansion and contraction at the 1.9 mm diameter tip of the needle. The hollow titanium needle is enveloped by a plastic sheath through which saline is flushed which acts as a lubricant and cools the needle. Through the hollow shaft, the irrigation fluid is sucked away together with dissected tissue particles. Due to this irrigation, there is always a small film of fluid present in the operation field. During surgery the needle is in light contact with the tissue providing 'tactile feedback'. The aspirated tissue can be used for hystopathology [5].

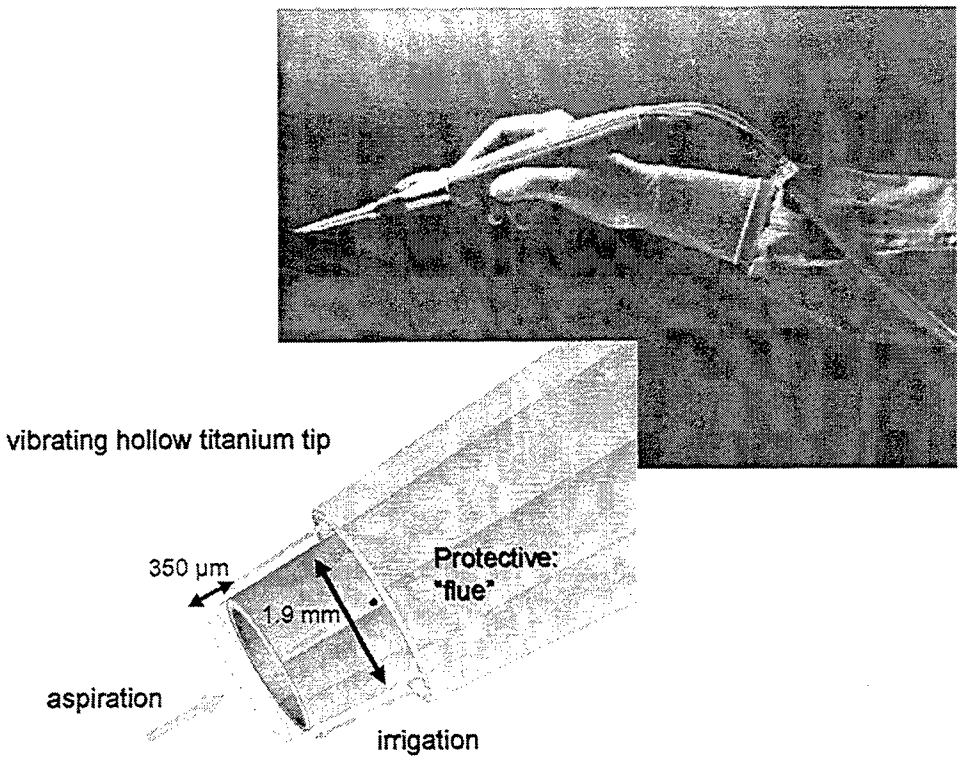

Figure 1: CUSA handpiece with schematic of tip

3. PHYSICS OF CAVITATIONAL SURGERY

Looking close-up to the needle as show in figure 1 we can imagine a metal ring is moving in and out a fluid like environment at very high speed. A simple calculation shows that the average speed of the needle tip is 16 m/s. There are various mechanisms that might be induced by this moving 'tube' [6 7].

3.1 Pressure waves

Ultrasonic waves can induce negative and positive pressures in the fluid and the surrounding tissue. Depending on the magnitude the pressure wave can 'break' the molecular cohesion in the fluid or tissue resulting in gas bubbles. The original size of the bubble will determine its lifetime. Smaller bubbles will resolve or implode directly, while bigger bubbles can expand and compress in a cyclic way induced and sustained by the ultrasonic energy emitted by the vibrating needle tip. At a molecular level, the difference between hard, elastic and soft tissue would explain the selectivity in tissue damage. Due to their behavior, these bubble are referred to as 'ultrasonic microcavitations' [8; 9] and are believed to have a major contribution to the ultrasonic surgery mechanism. However, these 'micro' cavitation bubbles have a different nature compared to the 'macro' cavitation bubbles described in the next paragraph.

3.2 Cavitation bubbles

The hollow needle itself can create big 'bubbles'. During tip retraction, the metal cylinder moves at high speed through a liquid environment. The fluid can have difficulty filling the gap that is left behind. This hole is empty or near vacuum. Due to the extreme underpressure, the surrounding fluid is sucked inward from all directions at the same time. The acceleration of the fluid is tremendous. During this process, fragments or layers of soft tissue near the cavitation bubble are separated from the underlying tissue. The moment the hole is filled, there will be collapse of fluid molecules near the center of the original gap. The forces associated with this collapse can be extremely high. Since this process is usually not symmetrical, so-called jet-streams are formed focussing the momentum of the accelerated fluid at particular positions preferentially at the surface of tissue. These jets can easily break both soft and hard tissues apart [10]. The mechanism described can be selective for tissue structure. Soft tissue is easily fragmented. Hard tissue does not give way and therefore amplifies the jet-streams focussed on the tissue surface which scatter it locally to pieces. Elastic tissue can partly follow the 'low' speed part of the expansion and implosions and deform without breaking and so stays intact.

3.3 Mechanical cutting and breaking

Another mechanism can be just 'ordinary' mechanical. When the titanium tip is in direct contact with the tissue, it will push against the tissue with extreme forces. The relatively sharp rim (90 degrees) of the tip can cut itself easily into the soft tissue. In combination with the suction the soft tissue is effectively removed. Elastic tissue, in contrast, will structurally give way and follow the motion of the needle without breaking. However, hard tissue in first instance does not deform at all. The weaker of the two materials colliding will break. In this case, the hard biological tissue is no competition for a metal like titanium. The metal tip will pound on the tissue surface shattering it to small pieces that are sucked away.

3.4 Friction

During vibration the tip will move at high speed through the fluid and tissue. Tissue in contact with the front and side surface of the needle will not follow the motion, Due to friction and mechanical resistance energy is dissipated, heating the position of contact. The temperature rise can be considerable due to the high motion speed and the friction. In the design of the tip is

accounted for friction using the irrigation fluid as a lubricant and cooling between the plastic protective sheet around the needle.

3.5 Mechanism of action of the CUSA

As more or less reflected by the summation of physical phenomena that can be involved during the action of the CUSA in a biological environment, it will be clear that the mechanism depends on conditions like presence of fluid, tissue type, extend of tissue contact etc. Although, it will probably be a combination of various physical interactions, it is not clear which mechanism is most dominant [6; 7].

3.6 Aim of study

To obtain a better perception what physical phenomena are involved during CUSA applications, a study was conduced to visualize with high spatial and time resolution the phenomena near the tip of the needle of Ultrasonic Surgery devices.

4. CLINICAL APPLICATION OF ULTRASONIC SURGERY

4.1 Tissue selectivity

As stated before, the CUSA is selectively resects tissue types in favor of elastic tissues. The elasticity of tissue is related to the moisture content. In table 1 tissue is differentiated in three tissue categories with representative examples. The efficacy of the CUSA in these tissues is graphically displayed in figure 2.

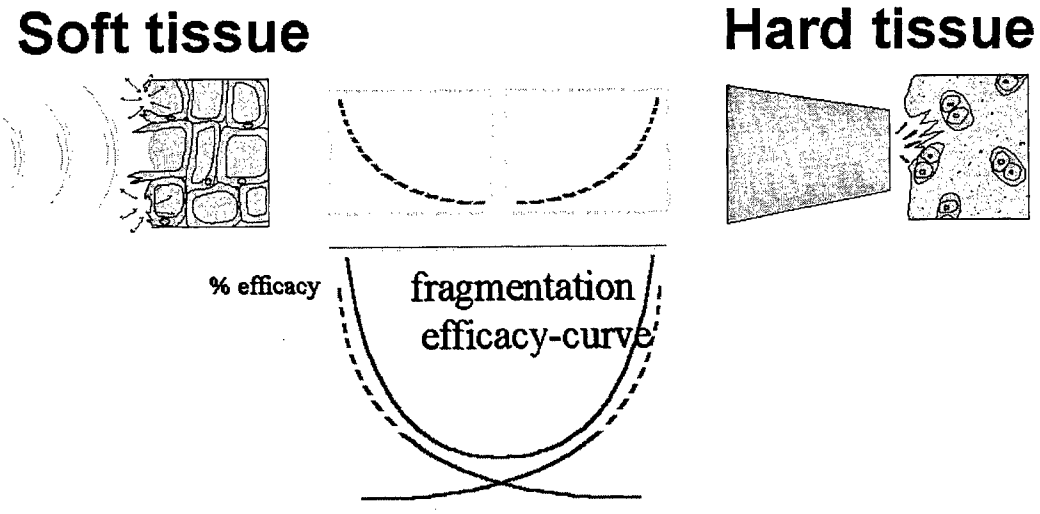

Figure 2: efficacy of CUSA depending on tissue type

moisture content	high	average	low
tissue type	soft	elastic	hard
example tissue	liver parenchyma	vessel, nerve, duct	calcified tissue

Tabel 1: differentiation of tissue types in relation to CUSA efficacy

4.2 New clinical applications

The areas of application of the CUSA are rapidly expanding. The most common application is in the field of neurosurgery for brain tumor resection and partial liver resection [3]. In tabel 2 an overview is presented of more recent areas of application and areas were the application is under investigation.

Gynecology[11 12]	Cardiac surgery [13]	Oncology [14]	Urology [15]	General Surgery (laparoscopy) [16]
➢ endometriosis ➢ hysterectomy ➢ vulvar mucosectomy ➢ condiloma	➢ prep. mammarian artery ➢ prep. annulus at valve replacement ➢ pericarditis	➢ debulking (reduction) of tumors ➢ lymphnode dissection ➢ pancreas-surgery	➢ partial nefrectomy ➢ Bricker	➢ Bowel resection ➢ cholecystectomy ➢ spleenectomy ➢ hernia repair

Tabel 2: Overview of recent applications for CUSA

4.3 Application modalities

Normally, the CUSA handpiece is applied in a continuous mode. The amplitude of the needle vibration can be adjusted by setting the percentage of activity between 10-100. However, by decreasing the amplitude, the action of the needle becomes less effective resulting in a lower fragmentation rate and in reduced tissue selectivity. Particular tissue types, which tend toward elastic tissue, need full power to be resected. At higher power settings, however, the resection become less controlled and power dissipation can result in unwanted thermal and mechanical damage in the environment. An alternative for effective and controlled dissection is offered by an adjustment in the active duty cycle of the tip. Instead of a continuous train of vibrations, the needle only vibrates one time at full amplitude and remains steady for some cycles before vibrating again .This way the therapeutic energy is equal however with conservation of the full fragmentation ability and full tissue selectivity. Due to the reduced fragmentation rate, the dissection is more controlled. These intermittent settings for CUSA are called the CAVI pulse modes which are numbered from 1 to 4 where 4 has the longest duty off time.

5. IMAGING TECHNIQUES

To obtain a better understanding of the mechanism of action of the CUSA various imaging techniques were applied as described below.

5.1 High speed Schlieren imaging

The schematic setup for high speed imaging is illustrated in figure 3. The CUSA probe is positioned in a medium within the object of a B&W Schlieren setup [17]. Schlieren techniques enable real-time image processing by e.g. subtracting the background light from an image leaving light that has been interacting with the CUSA probe to reconstruct an image captured using a video camera. Using light flashes of only 10 ns at 5 kHz generated by a copper vapor laser, it is possible to 'freeze' density waves that travel through the medium at sonic speeds and cavitation bubbles. The laser pulses are synchronized using a trigger from the CUSA generator that is

adjusted to the capture speed of the video camera (100 µs). By introducing a preset delay time (0-100 µs) relative to the duty cycle of the vibrating needle, it is possible to freeze a sequence of phenomena near the CUSA tip happening through the vibration cycle of the tip

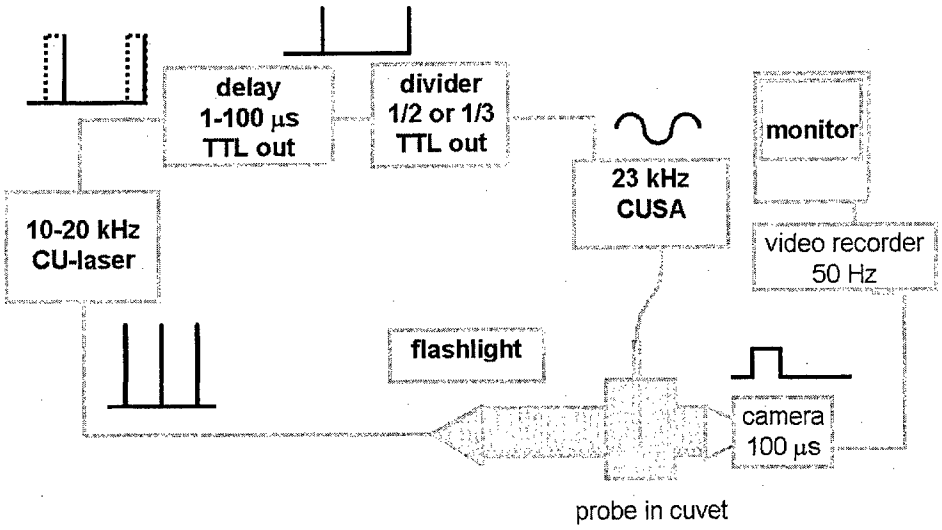

Figure 3: schematic of high speed Schlieren setup

5.2 High speed flash video imaging

The presence of cavitation phenomena near the tip of the CUSA can also be imaged using 'ordinary' high speed flash photography or video imaging [17]. In contrast to the shadow cast images provided by the Schlieren technique, these images have a natural appearance. Using again a trigger signal from the CUSA generator for synchronization, a stroboscope flashlight emitting 1 µs pulses at 50 Hz is used for illumination of the tip. Close-up images of the CUSA tip enable the visualization of cavitation phenomena through the duty cycle of the vibrating needle using a preset delay time (0-100 µs). The images are recorded on tape using a video camera with a shutter speed of 50 ms.

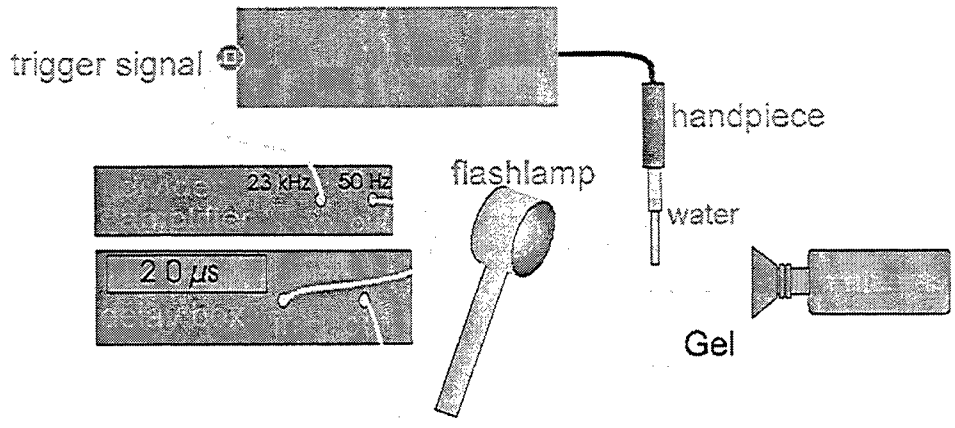

Figure 4: schematic of high speed flash photography setup

5.3 Color schlieren imaging

An imaging method based on color Schlieren techniques was used to visualize the temperature gradient in a phantom tissue [17]. The color Schlieren technique is explained in figure 5. Rays of a parallel beam of light from a continuous white light source will be deflected during their transit of a temperature field due to very small changes in the refractive index. An imaging lens collects the rays. The deflected rays are color coded in the focus plane by a filter, consisting of concentric rings colored in rainbow order ('rainbow filter, inlay in figure 5). The non-deflected rays are blocked by a black stop in the center of the filter. This results in a high-contrast color image in the image plane. Depending on the geometry of the temperature distribution, the colors in the image can be converted to real temperatures. The images are recorded in real time with a video camera with a standard shutter speed of 50 ms. The size of the close-up field is 10 x 15 mm with a resolution of 20 µm.

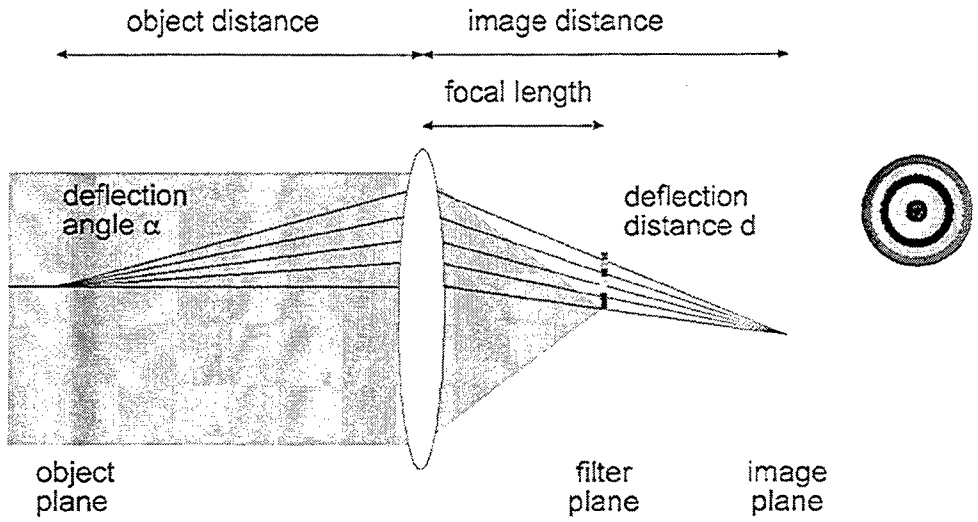

Figure 5: schematic of color Schlieren setup

5.4 Experimental conditions

The imaging was performed under various conditions as listed in table 3. It is assumed that under working condition the tip is always surrounded by a layer of water due to the irrigation around the tip. Therefore to simplify the imaging, the tip was always submerged several millimeter into a water bath.

Imaging Technique	*High Speed Schlieren (HSS)*	*High Speed Flash (HSF)*	*Color Schlieren (CS)*
power settings [%]	20, 40, 80, 100	20, 40, 80, 100	40,80
suction / irrigation	off , on	off , on	off , on
CAVI pulse mode	1,2,3,4	1,2,3,4	1,2,3,4
environment	water, water/gel	water, water/gel, water/tissue	water/gel,
angle of view	90, macro	45, 90, macro	90

Tabel 3: experimental conditions during imaging

In order to image the presence of cavitation and thermal effects at the surface and inside tissue, a transparent tissue model was used. This model consisted of a polyacrylamide gel from which the thermal and mechanical properties are assumed to be similar to soft biological tissues. Next to the artificial tissue also bovine subcutaneous tissue was used to visualize the working mechanism at the tissue surface.

6. RESULTS AND DISCUSSION

6.1 Visualization of CUSA interaction in a water environment

Using the high speed flash video imaging method, cavitation bubbles are observed with the needle freely vibrating in a water environment as was expected from the description of the working mechanism of the CUSA. A whole chain of cavitation bubbles with diameters of several hundreds of micrometer was present along the front end of the cylindrical needle (top left frame fig. 6). When suction was activated, the ring of small cavities shifted toward the inner rim of the hollow needle pushed by the inflow of irrigation fluid through the hollow channel of the needle (top right frame in fig.6). The cavitation bubble can be better appreciated looking at a macroscopic view near the rim of the tip (bottom right frame, fig.6). Many individual cavitation bubbles can be distinguished. During interaction with real tissue, the cavitation bubbles were clearly observed near the tissue surface while the soft tissue was effectively dissected and removed with the irrigation fluid (bottom right, fig.6). Whenever a small layer of liquid is present, as is the case using irrigation, the presence of cavitation bubbles is unquestionable.

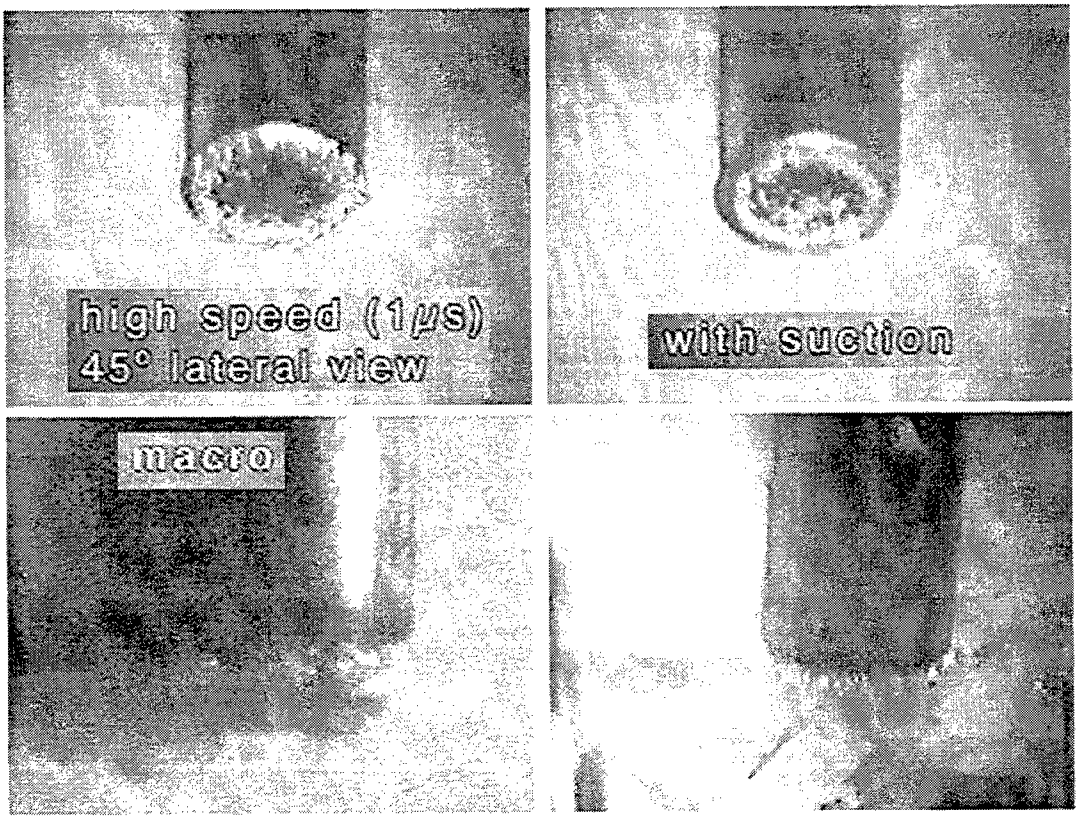

Figure 6: Still frames captured from high speed video images showing the presence of cavitation bubbles under various conditions.

6.2 Visualization of CUSA interaction at a tissue boundary

Using Schlieren techniques as described before, the presence and tissue interaction of the CUSA was visualized at the surface of the transparent tissue model. The top left frame of figure 7 shows the tip exactly at the water-tissue boundary. Underneath the tip, up to a depth of 400 μm, a hole is formed filled with water. Within this hole, the black 'shadow like' spots show that cavitation bubbles are present. If the tip is hold steady in this position, the surrounding tissue is not damaged illustrating the well-defined action radius of the CUSA tip. Looking at the thermal image (top right frame, fig.7), no thermal effects are visible, just a blurred looking image. Due to the vibration of the needle, the turbulence in the water effectively cools the surface and induces motion blurring in the 20 ms exposure of the image.

When the tip is advanced into the tissue while suction is applied, the irrigation channel is blocked by the tissue, which hampers the cooling. Since the needle is embedded in the tissue, the wall is moving at high frequency against the tissue. Due to friction, thermal energy is generated resulting is heating of the tissue represented by the white band along side the needle (bottom left frame, fig. 7). Since fluid is absent, cavitation bubbles are not observed. The penetration mechanism is probably due to a combined mechanical/thermal interaction. Preferable, this situation should be avoided in practical use by moving the needle around at the surface and making a large channel filled with water into the depth. The thermal image (bottom right frame, fig.7) shows the thermal zone around the tip in more detail.

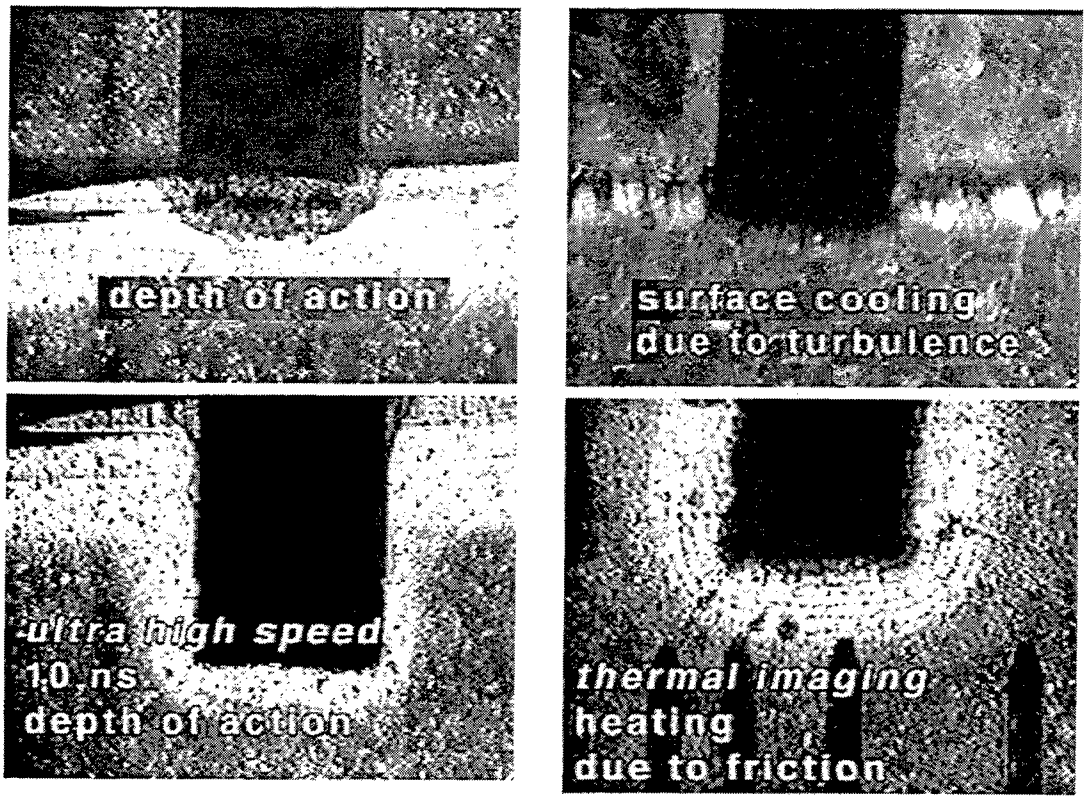

Figure 7: Ultra high speed and thermal Schlieren images showing the interaction of CUSA at the surface and inside tissue

6.3 Mechanism of action of CUSA resolved with ultra high speed Schlieren imaging

Although the images presented in the previous paragraphs already give a good perspective how the CUSA mechanism works, a better understanding can be obtained from the ultra high speed images which show a sequence through the duty cycle of one vibration (~ 40 μs). These images captured from still-frames of real time video imaging are presented in figure 8. The start of the duty cycle is defined by the motion of the tip forward into the medium: $\partial = 0$. During this motion it might induce a density wave in the liquid that moves from the tip near ultrasonic speed. However, it is not clear if this imaging technique is sensitive enough to visualize these waves. When the tip of the needle start retracting (near $\partial = 0.5$) it leaves a cylindrical cavity behind in the water since the liquid does not directly follow the near ultrasonic motion of the needle. This moment is shown in the first frame (top left) of figure 8. During further retraction the cylindrical shaped cavity falls apart in smaller collapsing cavitation bubbles since the water is starting to fill up the 'vacuum' left behind by the tip (top middle frame, fig.8). When the tip is slowing down towards its starting position, the smaller cavitation bubbles detach from the tip and implode rapidly towards their center of symmetry (top right frame). The momentum of the water mass focussed at the center of collapsing bubble is associated with such extreme forces that each individual bubble creates a shock wave that starts expanding at supersonic speed through the water (bottom row frames). The centers of collapse are situated 100-200 micrometer in front of the rim of the tip. These shock-waves associated with the CUSA have never been visualized before.

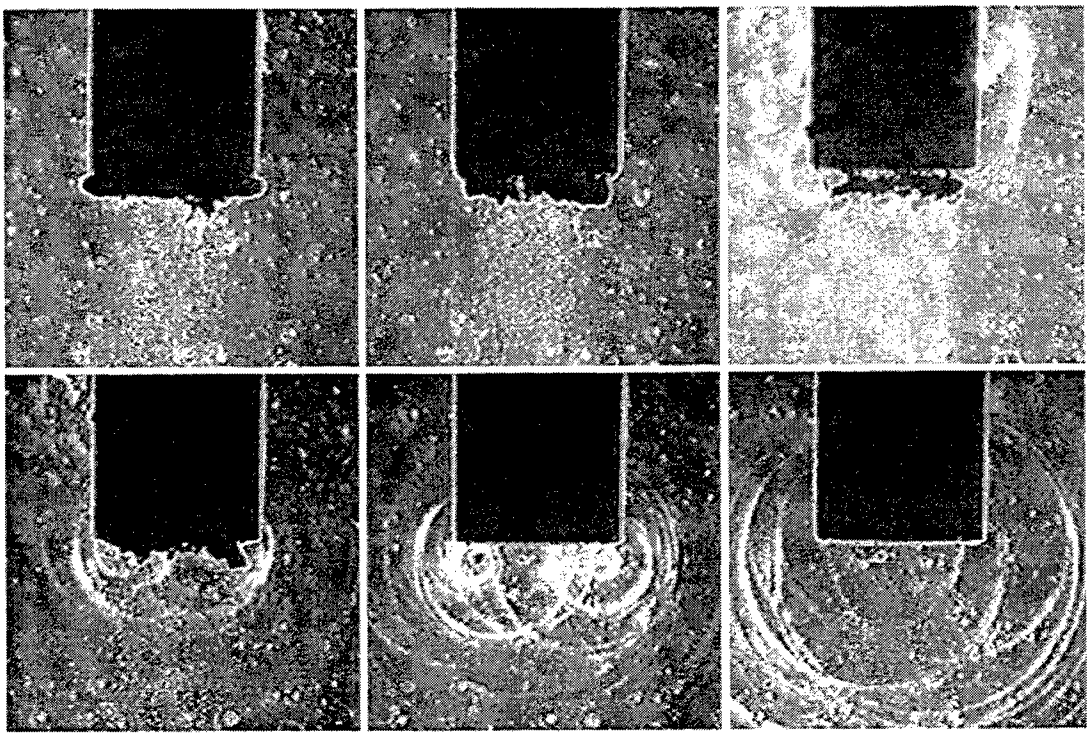

Figure 8: Sequence through the duty cycle (40 μs) of one vibration of the CUSA tips captured using ultra high speed Schlieren imaging showing collapsing cavitation bubbles and shock waves.

6.4 Interpretation of CUSA images: implications for mechanism of action

The sequence of the duty cycle of the CUSA as interpreted from the imaging techniques applied in this study is depicted in figure 9. The whole sequence is already discussed in the previous paragraph in conjunction with figure 8. However, some subjects remain unclear.

Cavitation phenomena

Other authors (Bond et al. [18] [19]) have not found any evidence of cavitation effects during CUSA interaction with tissue. Our images clearly show the presence of cavitation bubbles at the tissue surface (figures 6, 7) when a minimal layer of fluid is present as can be assumed in clinical settings. Either the irrigation fluid or blood in the operation field provides this layer. It could be, however, that other studies refer to the micro cavitation bubbles induced by density waves into the tissue. As explained in the introduction paragraph, these cavitation phenomena are from a different origin then the cavitation bubbles observed in this study. Also, in our study, we do not have any evidence of the presence of density wave and micro cavitation bubbles in liquid or tissue. In the literature, these 'micro' cavitation phenomena are described with ultrasonic devices working in a far higher frequency regime over several hundred kHz [20].

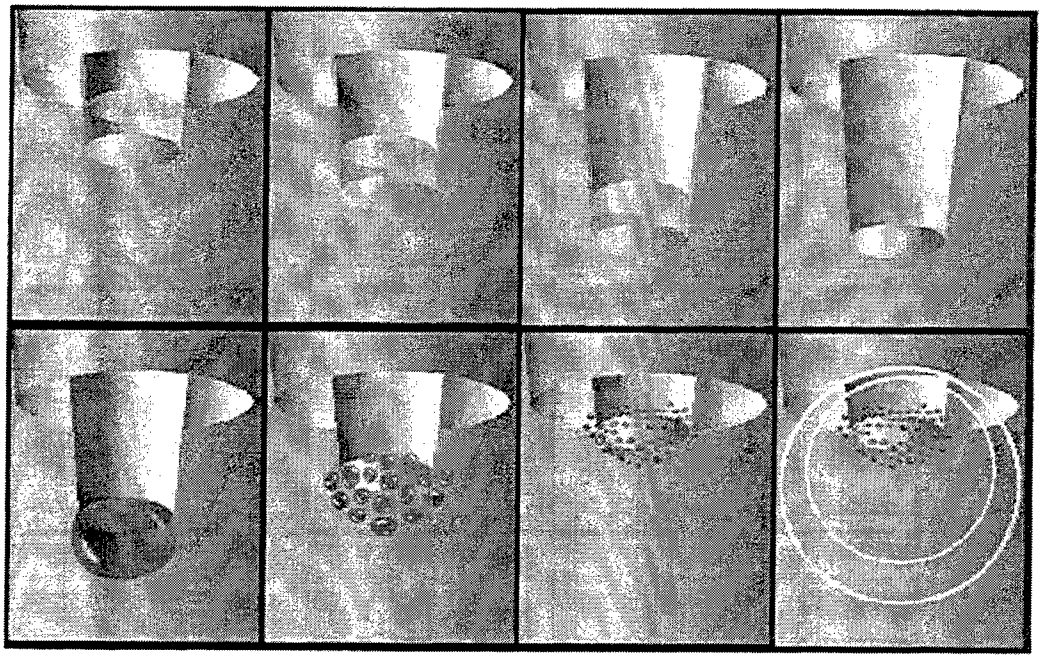

Figure 9: animation of the CUSA action during one sequence of the duty cycle of the needle.

Shock-waves

The visualization of shock waves associated with the CUSA mechanism of action has been revealing since is has not been reported before. At the same time, it might rise reasons for concern. In the field of medical laser applications, many reports deal with the adverse effects of pulsed laser induced shock waves [21]. The shock waves involved with pulsed lasers can however be of a total different order of magnitude. Although the biological effect of shock waves is still under investigation, some studies indeed show evidence for adverse effects [22] [23]. Since the CUSA has been applied already for many years in one of the most sensitive organs of our body; the brain, adverse effects should surely have been observed if present. Still, it might be an interesting topic for further investigation to quantify the pressure waves involved.

6.5 Further research of Ultrasonic Surgery devices

This study can be seen only as an initial study to explore the mechanism of action and the characterization of the CUSA. Besides the CUSA there are many surgical instruments similar to the CUSA or related like the phacoemulsification in ophthalmology, and more recently introduced, the harmonic knife for general surgery. There is a whole list of features that can be investigated with the imaging techniques described in this paper like:

- frequency range (23 - 55 kHz)
- tip amplitude (un)loaded
- shape and contact surface of tip
- fragmentation ability
- tissue selectivity
- intermittent vibration (CAVI-pulse)
- combination with electro surgery
- probe contamination and durability
- irrigation quality
- aspiration quality
- surgeons technique
- contact with tissue

These studies will contribute to a better understanding of the mechanism of action, improvement of instrumentation design and controllability and safety in accepted and new clinical applications

7. CONCLUSIONS

The Mechanism of Ultrasonic Surgery shows to be a combined effect of fragmentation induced by 'macro' cavitation bubble, mechanical cutting and thermal deterioration of tissue depending on the irrigation/aspiration flow intermittent vibration regime degree of tissue contact.

The impact of the shock waves observed at cavitation bubble implosion is undetermined yet.

Real-time imaging techniques contribute to the understanding of the working mechanism of Ultrasonic Surgery in relation to probe designs, US generator settings and tissue characteristics.

8. ACKNOWLEDGEMENTS

The authors like to thank Lex Beers of the Audiovisual Center of the University Hospital Utrecht.

9. REFERENCES

1. Brotchi J, Noterman J, Baleriaux D: Surgery of intramedullary spinal cord tumours. *Acta Neurochir.Wien.* 1992;116:176-178
2. Finley JL, Silverman JF, Dickens MA: Immunocytochemical evaluation of central nervous system tumors obtained by the Cavitron ultrasonic surgical aspirator. *Diagn.Cytopathol.* 1990;6:308-312
3. Fasulo F, Giori A, Fissi S, Bozzetti F, Doci R, Gennari L: Cavitron Ultrasonic Surgical Aspirator (CUSA) in liver resection. *Int.Surg* 1992;77:64-66
4. Storck BH, Rutgers EJ, Gortzak E, Zoetmulder FA: The impact of the CUSA ultrasonic dissection device on major liver resections. *Neth.J Surg* 1991;43:99-101
5. Malhotra V., Malik R., Gondal R., Beohar P.C., and Parkash B. Evaluation of histological appearance of tissues removed by Cavitron ultrasonic surgical aspirator (CUSA). *Acta Neurochir.Wien.* 1986;81:132-134

6. Bond LJ, Cimino WW: Physics of ultrasonic surgery using tissue fragmentation. *Ultrasonics.* 1996;34:579-585
7. Cimino WW, Bond LJ: Physics of Ultrasonic Surgery Using Tissue Fragmentation .1. *Ultrasound Med. Biol.* 1996;22:89-100
8. Madanshetty SI, Apfel RE: Acoustic microcavitation: enhancement and applications. *J Acoust.Soc.Am* 1991;90:1508-1514
9. Madanshetty SI, Roy RA, Apfel RE: Acoustic microcavitation: its active and passive acoustic detection. *J Acoust.Soc.Am* 1991;90:1515-1526
10. Rau HG, Meyer G, Jauch KW, Cohnert TU, Buttler E, Schildberg FW: Liver Resection by Water Jet Conventional and Laparoscopic. *Chirurg* 1996;67:546-551
11. Vasquez JM, Eisenberg E, Osteen KG, Hickerson D, Diamond MP: Laparoscopic ablation of endometriosis using the cavitational ultrasonic surgical aspirator. *J Am Assoc.Gynecol.Laparosc.* 1993;1:36-42
12. Van Dam P.A., Tjalma W., Weyler J., Van Oosterom A.T., Buytaert P.: Ultraradical debulking of epithelial ovarian cancer with the ultrasonic surgical aspirator: a prospective randomized trail. *Am J Obstet.Gynecol.* 1996;174:945-950
13. Baumgartner F, Pearsall P, Omari K, Robertson J: Aortic and mitral annular remodeling using ultrasonic decalcification. *Herz.* 1996;21:179-182
14. Millat B, Hay JM, Descottes B, Fingerhut A, Fagniez PL: Prospective evaluation of ultrasonic surgical dissectors in hepatic resection: a cooperative multicenter study. *HPB.Surg* 1992;5:135-144
15. Muraki J, Addonizio JC, Lastarria E, Eshghi M, Choudhury MS: New Cavitron system (CUSA/CEM): its application for kidney surgery. *Urology* 1993;41:195-198
16. Kato K, Matsuda M, Onodera K, Kasai S, Mito M, Saito T: An ultrasonically powered instrument for laparoscopic surgery: a brief technical report of preliminary success. *J Laparoendosc.Surg* 1995;5:31-36
17. Verdaasdonk RM: Imaging laser induced thermal fields and effects, in Jacques SL (ed): *Laser-Tissue interaction VI.* Bellingham, SPIE, 1995, pp 165-175
18. Cimino WW, Bond LJ: Physics of ultrasonic surgery using tissue fragmentation: Part I. *Ultrasound.Med Biol.* 1996;22:89-100
19. Bond LJ, Cimino WW: Physics of ultrasonic surgery using tissue fragmentation: Part II. *Ultrasound.Med Biol.* 1996;22:101-117
20. Holland CK, Apfel RE: Thresholds for transient cavitation produced by pulsed ultrasound in a controlled nuclei environment. *J Acoust.Soc.Am* 1990;88:2059-2069
21. Tomaru T, Geschwind HJ, Boussignac G, Lange F, Jea Tahk S: Characteristics of shock waves induced by pulsed lasers and their effects on arterial tissue: Comparison of excimer, pulse dye, and holmium YAG lasers. *Am.Heart J.* 1992;123:896-904
22. Prat F, Chapelon JY, Chauffert B, Ponchon T, Cathignol D: Cytotoxic effects of acoustic cavitation on HT-29 cells and a rat peritoneal carcinomatosis in vitro. *Cancer Res.* 1991;51:3024-3029
23. Delius M, Jordan M, Liebich HG, Brendel W: Biological effects of shock waves: effect of shock waves on the liver and gallbladder wall of dogs--administration rate dependence. *Ultrasound.Med Biol.* 1990;16:459-466

Experimental study and first clinical results with a cooled applicator system for interstitial laser coagulation (LITT)

A. Roggan[1], V. Knappe[2], M. G. Mack[3], T. J. Vogl[3],
D. Albrecht[4], C. T. Germer[4], J.-P. Ritz[4], F. Kniep[5], G. Müller[1,2]

[1]Institut für Medizinische/Technische Physik und Lasermedizin,
Universitätsklinikum Benjamin Franklin, Freie Universität Berlin
[2] Laser- und Medizin-Technologie gGmbH, Berlin
[3] Klinik und Poliklinik für Radiologie, Virchow-Klinikum, Humboldt-Universität zu Berlin
[4] Chirurgische Klinik und Poliklinik, Universtitätsklinikum Benjamin Franklin, Freie Universität Berlin
[5] Somatex, Medizintechnische Instrumente, Rietzneuendorf

ABSTRACT

Laser-induced interstitial thermotherapy (LITT) has proven to be an effective method for the treatment of different types of tumors. Until now the attainable coagulation volume was limited by the maximum applicable energy. The limiting factor was the high tissue temperature around the applicator which may have caused applicator damage. Consequently an internally cooled catheter system has been developed in order to reduce the temperature of the applicator surface and to allow for the application of higher laser powers. The optimal treatment parameters for the Nd:YAG laser were determined on the basis of *in vitro* studies with porcine tissue. Following these experimental studies, 127 patients with liver metastases were treated with the cooled system. The applicator position and the resulting tissue damage were verified using a MRI on-line monitoring system applying a FLASH-2D sequence. The optimal *in vivo* treatment parameters were found to be 25 watts for an exposure time of 20 minutes, resulting in coagulated volumes of up to 20 cm^3. The experimental and clinical results have proven that the combination of a scattering laser applicator with an internally flushed catheter enables a significant increase in the coagulation volume.

1 INTRODUCTION

During the last few years laser-induced interstitial thermotherapy (LITT) has become an effective method for the treatment of different types of tumors and of benign prostatic hyperplasia (BPH). The significance of this method is in fact increasing because it is a minimal invasive technique that permits the destruction of localized pathological tissue with limited damage to the surrounding healthy structures. The light source for interstitial coagulation is usually a Nd:YAG laser which penetrates deeply into biological tissue. The laser light is guided through a flexible quartz fiber that is directly punctured into the tumor region. The fiber has a special laser applicator at its distal end to provide a homogeneous interstitial photon distribution[1-5]. Subsequent photon absorption leads to temperatures up to 150 °C in the tumor region and provides a well-defined area of coagulation necrosis, subsequent degeneration, and finally tumor shrinkage (Fig. 1). In order to avoid direct contact between laser applicator and tissue, fiber and laser applicator should be inserted into a protecting catheter for patient safety [1]. The optimum applicator position within the tumor can be controlled with ultrasound, CT or Magnetic Resonance Imaging (MRI). The latter has also proven to be an ideal procedure for real time treatment monitoring of hyperthermic effects and the evaluation of the extent of coagulation necrosis [6-9].

In general, the coagulation efficiency is dependent on both the optical and thermal properties of tumor tissue and local blood perfusion as well as the applicator light emission distribution. The maximum input power is restricted by the power density on the applicator surface which causes a certain tissue temperature near the applicator. The maximum coagulation volume is therefore limited by this temperature because overheating can cause carbonization and subsequent applicator damage. Until now commonly used applicators were restricted to a maximum laser power of approximately 6 watts at 1064 nm and a maximum exposure time of 20 minutes[1-4], resulting in coagulation volumes of up to approximately 4 cm^3.

[1] Correspondence (A.R.):
Krahmerstr. 6-10, D-12207 Berlin; phone: ++49-30-844923-0; fax: ++49-30-844923-99; e-mail: lmzwe19@zedat.fu-berlin.de

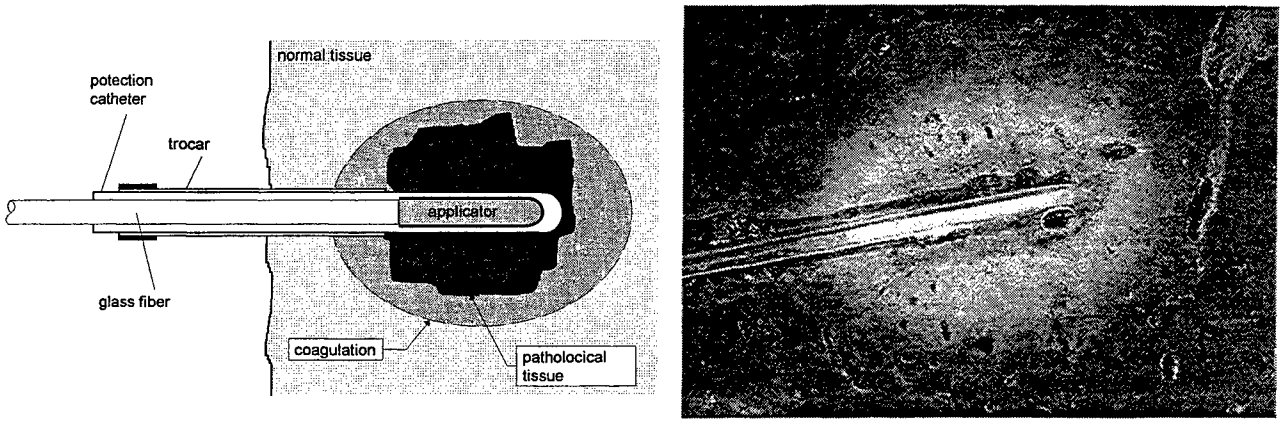

Fig. 1: Schematic diagram of interstitial laser coagulation and *in vitro* experiment in porcine liver with a scattering applicator (LMTB)

Clinical studies about palliative percutaneous LITT for the treatment of liver metastases have shown that tumors with a maximum diameter of 2 cm can be treated sufficiently, i.e. tumor destruction without recurrence[8]. However, in order to treat larger lesions or organs with a high perfusion, additional treatment techniques are required to ensure patient safety. Until now lesions between 2 and 4 cm in diameter have been treated either with a simultaneous multi-applicator technique or in pull-back technique with subsequent applications in the same puncture channel. The main disadvantage of the multi-applicator technique is that additional punctures are needed to treat larger lesions. Furthermore, radiation planning is a difficult procedure because the geometry of the resulting necrotic volumes is not as homogenous as with a single application. The risk remains that parts of the tumor, particularly on the edges, are not sufficiently damaged. The disadvantage of subsequent applications is that more treatment time is needed without a temperature adding effect. Additionally, the tumor extension should be large in the direction of the puncture axis and the lateral tumor dimensions should be less than 2 cm in diameter. To improve the LITT procedure an internally cooled applicator system was developed which enables an increase in the necrotic volumes in a single application without carbonization and vaporization.

2 COOLED APPLICATOR SYSTEM

Cooling the surface of a laser applicator modifies the radial temperature distribution so that the maximum temperature shifts into deeper tissue layers[3,4,11-13]. This was evaluated by computer simulations calculating the temperature distribution of different types of applicators in porcine liver by normalizing the input power to a maximum tissue temperature of 100 °C (Fig. 2)[10]. The temperature distribution at the cooled applicator is a combined effect of deep optical penetration of the Nd:YAG laser and cooling of the applicator surface. Hence the cooled applicator can be used at significantly higher laser powers than non-cooled systems without exceeding critical temperatures. Nevertheless, it has to be taken into consideration that part of the deposited energy does not become therapeutically effective because it is removed by the internal cooling flow. Computer simulations for the new applicator have demonstrated that the amount of lost energy reaches 20-40-30 %, depending on the type of tissue.

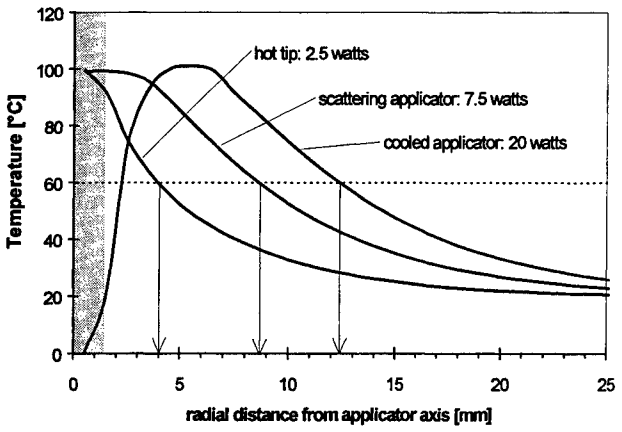

Fig. 2: Calculated radial temperature profile of different applicators in porcine liver (Simulation for Nd:YAG laser)

The newly designed cooled applicator system is a combination of a modified scattering applicator with a outer diameter of 0.95 mm (Fig. 3) and a double-tube PTFE-catheter that enables internal cooling with saline solution (Fig. 4). The catheter material is flexible, transparent for near infrared radiation and temperature stable up to 400 °C. After the catheter is positioned within the tumor the scattering applicator is introduced through a proximal sealing. The applicator is finally pushed forward to a position approximately 5 mm before the distal end of the catheter to provide a sufficient flushing rate. Figure 3 shows the axial intensity distribution of the application system (flushed with water), measured with a modified integrating sphere[14,15].

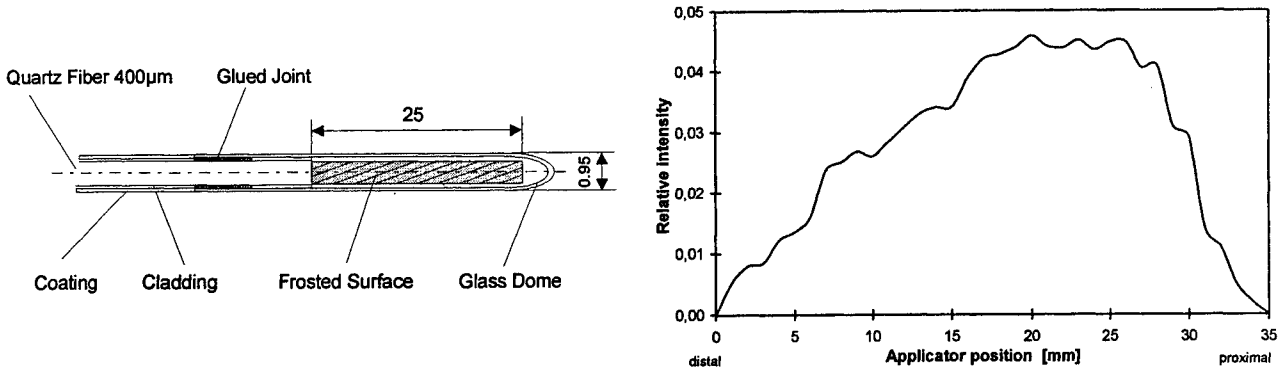

Fig. 3: Schematic diagram of the modified scattering applicator and its intensity distribution along the axis

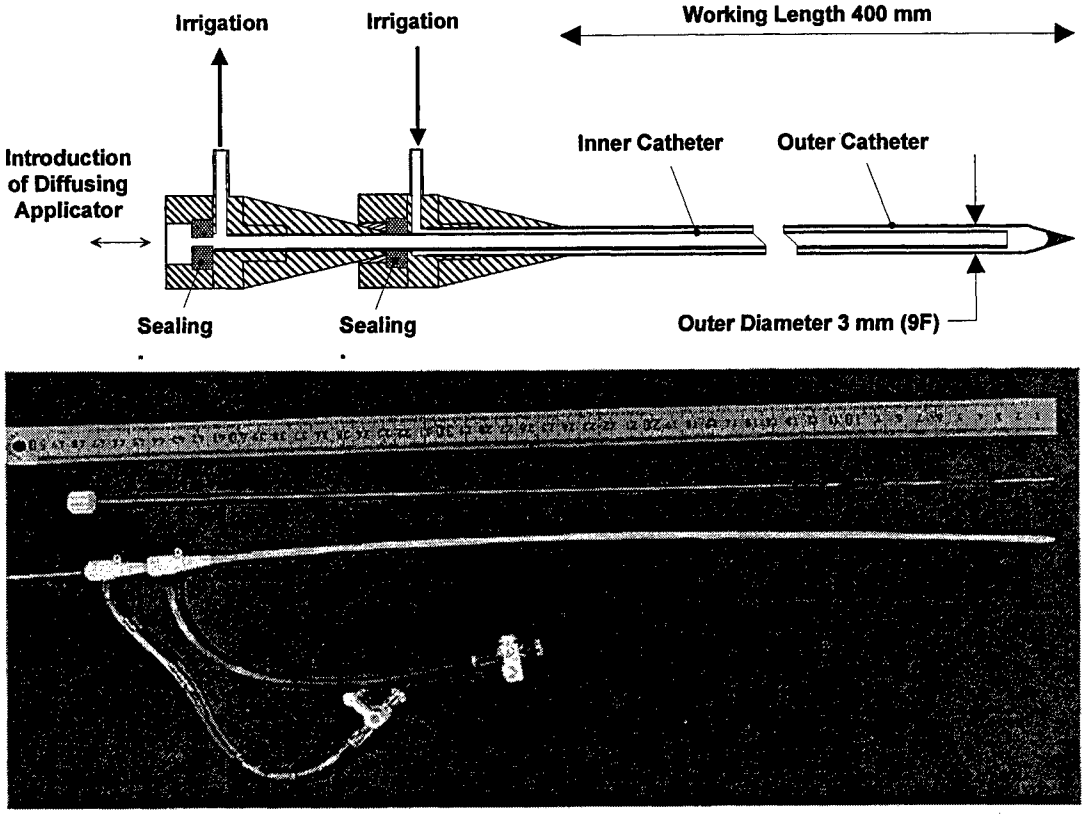

Fig. 4: Internally cooled laser application system with removed mandrin

The cooled applicator system was combined with a modified MR-compatible puncture equipment (needle, guide wire and 10 F-trocar) and permits the MR-guided percutaneous approach to liver tumors as well as intraoperative positioning. The catheter has a spiked end and a rigid mandrin allowing easy repositioning. The application system can be specified with following technical data:

Double-tube catheter:	outer diameter:	3.0 mm, 9 Fr
	length:	420 mm
	tube connection:	LUER-lock
	cooling medium:	saline solution
	cooling temperatures:	0 - 25°C
Scattering applicator:	fiber length:	12 m
	fiber core diameter:	400µm
	fiber type:	HCS
	fiber numerical aperture:	0.37
	laser connector:	SMA 905
	outer diameter:	0.95 mm
	active length:	25 mm

3 *IN VITRO* EXPERIMENTS

The optimal treatment parameters for the Nd:YAG laser (Dornier 5100 fibertom, 1064 nm) were determined *in vitro* by evaluating the volume of the resulting lesions in porcine liver and muscle at room temperature. The distal output power of the laser applicator was measured with an integrating sphere power meter (Hüttinger, MY-TEST). A peristaltic pump (Dornier) was used to ensure a continuous cooling flow rate of 60 ml/min. The experimental results showed that flow rates less than 40 ml per minute did not provide sufficient cooling, resulting in carbonization at laser powers above 20 watts and exposure times in excess of 10 minutes. On the other hand, a flow of over 100 ml per minute did not result in a higher damage threshold because the transfer of heat from the tissue into the cooling liquid was limited by heat conduction of the catheter material. The *in vitro* experiments were carried out at output powers of 20, 23, 25 and 30 watts with an exposure time of 10 minutes. Especially in liver tissue power settings above 30 watts resulted in slight charring in the region of the maximum temperature. Consequently laser powers above 30 watts were excluded from the investigation. Each experiment was repeated five times in order to calculate standard deviations. Fig. 5 shows the results for all investigated power settings. As expected, an increase in laser power led to an increase in the coagulated volume and slightly larger lesions for muscle tissue. All lesions were nearly spherical, a typical dimension in liver tissue was 4.0 x 3.2 cm at 25 watts laser power. The experiments showed, that the use of a cooled applicator resulted in a distinct increase in the coagulated volume compared to non-cooled laser applicators without the risk of carbonization and subsequent applicator damage.

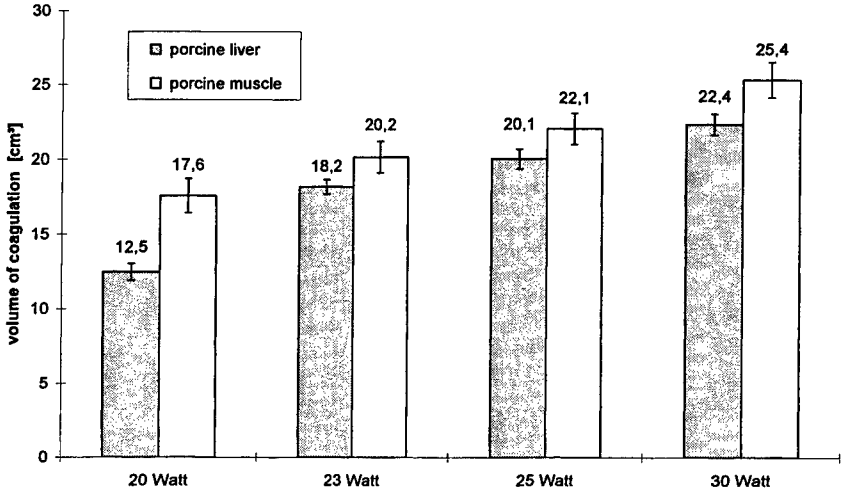

Fig. 5: Results of *in vitro* experiments with the cooled laser application system (25 mm active length, 20 °C saline solution, 60 ml/min); 10 minutes exposure time, 22 °C tissue temperature

Further *in vitro* experiments were performed in order to determine the interstitial temperature distribution around the cooled applicator. The applied method was described by Roggan et al.[15], using an infrared camera (Agema 900) and a tissue phantom which permits a book-like opening of two tissue layers (porcine liver), allowing a thermographic representation of the applicator plane. Fig. 6 shows the measured interstitial temperature distribution of a cooled applicator system (25 watts) in time intervals of 2 minutes. The last measurement was performed 2 minutes after the laser had been switched off. The thermographic pictures show the typical temperature distribution of a cooled applicator with a maximum temperature located a few millimeters away from the applicator surface. No hot spots were found which could cause subsequent applicator damage.

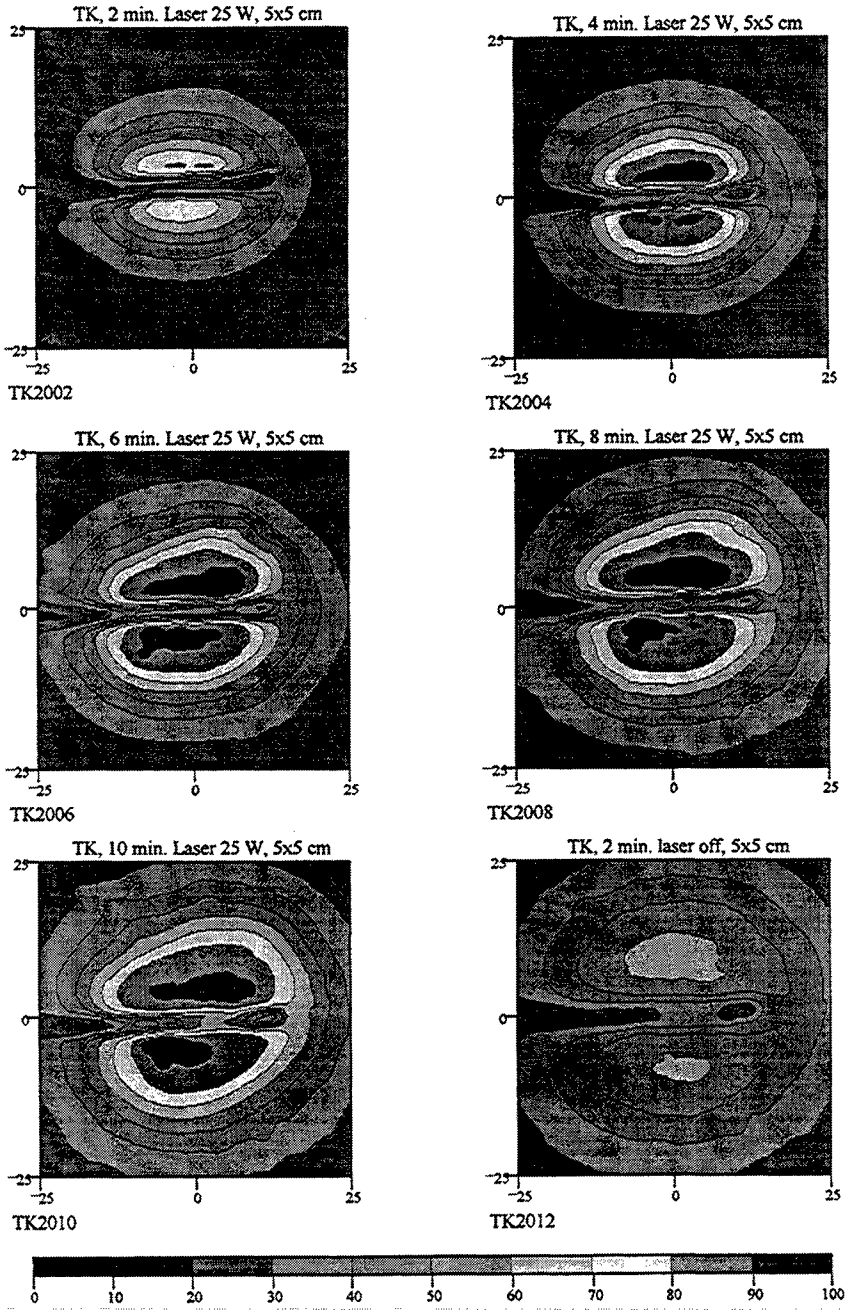

Fig. 6: Measured interstitial temperature distribution obtained with a cooled applicator system (25 mm active length, 20 °C saline solution, 60 ml/min), 25 W Nd:YAG laser, 10 minutes exposure time, porcine liver (20 °C)

4 CLINICAL USE OF THE COOLED APPLICATOR SYSTEM

Following the experimental *in vitro* studies a pilot clinical trial was carried out on patients with liver metastases of colorectal carcinoma. Surgical tumor resection is still the only potentially curative option for the treatment of intrahepatic colorectal metastases when the primary tumor has been totally removed. But only 20-40 % of the patients are suitable for surgical resection because of the presence of metastases in both hepatic lobes or a poor general condition[16-20]. This fact was the motivation to apply LITT as a therapeutic alternative for the treatment of non-resectable liver tumors.

In our clinical study 127 patients with a total of 317 liver metastases were treated from December 1996 to December 1997 with MR-guided laser-induced interstitial thermotherapy (LITT) in combination with the cooled applicator system. The primary tumor was colorectal cancer in 78 patients (61 %), breast cancer in 24 patients (19 %), hepatocellular carcinoma in 9 patients (7 %) and other primary tumors in 16 patients (13 %). LITT was carried out after approval from the local ethical committee and with the patients' informed consent. Localization and extension of the tumor were evaluated by MR-imaging prior to LITT with a conventional 1.5 Tesla MR unit (Siemens SP-4000), applying T1-weighted (SE, GE) and T2-weighted (SE) sequences plain as well as after administration of 0.1 mmol/kg body weight Gd-DTPA (Fig.7 a-c).

All patients received Pethidine (50-100 mg) intravenously before the treatment. The puncture of the catheter system was CT-guided in Seldinger technique[8] under local administration of 20 ml Lidocaine (1%). Then the patients were transferred to the MR-unit and a MRI marker was inserted into the catheter system to precisely locate its position. The laser applicator was finally introduced into the flushing catheter after the MRI marker had been removed. MR thermometry was used for on-line monitoring of the laser intervention applying FLASH-2D sequences (TR/TE/flip=102/8/15°) at intervals of 30 seconds. Hence the actual tissue damage and temperature development could easily been verified (Fig. 8a-c). A Nd:YAG laser served as light source (Dornier 5100, Martin My30). The mean laser power was 24.5 watts, providing a significant safety margin to the carbonization threshold. The mean treatment interval was 20 minutes and was increased in comparison to the *in vitro* experiments in order to compensate for heat losses due to the high blood perfusion of liver tissue. The cool flow of the catheter was provided by a peristaltic pump at a rate of 60 ml/min sterile saline solution at room temperature.

The laser-induced necrotic volumes were measured after intravenous injection of Gd-DTPA immediately after the treatment, showing an average coagulation diameter of 3.3 cm. Consequently tumors with more than 3 cm maximum extension were treated with two or more applications. Laser applicator and cooled catheter were finally removed and the puncture channel was closed by filling two components tissue glue into the trocar during its removal.

All patients tolerated the procedure well under local anesthesia without clinically relevant complications. The normal hospitation time was 1-2 days. The follow up of all patients included MR-imaging at two days, one month, three month and every six month after the LITT procedure. Qualitative and quantitative parameters were evaluated, including size, morphology, and contrast enhancement pattern at early and late follow up examinations.

For the discussion of survival rates we focused on patients with colorectal liver metastases because comparative statistical data are available for liver resection, chemotherapy and no treatment. Including 48 patients which were treated with the standard (non-cooled) applicator technique, a total of 126 patients with colorectal liver metastasis received LITT since 1992. The median survival among those patient with colorectal metastases was 34.9 months calculated according to Kaplan-Meier (maximum survival 54.5 months). For comparison, Scheele et al.[19] followed up 1718 consecutive patients with colorectal liver metastases, 469 of whom underwent hepatic resection (27 %). Among these, 434 resections were performed with curative intent (25 %). Operative mortality was 4.4 % while 16 % showed significant morbidity after resection. Median survival for the entire sample of patients undergoing liver resection with curative intent was 39.4 months, excluding 30-day mortality. For comparison, Stangl et al.[21] followed up 1099 patients with colorectal liver metastases, 566 of whom (52 %) received no treatment for their hepatic metastases, 340 (31 %) underwent hepatic resection; 123 (11 %) received regional chemotherapy; and 70 (6 %) received systemic chemotherapy. After hepatic resection the median survival was found to be 30 months for all patients but 41 months for those with complete tumor clearance. In patients who received regional or systemic chemotherapy, the median survival was 12.7 and 11.1 months, respectively. In the untreated group the median survival was 7.5 months.

In summary, MR-guided LITT has proven to be a safe and effective palliative treatment protocol for liver metastases because survival rates are significantly improved in comparison to untreated patients and chemotherapy. Further studies are required in order to compare laser-induced interstitial thermotherapy LITT with surgical resection of liver metastases and to investigate the combination of LITT with chemotherapy and other therapeutic protocols (e.g. embolization).

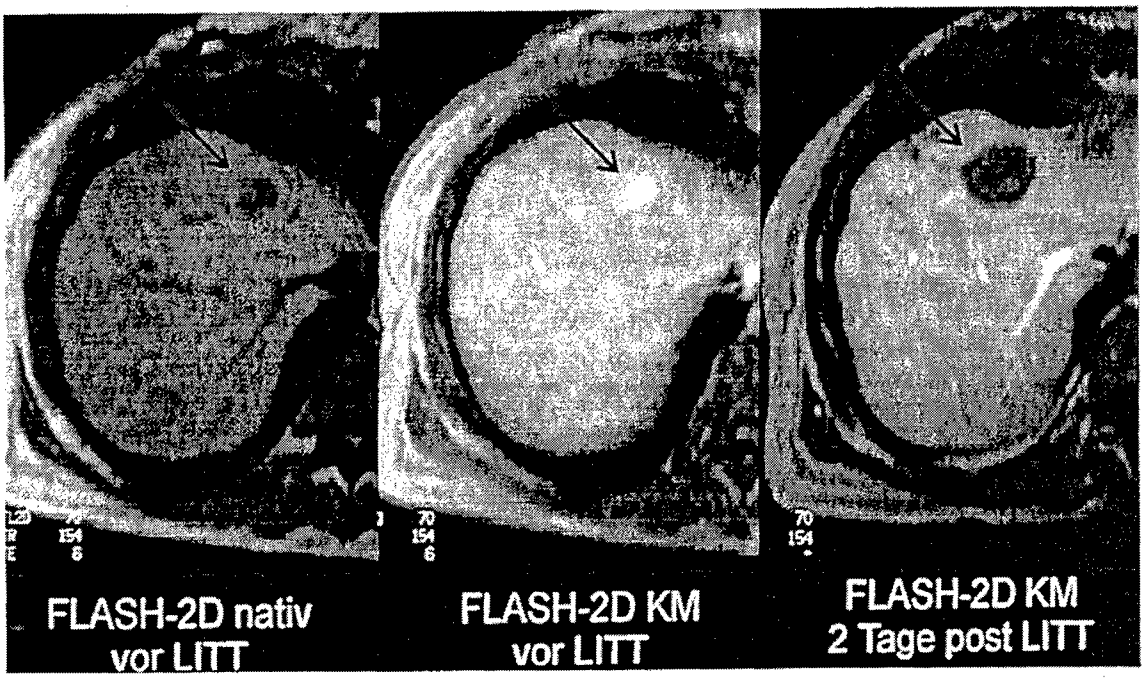

Fig. 7: FLASH-2D-sequence (TR/TE/Flip = 154/6/70°); a: Pre-therapy image, used for the intervention LITT-planning prior to treatment, b: Contrast enhanced FLASH-2D image before LITT with a distinct lesion enhancement after administration of 0.1 ml/kg body weight Gd-DTPA, c: Contrast enhanced FLASH-2D image two days after MR guided LITT clearly shows the resulting tissue necrosis

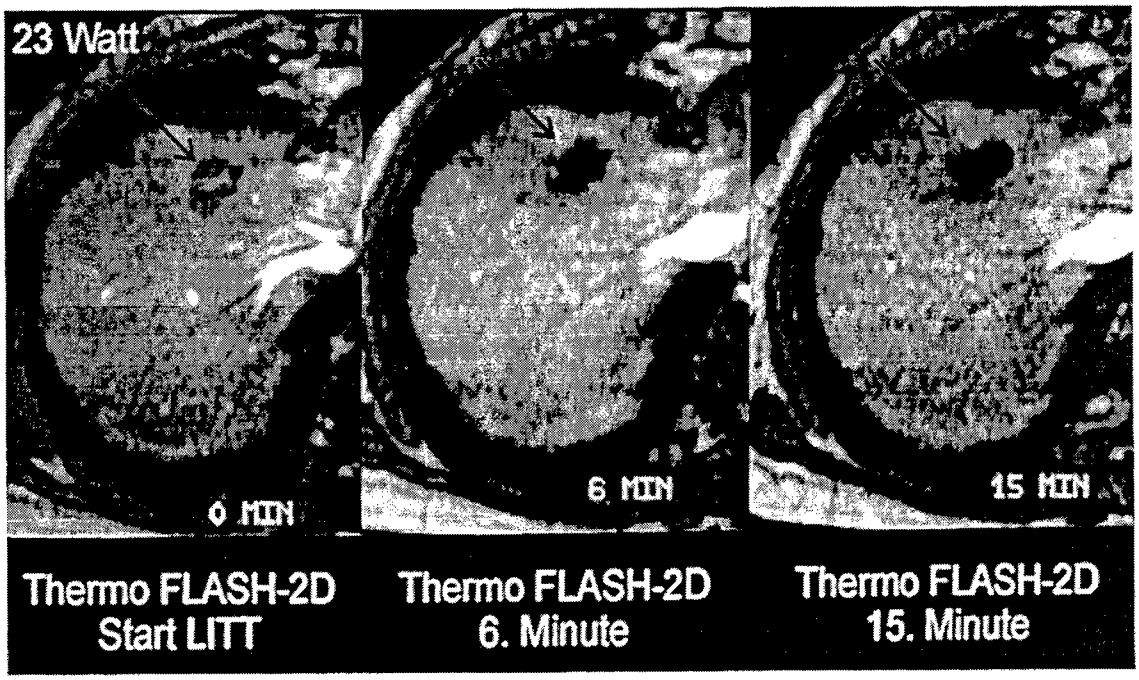

Fig. 8: FLASH-2D (TR/TE/Flip = 102/8/15°) image; a: Before LITT treatment with cooled applicator system, b: After 6 minutes of LITT treatment, c: After 15 minutes of LITT treatment

5 CONCLUSION

In vitro experiments with a cooled applicator system demonstrated that the coagulation volume of interstitially produced laser lesions can significantly be increased in comparison to non-cooled applicators. Nearly spherical damage volumes of 20 cm^3 were achieved with a laser power of 25 W and an exposure period of 10 minutes in porcine liver. Applying a cooling rate of 60 ml/min neither tissue carbonization nor damage of the applicator system was observed.
The clinical results confirmed the *in vitro* results, showing that the combination of a scattering laser applicator and an internally cooled catheter led to a significant growth of the coagulation volumes. This technique now provides the possibility of treating tumors with a diameter of up to 3 cm with a single application. Hence the comfort for the patient is drastically improved because the number of punctures have been reduced to 25 % and the risk of residual tumor tissue has been reduced significantly. MR-imaging has proved to be an ideal tool for on-line monitoring of interstitial laser coagulation with cooled applicators. Already one minute after starting the treatment distinct hypointense reactions were observed around the applicator region. The hypointense area increased during laser emission and disappeared a few minutes after the laser was switched off. The dimension of the hypointense area was found to correlate very well with the non-enhancing post treatment region after administration of Gd-DTPA. Follow-up evaluation of patient survival demonstrated that MR-guided LITT has proven to be an adequate tool to treat liver tumors very effective with a low strain for the patient.

6 ACKNOWLEDGMENT

Part of the work was supported by the Bundesministerium für Bildung, Wissenschaft, Forschung und Technologie (BMBF, Grants FKZ 13N6507 and FKZ 13N7064)

7 REFERENCES

(1) Hessel S., Frank F., "Technical prerequisites for the interstitial thermotherapy using the Nd:YAG laser". Proc. SPIE **1201**: 233-238, 1990
(2) Panjehpour M., Overholt BF., Milligan AJ., Swaggerty MW., Wilkinson JE., Klebanow ER, "Laser-induced interstitial hyperthermia using a long frosted contact probe". Lasers Surg Med **10**(1): 16-24, 1990
(3) Roggan A., Albrecht D., Berlin H.-P., Beuthan J., Fuchs B., Germer C. T., Mesecke v. Rheinbaben I., Rygiel R., Schründer S., Müller G., "Application equipment for intraoperative and percutaneous laser-induced interstitial thermotherapy (LITT)", *Laser-induced Interstitial Thermotherapy*, G. Müller, A. Roggan (Eds.), SPIE Optical Engineering Press, Bellingham, Washington, pp. 224-248, 1995
(4) Schwarzmaier H.-J., Kaufmann R., Kahn Th., Ulrich F.: "Applicators for laser-induced thermotherapy- Basic consideration and new developments", *Laser-induced Interstitial Thermotherapy*, G. Müller, A. Roggan (Eds.), SPIE Optical Engineering Press, Bellingham, Washington, pp. 249-262, 1995
(5) Heisterkamp J., van Hillegersberg R., Sinofsky E., Ijzermans JN, "Heat-resistant cylindrical diffuser for interstitial laser coagulation: comparison with the bare-tip fiber in a porcine liver model" .Lasers Surg Med **20**(3):304-309, 1997
(6) Gewiese B., Beuthan J., Fobbe F., Stiller D., Müller G., Boese-Landgraf J., Wolf KJ., Deimling M., "Magnetic resonance imaging-controlled laser-induced interstitial thermotherapy", Invest Radiol **29**: 345-51, 1994
(7) Kahn T., Bettag M., Ulrich F., Schwarzmaier HJ., Schober R., Fürst G., Mödder U., "MRI-guided laser-induced interstitial thermotherapy of cerebral neoplasms", J. Comp. Assist. Tomogr. **18**(4): 19-532, 1994
(8) Vogl TJ., Müller PK., Hammerstingl R., Weinhold N., Mack MG., Philipp C., Deimling M., Beuthan J., Pegios W., Riess H., Lemmens HP., Felix R., "Malignant Liver Tumors Treated with MR Imaging-guided Laser-induced Thermotherapy: Technique and Prospective Results", Radiology **196**: 257-265, 1995
(9) Bothnar R., Steiner P., Erhart P., Debatin J., Schulthess GK., "Absolute temperature quantification in near real-time with an open 0.5 Tesla interventional MR-Scanner", Proc. Int. Soc. Magn. Reson. Med. **3**:1957, 1997
(10) Roggan A., Müller G., "Dosimetry and computer-based irradiation planning for laser-induced interstitial thermotherapy (LITT)", *Laser-induced Interstitial Thermotherapy*, G. Müller, A. Roggan (Eds.), SPIE Optical Engineering Press, Bellingham, Washington, pp. 114-156, 1995
(11) Dowlatshahi K., Bangert JD., Haklin MF., Rhodes CK., Weinstein RS., Economou SG, " Protection of fiber function by para-axial fluid flow in interstitial therapy of malignant tumors", Lasers Surg Med 10(4):322-327, 1990

(12) Orth K., Russ D., Duerr J., Hibst R., Steiner R., Beger HG., " Thermo-controlled device for inducing deep coagulation in the liver with the Nd:YAG laser", Lasers Surg Med **20**(2): 149-156, 1997
(13) Sturesson C., Andersson-Engels S.," Tissue temperature control using a water-cooled applicator: implications for transurethral laser-induced thermotherapy of benign prostatic hyperplasia", Med Phys **24**(3): 461-470 1997
(14) Mesecke v. Rheinbaben I., Roggan A., Mollenhauer I., Müller G., Boenick U., "Entwicklung eines Meßplatzes zur Bestimmung des Abstrahlverhaltens von Streulichtapplikatoren für interstitielle Laseranwendungen", Biomedizinische **41**:60-63, 1996
(15) Roggan A., Mesecke v. Rheinbaben I., Schründer S., Müller G., "In-vitro measurements of two-dimensional temperature distributions during laser-induced interstitial thermotherapy (LITT) and comparison with theoretical calculations", Proc. SPIE **2623:** 245-261, 1995
(16) Adson MA., "Resection of liver metastases - When is it worthwhile ?", World J Surg **11**: 511-515, 1987
(17) Hughes K., Simon R., Songhorabodi S., "Registry of hepatic metastases; resection of the liver for colorectal carcinoma metastases - a multi institutional study for indications of the resection", Surgery **103:** 278-288, 1988
(18) Holm A., Bradley E., Aldrete JS. "Hepatic resection of metastases from colorectal carcinoma", J. Cancer **12**: 1622-1627, 1989
(19) Scheele J., Stangl R., Altendorf-Hofmann A., Paul M., "Resection of colorectal liver metastases", World J Surg **19**: 59-71, 1994
(20) Zavadsky KE., Lee YTM., "Liver metastases from colorectal carcinoma: incidence, resectability, and survival results", Ann Surg **60**: 929-932, 1994
(21) Stangl R., Altendorf Hofmann A., Charnley RM., Scheele J. "Factors influencing the natural history of colorectal liver metastases. Lancet **343**: 1405-1410, 1994

A New Application System for Simultaneous Laser and Ultrasonic Transmission in Endoscopic Surgery (LUST)

K. Desinger [a], J. Helfmann [b], T. Stein [b], K. Liebold [a], G. Müller [a, b]

[a] Laser- und Medizin-Technologie gGmbH, Krahmerstr. 6-10, D-12207 Berlin, Germany
Tel.: +49-30-844 9230, Fax: +49-30-844 923 99
e-mail: lmzwe19@ zedat.fu-berlin.de
[b] Institut für Med./Technische Physik und Lasermedizin, FU Berlin, Krahmerstr. 6-10, D-12207 Berlin
Tel.: +49-30-8445 37 58, Fax: +49-30-844 923 99

ABSTRACT

A new combined Laser and Ultrasound Surgical Therapy (LUST) device for an endoscopically suitable coagulation and tissue fragmentation based on the transmission of laser radiation and ultrasound via flexible silica glass fibers was developed at the LMTB [1]. The ultrasound tissue interaction is based on the well-known CUSA-technology, which enables the surgeon to cut various types of tissue with different degrees of effectiveness. This selective cutting performance is a very useful feature, e.g. for a brain tumor extirpation, where it must be guaranteed that vessels and nerves are not affected while ensuring a fast reduction of the tumor mass. Application fields are in oncology, neurosurgery and angioplasty. The laser radiation can be used for tissue coagulation purposes and homeostasis. With a fiber based LUST-system working at a resonance frequency of 30 kHz, using a laser-vibrometer, velocity amplitudes of up to 20 m/s could be detected at the distal end which corresponds to an elongation of more than 100 µm. The investigations have shown that the velocity amplitude, next to suction, frequency and cross section of the active fiber tip, has the greatest impact on the fragmentation rate. With a suction setting of 5 W, the following tissue fragmentation rates could be achieved with a 1.3 mm^2 fiber cross section and a tip amplitude velocity of 12 m/s: brain tissue 50 mg/s, liver 4,5 mg/s and kidney 4 mg/s. Laser radiation up to 25 watt was sufficient to coagulate soft tissue. This new approach in developing an application system for the therapeutical use of laser radiation and ultrasound via optical waveguides offers new possibilities in minimally invasive surgery, providing a complete new working sphere for the surgeon. The flexible opto-acoustic waveguide (∅ 400- 1700 µm) can be bent making areas accessible which were inaccessible before. The surgeon can use the laser radiation for tissue coagulation or cutting and the ultrasound for tissue fragmentation and tissue reduction without changing the instrumentation.

1. INTRODUCTION

A new combined endoscopical laser and ultrasound surgical therapy device has been investigated. The feasibility of ultrasound and laser transmission via silica glass fibers has been shown [2,3]. An active element of this medical applicator is a thin silica glass fiber (∅ 300 - 1700 µm), usually used only for laser transmission, which transfers the acoustic energy from a piezoelectric ultrasound transducer to biological tissue. The fiber consists of an amorphous silica core and cladding and a plastic coating to enhance the mechanical stability. The coatings of the used fibers are made of polymers (polyimide, acrylate). Regarding the ultrasound transmission, core and cladding of the fiber can be seen as a homogeneous structure (as core). In fig. 1, the results of our investigations on the ultrasound tissue interaction are presented : The efficiency of ultrasound tissue fragmentation as a function of tissue and the specific acoustic parameters.

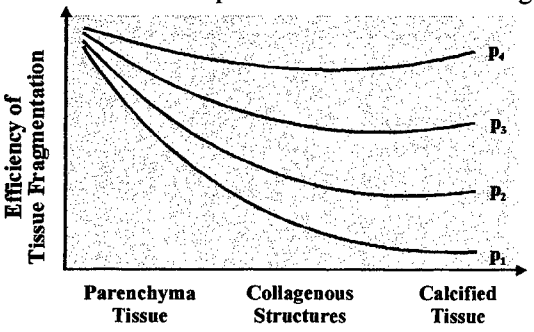

Fig.1 Efficiency of cutting with CUSA-technique for various types of tissue as a function of ultrasound power density p_n = f (frequency, amplitude, contact area) with $p_1 < p_2 < p_3 < p_4$

The ultrasound tissue interaction is based on CUSA-technology enabling the surgeon to cut various types of tissue with different degrees of effectiveness (fig.1). This selective cutting is a very useful feature for a brain tumour extirpation, for

SPIE Vol. 3249 • 0277-786X/98/$10.00

example, where it must be guaranteed that vessels and nerves will not affected [4]. This technology is established in neurosurgery [5], laparoscopy [6], gynaecology [7], urology [8], head and neck surgery [9] and angioplasty [10, 11].

Theoretical investigations were carried out to understand the acoustical behavior of coaxial layered optic fibers, which are mainly used for laser transmission. For the straight fiber waveguide the known theory of longitudinal acoustic waves in a rod can be applied to predict the vibratory response (transfer function) of the fiber [12]. An important problem concerns taking into account fiber bending which may appear during applications in endoscopy. For a curved fiber, the longitudinal and flexural waves cannot be propagated independently of one another. Only various composite „longitudinal-flexural" modes can exist, i.e. the displacements have both a longitudinal and a transversal component. We consider only one such mode which degenerates to the longitudinal bar mode at zero curvative and it is therefore called the quasi-longitudinal mode. A simple analytical formula is obtained for the transfer function, i.e., the ratio of the displacement at the working end of the fiber and that at the driven end. The transfer function depends on frequency, fiber length, output impedance, loss factor, and the mean-square curvative of the fiber. If the displacement at the driven end of the fiber is known, the power output of the applicator can be calculated from the known values of the tissue impedance and the transfer function [13].

As the transmission of high power ultrasound via metal waveguides (viscoelastic material with crystal structure) is highly attenuated, intrinsic losses have made an endoscopically controlled application impossible [14]. Between 10 and 100 kHz the losses are caused only by elastic deformation which means that although the process of oscillation in the metal is mechanically reversible, it is thermodynamically irreversible. In comparison, glass has an amorphous structure and does not show these losses. The coatings of the optical fibers are made of polymers and exhibit, as viscoelastical materials, the same losses as metals. These losses can be neglected for the first estimation compared to the whole waveguide mass.

2. MATERIALS AND METHODS

The concept of this application system is based on the transmission of laser radiation and ultrasound power via flexible silica glass fibers. Fig. 2 shows the opto-acoustic transmission system. The principle design of the LUST-applicator can be seen in Fig. 3. A piezo-ceramic transducer generates the ultrasound. The ultrasound is coupled into an amplitude transformer made of titanium and then into an optical fiber (e.g. silica-silica-acrylate, Ø: 300 - 1700 µm, length: up to 1.5 m) that is fixed by a high performance adhesive to a fiber coupler at the end of the amplitude transformer.

The applicator itself consists of a silica glass fiber mounted to a titanium coupling element (fig. 2). The coupling element with mounted fiber has a thread at its end and can be connected with the amplitude transformer of the ultrasound transducer (fig. 4). An efficient mounting method to connect the fiber to the metal coupling element can be realized by using high performance adhesives.

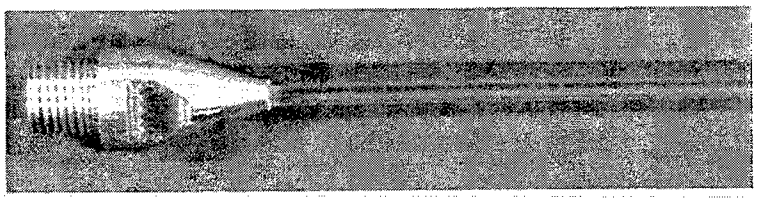

Fig. 2 Fiber coupler and opto-acoustic waveguide, bonded with high performance adhesive

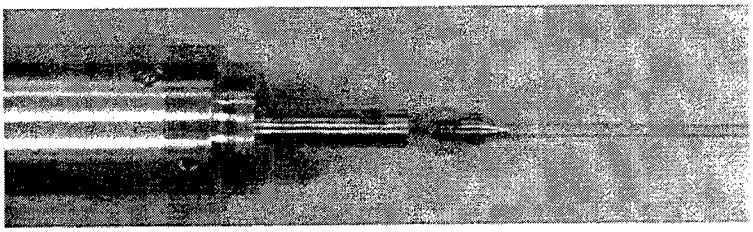

Fig. 3 Ultrasound transducer and opto-acoustic waveguide with fiber coupler

Another optical fiber (external laser coupling) coming from a laser (i.e. Nd:YAG, λ: 1064 nm) is guided axially through a central hole in the transducer. The laser radiation is transmitted into the ultrasound guiding fiber via an air gap in order to decouple the optical transmission from the acoustic oscillation.

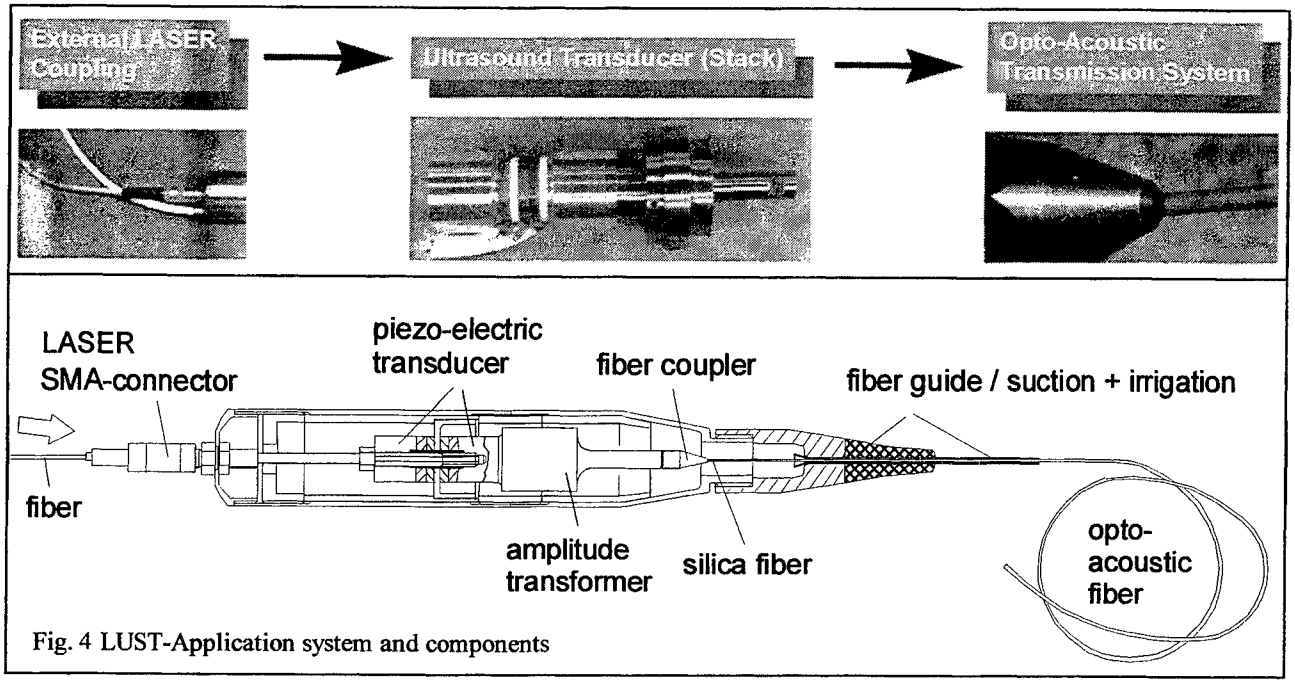

Fig. 4 LUST-Application system and components

A special fiber guide was designed, to avoid an excitation of transversal fiber modes. With this multi-layered fiber guide one can achieve the damping of the transversal excitation and further have the opportunity to use the guide for suction and irrigation, which is important when using the system as a Cavitron Ultrasonic Surgical Aspirator (CUSA).

The distal end of the flexible opto-acoustic transmission system is shown in Fig. 4. The central opto-acoustic waveguide is surrounded by two Teflon tubings, which are sealed at their proximal end to the system by a rubber valve. The lumen between the fiber and the inner tubing is used for flushing the target area with 0.9% saline solution, to dissolve the fragmented tissue particles. The inner tubing is connected via Luer-Lock to flushing pump with a flow rate of approx. 100 ml/h. The dissolved tissue fragments are sucked away continuously by the negative pressure flow (P=5W) of the suction channel between outer and inner Teflon tubing.

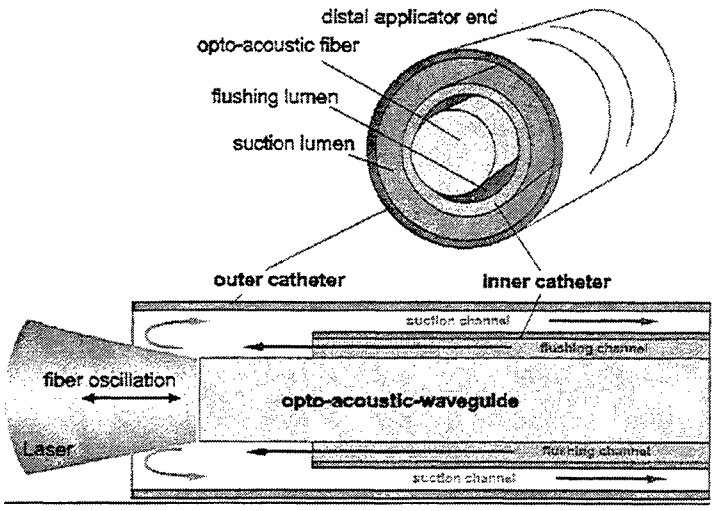

Fig. 5 Principle design of the fiber guide / suction and irrigation port

Several LUST-application systems were built up for clinical related investigations (in vitro and in vivo). Results will be presented in chapter 4 of this paper. The application system is shown in fig. 5 in its component parts. It is driven by a special designed US-generator of 20 Watt, which is amplitude and frequency controlled. The feedback controlled generator allows an infinitely variable adjustance of the amplitude which can be held constant even by treating tissues with different elastic properties. This is important with respect to reproducible tissue fragmentation rates.

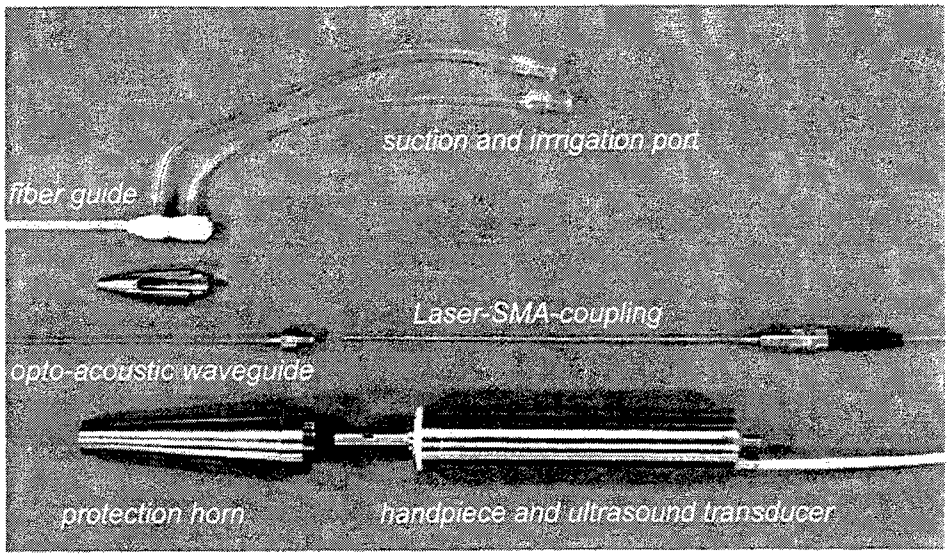

Fig. 6 30 kHz LUST application system in its component parts

3. TRANSMISSION OF ULTRASOUND VIA OPTICAL FIBERS

Investigations on the feasibility of high power ultrasound transmission at low frequencies were made using the set up in fig. 6. In one experiment, the optical fiber (silica-silica-acrylate, ∅: 600/680/1000 µm, length: 133.5 cm) was connected to the piezoelectric ultrasound transducer. The elongation at the distal tip of the fiber were measured for a straight and a bent fiber with a laser vibrometer. During the experiments the electric power to drive the transducer was constant. In the first experiment the fiber was bent 90° with a bending radius of 50 mm (fig. 6). After bending the fiber, a 10 % decrease in amplitude was measured as well as an insignificant frequency increase of the resonance frequency (15 Hz) which could be easily compensated by an amplitude feedback control circuit and an automatic frequency control unit (phase locked loop).

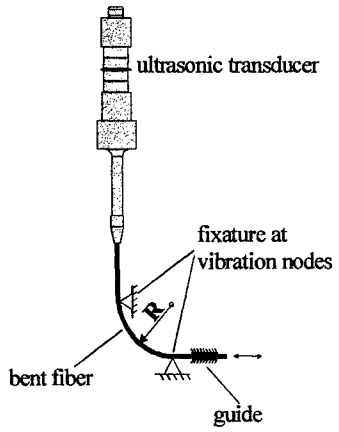

Fig. 7 Experimental set up for investigations of 90° - bending losses

The impact of the effect of bending on the acoustic transmission via a silica glass fibers was investigated in further experiments using a 385 µm polyimide coated silica glass fiber with a total length of 150 cm (fig. 7). The fiber was guided in an angioplasty diagnostic catheter and excited using a 85 kHz transducer (fig. 8). The velocity of the distal fiber tip was also measured with a laser vibrometer. For the straight fiber a velocity of 7.7 m/s and 14 µm amplitude could be detected. Subsequently, the catheter with fiber was bent 300 ° at one point with a bending radius of 12.5 mm. Nevertheless an amplitude of 6 - 7 µm at 85 kHz could be measured, accompanied by a resonance frequency shift of approx. 200 Hz. In several cases the transmission with a bent fiber/catheter generates high velocity amplitudes which are sometimes higher than without bending. This transmission behavior of the fibers may seem confusing but it is due to the difficult boundary conditions of the fiber. The transmitted amplitudes can be higher than the excitation amplitudes without fiber. This can occur because of resonance effects. This again is caused by a resonant amplification which is optimal with a certain degree of bending.

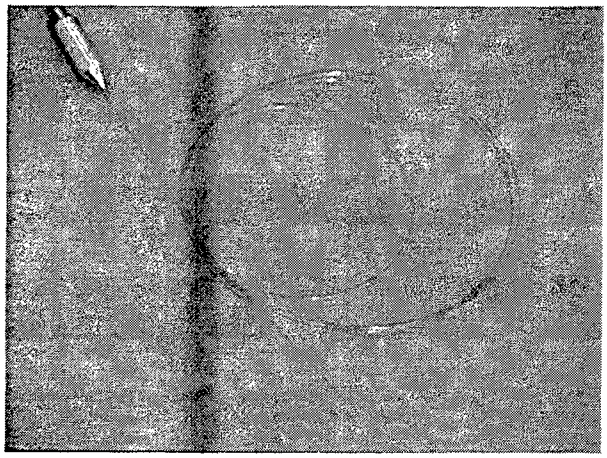

Fig. 8 Fiber with fiber coupler for 85 kHz, polyimide coated fiber

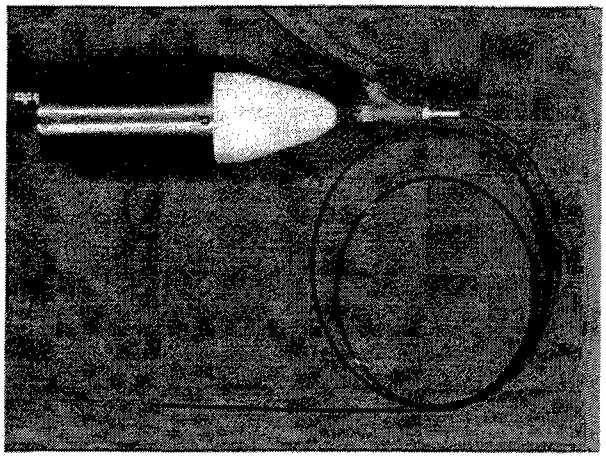

Fig. 9 Flexible acoustical delivery system: prototype design for angioplasty and drug delivery

In an experimental set up (destructive test) with a 1000 µm silica glass fiber with a length of 55 cm, a velocity of approx. 20 m/s of the distal fiber end could be measured which is equivalent to an axial elongation of up to 100 µm with respect to a frequency of 30 kHz. Higher amplitudes led to the destruction of the fiber. With amplitudes of more than 20 µm already typical ultrasound tissue interactions can be observed (e.g. cavitation). Amplitudes between 40 - 60 µm cause an efficient fragmentation rate of soft tissue (parenchymatous tissue e.g. liver). Longer application times (15-30 min) have shown that our opto-acoustic silica glass fibers (polyimide or acrylate coated) can withstand amplitudes of 60 - 80 µm continuously.

The feasibility of ultrasound transmission via silica glass fibers with high power at low frequencies (25-85 kHz) could be shown. The damping losses increase with bending. A maximum achieved elongation of ≈ 100 µm (v = 20 m/s) at 30 kHz was measured at the distal end of straight silica glass fiber.

A FEM-program (ULTRA© 2.1) was developed to calculate the transfer function of the opto-acoustic waveguide incl. the ultrasound transducer. It considers the transfer function of the acoustic waveguide dependent on excitation frequency of the ultrasound transducer, the mean-square curvative and the output impedance. The dimensions and material parameters of the used glass fiber type and of the ultrasound stack are required as input parameters. Fig. 9 shows the output shell of the program, where a 28 kHz ultrasound transducer including fiber was calculated.

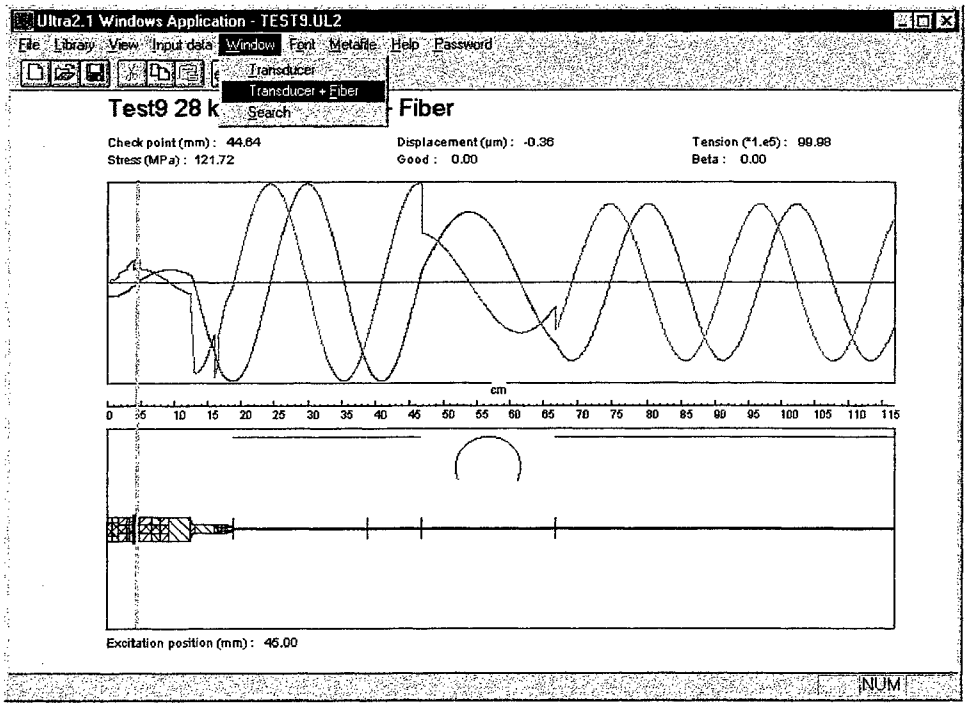

Fig. 10 Numerical simulation of the acoustic system with attached opto-acoustic waveguide, divided into segments with different bending angles and radii

4. IN VITRO EXPERIMENTS

The LUST-application system (Fig. 10) described here was evaluated using different tissue types: liver, kidney, brain and blood vessels.

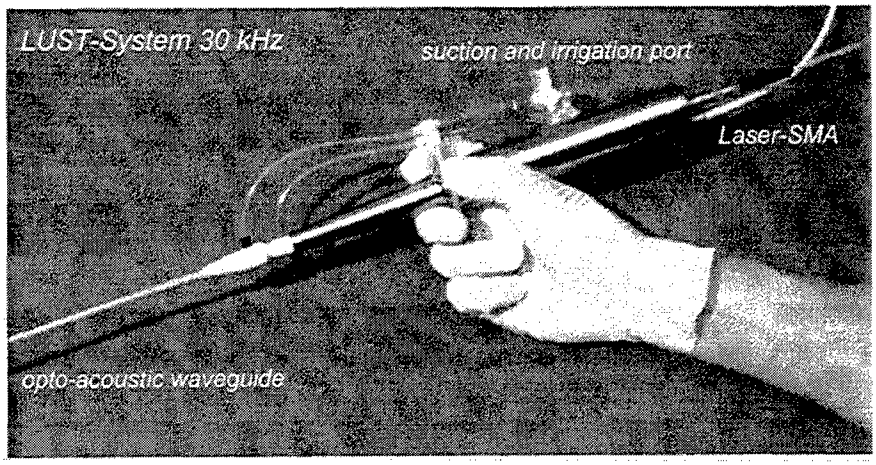

Fig. 11 LUST-system for a combined application of Laser and Ultrasound

The efficiency of the fiber based system of the Laser- und Medizin-Technologie gGmbH, Berlin (data LMTB), was compared to data of a conventional CUSA-systems, which was found in literature from Bond / Cimino in 1996 [15, 16]. In addition to the amplitude and the suction power, the active applicator area (tissue contact area) is of major significance for the removal of tissue. The efficiency of the LUST applicator with an active applicator area of 1.32 mm^2 ($\varnothing = 1.68$ mm) fits well into the parameter curves of the conventional CUSA systems with ring areas of 1 and 2 mm^2 (see Fig. 11).

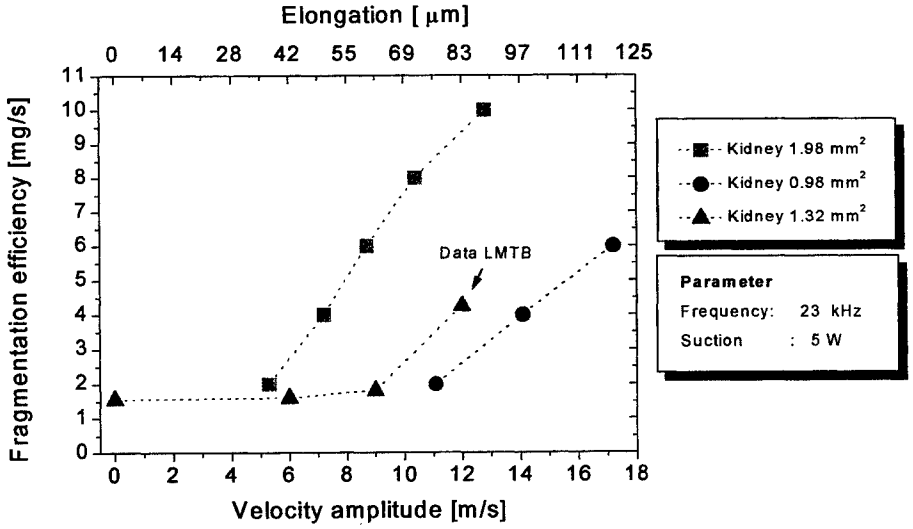

Fig. 12 Tissue fragmentation rate of conventional CUSA [15, 16] and fiber based LUST-systems (data LMTB)

In further in-vitro experiments with this system, different types of soft tissue were investigated with regard to the ultrasound induced fragmentation rate in dependence on the amplitude. The suction was held constant to 5 Watt. For these experimental investigations, a fiber with an active applicator area of 1.32 mm^2 ($\varnothing = 1.68$ mm) was used.

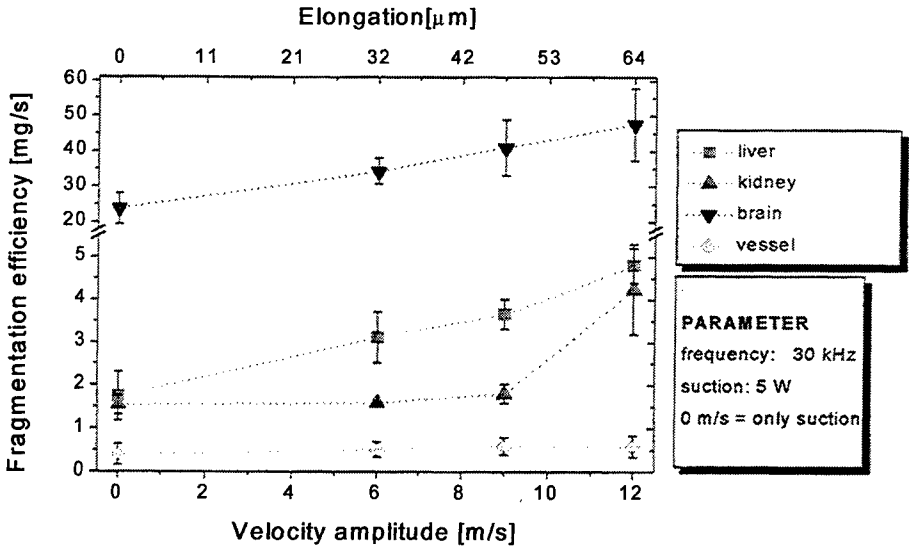

Fig. 13 Fragmentation rates for different soft tissue of the fiber based LUST-system

The result of first *in vitro* investigations is shown in fig. 13 and fig. 14. The ultrasound fragments the parenchymatous cell structure of the porcine liver (fig. 13). After suction of the fragmented cells the intact collagenous structures are clearly visible. Fig. 14 shows tissue that has been coagulated by laser radiation after exposure to ultrasound.

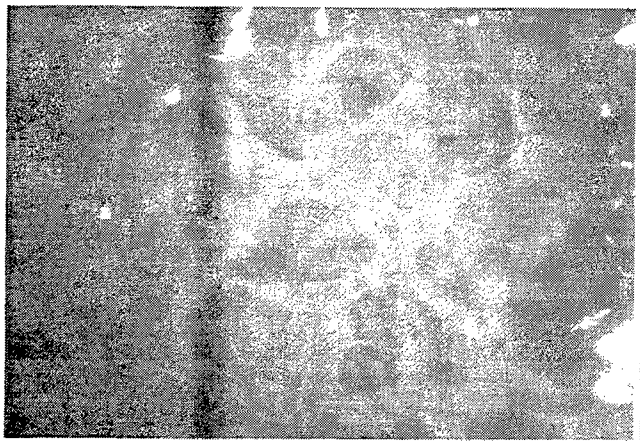

Fig. 14 Porcine liver after ultrasound exposition: the parenchyma cells have been removed, whereas the collagenous connective tissue is still intact

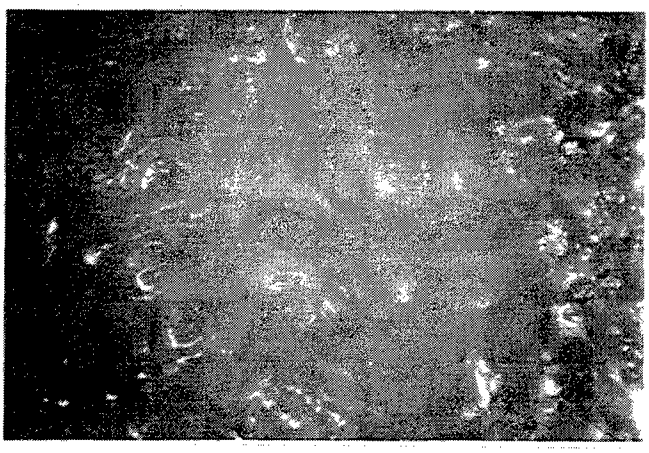

Fig. 15 Coagulation of ultrasound fragmented liver tissue by Nd:YAG-laser radiation

5. CONCLUSION

This new technique, developed at the LMTB, makes the combined application of laser and ultrasound in open and endoscopic surgery possible. Thus Laser Ultrasound Surgical Therapy could result in a whole new range of applications in MIM. Possible clinical applications could be in neurosurgery (excision of brain tumors) and angioplasty.

The fact that laser radiation up to 50 Watt and ultrasonic power up to 100 μm_{pp} can be transmitted without loss (no heating of the waveguide) via a fiber waveguide shows the possible endoscopic use of this multifunctional system.

A first clinical application prototype system for laser ultrasound surgical therapy (LUST) has already been realized for neuro-surgery. A prototype is also planned for a drug-delivery / angioplasty in order to test the clinical use of the technology.

With the transmission of high power ultrasound and laser radiation via a thin, flexible silica glass fiber, a combined endoscopical treatment of pathological tissue is possible. The fiber can be bent enabling previously inaccessible areas to be treated without the application system (the fiber) being heated up as a result.

6. REFERENCES

[1] MÜLLER G., TSCHEPE J.: Invasives/endoskopisches Instrument zur US-Chirurgie mittels optischer LWL. Patent Laser-Medizin-Zentrum, Berlin, D1 4224256.8

[2] DESINGER K., STEIN T., TSCHEPE J., MÜLLER G.: Laser Ultrasound Surgical Therapy; Minimal Invasive Medizin, Ecomed Verlag, 9(3), 121, (1996)

[3] TSCHEPE J., DESINGER K., MÜLLER G., STEIN T.: Simultane Übertragung von Laserstrahlung und Ultraschall über Quarzglasfasern, Laser und Optoelektronik, AT-Verlag Stuttgart, 28(4), August (1996)

[4] REINHARDT H. F.: Ultraschallresektion von Hirntumoren. Ultraschall 5, pp. 260-264, Georg Thieme Verlag Stuttgart, (1984)

[5] SCHÖCHE, J.D., HOHREIN, D., WEHNER, W.:Tumorentfernung mit Leistungsultraschall; Bericht über 50 Hirntumoroperationen, Zbl. Neurochir. 47, 277-284, (1986)

[6] WETTER, L. A., PAYNE, J. H., KIRSENBAUM, G., PODOLL, E. F., BACHINSKY, T., LAWRENCE, C., WAY, W.: The ultrasonic dissector facilitates laparoscopic cholecystectomy, Arch Surg, Vol 127, S. 1195-1199, (1992)

[7] DEPPE, G., MALVIYA, J.M., MALONE, J.M.: Debulking surgery of ovarian cancer with the cavitron ultrasonic surgical aspirator. A preliminary report, Gynecol. Oncol. 31, 223-226, (1988)

[8] ADDONIZIO, J.C., CHOUDHURY, M.S., SAYEGH, N.: Cavitron ultrasonic surgical aspirator. Applications in urologic surgery, Urology 23, S. 417-420, (1984)

[9] GILLESPIE, R.P., MARSHALL, P.: Use of the CUSA in removal of a recurrent intraorbital mucocele, Otolaryngol. Head &Neck Surg. 99, 71-72, (1988)

[10] SIEGEL R. J. ET AL.: Ultrasonic plaque ablation. A new method of recanalization of partially or totally occluded arteries. Circulation 78, pp. 1443-1447, (1988)

[11] WORLEY ET AL.: Electrohydraulic shock wave decalcification of stenotic aortic valves; postmortem and intraoperative studies. J Am Coll Cardiol, 12, pp. 458-462, (1988)

[12] THURSTON R.N.: Elastic waves in rods and clad rods, J.Acoust. Soc. Am., Vol. 64, pp. 1-37, (1978)

[13] MAKAROV S.N., OCHMANN M., DESINGER K.: The longitudinal vibration response of a curved fiber used for laser ultrasound surgical therapy, J. Acoust. Soc. Am., 102 (2), pp. 1191-1199, August 1997

[14] STUMPFF U.: Generation and transmission of high-intensity ultrasound in flexible waveguides in the 20 kHz - domain for therapeutic applications, Ph.D. Thesis, Aachen, Rheinisch-Westfälische Technische Hochschule, 137 p., (published in german), (1978)

[15] BOND L. J., CIMINO W. W.: Physics of ultrasonic surgery using tissue fragmentation, Part 2, Ultrasound in Medicine and Biology, Vol. 22, No. 1, pp. 101-117, (1996)

[16] CIMINO W. W., BOND L. J.: Physics of ultrasonic surgery using tissue fragmentation, Part 1, Ultrasound in Medicine and Biology, Vol. 22, No. 1, pp. 89-100, (1996)

SESSION 4

Therapeutic rf Devices and Techniques

Advances in Radiofrequency Tumor Ablation Therapy: Technical Considerations, Strategies for Increasing Coagulation Necrosis Volume, and Preliminary Clinical Results

S. Nahum Goldberg MD and G. Scott Gazelle MD, MPH

Department of Radiology, Massachusetts General Hospital, Boston, MA 02114

ABSTRACT

Radiofrequency (RF) tumor ablation has been demonstrated as a reliable method for creating thermally induced coagulation necrosis using either a percutaneous approach with image-guidance or direct surgical application of thin electrodes into treated tissues. Early clinical trials with this technology have studied the treatment of hepatic, cerebral, and bony malignancies. The extent of coagulation necrosis induced with conventional monopolar radiofrequency electrodes is dependent on overall energy deposition, the duration of RF application, and RF electrode tip length and gauge. This article will discuss these technical considerations with the goal of defining optimal parameters for RF ablation. Strategies to further increase induced coagulation necrosis including: multiprobe and bipolar arrays, and internally-cooled RF electrodes, with or without pulsed-RF or cluster technique will be presented. The development and laboratory results for many of these radiofrequency techniques, initial clinical results, and potential biophysical limitations to RF induced coagulation, such as perfusion mediated tissue cooling (vascular flow) will likewise be discussed.

1. INTRODUCTION

Percutaneous image-guided ablative therapies using thermal energy sources such as radiofrequency, microwave, high-intensity focused ultrasound (HIFU), and laser have received much recent attention as minimally invasive strategies for the treatment of focal malignant disease [1]. Potential benefits of these techniques include the ability for real-time imaging guidance, the ability to ablate tumor in non-surgical candidates, reduced morbidity as compared to surgery, and the potential to perform the procedure on an outpatient basis. In the past, a key limitation of these methods was the extent of coagulation produced for a single application of energy, for example 1.6 cm diameter of coagulation obtained from a single conventional radiofrequency electrode [2 - 4]. Because most potentially treatable tumors are larger than this, extended time and labor intensive treatment schedules, with repetitive electrode placements have traditionally been required to treat all but the smallest tumors [5, 6]. Thus, the aim for much subsequent development has been directed at enlarging the zone of necrosis produced from a single application of energy.

Radiofrequency (RF) induced tumor ablation has been used in early clinical trials for the treatment of hepatocellular carcinoma [5], hepatic [6 - 9], and cerebral metastases [10] and bony lesions such as osteoid osteomas [11]. Using CT, MR, or ultrasound imaging guidance, a thin (usually 21 - 14 gauge) electrode is placed percutaneously directly into the tumor. When attached to the appropriate generator, radiofrequency current is emitted from the exposed, non-insulated portion of the electrode. As the current attempts to find its path to ground, ion agitation is produced within the tissues surrounding the electrode. This agitation is converted by friction into heat, inducing cellular death via coagulative necrosis [12]. Several approaches have been used to increase the diameter of coagulation necrosis achieved using conventional RF techniques, including: the use of multiprobe [13], hooked [14 - 15], and bipolar arrays [16], saline injections during RF application [7], and the use of internally-cooled RF electrodes without and with pulsed or clustered technique [17 - 19]. In this article, we describe the development and laboratory results for many of these radiofrequency techniques, initial clinical results, and potential biophysical limitations to RF induced coagulation, especially perfusion mediated tissue cooling (vascular flow).

SPIE Vol. 3249 • 0277-786X/98/$10.00

2. MODIFICATION OF RF ELECTRODES: THE QUEST FOR INCREASED COAGULATION DIAMETER

2a. Conventional Monopolar Electrodes

Initial study of monopolar electrodes for percutaneous RF ablation therapy by other investigators involved the use of electrodes with no greater than 1 cm metallic tip exposure. This resulted in coagulation necrosis measuring up to 1.6 cm in diameter and length [2 - 3]. By applying RF current to ex-vivo liver tissue via 1.5 cm of exposed 0.38 mm guidewire, Sanchez et al. increased the length of induced coagulation to measuring 2 cm in length and diameter [20].

We initially investigated the effect of electrode size, tip temperature, and treatment duration on the extent of coagulation necrosis using conventional monopolar RF techniques in ex-vivo liver (n = 143) and muscle (n = 20) [4]. 500 KHz sinusoidal wave-form generators (Series 3, Radionics Inc., Burlington, MA) were used for all of our experiments. We found that the extent of necrosis varied not greater than 3 mm in diameter and not greater than 5 mm in length for each combination of variables, when tip temperatures of 90 ± 2° C were used. With 80 ± 2° C tip temperatures, coagulation necrosis was not uniform for electrodes greater than 5 cm in length. Increased duration of RF application from 1 to 6 minutes influenced lesion diameter, but not length. For example, with the 3 cm electrode, coagulation progressively increased from 0.7 ± 0.2 cm in liver at 1 minute to 1.4 ± 0.2 cm at 6 minutes. Increased RF application from 6 to 12 minutes did not increase coagulation necrosis. Increased electrode tip length from 0.5 to 8 cm was associated with a linear increase in the length of coagulation along the electrode shaft from 0.9 ± 0.1 cm to 8.0 cm ($r^2 = 0.996$). Using an 18 gauge electrode, coagulation diameter also increased from 0.8 ± 0.1 cm to 1.5 ± 0.1 cm in liver and from 0.7 ± 0.1 cm to 1.2 ± 0.1 cm in muscle as electrode tip length was increased from 0.5 - 3 cm. Maximum lesion diameter was achieved with an electrode tip of 3 cm, with longer electrodes yielding coagulation of equal diameter. Increasing electrode diameter from 24 gauge to 12 gauge increased coagulation necrosis from 0.7 ± 0.2 cm to 1.8 ± 0.1 cm.

Subsequent in-vivo studies demonstrated the feasibility of RF ablation in normal rabbit liver (n = 14) and lung (n = 8), as well as swine muscle (n = 21) [21 - 22]. The length of coagulation was comparable for all in-vivo tissues studied and similar to the previously noted ex-vivo results. Necrosis diameter, however, was tissue specific measuring 1.3 ± 0.2 cm for muscle, 0.9 ± 0.3 cm for liver, and 0.8 ± 0.2 cm for lung. Coagulation volume was significantly smaller for in-vivo liver and lung when compared to ex-vivo tissues ($p < 0.1$). Further studies demonstrated the feasibility of RF induced coagulation necrosis in VX2 carcinoma nodules in rabbit lung [23]. Seven 1.0 ± 0.2 cm tumor nodules were treated with a single CT-guided RF application. Pathologic examination 0 - 28 days post-procedure documented complete treatment of three nodules (43%) and greater than 95% tumor necrosis in the remainder. Recently, we have treated VX2 nodules implanted in liver (n = 8) and muscle (n = 6) with 21 gauge RF electrodes of 1 cm tip exposure. Coagulation necrosis diameter measured 0.8 to 1.4 cm in diameter. Viability of peripheral, untreated tumor and cell death in the treated regions has been confirmed by staining for mitochondrial enzyme activity with 2% 2,3,5-triphenyl tetrazolium chloride (TTC) and by vitalline dye staining using Evans blue.

The effect of electrode surface temperatures on RF-induced coagulation has subsequently been further defined [21]. RF was applied to ex-vivo liver (n = 76) for 6 minutes with constant tip temperature in 10° C increments from 60° C - 120° C, using 1 - 7 cm electrodes. Thermistors embedded within the electrodes enabled constant temperature monitoring at multiple sites along the electrode surface. Surface temperatures were non-uniform during RF application, with highest temperatures observed at the electrode ends. Increased temperature variation was seen both with higher tip temperatures and longer electrodes. The diameter of coagulation necrosis was a function of the local mean temperature during ablation. No coagulation was seen when the local temperature was less than 50° C. Temperatures above this threshold resulted in progressively greater necrosis, reaching 1 cm in diameter at 71° C. Further increases in necrosis diameter to 1.4 - 1.6 cm were seen at 80 ± 3° C. Temperatures equal to or greater than 110° C were associated with variable, and often reduced coagulation necrosis as tissue charring resulted in rising circuit impedance and markedly reduced RF output. The best fit logarithmic curve for temperatures less than 115° C was:

$$d = [1.4 + 0.03\ L]\ [1 - e\ (-\ 0.067(T_L - 49.5))]$$

d = lesion diameter
L = electrode tip length
T_L = local temperature.

R^2 was 0.986 with 0.14 cm standard deviation for each curve [21].

In-vivo confirmation of these results was performed in swine liver (n = 5) and muscle (n = 5) using 90° C tip temperatures with 3 cm and 5 cm electrodes [21]. The correlation of local temperature to necrosis diameter fit the same logarithmic relation as ex-vivo data, but the threshold for coagulation necrosis was 8.5° C higher for in-vivo specimens. In addition, greater variability in temperature was observed in-vivo with a resultant decrease in coagulation uniformity, particularly with the 5 cm electrode. These results therefore suggested that RF ablation with conventional electrodes will be most successful when high tip temperatures are achieved (90 - 100° C) using electrodes that have no greater than 3 cm tip exposure. These temperatures do not induce tissue boiling, vaporization, or charring, but will increase coagulation uniformity by maximizing the portion of the electrode surface reaching temperatures capable of causing tissue necrosis.

2b. Multiprobe arrays

We studied the feasibility of increasing the volume of tissue destroyed by a single RF application using multiple free-standing, 3 cm tip exposure, conventional RF electrodes in an array [13]. RF was applied to ex-vivo calf liver (n = 66) using arrays of two to five 18 gauge probes, for six minutes, at 70 - 90°C. Probe spacing (1 - 3 cm) and arrangement, as well as the method of radiofrequency application (simultaneous or sequential) was varied. Uniform tissue necrosis was observed with simultaneous radiofrequency application for probes spaced no greater than 1.5 cm apart. For each array, lesion size varied less than 3 mm in any dimension. Greater necrosis was accomplished when radiofrequency was applied simultaneously rather than sequentially.

At 1.5 cm, arrays of two probes produced coagulation with an elliptical cross-sectional area measuring 3.0 ± 0.1 cm in long axis and 1.4 ± 0.1 cm in short axis, and three equidistant probes with similar spacing produced spheroid shaped coagulation with a diameter of approximately 3.0 ± 0.2 cm. Arrays of four equidistant probes with 1.5 cm spacing produced cuboidal cross-sectional areas of coagulation measuring 3.2 ± 0.1 cm per side. Electrodes spaced 2 cm apart or greater produced independent foci of coagulation which measured 1.4 cm in diameter and had incomplete necrosis between probes. In the trials using five probe arrays, a 4 mm in diameter central region showed no visible evidence of tissue necrosis.

Alternate configurations of a four electrode array including linear, L-shaped and S-shaped arrays with 1.5 cm electrode spacing were also studied. Homogeneous coagulation necrosis, generally conforming to the shape of the array, was observed for the L-shaped and S-shaped arrays. For the L-shaped arrays, cross sectional length measured 4.5 ± 0.1 cm with width increasing from 1.4 ± 0.2 cm (the diameter of a lesion generated by a single probe) to 3.1 ± 0.2 cm at the base of the "L". The S - shaped array produced a uniform elliptical region of coagulation necrosis measuring 5.0 ± 0.2 cm along the long axis and 2.9 ± 0.2 cm in the short axis. Uniform necrosis was not observed for the four probe linear array as cylinders of coagulation measuring 1.4 ± 0.1 cm in diameter surrounded the outer two probes with variable coagulation necrosis observed along the middle two probes. Limited coagulation surrounding the inner electrodes was associated with lower tip temperatures and attributed to preferential RF emission at the non-electrically shielded outer electrodes.

Using this approach, volumes of coagulation necrosis of at least 40 cm^3 were generated by the simultaneous application of radiofrequency to multiprobe arrays. For the same treatment duration, this represented over an 800% increase in lesion volume created by an array of four probes of 3 cm tip exposure when compared to radiofrequency application using a single probe with identical tip exposure. Unfortunately, this strategy has been difficult to implement in clinical practice given the technical challenge of precisely positioning multiple needles simultaneously in percutaneous procedures [6].

One variation of a multiprobe system, the use of hooked electrodes has become available from two commercial vendors. These systems allow the deployment of an array of multiple, curved stiff wires in the shape of an umbrella from a single 14 or 16 gauge cannula [14 - 15]. Using a 12 hook array in in-vivo porcine liver, LeVeen has applied RF at 50 watts for five minutes with sequential 8% power increase up to 80 Watts for a total of 10 - 12 minutes to produce spherical regions of coagulation necrosis measuring up to 3.5 cm in diameter [14]. Similar results were found by Siperstein et al. who applied 30 - 50 Watts for 15 minutes to a four pronged electrode [15]. Reduction of blood flow by clamping of the porta hepatis, or repositioning of the electrodes (turning the electrode catheter 45° for a second insertion) were necessary to achieve reproducible 3.5 - 4.0 cm of coagulation in in-vivo pig liver. These investigators further treated 13 neuroendocrine tumors in 6 patients. Preliminary results (clinical and 3 month CT follow-up for 11 lesions) suggests complete ablation of these tumors [15].

2c. Bipolar arrays

McGahan et al. have used a bipolar radiofrequency ablation system in ex-vivo liver to increase the coagulation volume induced by a single application of RF compared to a conventional monopolar electrode [16]. In their work, a second, ground electrode was placed in close proximity (within four centimeters) to the active electrode. In these systems, heat is generated not only about the active electrode, but also the ground, resulting in larger, eliptiform zones of coagulation necrosis (up to 4.0 cm; long axis). However, the short axis of the cross-sectional area of induced coagulation measured only 1.4 ± 0.2 cm. Although this represents a volume increase compared to conventional monopolar RF, the shape of the induced necrosis does not conform to that of most tumors, so that the real gain in treatment effect is less significant. Thus, with this bipolar RF technique, multiple treatment sessions would be required in order to treat lesions greater than 1.5 cm in diameter.

2d. Saline injection during RF ablation

Another strategy used to increase the extent of coagulation using a single electrode insertion, is that of injecting normal saline into the tumor through tiny holes at the distal end of the electrode, during radiofrequency application. Using this technique, with continuous infusion of normal saline at 1 mL/min in experimental animal models, Livraghi et al. reported coagulation of up to 4.1 cm in diameter [7]. This strategy seemed to confirm an initial hypothesis that high local ion concentration from saline injection could increase the extent of coagulation necrosis by effectively increasing the area of the active surface electrode. Other possible explanations for the increase in coagulation include reduced effects of tissue vaporization (i.e. allowing for probe to tissue contact despite the formation of electrically insulating gases), or possibly diffusion of boiling saline into the tissues. Unfortunately, clinical results with this technique have been somewhat disappointing. In Livraghi's clinical series of 14 patients with tumors up to 4.5 cm in diameter, coagulation volume was unpredictable and irregularly shaped [7]. More importantly, partial necrosis was observed in some lesions smaller than 3 cm.

2e. Internally-cooled electrodes

We have recently characterized a novel, internally-cooled RF electrode capable of inducing increased coagulation when compared to conventional RF electrodes [17]. Two hollow lumens within an electrode enable internal cooling of the tip with chilled perfusate. As a result, heating of tissues nearest to the electrode is reduced. This allows for greater current deposition without tissue charring or impedance rises. We studied the effects of procedure duration (3 - 60 minutes), RF output (3 - 100 watts; 100 - 1,200 mA), electrode tip length (1 - 4 cm), and tip temperatures (15 - 90° C) in ex-vivo liver (n = 265) using an 18 gauge electrode [17, 24]. With internal electrode tip cooling, RF energy deposited into tissue and resultant coagulation necrosis were significantly greater ($p < 0.001$) than that achieved without electrode cooling. Maximum RF electrode tip cooling was 15 ± 2° C using 0° C saline as the perfusate. With this degree of cooling, a maximum of 350 mA, 550 mA, 750 mA, and 1,100 mA of RF current could be applied for 60 minutes using 1 cm, 2 cm, 3 cm, and 4 cm electrodes, respectively, without observed tissue charring. For all electrode lengths, coagulation volume increased progressively as treatment duration increased to 40 minutes, but did not increase with longer treatments. Maximum diameter of coagulation measured 2.5 ± 0.2 cm, 3.0 ± 0.1 cm, 4.5 ± 0.2 cm, and 4.4 ± 0.3 cm for the 1 cm, 2 cm, 3 cm, and 4 cm electrode tips, respectively. With tip temperatures of 25 - 35° C (less cooling), tissue charring occurred after only 750 mA (50 watts) had been applied to the 3 cm electrode tip for 12 minutes, resulting in necrosis measuring 3.0 ± 0.2 cm in diameter. Reduction of internal-cooling to maintain a tip temperatures of 45 - 55° C did not avoid tissue charring or permit increased RF current compared to conventional monopolar electrodes. As a result, necrosis diameter measured 1.5 ± 0.2 cm. As with conventional electrodes, reducing either the RF current or treatment duration resulted in smaller volumes of coagulation necrosis for any given tip temperature. Similar results have been reported by Lorentzen who applied RF to ex-vivo calf liver using a 14 gauge internally-cooled electrode and 20° C perfusate [18 - 25].

Subsequent ex-vivo thermometry studies compared the relative heat distribution in tissues surrounding 3 cm internally-cooled electrodes over 12 minutes of RF application with (n = 3) and without (n = 3) cooling [17]. Without cooling (90 ± 2° C tip temperature; 420 ± 20 mA), a rapid decrease in temperature was observed from the electrode surface so that lethal temperatures (50° C) were observed only 0.7 cm from the electrode. With internal cooling of the tip to 25 ± 2° C (750 ± 25 mA), however, temperatures increased to 90° C at 5 mm from the electrode and then decreased to 50° C at a distance of 1.6 ± 0.2 cm. Coagulation diameters were consistent with thermal data as 1.4 cm and 3.0 ± 0.1 cm of necrosis were seen without and with cooling respectively. Additional experiments (n = 12) have demonstrated that thermal equilibrium is not reached

within the greater volume of heated ex-vivo liver until 36 ± 4 minutes [24]. This finding likely accounts for the increased treatment duration required to obtain maximum coagulation with internally-cooled electrodes.

Confirmatory in-vivo studies using cooled-tip electrodes have been performed in normal swine muscle (n = 28) and liver (n = 11) with tip temperature ≤ 35° C [17, 25]. In muscle, 400 - 1,250 mA of RF current was deposited for 12 minutes. Diameter of coagulation increased with increasing RF current from 1.8 ± 0.1 cm to 5.4 ± 0.2 cm at maximum current. Following cessation of RF application and cooling, temperatures at the electrode tip increased to 82 ± 4° C within 60 seconds and remained above 60° C for a minimum of 2.5 minutes. In normal liver, however, only 2.3 ± 0.2 cm of coagulation was observed regardless of current applied (750 - 1,000 mA) or treatment duration (12 or 30 minutes). Necrosis was significantly smaller than that observed in ex-vivo trials using identical RF parameters ($p < 0.01$). Furthermore, temperatures at the electrode tip increased to only 64 ± 9° C and in all cases had decreased to 60° C within 60 seconds ($p < 0.05$ compared to muscle).

A study from our laboratory using internally-cooled RF electrodes in six rabbits with 1 cm VX2 tumor nodules in liver has demonstrated the feasibility of obtaining an adequate surgical resection margin for small tumors. Coagulation of the entire nodule and 5 - 8 mm of surrounding normal liver was seen in every case. The extent of coagulation, however, was no greater than 2.5 cm in diameter. In a clinical trial at our institution, 16 patients with primary (n = 3) or metastatic (n = 13) hepatic malignancy measuring 2.8 ± 0.4 cm have undergone treatment, with a single RF application using an internally-cooled electrode (12 - 20 minute duration at 600 - 1,000 mA) up to 5 days prior to scheduled metastasectomy [26]. For this study, the electrode tip was maintained at 90° C for 1 minute prior to internal-cooling of the electrode to ensure adequate ablation of the cooled portions of the tumor adjacent to the electrode. Pathologic analysis demonstrated a zone of continuous coagulation necrosis measuring 1.8 - 3.6 cm in diameter when RF deposition was greater than 850 mA. Complete treatment of the entire tumor, however, was achieved in only three cases.

2f. Pulsed RF

We conducted a set of experiment to determine if increased coagulation necrosis could be achieved with higher peak RF currents applied to internally-cooled electrodes in a pulsed fashion [19]. This strategy was chosen in an attempt to apply greater local current density to tissues while preventing tissue boiling near the electrode by allowing for heat dissipation in this region. RF was applied in ex-vivo (n = 68) and in-vivo porcine liver (n = 10) to electrodes of 3 - 5 cm tip length for 10 - 40 minutes with cooling of the electrode tip to 15 - 25° C using two strategies for RF application. In one group (n = 39), RF application was continuous at the maximum current achievable without impedance rises (750 - 1,350 mA; "constant RF"). In the second group (n = 39), RF was applied with the higher peak current sustainable for 15 seconds (1,500 - 2,000 mA) alternated with purposeful reduction of the current to 500 mA for 15 seconds ("pulsed RF"). The total duty cycle for this "pulsed" technique was 30 seconds. With 15 minutes of pulsed RF in ex-vivo liver, 3.6 ± 0.1 cm, 4.0 ± 0.2 cm, and 4.0 ± 0.1 cm coagulation diameter were achieved using 3, 4, and 5 cm electrodes, respectively. Necrosis was greater than that produced using constant RF application (2.9 ± 0.1 cm, 2.9 ± 0.2 cm, and 3.5 ± 0.1 cm diameters, respectively; $p < 0.05$). With 30 minutes of RF application, necrosis diameters were larger (4.1 - 4.5 cm), but no significant difference was seen between pulsed and constant RF technique. Remote thermometry experimentation (n = 8) demonstrated more rapid temperature increases at 10 and 20 mm from the electrode using pulsed RF technique. Coagulation produced in-vivo with 12 minutes of RF application (3 cm tip) was 2.8 ± 0.2 cm with pulsed RF as compared to 2.4 ± 0.2 cm with constant RF ($p < 0.01$). Thus, pulsed application of RF enabled overall greater energy deposition and more rapid heat deposition within treated tissues when compared to constant RF application to internally-cooled electrodes. Nevertheless, significant work is still required to determine the best parameters for delivering pulsed energy. It is currently unknown what duration of either peak energy or reduced energy deposition, or length of the duty cycle chosen is optimal for inducing the greatest volume of coagulation necrosis.

2g. Cluster RF

Initial experiments performed in ex-vivo liver (n = 36) determined that simultaneous RF application (1,100 mA for 10 minutes) to arrays of three, 2 cm tip exposure internally-cooled electrodes spaced equidistantly at 0.5 or 1 cm apart could produce a uniform circular cross-sectional area of coagulation necrosis measuring 4.1 ± 0.2 cm in diameter. Simultaneous RF application to arrays spaced 1.5 - 2.5 cm apart produced clover-leaf shaped lesions with maximum diameter of coagulation measuring up to 4.5 cm. However, within this area were peripheral areas of non-necrosis. With 3 cm spacing of the array,

three individual lesions measuring 2.5 ± 0.1 in diameter were seen. Smaller volumes of coagulation necrosis were produced when RF (550 mA) was applied sequentially in ex-vivo liver to each of the three electrodes for 10 minutes (total of 30 minutes) compared to simultaneous RF application ($p < 0.05$) with only 0.5 cm electrode spacing of the array resulting in a nearly circular cross-sectional area of coagulation (2.8 ± 0.2 cm in diameter.

Based upon these initial results, the effects of RF electrode tip length and the duration of RF application were studied using a cluster of three internally-cooled electrodes spaced equidistantly 0.5 cm apart. Radiofrequency was applied to ex-vivo liver (n = 68), in-vivo liver (n = 12) and muscle (n = 15) using electrode tip lengths of 1.5 - 3.0 cm with pulsed-RF deposition (1,400 - 2,150 peak mA) for 5 - 60 minutes. Pulsed technique was modified from prior experiments so that current was reduced from the peak current to 500 mA for 15 seconds only when impedance rose more than 10 ohms over baseline. This resulted in substantially fewer reductions in generator output, particularly during the first few minutes of RF deposition.

In ex-vivo liver, simultaneous RF application to internally-cooled electrode clusters for 15, 30 and 45 minutes produced 4.7 ± 0.1 cm, 6.2 ± 0.1 cm, and 7.0 ± 0.2 cm of coagulation, respectively (Figure 1). Application to a single electrode for 45 minutes resulted in coagulation measuring 2.7 ± 0.2 cm. Remote thermometry in ex-vivo liver (n = 8) using thermocouple probes placed 1 - 4 cm from the electrode surface demonstrated greater heat deposition over 45 minutes of RF application in tissues surrounding a cluster of three 2.5 cm tip electrodes compared to single 2.5 cm electrodes. In in-vivo liver and muscle, RF applied to electrode clusters for 12 minutes yielded 3.1 ± 0.2 cm and 7.3 ± 0.4 cm of coagulation, respectively. By comparison, only 1.8 cm of coagulation was induced in in-vivo liver and 4.3 cm in in-vivo muscle when single internally-cooled electrodes when otherwise similar technique was used ($p < 0.01$). Thus, the increase in coagulation diameter in in-vivo muscle from 4.0 cm to 7.3 cm compared to a single internally-cooled electrode represents an 83% increase in diameter and a 608% increase in volume. RF application (2,000 mA) to an electrode cluster for 30 minutes in in-vivo muscle produced coagulation measuring 9.5 ± 0.5 cm in diameter with coagulation extending into the retroperitoneum and into the overlying tissues.

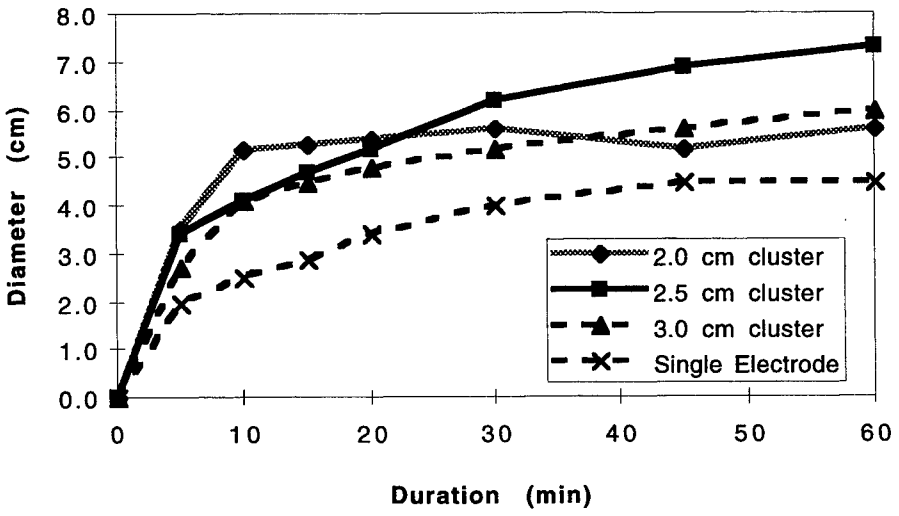

Figure 1: Duration of clustered RF application vs. coagulation diameter

The diameter of coagulation necrosis obtained by simultaneously applying RF to a single electrode or clusters of three internally-cooled electrodes spaced 0.5 cm apart in ex-vivo liver are presented. Peak currents applied using pulsed RF delivery were 1,200 mA, 1,900 mA, 2,100 mA, and 2,150 mA (maximum generator output) for the single 3 cm, and the clustered 2 cm, 2.5 cm, and 3.0 cm electrode tips, respectively. Results with the 3 cm electrode tip cluster suggest that greater generator output potential may have resulted in induction of even greater coagulative necrosis.

Ten patients with solitary intrahepatic colorectal metastases (4.2 - 7 cm) were also treated with RF ablation using cluster electrode technique (three internally-cooled electrodes spaced 0.5 cm apart). Each of the ten colorectal metastases were treated with a single 12 to 15 minute application of RF at 1,600 - 1,950 peak mA. Contrast enhanced spiral CT images acquired 1 - 10 days post-ablation demonstrated a minimum short axis diameter of coagulation necrosis of 4.2 cm with a mean of 5.3 ± 0.6 cm. Overall shape of the induced coagulation was not spherical in several cases, and generally conformed to the shape of the tumor. Large blood vessels limited the extent of coagulation in two cases. Coagulation extended a minimum of 5 mm beyond the tumor margin in 7 cases, and greater than one cm beyond all tumor margins in 5 cases. In three cases, coagulation necrosis extended approximately to the border of the tumor-liver interface with no margin of coagulated tissue surrounding the ablated tumor.

Simultaneous application of RF current to a cluster of three closely spaced internally-cooled electrodes, offers the potential of large volume coagulation necrosis for clinical tumor ablation therapy. RF application to electrodes spaced no greater than 1 cm apart produces larger, more spherical regions of coagulation than otherwise identical RF application to three electrodes spaced 2 cm apart or greater. While these results appear counterintuitive, this phenomenon of greater coagulation necrosis with relatively closely spaced electrodes can be explained by the electrodes functioning as if they were a single large electrode.

The use of clustered technique with high current densities (> 1,500 mA) has increased the risk of one significant potential complication, burns at the grounding pad site. For these high currents, larger area grounding pads are necessary to dissipate heat and prevent burns at the grounding pad site. Inadequate grounding pad surface area (96 cm^2) resulted in third degree burns at the grounding pad site following two 30 minute applications of RF at 2,000 mA. In subsequent trials of similar RF application in which larger grounding pads (400 cm^2) were employed to allow for greater heat dispersion, no burns were observed. However, even with this larger grounding surface area, a 1 x 2 cm second degree burn with blister formation was observed at the proximal edge of a grounding pad in the clinical trial. This lesion was treated with silvadine ointment, and healed within 2 weeks.

3. FACTORS LIMITING COAGULATION NECROSIS IN-VIVO

RF-induced coagulation necrosis has been more limited and variable in-vivo, particularly in clinical practice, compared to the reproducible results obtainable in ex-vivo tissues. Substantial evidence has been accumulated suggesting that perfusion mediated tissue cooling (vascular flow) reduces the extent of coagulation necrosis produced by RF. Decreased volume of coagulation has been observed in in-vivo liver compared to ex-vivo and non-perfused liver [15, 17] and coagulation necrosis in-vivo is often shaped by hepatic vasculature [6, 8, 14]. We therefore performed a series of experiments to determine to what extent the alteration of hepatic perfusion during RF ablation by mechanical or pharmacological means could account for the differences in observed coagulation, and whether perfusion-mediated tissue cooling can explain the reduced coagulation observed in-vivo [27]. The data to be presented strongly support the contention that hepatic blood flow is largely responsible for reduced coagulation observed in in-vivo liver. A heat-sink effect, similar to the cooling properties of the perfused internally-cooled needle, likely prevents the thermal build-up (50° C) in-vivo necessary to induce coagulation in tissues at a distance from the electrode.

3a. Mechanical occlusion

RF was applied using 3 cm tip internally-cooled electrodes (750 - 1,000 mA) to normal in-vivo porcine liver without (n = 8) and with balloon occlusion of the portal vein (n = 8), celiac artery (n = 3), or hepatic artery (n = 2), and to ex-vivo calf liver (n=10). A greater coagulation necrosis diameter was achieved when RF was applied for 12 minutes during portal venous occlusion than RF with applied unaltered blood flow (2.9 ± 0.1 cm vs. 2.4 ± 0.2 cm diameter; $p < 0.01$). The extent of coagulation obtained with portal venous occlusion was greater in every case than the extent of coagulation achieved in any trial with normal blood flow. With celiac and hepatic artery occlusion, coagulation diameter measured 2.7 ± 0.2 cm and 2.5 ± 0.1 cm, respectively. Coagulation in ex-vivo liver was also 2.9 ± 0.1 cm in diameter. The difference in coagulation diameter, therefore, correlated to an approximate reduction in hepatic blood flow. Concomitant administration of intraarterial or intravenous vasopressin (0.3 - 0.6 units / minute) to further reduce splanchnic blood flow, in addition to celiac (n = 7) or hepatic (n = 3) arterial occlusion produced a mean 3.4 ± 0.2 cm of necrosis. Intraarterial vasopressin infusion alone (n = 2), however, paradoxically decreased the extent of observed coagulation to 1.1 cm.

We have further studied the effects of mechanical occlusion on coagulation and heating during RF application in seven patients undergoing intraoperative RF therapy at our institution [27]. In three patients, two similar sized hepatic colorectal metastases (2.2 - 4.2 cm) were treated using internally-cooled RF electrodes with identical parameters of RF deposition (15 - 20° C tip, 900 - 1,000 mA, 12 minute duration). For each patient, one lesion was treated without altering blood flow, and the second was treated during portal inflow occlusion (Pringle maneuver). The extent of coagulation was greater in each case with inflow occlusion (4.0 ± 1.3 cm vs. (2.5 ± 0.8 cm; $p < 0.05$). In four additional patients with 2.4 - 3.8 cm colorectal metastases, remote thermometry demonstrated increased heating from 62° C to 72 °C at 1.0 cm and 39° C to 50 °C at 2.0 cm from the electrode within five minutes from initiation of portal inflow occlusion during constant RF application. The 10° C temperature increase observed 2 cm from the electrode was of extreme clinical significance as the threshold for induction of coagulation necrosis (50° C) [21] was reached by reduction of blood flow.

3b. Pharmacologic modulation of blood flow:

RF was applied for 10 minutes at constant current (500 mA) to exposed normal in-vivo porcine liver (n = 17) using 1.5 cm tip internally-cooled electrodes (15 - 20° C cooling). Blood flow was modulated using intraarterial vasopressin (0.3 - 0.6 units / minute; n = 5) or high dose halothane (3 - 5%; n = 5). Laser Doppler techniques quantified changes in hepatic blood flow and demonstrated a 33% increase in blood flow with vasopressin and a 66% decrease in blood flow with halothane. Coagulation diameter measured 1.3 ± 0.3 cm with vasopressin administration, 2.2 ± 0.4 cm with normal blood flow, and 3.2 ± 0.1 cm with halothane administration. Correlation of blood flow to coagulation diameter was good with $r^2 = 0.78$.

4. CLINICAL RESULTS

4a. Hepatic malignancy

Much of the interest in the development of radiofrequency tumor ablation has been directed at hepatic malignancies. For these lesions, minimally-invasive techniques particularly have the potential to dramatically alter patient outcomes, since existing therapies either are associated with significant morbidity and mortality, or have limited efficacy [1]. For example, hepatocellular carcinoma is often seen in the setting of hepatic cirrhosis, especially in high incidence areas such as Italy and the Far East. In these patients, liver dysfunction and associated coagulopathy combine to make surgical resection an unacceptably risky procedure. The development of in-situ ablative therapy using percutaneous ethanol instillation (PEI) has already provided an acceptable alternative to surgery for many of these patients [28]. RF tumor ablation offers another potential method for treating these lesions.

The rationale for local treatment of hepatic metastases is based primarily on the success achieved using a surgical approach. Without resection, the prognosis for patients with hepatic metastases from colorectal carcinoma is dismal, with 5-year survival reported to be less than 1% and median survival estimated at 9.6 months [29]. Unfortunately, systemic chemotherapy, radiation therapy, and PEI have been relatively unsuccessful in significantly improving patient outcomes, with the result that hepatic resection (metastasectomy) is the only widely available curative treatment for these patients. With resection, 30 - 35% 5-year survival can be achieved with proper patient selection [30 - 32]. However, despite its success in improving overall patient survival, metastasectomy is associated with significant morbidity, as well as a perioperative mortality rate of 2 - 10 % [30 - 32]. Furthermore, only a small fraction of patients with hepatic metastases can actually undergo metastasectomy as they are either deemed poor surgical risks, or the number and distribution of their tumors does not permit complete resection while at the same time leaving behind an adequate volume of normal liver to support life. Nevertheless, the success of hepatic metastasectomy in certain patients has led many investigators to speculate that similar results might be obtained with an effective in-situ ablative technique. In addition, because it would be less invasive than surgical resection, such a technique could be applicable to many patients who would not be considered for metastasectomy.

To date, five series using different methods of radiofrequency application for the treatment of hepatic malignancies have been reported as peer-reviewed, full length articles [5 - 8, 15]. These will be reviewed below. However, it cannot be stressed enough that these results are preliminary, and an assessment of safety and efficacy of RF tumor ablation cannot be adequately performed until the results of additional clinical trials are available. Abstract presentation of other series of RF treatment for hepatic malignancy have begun to appear, and should provide further insight into these questions [26, 33].

Rossi et al. [5] treated 39 patients with small hepatocellular carcinomas and 11 patients with 13 hepatic metastases using multiple insertions of conventional monopolar and bipolar radiofrequency electrodes over multiple treatment sessions. All but one of the tumors were less than 3.5 cm in diameter. For patients with hepatocellular carcinoma, median survival was 44 months, with less than 10% local recurrence over a mean follow-up of 22.6 months. For patients with metastases, only one patient was alive without evidence of tumor at one year, and local recurrence was evident at CT or pathology in 55% of patients.

Solbiati et al. [6] have treated 31 tumors in 16 patients with metastatic gastrointestinal carcinomas measuring 1.5 - 7.5 cm in diameter using conventional monopolar technique with and without multiprobe arrays. Complete treatment as defined as no evidence of local tumor growth by CT and MR imaging at 6 months of follow-up was achieved in 66.6% of these lesions; all of which were less than 3 cm in diameter. Disease free survival was achieved in 50% of patients with mean follow up of 16.6 months. Overall survival was 100% at one year and 61.5% at two years [34]. Solbiati et al. have also reported a series of 29 patients with 44 hepatic metastases from colorectal and other gastrointestinal malignancies measuring 1.5 - 4.5 cm in diameter who were treated using internally-cooled electrodes [8]. In this series, no more than two treatment sessions were required for any patient. No evidence of local recurrence was seen in 84% of these lesions with a mean follow-up of 7.9 months (range 3 - 15 months), and disease free survival was seen in 66.7 % of patients.

Livraghi et al. [7] treated 14 patients with 24 hepatic metastases (1.2 - 4.5 cm diameter) and one patient with cholangiocarcinoma using conventional radiofrequency electrodes and simultaneous intraparenchymal saline infusion. Complete necrosis of the tumor at six months follow-up was achieved in 52% of the lesions, all of which were smaller than 3.5 cm in diameter.

Siperstein et al. [15] treated 13 neuroendocrine tumors measuring from 1.5 - 8.0 cm in diameter in 6 patients using a laparascopic approach to deploy a hooked-electrode system. One to eight application of RF were used to apply 30 - 50 Watts for 5 - 15 minutes. Procedure duration lasted from 1:45 to 7:05 hours. Preliminary results were encouraging as 3 month CT follow-up for 11 lesions suggested complete ablation of these tumors, and the authors reported "symptomatic improvement in patients with secreting tumor". However, the extremely short duration of follow-up (less than the 6 months necessary to visualize residual tumor by CT [8, 9]) for 2/3 of the patients and the use of subjective patient symptoms over "incomplete" biochemical data as an endpoint strongly suggest that further follow-up is necessary before firm conclusions can be reached about this technique.

Few complications have been reported by these investigators. Rossi et al. and Siperstein et al. reported no complications in their series of 39 and 6 patients, respectively [5, 15]. Solbiati et al. observed two cases of self-remitting intra-peritoneal bleeding, one each using conventional and cooled-tip electrodes [6, 8]. One case of transient ascites was reported by Livraghi et al., and attributed to the saline infusion [7].

4b. Other neoplasms

Peer reviewed reports of RF tumor ablation have also been published for the treatment of brain tumors [10] and osteoid osteomas [11]. Additionally, we are aware of several ongoing, unpublished studies of RF ablation of primary prostatic and renal tumors, as well as osseous and pulmonary metastases.

Anzai et al. have used MR-guided stereotactic RF ablation to treat 14 brain tumors in 12 patients with primary and metastatic brain tumors [10]. Multiple RF applications were applied using a conventional electrode heated to 80° C for 1 minute. Repeated RF applications were performed until the entire tumor volume was destroyed. Sequential MR imaging for a minimum of 10 months follow-up suggested local control.

Rosenthal et al. have used conventional RF electrodes for in situ ablation of osteoid osteomas, small (< 1.5 cm), painful benign bony lesions [11, 35]. In their initial report, 18 patients were treated with a single 6 minute RF application with tip temperature of 90° C [11]. Pain was completely relieved in 16 (89%), and all patients resumed normal daily activities immediately. Their latest series which now includes over 100 patients (50 with greater than 2 year follow-up) reports complete treatment in over 95% of cases [35].

5. CONCLUSIONS

Percutaneous image-guided application of radiofrequency is a relatively new strategy for inducing thermally-mediated coagulation necrosis. As such, RF ablation may ultimately prove beneficial as a minimally invasive method for treating focal malignant disease. Because the goal of tumor eradication necessitates ablating the entire tumor and a 0.5 - 1 cm peripheral margin of grossly normal tissue, complete ablation of the entire neoplasm requires the induction of large volumes of coagulation necrosis. Several recent technical innovations, including RF application to multiple and/or internally-cooled electrodes enable increased energy deposition into tissues with a resultant increase in the volume of induced coagulation necrosis. These advances are timely because many sequential, overlapping applications of RF to a single electrode are required to treat all but the smallest of tumors using conventional monopolar electrodes which is difficult to accomplish in clinical practice. Simultaneous pulsed-RF application to a cluster of three closely spaced internally-cooled electrodes enables larger volume necrosis in ex-vivo liver, in-vivo tissues, and hepatic colorectal metastases than previously reported for a single application of radiofrequency or any other percutaneous technique. The use of clustered electrodes may therefore allow the treatment of larger metastases with a single application of radiofrequency.

Optimization of RF energy delivery and/or modulation of tumor or organ biology may allow tailoring of induced tissue destruction, thereby enabling adequate and predictable treatment of tumors. However, perfusion mediated tissue cooling limits both tissue heat deposition and the extent of coagulation necrosis induced by RF tumor ablation in vascular tissues and tumors. Development of strategies to reduce blood flow during RF tumor ablation may ultimately allow for improved treatment effect. Preliminary clinical studies encourage optimism about the future of RF ablation techniques, particularly for the treatment of hepatic neoplasms. However, further study is necessary to determine under which conditions a particular method will prove superior to others, and to determine whether any of these methods can improve patient outcomes.

6. REFERENCES

1. Goldberg SN, Livraghi T, Solbiati L, and Gazelle GS. In situ ablation of focal hepatic neoplasms. In: Hepatobiliary and pancreatic radiology: Imaging and Intervention. GS Gazelle, S Saini, and PR Mueller, Eds. Thieme Medical Pub. New York. 1997
2. McGahan JP, Brock JN, Tessluk H, Wei-Zhong G, Schneider P, Browning PD. Hepatic ablation with use of RF electrocautery in the animal model. JVIR 1992; 3:291-297
3. Rossi S, Fornari F, Pathies C, Buscarini L. Thermal lesions induced by 480 KHz localized current field in guinea pig and pig liver. Tumori 1990;76:54-57
4. Goldberg SN, Gazelle GS, Dawson SL, Rittman WJ, Mueller PR, and Rosenthal DI. Tissue ablation with radiofrequency: Effect of probe size, gauge, duration, and temperature on lesion volume. Academic Radiology, 1995; 2:399-404
5. Rossi S, DiStasi M, Buscarini E, Quaretti P, Garbagnati F, Squassante L, Paties CT, Silverman DE, and Buscarini L. Percutaneous RF interstitial thermal ablation in the treatment of hepatic cancer. AJR 1996; 167:759-768
6. Solbiati L, Ierace T, Goldberg SN, Livraghi T, Rizzatto G, Mueller PR, and Gazelle GS. Percutaneous US-guided RF tissue ablation of liver metastases: Long-term follow up. Radiology, 1997; 202:195-203
7. Livraghi T, Goldberg SN, Monti F, Bizzini A, Lazzaroni S, Meloni F, Pellicano S, and Solbiati L. Saline-enhanced radiofrequency tissue ablation in the treatment of liver metastases. Radiology 1997; 202:205-210
8. Solbiati L, Goldberg SN, Ierace T, Livraghi T, Sironi S, and Gazelle GS. Radiofrequency ablation of hepatic metastases with cooled-tip electrodes: Results in 29 patients. Radiology 1997; 205:367-374
9. Goldberg SN, Gazelle GS, Solbiati L, Livraghi T, Tanbe KK, Hahn PF, and Mueller PR. Percutaneous radiofrequency liver tumor ablation. AJR 1998 (in press)
10. Anzai Y, Lufkin R, DeSalles A, Hamilton DR, Farahani K, and Black KL. Preliminary experience with MR-guided thermal ablation of brain tumors. AJNR 1995; 16:39-48
11. Rosenthal DI, Springfield DS, Gebhart MC, Rosenberg AE, and Mankin HJ. Osteoid osteoma: Percutaneous radiofrequency ablation. Radiology 1995; 197:451-454
12. Cosman ER, Nashold BS, Ovelman-Levitt J. Theoretical aspects of radiofrequency lesions in the dorsal root entry zone. Neurosurg. 1984, 15:945-950
13. Goldberg SN, Gazelle GS, Dawson SL, Mueller PR, Rittman WJ and Rosenthal DI. Radiofrequency tissue ablation using multiprobe arrays: Greater tissue destruction than multiple probes operating alone. Academic Radiology, 1995; 2:670-674
14. Leveen RF. Laser hyperthermia and radiofrequency ablation of hepatic lesions. Semin Int Rad. 1997; 14:313-324
15. Siperstein AE, Rogers SJ, Hansen PD, and Gitomirsky A. Laparoscopic thermal ablation of hepatic neuroendocrine tumor metastases. Surgery 1997; 122:1147-1155

16. McGahan JP, Wei-Zhong G, Brock JM, Tesluk H, and Jones CD. Hepatic ablation using bipolar radiofrequency electrocautery. Acad Radiology, 1996; 3:418-422
17. Goldberg SN, Gazelle GS, Solbiati L, Rittman WJ, and Mueller PR. Radiofrequency tissue ablation: Increased lesion diameter with a perfusion electrode. Acad Radiology, 1996; 3:636-644
18. Lorentzen T. A cooled needle electrode for radiofrequency tissue ablation: Thermodynamic aspects of improved performance compared with conventional needle design. Acad Radiol 1996; 3:556-563
19. Goldberg SN, Gazelle GS, Solbiati L, Mullin K, Rittman WJ, and Mueller PR. Large volume radiofrequency tissue ablation: Increased coagulation with pulsed technique. Radiology 1997; 205:P258 (abstract)
20. Sanchez R, vanSonnnenberg E, D'Agostino H, Goodacre B, Esch O. Percutaneous tissue ablation by radiofrequency thermal energy as a preliminary to tumor ablation. Min Invasive Therapy 1993; 2:299-305.
21. Goldberg SN, Gazelle GS, Halpern EF, Rittman WJ, Mueller PR, and Rosenthal DI. Radiofrequency tissue ablation: Importance of local temperature along the electrode tip exposure in determining lesion shape and size. Acad Radiol, 1996; 3:212-218
22. Goldberg SN, Gazelle GS, Compton C, and McLoud TC. Radiofrequency tissue ablation in the lung: A safe, minimally invasive procedure. Academic Radiology, 1995; 2:776-784
23. Goldberg SN, Gazelle GS, Compton CC, Mueller PR, and McLoud TC. Radiofrequency tissue ablation of VX2 tumor nodules in the rabbit lung. Acad Radiology, 1996; 3:929-935
24 Goldberg SN, Gazelle GS, Solbiati L, Mullin K, Rittman WJ, and Mueller PR. Large volume radiofrequency tissue ablation: Increased coagulation with cooled-tip electrodes. Radiology 1996; 201:P387 (abstract)
25. Lorentzen T, Christensen NE, Nolsle CP, and Torp-Pedersen ST. Radiofrequency tissue ablation with a cooled needle in vitro: Ultrasonography, dose response, and lesion temperature. Acad Radiol 1997; 4:292-7
26. Goldberg SN, Tanabe KK, Solbiati L, Gazelle GS, Hahn PF, and Mueller PR. Treatment of intrahepatic malignancy with radiofrequency ablation: Radiologic-pathologic correlation in 16 patients. AJR 1997; 168:121 (abstract)
27. Goldberg SN, Hahn PF, Tanabe KK, Mueller PR, Schima S, Athanasoulis CA, Compton CC, Solbiati L, and Gazelle GS. Percutaneous radiofrequency tissue ablation: Does perfusion-mediated tissue cooling limit coagulation necrosis ? JVIR 1998; (in press)
28. Livraghi T, Giorgio A. Marin G et al. Hepatocellular carcinoma and cirrhosis in 746 patients: long-term results of percutaneous ethanol injection. Radiology 1995; 197:101-108
29. Ballantyne GH and Quin J. Surgical treatment of liver metastases in patients with colorectal cancer. Cancer 1993; 71:4252-66
30. Saenz NC, Cady B, McDermott WV, et al. Experience with colorectal carcinoma metastatic to the liver. Surg Clin North Am 1989; 69: 361-70
31. Cady B and Stone MD. The role of surgical resection of liver metastases in colorectal carcinoma. Sem Oncol 1991; 18: 399-406
32. Ridge JA and Daly JM. Collective review: treatment of colorectal hepatic metastases. Surg Gyn Obstet 1985; 161: 597-607
33. Dodd GD III, Halff GA, Rhim H, Chintapalli KN, Chopra S, Esola CC. Radiofrequency thermal ablation of hepatic tumors. Radiology 1997; 205:P723 (abstract)
34. Solbiati L, Goldberg SN, Ierace T, Livraghi T, Sironi S, and Gazelle GS. Five year follow-up of liver metastases treated with percutaneous radiofrequency ablation. Radiology 1997; 205:P200 (abstract)
35. Rosenthal DI, Hornicek FJ, Wolfe MW, Jennings LC, Gephart MC, and Mankin HJ. Changes in the management of osteoid osteoma. J Bone Joint Surg 1998 (in press)

Further author information:
S.N.G. (correspondence); E-mail: goldbern@helix.mgh.harvard.edu; Telephone: 617-726-8386; Fax: 617-726-4891

Quantitative and Qualitative Histopathological Comparisons of Multielectrode Balloon and Thermal Balloon Endometrial "Ablation".

S. Thomsen[a], T. Ryan[b], K. Kuk-Nagle[b], C. Soto[a], T. G. Vancaillie[c] and J. Garza-Leal[d].

[a]U. Texas M. D. Anderson Cancer Center, Houston TX. 77030
[b]Valleylab, Inc. Boulder, CO. 80301. [c]Methodist Plaza, San Antonio, TX 78229.
[d]University Hospital, Monterrey, Mexico

ABSTRACT

Quantitative and qualitative histopathologic techniques were used to compare the distribution, severity and depths of acute thermal lesions formed by *in vivo* placement of three different intracavitary thermal balloon instruments in the uteri of 19 women scheduled for hysterectromy. Thermal damage reflected by 1) Nitro Blue Tetrazolium stains separating "living" from "dead" tissues, 2) red zone formation and the 3) presence of a clear zone observed in histologic slides extended into the myometrium. One hysterectomy specimen removed 4 days after treatment showed superficial slough of the endometrium but solid, coagualtion necrosis of the deeper endometrium and adjacent myometrium. The treatment effect and success of intracavitary thermal coagulation may be related to a delicate balance of complete irradication of endometrium versus fibrous stricture and intracavitary adhesions of the uterus.

Key Words: thermal endometrial ablation, pathology

INTRODUCTION

Dysfunctional uterine bleeding is prolonged, high volume uterine hemorrhage that tends to occur at the time of menarche (onset of menses at puberty) and at the time of menopause. The bleeding is secondary to imbalanced secretions of pituitary and ovarian hormones leading to erratic and abnormal endometrial responses that culminate in hemorrhage. [1] Significant dysfunctional uterine bleeding can lead to significant blood loss and iron deficiency anemia. Symptomatically, the patient can suffer severe cramps and the nuisance of prolonged hemorrhage. Treatments have included supplemental hormonal therapy, mechanical curettage of the endometrium, hysterectomy and various energy applications for endometrial "ablation".

The desired clinical end point of endometrial "ablation" is to control ("ablate") dysfunctional uterine bleeding by removing ("ablating") the endometrium without causing unwanted complications. [2] Intracavitatary endometrial thermal coagulation using various instruments have been applied with some treatment success. [3-12]

The goal of the current study was to use qualitative and quantitative pathological techniques to describe the distribution and depths of acute thermal damage produced by three different intracavitary endometrial thermal coagulation instruments, 1) a multielectrode air-filled balloon, 2) a circulating heated fluid balloon and 3) a non-circulating heated fluid balloon.

MATERIALS AND METHODS

Nineteen women already scheduled for hysterectromy for dysfunctional uterine bleeding (n=14), pelvic relaxation syndrome (n=3) and leiomyomas (n=2) gave informed consent for application of one of the thermal instruments while under general anesthesia just before removal of the uterus. Before surgery, the women underwent physical examination, endometrial biopsy to rule-out endometrial hyperplasia and

neoplasia, ultrasound uterine measurements and were given oral birth control pills to regulate their menstrual cycle to the early proliferative phase (thin, regenerating endometrium). The women were divided into three treatment arms: 1) multielectrode balloon (n = 5), 2) circulating fluid balloon (n = 5) and non-circulating balloon (n =5). Two women had intracavitary application and expansion of balloons (multielectrode n = 1 and circulating n = 1) but no heating (sham operation controls). One woman underwent cavitary heating (multielectrode) but did not have her hysterectomy until four days after the thermal treatment. One uterine specimen was eliminated from the study because the patient was found to have pathologic endometrial hyperplasia requiring immediate detailed pathologic evaluation.

The general configurations of the intracavitary balloons are presented in Figure 1.

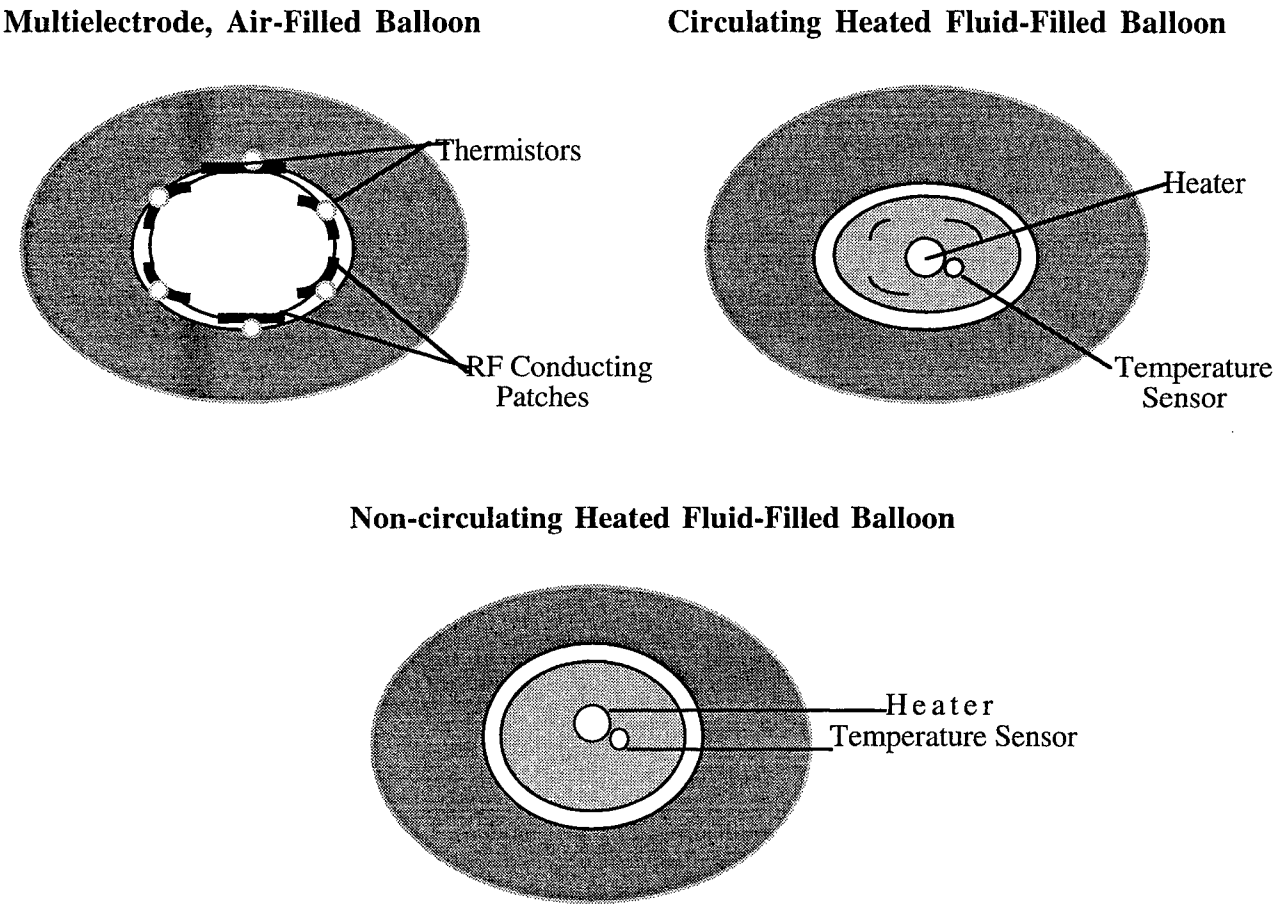

Figure 1. The balloons are filled with air (multielectrode) or fluid (circulating and non-circulating) and expanded to fill the uterine endometrial cavity. The uterus is heated by the 1) radiofrequency conducting patches applied to the endometrial surface by expansion of the balloon with air, 2) circulating and 3) non-circulating heated fluid within the balloons. The balloon temperature sensors monitor temperatures at the endometrial surface (multielectrode) or along the heater (circulating and non-circulating) and trigger temperature feedback systems to maintain the heating temperatures at preset levels.

After general anesthesia was obtained, the deflated balloons were inserted into the patient's endometrial cavities via the cervical canal, then inflated. After the heat-up intervals (ranges: 52.5-68.0

seconds), the treatment temperatures were maintained by temperature sensor-driven feedback systems for the recommended times . (Table 1).

Table 1.

Treatment Temperatures and Times

Balloon Type	Treatment Temperatures (°C)	Treatment Times (Minutes)
Multielectrode, Air-filled	75	4
Circulating, Fluid-filled	76-77	15
Non-circulating, Fluid-filled	87	8

After thermal treatment, the balloons were deflated and withdrawn. The patients then underwent vaginal or abdominal hysterectomy. Immediately upon removal of the uteri, they were opened along the left and superior and right sides and opened like a book to expose the endometrial and cervical canal surfaces. The entire uteri and cervices were dissected into blocks guided by a predetermined grid pattern to insure that each region of the uterus would be studied pathologically. Each block was a transmural section including endometrium (or cervical mucosa), myometrium and serosa. A total of 24 blocks of tissue were subjected to the following tests:

Vital Enzyme Staining with Nitro Blue Tetrazolium (NBT):

Selected blocks of fresh tissue (n = 12/uterus) were submerged in a solution of buffered aqueous NBT in tris buffer for 15 minutes, blotted and placed in 10% buffered formalin for fixation. This reagent demonstrates the presence of vital respiratory and metabolic enzymes, therefore is used to distinguish "living" from "dead" tissues in gross specimens. [13] The boundaries separating the non-colored ("dead") zone from the colored ("alive") zone were measured in the fixed specimens.

Red Zone of Thermal Damage:

The outer boundary of a red band (zone) of thermal damage was measured in the fixed specimens. This zone consists of thermally-induced vascular injury including hemorrhage, hemostasis and hyperrhemia [14,15] The surface red zone was obscured by the NBT reaction therefore, in the NBT specimens, the outer red zone boundary was measured of cut surfaces about 2 mm deep to the NBT stained surfaces.

Histological Clear Zone of Thermal Damage:

A clear zone with a boundary forms as a result of cellular thermal coagulation and shrinkage leading to formation of clear spaces within and among the cells. In addition, the clear zones were marked by dilatation of vascular spaces consistent with lymphatics. The boundaries of this clear change were measured macroscopically on tissue sections.

Measuring Techniques:

The individuals making the measurements did not know which specimen had received what treatment until all measurements were finished. All gross and microscopic section depth measurements were made with calibrated calipers measuring perpindicularly from the endometrial surface to the observable boundaries. Three measurements per transmural surface were made of the NBT and the outer red zone boundaries in the gross specimens and the clear zone boundaries for each histologic section using the calibrated calipers. Each measurement set was averaged, rounded off to the nearest 0.1 mm. and standard deviations were calculated. Because these measurements were made in fixed or paraffin processed specimens, the measurements are relative, not absolute.

Histology Preparation:

The superior, medial and inferior surfaces of each fixed tissue block were submitted for paraffin sections. Three microscopic slides stained with hematoxylin and eosin were prepared from each surface specimen. Microscopic evidence of thermal damage including tissue coagulation, cell shrinkage, glandular epithelial spindling, hemorrhage, hemostasis and hyperemia were evaluated.

RESULTS

As the result of hormonal pretreatment, most of the endometria were relatively thin with NBT, red zone and clear zone thermal damage boundaries extending through the endometrium into the subjacent myometrium in all three treatment groups. [Figure 2] However, the damage was variable in the circulating and non-circulating balloon groups with a significant number of very shallow ($\leq$ 1 mm) thermal lesions confined to the endometrium. In addition, the thermal lesions frequently did not involve endometrium at the narrow junction of the uterus to the tube (cornua) and in the narrowly angled lateral sides where the posterior and anterior uterine walls meet.

The NBT and outer red zone boundaries were distinct in most but not all of the multielectrode and circulating fluid balloon gross specimens but, frequently, were mottled in the non-circulating balloon specimens. In general, the inner boundaries of the red zones coincided with the NBT boundaries. And, the outer red zone boundaries were deeper than the NBT boundary in all treatment groups. [Table 2] The red zones were not as well developed in some non-circulating and circulating balloon specimens as in the multielectrode specimens yet measureable boundaries could be identified in many specimens. Distinct NBT boundaries and red zones were present in the proximal cervical canals in nearly all multielectrode and circulating fluid specimens including the 4 day uterus. Faint, dusky red cervical zones were present in the non-circulating fluid uteri. A rare small focus of NBT non-reaction was found in the sham specimens. Focal hemorrhage occured in the sham endometrial surfaces reflecting mechanical trauma from the insertion of the balloons.

Clear zone boundaries were distinct in the multielectrode balloon specimens but were less so in the circulating and non-circulating balloon specimens. The NBT, outer red zone and clear zone boundaries were very distinct in the hysterectomy specimen removed four days after a multielectrode heating treatment. [Figure 3] The clear zone depths coincided with the outer boundary depths of the red zone in the acute multielectrode specimens but not in the 4 day specimen. However, microscopically, the level of tissue coagulation necrosis in the 4 day multielectrode balloon specimen was at the outer boundary of the red zone. The clear zone boundaries of the circulating and non-circulating specimens did not coincide with their outer red zone boundaries. However, the large standard deviations reflect great measurement variation due to less than ideal boundary measurement conditions and uneven heating in some specimens. [Table 2]

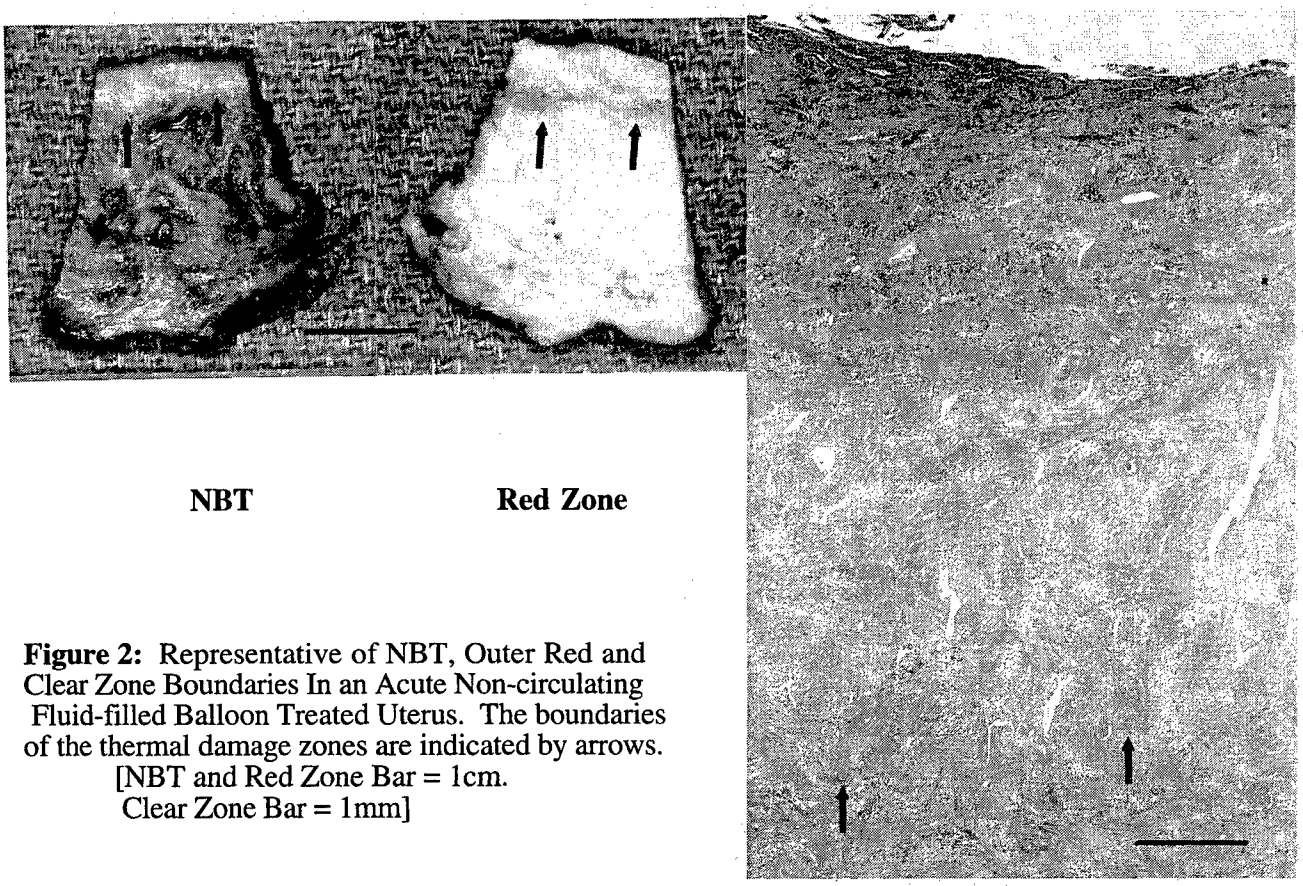

NBT **Red Zone**

Clear Zone

Figure 2: Representative of NBT, Outer Red and Clear Zone Boundaries In an Acute Non-circulating Fluid-filled Balloon Treated Uterus. The boundaries of the thermal damage zones are indicated by arrows. [NBT and Red Zone Bar = 1cm. Clear Zone Bar = 1mm]

Table 2.

Boundary Depths: NBT Zone and Outer Red Zone Boundary Depths

Instrument	NBT Zone Depth (mm)	Red Zone Depth (mm)	Clear Zone Depth (mm)
Multielectrode	2.7±1.2	4.3±1.5	4.2±1.5
Multielectrode 4 day	1.8±0.6	3.2±0.7	2.5±0.6
Circulating	3.1±1.4	6.1±1.2	4.8±2.8
Non-circulating	2.6±1.6	4.8 ±2.7	3.5± 2.7
Sham	0.1*	0.2*	0

* Less than 3 measuring points taken.

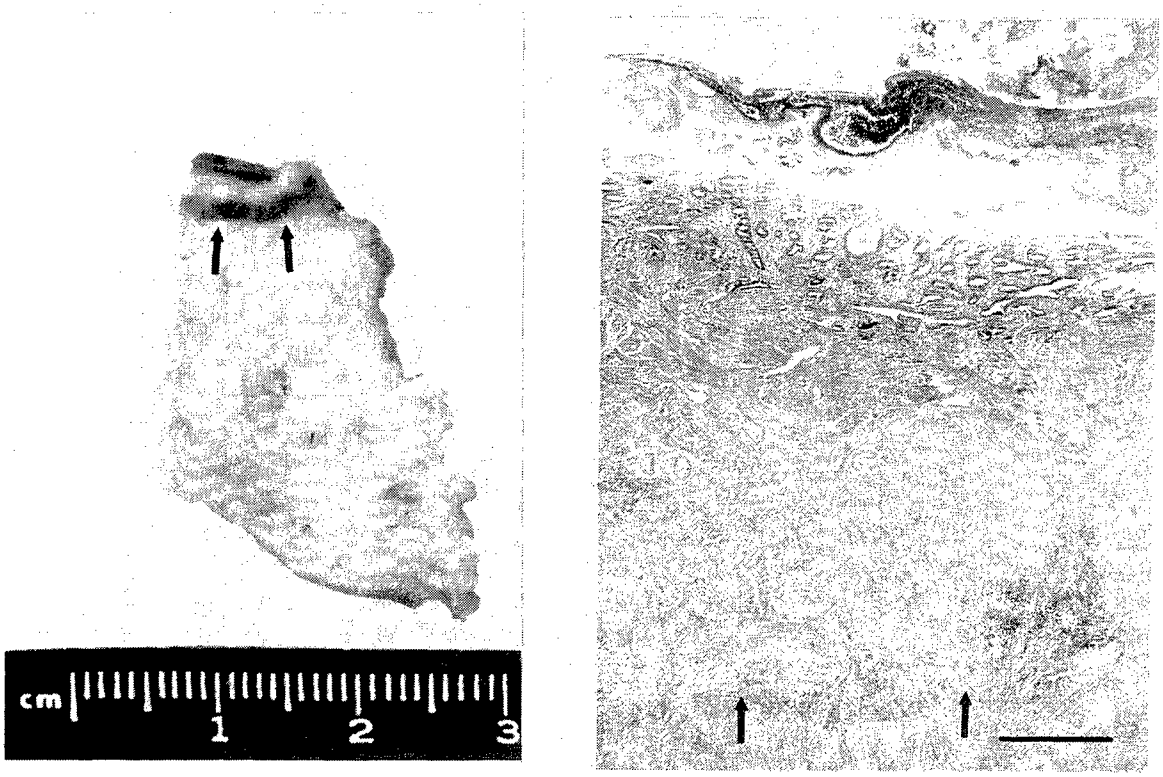

Red Zone **Clear Zone**

Figure 3: Representative of Red Zone and Clear Zone in 4 Day Multielectrode Balloon Uterus. The outer boundary of the red zone (arrows) is distinct. In the microscopic section shown, the clear zone, outer red zone and necrotic tissue boundaries coincide in the myometrium (arrows). A loose fragment of necrotic and hemorrhagic superficial endometrium is separated from the underlying deeper endometrium. This endometrium and the adjacent myometrium that extends to the clear/red boundary have undergone coagulation necrosis thus the full extent of lethal thermal damage is marked by the outer boundary of the red zone in these particular specimens. [Bar = 1mm]

Analyses of the damage depth distributions show that the multielectrode balloon damage depths were relatively tightly distributed around 5-6 mm depths for the outer boundary of the red thermal damage zone [Figure 4 A] and 5 mm for the clear boundary [Figure 5 B]. In contrast, the circulating and non-circulating balloon damage depths showed much wider distributions with a significant number of very shallow lesions ($\leq$ 1mm) and very deep lesions (8-11mm).

DISCUSSION

The pathologic evaluations of the uteri and cervices subjected to *in vivo* intracavitary thermal endometrial "ablation" reveal that the thermal damage extends into the myometrium (uterine muscular wall) in all three treatment groups. However, the thermal damage distributions and depths vary among patients and instruments. The instruments used are being developed and tested for clinical applications; therefore, the treatment temperatures and heating times used in this study were guided by preclinical and clinical indications. [3-6] The variations in thermal damage may be due to several factors.

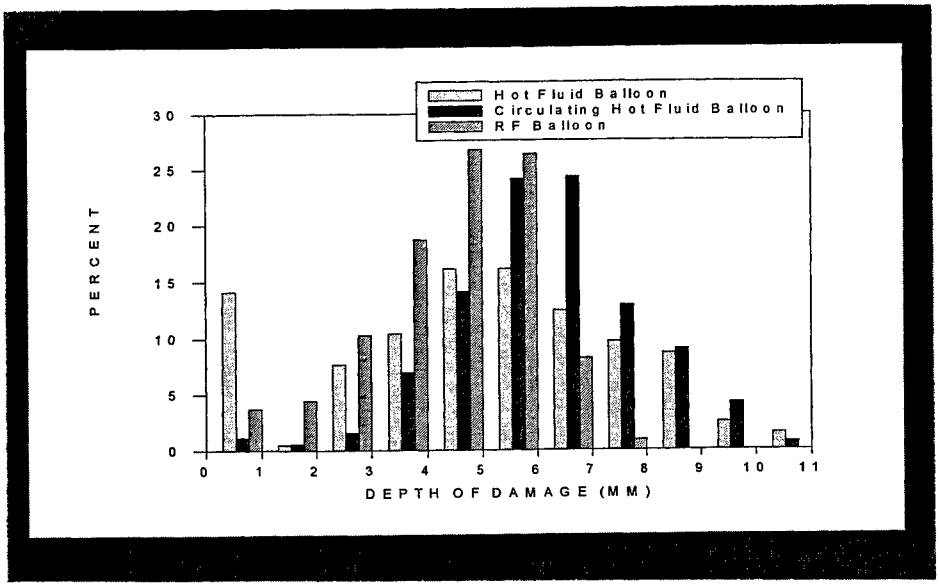

A. Red Zone Outer Boundary

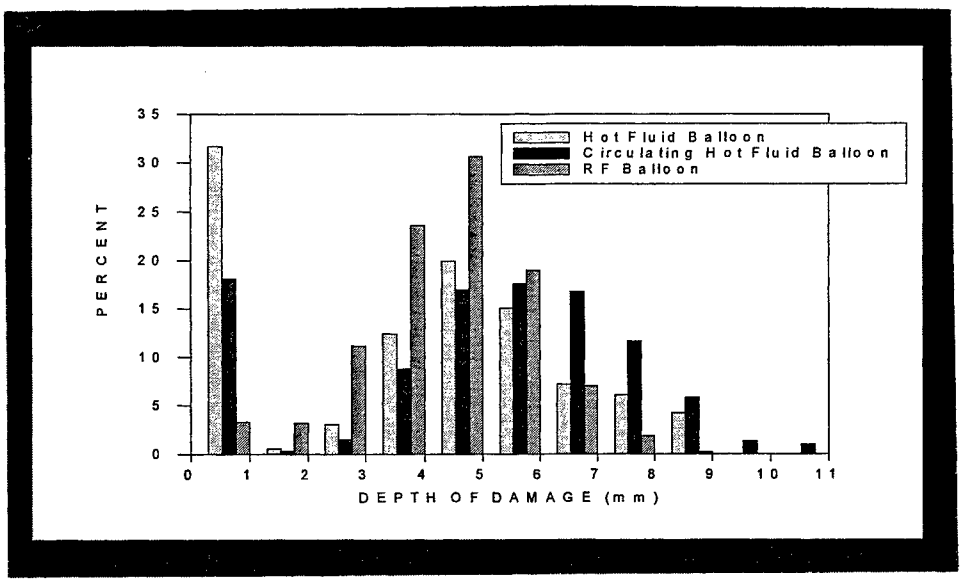

B. Clear Zone Boundary

Figure 4: Damage Depth Distributions for **A.** Outer Boundary of the Red Zone and **B.** Clear Zone Boundary. The labels in the graphs refer to the following instruments: Hot Fluid Balloon = Non-circulating fluid-filled balloon. Circulating Hot Fluid Balloon = Circulating fluid-filled balloon. RF Balloon = Multielectrode air-filled balloon.

The circulating fluid balloon uteri had longer treatment heating times than the multielectrode balloon uteri although both had similar treatment temperatures maintained by their respective feedback systems. The effects of longer heating time are reflected in the deeper average thermal damage depths (NBT, red and clear zone boundaries) in the circulating fluid balloon uteri than in the multielectrode or non-circulating fluid balloon uteri. The higher treatment temperatures (87°C) and intermediate heating time (8 min.) of the non-circulating fluid balloon treatments tended to be associated with more spotty damage depths as reflected by the large standard deviations and distributions of the measurements.

Although not shown in this report, several tissue blocks in this group had no measureable NBT, red damage and/or clear thus accounting for large number of observations in the 0-1mm range. [Figure 4]

The thermal damage depths were more uniform in the multielectrode balloon treatment group in which the regulating temperture measurements were taken at the endometrial surface rather than at the balloon/endometrial interface. These results suggest that temperature sensor placement may be important in production of more uniform tissue effect but adequacy of balloon/endometrial contact also may be important. Balloon/endometrial contact was was not tested in this study. The expanded balloon shapes in air differed among the three instruments: the multielectrode, air-filled balloon was triangular, the circulating fluid-filled balloon was an adjustable ellipsoid and the non-circulating fluid-filled balloon was ellipsoid. It is not clear how the balloon configurations were changed by inflation in the uterine cavity. In addition, the more spotty thermal effect seen in the non-circulating fluid-filled balloon uteri could be due to uneven thermal gradients in the non-moving fluid.

The patterns and progression of the healing of the thermal coagulation endometrial lesions could be through one or both of two major mechanisms, 1) slough of all necrotic tissue followed by endometrial regeneration and scar tissue formation and 2) gradual replacement of the necrotic tissue by regenerating endometrium and scar tissue. In the present study, one uterus specimen was obtained from a woman whose hysterectomy was 4 days after the multielectrode balloon heating treatment. Fragmented, hemorrhagic necrotic tissue covered the endometrial surfaces. Below the surface, an intact zone of solid coagulation necrosis extended through the endometrium into the myometrium to the depths roughly corresponding to areas of hemorrhage within the red zone. Early infiltrates of inflammatory cells including macrophages were begining to organize (literally "eat up") the necrotic myometrium at the boundary of necrotic/viable myometrium. This pathology suggests that slough of the superficial endometrium may occur but it is unclear what could happen to the coagulated deeper layers.

The histopathology of endometria treated with previous mechanical or electrosurgical curettage or rollerball or laser thermal endometrial coagulation have been reported. [1, 6, 9, 10, 12, 16] These endometria showed varied healing responses ranging from complete restitution of the endometrium, mixed endometrial regeneration and surface scarring, complete scarring of the endometrium, intrauterine adhesions and scarring stricture at the uterine/cervical os. Functionally, these patients ranged from amenorrhea (no normal or pathological uterine bleeding) to small or large (pathologic) volume periodic bleeding to completely normal menses. Since many of these reports were of small post-treatment biopsies or hysterectomies for recurrent dysfunctional uterine bleeding, detailed correlation of pathologic findings and functional status were not done.

Although, very superficial, endometrium-only thermal lesions were found mainly in the circulating and non-circulating balloon groups, all three heated balloon treatment groups in the current study showed thermal damage extending into the myometrium. Depths of acute thermal damage related to the number of passes of the rollerball [17] or the power delivered using electrosurgical curettage [10]. In the current study, maximal thermal damage depths were associated with longer heating times when the treatment temperatures were kept constant as was the case with the multielectrode and circulating water balloons.

The ideal depth for treatment of dysfunctional uterine bleeding is not known but removal of the entire functioning endometrium is a general goal for bleeding particularly in peri-menopausal women. This treatment effect may not be the desired effect in dysfunctional uterine bleeding the the peri-pubescent and younger women groups who may wish to have children. The sources of endometrial regeneration can come from 1) the narrow junction of the uterus with the fallopian tube (uterine cornua at the tubular ostia), 2) residual endometrial islands found within the myometrium (adenomyosis) and/or 3) residual suface endometrium missed by the treatment. The endometrium in the tubal os area (cornua) and in the narrow angles of the lateral wall escaped thermal damage in all three treatment groups showing that balloon contact and configuation are important instrument factors in thermal endometrial ablation and could be sources for normal or abnormal endometrial regeneration. Detailed studies are needed to

correlate instrument parameters, endometrial temperatures, treatment times with the pathology of acute and healing lesions examined at different intervals after treatment. These studies may help determine the most therapeutically efficacious lesion while minimizing unwanted complications including fibrous stricture, intracavitary fibrous adhesions and/or pregnancy in scarred uterine tissues.

CONCLUSION

This was a pathological study of acute (and 4 day post-treatment) thermal effect in human uteri treated *in vivo* for thermal endometrial "ablation". Comparisons of the pathologic effects of three different types of intracavitary balloons show that 1) thermal damage can extend beyond the endometrium into the myometrium, 2) some endometrium can escape thermal damage possibly because of balloon configuration and/or uneven distribution of heat and 3) superficial slough of endometrium and/or *in situ* organization of residual solid, thermally coagulated endometrium and myometrium may be the mechanisms of endometrial "ablation" for dysfunctional uterine bleeding. Thermal coagulation into the upper levels of myometrium may be necessary to obtain "ablation" of dysfunctional bleeding.

ACKNOWLEDGEMENTS

This work was supported by Valleylab, Inc., Boulder, CO. The authors wish to thank K. Nolan, HT (ASAP) for performance of last minute repeat histological preparations.

REFERENCES

1 R. J. Kurman, Editor. *Blaustein's Pathology of the Female Genital Tract.* 4th edition. Springer-Verlag. New York. 1994. pp. 327-409.

2. C. Wood. Alternative treatment. *Baillieres Clinical Obstetrics and Gynecology.* 9:373-397. 1995.

3. G. R. Vilos, E. C. Vilos and L. Pendley. Endometrial ablation with a thermal balloon for the treatment of menorrhagia. *J. Am. Asso. Gyne. Laproscopists.* 3:383-387. 1996

4. B. Friberg, B. R. Persson, R. Willen and M. Ahlgren. Endometrial destruction by heperthermia--a possible treatment of mnorrhagia: An experimental study. *Acta Obset . Gyne. Scand.* 75:330-335. 1996

5. R. S. Neuwirth, A. A. Duran, A. Singer, R. MacDonald and L. Bolduc. The endometrial ablator: A new instrument. *Obstet. Gyne.* 83 (5 Pt 1): 792-796. 1994

6. A. Singer, R. Almanza, A. Gutierrez, G. Haber, L. Bolduc and R. Neuwirth. Preliminary clinical experience witha thermal balloon endometrial ablation method to treat menorrhagia. *Obstet. Gyne.* 83 (5 Pt 1): 732-734. 1994.

7. N. C. Sharp, N. Cronin, I. Feldbery, M. Evans, D. Hodgson and S. Ellis. Microwaves for menorrhagia: A new fast technique for endometrial ablation. *Lancet.* 346:1003-1004. 1995.

8. V. J. Page. Anaesthesia and radiofrequency endometrial ablation. *Europ. J. Anaesthesiology.* 10:25-26. 1993.

9. A. Farnsworth, D. Itzkowic, M.Catt, J. Thurloe and C. Laverty. Roller ball endometrial ablation: A histological study in danazol pretreaated patients. *Austral. N. Zealand J. Obstet. Gyne.* 30:200-204. 1994.

10. G. S. Letterie, M. L. Hibbert, and B. A. Britton. Endometrial histology after electrocoagulation using different power settings. *Fert. Steril.* 60:647-651. 1993.

11. H. A. Goldfarb. A review of 35 endometrial ablations using the Nd:YAG laser for recurrent menometrorrhagia. *Obstet. Gyne.* 76 (5 Pt 1):833-835. 1990.

12. P. C. Reid, W. Thurrell, J. H. F. Smith, A. Kennedy and F. Sharp. Nd:YAG laser endometrial ablation: Histological aspects of uterine healing. *Int. J. Obstet. Gyne.* 11:174-179. 1992.

13. J. D. Bancroft and A. Stevens, *Theory and Practice of Histological Techniques* . 4th Ed. Churchill Livingstone. New York. 1996. pp. 391-420.

14. S. Thomsen. Identification of lethal thermal injury at the time of photothermal treatment. *Laser-induced Interstitial Thermotherapy.* G. Muller and A. Roggan. Eds. SPIE Publishers. Bellingham,WA. 1995 pp.459-467.

15. J. A. Pearce and S. Thomsen. Rate process analysis of thermal damage. *Optical-thermal Response of Laser -irradiated Tissue.* A. J. Welch and M. J. C. van Gemert. Plenum Press. New York. 1995 pp. 565-606.

16. T. A. McCulloch, B. Wagner, S. Duffy, S. Barik and J. H. Smith. The pathology of hysterectromy specimens following transcervical resection of the endometrium. *Histopathology.* 27:541-547. 1995.

17. A. M. McCausland and V.M. McCausland. Depth of endometrial penetration in adenomyosis helps determine outcome of rollerball ablation. *Am. J. Obstet. Gyne.* 174:1786-93. 1996.

Controlled Radio Frequency Vessel Sealing System for Surgical Applications

Jenifer Kennedy[a], Steve Buysse[a], James Chandler[a], Jeff Eggleston[a], Ken Taylor[a], and Sharon Thomsen[b]

[a]Valleylab Inc., 5920 Longbow Dr., Boulder CO, 80301
[b]U. Texas M. D. Anderson Cancer Center, Houston, TX 77030

ABSTRACT

A radio frequency tissue welding system has been developed for occlusion of vessels during surgery. The system is designed to replace commonly used mechanical clip and suture ligation techniques. Other energy based ligation techniques are limited to use on small structures ($\leq$ 2 mm) due to slow heating, unreliable sealing, and charring/sticking to the forceps. The system consists of forceps and an RF electrosurgery generator, both of which are specifically designed for optimal tissue sealing. The method combines optimal pressure delivery to the tissue and energy delivery consisting of a high heat cycle, a low heat cycle and a cooling cycle. The generator output is also voltage limited and delivers high current in order to remodel the collagen in approximately 5 seconds with no sticking or charring. The vessel sealing system was compared to other energy based ligation techniques including ultrasonic sealing and other bipolar systems. The pressure required to burst the vessel was used for comparison. Average burst pressures on 3-7 mm arteries were 126 $\pm$ 154 mmHg, 607 $\pm$ 314 mmHg, and 913 $\pm$ 304 mmHg for ultrasonic, standard bipolar, and vessel sealing, respectively. Histologic evaluation showed vessel wall fusion and minimal thermal damage to adjacent tissues for the vessel sealing system.

Keywords: electrosurgery, bipolar, tissue welding, radio frequency

INTRODUCTION

Vessel ligation is an integral part of nearly all surgical procedures. It is accomplished by many methods including use of ligatures, mechanical clips, ultrasonic coagulation and electrosurgical vessel coagulation (ES). ES coagulation is done using a standard radiofrequency electrosurgery generator with a frequency in the range of 300 to 500 kHz with either a monopolar or bipolar electrode configuration. In general, standard monopolar coagulation is not reliable on vessels greater than 2 mm in diameter. The same size limitation is seen in ultrasonic vessel coagulation which uses mechanical vibration to heat the vessel wall[1]. The use of bipolar forceps allows coagulation of larger vessels, but the seals are unreliable and time consuming with existing technology[2,3]. Often, multiple applications of energy are required resulting in thermal damage along several centimeters of vessel length. This is difficult to accomplish in the tight confines of most surgical procedures where damage to adjacent tissue structures must be avoided. The lack of reliability of this method can be explained by the mechanism which relies on vessel wall shrinkage and thrombus formation within the vessel[4]. Ligatures are the gold standard of vessel occlusion, but they are also slow. Mechanical clips were developed as a way to save time, however they are expensive, leave a foreign material in the body that may interfere with future diagnoses, and can be dislodged during manipulation of the tissue during surgery[5].

Electrosurgical vessel sealing has not been previously optimized with respect to generator output or instrument design. Standard electrosurgery generators deliver high voltage in the range of 3000-6000 V_{rms} and 500-800 V_{rms} for monopolar

and bipolar outputs respectively. Also, standard electrosurgery generators deliver relatively low current in the range of less than 1 amp. These outputs were designed for cutting and non contact coagulation, but were not optimized for contact coagulation with large surface area electrodes. The result when using the standard bipolar output for large vessel coagulation is that arcing is generated creating charring and sticking of the tissue to the electrodes. There are also explosive effects that may blow holes in the vessel walls causing bleeding. The instruments apply low force that is sufficient only to coapt vessel walls and stop the flow of blood. The force is too low to deform the vessel walls significantly. The goal of this study was to understand the mechanism of electrosurgical vessel welding and develop a system that would reliably seal vessels quickly and with a single application of energy.

MATERIALS AND METHODS

Vessel sealing parameters relating to the instrument and the generator were varied including voltage, current, electrode width, and applied force. A prototype generator with a data acquisition system was configured to control and monitor current, voltage, time and temperature. Temperature was monitored in order to help understand the mechanism, but was avoided as a control parameter because implementation in a product would be expensive and cumbersome. A prototype instrument was built with pressure control using a hydraulic cylinder. Prototype electrodes could be easily exchanged as well. The study was completed in vitro with porcine renal arteries because of their relatively large size (2-8 mm diameter) and accessability.

During optimization of sealing parameters, the burst strength of the seals were measured. The seal quality was also evaluated using transmission as well as polarized light microscopy. Birefringence loss was used as a marker of lateral thermal spread beyond the seal zone.[5] The burst testing was done using a syringe pump filled with saline and elevating the pressure at a rate of approximately 150 mmHg per minute. The pressure required to burst the seal was noted. A burst pressure of greater than 400 mmHg was considered a successful seal. This criterion was chosen based on the seals withstanding three times normal systolic blood pressure of 120 to 130 mmHg. This will account for pressure spikes that may be seen during post operative coughing or vomiting.

Once the sealing parameters were optimized, a comparative study to other ligation techniques was completed. Burst pressure values were compared for ES vessel sealing, standard bipolar coagulation, ultrasonic coagulation, clips and sutures. Statistical analysis was performed to determine probability of seal strength exceeding the 400 mmHg limit.

RESULTS

Parameters were identified that exhibited seals with high burst strengths characterized grossly by thin, translucent seal sites with plasticized molding of the adjacent vessel wall. The seal site was fully desiccated exhibiting a hard, plastic-like texture. Histologically, the seal zone was significantly compressed and the intimal layers of the vessel walls were fused (Figure 1). For successful seals, mural thermal damage characterized by collagen hyalinization and loss of native collagen birefringence was confined to less than 2 mm from the seal site edge.

The key parameters identified for successful electrosurgical vessel sealing were current, voltage, and applied pressure. The required electrosurgery output included high current (>2 amps) combined with low voltage (<160 V_{rms}) in order to seal the vessels reliably. Applied pressure requirements were found to be 11 to 14 kg/cm^2 (Figure 2). Outside these specified ranges for current, voltage, and pressure, seal quality degraded. Burst pressure decreased and correspondingly, percent success reduced significantly. At pressures above 14 kg/cm^2 the electrodes shorted out and arcing was observed.

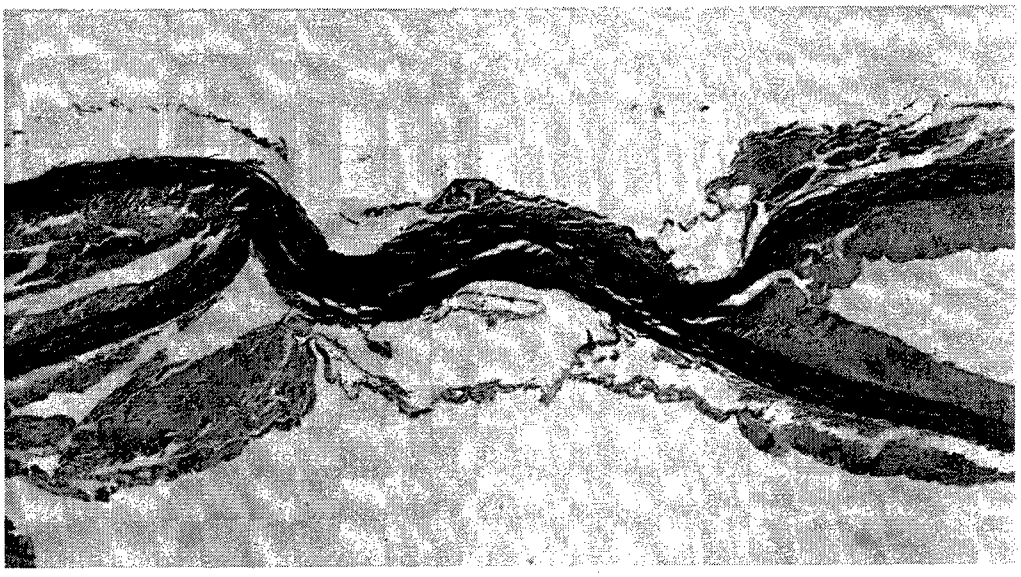

Figure 1: Longitudinal section of a pig femoral artery (Elastin stain). The media is significantly compressed in the seal zone (4 mm long) and the intimal surfaces are fused over the entire length of the seal. Permanent, curved plastic-like molding of the arterial walls adjacent to the seal is necessary to stabilize it. The remodeling is due to thermal denaturation (melting) then solidification of the denatured mural collagens and elastins upon cooling while the site is compressed.

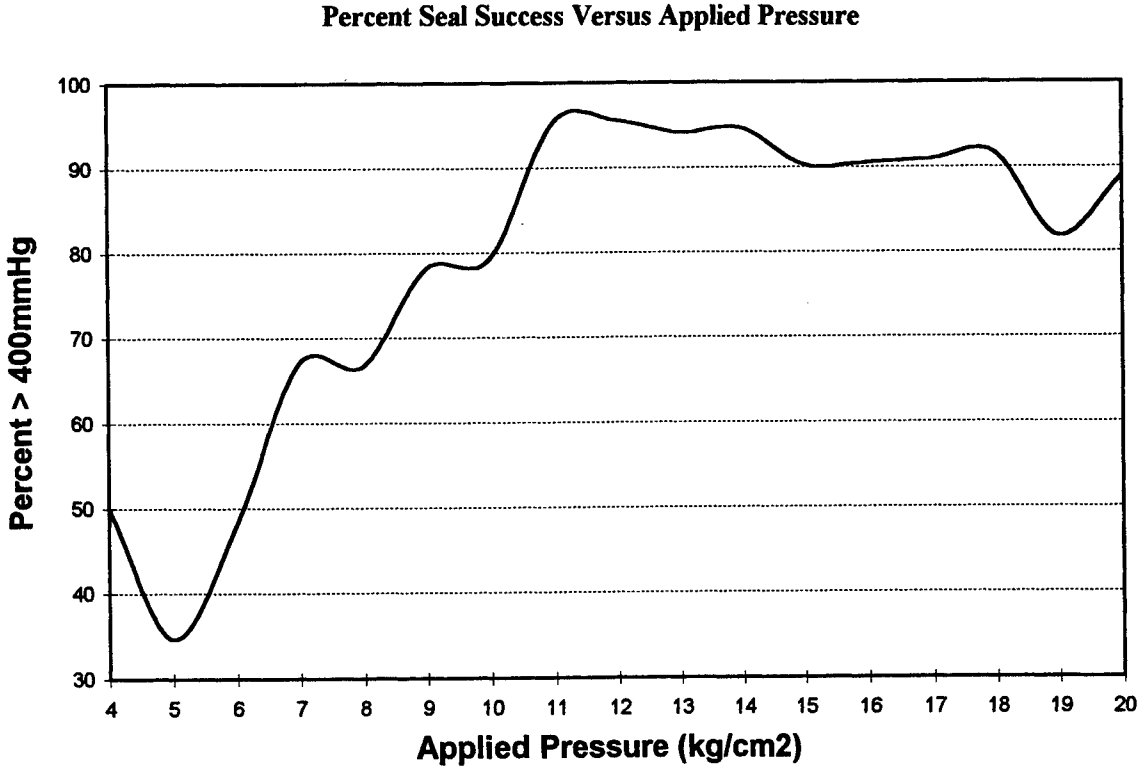

Figure 2: Seal success rates of approximately 95% were achieved at pressures between 11 and 14 kg/cm^2. A successful seal was defined as a burst strength greater than 400 mmHg. Vessel wall fusion was incomplete at lower pressures and complications due to arcing and shorting were seen at extremely high pressure settings.

The results of the comparative study with other ligation techniques are presented in Figure 3. The chart represents data on 3-7 mm arteries only and illustrates the probability that a burst test result would be less than 400 mmHg. The pressure transducer saturated at 900 mmHg which explains the maximum burst pressure on the chart. The probabilities ($\pm$ 90% confidence intervals) were 0.95 (0.82-1.00) for the ultrasonic coagulator, 0.28 (0.19-0.38) for standard bipolar coagulation, 0.02 (0.00-0.06) for the prototype electrosurgical vessel sealing system, 0.04 (0.00-0.13) for clips, and 0.00 (0.00-0.13) for ligatures. The probability of failure for both the ultrasonic coagulator and standard bipolar coagulation were significantly greater ($p<0.001$) than any of the other methods which were statistically indiscernible among themselves. See reference 6 for further information.

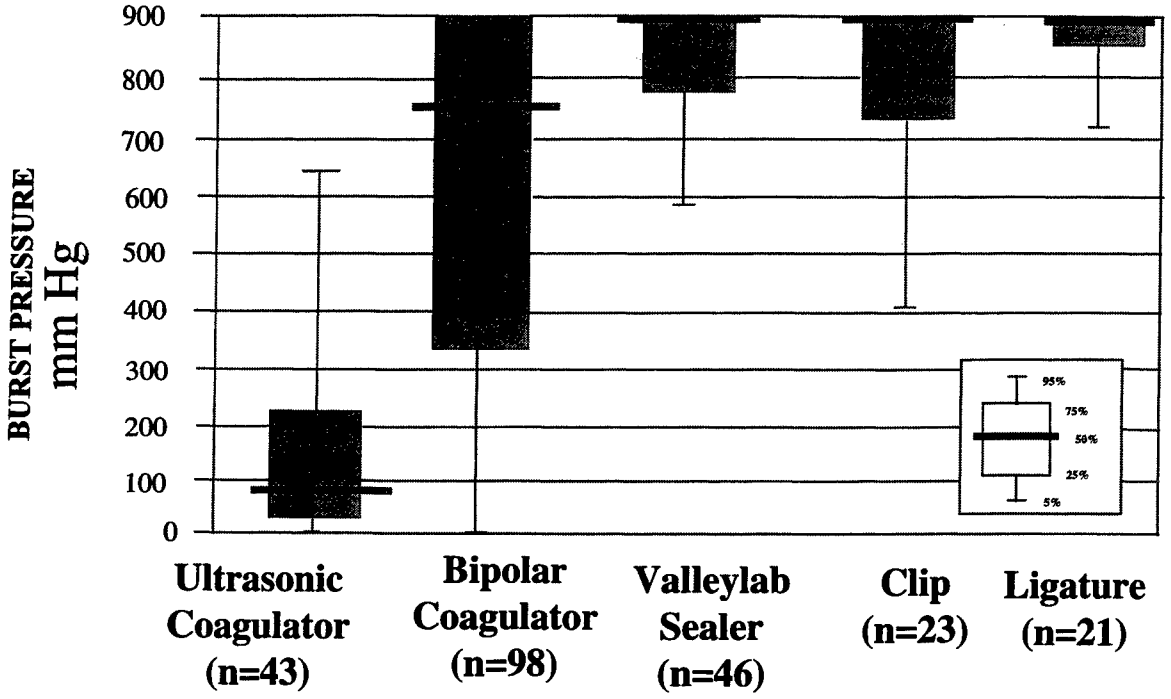

Figure 3: Comparative burst strength data for 3-7 mm arteries.

DISCUSSION AND CONCLUSIONS

This study has shown that it is feasible to fuse vessel walls with an optimized electrosurgical sealing technique. The seal site is translucent allowing the surgeon to visually verify lack of blood flow through the vessel. The plastic-like consistency of the seal site is due to collagen remodeling and acts like a plastic clip created from the body's own materials. Compared to other energy based ligation techniques on large vessels, this system is faster and the seals have more consistent, higher burst strengths. The system is comparable to ligatures and clips in terms of reliability.

The required generator output is significantly different than standard electrosurgery generator outputs in that it requires high current and low voltage. The high current resulted in seal times less than 5 seconds compared to 15 to 60 seconds for standard bipolar coagulation or ultrasonic coagulation. The low voltage limits arc formation and consequently removes the problems of charring, sticking and tissue cutting seen with existing ES systems. The high pressure delivered by the instrument creates the reformed seal site and reduces the chance of problems associated with explosive vaporization.

A limitation of the study is that it was completed on isolated renal arteries only. The parameters that have been defined must be optimized for other tissue types and also to account for potential differences between our animal model and human tissue. This vessel sealing technique, when optimized for human tissue has the potential to replace clips and ligatures in many surgical procedures.

REFERENCES

1. J. F. Amaral, "Ultrasonic dissection", *Endosc. Surg. and Allied Tech.* **2**, pp. 181-185, 1994.

2. J. D. Harrison, D. L. Morris, "Does bipolar electrocoagulation time affect vessel weld strength?", *Gut* **32**, pp. 188-190, 1991.

3. K. J. Barry, J. Kaplan, R. J. Connolly, P. Nardella, B. I. Lee, G. J. Becker, B. F. Waller, and A. D. Callow, "The effect of radiofrequency generated thermal energy on the mechanical and histologic characteristics of the arterial wall in vivo: implications for radiofrequency angioplasty", *Am. Heart. J.* **117(2)**, pp. 332-341, 1989.

4. B. Sigel, and M. R. Dunn, "The mechanism of blood vessel closure by high frequency electrocoagulation", *Surg. Gynecol. Obstet.* **121**, pp. 823-831, 1965.

5. M. T. Nelson, N. Nakashima, and S. J. Mulvihill, "How secure are laparoscopically placed clips?" *Arch. Surg.* **127**, pp. 718-720, 1992.

6. J. S. Kennedy, P. L. Stranahan, K. D. Taylor, and J. G. Chandler, "High burst strength, feedback controlled bipolar vessel sealing", *Surg. Endosc.*, Accepted for publication.

Heating Stents with Radiofrequency Energy to Prevent Tumor Ingrowth: Modeling and Experimental Results

Thomas P. Ryan[a], Kate Lawes[a], and S. Nahum Goldberg[b]
[a]Valleylab, Boulder, CO, 80301, USA
[b]Dept. of Radiology, Massachusetts General Hospital, Boston, MA, 02114, USA

ABSTRACT

Stents are often inserted into internal orifices to treat blockage due to tumor ingrowth. Stents are favored due to their minimally invasive nature, possible avoidance of a surgical procedure, and their ability to palliate surgically non-resectable disease. Because of rapid tumor growth however, a treatment means to prevent overgrowth through the stent and resultant blockage is required. To further this goal, experiments were performed in which a stent was placed in tissue and heated with radiofrequency (RF) energy to coagulate a cylinder of tissue, thereby eradicating viable tissue in the proximity of the stent. Temperatures were measured at the central stent surface and edges over time during a 5-10 minute heating in phantom and in fresh tissue. In addition, a finite element model was used to simulate the electric field and temperature distribution. Blood flow was also introduced in the model by evaluating RF application to stents to determine effectiveness of the energy applications. Changing perfusion and tissue electrical conductivity as a function of temperature was applied as the tissue was heated to 100°C. Results from the electric field model will be shown as well as the thermal distribution over time from the simulations. Lastly, results from the damage integral will be discussed.

Keywords: stents, radio frequency, tumor, blood flow, tissue heating, simulations, finite element model

1. INTRODUCTION

In tumors that grow along tubular structures, simple percutaneous ablation is difficult due to problems in visualization and targeting. One potential palliative strategy is the placement of metallic stents to open the obstruction. Stents are composed of a wire mesh that can be elongated and flattened during insertion, but are self-expanding or can be expanded by a balloon during deployment. Endoluminal stents have been placed to alleviate obstruction of tumors in the biliary, GI, and respiratory systems. Due to the gaps in the stent mesh, however, tumor may grow through the stent and cause re-occlusion (LaBerge et al. 1990). This regrowth could be prevented or delayed by energizing the stent with RF current to induce heating of a cylinder of tissue surrounding the stent. This would induce necrosis and potentially form a fibrotic layer around the stent. Image guidance greatly assists in the placement of these stents in the liver or biliary tree.

To aid in prolonging patency in these stents, RF energy was applied (Goldberg et al. 1995, 1997). The stent was energized by central or longitudinal contact for best power deposition due to the stent resistance which can range from 15 to 20 Ω along its length. Initial tests were done in phantom and then progressed to in-vitro liver and then to an in-vivo porcine liver model. The finite element model was used for simulations of all of these studies (Humphries et al. 1997, Ryan et al. 1997). In addition, evaluation of the changing electrical properties of tissue was performed in our laboratory (Dadd et al. 1996; Ryan et al. 1997), since no data were available for 500 kHz. Simulations included the incorporation of perfusion and tissue electrical conductivity as a function of temperature into the bioheat equation (Ryan et al. 1997). The damage integral was used to evaluate the time temperature history of each element in the model.

SPIE Vol. 3249 • 0277-786X/98/$10.00

2. METHODS AND MATERIALS

2a. Phantom experiments

A stent (Schneider, Minneapolis, MN) of Elgiloy alloy was placed in translucent, viscous phantom material (Hartsgrove et al. 1987) with electrical conductivity and permittivity as well as specific heat and thermal conduction close to that of human tissue. Liquid crystal paper with a sensitivity range of 35-40°C was placed 5 cm below the surface, horizontally and along the central axis of the stent (Goldberg et al. 1995, 1997). The liquid crystal paper had an appropriate cutout to snugly house the stent in its midplane, along its longitudinal axis. The stent was internally occluded by a balloon to mimic actual usage which would prevent conductive liquids from entering the interior of the stent during RF heating at 500 kHz (Force FX, Valleylab, Boulder, CO). The container was covered on its inner surfaces with conductive material to act as an extensive return electrode for volume conduction, as in the body. Power was gradually adjusted so as not to overheat the phantom material since phantom materials degrade at temperatures above 40°C (Ryan et al. 1991). A special low light video camera was placed over the phantom to capture the liquid crystal heating at discrete time intervals. A computer based video capture system (Quantimet 500+, Leica, England) was used to analyze the captured images over time. A range of stent sizes was tested with diameters of 5 to 16 mm and lengths of 20 to 68 mm.

2b. In-vitro experiments

Fresh, whole bovine liver was acquired immediately prior to experimentation. A large metal container was used to provide a sufficient ground path. For in-vitro experiments, a cylindrical cavity was made in fresh, whole bovine liver. The stent was then inserted followed by a balloon to expand it to its working dimensions. Thermocouples were placed in relation to the stent location, either at fixed radial distances or along the stent/tissue interface. Initial power was 60 to 110 W, scaled to the surface area of the stent. Temperatures were read every 10 s. For most of the experiments, temperatures were maintained at 95±0.5°C by adjusting power. Following RF application for five minutes at 95°C, a second five minute interval of cooldown was recorded. The liver was then sectioned, measured and photographed. Temperatures were measured either by thermocouples (Physiotemp, Clifton, NJ) or by fiberoptic probes (Luxtron, Santa Clara, CA). Temperatures at the stent central surface were kept at 90-100°C to avoid charring the tissue and excessive steam formation. A custom data acquisition system was used (FACT system, Valleylab, Boulder, CO) to monitor power, voltage, current, impedance, leakage, energy, temperature, and phase. These data were acquired at 10 Hz and proportional control was implemented to control power to attain and hold the target temperature.

2c. Finite element model

A finite element model was created (Humphries et al., 1997) based on the bioheat equation (Pennes 1948). A finite element model for tissue heating by electromagnetic energy was used to predict temperatures over time intervals associated with clinical treatments (Ryan 1993). Thermal and electrical properties of tissue as well as perfusion are input as functions of temperature. The software recalculates power absorption and temperature distribution based on updates of tissue properties which may change due to the thermal dose history. Although a common assumption is that thermal and electrical properties in tissue change little with temperature elevation, electrical conductivity is assumed to increase 2%/°C (Schwan and Foster, 1980), up to 100°C (Labonte 1994). We used our own measurements for changes in electrical conductivity since there were no data at 500 kHz. A damage integral overlay was implemented to predict the extent of necrosis. The modeling code was developed and allowed thermal and electrical properties to vary with temperature, time, or location. Both changing electrical conductivity and perfusion parameters were simulated by the model. The modified bioheat equation is shown below.

$$\rho_t(r,z,T)\, c_t(r,z,T)\, \partial T(r,z,t)/\partial t = \nabla\, (k_t(r,z,T)\, \nabla T)$$

$$- c_b(T)\, \rho_b\, m(r,z,T)\, \rho_t\, (T - T_b) + Q_p\, (r,z,t) + Q_m$$

r,z = coordinates of element location
$\rho_{t,b}$ = density of tissue, blood (kg/m^3)
$c_{t,b}$ = specific heat of tissue, blood (W s/kg/°C)
k_t = thermal conductivity ($W/m^{-1}/°C^{-1}$)
m = perfusion (flow rate of blood/unit mass tissue) (m^3/kg s)
Q_p = power absorbed/ unit volume tissue (W/m^3)

Q_m = metabolic heating/ unit volume of tissue (W/m^3)
x,y = location in the 2D model
T = temperature (°C)
t = time (s)
Q_m is assumed to be small and is neglected.

The stent was modeled in cylindrical coordinates as an infinitely thin, stainless steel cylinder. The cylinder was air filled and placed in muscle tissue. The stent was 68 mm long with a 10 mm diameter, as in the phantom experiments.

2d. Damage integral for thermal dose assessment

Tissue thermal dose was assessed by utilizing the damage integral to designates areas of both reversible and irreversible damage as heat is applied over time (Henriques 1947).

$$\Omega = P \int_0^t e^{-\Delta E/RT} \, dt$$

where
Ω = thermal damage function
where $\Omega \geq 1.0$ (irreversible damage);
and $\Omega \leq 0.5$ (reversible damage)
P = constant (s^{-1})
ΔE = activation energy (J mol^{-1})
R = ideal gas constant (J mol^{-1} K^{-1})
T = time dependent temperature (K)
t = time (s)

3. RESULTS

The results of the model are shown below. Both electric field results as well as temperature results are shown.

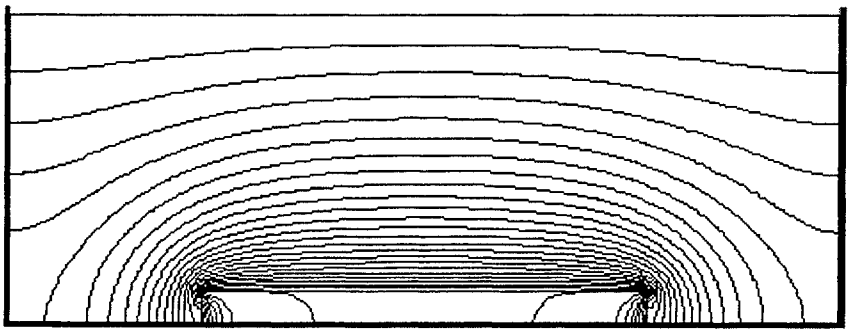

FIGURE 1

LINES OF EQUAL POTENTIAL OF THE STENT EMBEDDED IN TISSUE

The results of the electrical field calculation are displayed as lines of equal potential. The stent is at the bottom of Figure 1 and the upper boundary is ground. The stent is air filled and embedded in a block of tissue with electrical and thermal properties of human liver.

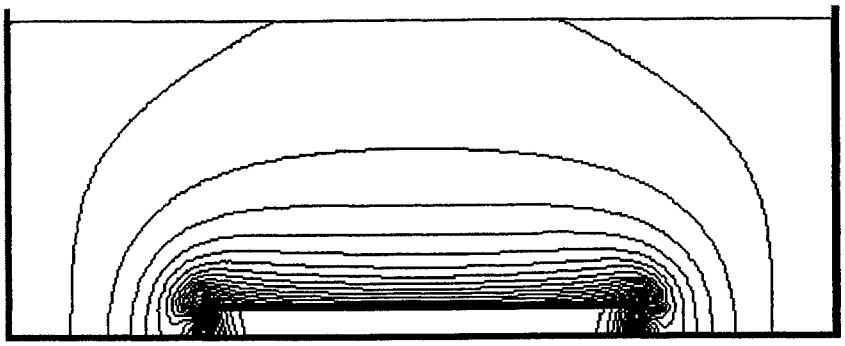

FIGURE 2

MAGNITUDE OF THE ELECTRIC FIELD OF THE STENT EMBEDDED IN TISSUE

The results show the concentration of the electric field magnitude at the stent edges and the relatively flat magnitude parallel to the stent surface in tissue. The iso-electric field lines continue well beyond the ends of the stent.

3a. Phantom experiments

The phantom experiments displayed a heating pattern in the 35-40°C range as seen in figure 3. The dog-bone shaped pattern is due to the edge effects of the stent where a large discontinuity exists. The model of the phantom with zero perfusion is shown in figure 4. Note the similarity in shape and size between the two figures. The model predicted the large side zone of heating at the ends of the stent and the heating beyond the open ends as observed in the pohantom.

FIGURE 3

PHANTOM RESULTS OF HEATING AT 75 W FOR 60 SECONDS

Figure 3 shows the results of the heating pattern of a stent placed in phantom in the plane of a liquid crystal sheet sensitive to 35-40°C. RF power was applied at a constant level for 60s. The white image inside the wire stent is an insulator to shield RF current.

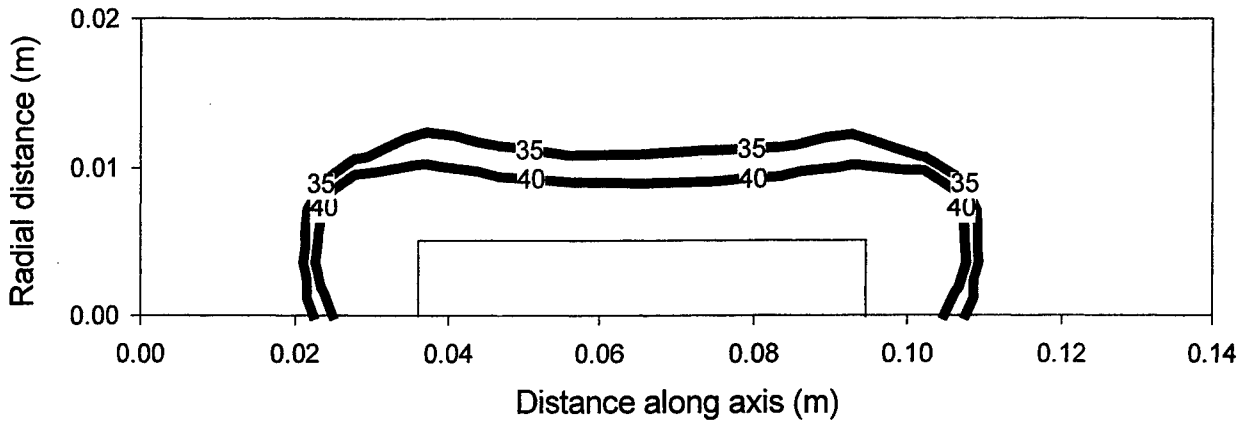

FIGURE 4

SIMULATED RESULTS OF 60 SECONDS OF HEATING

Figure 4 shows a simulation from the model of a stent, show by the rectangular outline. Only half of the plane is shown. The edge effects cause heating beyond the ends of the stent, as well as a broadening of the diameter of heating near the edge.

To more accurately assess heating at temperatures over 60°C, changing electrical conductivity of liver was measured (Figure 5) and then placed in the model. The difference at a point is then shown in Figure 6.

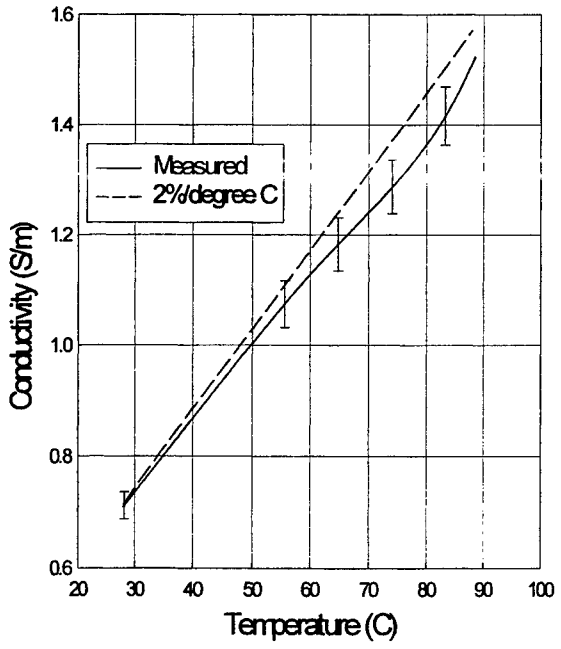

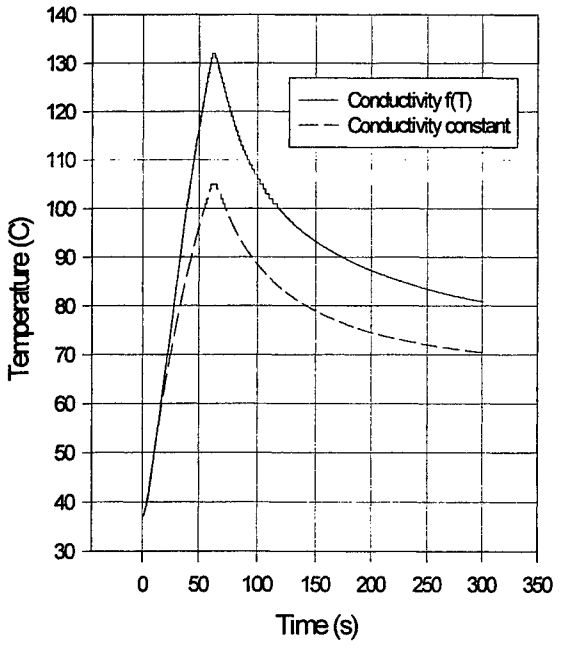

FIGURE 5
ELECTRICAL CONDUCTIVITY
OF LIVER WITH TEMPERATURE
ELEVATION

FIGURE 6
CHANGE IN TEMPERATURE
ELEVATION WITH CHANGE
IN CONDUCTIVITY

Figure 5 shows empirical results in liver of electrical conductivity changes with temperature elevation. The common assumption used by those that change conductivity using tissue heating is a rise of 2%/°C. The actual curve measured is less than the assumed value and will vary depending on tissue type (Dadd et al. 1996). Figure 6 shows the difference at a point of the temperature elevation over time as conductivity is kept constant vs. conductivity as a function of temperature.

3b. In-vitro

For in-vitro stent experiments, RF current ranged from 900-1300 mA and voltage ranged from 25-50 V. Initial contact impedance was 30 Ω and reduced to 15-20 Ω while power was applied. The whole bovine liver was used to induce more uniformly circumferential, unaffected by the location of the grounding pad. Power was modulated such that the stent surface did not exceed 95°C, to prevent a rise in impedance due to excessive tissue desiccation.

In-vitro liver experiments with radial temperatures over time were measured and displayed in Figure 7. A simulation with measurements at the same positions was done with normothermic temperatures to illustrate similar excursions with power on and during cooldown with zero perfusion (Figure 8).

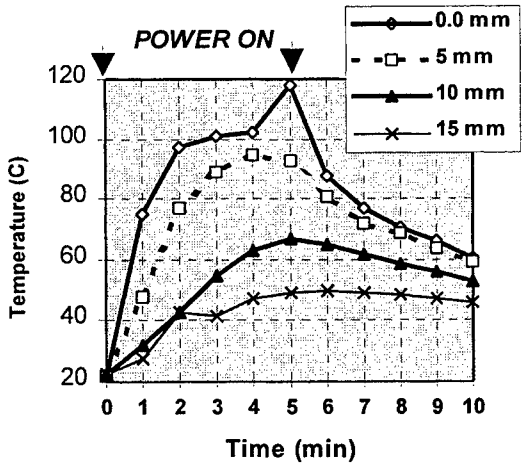

FIGURE 7
RADIAL TEMPERATURES FROM THE STENT DURING IN-VITRO RF HEATING

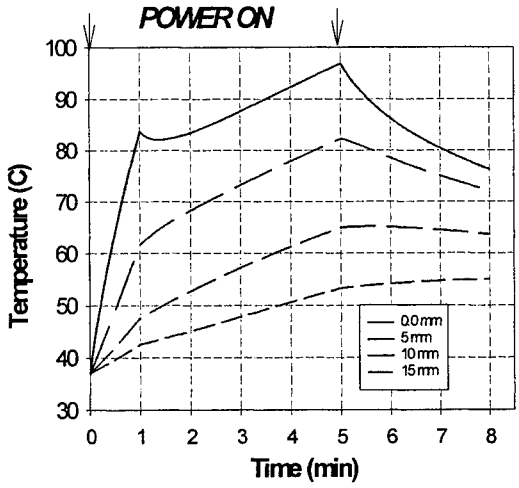

FIGURE 8
RADIAL TEMPERATURES FROM SIMULATION STUDIES

Figure 7 shows results of a 2.5 cm (8 mm diameter) stent placed in fresh bovine liver. Power was constant during the measurements. Thermocouples were placed in the central plane of the stent, perpendicular to the central axis at distances 0.0, 5.0, 10, and 15 mm from the surface of the stent. Note that power was applied for 5 minutes and then 5 minutes of cooldown data were recorded.

Figure 8 shows the temperature elevation during a simulation with higher power the first minute and finally, a leveling off of power during the next 4 minutes. This is typical when controlling power in in-vivo and ex-vivo experiments. Cooldown took place during the last 3 minutes. The temperature spread in this non-perfused tissue mimics the in-vitro data.

A series of simulations were computed. Figure 9 simulates a stent in tissue with no perfusion to mimic our in-vitro work. This figure shows results at 5 minutes of applied power and Figure 10 shows the results after 3 minutes of cooldown is done. Figure 11 adds a high level of perfusion with 5 minutes of power and Figure 12 has 3 minutes of cooldown. Finally, varying electrical conductivity and perfusion with temperature rise is shown in Figures 13 and 14. For simulations in Figures 9 and 11, the stent surface temperature was limited to 97°C.

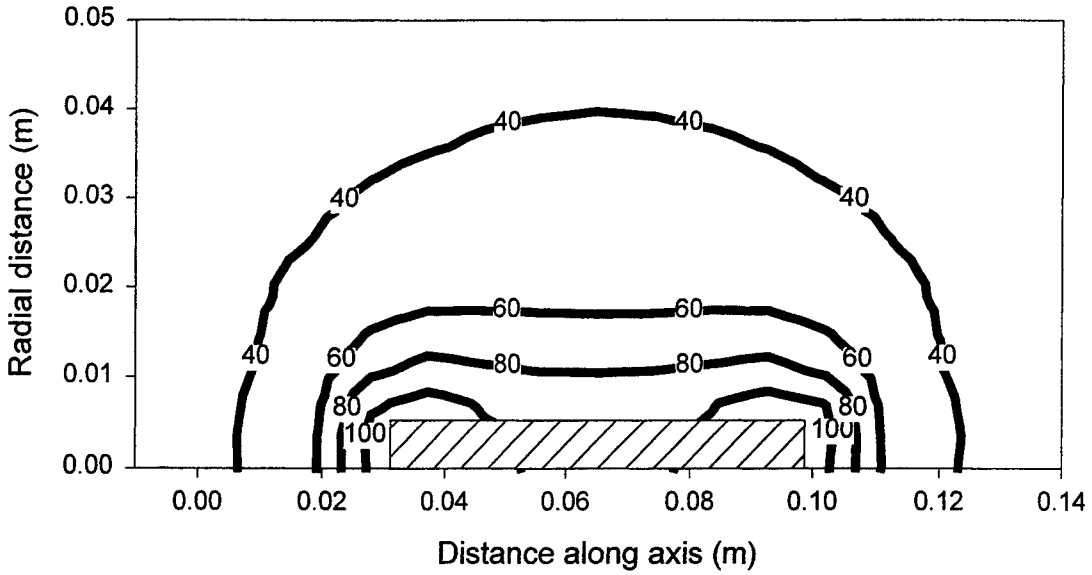

FIGURE 9

SIMULATED HEATING PATTERN AT 5 MINUTES WITH ZERO PERFUSION

Figure 9 displays the results of a simulation of a stent embedded in tissue. Temperatures are controlled such that the central surface stent temperature is allowed to rise to 97°C with power on for five minutes. The tissue has the same electrical and thermal properties as liver. Perfusion is set at zero to mimic in-vitro experiments. Note the higher temperatures at the ends of the stent as predicted by the magnitude of the electric field. Voltage was 40 V for 1 minute and 22 V for 4 minutes.

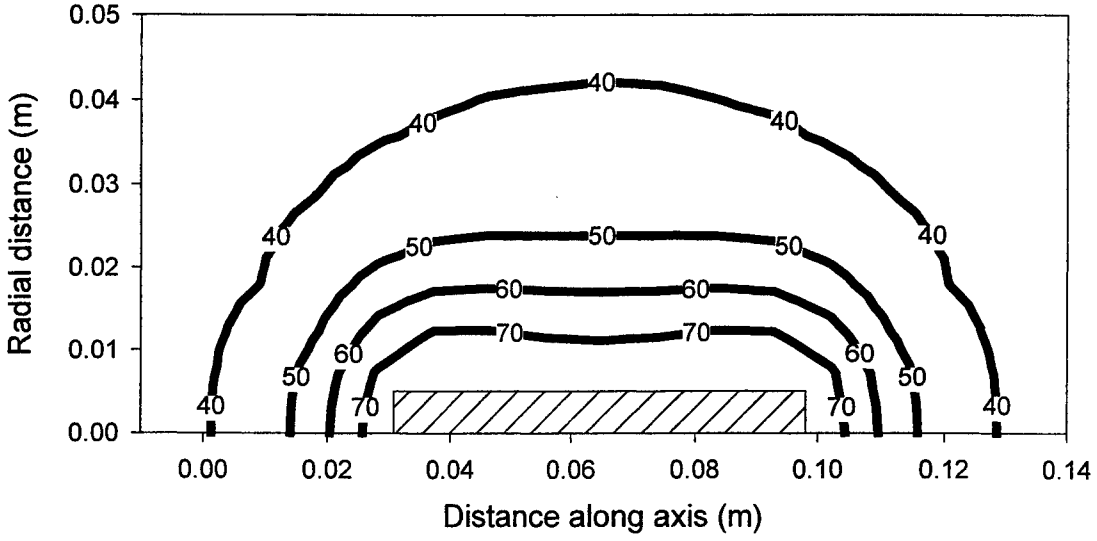

FIGURE 10

SIMULATED HEATING PATTERN AT 8 MINUTES WITH ZERO PERFUSION

The stent set up is the same as in figure 9. Figure 10 shows the simulated results with 5 minutes of heating and 3 minutes of cooldown. Note the smoothing of hot spots at the stent ends.

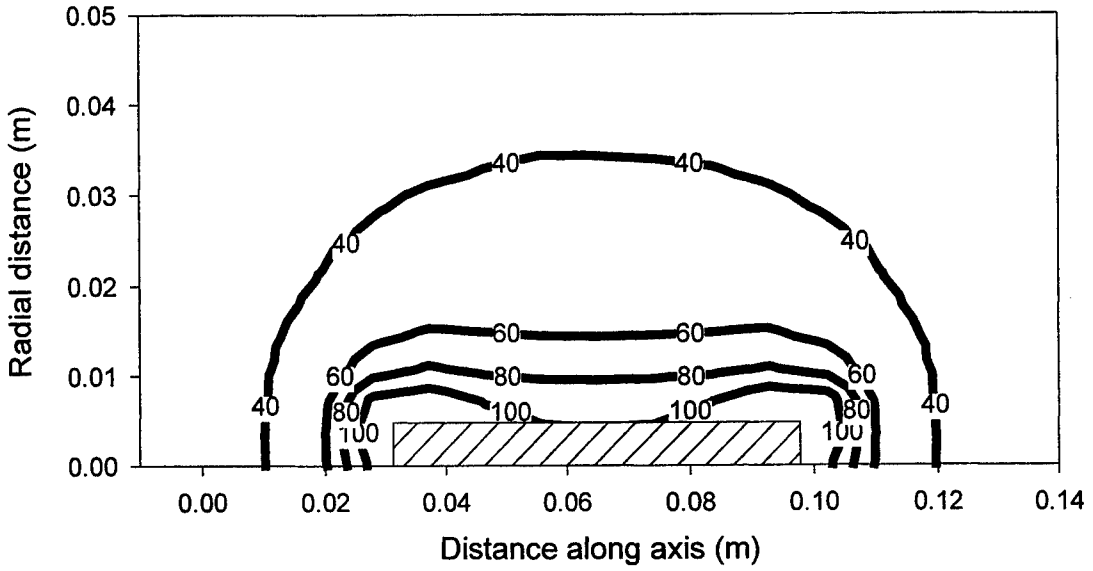

FIGURE 11

SIMULATED HEATING PATTERN AT 5 MINUTES WITH 8.4 kg/m^3/s PERFUSION

This simulation is similar to figure 9 but with perfusion of 8.4 kg/m^3/s as may be found in a tumor with rapidly developing neovasculature. Note the difference when compared to the non-perfusion case in figure 9. The penetration in tissue is greatly affected and the depth of damage will be lessened. Power was on for five minutes and the stent central surface was not to exceed 100°C. Voltage was 40 V for 5 minutes.

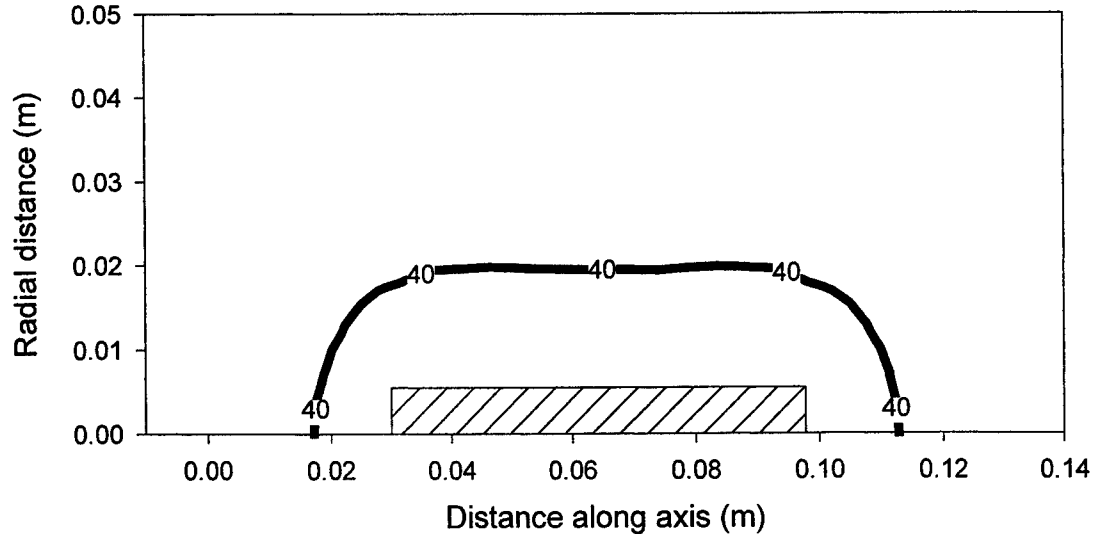

FIGURE 12

SIMULATED HEATING PATTERN AT 8 MINUTES WITH 8.4 kg/m^3/s PERFUSION

This figure is similar to figure 9 except three minutes of cooldown have elapsed. Power was on for five minutes.

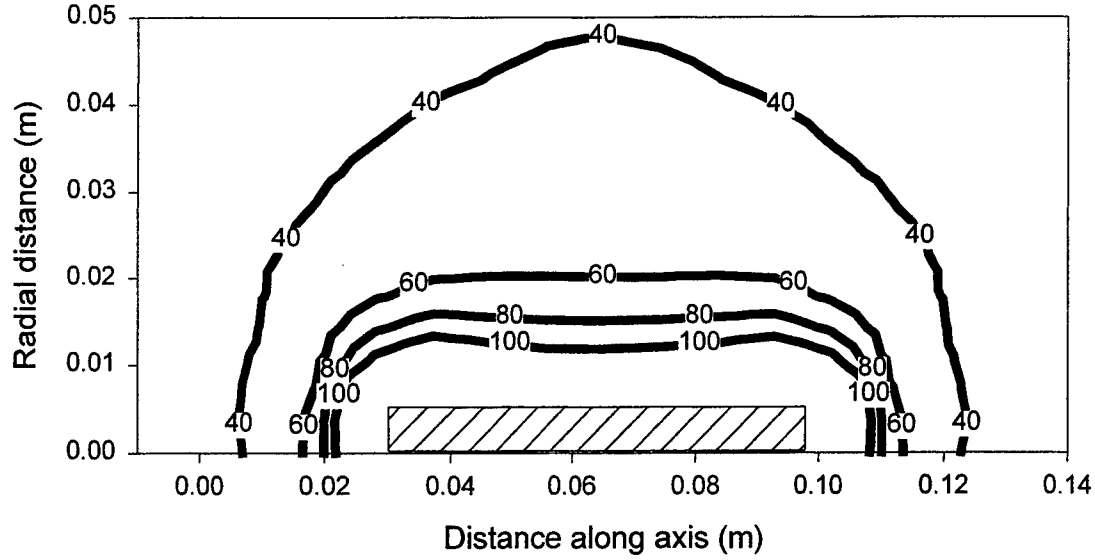

FIGURE 13

SIMULATED HEATING PATTERN AT 5 MINUTES WITH PERFUSION(T), $\sigma(T)$

In Figure 13, RF power was on for five minutes. Perfusion was input as a function of temperature such that it equaled 8.4 kg/m^3/s for elements in the model less then 60°C. If any element exceeds 60°C, perfusion goes to zero due to coagulation of blood at this temperature. In addition, electrical conductivity changes with temperature according to figure 5 were input. Both of these changing factors will cause increased temperature spread. Voltage was 40 V for 1 minute and 22 V for 4 minutes.

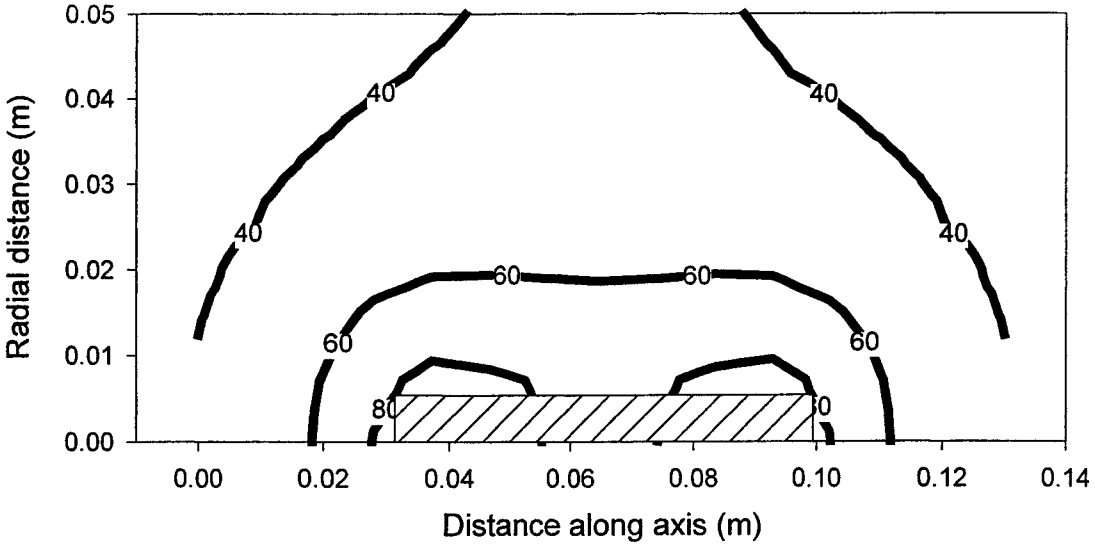

FIGURE 14

SIMULATED HEATING PATTERN AT 8 MINUTES WITH PERFUSION(T), $\sigma(T)$

This simulation uses changing electrical conductivity and perfusion as a function of temperature. Power was on for five minutes and thus this plot incorporates three minutes of cooldown.

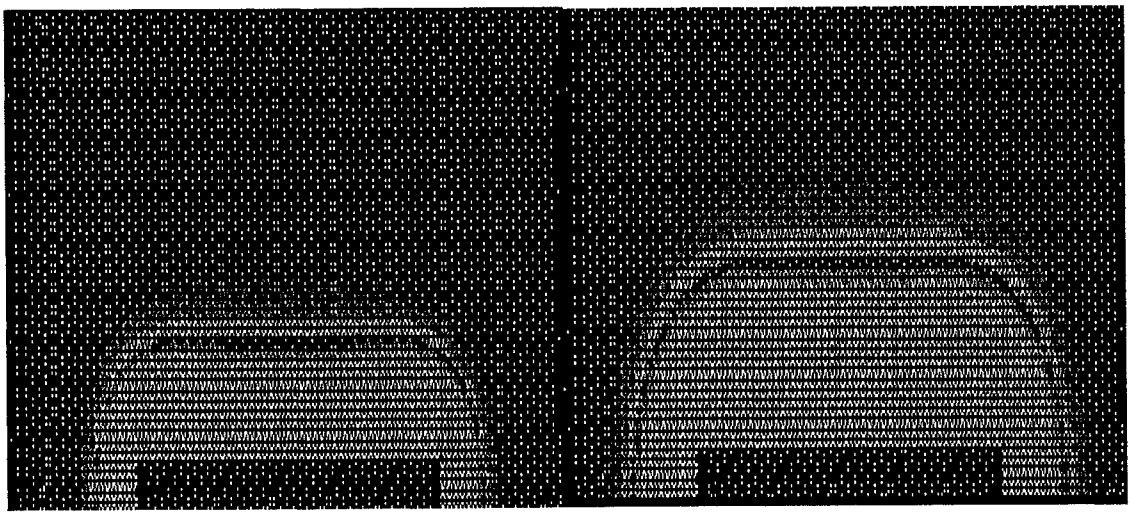

FIGURE 15 *FIGURE 16*

SIMULATION OF DAMAGE INTEGRAL RESULTS FOR STENT HEATING

Figure 15 shows the damage integral results for 5 minutes of heating with constant perfusion and conductivity. Perfusion equals 8.4 kg/m^3/s. The zone of damage extends to 2.8 cm.
Figure 16 shows the damage integral results after 5 minutes of heating and 3 minutes of cooldown. Initial perfusion values are 8.4 kg/m^3/s, but return to zero at mesh elements above 60°C. Electrical conductivity is also a function of temperature using the data from Figure 5. The zone of damage extends to 4.1 cm.

4. DISCUSSION

It has been demonstrated that RF power deposition in stents may be performed to induce uniform, circumferential, transmural coagulation necrosis both in-vitro and in-vivo. In phantom experiments it was found that the tighter the stent mesh, the less electrical resistance and the quicker the heat distribution becomes uniform around the stent. Higher resistance alloys show more of a non-uniform heating nature, taking longer to heat up along the stent. Comparing the resistance along a stent to a standard can therefore give an indication of the expected time to a uniform heating pattern.

In-vitro results show good uniformity of heat distribution for various stent sizes and lengths if energized with central contact. The ability to uniformly heat the various stent sizes and configurations argues favorably for placing stents in various locations throughout the body, according to required size and length. The model demonstrates the ability to simulate the zero perfusion case which matches the in-vitro work in liver. The model also simulated changing electrical conductivity. By increasing the conductivity with temperature rise, an increase in predicted temperatures was seen, depending on the amount of heating at any location.

To transition to the in-vivo case, blood flow was modeled with both fixed perfusion values as well as perfusion as a function of temperature. Assumptions that perfusion shuts down beyond 60°C causes greater heating in the elevated temperature sites. Waiting three minutes beyond the power application time may also more accurately model the damage since the tissue cools slowly and yet is still at therapeutic temperatures.

All in-vivo studies were performed with 4 pigs. Initially, a guide wire was placed via jugular vein access through the heart into hepatic veins under fluoroscopic guidance. The stent delivery catheter was placed over-the-wire. A balloon catheter was placed to fill the interior of the stent, preventing stray conductive fluid or blood from carrying RF current. A second insulated wire was placed to provide a path for RF current to the stent. Separate catheters were placed percutaneously under fluoroscopic guidance to deliver four fiberoptic probes to measure temperatures. Animals underwent CT imaging immediately following the ablation procedure. Additional details have been previous described (Goldberg et al. 1997). RF power was controlled to 90 W, until the stent surface achieved 90°C. The stents were 2 cm in length. Once the target temperature was reached, the power required was 35 W. Following the RF heating, a non-contrast-enhanced CT series was done. Hypoattenuated regions extending 8-10 mm from the stent were seen. This agreed well with the firm, tan region of coagulation necrosis seen on pathological examination. Thus, it was demonstrated that in-vivo stent delivery and heating could be performed under fluoroscopic guidance, the treatment assessed with percutaneously placed thermometry, and the lesion assessed with CT imaging.

Penetration of heating in tissue was simulated with 3 cases: non-perfused (Figures 9 and 10), perfused (Figures 11 and 12), and perfusion and electrical conductivity as a function of temperature (Figures 13 and 14). The perfused case showed less heat penetration, as expected, when the stent surface temperature is limited to less than 100°C (Figure 11). This limit assures minimal steam formation and popping-induced mechanical damage to tissue. Cooldown is prominent in the perfused case in Figure 12. Figure 13 displays the enhanced penetration of heat when electrical conductivity increases with temperature and blood flow shuts down after 60°C. This suggests a more rounded heat distribution as seen in liver studies.

The variety of parameters that may be related to time, temperature, or location in the model make it ideal for tissue damage predictions. All that are lacking may be the thermal or electrical parameter changes with temperature which need to be determined empirically and depend on the type of tissue.

5. ACKNOWLEDGMENTS

Dr. Robert Platt was most helpful in reviewing the finite element model. Jeff Dadd is acknowledged for his assistance in making electrical conductivity measurements and Dr. Mike Schollmeyer and John Stinson for donation of the stents.

6. REFERENCES

1. J.S. Dadd, T.P. Ryan, R.C. Platt, "Tissue impedance as a function of temperature and time", *Biomed Sci Instrum* **32,** 205-14, 1996.

2. S.N. Goldberg, T.P. Ryan, G.S. Gazelle, K.R. Lawes, S.L. Dawsen, P.R. Meuller, "Radiofrequency tissue ablation: transluminal application via metallic stents", *Radiology* **197,** p.382, 1995.

3. S.N. Goldberg, T.P. Ryan, P.F. Hahn, W. Schima, S.L. Dawson, K.R. Lawes, P.R. Mueller, G.S. Gazelle, "Transluminal radiofrequency tissue ablation using metallic stents", *J Vascular Interventional Radiol* **8,** 835-843, 1997.

4. G. Hartsgrove, A. Kraszewski, and A. Surowiec, "Simulated biological materials for electromagnetic radiation absorption studies", *Bioelectromagnetics*, **8**, pp. 29-36, 1987.

5. F.C. Henriques, "Studies of thermal injury," *Archives of Pathology,* **5**, pp. 489-502, 1947.

6. S. Humphries, R.C. Platt, T.P. Ryan, "Finite-element codes to model electrical heating and non-linear transport in biological media", *Advances In Heat And Mass Transfer In Biotechnology,* **HTD-Vol. 355/BED Vol.37**, pp 131-134, 1997.

7. J.M. Laberge, M. Doherty, R.L. Gordon, E.J. Ring, "Hilar malignancy: treatment with an expandable metallic transhepatic biliary stent", *Radiology* **177,** 793-797, 1990.

8. S. Labonte, "Numerical model for radio-frequency ablation of the endocardium and its experimental validation," *IEEE Transactions on Biomedical Engineering,* **41**, pp. 108-115, 1994.

9. H.H Pennes, "Analysis of tissue and arterial blood temperatures in the resting human forearm," *Journal of Applied Physiology,* **1**, pp. 93-122, 1948.

10. T.P. Ryan, P.J. Hoopes, J.M. Taylor, J.W. Strohbehn, D.W. Roberts, E.B. Douple, and C.T. Coughlin, "Experimental brain hyperthermia: techniques for heat delivery and thermometry," *International Journal of Hyperthermia,* **20**, pp. 739-750, 1991.

11. T.P. Ryan, "Methods of thermal modelling and their impact on interstitial hyperthermia treatment planning, 1993, *Medical Radiology- Diagnostic Imaging and Radiation Oncology: Interstitial and Intracavitary Thermo-Radiotherapy*, HM Seegenschmiedt and R Sauer, eds, Springer-Verlag, Berlin, pp. 95-116, 1993.

12. T.P. Ryan, R.C. Platt, J.S. Dadd, S. Humphries, "Tissue electrical properties as a function of thermal dose for use in a finite element model", *Advances In Heat And Mass Transfer In Biotechnology*, **HTD-Vol. 355/BED/Vol.37**, pp 167-171, 1997.

13. H.P. Schwan and K.R. Foster, "RF-field interactions with biological systems: electrical properties and biophysical mechanisms", *Proceedings of the IEEE,* **68**, pp. 104-113, 1980.

Further author information;
TPR Email: tryan@fortnet.org; TEL 303-581-6752; FAX 303-530-6277
SNG Email goldbern@helix.mgh.harvard.edu

A New Electrosurgical Ball Electrode with Non-Stick Properties

Joseph Rondinone[a], James Brassell[b], Scott Miller, III[b], Jonathan O. Thorne[b], David Rondinone[c], Jason Safabash[a], and Felix Vega[a]

[a]Fusion Medical Technologies, Inc., Mountain View, CA 94043
[b]Battelle Product Development Group, Boulder, CO 80301
[c]Berkeley Engineering and Research, Berkeley, CA 94710

ABSTRACT

A new electrosurgical ball electrode (SilverBullet™) has been developed for applying radiofrequency (RF) energy to fuse biological and other materials to tissue surfaces. Specifically, the electrode was developed for use in conjunction with the Fusion Medical Technologies, Inc. gelatin patch (RapiSeal®) for use in pulmonary surgery to seal air leaks, and in solid abdominal organ surgeries to provide hemostatic tamponade. The new electrode allows for the application of RF energy in contact mode without the problems of the electrode sticking to the gelatin patch or the underlying tissue.

Designed for use with commercially available electrosurgical handpieces, the electrode consists of a stainless steel connector that fits into the hand-piece, and an electrode assembly made from silver that includes a shank region, and a tip extension extending distally from the shank region. The distal tip of the tip extension is rounded and has a length of about 10 mm. The uniqueness of this electrode is the shank region which has a cross sectional area that is larger than the tip extension. The shank region acts as a heat sink to draw away heat from the tip extension while the tip extension itself remains sufficiently small to access desired target sites and display the desired energy transfer properties. In addition to the physical design, the use of silver as the core element provides a material with high electrical and thermal conductivities. The bulk of the electrode is appropriately insulated.

Keywords: Electrosurgery, electrode, welding

1. INTRODUCTION

Patches made of gelatin or collagen can be welded to tissue using energy sources such as argon enhanced coagulators or lasers. The welding process requires a patch-tissue interface temperature of approximately 200° F and involves protein denaturation and dehydration of the patch and underlying tissue. Since intimate contact between the patch material and the underlying tissue is required for good attachment, energy which is applied in contact mode can be expected to yield a better weld joint. However, the contact electrode must not stick to the patch or tissue if it is to be effective. Another important consideration is that such operations usually involve large areas over which the energy must be applied.

Temperature of the contact surface is critical for effective electrode operation. Excessive temperatures of the electrode contact surface can result in unwanted degradation of tissue, as well as sticking of proteins to the electrode. Important factors which influence the electrode temperature include electrical conductivity, thermal conductivity, heat capacity, and geometry. High electrical conductivity minimizes resistive heating of the electrode. High thermal conductivity and heat capacity reduce the contact surface temperature by enhancing the flow of thermal energy away from the hot tissue surface. Finally, the geometric properties determine the efficiency with which the electrode acts as a heat sink. A larger electrode with a cross-sectional area which increases with distance from the contact surface will be a more efficient heat sink.

The effects of thermal properties and geometry have been modeled using a finite element solution to the heat diffusion equation. In vitro measurement of the weld strength of the RapiSeal Patch produced by the argon beam coagulator was compared to that provided by the SilverBullet.

2. MATERIALS AND METHODS

In order to study the effects of material and geometry on electrode surface heating, a model system was developed using COSMOS/M software (Structural Research and Analysis Corp., Los Angeles). The components of the system included an electrode, tissue, and air, as shown in Figure 1. Two different electrode shapes were studied. The first was similar to the

SPIE Vol. 3249 • 0277-786X/98/$10.00

SilverBullet, with an overall length of 1.4" and diameters of 0.38 and 0.18" at the shank and tip, respectively. The second electrode shape was a ball with diameter of 0.18" attached to a shaft with diameter of 0.094" with overall length of 1.4" . For each of these shapes, two materials were studied - silver (k = $5.6X10^{-3}$ BTU/in/s deg F , Cp = 22 BTU in/lb/s/s/F°) and stainless steel (k=$2.4X10^{-4}$ BTU/in/s deg F , Cp = 42 BTU in/lb/s/s/F°). Tissue was modeled as having the same thermal properties as water (k = $8.2X10^{-6}$ BTU/in/s deg F, Cp = 390 BTU in/lb/s/s/F°) . Air was modeled as an insulator with zero thermal conductivity.

Joule heating of the tissue was modeled two ways. In the first set of simulations, temperature transients resulting from a 500 ms activation of the electrosurgical generator at 35 watts were modeled. These conditions were chosen to simulate the approximate energy required to "spot weld" a patch to tissue. Joule heating of the tissue was modeled with concentric hemispheres, each with heat generation per unit volume inversely proportional to the square of the distance from the center of the sphere defining the electrode interface. Heat generation was normalized so that the total heat generated in the sum of hemispherical elements was equal to the total power output of the generator. In the second set of simulations, the temperature of a hemispherical shell at .012 inches from the electrode interface was held at 212°F for 3 seconds. This simulates the longer term temperature profile as the boiling point of water is reached.

To measure the difference in welding performance between the SilverBullet and the argon beam coagulator, a total of 14 pieces of RapiSeal Patch, sampled from 3 different lots, measuring 2x4 cm were welded to the pleural surfaces of slabs of fresh porcine lung, warmed to 37°C. Welding was performed using either the Birtcher model 6400 argon beam coagulator (ABC) at 40W, 2 l/min, or with the SilverBullet electrode attached to the Valleylab Force 40 electrosurgical generator set to 35 W, spray coagulation mode. Paired pieces of RapiSeal patch from the same lot were welded using the ABC and the SilverBullet side by side at the same time. A Chatillon TCD200 was used to measure the total energy required to peel each piece at 3 minutes post weld. Peel strengths of welds made with the ABC and SilverBullet were compared using a paired Student's t-test.

3. RESULTS

Figure 1 shows the calculated isotherms of the model system at 500 ms after the start of a simulated 35 W activation of the electrosurgical generator through the SilverBullet and the silver ball electrodes. Figure 2 shows the calculated temperatures along the symmetry axis at 200 and 500 ms, during generator activation, and at 9.5 seconds after the generator had been stopped. Note that the peak temperature at 500 ms is at a depth of .012 in (305 microns) into the tissue, and not at the surface, where current density, and therefore joule heating, is greatest. Note also that temperature in the electrode is equilibrated by 9.5 sec after inactivation of the generator.

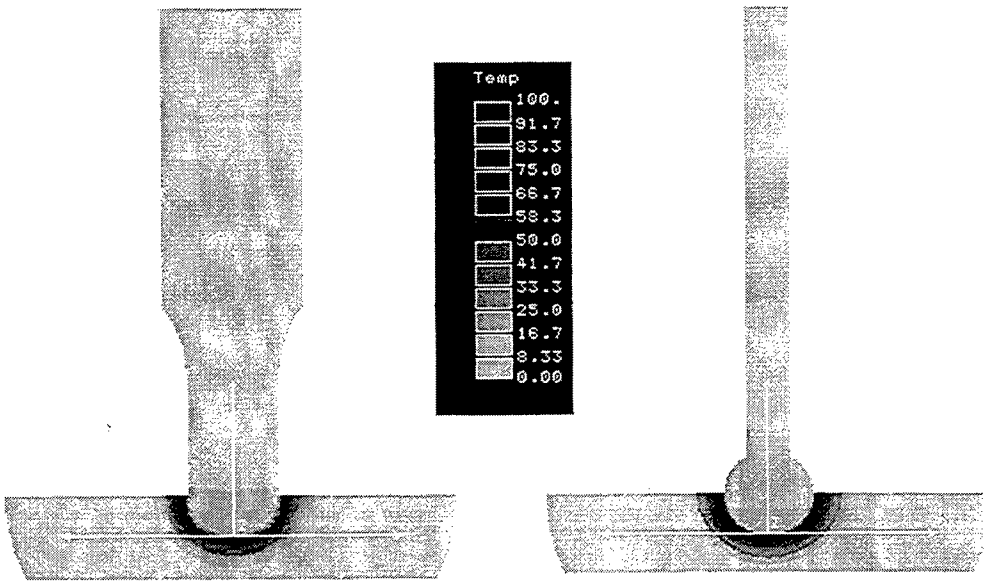

Figure 1. Temperature isotherms for the SilverBullet (left) and silver ball electrode(right) at the end of 500 ms, 35 watt activation of the electrosurgical generator.

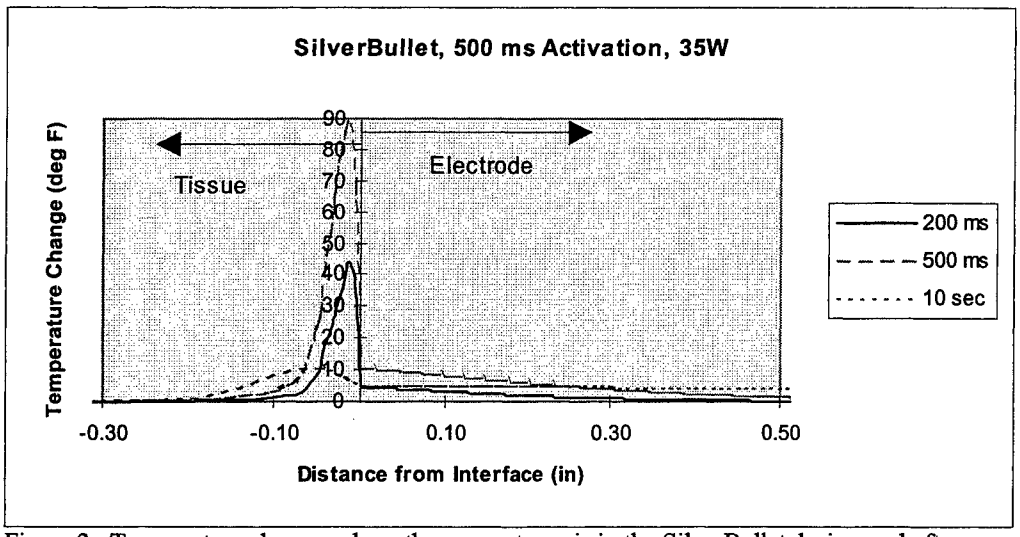

Figure 2. Temperature changes along the symmetry axis in the SilverBullet during and after a 500 ms activation of the electrosurgical generator at 35 watts. Electrode-tissue interface is at x = 0.

Figure 3 shows the temperature along the symmetry axis following a 500 ms, 35 watt activation of the generator for the SilverBullet, a silver ball electrode of with the same contact surface as the SilverBullet , and a stainless steel electrode (steel bullet) with the same shape and size as the SilverBullet. Peak temperature in the tissue is similar for all three electrodes, but changes in electrode surface temperatures are 10.8, 14.2, and 32.4 degrees F for the SilverBullet, silver ball, and steel bullet, respectively.

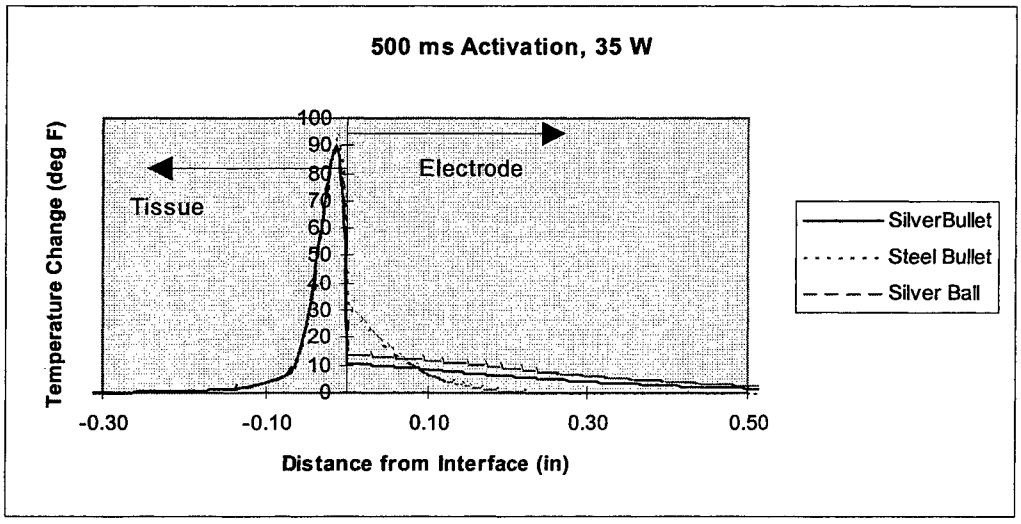

Figure 3. Temperature changes along the symmetry axis for the SilverBullet, steel bullet, and silver ball electrode following 500 ms activation of the electrosurgical generator at 35 watts.

Figure 4 shows the time dependence of temperature at the center of the electrode-tissue interface when the hemispherical shell at 0.012" is held at +140° F above ambient (approximately the boiling temperature of water) for 3 seconds. Temperature changes at 3 seconds are 21.4, 36.7, 66.3, and 71.3 degrees F for the SilverBullet, silver ball electrode, the steel bullet, and a stainless steel ball electrode having the same size and shape as the model silver ball electrode, respectively.

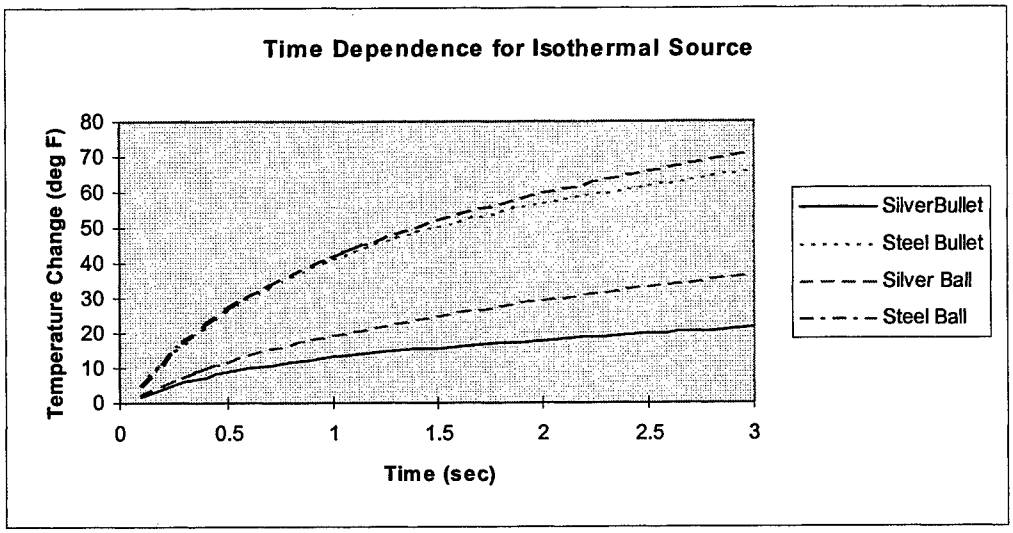

Figure 4. Temperature changes at the center of the electrode-tissue interface for isothermal condition in tissue .

Figure 5 shows the peel strength measured in vitro using patches welded with the argon beam coagulator and the SilverBullet. Peel strengths of patches welded with the argon beam coagulator and the SilverBullet were (mean $\pm$ standard deviation) 1.3 $\pm$ 0.5 mJ and 3.0 $\pm$ 0.9 mJ, respectively. These results are statistically significant by paired Student's t-test (p=.00001).

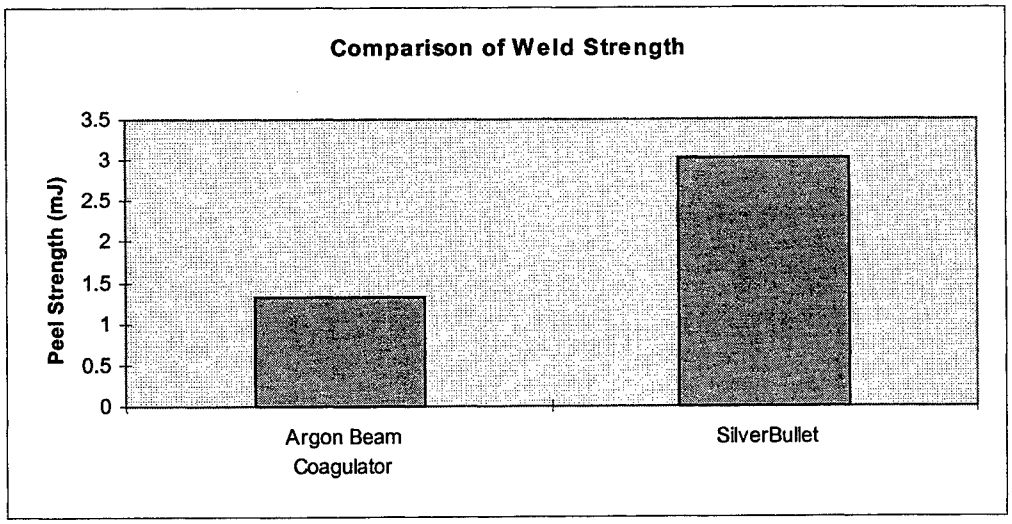

Figure 5. See text.

4. DISCUSSION

Temperature of the surface of a contact electrosurgical electrode is critical for its performance, whether the electrode is used for welding patches or simply as a coagulation electrode. Two factors which have a profound effect on electrode temperature are electrode material and geometry. The effect of thermal conductivity and heat capacity on the ability of an electrode to act as a heat sink have been studied by comparing thermal calculations modeled with electrodes having the same size and shape, but different materials. The thermal conductivity of silver is an order of magnitude larger than that of stainless steel, a material commonly used for electrosurgical electrodes. In the particular geometry studied, the silver electrode heated to only about 35% of the temperature change in a similar stainless steel electrode.

Geometry also has an important effect on electrode heating. The SilverBullet was specifically designed to act as an efficient heat sink. Compared to a simple ball electrode having the same interface, the increased mass and cross sectional surface area of the SilverBullet result in a 25 - 40% reduction in temperature change in the conditions studied. These differences are most pronounced when the electrode is activated for longer times, such as when welding a patch with a relatively large surface area. Although a larger electrode with larger cross sectional area would be a better heat sink, practical considerations limit the size of a commercial electrode useful for surgery.

Finally, the ability of the SilverBullet electrode to effectively weld a RapiSeal Patch to tissue is clearly superior to the non-contact argon beam coagulator. This difference almost certainly arises from the improved apposition of the patch to the tissue surface which results from contact application of energy. The heat sink ability of the electrode also allows the tissue-patch interface to reach a higher temperature than the patch-electrode interface, thereby improving the weld while reducing the tendency of the electrode to stick to the patch.

5. CONCLUSION

A new electrosurgical electrode well suited for welding gelatin patches to tissue has been described. It combines the effects of the high electrical and thermal conductivity of silver with an advantageous size and shape to provide an electrode capable of heating a large surface in contact mode, over prolonged time, without heating to the point where sticking becomes a problem. Patches welded in vitro to porcine lung with the SilverBullet have approximately twice the peel strength as patches applied with the argon beam coagulator. The device has also been used clinically as a coagulation electrode at high powers with minimal sticking. Although the materials are relatively expensive, the device withstands autoclaving and can be reused, making it cost effective.

Interstitial bipolar RF-thermotherapy (RFITT) Therapy planning by computer simulation and MRI-monitoring - A new concept for minimally invasive procedures -

K. Desinger [1], T. Stein [2], G. Müller [1,2], M. Mack [3], T.J. Vogl [3]

[1] Laser- und Medizin Technologie gGmbH, Berlin, Krahmerstr. 6-10, D-12207 Berlin *

[2] Institut für Medizinische/Technische Physik und Lasermedizin, Universitätsklinikum Benjamin Franklin, FU Berlin, Kramerstr. 6-10, D-12207 Berlin

[3] Universitäts Klinikum Rudolf Virchow, Abt. f. Radiologie Humboldt Univ. Berlin, Augustenburger Platz 1, D-13353 Berlin

ABSTRACT

In addition to the laser, microwave or other energy sources, interstitial thermotherapy with radio-frequency current (RFITT) in bipolar technique has already been shown *in vitro* to be a safe and an economical alternative energy source with a comparable operating performance [1, 2]. The therapeutical application efficiency of these bipolar RF-needle applicators was evaluated using 3 different types of probes: standard, flushed and high performance cooled RF-probes (∅ 3 mm). These can be used to create large coagulation volumes in tissue such as for the palliative treatment of liver metastases or the therapy of the benign prostate hyperplasia (BPH). It was shown that the achievable lesion size resulting from the cooled RF-probes could be increased by a factor of three compared to a standard bipolar probe. With these bipolar power RF-applicators, coagulation dimensions of 5 cm length and 4 cm diameter with a power input of 40 watt could be achieved within 20 minutes. No carbonization and electrode tissue adherence was observed. Investigations *in vitro* with adapted RFITT-probes, using paramagnetic materials such as titanium alloys and high performance plastic, have shown that monitoring under MRI (Siemens Magnetom, 1.5 Tesla) allows visualization of the development of the spatial temperature distribution in tissue using an intermittent diagnostic and therapeutical application. This is no loss in performance compared to continuous applications. A ratio of 1:4 (15 s Thermo Flash MRI, 60 s RF-energy) has shown to be feasible. A computer simulation of the temperature and damage distribution during a bipolar RFITT application has been developed. The simulation works on-line with a RF-generator and measures the output power continuously. The electric power density (heat generating term) and the damage distribution is displayed graphically in real time.

1. INTRODUCTION

Investigations on the suitability of bipolar electrosurgery devices for the interstitial thermotherapy (RFITT) will be presented in this paper. An efficient treatment of liver tumors and benign prostate hyperplasia (BPH) is feasible where primary large coagulation volumes have to be achieved. An enhanced bipolar application device was designed and tested to produce large tissue coagulation lesions. These liquid flushed and cooled flexible applicators allow a time-reduced and enhanced interstitial coagulation of large tissue areas.

Using (non-cooled) standard applicators the power which can be applied is limited due to the dessication of the surrounding tissue volume. The maximum power setting for a 3 mm standard probe was found to be 10 watt. Higher power settings led to a premature breakdown in the proceedings; the power output of the RF-generator breaks down at an early stage of the procedure because of an extreme impedance rise caused by tissue desiccation. The concept of the liquid flushed (saline solution) probes is based on the irrigation of the electrode surface to achieve an efficient electrical coupling during the whole procedure but at the same time avoid tissue dehydration and tissue overheating. This method which was already realized in the early 80's from [3] who developed this EHT[1]-method to cool down and irrigate the indifferent

* Further author information:
K.D. (correspondence): Phone: +49 30 844 923-0 • FAX:+49 30 844 923-99 • E-mail: lmzwe19@zedat.fu-berlin.de

[1] EHT = electrohydrothermosation

electrode(s) of quasi-bipolar cutting or coagulation devices. Returning to RFITT, the power input which could be applied to the tissue could be increased by a factor of two up to 20 watt using these liquid rinsed bipolar probes.

A further method to enhance performance is the use of an internal cooling circuit which enabling the electrode to be held at a constant temperature and avoiding tissue contact with the cooling medium. With these RF-power-probes, the highest temperature peak will be shifted from the surface of the electrode into deeper tissue areas far removed from the critical electrode surface (see Fig. 10). As a consequence, an increase in the virtual heating source can be achieved resulting in the application of power settings over 80 W without causing an increase in the load impedance of the tissue during the procedure.

All interstitial treatment methods have one requirement in the common namely that they require a monitoring system such as sonography, CT or MRI in order to control the progress of therapy, i. e. the temperature distribution or the increase of coagulation volume. A computer program for the on-line simulation of the temperature distribution would be an additional quasi-monitoring system for the surgeon in addition to a tool for therapy planning prior to an operation. For developers of RF-needle applicators the simulation is also helpful when investigating the impact of design variations on the coagulation process. A simulation software (LITCIT) has already been developed at our institute for the laser-induced interstitial thermotherapy (LITT) with sufficient accuracy for medical applications. This program now has been extended with a module for RFITT (radio-frequency current induced interstitial thermotherapy) applications.

Firstly a differential equation to describe the electrical potential distribution (combination of Maxwell's equations) of a bipolar RFITT applicator is set up in cylindrical coordinates. With knowledge of the electrical properties of the tissue and the boundary conditions (Dirichlet and Neumann) of the region of interest, the equation is solved numerically by the Finite Difference Method (FDM). Then the electrical power density is calculated as the heat generating term. The power density is standardized to the output power of the RF-generator so that any variation of power during application will be taken into consideration by the program. A further FDM calculation of the heat transfer is necessary for the determination of the temperature distribution. By solving the damage integral (Arrhenius formalism) the degree of tissue damage can be calculated and displayed on a monitor. This procedure is repeated at short time intervals allowing varying parameters and heat transport processes to be taken into consideration.

The electrical properties of the tissue and their dependence on temperature were determined in preliminary experiments. A linear approximation of the dynamic conductivity gave good simulation results.

With a feedback controlled system which may be part of an already developed RF-dosimetry computer program, the cooling circuit of the RFITT-probe and an on-line impedance measurement could be used to actively control the radiation of the process via power input and cooling temperature.

Furthermore, preliminary investigations with these bipolar RFITT-probes showed that monitoring under MRI is also feasible in order to visualize the course of the spatial tissue coagulation using *Flash 2D-Thermo-Sequences.*

2. MATERIAL AND METHODS

Bipolar needle probes with an in-line configuration, different configurations and diameters between 1-3 mm were tested in vitro on different types of tissue. The geometry dependent efficiency of the bipolar probes was optimized using a FEM computer program for obtaining numerical solutions of the specific electromagnetic field distribution. In addition to a standard bipolar needle probe, a 3 mm needle probe was modified by integrating a tip irrigation port (saline solution: 30-100 ml/h). Another 3 mm needle probe was modified with an internal cooling circuit to investigate the influence on the resulting probe performance.

Three different kinds of bipolar applicators were investigated (Fig. 1):

1. *bipolar standard probes*
2. *bipolar probes with electrode surface flushing using physiological saline solution*
3. *bipolar probes with internal cooled electrodes*

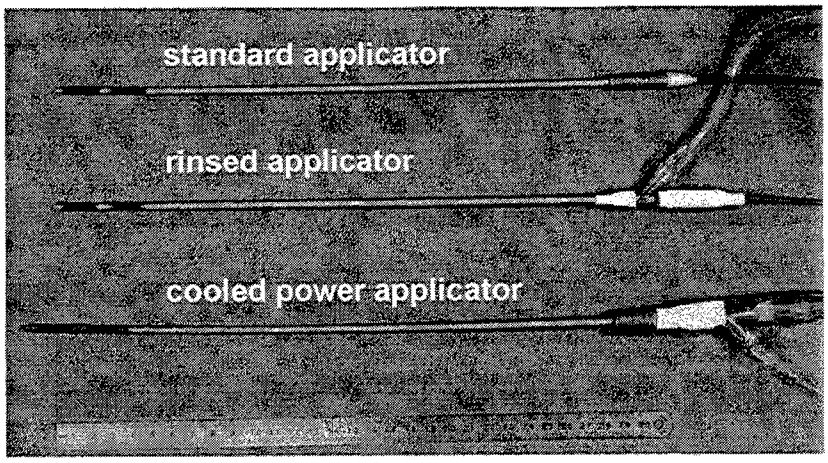

Fig. 1: The RFITT-probes tested

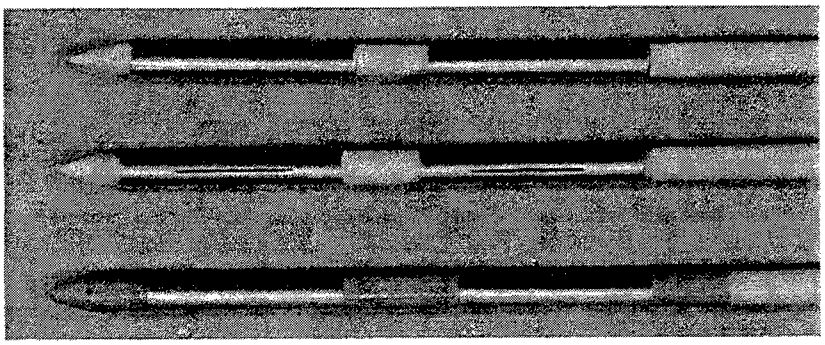

Fig. 2: Applicator tips; standard -, rinsed- and cooled power-applicator tip (top to bottom)

The *in vitro* investigations were performed in porcine liver tissue. The bipolar unit of a Martin ME 80 generator was used for the RF-power supply. To rinse the electrodes of the applicator, an irrigation pump was need which allowed the flow rate to be set between 20 - 40 ml/h. The irrigation liquid used was a physiological saline solution. A Dornier irrigation pump was used for the internal cooling circuit of the cooled RF power probe with a flow rate of 40 - 80 ml/min. The cooling medium used here was sterile, distilled water. The power and the load impedance of the needle in tissue were measured continuously (on-line) during the application with a programmable digital oscilloscope (LeCroy 4030) at time intervals of 1 s. Measurement data were automatically saved and evaluated by a personal computer (Fig. 3).

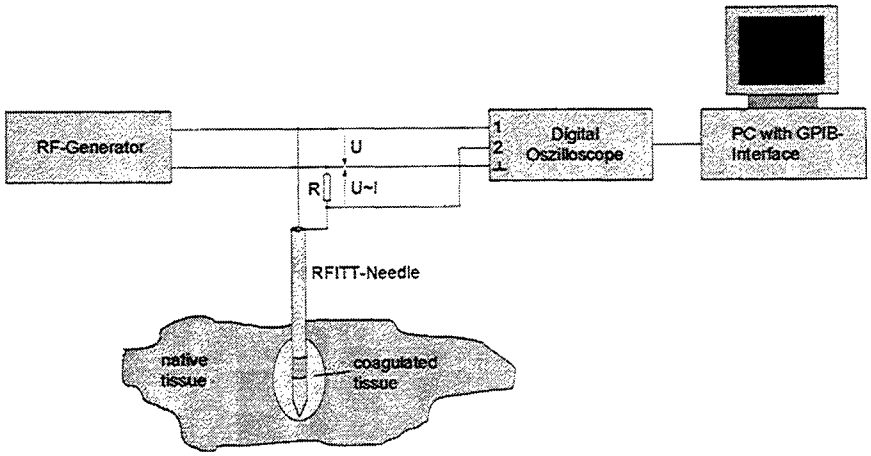

Fig. 3: Experimental set up for an on-line parameter measurement

3. EXPERIMENTAL INVESTIGATIONS

The following chapter describes the *in vitro* investigations carried out using three different types of bipolar RF-applicators. The achievable coagulation volumes and the performance of the applicators were used as evaluation parameters. A comparison was made between the standard probe, the saline solution flushed probe and the cooled applicator. To aid comparison of the applicators the application time in all experiments was set at 10 min and the power settings listed in the tables 1 - 3 gave the optimal coagulation volume within 10 min. Other observations such as carbonization or electrode tissue adhesion were noted.

Standard Applicator

Four conventional applicators with different geometry were tested regarding their efficiency, i.e. achievable coagulation volume within 10 min. The power setting was adapted to the geometry of the applicator. In Tab. 1 only the results of those power settings are listed which led to the a maximum coagulation volume. Further information about the experiments carried out to find the optimal power setting can be found in [2].

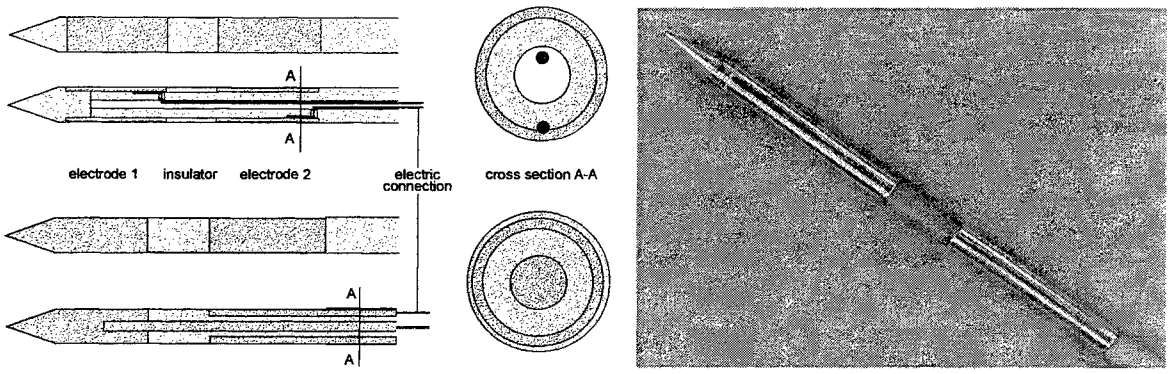

Fig. 4: Possibilities of RFITT-applicator realization, bipolar standard probe

Using a conventional bipolar applicator, the coagulation volume is limited due to the effect of tissue dehydration. The tissue dehydration is a secondary effect of the generated heat caused by the current density distribution along the electrode. The tissue load impedance (R_L) increases due to the gradual dehydration of the tissue during treatment and consequently leads to a mismatching of the internal generator impedance (R_i).

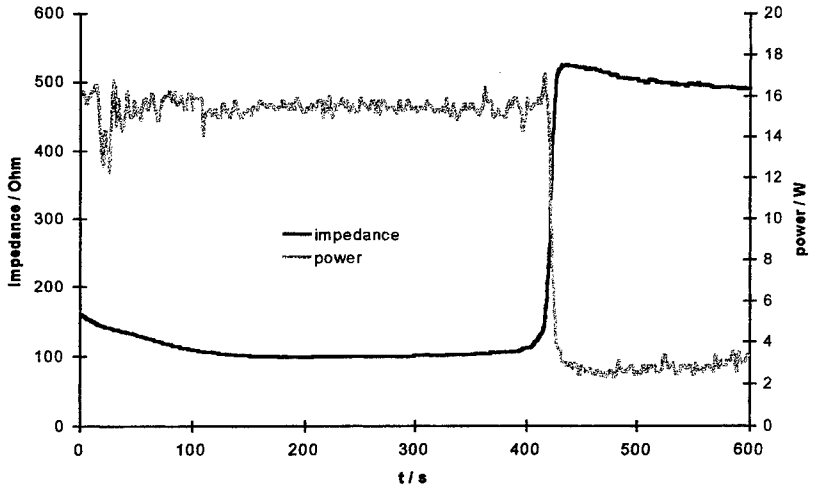

Fig. 5: Typical course of power and impedance of a standard applicator

RF-generators are usually designed to match a load impedance about 100 Ω at which the generator has its optimal power output of 100%. As a result of an increased load impedance due to tissue dehydration (decrease of conductivity) the power output decreases dramatically and only a percentage of the power can be further applied to the tissue (Fig. 5).

It is remarkable that during our investigations with these standard applicators no carbonization occurred at any time. The reason for this is the above mentioned increase in impedance of the dried up tissue and the consequent decline in electric power released by the RF-generator. When the tissue is dried up, the power density is not high enough to heat the tissue beyond the critical temperature of carbonization (provided that the initial power setting is kept constant). But a second and more important effect of the power decline is that there is no further significant increase in the coagulation volume and the thermal heating process stops immediately. Even if one were to increase the power setting, no significant enlargement of the necrosis would be observed, apart from severe carbonization at the electrode surface.

Tab. 1 Achieved coagulation volumes in liver tissue (θ of tissue before application: 20 - 23°C)

diameter of needle [mm]	length of e_1 / ins. / e_2 [mm]	irrigation	power setting [W]	time [s]	electrical energy [J]	coag.-diameter [mm]	coag.-length [mm]	coag.-volume [mm³]
1	10 / 2 / 10	-	4	600	1800	11	23	1400
2	13 / 4 / 14	-	7	600	5100	15	37	4400
3	16 / 6 / 16	-	10	600	6200	24	41	12200
3	**18 / 6 / 18**	-	**10**	**600**	**6200**	**24**	**46**	**13900**

Saline flushed applicator

Using saline solution rinsed electrodes, the electrical coupling between electrode and tissue can be improved at each stage of the process, provided a steady liquid layer is maintained around the electrode. Using this technique, the optimal power which could be applied with this RF-probe to tissue without increasing the tissue impedance by dehydration, was found to be 20 watt, double the value achieved for the standard applicator.

During the course of the experiment several problems became obvious. The adjustment of the optimal flushing rate proved very difficult. When the flushing rate is too low, there is a high probability that the flushing ports (bores or slits) will become blocked by coagulated tissue or biological liquids (e.g. blood) and the flushing process will come to a halt. As a consequence dehydration of the tissue and an increase in tissue impedance occurs. Furthermore contact of the rinsing solution with the biological tissue is unavoidable (hygiene !).

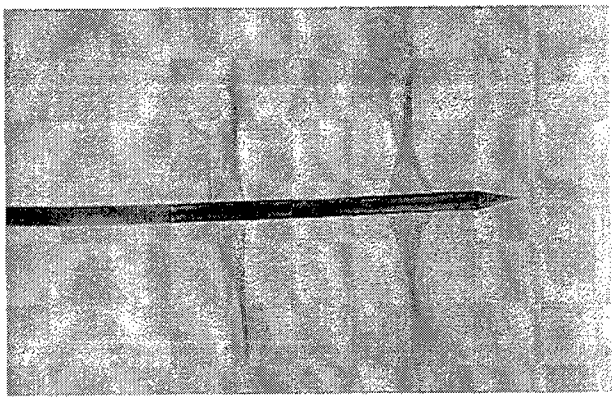

Fig. 6: Tip-flushed bipolar RFITT-Probe

It is therefore advisable to start the flushing of the electrode surface before the application begins. If the flushing rate is higher than is necessary for compensation of the dehydration process (usually 20-40 ml/h), the heated saline solution which flows along the needle path and emerges from the puncture point can lead to unintended coagulation of other native tissue areas along its rinsing path. However, high flushing of rates over 60 ml/min, which have been cited by other groups

as enhancing the performance of monopolar needle probes (e.g. 110 -150 ml/h) [4, 5], initially appeared to achieve larger coagulation volumes because of an active infiltration of the heated saline solution into the interstitium. The biggest disadvantage of such a *high-rate flushing* is the uncontrollable flow path (cavities, vessels) and the coagulation lesions resulting from this RF-enhanced hot water irrigation. As a consequence the course of the spatial coagulation distribution is unpredictable with this method. This could be observed during our recent investigations, shown by one representative in vitro experiment in Fig. 7. All in all, an increase in coagulation volume could be verified but the transition area between native and coagulated tissue is not well-defined because the saline solution penetrated into deeper tissue layers. When the applicator was located in a region with vessels, during the *in vitro* experiment, the heated flushing medium was able to flow along a major vessel and overheat tissue regions far removed from the area of treatment (Fig. 7).

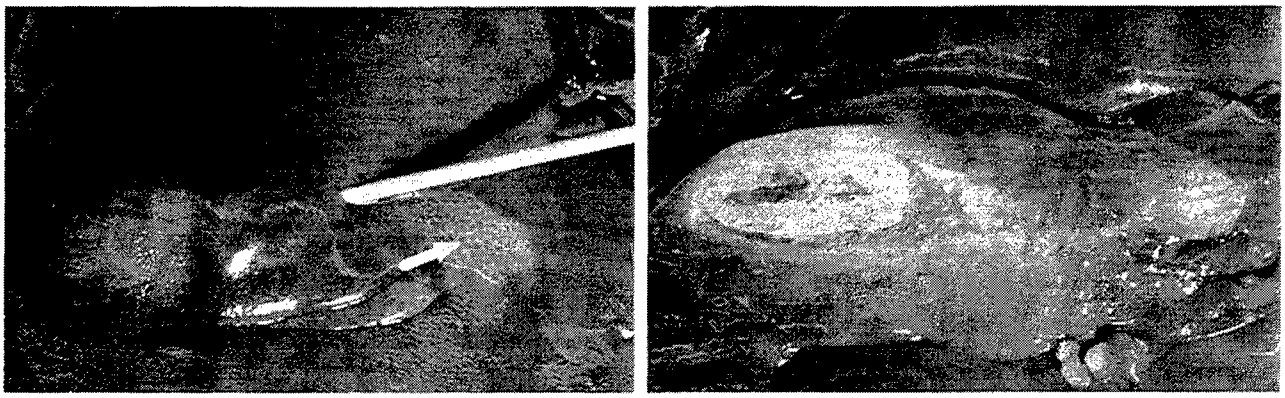

Fig. 7 Uncontrolled RF-application with a flushed needle probe (80 ml/h). Superficially demarkable thermal induced lesion (marker) next to the primary target area (left fig.). Secondary coagulation lesion caused by interstitial rinsing path along a major vessel (right fig.).

When using an applicator with an electrode irrigation system, a higher initial power setting can be applied compared to the standard applicator (see Tab. 2). The dehydration of the tissue is prevented and thus the electric coupling can be guaranteed for the whole application time. The typical power decline of the standard applicator does not occur so that the tissue can be heated up more efficiently because of a higher energy deposition (Fig. 8).

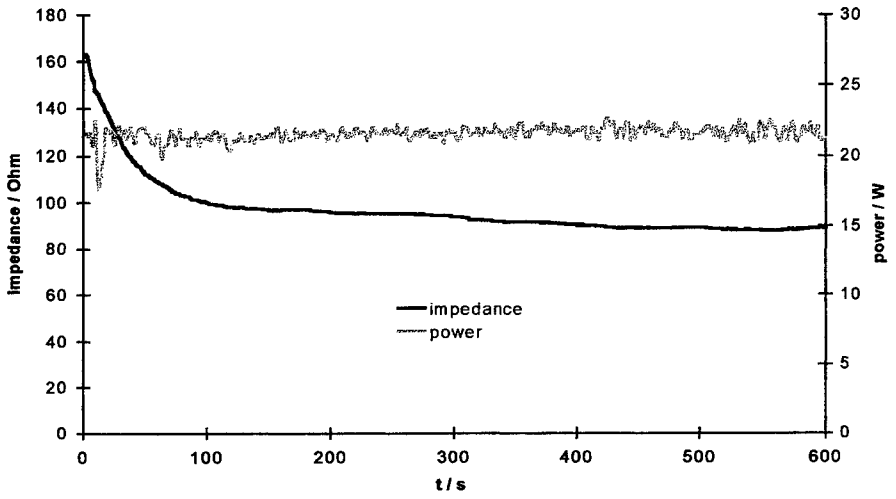

Fig. 8: Typical course of power and impedance of a rinsed applicator

The coagulation volume dimensions are difficult to determine because of the inhomogenity of the thermal lesion. The values in table 2 represent the results of more than 30 measurements with a liquid rinsed RF-applicator tip. An optimum flushing rate was found to be between 40-60 ml/h at a the power setting of 20 watts.

Tab. 2: Achieved coagulation volumes in liver tissue (θ of tissue before application: 20 - 23°C, θ of saline solution: 23°C)

diameter of needle [mm]	length of e_1 / ins. / e_2 [mm]	irrigation [ml/h]	power setting [W]	time [s]	electrical energy [J]	coag.-diameter [mm]	coag.-length [mm]	coag.-volume [mm³]
3	18 / 6 / 18	40	20	600	8400	25	46	15100
3	18 / 6 / 18	60	20	600	12300	26	47	16600
3	18 / 6 / 18	80	20	600	12300	26	47	16600

Cooled applicator

Most of the problems associated with both the standard applicator and the flushed applicator can be avoided by cooling the electrodes internally. When the surface of the electrodes is kept at a low and constant temperature ie. 20-30° C, the temperature of the tissue in the vicinity of the electrodes will not exceed 100°C, which means that at least initially, local dehydration can be prevented. The principle design of a bipolar internal cooled RF-power applicator is shown in Fig. 9. The diameter of this probe is 3 mm, the length of each electrode being 18 mm. The RF-applicator is flexible and heat resistant up to 200 °C.

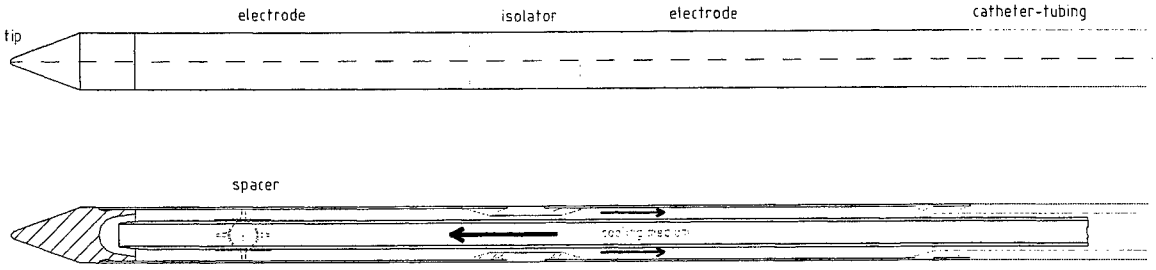

Fig. 9 Principle design of the RF-power applicator with internal cooling circuit

The second and most important feature is that the cooling shifts the hottest spots some millimeters away from the surface into deeper tissue layers (in conventional applicators they are on the electrode surface, depending on the power and cooling)(Fig. 10). In the *hot spot regions* temperatures of up to 150° C can occur but a small area around the electrodes is always electrically conductive which allows conversion of electrical current into heat throughout the entire application time. With power settings > 80 W and application times > 20 min severe tissue dehydration and carbonization are observed at the *hot spot regions*. No carbonization in the tissue surrounding the electrode or tissue adhering to the electrodes was observed, even at power settings > 80 W.

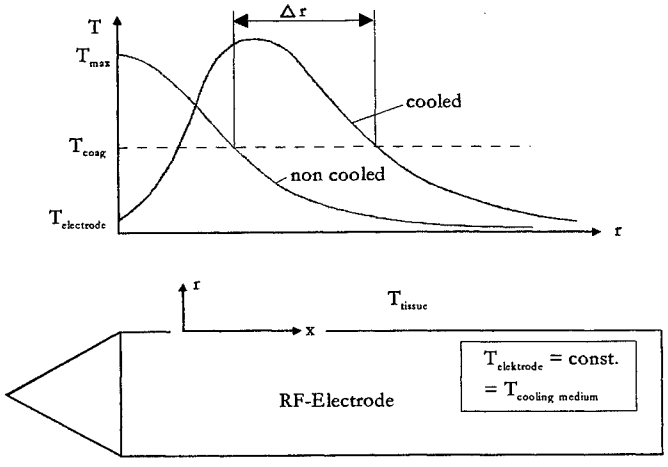

Fig. 10: Principle of thermal peak shift due to electrode cooling

A flow rate of between 40 - 200 ml/min depending on the power setting, is sufficient for effective cooling of the electrodes during an application as a large percentage of the heat energy will be cooled away from the electrodes. The temperature of the coolant before and after electrode contact had a maximum difference of 5°C. This suggests that neither a pre-cooling of

the coolant to a temperature lower than ambient temperature nor higher irrigation rates would have a major impact on the coagulation process. Tab. 3 shows the values of the *in vitro* measurements.

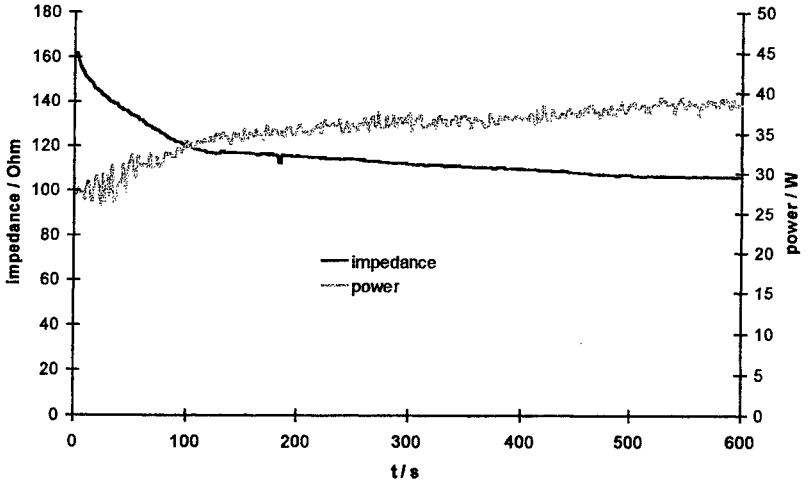

Fig. 11: Typical course of power and impedance of a cooled applicator

Tab. 3 Achieved coagulation volumes in liver tissue (θ of tissue before application: 20 - 23°C; θ of coolant (distilled water): 23°C)

diameter of needle [mm]	length of e_1 /ins. / e_2 [mm]	irrigation [ml/min]	power setting [W]	time [s]	electrical energy [J]	coag.-diameter [mm]	coag.-length [mm]	coag.-volume [mm³]
3	18 / 8 / 18	130	40	600	21500	34	45	27200
3	18 / 8 / 18	130	60	600	30500	32	46	24600
3	18 / 8 / 18	130	70	600	26300	31	46	23200
3	**18 / 8 / 18**	**40**	**40**	**600**	**21500**	**34**	**46**	**27800**
3	18 / 8 / 18	70	40	600	21500	33	45	25600
3	18 / 8 / 18	100	40	600	21500	33	44	25100

In-vitro-Results

Using 3 mm bipolar RF-probes, porcine liver tissue could be efficiently coagulated *in vitro* within 10 minutes whereby the efficiency depends on the primary energy input of the investigated types of RF-application probes (see Fig. 2).

The resulting coagulation, which is representative for a bipolar standard applicator, is shown in Fig. 12. The spatial coagulation expansion is more elliptical because of the limited current density. The diameter/length-ratio is approximately 2/4.

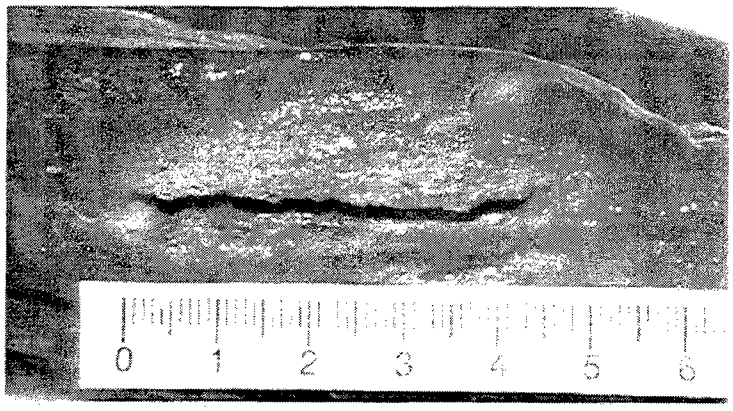

Fig. 12: RF-induced thermal lesion in porcine liver, performed with a bipolar standard applicator (10 W/10 min)

The performance of the tested 3 mm probes could be increased by a factor of two, using flushed needle tips which avoid desiccation and carbonization of the tissue surrounding the probe. However this application is not without danger because of a possible unintended flow of the saline solution in the interstitium or along the needle insertion path. The results of the experiments with the cooled RF-power-applicator showed several positive features:

1. Higher power settings are possible without dehydrating the tissue in the vicinity of the applicator. As a consequence within the same application time, a larger coagulation volume is generated. The volume is more than twice as large c.f. the standard applicator.
2. Furthermore the shape of the coagulated area is more spherical. The diameter/length-ratio is 2/3 in contrast to 2/4 c.f. unflushed applicator.
3. After the procedure, the applicator can be easily withdrawn from the tissue because the tissue does not adhere to the cooled electrodes.

Fig. 13 shows the resulting tissue coagulation after treatment with a 3 mm cooled RF-power applicator. The power setting was 40 Watt over a time period of 20 minutes and a cooling rate of 100 ml/min.

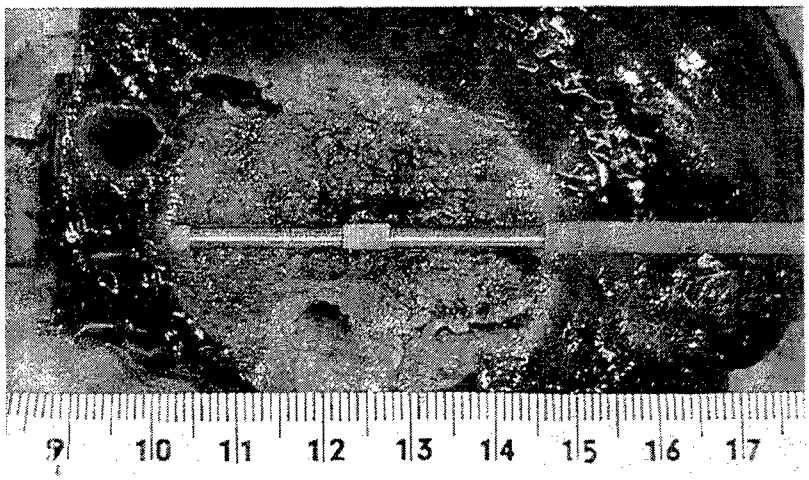

Fig. 13: Spherical RF-induced thermal lesion in liver tissue with cooled bipolar RF-power-applicator

4. COMPUTER PROGRAM FOR DOSIMETRY

The following text presents the theoretical basis necessary for the realization of the computer simulation. At first a differential equation to describe the electric field problem is derived from Maxwell's equations. To allow a numerical solution, the area of calculation ('region of interest') is separated into discrete volume elements and the partial derivatives are approximated by finite differences. With the finite difference method (FDM) the distribution of the heat source is calculated, which is in the case of RFITT, the electric power density. After the electrical problem has been solved the heat diffusion is determined. This is also done by FDM. With the resulting temperature distribution and the chronological course of the temperature, the tissue damage is calculated and can be displayed graphically.

Further details on the theoretical background of the computer model and the FDM-algorithms can be found in [6].

After the implementation of the different parts of calculation (determination of electrical power density, calculation of temperature increase and heat conduction, solving the damage integral) the algorithms were combined into a hybrid model for the dosimetry of interstitial application of RF-current (fig. 14). The correct model version is shown on the left side of the figure. The electric and the thermal problem is calculated cyclically. The change of the electric and the thermal parameters with temperature is considered before each calculation cycle. A simplified model can be seen on the right side. Here the electric field is calculated only once after starting the simulation with the assumption of a constant distribution of the electric conductivity. The heat transfer is calculated cyclically taking account of changing thermic parameters.

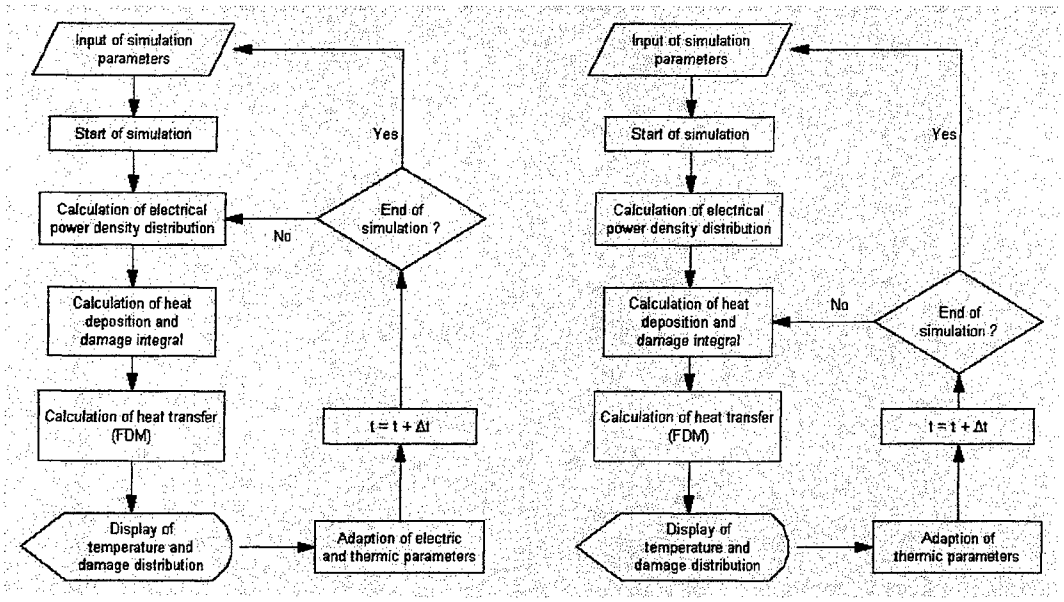

Fig. 14: Floating diagram of the simulation program for dosimetry in interstitial thermotherapy with RF-current; left: accurate, right: simplified version.

As basic investigations have shown, the electric tissue properties are dependent on temperature. The left diagram of fig. 14 shows the result of a temperature dependence measurement performed with a special fillable capacitor. For implementation in the simulation program, the temperature dependence of the specific conductivity has been estimated by a linear approximation. Therefore the measured course was extrapolated knowing that the measured decline of conductivity after 65°C is caused by the measurement set-up and not by the tissue and that the conductivity will increase until the dehydration of tissue begins after 100°C due to the boiling of water.

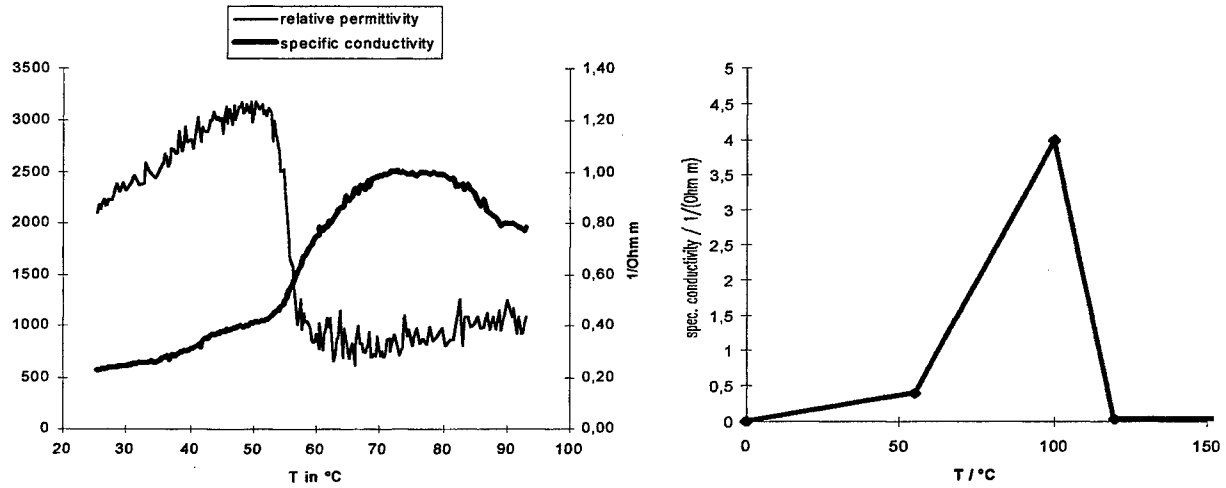

Fig. 15: Left: Measured course of specific conductivity and relative permittivity in a temperature interval from 25 - 70°C. Right: Linear approximation of time dependence of specific conductivity for an interval from 0 - 150°C (porcine liver).

For the implementation of the RF calculation a different region of interest (fig. 16) and different element dimensions as for the heat transfer are used.

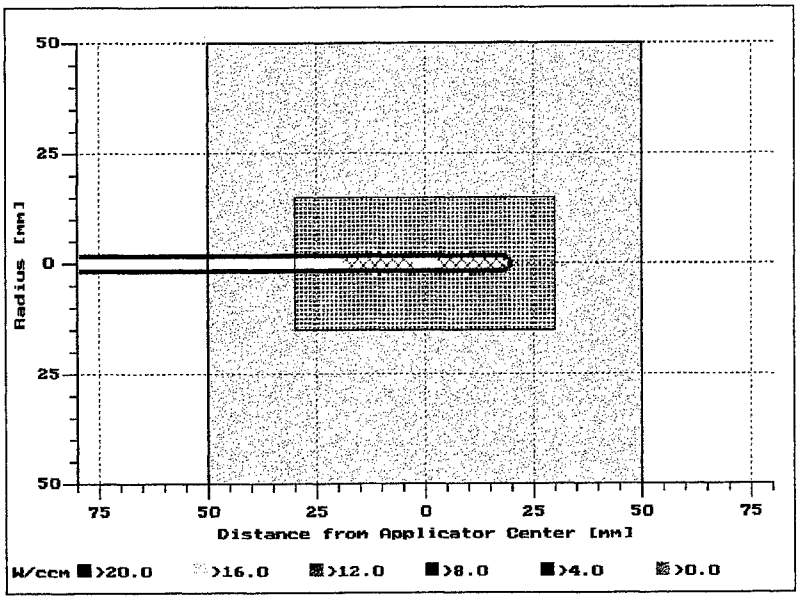

Fig. 16: Possible regions of interest for RF-field calculation (60 x 30 mm) and heat distribution (100 x 100 mm)

The accuracy of an on-line dosimetry (using the simple model) can be increased by measuring the actual RF-power during the application and rescaling the power density distribution. The output power of the RF-generator therefore has to be transformed into a proportional voltage signal and given to an A/D-converter.

5. EVALUATION OF COMPUTER MODEL

Figure 17 (left) shows the simulated damage distribution of an applicator with 3 mm diameter. The RF-power during the application of 10 min was 10 W. The photo on the right side shows the result of the corresponding in vitro experiment. Volume and shape of the simulated and the real necrosis are almost the same. The simulation was performed with the accurate model.

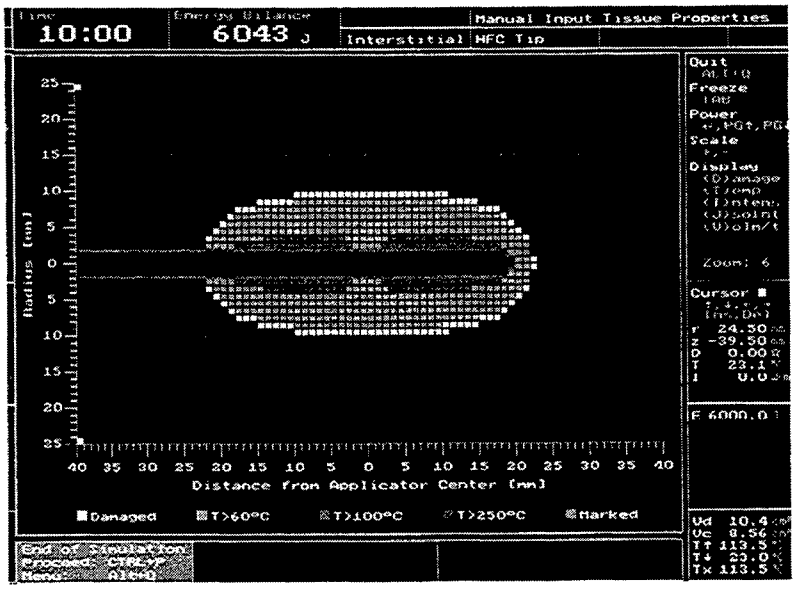

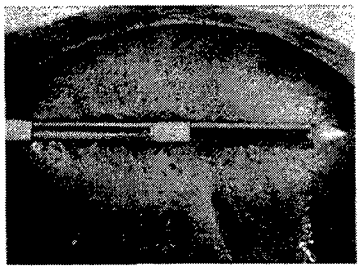

Fig. 17: Simulation and in vitro experiment;
3 mm applicator
10 W, 10 min

Due to the fact that the calculation of the electric potential requires a few seconds on a PC with Pentium 90 processor, even with a low resolution ($\Delta r = 0.5$mm, $\Delta z = 1$mm), the model with dynamic electric conductivity can not yet run at real time because the electric potential is calculated in every program cycle.

A real time simulation can be performed with the simple model because here the potential is only calculated once after starting the program, and then only the heat transfer is calculated which occurs very rapidly. A disadvantage of the simple model is the deviation of the shape of the necrosis especially in the first minutes of the simulation before the heat conduction has the major impact on the coagulation volume.

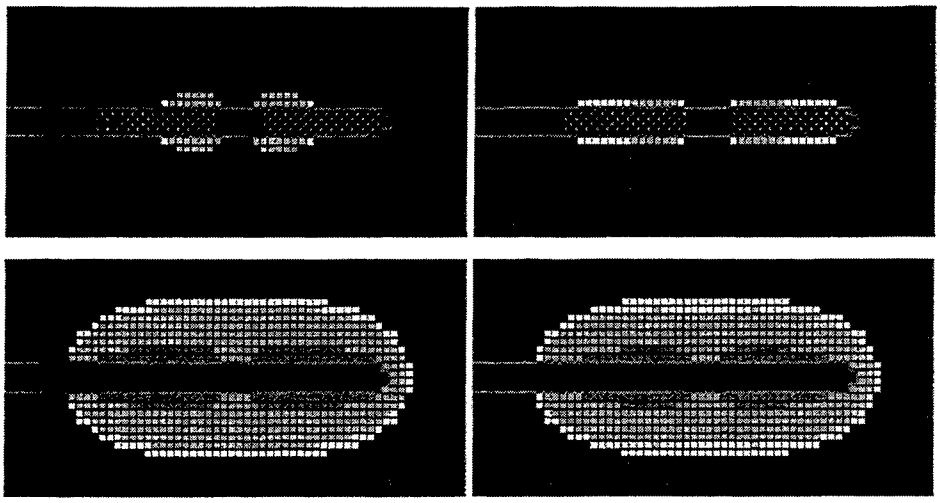

Fig. 18: Damage distributions simulated with the accurate model (dynamic conductivity) (left side) and the simple model (right side). A power of 10 W was applied 10 min with a 3 mm applicator (see fig. 17). The last two pictures show the degree of damage two minutes after switching off the power.

6. MONITORING WITH MRI

Preliminary investigations were carried out regarding the feasibility of MRI monitoring (Siemens MAGNETOM, 1.5 T) during the RFITT-therapy using *Flash 2D-Thermo-Sequences* for the monitoring of the thermal heat distribution. For this experiment a cooled RF-power applicator was modified for MRI, using special titanium alloy electrodes from SOMATEX Corp., Berlin, and other suitable non-magnetic materials. The first results of the material testing with a head coil and applicator in contrast medium are shown in fig. 19. Fig. 19 (left side) shows the applicator tip with clearly demarkable electrode artifacts which allows the radiologist to precise position the applicator probe in the target area. The length of the insulator was measured between both electrodes and the electrode itself. They exactly fitted the probe values. Measurements were performed with 5 Watt RF-power in order to visualize the artifacts caused by the interference of the 500 kHz field of the RF-generator.

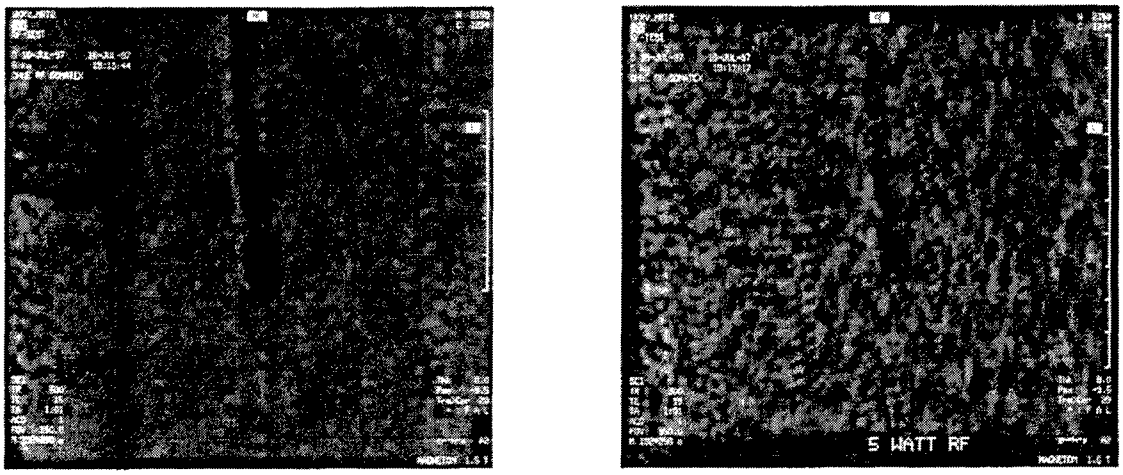

Fig. 19: MRI monitoring tests of a bipolar RF-applicator without (left) and with RF-current flow (right)

Consequently, an electrosurgical application for RFITT under MRI control should not be applied continuously but intermittently to avoid causing severe artifacts in the MRI monitoring.

IN VITRO INVESTIGATIONS WITH MRI MONITORING

In vitro experiments were performed to evaluate the RFITT with MRI-monitoring. Intermittent MRI measurements of 15 s were followed by RF-current application for about 60 s. With this ratio the efficiency regarding the coagulation volume of the procedure is similar to a continuous RF-current application, - no significant difference could be measured between the coagulation volumes achieved.

In fig. 20 a sequence of 6 measurements was evaluated using *Flash-2D Thermo-MRI-Sequences*. The course of the thermo signal sequence is shown. The point of measurement is highlighted (No.1). The amount of signal decrease caused by RF-induced tissue heating of porcine liver with a bipolar standard RFITT-applicator is comparable to the results which could be performed with a standard LITT-applicator.

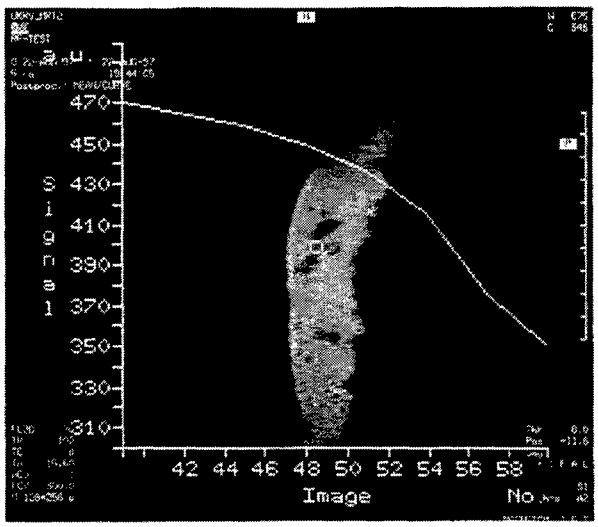

Fig. 20: I*n vitro r*esult of *Flash-2D Thermo-MRI-Sequences*

7. CONCLUSIONS

The coagulation volumes achieved in tissue, using cooled, irrigated and 3 mm standard needle applicators are comparable to those of the *Laser Induced Thermotherapy* (LITT) using the same energy input [7, 8]. Thus the RFITT could be an economical alternative or addition to LITT. Furthermore, MRI monitoring is also suitable for RFITT procedures. The feasibility of RFITT-planning and -monitoring with the developed simulation program was also shown. This could be a very useful tool for the surgeon. The difference between simulated and real coagulation volume is already quite acceptable. A further increase in accuracy would be possible by improving the implementation of the temperature dependence of the electric conductivity, for example, with a look-up table of measurement values. Research supported by the BMBF (13 N 6685).

8. REFERENCES

1. K. Desinger, G. Müller, T. Stein, J. Tschepe: *„Radiofrequency current application for interstitial thermotherapy (RF-ITT), an alternative or completion to LITT ? - Future Prospects -"*, SPIE-Symposium, Institute on Laser- induced interstitial thermotherapy, SPIE Vol. PM25, Berlin 6/1995
2. K. Desinger, T. Stein, G. Müller: „Investigations on High-Frequency Current Application in Bipolar Technique for Interstitial Thermotherapy (HFITT)", SPIE-Press; Vol. 2970, p. 526-535, BiOS San José, USA, 2/1997
3. H.-D. Reidenbach : „Fundamentals of Bipolar High-Frequency Surgery", End. Surg.; 1: p. 85 - 90,. Georg Thieme Verlag Stuttgart - New York, 8/1993
4. W. Müller, H. Haendle: „A short characterization of the methods of the high-frequency-thermo-therapy (HFTT) with rinsed HFTT-needle-applicators", submitted Abstract, Session 9: Photothermal therapies: Interstitial Thermotherapy II, Wien, 7-10 September 1996
5. C. Thiel, K. Fastenmeier: „Minimalinvasive Zerstörung großer Gewebevolumina mit Hochfrequenzstrom", Biomedizinische Technik, Band 41, Ergänzungsband 1, p. 498 -499, 1996
6. T. Stein, K. Desinger, A. Roggan, G. Müller: „Computer Simulation to model interstitial bipolar RF-coagulation", BiOS-Europe '97, SPIE-Press, Vol. 3139, San Remo; Italy, 1997
7. G. Müller, A. Roggan, „Laser-induced interstitial thermotherapy", SPIE Optical Engineering Press, Washington,1995
8. A. Roggan, „Dosimetrie thermischer Laseranwendungen in der Medizin", Dissertation, ecomed Verlag, Landsberg, 1997

SESSION 5

Image Guidance and Thermal Imaging

MR imaging guidance for minimally invasive procedures

Terence Z. Wong, Joachim Kettenbach, Stuart G. Silverman,
Richard B. Schwartz, Paul R. Morrison, Daniel F. Kacher, and Ferenc A. Jolesz

Department of Radiology, Brigham and Women's Hospital,
Harvard Medical School, Boston, MA 02115

ABSTRACT

Image guidance is one of the major challenges common to all minimally invasive procedures including biopsy, thermal ablation, endoscopy, and laparoscopy. This is essential for 1) identifying the target lesion, 2) planning the minimally invasive approach, and 3) monitoring the therapy as it progresses. MRI is an ideal imaging modality for this purpose, providing high soft tissue contrast and multiplanar imaging capability with no ionizing radiation. An interventional/surgical MRI suite has been developed at Brigham and Women's Hospital which provides multiplanar imaging guidance during surgery, biopsy, and thermal ablation procedures. The 0.5T MRI system (General Electric Signa SP) features open vertical access, allowing intraoperative imaging to be performed. An integrated navigational system permits near real-time control of imaging planes, and provides interactive guidance for positioning various diagnostic and therapeutic probes. MR imaging can also be used to monitor cryotherapy as well as high temperature thermal ablation procedures using RF, laser, microwave, or focused ultrasound.

Design features of the interventional MRI system will be discussed, and techniques will be described for interactive image acquisition and tracking of interventional instruments. Applications for interactive and near-real-time imaging will be presented as well as examples of specific procedures performed using MRI guidance.

Keywords: MRI, interventional, surgery, ablation, percutaneous, endoscopy, biopsy, laser, minimally invasice therapy

1. INTRODUCTION

Minimally invasive procedures may be divided into diagnostic and therapeutic applications. One major diagnostic procedure is biopsy using either fine needle aspiration or automated biopsy needles to obtain tissue cores. Cross sectional imaging modalities, including computed tomography (CT), ultrasound, and magnetic resonance imaging (MRI) permit tissue targeting, trajectory planning, and guidance during insertion of the biopsy device. Other advantages of image guidance include verification of the sample location and early recognition of complications, such as hematoma. State-of-the-art fluoro, ultrasound, ultrafast fluoro-CT scanners, and interventional MRI systems allow essentially real-time imaging during the biopsy procedure. MRI offers several significant advantages over the other imaging techniques. First, MRI produces excellent soft tissue contrast and in some cases may be the only imaging modality to demonstrate the abnormality. Some lesions may enhance on CT, but may become less conspicuous with time, making adequate targeting impossible. Second, MRI allows multiplanar imaging, and image plane selection may be interactively directed by the biopsy device. While ultrasound also permits real time and multiplanar imaging, it is limited by its inability to penetrate air-filled structures such as bowel or lung. MR images form a 3-dimensional data set which

SPIE Vol. 3249 • 0277-786X/98/$10.00

can be integrated with other imaging modalities, such as positron emission tomography (PET) or single photon emission tomography (SPECT). In addition, MRI sequences sensitive to activity or function are being developed. This can allow tissue targeting based on functional as well as anatomic information.

A logical extension of the percutaneous biopsy technique is insertion of a therapeutic probe into the target lesion using image guidance. Of the cross sectional imaging modalities, MRI is the most sensitive for monitoring the tissue changes resulting from minimally invasive therapies. While CT and ultrasound may detect necrosis and irreversible changes from thermal ablation, MRI is the only method which is sensitive enough to detect subtherapeutic thermal changes. This is an important advantage which can be utilized for treatment planning[1].

The second major category of minimally invasive diagnostic or therapeutic procedures is endoscopy. Imaging can be a powerful adjunct to endoscopic procedures and provides information on the position of the endoscope relative to surrounding tissues. MRI is the only modality which permits noninvasive tracking and image selection based on the position of the endoscope. Miniature RF coils[2] located on catheters, needles, endoscopes, or laparoscopes can be used to detect MR signal and establish spatial coordinates, permitting MRI localization of these devices within tissues (MR tracking).

2. INTERVENTIONAL MRI DESIGN

Several magnet configurations are currently used for MRI-guided procedures[2]. These include 1) modification of the conventional long bore configuration, 2) short bore design, 3) horizontal gap open-configuration, and 4) vertical gap open-configuration. These are summarized in Table 1.

TABLE 1: Possible MRI configurations for interventional imaging.

CONFIGURATION	FIELD	ACCESS	ADVANTAGES
Long bore (closed)	1 - 3 T	Poor	Highest image quality
Short bore (closed)	1 - 1.5 T	Fair	Fast gradients, cardiac/vascular applications
Horizontal open gap	0.02 - 0.6 T	Good	Maximum safety and instrument compatibility
Vertical open gap	0.5 T	Very Good	Intraoperative imaging, flexible positioning

While the conventional closed long-bore configuration will provide the highest image quality, it offers the least patient access. However, this design is compatible with certain minimally invasive procedures; interstitial radiofrequency (RF), laser, microwave, or cryo probes can be positioned (using ultrasound guidance, for example) prior to sliding the patient into the scanner, and subsequent high-field MR imaging can be used to monitor the thermal ablation therapy. Alternatively, the minimally invasive device, for example focused ultrasound, can be incorporated into the MRI scanner. The focused ultrasound technique may be the ultimate minimally invasive therapy, as energy is delivered through the body surface and focussed deeply, eliminating the need for insertion of any probe. The major disadvantage is the inability of ultrasound to penetrate gas-containing structures such as lung or bowel.

The closed short-bore configuration with flanged bore openings permits slightly improved patient access, and may be most useful for cardiac and vascular applications. Miniature endovascular coils mounted on catheters permits tracking of the catheters as they are positioned within the vessels. Their position can be superimposed on flow-sensitive MR images, creating a "roadmap" type of catheter localization[4]. In addition, endovascular coils enable imaging of the vessel walls for evaluation of plaque and response to intervention such as angioplasty.

The horizontal gap MRI design provides horizontal access to the patient, allowing most radiologic percutaneous procedures to be performed. The low field minimizes the need for shielding of equipment, but also potentially limits imaging capability. The overlying magnet structure precludes open surgical procedures while the patient is within the imaging field, but intraoperative imaging is possible by physically moving the patient into and out of the MRI system to obtain images.

A vertical gap mid-field strength MRI system was developed by General Electric (Signa SP, Milwaukee, WI) in collaboration with Brigham and Women's Hospital in 1993. This is the only design which permits true intraoperative MR imaging without moving the patient. The MRI system has been described in detail[5,6,7], and consists of two vertically oriented superconducting coils separated by a 56 cm gap, within which a 30 cm sphere of uniform static magnetic field is maintained for imaging. Flexible transmit/receive coils have been designed to be placed on the patient in close proximity to the imaging volume, while simultaneously allowing surgical and interventional access. The MRI system is maintained in an operating room environment, with adjacent clean and scrub areas, and the design of the intraoperative MRI interventional suite at Brigham and Women's Hospital has been reported in detail[8]. Anesthesia equipment, surgical instruments, patient monitors, and electrocautery devices were modified to be MRI compatible. Specialized devices such as a pneumatic neurosurgical drill or a MR-compatible microscope have also been developed[10].

The environment of the MRI system permits it to be used for both *interventional* and *intraoperative* applications[8]. Although open surgery is by definition not a minimally invasive procedure, image guidance can, by accurate targeting and presurgical planning, minimize the damage to healthy tissue and maximize removal of the abnormality; this minimizes the invasiveness of the surgical intervention. In the remainder of this paper, we will summarize our experience with MR imaging guided interventional and intraoperative procedures using the vertical gap 0.5T MRI system (Figure 1).

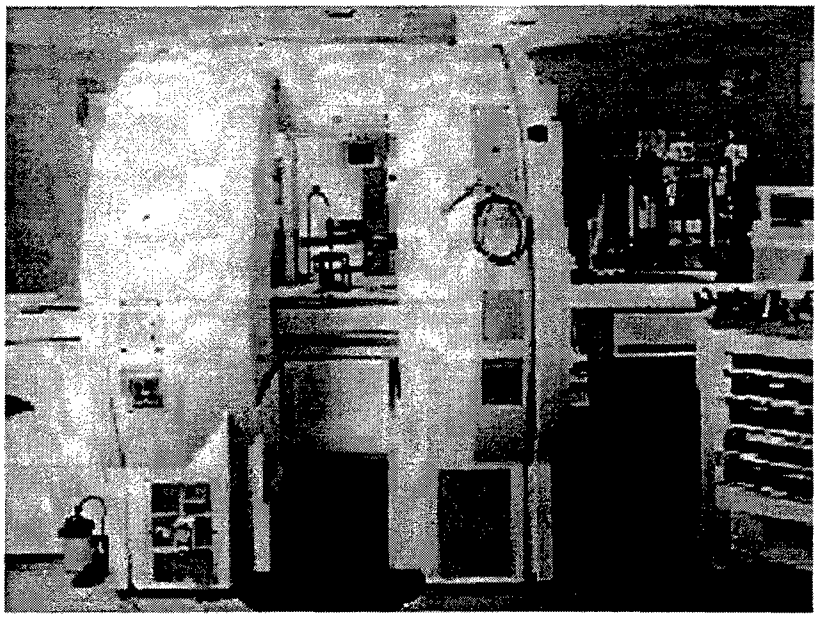

FIGURE 1: The GE Signa SP 0.5T MRI system is designed for both interventional and intraoperative procedures. Vertical access is provided on either side of the patient between two superconducting coils. LCD displays are mounted on both sides of the work area at eye level.

(Courtesy GE Medical Systems, Inc.)

3. CLINICAL EXPERIENCE AT BRIGHAM AND WOMEN'S HOSPITAL

At this time, the major clinical application of the interventional / intraoperative MRI system at Brigham and Women's Hospital is imaging guidance during open craniotomies[9]. To date, over 120 MRI-directed craniotomies have been performed. MRI-guided intracranial biopsies are the second most

common procedure[9]. In total, over 200 MRI-guided neurosurgical procedures have been performed. The expected benefits of improved biopsy targeting and tissue selection for resection are apparent during surgery[10], but the cost effectiveness of MRI guidance awaits further clinical experience. However, it should be noted that MR-guided, frameless streotactic biopsies significantly shortened the total procedure time[11].

Therapeutic interventions that have been performed on the open-configuration MRI system are summarized in Table 3. This includes eleven laser ablations: 7 in the liver, 3 in the brain, and 1 in the epipharynx. Endoscopic sinus surgery and transphenoidal pituitary resections have also been performed. MR imaging permits identification of structures deep to the surgical exposure[7,12,13]. In several of the transphenoidal cases, MR imaging identified additional tissue that was not visible through the endoscope[9].

TABLE 2: MRI-guided biopsies at Brigham and Women's Hospital (10/97).

Brain	70
Liver	32
Other abdomen/pelvis	29
Head and neck	16
Extremeties	8
Other sites	9
TOTAL	**164**

TABLE 3: MR image-guided therapeutic interventions at Brigham and Women's Hospital (10/97).

Drainage procedures	13
Laser ablation	11
Endoscopic sinus surgery	11
Transphenoidal pituitary resections	5
TOTAL	**40**

Abdominal/pelvic biopsies are performed in the MRI system in a manner similar to using CT or ultrasound guidance. Potential advantages or MRI include true three-plane imaging, the ability to visualize major vessels, and the lack of exposure to ionizing radiation. Some lesions are only visible on MRI, making this the guidance modality of choice. Nonetheless, many image-guided biopsy procedures in the abdomen or pelvis are just as easily done under ultrasound or CT image guidance, particularly with the advent of ultrafast CT units. Our experience with MRI-guided interventions involving the genitourinary system is described elsewhere[14].

4. INTERACTIVE IMAGING AND NAVIGATION

To provide interactive information to the interventional radiologist or surgeon, two color liquid crystal display (LCD) screens are mounted on the bore of the MRI unit at eye level. These can be used to display images directly from the MR scanner, or can show the near-real-time images to the interventionalist as they are acquired[8,14].

An optical tracking system (Flashpoint, Boulder, CO) is built into the MRI unit[2,8]. Interactive probes equipped with infrared light emitting diodes (LEDs) are attached to biopsy needles or other interventional instruments. The locations of the LEDs are tracked by a video system mounted in the bore of the magnet above the imaging volume, and the coordinates of the interventional device calculated for interactive prescription of MR imaging planes. For example, the user can select MR images to be obtained in the plane of the biopsy (or interventional) probe, or perpendicular to the probe axis. Depending on the MR imaging sequence selected, continuous scanning provides updated MR images every 2 to 20 seconds. Graphic annotation allows visualization of the "virtual needle" for trajectory planning. A "fast needle graphics" feature allows the user to make fine adjustments to the virtual needle trajectory which is displayed in real time between image acquisitions. These features facilitate the feedback loop between the interventionalist or surgeon and the MR imaging system.

Interactive MR imaging can be used in several ways for planning and performing interventional and surgical procedures. For *interactive imaging*, the interventionalist uses the interactive probes to navigate through the region of interest, in a manner similar to ultrasonography. This technique is particularly useful for establishing the relationship between surface landmarks and underlying structures, and planning the interventional or surgical approach. In the *targeting* mode, specific annotation is added to the acquired images, which enable the operator to view the needle path and tip. The trajectory and target can then be verified by imaging in three orthogonal planes. When the desired trajectory and target point has been established, the interventional probe can be advanced, and its progress observed on the MR images as they are acquired in near-real-time; this is termed the *tracking* mode, and confirms satisfactory positioning of the biopsy needle or therapeutic probe.

Figure 2 illustrates an example of an intracranial biopsy performed using interactive MRI guidance. In this case, the lesion is a small enhancing focus in the suprasellar region. Initially, a trajectory is selected prior to insertion of the biopsy needle by positioning the biopsy guide equipped with optical tracking. Needle annotation (representing a "virtual needle") with user-selectable lengths can then be displayed to target the lesion. Once the trajectory is established, the needle can be advanced and observed in near real-time. This is done in a step-wise manner as the needle approaches the target. In Figure 2 (a and b), the needle annotation is seen along with the signal void caused by the biopsy needle. The actual biopsy needle is seen to extend slightly beyond the "virtual" needle tip because the actual tissue sampling is from a side port is just proximal to the needle tip.

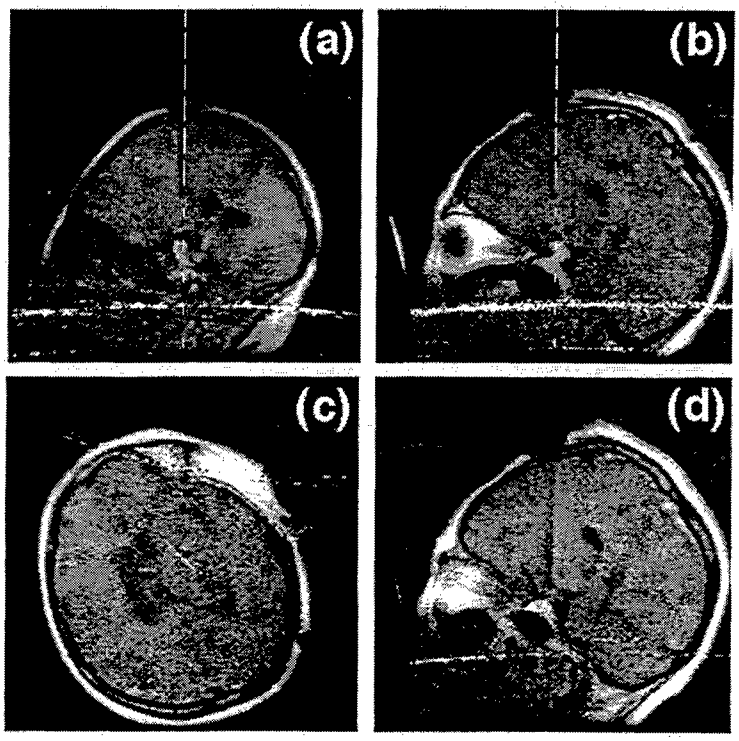

FIGURE 2: Example of MRI-guided biopsy of a deep suprasellar lesion. Near real time T1W images were obtained following intravenous gadolinium. Target is the small focus of suprasellar enhancement. Signal void from the biopsy needle is seen superimposed on the needle annotation in two planes (a,b). Target is confirmed in the plane perpendicular to the needle (c). Biopsy site is confirmed at time of sampling on parasagittal image with annotation removed (d).

In neurosurgical applications, MRI guidance has several advantages over conventional stereotactic biopsies. First, MRI is the most sensitive imaging technique for defining intracranial abnormalities, and may demonstrate the target lesion more clearly than CT. Second, the stereotactic frame and pre-procedure CT are unnecessary, saving time and eliminating the possible risks associated with iodinated contrast. Third, imaging during the procedure allows the location of the actual biopsy to be confirmed, which may reduce the number of repeat biopsies and indeterminate pathology results. Finally, any resulting complications (i.e. bleeding) can be detected early.

There are several potential advantages of MR imaging guidance during open craniotomies for resection of intracranial lesions. First, MRI can be used to plan the approach and degree of resection. The craniotomy site can be precisely positioned and minimized in size. Secondly, since the intracranial abnormalities are often clearly demonstrated by MRI, serial images permits the progress of the resection to be followed for accurate removal of the desired portions of the lesion. The completeness with which a lesion can be removed depends largely on its proximity to critical functional regions of the brain, such as motor, speech, or visual areas. Serial MR imaging allows these critical areas to be identified and avoided. Other coordinate-based imaging techniques for guiding craniotomies depend on presurgical imaging and cannot account for shifts in brain and lesion position which occur during the resection. In addition to anatomic guidance for neurosurgery, MRI can provide physiologic information, either through functional MRI (e.g. to identify speech areas). We have done a pilot study demonstrating the effectiveness of dynamic MR imaging in distinguishing tumor recurrence from prost-treatment necrosis in glioblastoma patients who have been previously irradiated[15]. These MR techniques can aid the neurosurgeon in further refining the target tissue to be biopsied or resected, and thus reduce the invasiveness of the intervention. Finally, as previously mentioned, MR imaging allows early diagnosis of any immediate intraoperative or post-operative complication, such as hemorrhage.

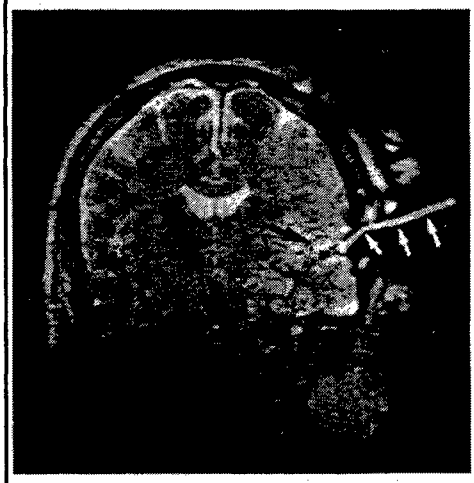

FIGURE 3: MRI guidance for craniotomy. This small vascular malformation (black arrow) is below the cortical surface and not visible to the surgeon. A saline-containing pointer has been inserted (white arrows).

Figure 3 illustrates MR guidance for resection of a small vascular malformation in a patient with seizures. Situated below the cortex, this lesion was not visible to the surgeon. A saline marker was used to mark a fissure and imaged. The precise position of the leison relative to the pointer could then be reported to the surgeon, who could then redirect the microscope to the appropriate location. Although not a minimally invasive procedure per se, MRI guidance allows surgical resection of lesions such as this with minimal damage to overlying normal tissue, and therefore minimizes invasiveness of the procedure.

5. THERMAL ABLATION

Ultimately, one of the most significant applications of interventional MRI and MR imaging guidance will be in thermal ablation of various neoplasms. MRI is clearly the modality of choice for these procedures, because it can be used both to guide placement of the ablation probes and monitor the thermal treatment. Techniques for creating thermal ablation lesions are discussed in detail elsewhere in these proceedings, and will therefore only be briefly mentioned. Thermal ablation methods include laser, radiofrequency (RF), ultrasound (US), and microwave energy. Temperatures above 56-60°C cause irreversible tissue damage, and the pathophysiology is similar regardless of the energy source.

Laser energy, delivered to tissue by optical fibers, has the advantage of small diameter and efficient energy delivery to the treatment site. Being non-metallic, the laser fibers are MRI compatible. The major disadvantage of lasers is the relatively limited penetration depth and therefore relatively small lesion size (Fig. 4).

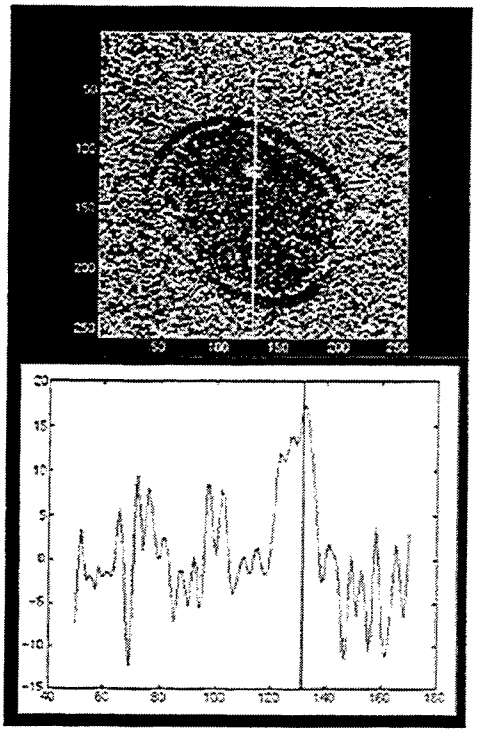

FIGURE 4: Chemical Shift-based imaging with phase mapping of a left parietal brain tumor (recurrent glioma). On the resultant phase image (upper window) thermal changes are highlighted within the tumor during laser therapy (single fiber, 3 Watt, 1 minute). Temperature gradients were then calculated along a line through the tumor, demonstrating a temperature elevation of more than 15 degrees Celsius above body temperature (lower window) within the tumor.

RF energy can be delivered simply through needles implanted in the target lesion. Large lesions can be created with this technique by implanting a tight array of needles, by cooling the needles, and by pulsing RF power[16,17]. One disadvantage of RF heating is the interference between the energy source and the MRI system, precluding imaging while the RF device is on, although some groups are addressing this problem. Microwave energy has the potential to penetrate deeper into tissues than either laser or RF methods, but small implantable antennas are much more complex to design, and this technique is not in common use a t this time.

Finally, one of the most promising techniques for thermal ablation, when combined with MR imaging, may be high intensity focused ultrasound (HIFU). A system has been incorporated into a standard 1.5T MRI system (GE Medical Systems, Milwaukee, WI) at Brigham and Women's Hospital[18,19]. An MRI compatible 1.5 Mhz ultrasound transducer is coupled to the body surface by a water bath and focused to a deep tissue target. The focal spot is controlled by computer based on MR imaging, and permits irregular volumes to be precisely treated. It has been shown that MRI can readily detect temperature changes of 7-8°C, therefore detecting temperature elevations below the threshold for causing irreversible tissue damage[19,20]. This permits a low power sonication to be used to verify the treatment focus prior to increasing the ultrasound power to ablate the tissue. A precise spatial control of the tissue ablation beyond what is possible with interstitial methods is achieved (Fig.5).
In addition, this technique requires no needle insertions and is therefore the least invasive of the minimally invasive therapies. The major disadvantages with the technique are 1) inablility of ultrasound to penetrate gas or bone, 2) small treatment volume (focus is only several millimeters in size) of each focused ablation, making treatment times longer than for other methods, and 3) patient motion is more problematic, since probes are not physically positioned within the target lesion.

FIGURE 5: Focused ultrasound of a fibroadenoma in the breast; The enhancing tumor on a T1 weighted image, just before the treatment (left). A week later no tumor was seen an a follow-up (right).

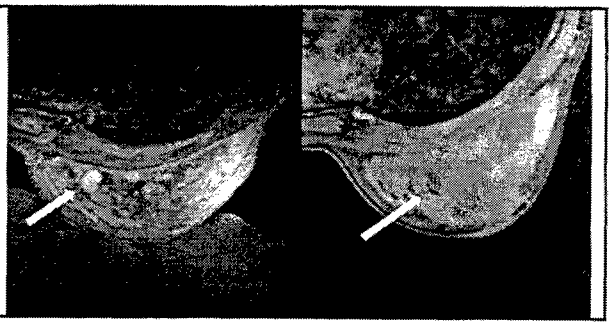

Several MR techniques are available for determining temperature changes from thermal ablation procedures. Molecular diffusion methods can be used, but are sensitive to patient motion, making this technique less desirable[19]. Small temperature-dependent shifts in proton resonant frequency can be evaluated with fast spoiled gradient echo sequences[20,21,22]. Using this technique, Hynynen et al.[1] found the temperature coefficient for the frequency shift to be 0.011 ppm/°C in rabbit brain. This allows temperature changes to be related to phase changes observed on the gradient echo images. Using this technique, temperature elevations below the threshold for tissue damage can be detected for localization and verification of the ultrasonic focus prior to therapeutic sonication. Irreversible tissue damage caused by temperatures exceeding 60°C are evident on T1W and T2W conventional spin-echo images[23].

6. CONCLUSION

The addition of MR imaging guidance can greatly enhance the abilities of current minimally invasive procedures by providing information about the relationship of the interventional device to the target lesion and the surrounding anatomic structures. The major advantages of MRI over other cross-sectional imaging modalities is the high tissue contrast, multiplanar imaging capability, and sensitivity to parameters such as temperature, which allow monitoring of therapeutic interventions during the treatment. The major disadvantages of MRI-guided interventions include the high cost of the imaging system and the high magnetic field environment which complicates design of interventional devices and associated electronic equipment. Access to the patient for interventional procedures is a problem that has been solved to a large extent, but at this time no MRI system exists which combines the advantages of high field strength and open patient access. Interactive MR imaging is made available by navigational devices which control the plane of image acquisition and permit direct visual feedback to the interventionalist or surgeon. This allows near real-time control during the interventional procedure.

In spite of its relatively high cost, MRI is unique in its abilities to detect subtle abnormalites and to actively monitor minimally invasive therapies, such as thermal ablations. Providing that the thermal ablation apparatus is MRI compatible, MRI monitoring can be applied to any thermal ablation modality (laser, RF, ultrasound, or microwave energy). The development of faster and more sensitive imaging sequences, along with functional MR imaging will only further enhance the utility of MRI-assisted interventions and surgery.

7. ACKNOWLEDGMENTS

Neurosurgeons involved with the intraoperative MRI project include Peter Black, MD, PhD, Eben Alexander III, M.D., Philip Steig, M.D., and Claudia Martin, M.D. The authors wish to thank Ray Kelley for technical assistance, and MRI technologists Holly Isbister, Sharon Spaulding, and Cheryl Cahill. This work was supported in part by grants from the National Institutes of Health, National Science Foundation, and GE Medical Systems.

8. REFERENCES

1. K. Hynynen, N. I. Vykhodtseva, A. H. Chung, et. al., "Thermal effects of focused ultrasound on the brain: determination with MR imaging", *Radiology* **204**, pp. 247-253, 1997.
2. K. D. Hagspiel, K. Kandarpa, and F. A. Jolesz, "Interventional MR imaging", *JVIR* **8**, pp. 745-758, 1997.
3. D. A. Leung, J. F. Debatin, S. Wildermuth, et. al., "Real-time biplanar needle tracking for interventional MR imaging procedures", *Radiology* **197**, pp. 485-488, 1995.

4. D. A. Leung, J. F. Debatin, S. Wildermuth, et. al., "Intravascular MR tracking catheter: preliminary experimental evaluation", *AJR* **164**, pp. 1265-1270, 1995.
5. F.A. Jolesz, F. Shtern, "The operating room of the future: report of the National Cancer Institute workshop, image-guided stereotactic tumor diagnosis and treatment", *Invest Radiol* 27, pp. 326-328, 1992.
6. F. J. Schenck, F. A. Jolesz, P. B. Roemer, et al., "Superconducting open-configuration MR imaging system for image-guided therapy", *Radiology* **195**, pp. 805-814, 1995.
7. F. A. Jolesz, "Image-guided procedures and the operating room of the future", *Radiology* **204**, pp. 601-612, 1997.
8. S. G. Silverman, F. A. Jolesz, R. W. Newman et al., "Design and implementation of an interventional MR imaging suite", *Am. J. Roentgenol.* **168**, pp. 1465-1471, 1997.
9. R. B. Schwartz, L. Hsu, J. Kettenbach, et. al., "Recent experience with intraoperative MR imaging in intracranial procedures", (Abstr.), *Radiology* **205(P)**, pp. 403-404, 1997.
10. P. Black, T. Moriarty, E. Alexander, et al., "Development and implementation of intraoperative magnetic resonance imaging and its neurosurgical applications", *Neurosurgery* **41**, pp. 831-845, 1997.
11. L. Hsu, R. B. Schwartz, T. M. Moriarty, "MRI-guided neuro-interventions", *Proc. of 4th ISMRM*, pp.55, 1996.
12. L. Hsu, F. A. Jolesz, and M. P. Fried, "Interactive MR-guided sinus endoscopy" (abstr.), *Radiology* **197(P)**, p. 237, 1995.
13. M. P. Fried, F. A. Jolesz, and P. R. Morrison, "Image guidance with laser applications", *Otolaryngol. Clin. North Am.* **29**, pp. 1063-1078, 1996.
14. T. Z. Wong, S. G. Silverman, J. R. Fielding, et al., "Open-configuration MR imaging, intervention, and surgery of the urinary tract", *Urol. Clins. North Am.*, in press, 1998.
15. R. B. Schwartz, L. Hsu, S. Okon, et. al., "Intraoperative dynamic MR imaging: localization of sites of brain tumor recurrence after high-dose radiotherapy", *J. Magn. Reson.*, in press.
16. S. N. Goldberg, G. S. Gazelle, L. Solbiati, et. al., "Radiofrequency tissue ablation: increased lesion diameter with a perfusion electrode", *Acad. Radiol.* **3**, pp. 636-644, 1996.
17. S. N. Goldberg, L. Solbiati, P. R. Mueller, et. al., "Radiofrequency ablation: larger volume tissue necrosis using a pulsed, high current technique" (Abstr.), *Radiology* **205(P)**, p. 258, 1997.
18. H. E. Cline, K. Hynynen, R. D. Watkins, et al., "A focused ultrasound system for MRI guided ablation", *Radiology* **194**, pp. 731-737, 1995.
19. K. Hynynen, W. R. Freund, H. E. Cline, et. al., "A clinical, noninvasive, MR imaging-monitored ultrasound surgery method", *Radiographics* **16**, pp. 185-195, 1996.
20. H. E. Cline, K. Hynynen, C. J. Hardy, et al., "MR temperature mapping of focused ultrasound surgery. *Magn. Reson. Med.* **31**, pp. 628-636, 1994.
21. J. Kettenbach, S.G. Silverman, N. Hata, K. Kuroda, P. Saiviroonporn, G.P. Zientara et al, "Monitoring and visualization techniques for MR-guided laser abaltion", *JMRI*, in press, 1998.
22. A. Chung, K. Hynynen, H. E. Cline, et. al., "Optimization of spoiled gradient-echo phase imaging for in vivo localization of focused ultrasound beam", *Magn. Reson. Med.* **36**, pp. 745-752, 1996.
23. F. A. Jolesz, A. R. Bleier, P. Jakab, et. al., "MR imaging of laser-tissue interactions", *Radiology* **168**, pp. 249-253, 1988.

Towards a Clinical Implementation of a Non-Invasive Microwave Imaging System for Temperature Monitoring

Paul M. Meaney*, Keith D. Paulsen*+, John T. Chang*, Margaret Fanning*

* Thayer School of Engineering, Dartmouth College, Hanover, NH 03755
+ Norris Cotton Cancer Center, Lebanon, NH 03756

ABSTRACT

A laboratory scale multi-illumination microwave imaging system has been successfully demonstrated for the reconstruction of biologically relevant materials and has also been shown to be sensitive to thermally induced electrical property changes. Several challenges are currently being addressed in an effort to bring the system to the clinic for use in non-invasive thermometry. These include: (1) increasing the size of the imaging region, (2) reducing image artifacts due to the presence of multiple antennas during illumination, and (3) developing a solid illumination chamber to replace the saline bath tank. The first two are intimately related. As the imaging system size is increased to clinically useful dimensions, we must inevitably reduce the lossiness of the surrounding medium which will subsequently increase the antenna-antenna interactions. This is being addressed both in terms of the design of the individual antennas and in terms of introducing compensating techniques into the numerical model. Investigating these areas will provide insight into the ultimate capability of this imaging modality. Additionally, a solid material is being developed with electrical properties close to that of saline. Working in such a lossy medium has significant advantages in terms of the antenna performance and the reduction of unwanted multi-path signals propagating into and out of the desired imaging plane. With these tasks completed, quantification of the system's ability to recover electrical property distributions and thermal profiles based on difference imaging techniques will be investigated for both phantom and *in vitro* experiments.

Keywords: microwave, imaging, iterative, reconstruction, multi-illumination, electrical properties, temperature monitoring

1. INTRODUCTION

During the past six years we have been developing a 2D multi-illumination microwave imaging system for biomedical applications.[1,2,3,4,5] This work was started with a thorough analysis using numerical simulations which led to the choice of a hybrid scheme of the finite and boundary element methods for our forward computation models and a Newton-Raphson iterative technique for image reconstruction.[1,2] Initial phantom experiments were performed utilizing a manually moveable single transmitter and receiver data acquisition system which was eventually upgraded to a fixed 16 channel system with each antenna electronically selectable for either transmit or receive.[3,4]

Several important discoveries have been made at the various stages of development which have significantly impacted our subsequent upgrades. Primarily, we determined that performing the experiments in a lossy saline bath was beneficial for several reasons.[3] First, it dramatically improved the impedance match of the various antennas we employed over a broad bandwidth and reduced any surface currents that might have been excited. Second, it attenuated the signals

* Further Author Information -
P.M.M.(correspondence): Email: paul.meaney@dartmouth.edu; Telephone: 603-646-3939; FAX: 603-646-3856

propagating out of the imaging plane to such an extent that when they were reflected back into the plane by some object, their resultant contribution was negligible. The downside to using this lossy medium has been the reduction in desired signal strength and the subsequent limitations on the size of our imaging region. Until now, we have performed most of the experiments using a 14 cm diameter imaging area.[3,4,5] Obviously the goal is to increase this, and while we do not show such results here, we are presently constructing a 28 cm diameter array with 32 antennas. The results presented here represent the necessary studies required before its implementation.

Additionally, as we increase the size of the imaging area, we are also concerned with maintaining and possibly improving both the spatial and contrast resolutions. With the type of image reconstruction employed here, the number of points at which the electrical properties can be recovered is proportional to the amount of observation data. This led to the choice of the monopole antenna design employed in a TM illumination mode because we could physically configure many of these close together while also being relatively close to the target region. Using these does have drawbacks such as zero directivity which reduces the signal propagation distance even further. An important advantage to its use in terms of our 2D model is that they could be considered point sources. We have demonstrated excellent agreement between field measurements and the computed values.[5]

However, there is a limit as to how close we can pack the antennas before seeing adverse effects in our system. We have been able to observe significant field perturbations between the case where only one transmitter and one receiver are present to the case where the full array is present for a range of operating frequencies and varying saline levels. We will show results where we are working to represent these effects in the forward model along with hardware approaches for reducing the effects in the reconstruction algorithm. We will show that these issues are being considered thoroughly as we go to the larger target regions.

The last major challenge as we proceed towards a clinical implementation is the construction of a solid illumination chamber to replace the saline bath. While saline is ideal in terms of its high dielectric constant for matching to human tissue and its easily adjustable attenuation coefficient via manipulation of the salt concentration, it would be difficult to use in a clinical situation. We have been working to develop a solid material with roughly the same electrical properties as saline to use in a solid illumination chamber. At present we have produced a preliminary chamber made from carbon loaded polyethylmethacrylate (PEMA) that demonstrates the desirable properties for the frequencies of interest.

Finally, with the ultimate goal of this system to be able to monitor temperature distributions, we show phantom results demonstrating the ability to monitor temperature distributions along with images for the case of a perfused kidney with saline heated to different temperatures.[6]

2. RECENT EFFORTS

A. Increased Imaging Region Size

As mentioned in the introduction, one of our primary goals is to increase the overall size of our imaging region to something that is useful in a clinical setting. Before committing to the costly and time-consuming task of building a larger system with a solid illumination chamber, we felt it was imperative to study various problems that might occur in our saline-based configuration. Figure 1 is a photograph of the upgraded, 32 channel microwave switching matrix and Figure 2 is the new antenna array mounting configuration with a 28 cm diameter imaging region. Some of the more fundamental issues which will be studied in this latest upgrade will be: *1) 32 channel switching matrix compared with the old 16 channel system* - In order to maintain comparable spatial and contrast resolution as we increase the size of the imaging region, the amount of measurement data must be increased. One way to do this is simply to increase the number of radiating/receiving antennas in the array which we have allowed for here. *2) Allowing for nominal manual array rotation to*

increase the amount of measurement data - A second way to increase the amount of measurement data is to rotate the entire array slightly to increase the number of illumination and receiver positions. This is attractive for a number of reasons. First it reduces the overall number of data acquisition channels and antennas, thus reducing the cost of electronic components. Second, as will be discussed in **Section B**, the closer the antennas are packed together, the more the switched OFF antennas will perturb the transmitted signal. Therefore, there is a premium on keeping the number of antennas in the array down. One potentially detrimental effect of the mechanical motion to the overall system is that the flexible cables attached to the antennas may change their phase and amplitude characteristics during rotation. Special cables have been purchased along with making significant modifications to the antenna mounting fixture for this purpose while modifications to the calibration procedure may also be required to account for these effects. *3) Reduced saline concentration* - As the imaging region is increased, the distance that the microwave signals must travel between transmitter and receiver also increases. Because this transmission distance is generally proportional to the lossiness of the medium, we will inevitably have to reduce the lossiness by decreasing the saline concentration. This will have two potential adverse effects. First, it will most likely increase the antenna-antenna interaction alluded to above. Secondly, it will reduce the amount that possible surface waves on the antennas are attenuated. The current monopole antenna design generally excites considerable surface waves in a low loss environment. While these antennas are easily constructed and modeled, their use is limited because of the high level of surface wave activity. We have been able to deal with this effectively by operating in a high loss medium. As we move from a high loss medium to a lower loss situation, we will have to verify that the operation of these antennas is still acceptable.

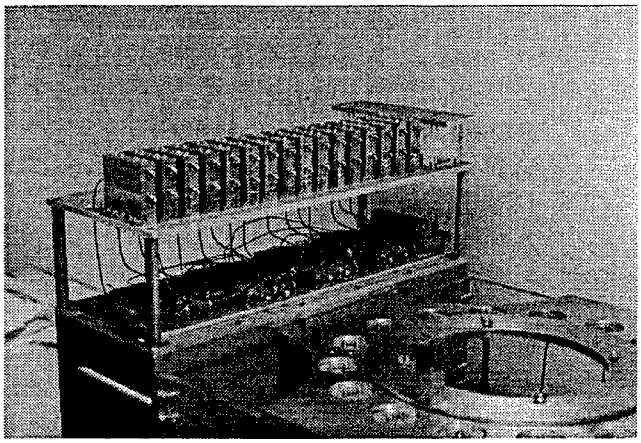

Figure 1. 32 channel microwave switching matrix.

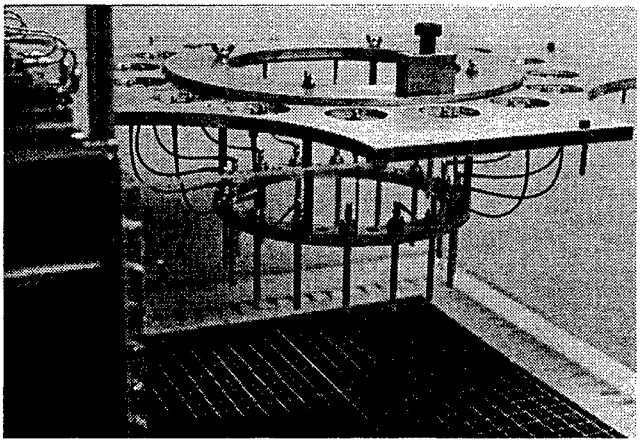

Figure 2. Antenna array mounting configuration - 28 cm imaging region.

B. Full Array Issues and Workarounds

1) Background Saline Concentration and Array Element Number Effects on the Current System:

Previous efforts showed excellent results in reconstructing images for a 16 channel system, with a 14 cm diameter imaging region operating in a 0.9% saline solution as the background medium. Figure 3a shows the reconstructed image for three targets in the region: a 4.4 cm diameter plexiglas® cylinder filled with a 0.3% saline-agar gel, and a 4.3 and a 2.5 cm diameter bone/fat equivalent phantoms (The exact desired image is shown in Figure 3b). These show good spatial resolution of the objects and generally good contrast resolution for the larger diameter objects. It is also interesting to note that the system is also capable of discerning the presence of the 0.3 cm thick plexiglas® ring. As a precursor to the studies that will be undertaken with the new prototype system, we studied how the imaging capability would be affected by reducing the saline concentration and then by simulating the array rotation concept with less antennas by rotating the phantom during the data acquisition. In the 16 fixed antenna array configuration, for each transmitter the opposing nine antennas are used as receivers yielding a total of 144 (16 x 9) pieces of measurement data. In the 8 rotating antenna array configuration, for each transmitter the opposing five antennas are used as receivers for the four rotation positions yielding a total of 160 (8 x 5 x 4)

pieces of measurement data. Figure 4 illustrates the results achieved using the two configurations for two bone/fat equivalent phantoms (4.3 cm and 2.5 cm diameters) spaced 0.25 cm apart and the 0.9 and 0.6% saline backgrounds. Note that the case for the fixed array in the 0.6% saline background did not converge and is not shown. It is clear that while the algorithm did converge for both the fixed and rotation array configurations in the 0.9% saline background, the image for the rotation case is better in terms of smoothness of the background and the definition of the objects. In comparing the rotation antenna array in the two background saline concentrations, it is again clear that the image is better for the higher concentration medium. This illustrates that the issues of array element number and background medium concentration will be significant in the development of the larger system.

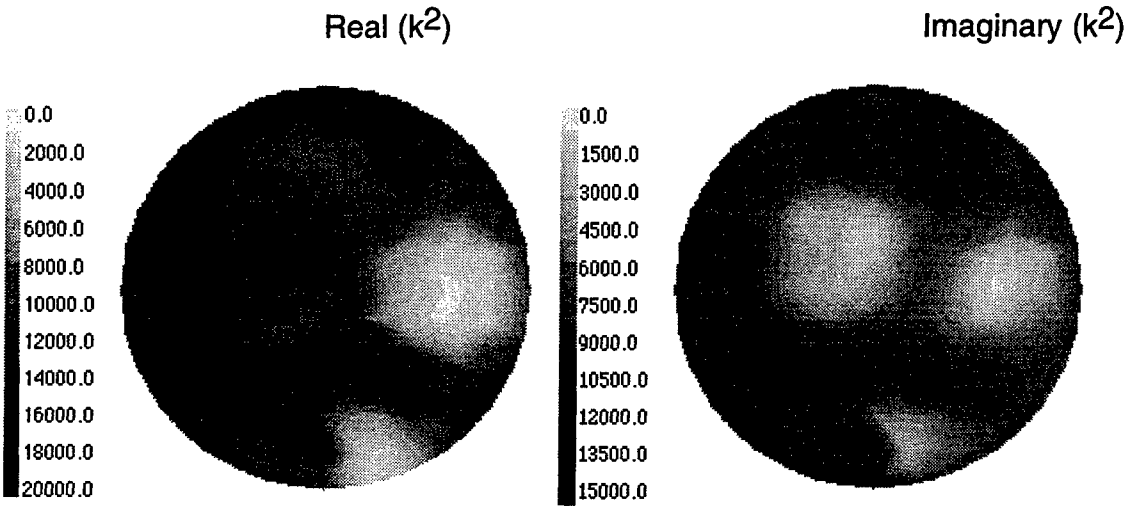

Figure 3. a) Real and imaginary components of a reconstructed image for the target region containing 1) a 3.8 cm diameter plexiglas® cylinder filled with a 0.3% saline-agar gel, and 2) 2.5 and 3.8 cm diameter bone/fat equivalent cylinders within a 0.9% saline background. b) Exact representation of the image expected with the three objects described in (a).

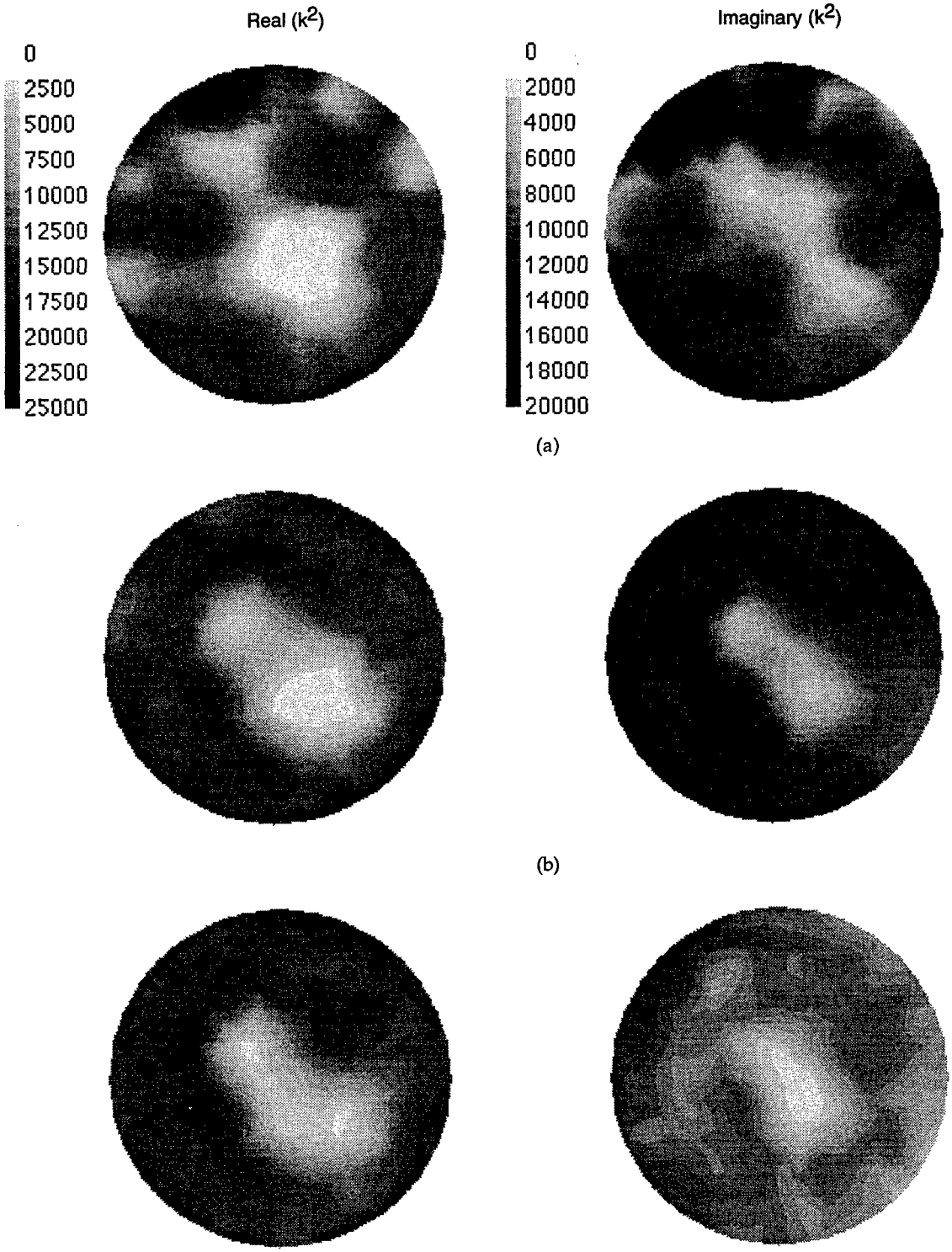

Figure 4. a) Real and imaginary components of a reconstructed image for the target region containing a 2.5 and a 3.8 cm diameter bone/fat equivalent cylinders separated by 0.25 cm within a 0.9% saline background medium utilizing the 16 fixed antenna array at 700 MHz. b) Image for the for the same case as (a) except for using the 8 rotating antenna array configuration. c) Image for the same case as (b) except for a 0.6% background medium.

2) Numerical Model Simulations for Incorporating the Presence of Extra Antennas

An alternative approach which is being investigated is the incorporation of the presence of the extra antennas into the forward solution of the numerical model. In general, our philosophy to this system development has been that the best possible images will be produced when we have achieved the best match between the forward solution model and the measurement configuration. For the case of the extra antennas present while transmitting from one antenna and receiving with another, we will treat each as very small but finite circle within the boundary element model domain with appropriate boundary conditions. The choice of the boundary conditions at this point is non-trivial and has considerable impact on the hardware design. Treating these antennas as simple wires is inappropriate in that after the signal has been coupled to the wire, it is not immediately re-radiated out into the medium[7]. Because the antennas are well matched over our operating bandwidth (greater than 15 dB return loss from 300 to 900 MHz), much of the signal will propagate up the coaxial cables to the first significant discontinuity and reflect back towards the antenna for re-radiation. With the unknowns in the exact cable lengths for each antenna and the exact impedance match of the OFF switches, replicating this condition within the numerical model would be difficult. We chose instead to use a radiation boundary condition for each of the extra antennas while empirically determining their numerical impedance condition. Critical to this was the incorporation of "matched" single-pole, single-throw (SPST) switches as the last component within the microwave switching matrix to guarantee an impedance match of 15 dB or better over the working bandwidth. For the most part, any signal coupled to the extra antennas will travel up the cable with a minimum being re-radiated out into the medium. Generally this is what is implied when implementing a radiation boundary condition.

Figure 5 illustrates the measured and numerically generated amplitude and phase perturbations while propagating a signal from one antenna to another in a homogeneous medium when changing from the condition of no extra antennas present to the case where the entire antenna array is present. The radius and impedance condition for the extra antennas at each frequency were determined empirically by finding the best least squares fit of the computed values to both the amplitude and phase differences of the measured perturbation data. In general the agreement between the measured and computed quantities is quite good especially considering that the overall magnitudes of the amplitude and phase differences were quite small. The resultant antenna radii and impedance values generally followed a well behaved pattern suggesting that we had not chanced on some unwanted local-minimal condition for the given frequencies. Work is still being done to incorporate these results into the reconstruction algorithm.

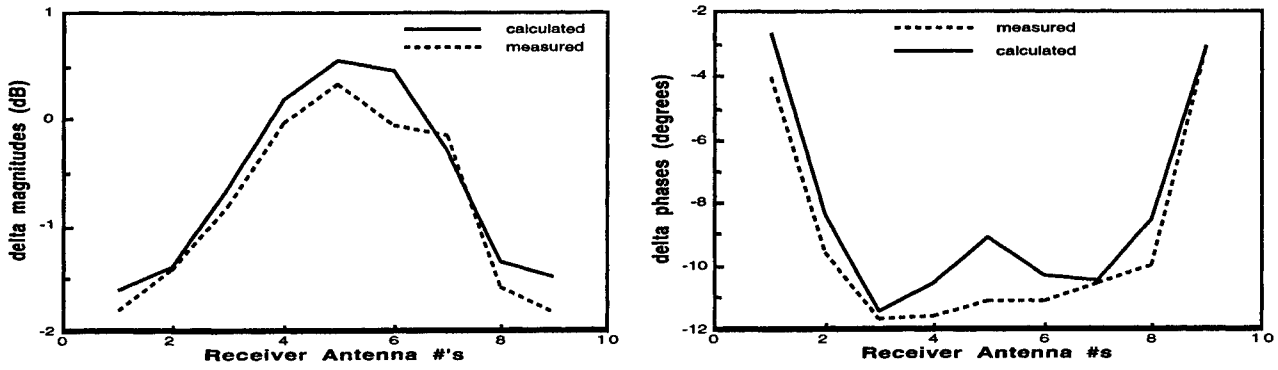

300 MHz

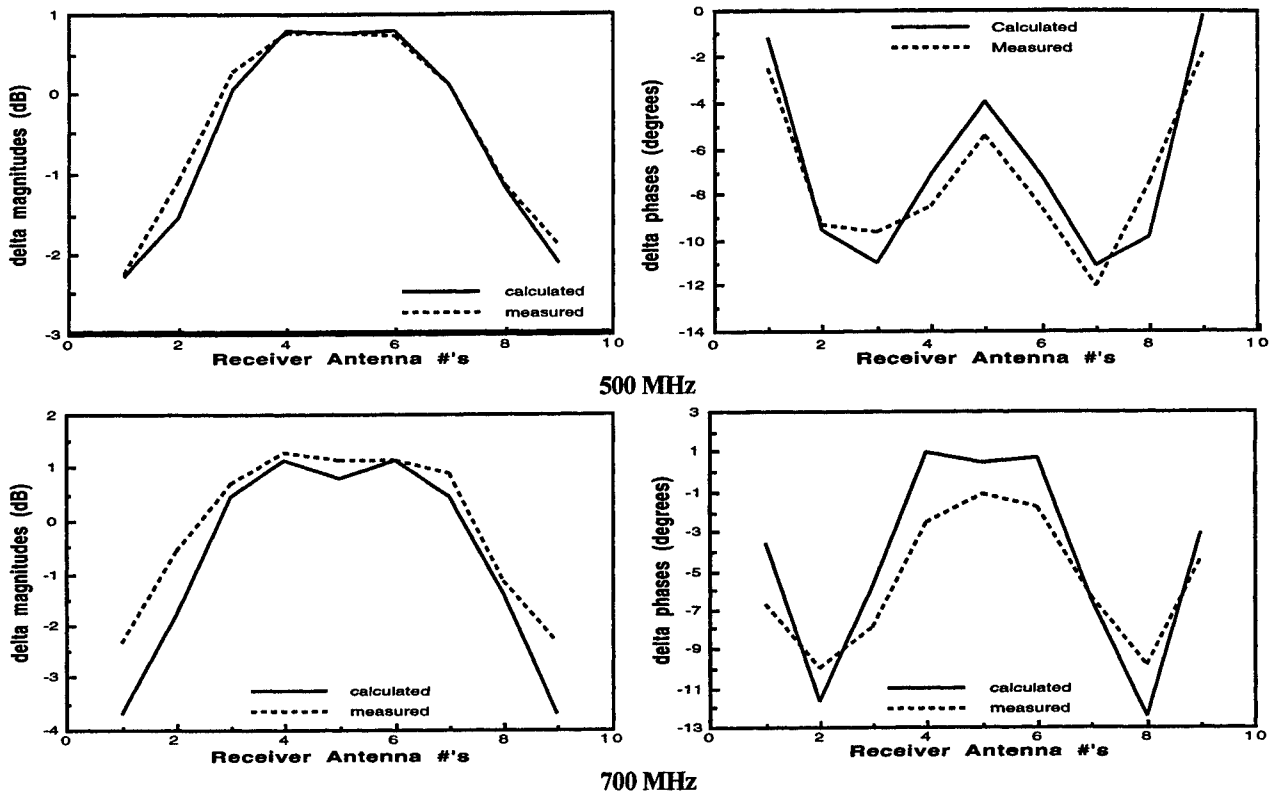

Figure 5. Calculated and measured amplitude and phase perturbation values while propagating from a single transmit to a single receive antenna in a 0.9% homogeneous saline medium between no extra antennas present and the entire array present. (a) 300 MHz, (b) 500 MHz, (c) 700 MHz.

C. Solid Illumination Chamber

Figure 6 shows a photograph of a solid illumination chamber having an inner bore diameter of 11.0 cm with an array of 16 monopole antennas embedded in it. The solid is constructed from PEMA loaded with finely ground carbon powder. For this sample the electrical properties were $\varepsilon_r \approx 40$ and $\sigma \approx 2.4$ at 500 MHz. While not exactly the values of our saline bath it demonstrates the ability to manufacture high dielectric/high loss materials and is more than adequate in terms of electrically matching to biological tissue while maintaining a high attenuation coefficient. Issues such as achieving intimate contact between the antennas and the solid have been addressed and imaging experiments are currently being performed.

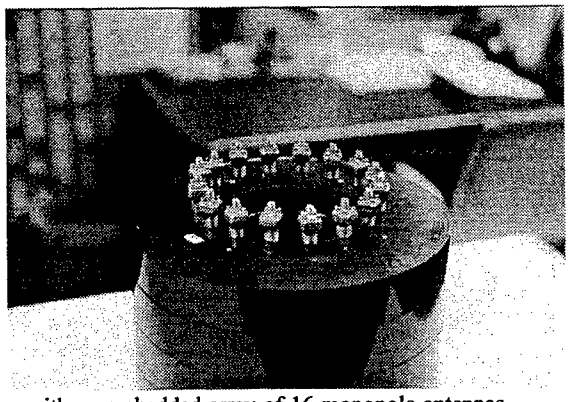

Figure 6. A solid illumination chamber with an embedded array of 16 monopole antennas.

D. Thermal Imaging Results

Figures 7 and 8 demonstrate the results of initial phantom imaging experiments. For this case, the background medium was 0.9% saline in which there were two objects: (a) a 4.3 cm diameter bone/fat equivalent cylinder, and (b) a 6.0 cm diameter carbon loaded PEMA cylinder with 0.9% saline flowing through it. The carbon shell had a relative dielectric constant of 40 and conductivity of 2.4 s/m at 500 MHz (the electrical properties for the 0.9% saline at 20°C were $\varepsilon_r = 76$ and $\sigma = 1.8$ s/m). For these tests the temperature of the flowing saline was set to various levels to ±0.1°C accuracy. Figure 7 shows the static image achieved at 500 MHz when the temperature of the saline in the cylinder was the same as that of the background. The image is interesting in that it does recover all of the relevant objects including the shell. In the real part of the image there is some blurring of the bone/fat cylinder and the carbon-loaded shell due to the relatively small separation of 2.1 cm. This ability to image the material properties of objects within a high contrast shell has been demonstrated in earlier work and has many potential applications. As the temperature was varied for the subsequent reconstructed images, the only thing that should change is the electrical properties of the flowing saline (For this case, the change with temperature for the real part of k^2 is minimal with respect to the imaginary part and is not shown). Figure 8 shows the sequence of difference images for the imaginary part of k^2 (the 20°C image was used as the baseline). For the most part, the backgrounds of the images are quite uniform except for the center of the cylinder which shows a progressive increase in conductivity with increased temperature. These images illustrate the system's ability to monitor the temperature dependent electrical properties while still recovering good images of high contrast, complex phantoms.

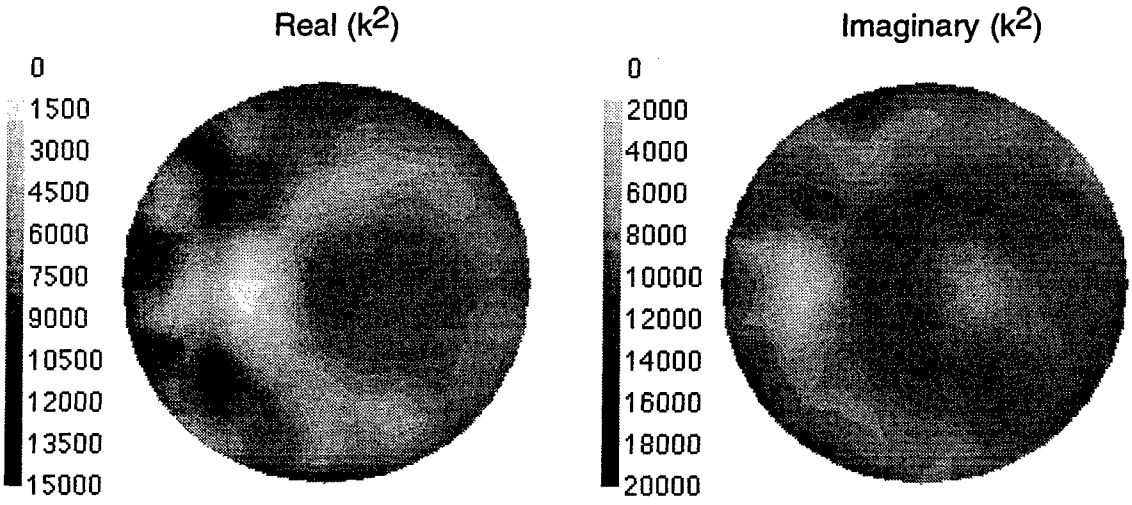

Figure 7. The real and imaginary parts of the k^2 images recovered for a bone/fat cylinder and a carbon loaded PEMA cylinder with 0.9% saline inside.

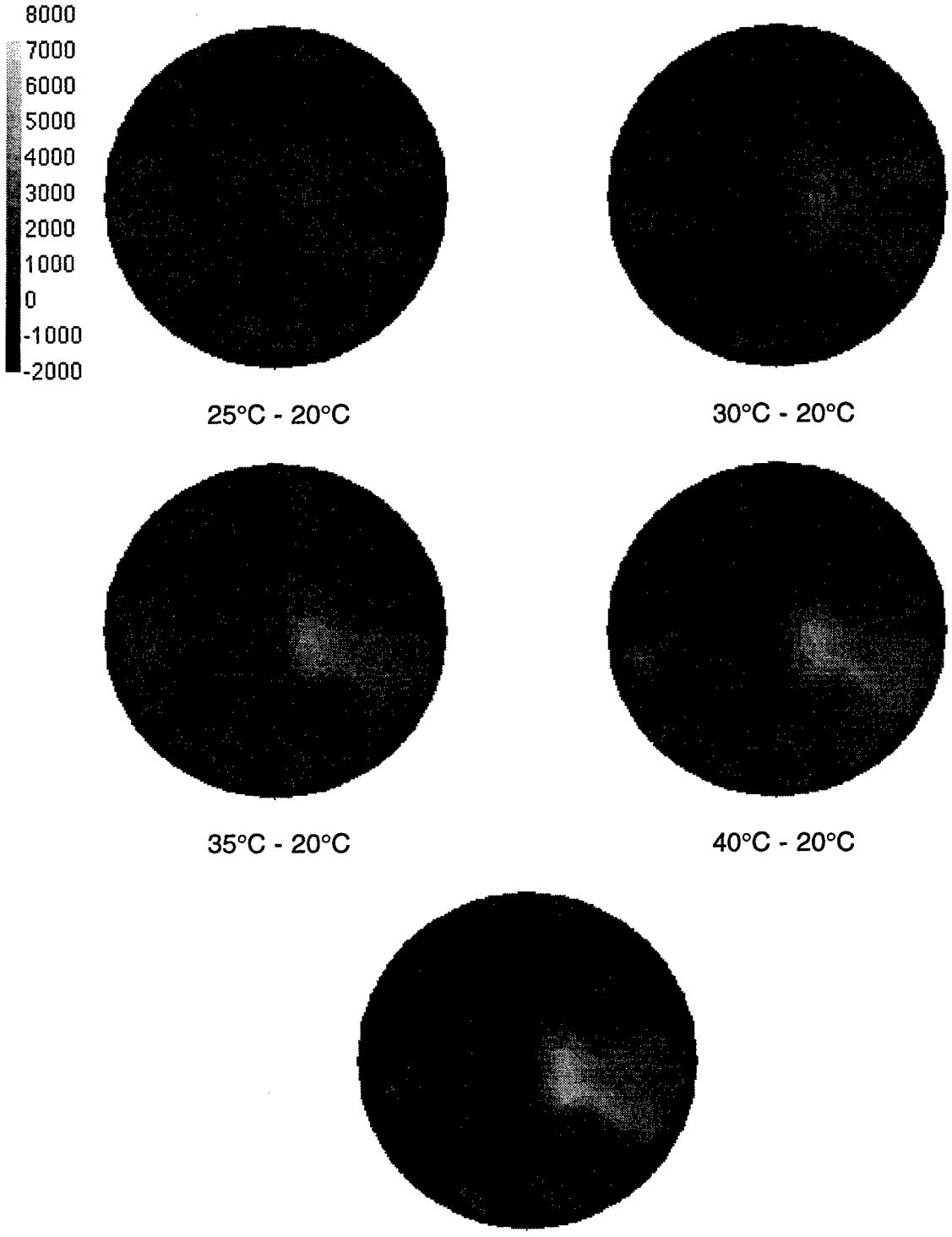

Figure 8. Difference images of the imaginary parts of k^2 for exactly the same situation as shown in Figure 7 except that the pumped saline temperature is varied up to 45°C.

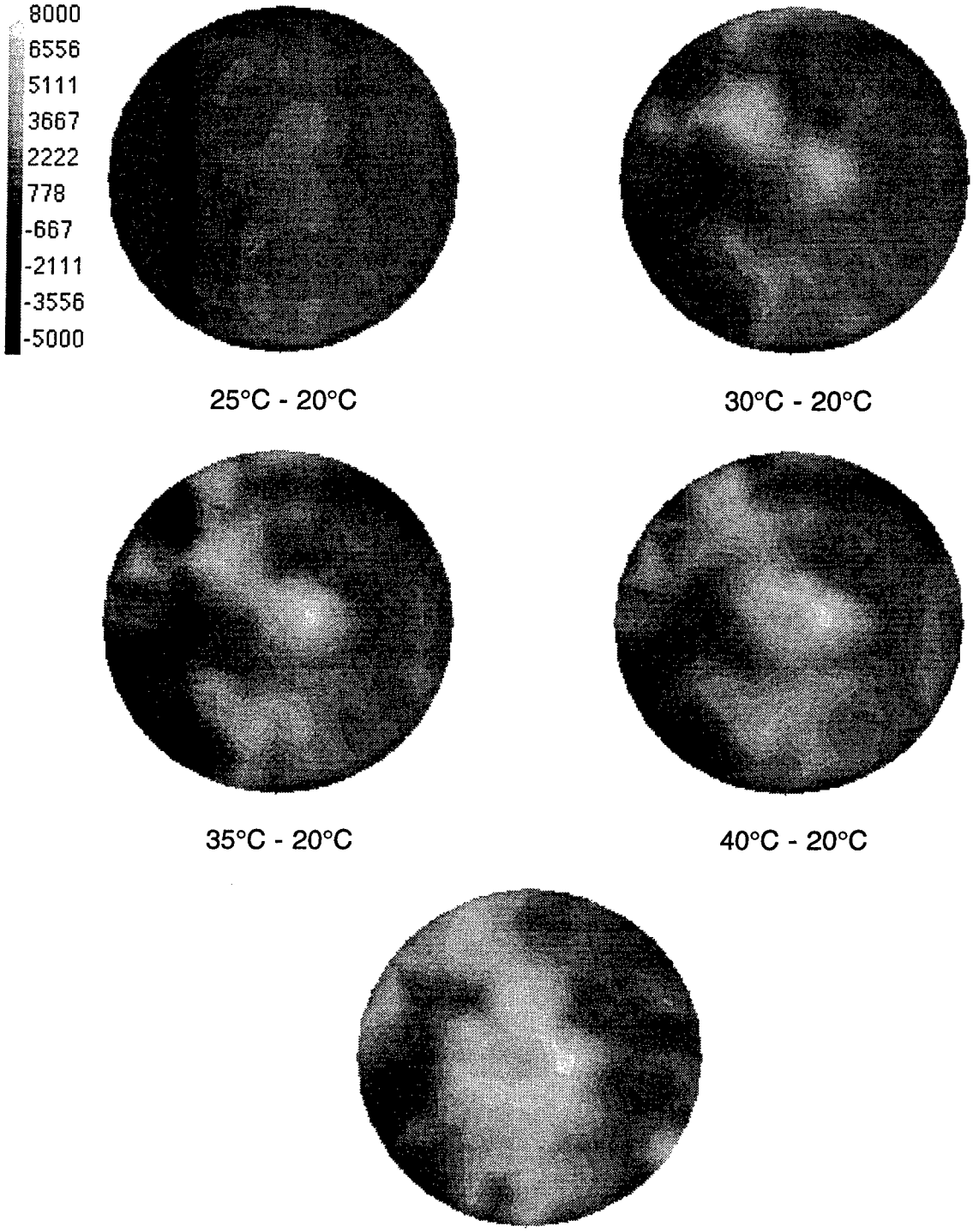

Figure 9. Difference images performed at 900 MHz of the imaginary parts of k^2 for the case of an excised kidney that is being perfused with a 0.9% saline solution, varying in temperature from 20°C to 45°C (the 20°C image is used as the baseline).

Finally, Figure 9 shows difference images of the imaginary part of k^2 performed at 900 MHz for an excised kidney which is being perfused with temperature varying, 0.9% saline solution (Here, again, the variations in the real part were insignificant with respect to the imaginary part and are not shown). These images illustrate a couple of interesting features. First, the 25°C-20°C image shows very minor heating; however, the area that is heated more or less shows the outline of the kidney (It should be noted that the kidney is positioned more or less vertically with respect to the imaging regions shown and that the heated saline solution enters and leaves from the center of the right side). The following three images clearly show two hot spots that may correspond to where the predominant flow is in the kidney. As the temperature reaches the maximum for these experiments, it appears that the bulk of the center of the kidney is heated to a high temperature and diminishes towards the periphery.

3. ACKNOWLEDGMENTS

This effort was supported by an NIH/NCI grant, # RO1 CA55034-05.

4. REFERENCES

1. P. M. Meaney, K. D. Paulsen, T. P. Ryan, "Two-dimensional hybrid element image reconstruction for TM illumination", *IEEE Trans. Ant. and Prop.*, **43**, pp. 239-247, 1995.
2. K. D. Paulsen, P. M. Meaney, M. J. Moskowitz, J. M. Sullivan, Jr., "A dual mesh scheme for finite element based reconstruction algorithms", *IEEE Trans. on Med. Imag.*; **14**, pp. 504-514, 1995.
3. P. M. Meaney, K. D. Paulsen, A. Hartov, R. K. Crane, "An active microwave imaging system for reconstruction of 2-D electrical property distributions", *IEEE Trans. Biomed. Eng.*; **42**, pp. 1017-1026, 1995.
4. P. M. Meaney, K. D. Paulsen, A. Hartov, R. K. Crane, "Microwave imaging for tissue assessment: initial evaluation in multitarget tissue-equivalent phantoms", *IEEE Trans. Biomed. Eng.*; **43**, pp. 878-890, 1996.
5. P. M. Meaney, K. D. Paulsen, J. T. Chang, "Near-field microwave imaging of biologically based materials using a monopole transceiver system", *IEEE Trans. on Microwave Theor. and Tech.*, January 1998 (in press).
6. J. T. Chang, K. D. Paulsen, P. M. Meaney, "Non-invasive thermal assessment of phantom biological tissues using an active microwave imaging technique", *Int. J. Hyperthermia*, (to be submitted).
7. C. A. Balanis, Antenna Theory: Analysis and Design, Harper and Row Publishers, New York, NY, pp.64-67, 1982.

Motion compensation algorithm for non-invasive two-dimensional temperature estimation using diagnostic pulse-echo ultrasound

Claudio Simon Philip VanBaren Emad Ebbini

Department of Electrical Engineering and Computer Science
University of Michigan, Ann Arbor, MI 48109-2122, USA

ABSTRACT

The feasibility of real-time non-invasive spatio-temporal temperature estimation from pulse-echo diagnostic ultrasound data has been previously demonstrated in stationary phantoms. The method is based on first estimating the axial shifts of the RF-echo data due to local changes in the speed of sound and thermal expansion in the propagating medium, and then differentiating these estimates along axial direction to obtain the temperature rise map. In a clinical setup, however, translation, rotation and deformation affect the estimates. In this paper we introduce an algorithm to compensate for tissue translation and uniform deformation along the axial and lateral directions of the ultrasonic imaging plane. This is achieved by separating the components of the time-shift map due to temperature rise (a local effect, occurring within the vicinity of the heated region) from the component due to translation and deformation (effect observed over a larger region). A rubber phantom experiment was designed where high intensity focused ultrasound was used to generate localized heating while motion was applied to the phantom and/or imaging transducer. Temperature profiles were successfully estimated while the phantom was translated by 30 mm and axially deformed by 13%.

Keywords: Temperature estimation, motion compensation, ultrasound, image-guidance, medical imaging

1. INTRODUCTION

It has long been recognized that the lack of real-time non-invasive multidimensional temperature feedback is a major hindrance against the use of high intensity focused ultrasound (HIFU) for a range of deep localized thermotherapies. Thermal imaging techniques based on magnetic resonance imaging,[1] impedance tomography,[2] microwave radiometry,[3] and backscattered ultrasound[4,5] have been suggested in the last few years. Each of these techniques has its particular advantages and limitations, however, motion imposes limitations for most of these non-invasive temperature imaging modalities, including magnetic resonance imaging and ultrasound. In the case of ultrasound, the data collection is inherently performed in real-time, so that the data collection itself is usually not affected by motion. However, the temperature estimates are computed based on the estimation of changes in the speckle pattern, by comparing frames collected prior to and after the therapeutic energy is delivered. Therefore, motion has to be tracked and compensated in order to obtain meaningful estimates of the temperature profile.

A one-dimensional technique for non-invasive temperature estimation based on backscattered diagnostic ultrasound was proposed in Refs. 4,6. The technique is based on the estimation of the axial time-shift observed in the ultrasound echo due to thermally induced local changes in the speed of sound and thermal expansion in the propagating medium. The time-shift estimates are differentiated along the axial direction and scaled to obtain the temperature estimates. In Refs. 5,7 the temperature estimation technique was modified to provide two-dimensional maps of the temperature profile. Although motion affects the temperature estimates obtained with this technique, as it is based on speckle tracking, most of the thermal images produced so far using this technique have assumed a motion-free environment.[8–10]

The effect on the ultrasound echo introduced by local temperature changes is typically small when compared to the extent of motion that can occur in clinical settings. As an example, a temperature change of 5°C in a 5 mm diameter heated region in muscle tissue will cause the ultrasound echo to shift by only 30 ns, corresponding to an apparent shift of approximately 20 μm. On the other hand, if the imaging transducer is physically translated by

E-mail: claudio@eecs.umich.edu phillipv@eecs.umich.edu emad@eecs.umich.edu
http://bul.eecs.umich.edu/research/

SPIE Vol. 3249 • 0277-786X/98/$10.00

as little as 1 mm along its axial direction, the ultrasound echo will shift by 1300 ns, an effect almost two orders of magnitude larger than the thermal effect we are trying to measure. In Ref. 4 a method for compensating for axial translation, while estimating temperature changes along one dimension was considered. Axial translation was compensated by tracking the echo from a region where the temperature was known to remain constant.

Meunier and Bertrand[11] developed a theoretical model to predict the change in perceived ultrasound speckle pattern as the imaged object undergoes translation, rotation or deformation in the imaged plane. The echo was modeled as the convolution of the scattering structure in the object with the point spread function of the imaging system. Using this model to simulate the echo of objects undergoing motion, they confirmed the validity of their model. They have shown that most of the structure of the ultrasound echo is preserved when the object undergoes axial and lateral translations. In the case of temperature estimation, it is therefore possible to compensate for these by realigning the data. On the other hand, rotation and deformation induce interframe speckle decorrelation. In Ref. 11 it was shown that the decorrelation is proportional to the extent of the rotation and deformation.

Speckle decorrelation due to axial deformation has been largely studied in ultrasound elasticity imaging.[12] In this imaging modality, a reference frame of backscattered ultrasound RF-data is first collected. The interrogated object is then subjected to deformation, and a second frame is acquired. Speckle tracking is used to estimate the axial and lateral shifts, that are then used to obtain two-dimensional estimates of the local strain vectors and Young's modulus. It has been shown that speckle decorrelation is one of the factors limiting the elasticity signal to noise ratio achievable with such systems. In Ref. 12 it was shown that this limitation can be partly overcome if a sequence of frames is acquired while the deformation is applied and speckle tracking is performed between successive frames. This procedure reduces the overall error introduced by speckle decorrelation, as the cross-correlation between successive frames is typically high. This idea is utilized in this paper, where a sequence of frames is collected while the imaged object experiences heating, translation and deformation.

Axial deformation also produces echo contraction or stretching, an effect that can inadvertently be interpreted as thermally induced change in the speed of sound, or thermal expansion in the medium. In order to account for axial deformation, we make the assumption that the elastic properties of the region of the medium undergoing deformation are homogeneous and the force creating deformation is homogeneous as well. In this case, we show that it is possible to separate the component of the axial shift due to deformation, an effect that occurs over a large region, from the thermal component, a local effect.

2. TEMPERATURE ESTIMATION WITH MOTION COMPENSATION

Temperature estimates obtained at a frame rate of one frame per second will typically suffice to capture the relatively slow thermal dynamics in tissue undergoing thermotherapy. At this frame rate, the interframe axial and lateral shifts caused by translation and deformation can typically achieve a few millimeters. Due to the relatively homogeneous texture seen in ultrasound images it is necessary to use rather large window sizes when performing correlation based motion tracking, so that each window encompasses a number of scattering centers. This reduces the occurrence of false peaks in the computed auto-correlation function. On the other hand, in order to obtain meaningful temperature estimates with good spatial resolution, it is necessary to have estimates of the axial shift on a fine spatial sampling grid,[9] therefore smaller window sizes are desired.

In this paper we suggest a three-step approach to meet both of these requirements. The first step consists of subdividing the 2-D data frame into large windows and then computing, for each window, a coarse estimate of the axial and lateral shifts introduced by translation and deformation. In a second step, smaller windows are used to obtain fine local estimates of the lateral and axial shift components on the order of the sampling period of the RF-data. The last step consists of estimating the lateral and axial shifts with sub-sample resolution. Lateral shifts are estimated by interpolating the normalized auto-correlation function along the lateral direction. Axial shifts are estimated from the phase information of the RF-signal along the axial direction. A detailed description of each step is provided in Appendix A.

It is shown in Ref. 9 that, when the medium is not undergoing axial deformation, the spatial (axial) derivative of the axial shift estimates obtained from the procedure described above are linearly proportional to the local change in temperature in the propagating medium. However, if the medium experiences axial deformation between the acquisition of the reference echo data (performed at base-line initial temperature) and the acquisition of the echo data from which the temperature estimates are to be computed, the axial shift estimates will reflect the superposition of the effects due to axial deformation and local changes in temperature. It is therefore necessary to subtract the effect

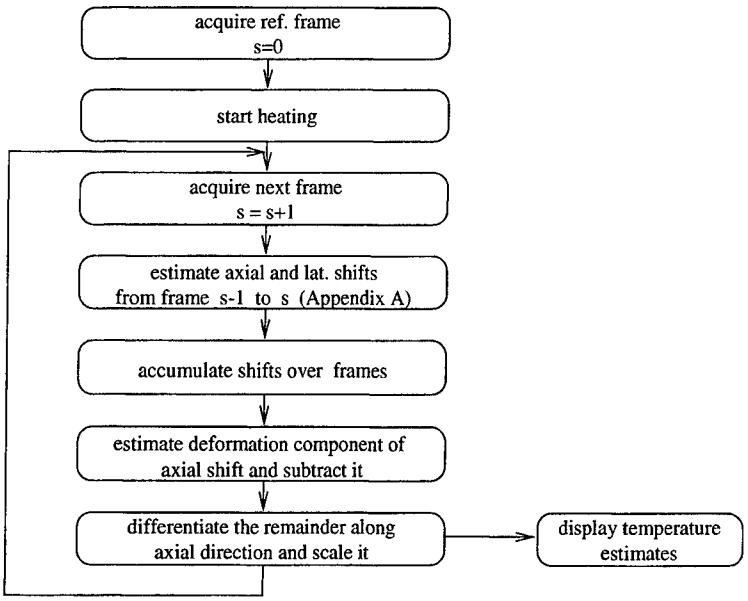

Figure 1. Block diagram of the temperature estimation algorithm with motion compensation.

caused by deformation prior to computing the temperature estimates. However an additional difficulty comes from the fact that the axial deformation is usually unknown, therefore a need to estimate this effect prior to compensation. To solve this problem, we make the assumption that the elastic properties in the medium undergoing deformation are spatially homogeneous, and we assume the force causing deformation to be spatially constant within a region of interest. In this case, the medium experiences uniform deformation, being constant over a relatively large region. On the other hand, the effect due to temperature change is typically very localized, being restricted to the region close to the focus of the HIFU field. In this case, by spatially low-pass filtering the estimates of the axial shift, it is possible to obtain an estimate of the component due to deformation. This component is then subtracted from the originally estimated axial shifts, the resulting quantity being differentiated along axial direction to obtain the temperature estimates.

2.1. Periodic motion

In a clinical environment, a significant component of the motion will have a periodic behavior, mostly due to cardiac and breathing cycles. In this case, it is possible to modify the algorithm in Fig. 1 to exploit this periodicity. A collection of reference frames is acquired prior to any heating (baseline temperature), corresponding to the different stages of the approximately periodic motion. After heating has started, whenever a new frame is acquired, it is first compared to the collection of reference frames, to determine the one that most closely resembles it. The axial and lateral shifts are then estimated using the speckle tracking algorithm described in appendix A with these two frames. The axial and lateral shifts will typically contain a residual component due to motion between the acquisition of the two frames, as well as information on the temperature change. The compensation method described in the previous section can be used to account for the effect introduced by the first component. Nevertheless, the amount of translation and deformation that has to be compensated between the frame for which the temperatures are being estimated and the reference frame is reduced. Furthermore, inhomogeneities in the elastic properties of the medium and in the force causing deformation, as well as rotation and out-of-plane motion are partially compensated using this approach.

3. EXPERIMENTAL SETUP

A combined imaging and therapy ultrasound system is shown in Fig. 2 and described in detail elsewhere.[7,9] The therapeutic system uses a 1 MHz spherically shaped 1-D 64-element array transducer, and provides individual control

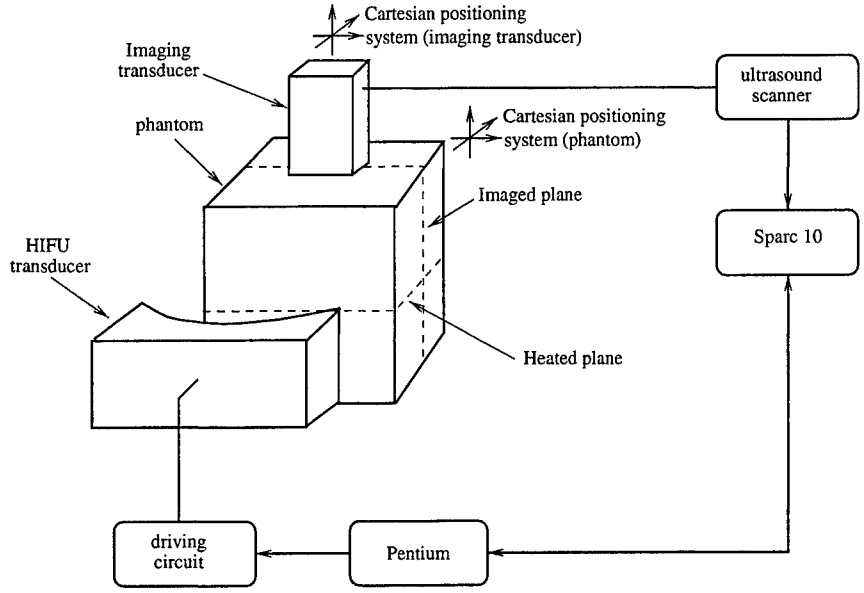

Figure 2. Experimental setup showing the dual ultrasound system and the two Cartesian positioning systems.

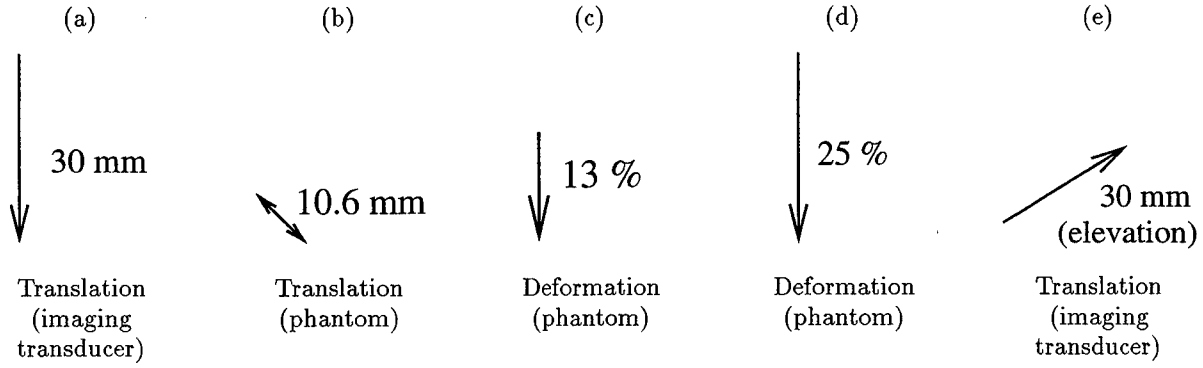

Figure 3. Vectors indicating the applied motion for each of the experiments. The double arrow in (b) indicates periodic motion of the phantom.

of the amplitudes and phases of each element. The imaging system consists of an ATL UM9 ultrasound scanner that has been adapted to provide beamformed RF-data collection in real time. A 3.5-5.0 MHz linear array probe was used. The imaging transducer and the phantom were mounted on separate stepper-motor driven Cartesian manipulators used to create the motion patterns shown in Fig. 3.

4. RESULTS

A series of experiments was performed on a custom made rubber phantom[9] to test the effectiveness of the algorithm described.

4.1. Axial translation of the imaging transducer

In the first experiment the imaging transducer was mechanically displaced along its axial direction at a constant speed of 1.5 mm/s (Fig 3(a)). Two-dimensional frames of beamformed RF-data were captured every 0.9 s, and processed

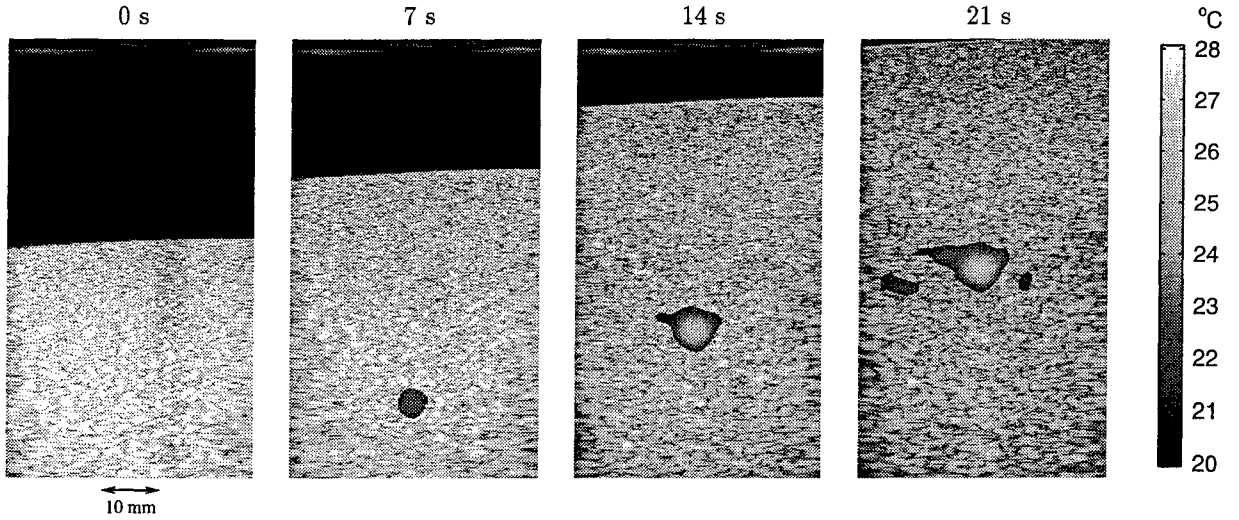

Figure 4. Temperature estimates obtained for a heating experiment where the imaging transducer was translated along its axial direction, as indicated in Fig. 3(a).

off-line. The HIFU therapeutic beam (5 W) was switched on at 3.6 s and switched off at 17.1 s. Two-dimensional temperature profiles were estimated and overlayed to the corresponding gray-scale B-scan images. Fig. 4 shows the frames obtained at 0 s, 7 s, 14 s and 21 s. The top (dark) part of the first 3 frames corresponds to water, used to provide acoustical coupling between the phantom and the ultrasound systems. In the first frame, the phantom is at baseline temperature, 20 °C. At 7 s the temperature rise at the focus of the therapeutic beam starts to be seen. At 14 s the temperature at the focus has increased. It can be seen that the algorithm correctly compensates for the axial translation, and tracks the apparent motion of the heated spot. At 21 s, corresponding to a total axial translation of approximately 30 mm, some artifacts start to be seen. These are caused by echo decorrelation due to changes in the point spread function of the imaging system, as the imaging transducer is axially translated.

4.2. Axial and lateral translation of the object

A situation that may occur more often during treatment of abdominal organs is motion of the tissue being treated with respect to the therapeutic and imaging transducers, instead of motion of the imaging transducer alone, as was considered in the previous section. In this case, even though the therapeutic beam is focused at a single location, an extended region could be inadvertently heated due to tissue motion during treatment. To illustrate how the non-invasive temperature estimation method developed in this paper can be used to detect this effect while the tissue is undergoing motion, an experiment was designed where periodic motion was applied to the phantom.

The phantom was periodically translated along a 135° diagonal (axial-lateral), at the speed of 1.4 mm/s over a linear extension of 10.6 mm, as indicated in Fig. 3(b). Ultrasound frames of RF-data were collected every 0.9 s. Starting at 28 s, a therapeutic beam (7.5 W) focused at the geometric center of the HIFU transducer was applied. The temperature estimates overlayed to the gray-scale B-scan images corresponding to 34 s, 42 s, 50 s and 58 s are seen in Fig. 5. The frame at 34 s (corresponding to 6 s after the heating has started) starts to show a very weakly heated region, if compared to the frame at 7 s in Fig. 4, where the phantom was heated for only 3.4 s. Furthermore, the power of the therapeutic beam was 50% larger for the case shown in Fig. 5. This is in good agreement with the fact that the therapeutic power is being applied to an extended region, due to motion. The frames at 50 s and 58 s show a diagonally extended heated region, which is consistent with the applied periodic translation (Fig 3(b)).

4.3. Deformation

The two previous examples only involved translation. Linear motion in a plane can also include deformation and rotation. Both cause the ultrasound echo to decorrelate from one frame to the next, as shown in Ref. 11. Furthermore estimates of the axial shift sum the effects of both axial deformation and thermally induced axial shift, the latter

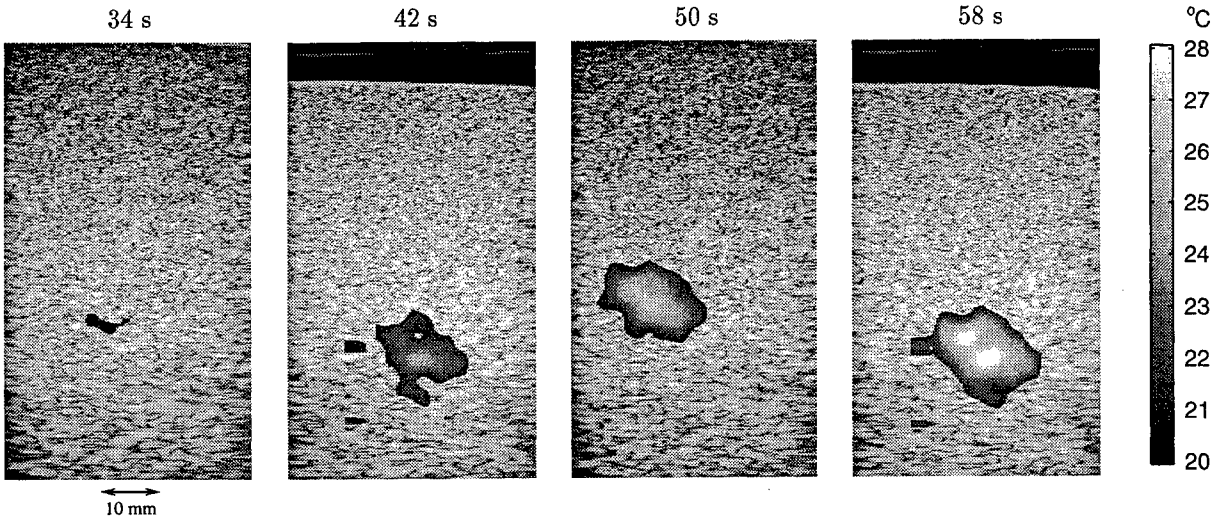

Figure 5. Temperature estimates obtained for a heating experiment where the phantom was periodically translated along a 135° diagonal, as indicated in Fig. 3(b).

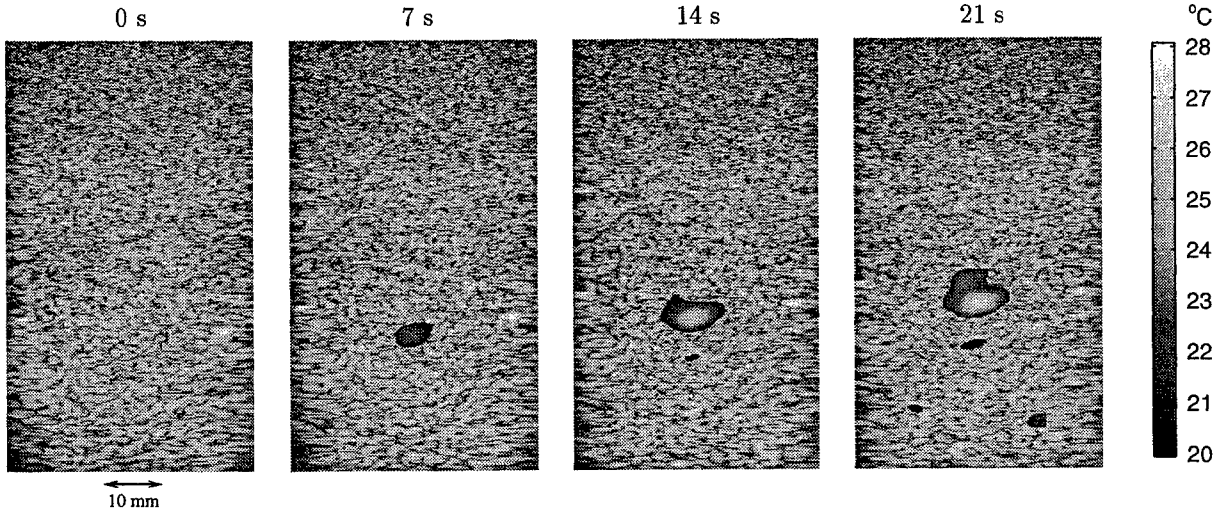

Figure 6. Temperature estimates obtained for a heating experiment where the imaging transducer was translated in order to apply axial deformation to the phantom, as indicated in Fig. 3(c).

used to measure temperature changes in the medium. The algorithm suggested in Fig. 1 can separate these two components, provided that the deformation is homogeneous. In order to test the algorithm in such a scenario, the setup in Fig. 2 was adapted so that the imaging transducer could apply linear deformation to the phantom along the imaging axial direction, as regularly performed in elasticity imaging.[12]

The axial strain applied to the phantom was linearly increased from 0 to 13%, at a rate of 0.6%/s (Fig. 3(c)). The therapeutic beam (5 W) was switched on at 3.6 s. The estimated temperature images are shown in Fig. 6 for the frames obtained at 0 s, 7 s, 14 s and 21 s, corresponding respectively to 0%, 4%, 9% and 13% of applied axial strain.

Figure 7(a) shows estimates of the cumulative axial shift for the A-line that passes through the center of the

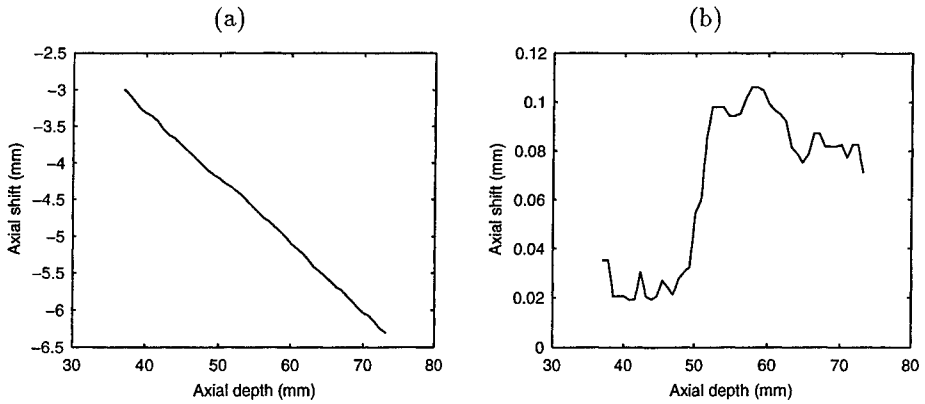

Figure 7. Example of deformation compensation. (a) original axial shift estimates, including the thermal and deformation effects. (b) estimated thermal component after deformation compensation. Note that the two plots have different vertical scales.

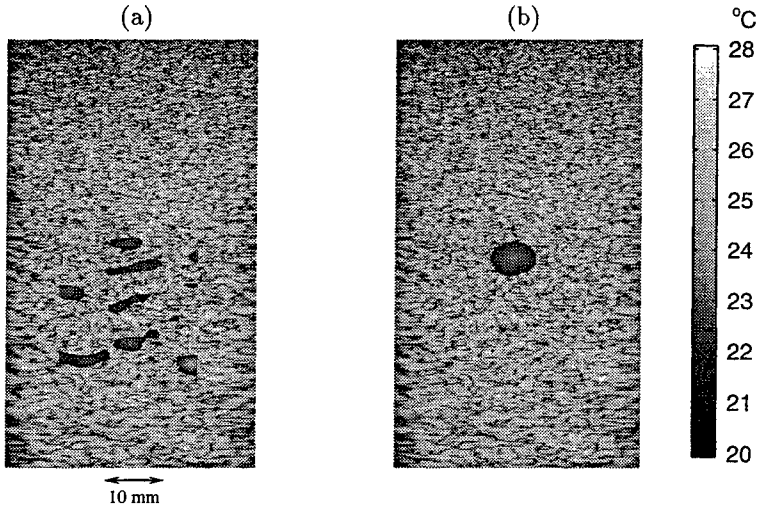

Figure 8. Temperature estimates obtained at 21 s in a heating experiment where the imaging transducer was translated in order to apply axial deformation to the phantom, as indicated in Fig. 3(d). (a) using the algorithm in Fig. 1. (b) using the algorithm described in Section 2.1, that assumes motion to be periodic.

heated region, for the 9% strain case (14 s frame, Fig. 6). The axial shift due to temperature change is hardly seen in this plot, as the effect due to axial strain is dominant. Using the algorithm described in Section 2, the axial average strain component was removed. The remaining component, that corresponds to the thermal effect we are trying to estimate, is represented in Fig. 7(b). The positive slope at 50 mm corresponds to the local change in temperature in the heated region. It is seen from Figs. 6 and 7 that the compensation algorithm is capable of separating the two components of the axial shift in this example.

A second experiment was performed using the setup configuration previously described, where the applied axial strain was increased from 0% to 25% at a rate of 1.2%/s (Fig. 3(d)). The remaining experimental parameters were unchanged. The temperature image obtained at 21 s (corresponding to 25% strain) is shown in Fig. 8(a). In this case, the interframe speckle decorrelation became more significant, due to the increase in average strain. The cumulative error introduced by speckle decorrelation in the estimates of the axial shift was dominant with respect to the thermal

effect, corrupting the temperature estimates as seen in Fig. 8(a).

As described in Section 2.1, if the motion is periodic, it is possible to acquire a collection of reference frames, and estimate the temperature at a given time using the current frame and the reference frame that most closely resembles it. In order to illustrate this, a collection of reference frames was acquired for the 25% strain experiment, prior to the actual heating experiment described in the previous paragraph. Therefore, during the acquisition of reference frames, the temperature in the phantom was constant, the phantom being imaged while the deformation was applied. The external force used to deform the phantom was then removed, and the phantom returned to its undeformed shape. The actual heating experiment described in the previous paragraph was then performed.

The interframe speckle tracking algorithm described in appendix A was used to estimate the axial and lateral shift between the frame represented in Fig. 8(a) and the corresponding frame from the collection of reference frames. The temperature image obtained in this way is shown in Fig. 8(b). It is seen that the temperature profile could be reliably estimated in this case.

5. DISCUSSION

Rotation of the imaged object also affects the ultrasound echo. It is shown in Ref. 11 that rotation in the imaged plane, similarly to deformation, causes speckle decorrelation. It is expected that the algorithm presented in this paper will be able to partially compensate for this effect, however this has not been tested. Such compensation would be obtained by acquiring a sequence of frames and computing interframe shifts, that are then accumulated. This same principle was shown to be effective in reducing speckle decorrelation due to deformation.

In this paper we only considered motion in the imaged plane. However, in a clinical application, motion in the elevation direction will also be present. It is known that motion in the elevation direction will cause speckle decorrelation, limiting the performance of the temperature estimation technique. If the motion is periodic, it is possible to partially compensate for it by synchronizing the temperature estimation with a collection of reference frames, as described in Section 2.1.

The spatial accuracy achievable with the temperature estimation technique described is limited by a thermo-acoustic lens effect, as discussed in detail in Refs. 8–10. Briefly, local changes in the speed of sound introduced by the change in temperature act like aberrators to the imaging system, causing the echo from regions behind heated spots to decorrelate. This creates ripple in the temperature estimates obtained in these regions. In Ref. 9 it is shown how a bandlimited spatial filter can be used to control the tradeoff between ripple and achievable spatial resolution.

The technique used to compensate for deformation relies on the homogeneity of the deformation force and elastic properties in the medium. If the medium is inhomogeneous, the estimates of the axial shift will contain information on local elastic properties of the medium. However, the algorithm described cannot differentiate between this information and thermally induced axial shifts. Furthermore, the compensation technique is based on the assumption that only a localized region is being heated, which holds for highly focused therapeutic beams over short periods of time. On the other hand, if large volumes are heated, either by scanned or unfocused therapeutic beams or by thermal conduction, the compensation technique has to be modified.

5.1. Temperature estimates in a 3-D volume

The algorithm described in Section 2.1 can easily be modified to obtain temperature estimates in a 3-D volume, in the case of non-moving objects. To illustrate this, the imaging transducer was mechanically scanned along its elevation direction at the speed of 2 mm/s (Fig. 3(e)). A collection of 90 reference frames was acquired at the rate of 6 frames per second while scanning the imaging transducer. The imaging transducer was returned to its original position, and a quickly scanned double focus pattern was used to heat the phantom for 1.5 s. A new scan of the imaging transducer was performed, acquiring another collection of 90 frames.

The temperature profile at each imaged plane was estimated using the algorithm described in Section 2.1 between the frame collected after heating and its corresponding reference frame. This way, temperature estimates in a $65\times38\times30$ mm^3 volume were obtained . Temperature estimates obtained for the plane scanned by the HIFU transducer (therefore transversal to the imaged planes) are shown in Fig. 9(a), where each contour line corresponds to a temperature change of 1 °C. Figure 9(b) shows a crude estimate of the predicted temperature profile in the phantom, obtained by spatially smoothing the simulated HIFU acoustic intensity used to heat the phantom. A 3.7×3.7 mm^2 moving average spatial filter was used to smooth the acoustic intensity, partially accounting for thermal conduction

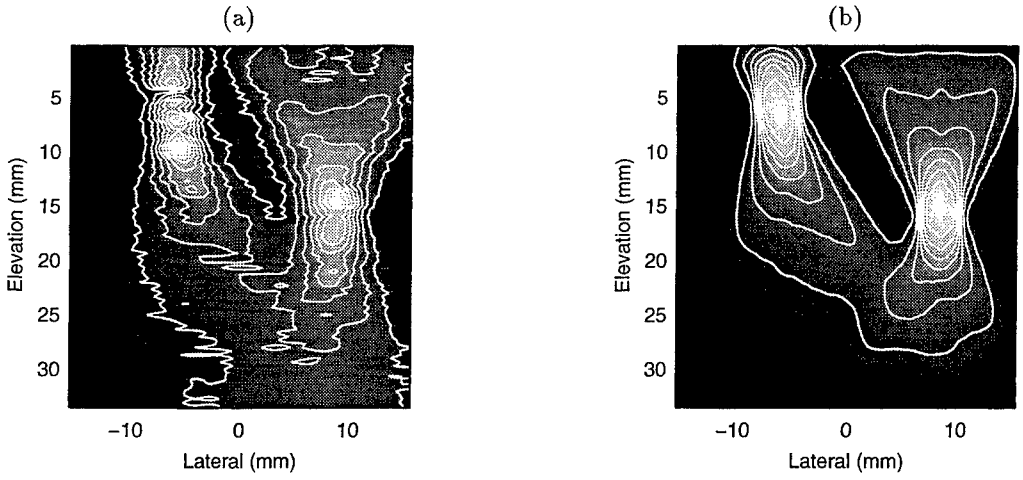

Figure 9. (a) Temperature estimates at a plane transversal to the imaging plane. (b) Simulated profile of the temperature distribution.

in the phantom as well as the spatially bandlimited characteristic of the temperature estimation method. It is seen that the temperature estimates in Fig. 9(a) strongly resemble the simulated HIFU heating pattern.

6. CONCLUSION

A method capable of non-invasively estimating temperature changes while the medium undergoes planar translation and deformation was presented and successfully tested in a tissue-mimicking phantom. Rotation and out-of-plane motion were not considered in this preliminary study, however these should be studied and solved prior to application of this technique in the clinic. Periodicity in motion and deformation can be exploited to minimize the effects of speckle decorrelation on the compensation schemes. Finally, further development is needed to account for spatially varying motion and deformation models encountered in clinical situations.

APPENDIX A. ALGORITHM FOR AXIAL AND LATERAL SHIFT ESTIMATION

In this appendix we describe the steps used to estimate the interframe lateral and axial shifts experienced by the speckle structure at location (m, n) from frame $s-1$ to frame s, where m and n are the indices of the sampled data along the axial and lateral directions, respectively.

Let $r(m, n, s)$ represent the discrete-time sampled RF-echo data. The Hilbert transform of the signal, the analytic signal and the envelope detected signal are, respectively, given by[13]:

$$\check{r}(m, n, s) = r(m, n, s) * h(m), \tag{1}$$

$$\hat{r}(m, n, s) = r(m, n, s) - j\check{r}(m, n, s), \tag{2}$$

$$\tilde{r}(m, n, s) = |\hat{r}(m, n, s)|, \tag{3}$$

where $*$ denotes convolution, $|\cdot|$ denotes absolute value, $h(m)$ is the 1-D FIR Hilbert Transformer and $j = \sqrt{-1}$.

Let us define the function:

$$\psi_{s_1,s_2}(m, n; q, l) = \sum_{m'=-\frac{M_1}{2}}^{\frac{M_1}{2}-1} \sum_{n'=-\frac{N_1}{2}}^{\frac{N_1}{2}-1} \tilde{r}(m + m', n + n', s_1) \cdot \tilde{r}(m + m' + q, n + n' + l, s_2), \tag{4}$$

where M_1 and N_1 are the (large) window sizes in the first step of the algorithm. The normalized auto-correlation of the envelope detected data is then computed by:

$$\tilde{\rho}(m,n;q,l) = \frac{\psi_{s-1,s}(m,n;q,l)}{\sqrt{\psi_{s-1,s-1}(m,n;0,0)\cdot\psi_{s,s}(m+q,n+l;0,0)}}. \tag{5}$$

The first estimate of the axial and lateral shifts will be given by the lag (q_1, l_1) that maximizes the quantity $\tilde{\rho}(m,n;q,l)$ within the search region given by $|q| \leq Q_1$, $|l| \leq L_1$.

In the second step this estimate is refined, by using a smaller window size (M_2, N_2), and searching in a smaller region around the lag (q_1, l_1) obtained above. Furthermore, the analytic signal is used in this case. Let us define the function:

$$\varphi_{s_1,s_2}(m,n;q,l) = \sum_{m'=-\frac{M_2}{2}}^{\frac{M_2}{2}-1}\sum_{n'=-\frac{N_2}{2}}^{\frac{N_2}{2}-1} \hat{r}(m+m',n+n',s_1)\cdot\hat{r}^*(m+m'+q,n+n'+l,s_2), \tag{6}$$

where the superscript * denotes complex conjugation. The normalized auto-correlation of the analytic signal is given by:

$$\hat{\rho}(m,n;q,l) = \frac{\varphi_{s-1,s}(m,n;q,l)}{\sqrt{\varphi_{s-1,s-1}(m,n;0,0)\cdot\varphi_{s,s}(m+q,n+l;0,0)}}. \tag{7}$$

The refined estimate of the axial and lateral shifts is the lag (q_2, l_2) that maximizes $|\hat{\rho}(m,n;q,l)|$ within the confined search region $|q-q_1| \leq Q_2$, $|l-l_1| \leq L_2$.

In order to obtain sub-sample estimates of the lateral shift, a 2nd order polynomial is fit to $|\hat{\rho}(m,n;q_2,l_2+i)|$, $i \in -1,0,+1$. The lag of the peak of the fitted polynomial is used as the final estimate of the lateral shift, l_3.

For the axial direction it is possible to make use of the phase information present in the backscattered echo signal. Let $\underline{l_3}$ and $\overline{l_3}$ be the nearest integers to l_3 when rounded towards $-\infty$ and $+\infty$, respectively. The sub-sample estimate of the axial shift at lateral lag $\underline{l_3}$ is then computed by:

$$\underline{q_3} = q_2 + \frac{2\angle\hat{\rho}(m,n;q_2,\underline{l_3})}{\angle\hat{\rho}(m,n;q_2+1,\underline{l_3}) - \angle\hat{\rho}(m,n;q_2-1,\underline{l_3})}, \tag{8}$$

where $\angle$ is the angle operator. The sub-sample estimate of the axial shift at lateral lag $\overline{l_3}$, $\overline{q_3}$, is computed in a similar way. The final estimate of the axial shift, q_3 is computed using a weighted average:

$$q_3 = \underline{q_3}\cdot(\overline{l_3} - l_3) + \overline{q_3}\cdot(l_3 - \underline{l_3}). \tag{9}$$

ACKNOWLEDGMENTS

The authors thank *Matthew O'Donnell* and *Mark Lubinski* for their valuable suggestions, *Stanislav Emelianov, Jan-Ulco Kluiwstra, Ramon Erkamp* and *Timothy Hall* for setting up some of the tools used in the experiments. The first author thanks *CAPES* (Brazil) for partially supporting him during his graduate studies. This work was partially funded by *NSF* Young Investigator Award ECS 9358301 and *NIH* Grant CA66602. *ATL* provided the HDI-Ultramark 9 ultrasound scanner. The therapeutic array was acquired with funds from the *Office of Vice President for Research at University of Michigan.*

REFERENCES

1. K. Hynynen, A. Chung, T. Fjield, M. Buchanan, D. Daum, V. Colucci, P. Lopath, and F. Jolesz, "Feasibility of using ultrasound phased arrays for MRI monitored noninvasive surgery," *IEEE Trans. Ultrason., Ferroelec., Freq. Contr.*, vol. 43, no. 6, pp. 1043–1053, Nov. 1996.
2. K.Paulsen, M.Moskowitz, T.Ryan, S.Mitchell, and P.Hoopes, "Initial *in vivo* experience with EIT as a thermal estimator during hyperthermia," *Int. J. Hyperthermia*, vol. 12, no. 5, pp. 573–591, Sept. 1996.
3. P.Meaney, K.Paulsen, A.Hartov, and R.Crane, "Microwave imaging for tissue assessment: Initial evaluation in multitarget tissue-equivalent phantoms," *IEEE Trans. Biomed Eng.*, vol. 43, no. 9, pp. 878–890, Sept. 1996.

4. R. Moreno, C. Damianou, and N. Sanghvi, "Tissue temperature estimation *in-vivo* with pulse-echo," *IEEE Ultrason. Symp.*, pp. 1225–1229, Nov. 1995.
5. R.Seip, P.VanBaren, C.Simon, and E.Ebbini, "Non-invasive spatio-temporal temperature change estimation using diagnostic ultrasound," *IEEE Ultrason. Symp. Proc.*, pp.1613–1616, Nov. 1995.
6. R. Seip, P. VanBaren, C. Cain, and E. Ebbini, "Non-invasive real-time multipoint temperature control for ultrasound phased array treatments," *IEEE Trans. Ultrason., Ferroelec., Freq. Contr.*, vol. 43, no. 6, pp. 1063–1073, Nov. 1996.
7. P. VanBaren, C. Simon, R. Seip, T. Solf, C. Cain, and E. Ebbini, "Image-guided phased array system for ultrasound thermotherapy," *IEEE Ultrason. Symp.*, pp. 1269–1272, Nov. 1996.
8. C. Simon, P. VanBaren, and E. Ebbini, "Quantitative analysis and applications of non-invasive temperature estimation using diagnostic ultrasound," *IEEE Ultrason. Symp.*, Oct. 1997.
9. C. Simon, P. VanBaren, and E. Ebbini, "Two-dimensional temperature estimation for ultrasound thermotherapy using diagnostic ultrasound," submitted to *IEEE Trans. UFFC*, Sep. 1997.
10. C. Floch, and M. Fink, "Ultrasonic mapping of the temperature distribution in hyperthermia: the thermal lens effect," *IEEE Ultrason. Symp.*, Oct. 1997.
11. J. Meunier, and M. Bertrand, "Ultrasonic texture motion analysis: theory and simulation," *IEEE Trans. Med. Imag.*, vol. 14, no. 2, pp. 293–300, June 1995.
12. M. O'Donnell, A. Skovoroda, B. Shapo, and S. Emelianov, "Internal displacement and strain imaging using ultrasonic speckle tracking," *IEEE Trans. Ultrason., Ferroelec., Freq. Contr.*, vol. 41, no. 3, pp. 314–325, May 1994.
13. A. Oppenheim, and R. Schafer, *Discrete-Time Signal Processing,* Prentice-Hall, Englewood Cliffs, 1989.

Electrical Impedance Imaging For Tissue Monitoring And Assessment During Thermal Therapy

Keith D. Paulsen*+, Alex Hartov*#, Kendra S. Osterman*, Rob Mazzarese*, Todd Kerner*#

* Thayer School of Engineering, Dartmouth College, Hanover, NH 03755
#Dartmouth Hitchcock Medical Center, Lebanon, NH 03756
+ Norris Cotton Cancer Center, Lebanon, NH 03756

ABSTRACT

Electrical properties of tissues in the 10KHz to 10MHz range are known to be temperature sensitive making the monitoring and assessment of thermal insult delivered for therapeutic purposes possible through imaging schemes which spatially resolve these changes. We have been developing electrical impedance imaging technology from both the hardware data acquisition and software image reconstruction perspectives in order to realize the capability of spectroscopically examining the electrical property response of tissues undergoing hyperthermia therapy. Results from simulations, in vitro phantom experiments and in vivo studies including in human patients are presented. Specifically, a new prototype multi-frequency data acquisition system which is functional to 1MHz in both voltage and current modes is described. In addition, recent advances in image reconstruction methods which include the enhancement techniques of total variation minimization, dual meshing and spatial filtering are discussed. It is also clear that the electrical impedance spectrum of tissue has the potential to monitor other types of treatment-induced injury. Preliminary *in vivo* electrical impedance measurements in a rat leg model suggest that the tissue damage from radiation therapy can be tracked with this technique. Both dose and time-dependent responses have been observed in the electrical impedance data when compared to measurements recorded in an untreated control. Correlations with histological examination have also been performed and indicate that electrical impedance spectroscopy may provide unique information regarding tissue functional status and cellular morphology. Representative results from these studies are reported.

Keywords: electrical impedance imaging, electrical impedance spectroscopy, thermal imaging, tissue damage assessment

1. INTRODUCTION

Electrical impedance tomography (EIT) or spectroscopy (EIS) involves the injection of low frequency electric currents, typically over the range 10KHz to 10MHz, and measurement of the subsequent potential distribution that develops at a discrete set of electrodes positioned on the skin surface. The electrical properties, represented through bulk media parameters, the electrical conductivity and electrical permittivity, are tissue and frequency dependent; hence, the imaging problem becomes one of determining the electrical property distribution (i.e. conductivity and permittivity) which is needed to sustain the measured voltage distribution subject to the applied currents. Because the excitation frequencies are relatively low, direct or conducting medium contact is required. However, data acquisition is relatively simple and can generally be realized through low cost, off-the-shelf integrated circuit components. This is a potentially major advantage of the technique: that it is inexpensive to develop, portable, safe and easy to use.

Electrical impedance imaging is under investigation as a noninvasive method of monitoring subsurface temperature

* Further Author Information -
KDP (correspondence): email: keith.paulsen@dartmouth.edu; Telephone: 603-646-2695; FAX: 603-646-3856

distributions and/or associated cellular response during thermal therapy or other forms of treatment which cause a progression in tissue injury such as radiation therapy[1-6]. Imaging the thermal response in terms of estimating tissue temperature is based on the observation that the electrical properties of tissue, most notably the electrical conductivity, vary with temperature on the order of 2%/°C[7]. Laboratory studies involving tissue equivalent phantoms having this level of linear electrical conductivity variation with temperature have confirmed that temperature sensing to within 1°C or better over regions relevant to clinical treatment are possible[8]. In addition, some *in vivo* results in animal and human subjects have appeared which suggest that the technique is viable in the clinical setting[2,9].

However, carefully controlled experiments in mouse tumor systems have demonstrated that temperature effects on the conductivity change occur during the onset of temperature rise in tissue but diminish in importance giving way to cellular-based changes in electrical impedance resulting from hyperthermia-induced cytotoxicity[3]. Spectroscopic response has been found to be essential in separating these temporal events. In fact, it now appears that the most promising utilization of EIS imaging will be as a marker of thermal therapy insult rather than as a direct temperature probe. Further, this concept of exploiting the electrical impedance signature of tissues as a measure of tissue injury is extendible to other forms of treatment. The emerging results of Osterman et. al. are the first evidence which supports the notion that the ability of EIS to follow the progression of tissue injury from thermal insult can be generalized to other types of therapies.

As a result, there is considerable rational for exploring and developing electrical impedance imaging. There are basically three aspects to realizing an EIS or EIT system. First, some measurements of tissue electrical response to a controlled stimulus (e.g. current injection) need to be acquired in a region of interest; that is, some form of data acquisition hardware is required. Second, an image must be formed from the measurements. In EIS imaging, the raw data cannot be used directly to create an image; rather, model-based image reconstruction is needed to extract the conductivity distribution from the measured observations. Hence, advanced computational methods are an essential ingredient for successful EIS imaging. Third, electrical property imaging requires the integration of the hardware and software (image recovery) systems as a single functioning entity. This is not a trivial matter in that issues of data calibration and data-model match become critical.

In this paper, we will explore our recent progress on there fronts. In particular, advances in realizing a new, dual mode (current or voltage excitation), multi-channel, multi-frequency hardware system will be described. Recent progress in developing multi-component objective function imaging which incorporates the image enhancement schemes of total variation minimization, dual meshing and spatial filtering will be discussed and samples of image reconstruction performance will be provided. Examples of thermal imaging simulations and experiments in phantom and human subjects will be presented. New data suggesting the general role for EIS imaging in the monitoring of the progression of tissue injury will be highlighted from radiation therapy experiments in rodent muscle.

2. DATA ACQUISITION SYSTEM

Recent literature describes a number of EIT hardware systems which have focused on various aspects of instrumentation design. Koukourlis et. al.[10] constructed a 32-electrode, 25 KHz system with an emphasis on data acquisition techniques. Smith et. al.[11] realized a 16-electrode, 20 KHz instrument where the design effort targeted achieving real-time imaging speeds. Cook et. al.[12] developed a 32-electrode, 30 KHz system with the goal of real-time imaging with true 16-bit measurement precision.

Our approach represents a departure from these design strategies in that we have sought to produce a multi-frequency instrument with both high analog bandwidth and 16-bit measurement precision. In addition, we have incorporated the concept of dual mode operation whereby either an impressed current or applied voltage can be sustained at the stimulating

electrodes. An overview block diagram of the system is illustrated in Figure 1. We have incorporated high-quality commercial products where possible to achieve certain instrumentation functionality. For example, waveform generation and 16-bit data acquisition are performed through PC cards purchased from commercial vendors. The modular EIS circuit boards then rely on analog electronics to distribute the input waveform (in either current or voltage mode) over a number of channels and digital circuitry to multiplex the corresponding output measurements.

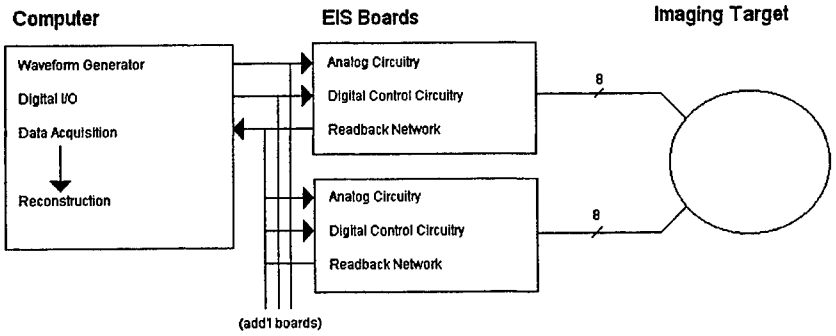

Figure 1: EIS system overview

The EIS circuit boards represent a new electronic design implemented on a 9" x 12.5" four-layer printed circuit card which fits directly into standard 9U sub-rack assemblies with a custom backplane. The four-layer design permits dedicated copper layers for ground and powder. This minimizes lead lengths for bypass capacitors and ensures minimal return paths for ground currents which maintain the low self-inductance essential to the proper performance of high bandwidth analog components. Digital and analog power planes are physically separated to reduce noise.

A 32-bit digital bus controls the EIS system from a PC using a standard digital I/O card. The digital board selection scheme permits use of an arbitrary number of EIS boards expandable up to 128 or 1024 output channels. The board select function shown in Figure 2 is an 8-bit comparison of an on-board DIP switch selection with an 8-bit word on the digital I/O bus. Once a specific EIS board is selected, inputs to that board are enabled through line drivers with further signal decoding to specify functions and scaling for each output channel. Data acquisition read-back multiplexing operates from the same switching network to permit measurements for an arbitrary number of electrodes using a single, two-channel A/D card. While the digital I/O hardware and software drivers have yet to be optimized, the EIS board's high-speed switching networks should allow optimal current pattern acquisition times under 100 ms for a 32-electrode implementation (assuming 100 data points are collected for each measurement).

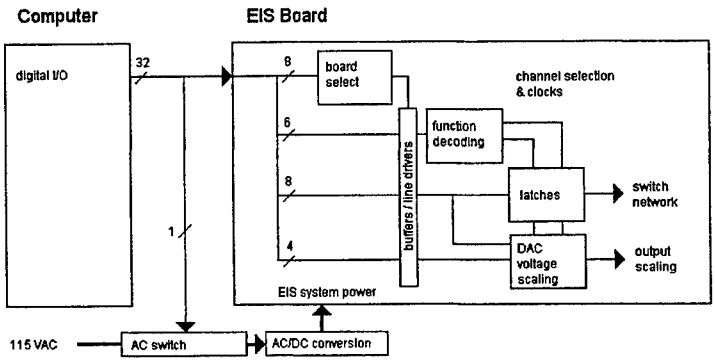

Figure 2: Digital system functional overview

The analog system was designed to accurately distribute the driving signal over a large number of channels. Figure 3 illustrates a functional diagram of the analog architecture used for each output channel. An analog multiplier scales the input waveform at each channel by multiplication with a DC value stored in a 12-bit DAC. This scaled signal is then converted to a voltage or current depending on the mode of operation selected. Measurements are achieved through a buffered read-back network under digital control. The voltage source is an op-amp configured for noninverting gain with external trimming to guarantee DC offsets in the applied signal smaller than 125μV. The current source is a transconductance amplifier. Although strict component tolerance is maintained, a final system wide digital calibration ensures accurate specification of output signal magnitude within the DAC's 12-bit resolution.

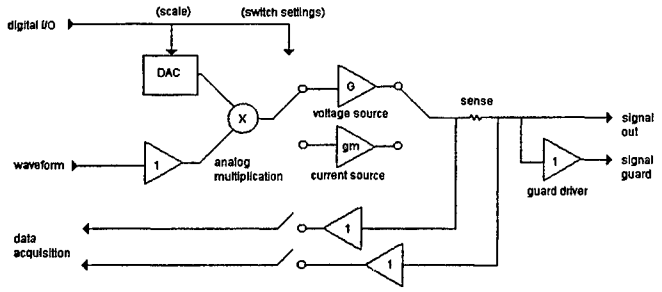

Figure 3: Analog system functional overview

High performance is required from the analog multiplier, the voltage source, and the current source. The multiplier is Burr-Brown's MPY600 which offers high-bandwidth, good linearity and relatively low harmonic distortion. For a voltage source, we have used Analog Device's AD817, a high-bandwidth, low-offset op-amp capable of driving the capacitive loads typical in an EIS imaging environment. For a current source, we are presently using Burr-Brown's OPA2662 as a high bandwidth, high current output, transconductance amplifier. However, the OPA2662 has very low output impedance (4.5 kΩ// 6.5pF) and requires active digital trimming to maintain accurate applied signals. The OPA2662 also exhibits a significant DC off-set which is removed with additional external analog circuitry (a feedback inverting integrator). Other current sources are under investigation such as Harris's CA3280 which will limit peak output current to a few milliamperes but offers the high output impedance (>63 MΩ// 7.5 pF) required for 16-bit resolution.

In order to capture phase information, voltage and current are sampled simultaneously for each channel. The results are converted to magnitude and phase by evaluating the discrete transform of the time domain sample set at the driving frequency (phase sensitive detection). A 32-channel implementation of this system has been realized and evaluated in terms of a number of performance criteria. Figure 4 shows of photographs of the present system which is currently being tested in tank experiments with physiological saline. The performance evaluation is summarized and compared to other recently described systems in Table 1.

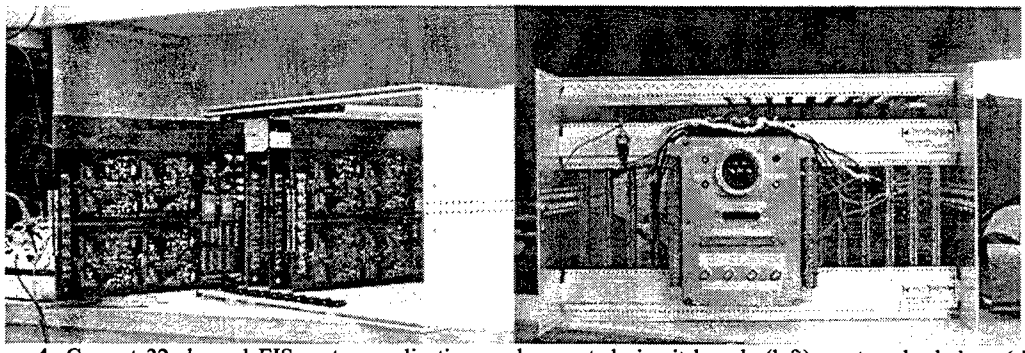

Figure 4: Current 32-channel EIS system realization: rack-mounted circuit boards (left), custom backplane (right)

SPECIFICATION	RESEARCH GROUP			UNITS
	RPI (1994)	Sheffield (1995)	Thayer (1998)	
OUTPUT				
Output Channels	32	16	8-1024	
Operating Frequency	30	20	0.1-1500	kHz
Frequency Scaling	n/a	n/a	1.2	kHz
Peak Output Current	0.5	2.5	75	mA
Output Scaling	12-bit	12-bit	12-bit	full scale
Phase Coherence	0.01	2	0.05	%
THD				
2nd harm.	n/a	n/a	-70	dB
3rd harm.	n/a	n/a	-50	dB
4th harm.	n/a	n/a	-80	dB
DATA ACQUISITION				
Frame Rate	7.5	25	0.22	images/s
SNR	104	65	90	dB
Digital Precision	16	n/a	16	bits
Absolute Accuracy	99.5	99.9		%
Data Acquistion Bandwidth	n/a	n/a	1.5	MHz

Table 1: EIT system performance comparison: RPI[12], Sheffield[11]

3. RECONSTRUCTION ALGORITHM

We are using a finite element based approach to simultaneously recover both the real and reactive components of the electrical property profile. It consists of a multi-component objective function method which minimizes the difference between a series of measurements and values computed from a computational model by determining the best-fit electrical property distribution that reproduces the measured data given the applied excitation. Key to this approach has been the identification of three image enhancement strategies: (1) total variation minimization (2) dual meshing, and (3) spatial low-pass filtering. Recent results[13] demonstrate a number of important findings including more than an order of magnitude increase in the tolerable noise level (more than 1%) relative to earlier algorithms. These findings also suggest the possibility of achieving absolute image reconstruction with quantitative recovery of the tissue electrical properties.

In the low frequency case, the electric potential within the body can be described by the generalized form of Laplace's equation

$$\nabla \cdot (\sigma - i\omega\varepsilon)\nabla\Phi = 0$$

where σ is the electrical conductivity, ε is the permittivity, ω is the angular frequency of the applied currents, i is the square root of -1, and Φ is the resulting electrical potential. The potential distribution is driven by an enforced current density distribution on the body surface at the electrode sites such that

$$(\sigma - i\omega\varepsilon)\hat{n} \cdot \nabla\Phi = \begin{cases} -J_{in} \cdot \hat{n} & \text{on the electrode} \\ 0 & \text{elsewhere} \end{cases}$$

where $\hat{n}$ is the outward-pointing normal direction on the body surface and J_{in} is the applied current density.

The reconstruction algorithm adopts a nonlinear optimization approach which minimizes the sum of the difference between a set of observed and calculated potentials at a finite number of surface electrodes, L, for a fixed number of applied current patterns, M, and the total variation of the electrical property distribution estimation written as

$$F(\Phi,\sigma,\omega\varepsilon) = \sum_{l=1}^{LM}\left(\Phi_l^0 - \Phi_l^c\right)\left(\Phi_l^0 - \Phi_l^c\right)^* + \left\langle \left(W_\sigma^2|\nabla\sigma|^2 + W_\varepsilon^2|\nabla\varepsilon|^2 + \gamma^2\right)^{\frac{1}{2}} \right\rangle$$

where Φ_l^0 and Φ_l^c are the observed and calculated potentials at the electrode sites; W_σ, W_ε and γ are typically small positive parameters which are determined empirically, and < > indicates integration over the image. The second term in F represents the total variation contribution to the minimization process which measures the oscillations in the property functions and does not unduly filter (i.e. smooth) discontinuities.

The minimization of F proceeds by differentiation with respect to each of the discrete parameters that comprise the σ and ωε distributions and simultaneously setting all of these relationships to zero. This nonlinear system of equations can then be solved with Newton's method using a regularized iteration

$$\left(2J^TJ + R + \lambda I\right)\Delta X = 2J^T\left(\Phi^0 - \Phi^c\right) - V$$

where ΔX is the change in property distribution vector, J is an $L \cdot M \times K$ matrix composed of the derivatives of Φ_l^c with respect to each of the K parameters forming the electrical property distribution, R is a $K \times K$ matrix having the derivatives of the total variation term, V, differentiated and distributed as

$$R = \begin{bmatrix} \dfrac{\partial V_i}{\partial \sigma_j} & \dfrac{\partial V_i}{\partial \omega\varepsilon_j} \\ \dfrac{\partial V_i}{\partial \sigma_j} & \dfrac{\partial V_i}{\partial \omega\varepsilon_j} \end{bmatrix}$$

The dual meshing concept[14] defines arbitrarily overlapping but separate meshes each having its own sampling rate. This provides a fine mesh for accurate potential solution and a courser mesh for representing the electrical property distribution, the combination of which maintains the integrity of image formation while reducing overall problem size and associated computational costs along with the amount of measured data that may be needed for image reconstruction. Spatial low-pass filtering is applied during each Newton method iteration as an averaging of the evolving σ and ωε values at each node with those of the neighboring nodes in a manner whereby the influence of the surrounding nodal values can be systematically controlled.

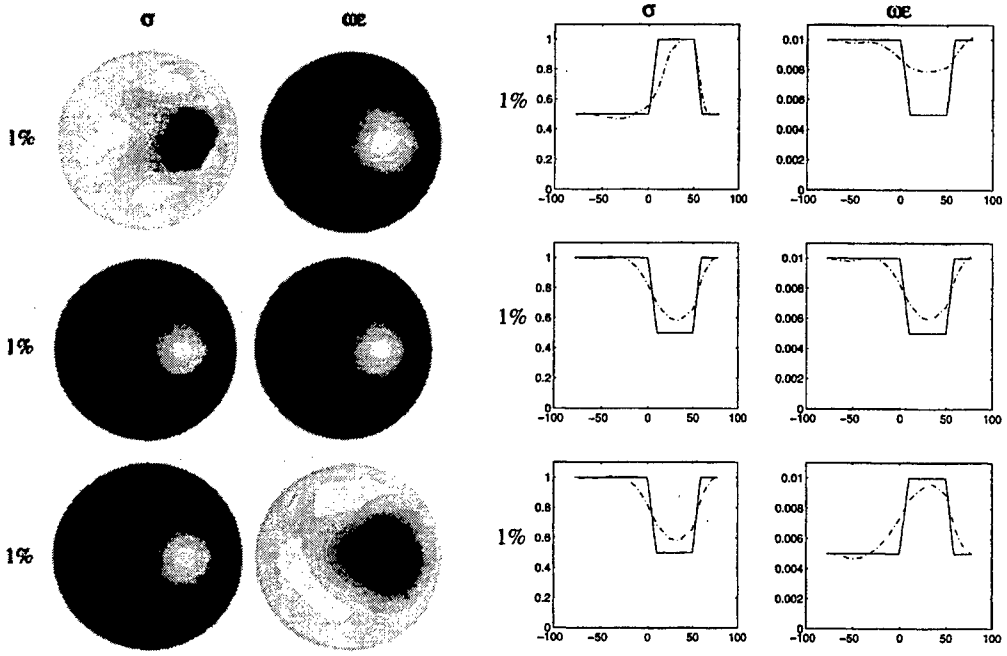

Figure 5: Electrical property image reconstructions for a two region problem in the presence of 1% noise

As an example of the image reconstruction performance attained with this approach, Figure 5 is included. In this case a two-region distribution with 2:1 and 1:2 property contrasts (ratio of background to target zone) in the conductivity and permittivity is considered. Sixteen surface electrodes have been used and a measurement noise level of 1% has been assumed. The images shown on the left in Figure 5 represent different combinations of property contrast with the background for the conductivity and permittivity. They are spatially and property-value accurate. The right-side of Figure 5 demonstrates this point by presenting profiles of the exact and recovered electrical property distributions for these images along a horizontal transect. A study of image errors for a number of similar imaging experiments has been performed as a function of noise level from 0-10%. Errors are determined as averages taken over the target zone and the background for several different property contrast arrangements. The results are impressive and illustrate that property values can be reconstructed to within 10-20% of their true values in most cases for noise levels as high as 5% or more.

More complex electrical property distributions are recovered in Figure 6 with the concomitant quantitative comparison also shown as a function of angle at a fixed radius (equal to one-half the maximum radius of the image region). Here, the electrical properties, both conductivity and permittivity, are continuously varying throughout the imaging domain with $\sigma=0.01\omega\varepsilon$ or $\sigma=0.001\omega\varepsilon$. Again, the fidelity of the images, both spatially and with respect to property values, is encouraging.

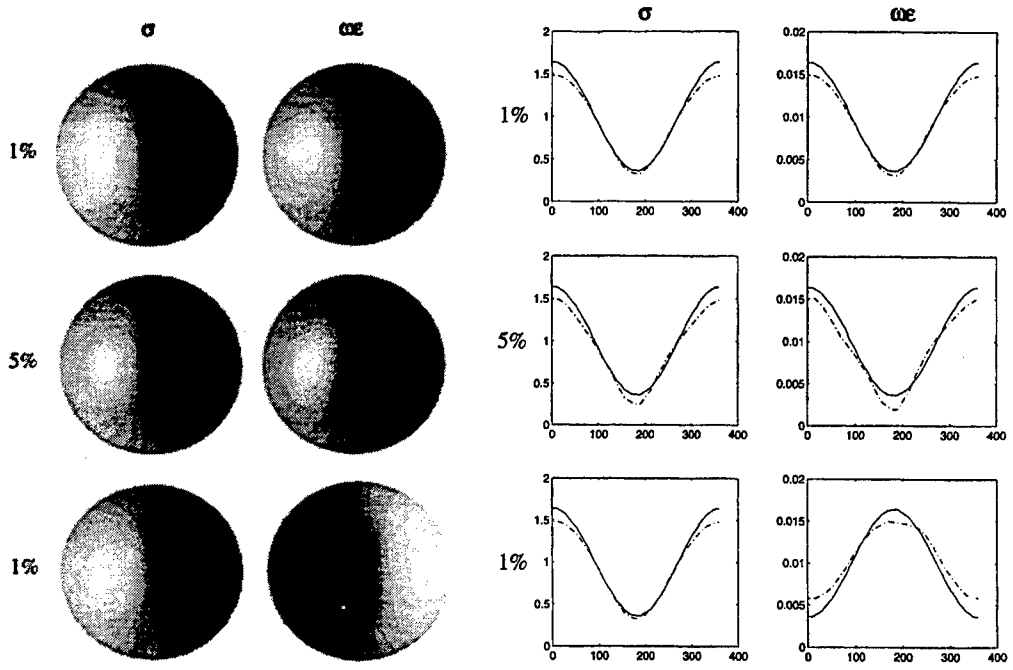

Figure 6: Electrical property images for a continuous distribution in the presence of 1% and 5% noise levels

4. THERMAL IMAGING

Thermal imaging experiments have been conducted based on simulations, phantoms and *in vivo* studies. Representative examples are presented in this section. On the simulation front, the most complex cases we have considered are those involving a CT-based pelvic tumor model where noninvasive heating by an external phased array applicator is modeled. The resulting temperature distribution is superimposed on the electrical property profile which is then adjusted continuously at the nominal rate of 2%/°C. Figure 7 presents difference images (between normothermic and hyperthermic conditions) as information that can be interpreted as thermal reconstructions. Figure 7 also shows transects through the tumor and surrounding tissue region which compare reconstructed change in electrical conductivity with exact values.

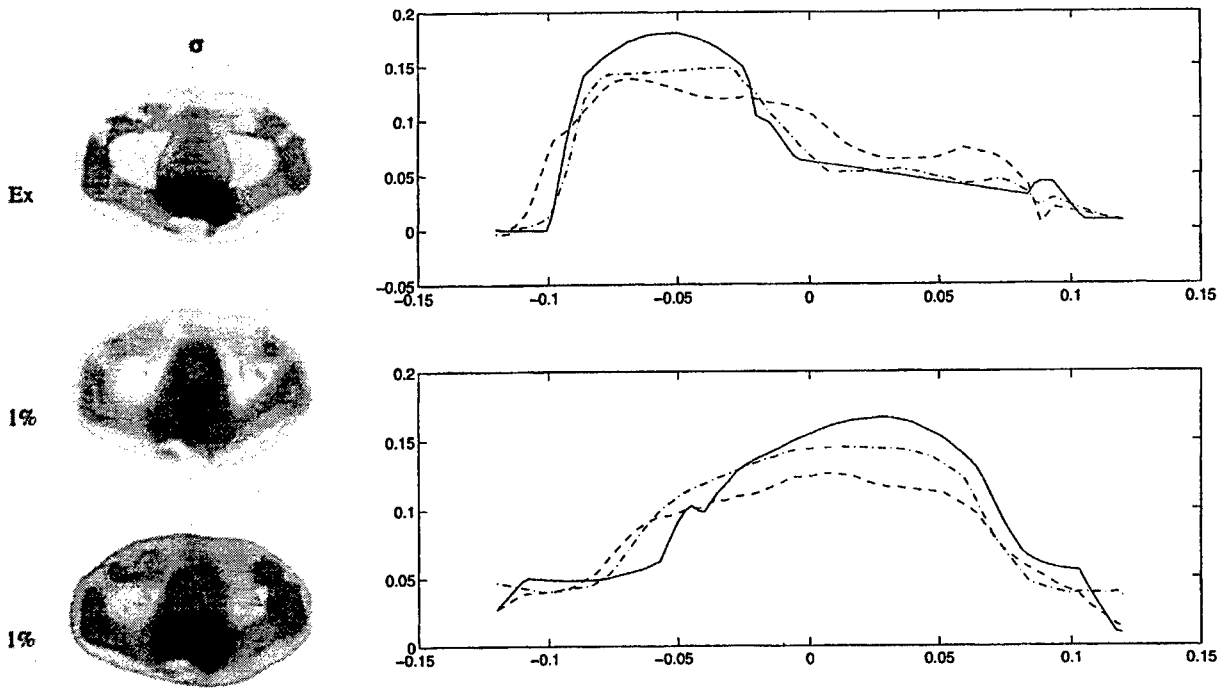

Figure 7: Thermal imaging simulations in a CT-scan model with and without *apriori* knowledge. Difference images are presented on the left (top image is exact, middle image without *apriori* knowledge, bottom image with priors) and corresponding vertical (top plot) and horizontal (bottom plot) transects on the right with (dash-dot line) and without (dashed line) priors compared to the exact distribution (solid line).

In the first reconstruction of Figure 7, no *apriori* information has been assumed about the initial electrical property distribution and noise levels of 1% have been imposed on the measurement data. Analysis of the track data in Figure 7 (right) reveals that the average temperature error is 1.2° C for this case with a maximum error of 3.4° C occurring along the horizontal transect (bottom plot). In thermal therapy delivery, pretreament image data is often available; hence, it is of interest to study the level of thermal imaging improvement that might be anticipated if *apriori* anatomical information were incorporated into the image reconstruction process. The second result in Figure 7 (bottom image) illustrates the case when the starting anatomy is known, but the initial estimates of the electrical properties are uncertain to ± 25%. Under these assumptions track data analysis (Figure 7, right: dash-dot line) shows that the average temperature error is improved to 0.66° C with a maximum error of less than 2° C.

In vivo experimental results have also been produced in both animals and human subjects. Photographs of representative situations are shown in Figure 8. In the animal experiment illustrated, the heating takes place on the thigh and is accomplished with a microwave spiral antenna operating at 433 MHz. A 32-electrode array arranged in a circumferential geometry is used to drive current and measure voltage. Electrodes were constructed using wet-etch printed circuit board techniques and were custom-sized based on pretreatment anatomical measurements. Temperature data was recorded along eight subsurface tracks with fiberoptic probes that were manually translated back and forth inside of catheters in 5 mm increments. The clinical case presented in Figure 8 consisted of a scalp tumor which was also heated with a 433 MHz microwave spiral applicator. The electrodes were designed to lie flat on the scalp in a co-planar configuration in order to be positioned around the lesion. 32 electrodes were incorporated into a flexible array which was wet-etched on a thin polyimide sheet to produce the required circuit pattern as in the animal experiments. Temperature data was recorded along two parallel tracks through the tumor region every 2-3 minutes during the course of the therapy session and for several minutes at the end of treatment once power to the heating applicator had been turned off.

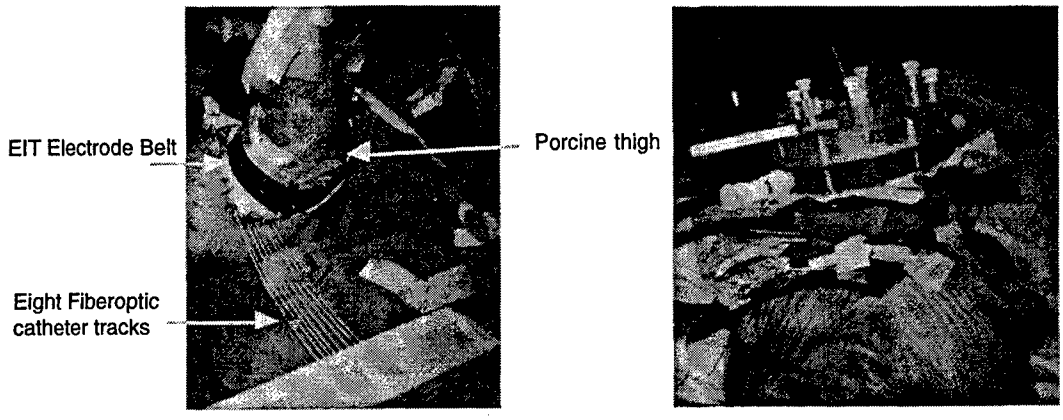

Figure 8: Photographs of typical *in vivo* imaging experiments: animal subject (left), human subject (right)

Typical results from this type of clinical heating are presented in Figure 9. Figure 9 (top) shows reconstructed difference images over the time course of heating (including after power had been terminated). There is a clear progression of heating, then cooling which takes place as evidenced by a recovered increase, then decrease in electrical conductivity relative to baseline conditions. The areas of maximal change in conductivity also correlated to regions of highest measured temperature during most of the treatment. If an assumed relationship between conductivity change and temperature rise in tissue is taken and the image conductivity maps are translated into temperature estimates using this assumed temperature coefficient, direct comparisons can be made, as illustrated in the bottom portion of Figure 9, between the images and actual

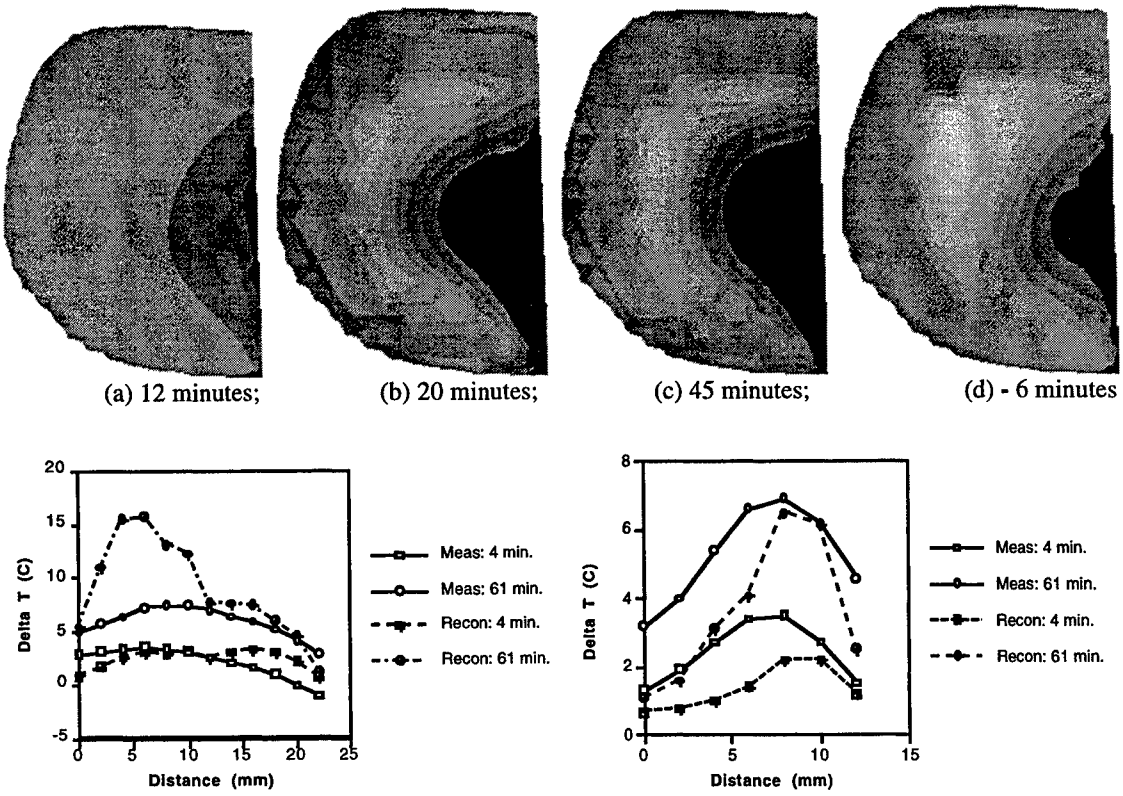

Figure 9: Difference images (top) recovered during the course of treatment at the time point indicated. Increasing temperature corresponds to conductivity increases presented as darker areas in the images. Comparison (bottom) of measured temperature values with predicted estimates along two catheter tracks in a tumor at early and late treatment time-points.

temperature measurements. Analysis of data such as that in Figure 9 has demonstrated that temperature accuracies have been approximately, 1.3° C on average, although maximum deviations can be 10° C or more. Figure 9 shows that general trends are determinable from the images; however, there are places where increasing conductivity did not translate into increasing temperature, especially at later time-points during treatment.

These results suggest that permanent change may have taken place in the heated tissue which are responsible for nonlinear behavior in the conductivity change that has been imaged. Cool down data also supports this hypothesis as the images produced some time after power is turned off (see Figure 9, for example) have conductivity distributions that do not return to their starting distribution (i.e., at the beginning of treatment) and the largest deviations from baseline correlate with those areas which sustained the most thermal dose. Data in the literature in mouse tumor models[3] also demonstrates the concept that linear variation in conductivity with temperature occurs during an initial heat-up phase in tissue, but gives way to nonlinear behavior as the amount of tissue injury from thermal exposure progresses during treatment. The idea that EIT imaging could follow this type of tissue injury progression due to thermal insult is intriguing and potentially more important and/or useful than monitoring temperature change which is, in essence, an indirect vehicle for estimating the thermal dose delivered to tissue.

5. TISSUE INJURY MONITORING

We have also been pursuing the notion that electrical impedance signatures can serve as indicators of the progression of tissue injury in other treatment settings, in particular, radiotherapy. The frequency response is critical in this regard. To illustrate this concept, we show some sample results from a study where we have used *in vivo* EIS to evaluate the progression of injury in irradiated muscle tissue. Since normal tissue is always in the radiation field and its response limits the dose that can be delivered, if the architectural integrity of the treatment site could be accurately assessed, the success rates of radiation therapy would likely increase.

Each EIS data set consists of fifty complex impedance values measured from 1 KHz to 1 MHz. Readings were obtained at 50 frequencies using a PC interfaced with a precision LCR meter. Two electrodes, mounted on the parallel arms of a caliper, applied a 0.15 mA current and measured the subsequent voltage. Recessed, 8 mm diameter platinized stainless steel and solid matrix Ag-AgCl electrodes were used. The cavities of these electrodes were filled with electrode gel and residual polarization impedances were calibrated by shorting the electrode pairs across the gel.

Animal hind legs were exposed to single does of 70, 90 and 150 Gy and followed over a 3-5 month period with measurements performed monthly. The impedance spectra obtained indicate that there are both dose and time dependent responses occurring in the tissue. Figures 9-10 illustrate representative effects. Initial shifts are most pronounced in the low frequency resistive component of the EIS signature, a change typically associated with edema or cell shrinkage. At later times and increasing doses, the tissue conductivity continues to increase and there is a significant shift in the dispersion frequency known to relate to cell membrane integrity.

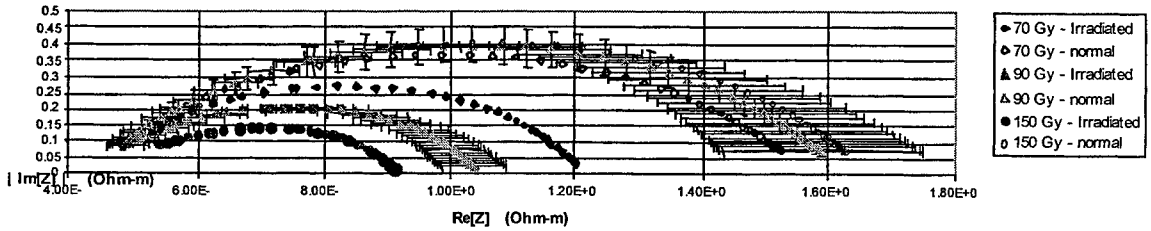

Figure10: Average impedance spectra from data collected 2 months post irradiation. Sixteen measurement sets averaged; error bars are one standard deviation

A histological grading system has been developed for independent quantification of damage. Four criterion: interstitial edema, interstitial fibrosis, muscle necrosis, and vascular damage have been evaluated. A score was assigned based on the most severe changes present in three or more 25x magnification fields with zero indicating a healthy appearance and three indicating greatest degree of change for a total possible score of twelve. All samples were scored in a single sitting without knowledge of radiation levels or sacrifice times. Representative results are presented in Table 2.

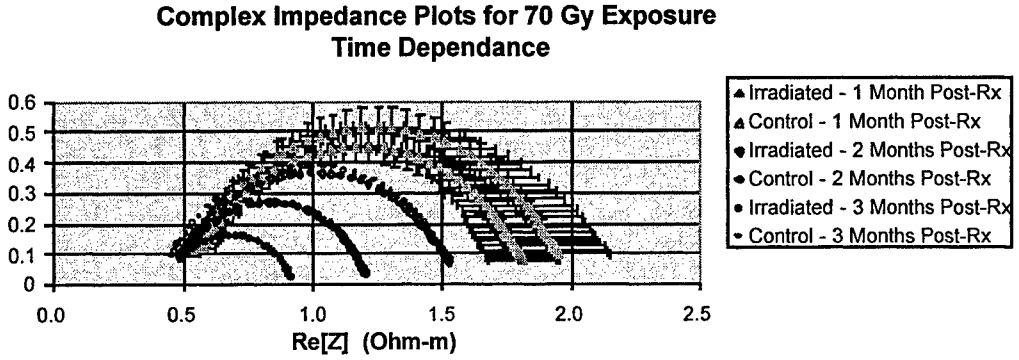

Figure 11: Time dependent response in EIS signature post radiation exposure at 70 Gy

Doses (Gy)	Vascular Damage	Muscle Damage	Interstitial Inflammation/Edema	Interstitial Fibrosis	Total Score
70	1.0	1.0	1.0	0	3.0
90	1.5	1.5	2.5	1.5	6.0
150	2.0	2.0	2.5	2.0	8.5
control	0	0	0.5	0.5	1.0

Table 2. Histopathological Scoring of Irradiated Muscle Tissue 2 months Post-Irradiation

Minimal injury is seen at the earlier times and lower doses. For example, 70 Gy at one month received a score of one while 70 Gy at two months attained a score of three. A progression of necrosis and vascular damage is observed as dose increases and post-irradiation time lengthens. In this regard, 70 Gy at three months received a score of nine. The dose/time trends seen with EIS, as illustrated in Figures 9-10, track those in the histological assessment (Table 2) and suggest that EIS has the potential to noninvasively monitor injury in irradiated tissue.

6. ACKNOWLEDGMENTS

This work was supported in part by NIH grant number R01 CA64588 awarded by the National Cancer Institute.

7.REFERENCES

1. M.S. Hawley, J. Conway, H. Amasha, Y.F. Mangnall, and G.C. Van Rhoon, "Electrical impedance tomography: prospects for non-invasive control of deep hyperthermia treatments", *Frontiers in Medical and Biological Engineering,* **4**, pp. 119-128, 1992.
2. K.D. Paulsen, M.J. Moskowitz, T.P. Ryan, S.E. Mitchell, and P.J. Hoopes, "Initial in vivo experience with EIT as a thermal estimator during hyperthermia", *International Journal of Hyperthermia,* **12**, pp. 573-591, 1996.
3. D.A. McRae and M.A. Esrick, "Deconvolved electrical impedance spectra track distinct cell morphology changes, *IEEE Transactions on Biomedical Engineering,* **43**, pp. 607-618, 1996.
4. H. Griffiths and J. Jossinet, "Bioelectric tissue spectroscopy from multi-frequency EIT, *Physiological Measurements*, **15**

(Supplement 2A), pp. 29-35, 1994.

5. H. Griffiths "Tissue spectroscopy with electrical impedance tomography: computer simulations, *IEEE Transactions on Biomedical Engineering,* **42**, pp. 948-954, 1995.
6. K.S. Osterman, K.D. Paulsen, J.P. Hoopes, and A. Hartov, "In vivo Electrical Impedance Spectroscopy of Irradiated Muscle Tissue", *Proceedings of the 19th Annual International Conference of the IEEE Engineering in Medicine and Biology Society, Chicago, IL*, pp. 2512-2515, 1997.
7. F.A. Duck, "Physical Properties of Tissue: A Comprehensive Reference Book (London: Academic Press) 1990.
8. M.J. Moskowitz, K.D. Paulsen, T.P. Ryan, and D. Pang, "Temperature field estimation using electrical impedance profiling methods: II. experimental system description and phantom results, *International Journal of Hyperthermia,* **10**, pp. 229-245, 1994.
9. M.J. Moskowitz, T.P. Ryan, K.D. Paulsen, and S.E. Mitchell, "Clinical implementation of electrical impedance tomography with hyperthermia, *International Journal of Hyperthermia,* **11**, pp. 141-149, 1995.
10. C.S. Koukourlis, G.A. Kyriacou, and J.N. Sahalos, "A 32-electrode Data Collection System for Electrical Impedance Tomography" *IEEE Transactions on Biomedical Engineering*, **42-6**, pp. 632-636, 1995.
11. R.W.M. Smith, I.L. Freeston, and B.H. Brown, " A Real-Time Electrical Impedance Tomography System for Clinical Use - Design and Preliminary Results", *IEEE Transactions on Biomedical Engineering*, **42-2**, pp. 133-140, 1995.
12. R.D. Cook, G.J. Soulnier, D.G. Gisser, J.C. Goble, J.C. Newell, and D. Isaacson, "ACT3: A High-Speed, High-Precision Electrical Impedance Tomograph, *IEEE Transactions on Biomedical Engineering*, **41-8**, pp. 713-722, 1994.
13. K.D. Paulsen, H. Jaing, "An Enhanced Electrical Impedance Imaging Algorithm For Hyperthermia Applications, *International Journal of Hyperthermia*, **13**, pp. 459-480, 1997.
14. K. D. Paulsen, P. M. Meaney, M. J. Moskowitz, J. M. Sullivan, Jr., "A dual mesh scheme for finite element based reconstruction algorithms", *IEEE Trans. on Med. Imag.*; **14**, pp. 504-514, 1995.

SESSION 6

Modeling of Therapeutic Devices

Finite Element Model for Endometrial Ablation Systems

Thomas P Ryan[a], Robert C Platt[a], Stanley Humphries[b]

[a]Valleylab, Boulder, CO, 80301, USA
[b]Field Precision, Albuquerque, NM, 87192, USA

ABSTRACT

Ablation of the endometrium has become a viable treatment for dysfunctional bleeding of the uterus in women. Surgical applications of thermal ablation utilized a rolling electrode to ablate the inner uterine lining, but required practiced surgical skills and made it difficult to assess subsurface damage. Recently, various energy systems have been applied to the endometrium such as lasers, microwaves, RF electrodes, hot water balloons, and cryotherapy. A finite element model is presented to compare a multi-electrode, multiplexed RF device with a balloon containing hot fluid. The temperature fields in the uterine wall are plotted over time for various blood flow values. Assumptions of constant electrical conductivity are compared to temperature-dependent electrical conductivity. Temperatures are shown to be a maximum of about 10-20°C higher when varying electrical conductivity is used. Results are also shown for cases with a 2 mm blood vessel in the field and how each device adjusts its operation to compensate for this heat sink. Damage integral results will be shown according to the time and temperature of the treatments.

Keywords: finite element model, radio frequency, endometrial ablation, uterus, dysfunctional bleeding

1. INTRODUCTION

Dysfunctional uterine bleeding has been a common problem for women throughout the world. The choices for women are limited: hysterectomy or removal of the uterus, medical treatment that induces a peri-menopausal state, or living with the discomfort. The bleeding originates in the endometrium, the inner layer of the uterus. If proper transcervical access is attained using small endoscopes (hysteroscopes), the endometrium becomes accessible. A recent surgical treatment performed under video guidance has been to apply radiofrequency (RF) energy to a rolling ball for ablation of the endometrium. By ablating the endometrium, it is possible to stop or at least reduce the bleeding so that women can lead a more normal life. Unfortunately, the complex geometry of the endometrial surface combined with the lack of assessment of deep thermal damage with superficial observation in a 2-D scope system make rollerball ablation dependent on the skill of the user.

Recently, there have been several attempts at applying heat treatments for thermal ablation in an office-based procedure that does not require surgery. This treatment is composed of utilizing either a hot fluid filled balloon for conductive heating or RF patches on the outside of a balloon to make contact with the endometrial wall. The latter applies RF energy and deposits power in the superficial layers of the endometrium. The target depth of ablation is approximately 5 mm. Due to the wide variety of parameters that effect heating, a finite element model was created to predict temperature distribution and extent of thermal damage in the uterus. Some of the parameters studied include blood flow, heat source temperature, type of heat source, heat application time, blood vessel presence, and temperature dependent electrical properties and perfusion. The paper will develop two numerical models for a conductive and an RF heating system for treatment of the endometrium based on the bioheat equation (Pennes 1948).

Lesions produced by RF ablation are thermal and depend on the temperature distribution resulting from the electric field distribution in the tissue layers. Although other works in the literature have modeled heating in tissue, the temperatures achieved were in the hyperthermia range of 40-55°C (Strohbehn 1983, Paulsen et al. 1993, Mechling et al. 1992, Ryan 1993), typically with temperatures limited to 45°C maximum (Strohbehn 1983). This limit simplifies the model somewhat since the initial thermal and electrical properties of tissue remain substantially constant. Our target temperature for tissue is in the range of 60-110°C, where tissue desiccates and electrical properties change substantially and non-linearly (Dadd et al. 1996). In addition, if temperatures exceed 41°C, damage to living tissue is a function of both temperature elevation and

SPIE Vol. 3249 • 0277-786X/98/$10.00

duration of exposure (Sapareto and Dewey, 1984). This is also characterized in the damage integral (Henriques 1947) which easily handles higher temperatures.

Since values of conductivity with changing temperatures for the tissues of interest for this model at 500 kHz were not available, we proceeded to measure the electrical conductivity over time at various temperatures as input to the model. Other works that assume changes in conductivity with temperature, assume that conductivity increases 2%/°C (Schwan and Foster, 1980), up to 100°C (Labonte 1994).

Having a blood flow or perfusion term in the model, especially one that can be varied with time or temperature is important. The tissue perfusion term is rate of mass flow of blood per unit mass of tissue. Flow is considered to occur at the capillary level and due to the convoluted nature of these capillary beds, causes it to be non-directional (Patel et al. 1987). Blood perfusion is also a temperature dependent function that can be rescaled due to tissue reaction to heating which will increase flow in normal but not in pathologic tissue, and decrease due to desiccation and capillary shutdown. In addition, our own experiments showed that blood coagulates at 60°C.

2. SIMULATION OF ENDOMETRIAL TREATMENT DEVICE

Modeling code was developed (Humphries et al. 1997, Ryan et al. 1997) and allowed thermal and electrical properties to vary with temperature, time or location. It was able to simulate both RF devices that deposit power in tissue and purely conductive heating devices. It was based on the bioheat equation (Pennes 1948) as shown below:

$$\rho_t(r,T)\, c_t(r,T)\, \partial T(r,t)/\partial t = \nabla\,(k_t(r,T)\,\nabla T) - c_b(T)\,\rho_b\, m(r,T)\,\rho_t\,(T - T_b) + Q_p\,(r,t) + Q_m$$

$\rho_{t,b}$ = *density of tissue, blood (kg/m^3)*
$c_{t,b}$ = *specific heat of tissue, blood (W s/kg/°C)*
k_t = *thermal conductivity (W/m/°C)*
m = *perfusion (flow rate of blood/unit mass tissue) (m^3/kg s)*
Q_p = *power absorbed/ unit volume tissue (W/m^3)*
Q_m = *metabolic heating/ unit volume of tissue (W/m^3)*
T = *temperature (°C)*
t = *time (s)*
Q_m *is assumed to be small and is neglected.*

3. DAMAGE INTEGRAL FOR THERMAL DOSE ASSESSMENT

The damage integral designates areas of both reversible and irreversible damage as heat is applied (Henriques 1947). It is a function of both time and temperature. Our model plots the damage integral results over a range of levels for application to different tissue types with varying levels of sensitivity.

$$\Omega = P \int_0^t e^{-\Delta E/RT}\, dt$$

where

Ω = *thermal damage function*
where $\Omega \geq 1.0$ *(irreversible damage);*
and $\Omega \leq 0.5$ *(reversible damage)*
P = *constant (s^{-1})*
ΔE = *activation energy (J mol^{-1})*
R = *ideal gas constant (J mol^{-1} K^{-1})*
T = *time dependent temperature (K)*
t = *time (s)*

4. MODEL OF RF AND CONDUCTIVE HEATING DEVICES

Two devices presently in clinical trials were modeled. The device requirements for treatment are to heat and ablate the endometrium, the inner lining of the uterus, with a single application of heat in under 10 minutes. A cross section of the RF device as modeled in two-dimensions is shown in Figure 1. The silastic membrane in Figure 1 has electrodes composed of copper patches, each with a central thermistor in contact with tissue. The electrodes are mounted on an air filled membrane which when inflated may lower perfusion in adjacent tissue. RF current is multiplexed among the electrodes which share a common return electrode mounted elsewhere on the body. The thermistors in the center of each electrode are controlled to 72 or 75°C for four minutes, after a one minute heatup.

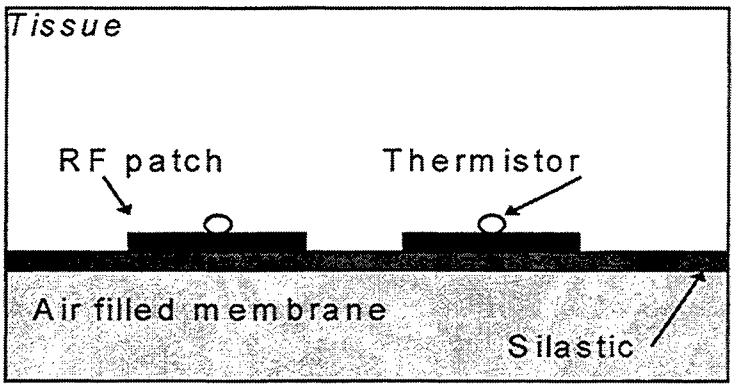

FIGURE 1
DIAGRAM OF MODEL OF RF ENDOMETRIAL ABLATION TREATMENT DEVICE

In order to characterize electrical conductivity in our laboratory, we performed heating tests while measuring electrical conductivity at 500 kHz to gage the effects of thermal dose (Dadd et al. 1996). There were no tissue results in the literature at this frequency. Attempts to heat tissue beyond 90°C resulted in severe tissue shrinkage, causing unreliable endplate electrode contact and producing artifactual readings.

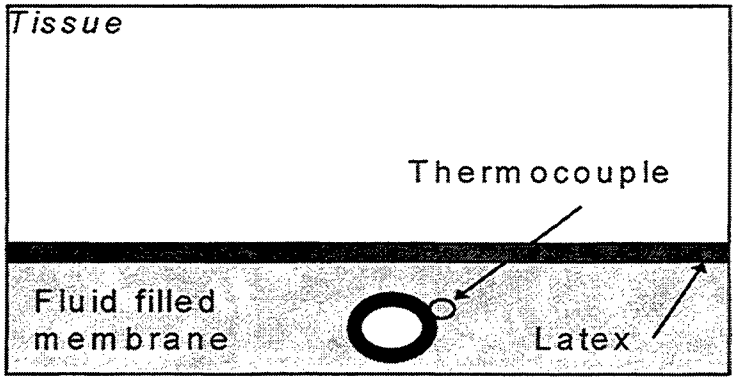

FIGURE 2
DIAGRAM OF MODEL OF CONDUCTIVE ENDOMETRIAL ABLATION TREATMENT DEVICE

Figure 2 is a model of a conductive endometrial ablation device. The central heater is held at 87°C, as measured by a thermocouple affixed to the wall of the heater. The fluid carries the heat to the tissue through the balloon wall. The heater takes one minute to reach target temperature and is then held constant at 87°C for eight minutes.

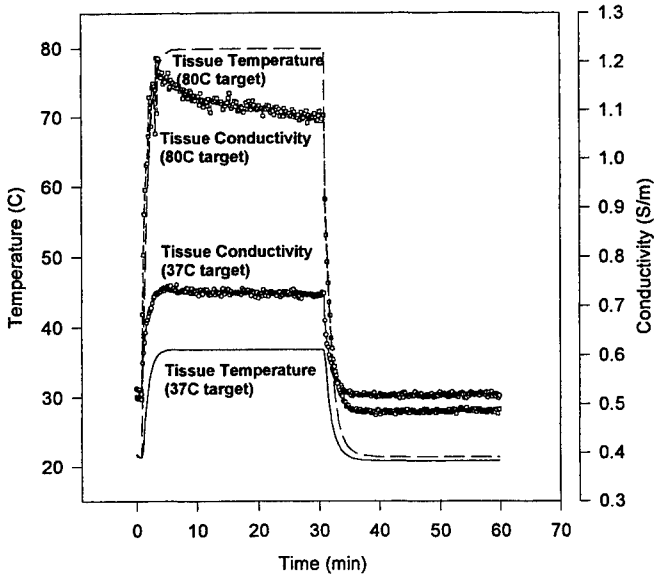

FIGURE 3

CONDUCTIVITY EXAMPLES OF TWO SAMPLES HEATED TO 37°C AND 87°C.

Figure 3 shows the effects of heating muscle tissue for 30 minutes at either 37°C (normothermic body temperature) or 80°C. After heating, the tissue was rapidly cooled to the baseline temperature and electrical conductivity carefully monitored. Baseline conductivities were nearly the same until rapid heating caused an increase in conductivity. The normothermic sample retained its conductivity whereas the 80°C sample decreased in conductivity over the time interval. As expected, the conductivity for the 37°C sample resumed baseline values when the sample returned to starting temperature. However, the sample heated to 80°C when cooled to baseline, decreased in conductivity about 0.14 S/m, suggesting irreversible damage

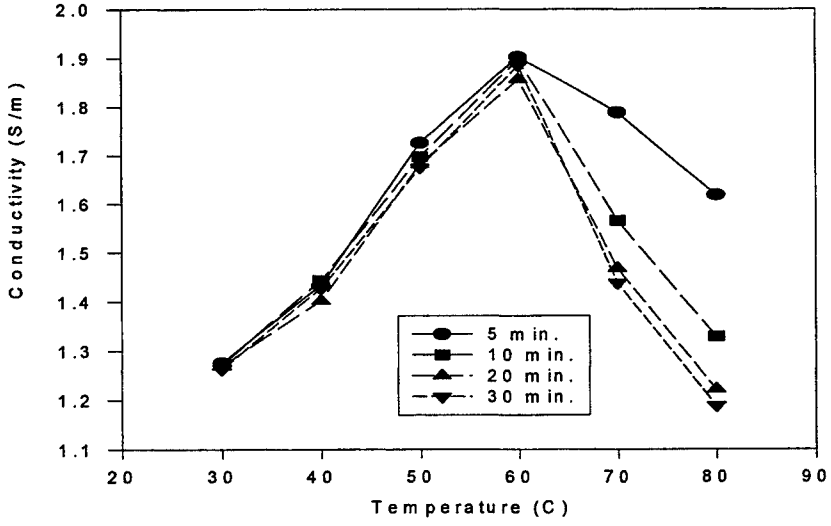

FIGURE 4

PLOT OF CHANGES OF CONDUCTIVITY IN MUSCLE OVER TIME

Figure 4 shows a family of curves for conductivity vs. temperature over a range of time intervals. It is noted that at 60°C and below, tissue conductivities are not time dependent. However, at 70 and 80°C, there is an obvious change in conductivity with the conductivity continuing to decrease with time. Overlap among the various time points is seen until a breakpoint at 60°C, with divergence of the curves at higher temperatures.

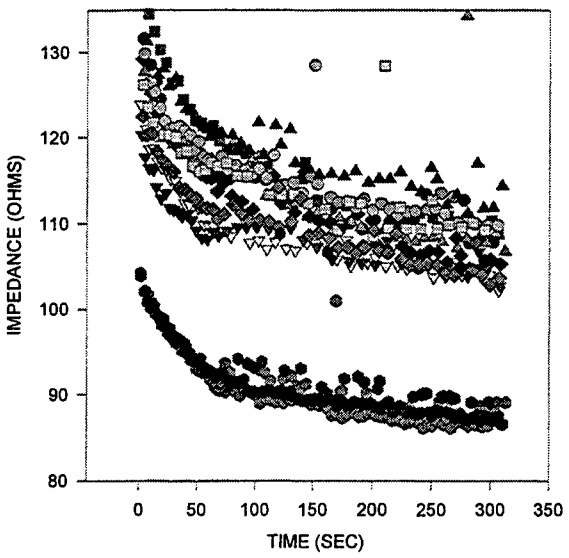

FIGURE 5

MEASURED IMPEDANCE OF THE 12 RF ELECTRODES DURING PATIENT TREATMENT.

Figure 5 shows impedances measured during a patient treatment. Each curve represents data taken at an electrode site in contact with tissue during RF heating of the endometrium. The curves with lower impedance starting values are due to two electrodes which are larger in area. As the electrode-tissue interface is heating during the first 60 s, impedance decreases as expected. In the first 60 s, power is continuously on until the target temperature of 72 or 75°C is reached. During the next four minutes, power is controlled such that temperatures begin to level off. All channels decreased in resistivity with increased temperature.

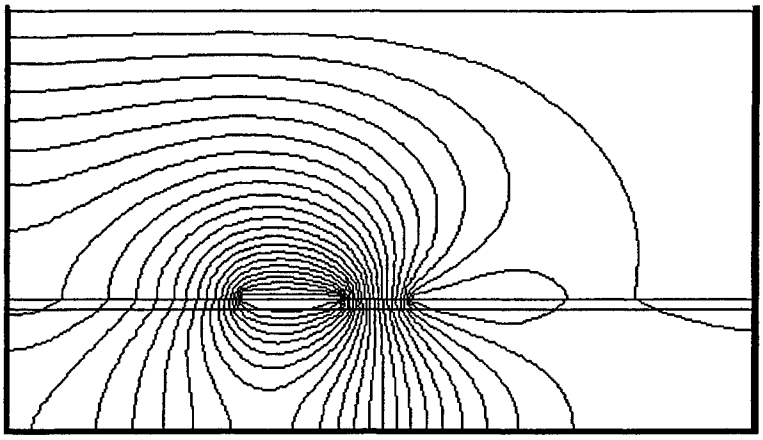

FIGURE 6

THE PLOT OF CONSTANT POTENTIAL OF A SINGLE ELECTRODE ENERGIZED OF AN ELECTRODE PAIR IN TISSUE.

Figure 6 shows lines of constant potential. Since the system is multiplexed, only a single electrode is on. The right hand electrode reshapes the electric field of the left electrode. Note the intensity in the gap between the electrodes. The electrodes are 8 mm width separated by 6 mm.

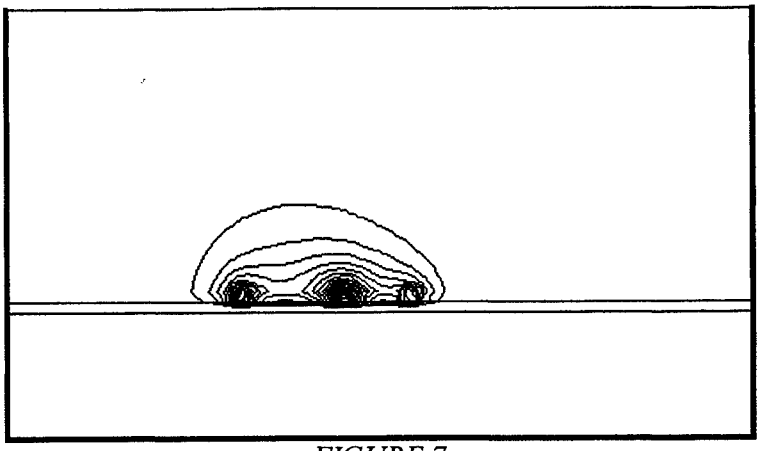

FIGURE 7

THE POWER DENSITY OF A SINGLE ELECTRODE ENERGIZED OF AN ELECTRODE PAIR IN TISSUE.

Figure 7 shows the power deposition of a single electrode in a multiplexed system. The electrodes alternate being energized, each on for 0.5 s. The left electrode is the only electrode energized in this simulation. The influence of the right electrode is easily visualized. The electrodes are 8 mm width separated by 6 mm.

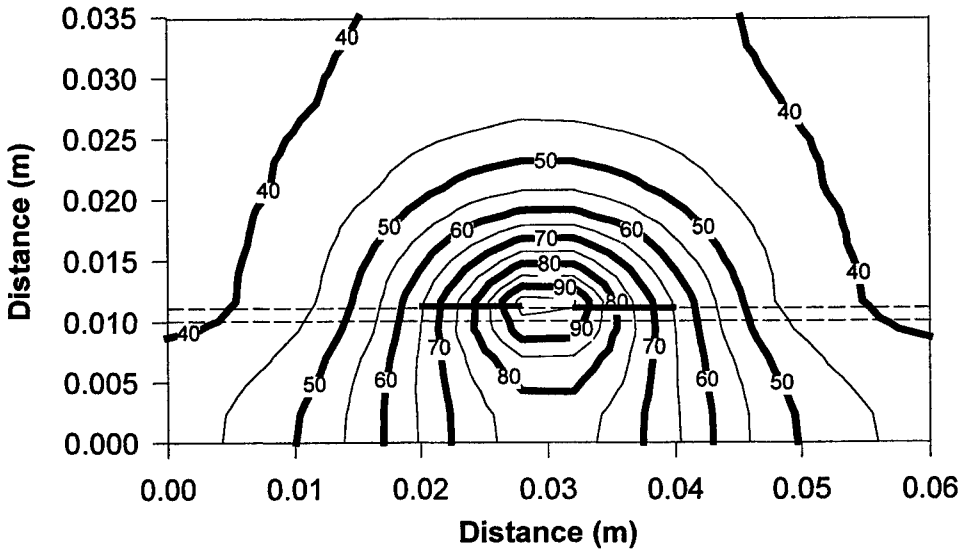

FIGURE 8

TWO ELECTRODES HEATING PERFUSED TISSUE AT 300 SECONDS

Both electrodes are multiplexed and controlled such that the central electrode temperatures are maintained at 75°C. Perfusion is constant at 3.34 kg/m^3/s . The electrodes are 8 mm width separated by 6 mm. The dashed lines demarcate the insulating silicone layer with air filling the interior below the silicone. The electrodes ride on this layer as shown by the horizontal lines. Note the outer uterine wall achieves 40°C. Electrical conductivity was a function of temperature.

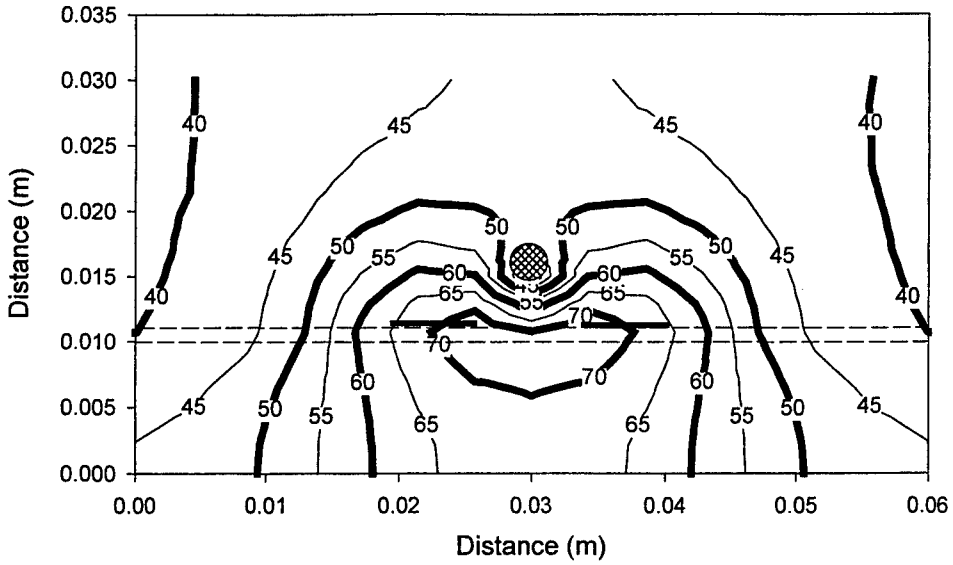

FIGURE 9

TEMPERATURE DISTRIBUTION FOR A PAIR OF RF ELECTRODES WITH A 2 MM VESSEL

The temperature distribution is shown in Figure 9 for a block of tissue containing a 2 mm diameter vessel. Between the dashed lines lies the layer of silicone. The two electrodes are represented by the short horizontal lines. The electrodes are 8 mm width separated by 6 mm. Temperature is controlled to 75°C at the center of each electrode. The target temperature is achieved in 60 s and held for an additional 4 minutes. The perfusion is 3.34 kg/m^3/s. There is a 2 mm vessel denoted by the shaded circle.

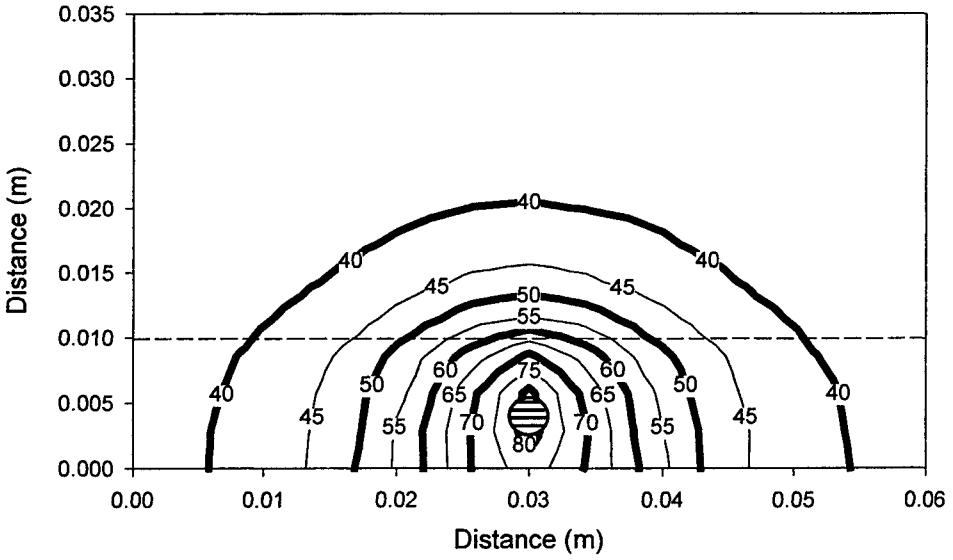

FIGURE 10

TEMPERATURE RESULTS FROM A CONDUCTIVE SOURCE AT 8 MINUTES

Figure 10 shows results from a hot source with 1 minute of heatup and 8 minutes of steady state as measured at the hot source which is held at 87°C. Perfusion is 3.34 kg/m^3/s. The dashed line demarcates a latex membrane, below which is a fluid filled balloon with the conductive heater.

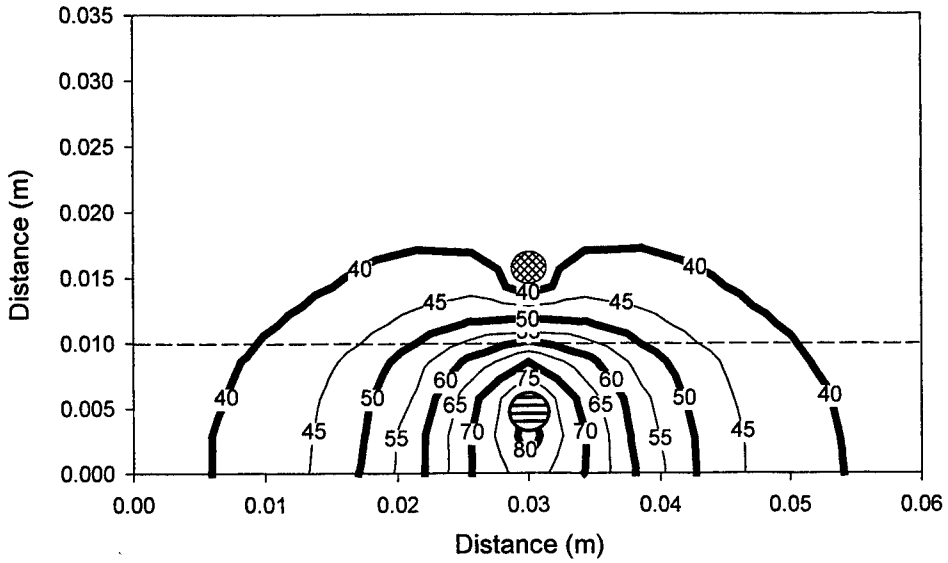

FIGURE 11

TEMPERATURE DISTRIBUTION WITH A CONDUCTIVE HEATER IN FLUID INFLUENCED BY A BLOOD VESSEL

Figure 11 shows the temperature distribution as in Figure 10, but with a 2 mm blood vessel embedded in tissue. Note the influence on the temperature distribution. Perfusion is 3.34 kg/m^3/s. Heating is for 8 minutes, following a one minute heatup to 87°C at the hot source.

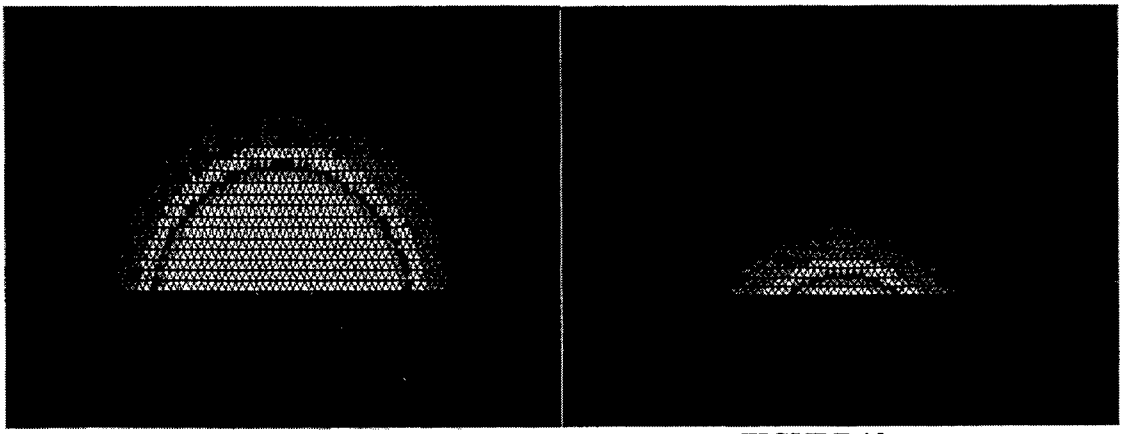

FIGURE 12

FIGURE 13

Figure 12 shows the prediction of the damage integral a pair of RF electrodes on an air filled balloon. Electrical conductivity is a function of temperature. The lower, non-shaded portion represents the balloon as shown in Figure 1. The various shaded represent the predictions of the damage integral depending on the sensitivity of the tissue. The inner zone represents irreversible damage. The outer layer represents the zone of reversible damage.

Figure 13 shows results of the damage integral of the conductive heating device as shown in Figure 2. The shading of zones of damage is of equal value to Figure 12. Perfusion in both figures is 3.34 kg/m^3/s.

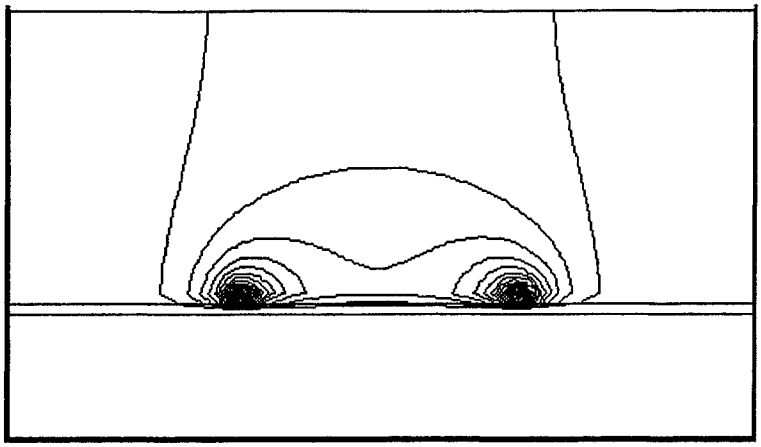

FIGURE 14

POWER DENSITY FOR RF HEATING WITH ONE LARGE ELECTRODE IN TISSUE

Figure 14 shows the power density for a single large electrode replacing the two electrodes in previous examples. The ends of the previous electrodes are now the ends of the new electrodes with the gap being spanned. The end effects at the electrode ends due to the discontinuities are the locations of concentrations of power. This figure shows much broader power deposition than a single electrode shown in Figure 7. The electrode width is 20 mm.

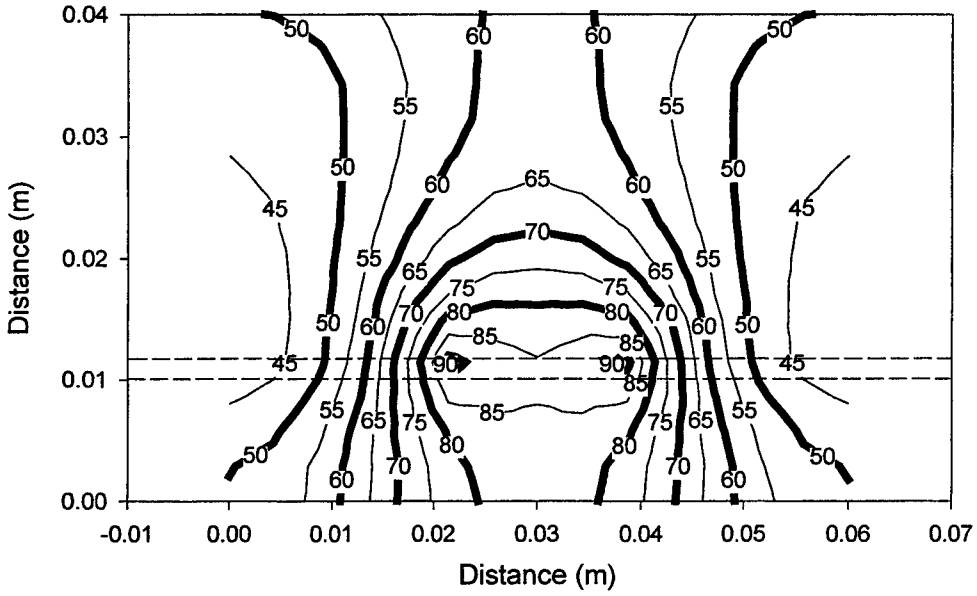

FIGURE 15

TEMPERATURE DISTRIBUTION FOR MULTIPLE SMALL ELECTRODES

Figure 15 shows the temperature distribution for tissue with 5 small RF electrodes replacing the pair found in Figure 1. The electrodes are 2 mm width and spaced by 2 mm. All electrodes are energized simultaneously. The penetration is significantly changed relative to the paired electrodes seen previously. The center of the electrode array is held to 75°C during one minute heatup and four minute hold. Perfusion is 3.34 kg/m^3/s.

6. DISCUSSION

We have shown that when heating beyond 60°C the electrical conductivity of tissue changes enough to make a visible difference in the predicted temperature distribution. Thus, a versatile model should have the capability of inputting changing tissue parameters when temperatures are high enough to affect results and thus will better predict tissue thermal events in biological systems. Trends show that as temperature rises, conductivity increases, but not exactly as 2%/°C (Schwan and Foster, 1980) estimates predict. Conductivity values for muscle tissue actually decreased over time at 70°C and above. Thermal doses of time and temperature affect various tissues differently, however, depending on the temperature level, the tissue could be irreversibly altered. These results agree with work at lower frequencies (Moskowitz et al. 1995) that demonstrated the effects of irreversible damage. Only at lower temperatures in our study did tissue samples return to baseline values and show complete reversibility due to lack of damage by the thermal dose. Lastly, since the damage integral is built into the code, we can track estimates of irreversible tissue damage due to the thermal history at each location in the mesh.

The development of the devices shown here can be greatly aided by numerical simulations that allow parameter changes such as material thicknesses, heat source temperatures, device dimensions, and others. The design process may be sped up by letting the model compare various designs prior to prototyping and bench testing. Modeling can help guide us to a few good design concepts that we can test. Hopefully, application of a good model may reduce time to commence clinical trials and make the devices available to the medical treatment community so that patients can ultimately benefit.

In both the RF and conductive heating designs, the simulations are useful in designing the dimensions of the products. In the conductive heating system, the model will help predict the extent of thermal damage if the time or control temperature is changed. If the balloon thickness or material is changed, the model can show the differences in outcome. If the tissue is pathological and has different thermal properties or perfusion, these can be input. For the RF balloon, the model can assist in sizing the electrodes and spacing them apart from one another, as well as choosing the number and how they are multiplexed. Changing the set point temperatures can be modeled. If the system was bipolar such that current only traveled between electrodes, the model can easily simulate this type of device.

7. ACKNOWLEDGMENTS

This work was supported by Valleylab. Special acknowledgment to Jeff Dadd for doing initial tissue testing.

8. REFERENCES

1. J.S. Dadd, T.P. Ryan, and R. Platt, "Tissue impedance as a function of temperature and time," *Biomedical and Scientific Instrumentation,* **32**, pp. 205-14, 1996. .
2. F.C. Henriques, "Studies of thermal injury," *Archives of Pathology,* **5**, pp. 489-502, 1947.
3. S. Humphries, R.C. Platt, T.P. Ryan, "Finite-element codes to model electrical heating and non-linear transport in biological media", Advances In Heat And Mass Transfer In Biotechnology, **HTD-Vol. 355/BED Vol.37**, pp 131-134, 1997.
4. S. Labonte, "Numerical model for radio-frequency ablation of the endocardium and its experimental validation," *IEEE Transactions on Biomedical Engineering,* **41**, pp. 108-115, 1994.
5. J.A. Mechling and J.W. Strohbehn, "Three-dimensional theoretical SAR and temperature distributions created in brain tissue by 915 and 2450 MHz dipole antennas with varying insertion depths," *International Journal of Hyperthermia,* **8**, pp. 529-542, 1992.
6. M.J. Moskowitz, T.P. Ryan, K.D. Paulsen, and S.E. Mitchell, "Clinical implementation of electrical impedance tomography with hyperthermia," *International Journal of Hyperthermia,* **11**, pp. 141-149, 1995.
7. P.A. Patel, J.W. Valvano, J.A. Pearce, S.A. Prahl, C.R. Denham, "A self-heated thermistor technique to measure effective thermal properties from the tissue surface" Trans ASME: **109**, pp. 330-335, 1987.
8. K.D. Paulsen, X. Jia, and J.M. Sullivan, "Finite element computations of specific absorption rates in anatomically conforming full-body models for hyperthermia treatment analysis," *IEEE Transactions on Biomedical Engineering,* **40**, pp. 933-945, 1993.
9. H.H. Pennes, "Analysis of tissue and arterial blood temperatures in the resting human forearm," *Journal of Applied Physiology,* **1**, pp. 93-122, 1948.
10. T.P. Ryan, "Methods of thermal modelling and their impact on interstitial hyperthermia treatment planning", *Medical Radiology-Diagnostic Imaging and Radiation Oncology: Interstitial and Intracavitary Thermo-Radiotherapy*, HM Seegenschmiedt and R Sauer, eds, Springer-Verlag, Berlin, 1993, pp. 95-116, 1993.
11. T.P. Ryan, R.C. Platt, J.S. Dadd, S. Humphries, "Tissue electrical properties as a function of thermal dose for use in a finite element model", Advances In Heat And Mass Transfer In Biotechnology, **HTD-Vol. 355/BED Vol.37**, pp 167-171, 1997.
12. S.A. Saparetto and W.C. Dewey, "Thermal dose determination in cancer therapy," *International Journal of Radiation Oncology, Biology and Physics,* **10**, pp. 787-800, 1984.
13. H.P. Schwan and K.R. Foster, "RF-field interactions with biological systems: electrical properties and biophysical mechanisms", *Proceedings of the IEEE,* **68**, pp. 104-113, 1980.
14. J.W. Strohbehn, "Temperature distributions from interstitial RF electrode hypothermia systems: theoretical predictions," *International Journal of Radiation Oncology, Biology and Physics,* **9**, pp. 1655-1667, 1983.

Further author information:
TPR Email: tryan@fortnet.org TEL:303-581-6752; FAX 303-530-6277
RCP Email plattrcjr@aol.com
SF Email fieldp@rt66.com

The effect of vessel architecture on fusion by radio frequency current

John Pearce* and Sharon Thomsen**

* Biomedical Engineering Program, The University of Texas at Austin
Austin, TX 78712

** Laser Biology Research Laboratory
University of Texas/M.D. Anderson Cancer Center, Houston, TX 77030

ABSTRACT

Sealing and fusion of vessels by electrosurgical current is strongly influenced by the inhomogeneous architecture of the tissue constituents, particularly in the large arteries. Inhomogeneities in electrical properties of the constituents, specifically smooth muscle, collagen and elastin, lead to sharp spatial gradients in volumetric power deposition which results in uneven heating. The mechanical properties of the various tissue constituents are also of considerable importance. Vessel collagen and elastin distribution varies from vessel to vessel, species to species in the same artery, and point to point in the same vessel of the same animal or person. We present histologic evidence of vascular constituent variations, measurements of germane tissue electrical properties and numerical model studies of their effect on local heating rates and temperature rise in geometrically realistic finite difference vessel models. Comparisons between predicted and measured damage boundaries showed favorable agreement.

Keywords: electrosurgery, vessel sealing, tissue fusion, vessel architecture, numerical models

1. INTRODUCTION

Since the early 1930's electrosurgical current at radio frequencies (RF) between 500 kHz and 5 MHz has been used to cut fuse, seal or coagulate resected and transected blood vessels. Common surgical wisdom holds that sealing vessels larger in diameter than about 2mm is better accomplished with staples or ligatures, whether artery or vein. We have experimented with various temperature control strategies in order to seal larger vessels [1, 2] and have been frequently frustrated by apparently random failures, particularly in larger arteries. Histologic studies of vessels reveal significant species-dependent differences in the spatial distribution of the vessel constituents (vascular architecture) of analogous vessels; and significant architectural differences from location to location along the same vessel in the same species, particularly in the large arteries. These variations, both in the electrical and mechanical senses, are the likely source of most of the randomness in the outcomes.

Collagen alteration is apparently an important prerequisite to successful tissue fusion, [3,4,5, 6, 7] and, by analogy, in the vessel sealing process. Electron microscopic (EM) studies suggest that the fusion process in blood vessels may be dominated by random re-entwinement of thermally dissociated adventitial collagen fibrils (Type I) during the end stage heating and early cooling phases [6]. Successful welds have been experimentally obtained in many tissues[7] as well as vessels[8]; and we have also obtained successful seals [9, 10]. Yet, the thermodynamics of vessel sealing by RF current remain to be investigated. We have studied the governing processes in geometrically and electrically accurate finite difference method (FDM) numerical models.

2. COMPARATIVE VESSEL ARCHITECTURE

Tissue specimens studied included: 1) canine carotid and femoral arteries, femoral veins, and 2) bovine *dura mater* and *ligamentum nuchae*. The tissue specimens were fixed by immersion in 10% neutral buffered formalin. After dehydration in graded alcohols and xylenes, the specimens were embedded in paraffin. Serial 5 μm sections were stained with Weigert-vanGieson elastin stain, and Mallory's trichrome stain.

Two sections of the canine carotid artery are shown in Figure 1. The specimen shown in Figure 1a was collected near the origin of the carotid artery at the aorta and the specimen in 1b is from the middle of the common carotid.

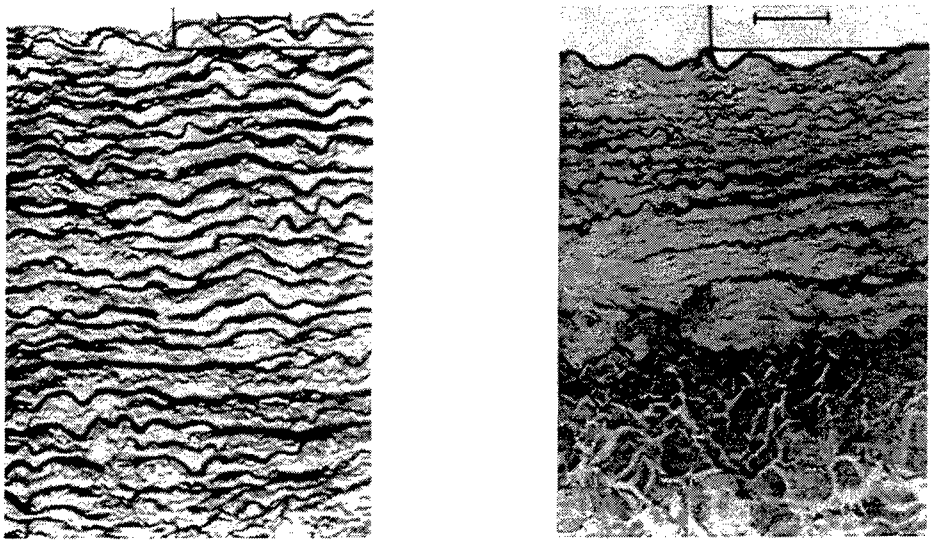

(a) (b)

Figure 1. Proximal Carotid Artery (a) and Middle Carotid Artery (b). The elastin is black, the collagen, medium gray, and vascular smooth muscle, light gray. The intimal (lumenal) surfaces are at the top of the illustrations. [Elastin Stains. Bar = 62 microns]

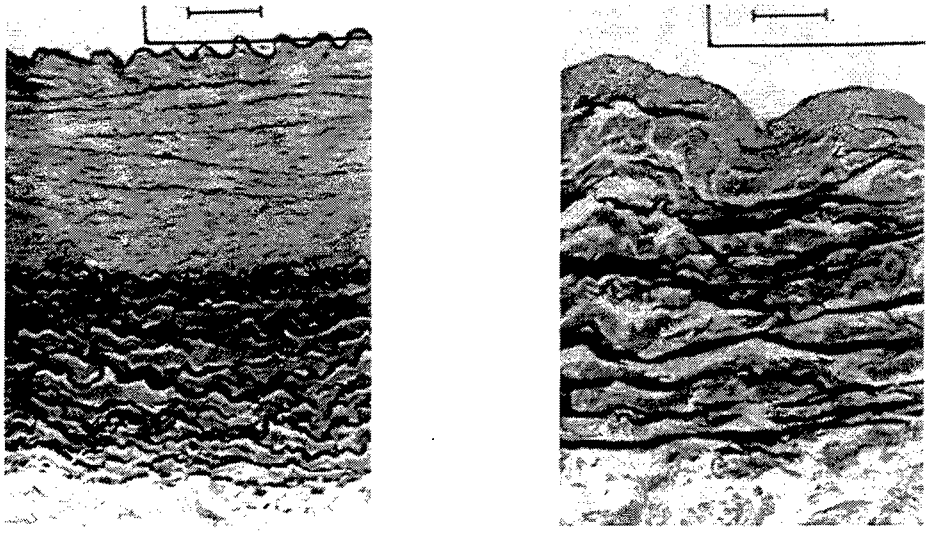

(a) (b)

Figure 2. Canine Femoral Artery (a) and Vein (b). The intimal surfaces are at the top of the figures.[Elastin Stains. Bar (a) = 99 microns and (b) = 62 microns].

The proximal carotid artery has a thick media composed of prominent elastin plates connected by a collagenous scaffolding in which smooth muscle cells are found. The internal elastic lamina (luminal surface) is thin and mingles with the medial elastin. The adventitia [not shown] consists of a dense feltwork of collagen. On the other hand, the intimal surface of the middle carotid artery is separated from the media by a continuous (except for very small pores) elastic

membrane, the internal elastic lamina. The media is composed of sheets of smooth muscle cells separated by irregular elastin plates and ribbons and by collagen. The proximal adventitia is a dense feltwork of elastin fibers that gradually intermixes with the collagen of the more peripheral adventitia.

Figure 2 illustrates the typical architecture of the canine femoral artery and vein. The femoral arterial media is separated from the intima by a prominent lamina propria. The media consists mainly of smooth muscle cells supported by a collagen framework and spare, thin elastin plates. In the dog, the femoral arterial adventitia is composed of a thick elastin feltwork that is almost as thick as the media. The femoral vein has a thinner wall with no internal elastic lamina and ribbons of elastin interspersed with dense collagen fibers and smooth muscle cells.

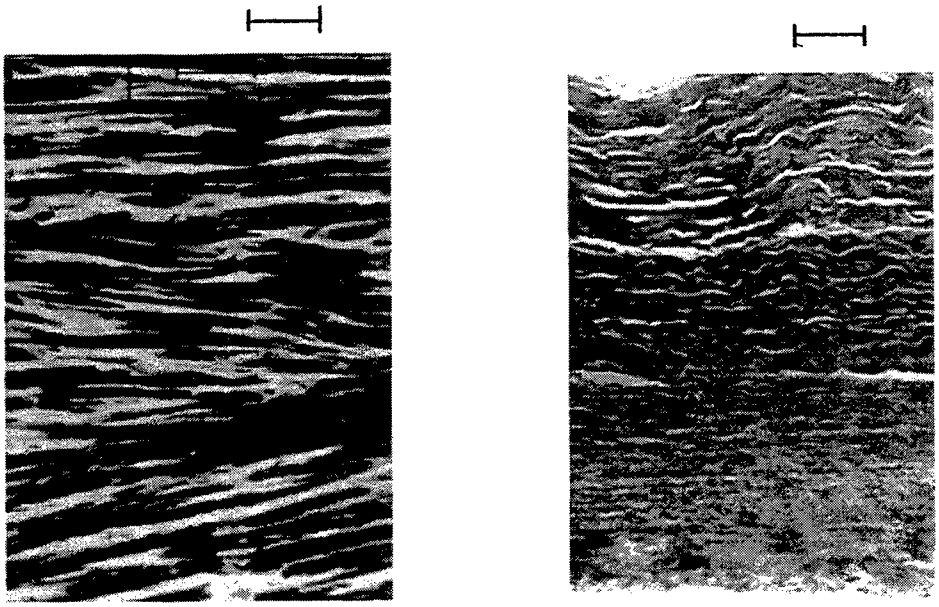

(a) (b)

Figure 3. Bovine *Ligamentum Nuchae* (a) and Bovine *Dura Mater* (b). [Elastin stains. Bar (a) = 31 microns and (b) = 25 microns].

Plainly, collagen and elastin are dominant constituents in the vessels, and they might reasonably be expected to have differing electrical properties. We used two model tissues to study them separately: *Ligamentum nuchae*, a large elastic ligament and *dura mater* a collagenous sheet covering the interior surface of the skull.

Figure 3a is an elastin stain section of bovine *ligamentum nuchae*. The *ligamentum nuchae* is constructed of darkly staining, densely packed, thick elastin ribbons (75-80%) separated by collagenous bands (light gray). The ligamentum nuchae is found in most mammalian species and in large four-footed grazing animals in whom the structure assists in the support and raising and lowering of the head. The *ligamentum nuchea* is the "purest" and most readily available biologically intact elastic tissue that can be used for *in vitro* experiments, and thus was used as the elastin tissue source for these studies.

Figure 3b is a trichrome stain section of bovine *dura mater*. The *dura mater* is the collagenous membrane that separates the skull from the underlying vascular meninges and brain tissue. The *dura* is composed of densely packed Type I collagen fibers with a very small amount of elastin (less than 5%) The fibrous nature of the collagen sheet is clearly visible in the section.

3. TISSUE ELECTRICAL PROPERTIES

The electrical conductivity of the tissues was estimated from impedance measurements in an approximately uniform electric field. Tissue samples were thin rectangles less than 2 mm thick and approximately 4 to 10 mm wide by 10 to 25 mm

long. The measurement electrodes were configured to establish an electric field either transverse or longitudinal to the dominant tissue axes, as in Figure 4.

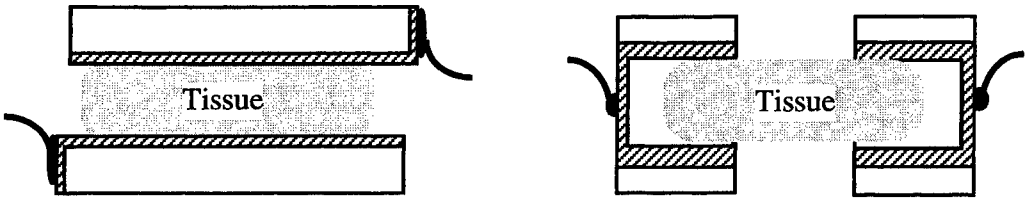

Figure 4 Electrode configurations for a) transverse E-field measurement, and b) longitudinal E-field measurement.

Impedance data were collected at 201 points between 10 kHz and 10 MHz using a Hewlett-Packard 4194A Impedance/Gain-Phase analyzer. Electrical conductivity was calculated assuming a uniform E-field according to:

$$\sigma = \frac{d}{RA} \tag{1}$$

where σ = conductivity (S/m), d is the dimension in the direction of the electric field (m), R is the measured resistance (Ω), and A is the area transverse to the electric field (m^2). In both cases the limitation in estimation of the electrical conductivity is dominated by uncertainties in the thickness of the tissue sample.

A typical impedance sweep is illustrated in Figure 5, a longitudinal measurement on canine femoral artery. The magnitude is between 1.4 and 1.8 kΩ and phase angle is between -6 and -2 degrees, slightly capacitive, especially at the higher frequencies. Figure 6 shows five estimates of conductivity in the transverse measurement for bovine *dura mater*. The complete results are summarized in Table 1. Each table entry is the average of swept frequency measurements on five separate tissue samples. Each of the five sample measurements is the average of 16 sweeps over the range of frequencies with a "medium" integration time at each sample point, i.e. 5 ms.

There is no significant difference between electrical conductivities at the representative electrosurgical frequencies of 500 kHz and 2 MHz, as was expected. As reflected by the standard deviations, the uncertainty in the transverse measurements is uniformly smaller than for the longitudinal measurements, as expected from preliminary estimates. Unexpectedly, there is no significant difference between the longitudinal and transverse conductivities of canine femoral artery. The other tissues studied exhibited significant anisotropy, with the longitudinal conductivity about twice that of the transverse conductivity.

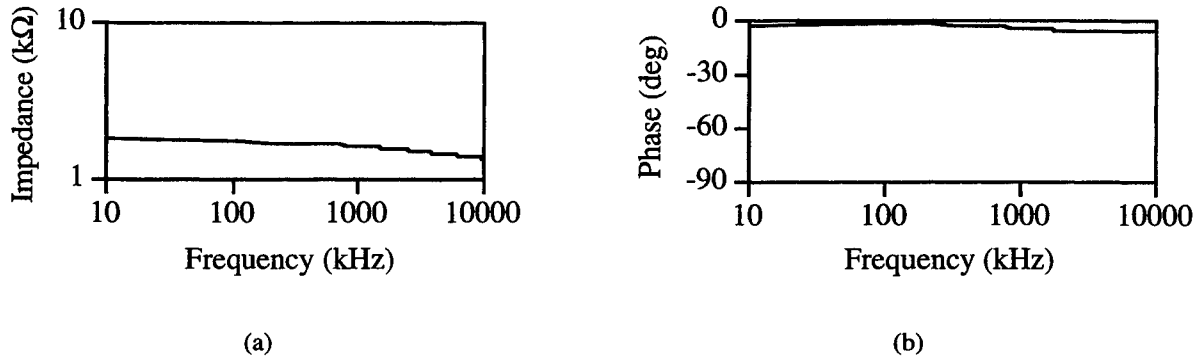

Figure 5 Longitudinal impedance of canine femoral artery a) Magnitude and b) Phase angle.

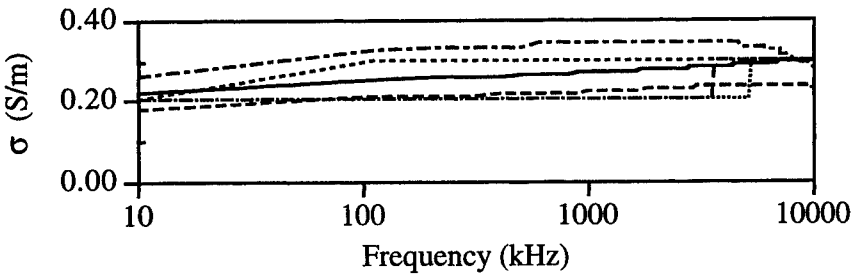

Figure 6 Five estimates of the transverse electrical conductivity of *dura mater*.

Tissue	Electrical Conductivity (S/m) (S.D.) 500 kHz	2 MHz
Canine Femoral Artery (trans)	0.75 (0.03)	0.85 (0.05)
Canine Femoral Artery (long)	0.64 (0.12)	0.70 (0.11)
Canine Femoral Vein (trans)	0.57 (0.10)	0.60 (0.11)
Canine Femoral Vein (long)	1.04 (0.18)	1.05 (0.17)
Bovine *Dura Mater* (trans)	0.26 (0.05)	0.27 (0.05)
Bovine *Dura Mater* (long)	0.41 (0.17)	0.43 (0.17)
Bovine *Ligamentum N.* (trans)	0.67 (0.02)	0.68 (0.02)
Bovine *Ligamentum N.* (long)	0.99 (0.14)	1.0 (0.14)

Table 1 Longitudinal and transverse electrical conductivity. Numbers are averages of five samples and (standard deviation).

4. NUMERICAL METHODS

Numerical models are never able to accurately predict specific experimental results owing to uncertainty in physical properties and randomness in tissue structure. However, they do permit study of the governing processes on fine spatial and temporal scales which cannot be obtained in experiments. When numerical models are sufficiently well behaved they can be used to study transient micro structural thermodynamic events, and to compare dominant processes and effects. Thus they can be used to provide substantial insight into the clinical problem.

Electric Field Model

We have relaxed some of the usual assumptions about tissue in these models: we do not assume globally homogeneous electrical properties. Instead, measured electrical properties for collagen, elastin and estimated values for smooth muscle were used to study inhomogeneous vessels. At present, each tissue constituent is assumed isotropic; however, the effect of discrete regions of each tissue type is to make the vessel model globally anisotropic even though locally isotropic. The thermal properties of the soft tissues vary little, and so the model thermal properties are presently homogeneous and isotropic. The model solves the quasi static Laplace equation:

$$\nabla^2 V = 0 \qquad (2)$$

as a boundary value problem by iterative use of successive approximation. The criterion for convergence was the calculated total active electrode current. Iteration proceeded until the change in electrode current was less than a specifiable maximum magnitude in a selectable number of iterations. Double precision was used for the potential matrices.

The model space consists of the first quadrant (I) of the symmetrical system composed of two bipolar flat plate electrodes clamped transversely around a vessel of arbitrary thickness and composition, as shown in Figure 7. The electrodes are of arbitrary size and potential and an insulated thermocouple (t/c) of arbitrary size can be included. Electrical boundary conditions are: 1) zero flux at x = 0, 2) V = 0 at y = 0, 3) constant potential under the electrode and zero flux outside the electrode at y = maximum, and 4) either a mixed boundary condition (simulating leakage flux) or a zero flux boundary at x = maximum. The model space used in the model was 81H X 21V nodes capable of 9 tissue layers. This particular size was

used so that the time step required in the thermal model would be sufficiently long that a reasonable execution time could be achieved. The tissue layers may have arbitrary thickness and electrical conductivity and be represented by a selectable number of node spaces. Interfaces between tissues are constrained to lie along node planes. Calculations of electrode current and power are on a per unit length basis along the Z-axis.

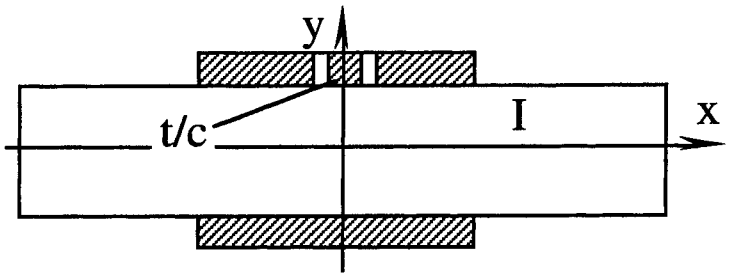

Figure 7 Idealized Cartesian 2-D model space of the first quadrant of bipolar electrodes (cross-hatched) clamped symmetrically around a vessel. Thermocouple (t/c) may be included.

The electrical conductivities used in the calculations were: 1) for collagen, σ_c = 0.26 S/m (transverse), 2) for elastin, σ_e = 0.67 S/m (transverse), 3) for smooth muscle no published values are available — an estimate was formed using published values for cardiac muscle (values range from 0.11 to 0.47 S/m[12]) the geometric mean of σ_m = 0.23 S/m was used for these calculations. Transverse conductivities were chosen because the primary electric field direction was transverse to the fibers and plates. Cardiac muscle is thought to be a more effective electrical analog of smooth muscle than skeletal muscle since it is essentially devoid of the cascade of collagenous connective tissue shrouds which electrically and mechanically isolate the skeletal muscle fibers.

Thermal Model

The thermal model space matches the electrical geometry in dimension and node placement; however, the tissue was treated as thermally homogeneous and isotropic. Boundary conditions in the thermal model are: 1) zero flux at x = 0 and at y = 0, 2) surface evaporation, convection and radiation at y = maximum, 3) either a mixed boundary condition or zero flux (selectable) at x = maximum. Surface evaporation is not allowed under the electrode and thermocouple, however convection and radiation are included at the electrode surface. The thermal mass of the electrode is significant and is included in the model. The transient thermal model incorporates proportional control, reducing electrode power proportionally within a selectable error band of the set point temperature, simulating the function of the experimental apparatus.

Temperature fields

The model space was a transient Cartesian finite difference model. The time step used was 40 μs in order to ensure stability in the solution. A typical 4 second activation with 1 second cooling phase required 9 hours to solve on a Macintosh Quadra 840 AV (68040 CPU with floating point processor).

The local volumetric power generation term, Q_{gen} (W/mm^3), was determined from:

$$Q_{gen} = \sigma |\mathbf{E}|^2 \tag{2}$$

where Q_{gen} = volume power deposition, σ = electrical conductivity (S/mm) and **E** is the electric field (V/mm).

The power generation term was the source term for the energy balance:

$$\rho c\left[\frac{\partial T}{\partial t}\right] = k\nabla^2 T + Q_{gen} + Q_{fg} - \text{Surface Losses} \tag{3}$$

where ρ = density (gm/mm^3), c = specific heat (J/gm-°C), k = thermal conductivity, (W/mm-°C), and Q_{fg} is the phase change term due to vaporization (from the surface or when tissue temperature is 100 °C). Tissue thermal properties were

assumed similar to those of water[13] and we have assumed a linear homogeneous isotropic material. The thermal conductivity turns out to be a particularly strong influence on the results in the vertical direction since the vessels are very thin and the thermal mass of the electrode is significant. Thermal conduction in the horizontal direction is negligible. Tissue density is very close to that of water and was assumed constant. The specific heat is a particularly sensitive parameter; however, no data are available on the relationship between specific heat and remaining water content, so constant properties were assumed.

Surface evaporation was modeled using Snelling's formula with empirical coefficients derived from solar pond data. Water vaporization (i.e. boiling) was assumed to occur at rates low enough that no significant tissue pressure increases resulted. Consequently, all vaporization processes occurred at or below 100 °C. That is, all Q_{gen} in excess of that required to supply local heat transfer processes was assumed to apply to local equilibrium boiling at 100 °C. Tissue was allowed to increase in temperature above 100 °C only if fully desiccated.

Damage process model

Kinetic models of thermal damage processes based on an Arrhenius formulation have been used for many years to describe different forms of thermal damage[7] :

$$\Omega(\tau) = ln\left\{\frac{C(0)}{C(\tau)}\right\} = \int_0^{\tau} A\, e^{-\left[\frac{E}{RT}\right]}\, dt \qquad (4)$$

Here Ω is the dimensionless damage, A is a measure of the molecular collision frequency (s^{-1}), E is an energy barrier the molecules surmount in order to denature (J/mole), R is the gas constant (J/mole-K), T is the absolute temperature (K) and t the time (s). The physical significance of the dimensionless damage, Ω, is that it is the logarithm of the ratio of the initial concentration of undamaged material, C(0), to the remaining undamaged material at the conclusion of the exposure, $C(\tau)$. The process coefficients, A and E, must be experimentally determined. This model assumes that only one first-order process is active — the model can be used in multiple-process damage accumulation if each process is thermodynamically independent with its own set of coefficients. We have used damage coefficients derived from experiment and literature to model collagen denaturation, smooth muscle denaturation, and skin damage.

The kinetic coefficients used for collagen damage were those derived by us from measurements of collagen birefringence loss in rat skin and are: $A_{col} = 1.606 \times 10^{45}$ (s^{-1}) and $E_{col} = 3.06 \times 10^5$ (J/mole).[9] The values used for smooth muscle were estimated from two sets of measured coefficients in cardiac muscle, one set for short exposures and one set for long exposures: $A_{mus} = 1.28 \times 10^{22}$ (s^{-1}) and $E_{mus} = 1.45 \times 10^5$ (J/mole). The estimate was created by taking the geometric mean of the E values and selecting A to obtain threshold damage at the temperatures measured and previously reported[10]. The reported coefficients of Henriques and Moritz[11] were used to predict "skin" damage boundaries: $A_{skn} = 3.0 \times 10^{98}$ (s^{-1}) and $E_{skn} = 6.28 \times 10^5$ (J/mole). These were used as a means of comparison, only since, of course, there is no "skin" in a vessel. However, the intima is composed of endothelial cells which may exhibit a thermal sensitivity similar to that of the epithelial cells of the skin; also, the skin coefficients are known to be the most sensitive of all of the reported values to date and have been used in other thermal models, and therefore make a useful standard of comparison. The three damage processes were allowed to progress independently.

5. MODEL RESULTS

The geometry used for the carotid and femoral arteries in the low resolution model is shown in Figure 8. Both models have an "intima" 10 μm thick (actual dimensions are closer to 1 to 3 μm) modeled by muscle properties and an "internal elastic lamina" 20 μm thick (close to the actual dimension) for which elastin properties were used. For both models the electrode was 0.5 mm thick and 4mm across (assigned nodes 1 to 41) with no specific thermocouple site. The major difference between the models is the location of the elastin plates: in the media for the carotid artery and in the adventitia for the femoral artery.

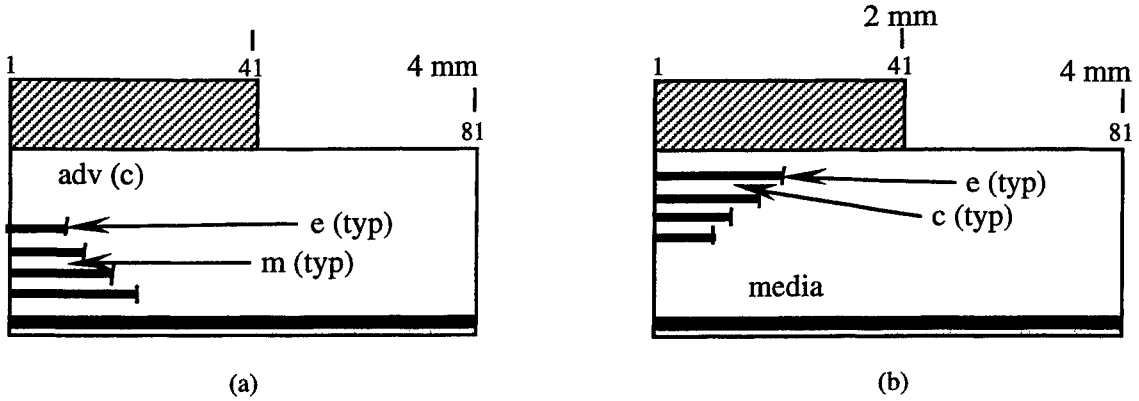

(a) (b)

Figure 8. Vessel model dimensions in the 81 X 21 model space a) carotid artery b) femoral artery. Tissue constituents are collagen (c), elastin (e) and muscle (m). Both models have an intima 10 μm thick (bottom) and an internal elastic lamina 20 μm thick just above it.

Specific dimensions in the carotid artery model are: 1) 0.38 mm thick overall with 2) an adventitia (collagen mat) 0.17 mm thick, assigned 4 node spaces, 2) four pairs of elastin/muscle layers, each elastin layer 10 μm thick and each muscle layer 50 μm thick, assigned 2 node spaces for each layer.

Specific dimensions for the femoral artery are: 1) 0.46 mm thick overall with 2) an adventitia composed of four pairs of elastin/collagen layers, each elastin layer 10 μm thick and each collagen layer 50 μm thick (except for the upper-most collagen layer which was 80 mm thick), assigned 2 node spaces for each layer, and 3) the media (muscle) 0.22 mm thick, assigned 4 node spaces.

Canine carotid artery model.

The electrical model converged to a maximum electrode current change of 0.001% in 10 iterations after 3460 iterations. For a single electrode potential of 50 volts (100 v bipolar) the current per unit length was 84.4 mA/mm and resistance per unit length was 592 Ω/mm. For 7 mm of vessel in contact with the electrode, this would correspond to a total current of 591 mA and inter-electrode resistance of 85 Ω, both reasonable values in the light of experimental results.

The potential field is shown in Figure 9a while the volumetric power density (W/mm^3) is in Figure 9b. The maximum of the power density was to 27 W/mm^3, and the gray scale covers 0 to 10 W/mm^3.

(a) (b)

Figure 9. Geometrically scaled carotid artery E-field model results. a) Potential field (0 to 50 V, interpolated) and b) power density (0 to 10 W/mm^3, no interpolation used).

The voltage gradient is very strong at the edge of the electrode, as expected, with a correspondingly high power density located there. The high edge power density is moderated by strong heat transfer effects in the thermal model. The variation in electrical properties of the elastin and muscle in the media is plainly visible in the power density field.

The temperature and damage fields were calculated for two heating protocols. In both models the set control point temperature was 90 °C with a proportioning band of 10 °C. The first was a rapid heating protocol; current adjusted to 169 mA/mm, heating time 0.02 s with a 0.05 s cooling period, Figures 10 and 11, and required 3 minutes to calculate at $\Delta t = 40$ μs. The second was a 4 second heating time (current adjusted to 42.2 mA/mm) with a 1 s cooling period, Figures 12 and 13, and required 9 hours to calculate (for the same time step).

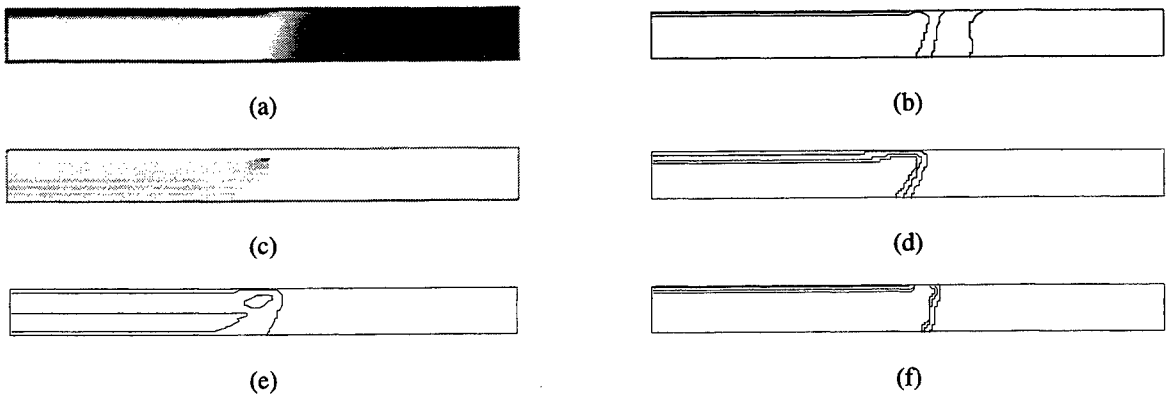

Figure 10. Geometrically scaled results for the carotid artery model with rapid heating (at 0.02 s, end of heating; 0.025 s total). a) Temperature field (0 to 100 °C, interpolated). b) contour plot (40 to 100 °C, by 20 °C). c) water vaporization boundaries (range 21, gray, to 55%, white, by volume). d) collagen damage boundaries with contours at 10%, 63% ($\Omega = 1$) and 90% damaged tissue. e) muscle damage (10% and 63%) and f) skin damage (10, 63, and 90%).

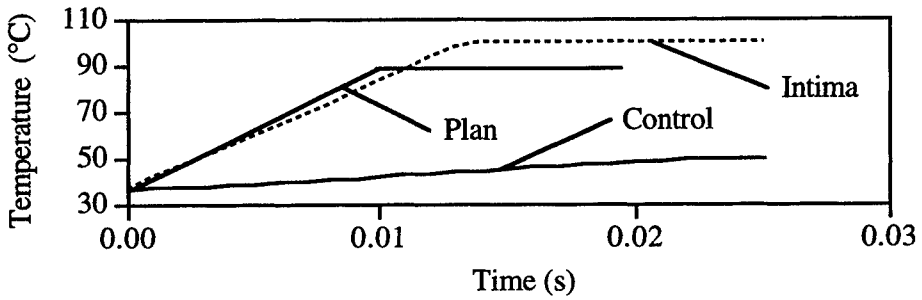

Figure 11. Plot of calculated temperatures at the adventitial control point (x = 0 to 0.2 mm, y = 0.38 mm) and intimal surface temperature (x = 0 to 0.2 mm, y = 0) and the planned heating curve.

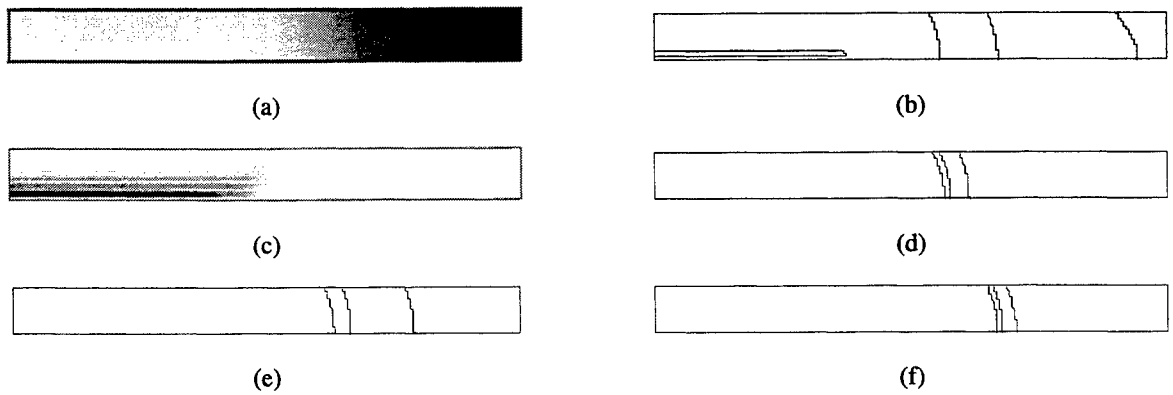

Figure 12. Geometrically scaled results for the carotid artery model with slow heating (at 4 s, end of heating; 5 s total). a) Temperature field (0 to 100 °C, interpolated). b) contour plot (40 to 100 °C, by 20 °C). c) water vaporization boundaries (range 0, black, to 55%, white, by volume). d) collagen damage boundaries with contours at 10%, 63% ($\Omega = 1$) and 90% damaged tissue. e) muscle damage (10, 63 and 90%) and f) skin damage (10, 63, 90%).

In the rapid heating protocol of Figures 10 and 11, it is apparent that the thermal mass of the electrode has limited surface temperature rise and thus the evaporation (10c) and damage (10d-f). The locally high power density near the electrode edge has been moderated to the extent that the boiling peak is below the surface (10c). Figure 11 is a plot of the adventitial and intimal surface temperatures between nodes 1 and 5 (under the center of the electrode) as the heating progressed. The results contain the seemingly nonsense result that the predicted muscle damage boundaries are inside of the collagen damage boundaries — and, in fact, the muscle damage process is not complete since a 90% contour doesn't exist (the maximum muscle damage was predicted to be 73%).

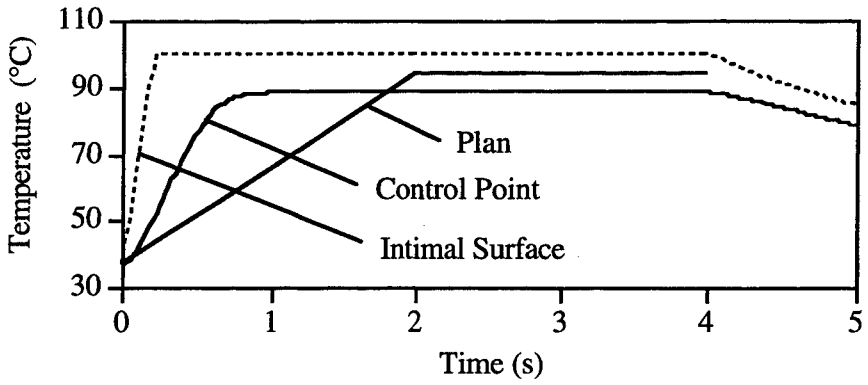

Figure 13. Plot of calculated temperatures at the adventitial control point (x = 0 to 0.2 mm, y = 0.38 mm) and intimal surface temperature (x = 0 to 0.2 mm, y = 0) and the planned heating curve.

In the slow heating model the skin, muscle and collagen damage areas are nested in the expected sequence. The effects of lateral heat transfer are significant and readily observed in this longer activation.

Canine femoral artery model

The electrical model converged to a maximum electrode current change of 0.001% in 10 iterations after 1660 iterations. For a single electrode potential of 50 volts (100 v bipolar) the current per unit length was 62.1 mA/mm and resistance per unit length was 805 Ω/mm, higher than the carotid artery model. For 7 mm of vessel in contact with the electrode, this would correspond to a total current of 435 mA and inter-electrode resistance of 115 Ω, both reasonable values in the light of experimental results, and following the trend observed in the experiments.

The potential field is shown in Figure 14a while the volumetric power density (W/mm^3) is in Figure 14b. The maximum of the power density was to 15.6 W/mm^3, and the gray scale covers 0 to 10 W/mm^3. Both the potential and power density fields have a markedly different appearance than for the carotid artery model.

(a) (b)

Figure 14. Geometrically scaled femoral artery E-field model results. a) Potential field (0 to 50 V, interpolated) and b) power density (0 to 10 W/mm^3, no interpolation used).

Again, the voltage gradient is very strong at the edge of the electrode with a correspondingly high power density located there. The variation in electrical properties of the elastin and collagen in the adventitia is not visible in the power density field, however.

The temperature and damage fields were calculated for 4 second heating time with a 1 s cooling period, Figures 15 and 16, and required 9 hours to calculate (for the same time step). The planned heating was to mimic that of the carotid artery

model, 2 seconds ramp to 90 °C with 2 s at 90 and then a 1 second cooling period. The same current was used as for the carotid artery model, 42.2 mA/mm.

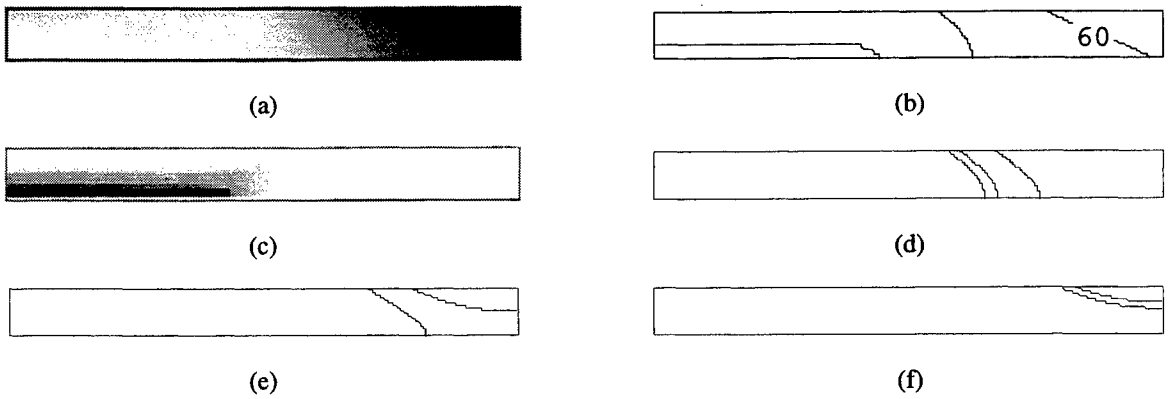

Figure 15. Geometrically scaled results for the carotid artery model with rapid heating (at 4 s, end of heating; 5 s total). a) Temperature field (0 to 100 °C, interpolated). b) contour plot (60 to 100 °C, by 20 °C). c) water vaporization boundaries (range 0, black, to 55%, white, by volume). d) collagen damage boundaries with contours at 10%, 63% ($\Omega = 1$) and 90% damaged tissue. e) muscle damage (63% and 90%) and f) skin damage (63, and 90%).

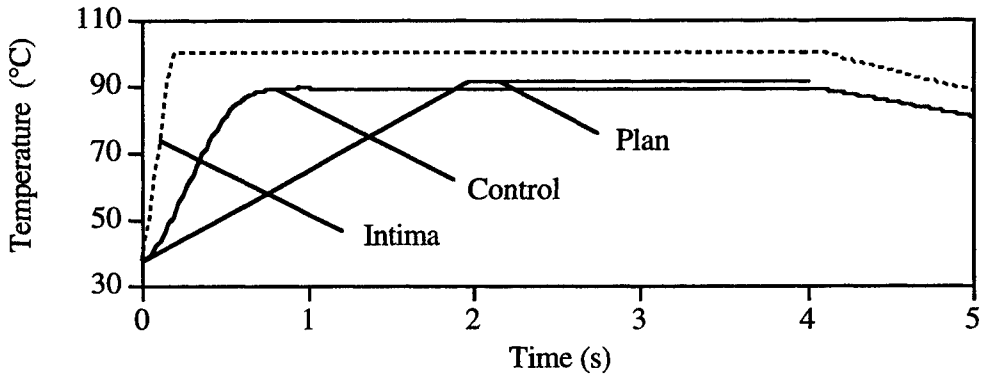

Figure 16. Plot of calculated temperatures at the adventitial control point (x = 0 to 0.2 mm, y = 0.38 mm) and intimal surface temperature (x = 0 to 0.2 mm, y = 0) and the planned heating curve.

The predicted desiccation boundary is substantially similar to the carotid artery case. Muscle damage has a minimum of 38% and skin 12%, so only the 63% and 90% contours are shown in those plots. The temperatures are higher and the damage is more severe in this model when compared with the carotid artery case.

6. CONCLUSIONS

The numerical modeling results compare favorably with experiment in spite of the geometric simplifications used in their formulation. The numerical models can be used to study microscale thermodynamic events in the tissue, and in future will be modified to include temperature dependent thermal and electrical properties.

7. ACKNOWLEDGEMENTS

The authors would like to express their appreciation to the Texas Higher Education Coordinating Board (grant number ARP-138) and to Valleylab Inc. for partial support of this work. Many of the tissue property measurements were made by Tadija Janjic.

8. REFERENCES

1. T.A. Magnusen and J.A. Pearce, Temperature Controlled Electrosurgical Vessel Sealing, *Proc. IEEE-EMBS 16th Annual Meeting,* 1994.

2. J.S. Kennedy J.A. Pearce and S. Thomsen, Mechanisms of Electrosurgical Fusion for Large Vessel Hemostasis, *Proc. 7th Intl. Mtng, Soc. Min. Invas. Therapy* (in J. *Min. Invas. Therap.*, **4** Suppl 1, p19), 1995.

3. G.M. Lemole, R.R. Anderson and S. DeCoste; "Preliminary evaluation of collagen as a component in the thermally-induced 'weld' " *Proc. SPIE* **1422**:116-22, 1991.

4. R.A. White, G.E. Kopchok and G. White, "Vascular tissue bonding using laser surgery" Lasers in Cardiovascular Medicine and Surgery: Fundamentals and Techniques. G. Abela ed. pp361-372, Kluwer Academic Press. Boston, 1990.

5. G.E. Kopchock, R.A. White, H.J. White et al; "CO_2 and argon laser vascular welding: acute histologic an thermodynamic comparison" *Lasers in Surgery and Medicine* **8**(6)584-8, 1988.

6. R. Schober, F. Ulrich, T. Sander, H. Durselen and S. Hessel; "Laser-induced alteration of collagen substructure allows microsurgical tissue welding" *Science* **232**:1421-11, 1986.

7. M.R. Treat, Mehmet, C.O., and Bass, L.S.; "New technologies and future applications of surgical lasers" Surgical Clinics of North America **72**(3): 705-42, 1992.

8. C.R. Neblett, J.R. Morris and S. Thomsen; "Laser-assisted microsurgical anastomosis" *Neurosurgery* **19**:914-34, 1986.

9. J.A. Pearce, S. Thomsen, H. Vijverberg and T. McMurray; "Kinetics for birefringence changes in thermally coagulated rat skin collagen", *Proc. SPIE* **1876**:180-186, 1993.

10. S. Thomsen, J.A. Pearce and W. F. Cheong; Loss of birefringence as a low temperature marker of thermal damage in tissues, *IEEE Transactions on Biomedical Engineering* **BME-36** (12), 1174-1179, December 1989.

11. A.R. Moritz and Henriques F.C.; "Studies in thermal injury: II the relative importance of time and surface temperature in the causation of cutaneous burns" *Am. J. Pathol.* **23**(5):695-720, 1947.

12. L.A. Geddes and L.E. Baker; The specific resistance of biological material — a compendium of data for the biomedical engineer and physiologist, *Med. & Biol. Engr.* **5**, pp271-293, 1967.

13. H.F. Bowman, E.G. Cravalho and M. Woods; Theory, measurement and application of thermal properties of biological materials, Ann. Rev. of Biophys & Bioengr. **4**, pp43-80, 1975.

SESSION 7

Focused Ultrasound for Tissue Therapy I

Image-guided noninvasive surgery with ultrasound phased arrays

Emad S. Ebbini, Philip D. VanBaren and Claudio Simon

Department of Electrical Engineering and Computer Science
The University of Michigan, Ann Arbor, MI 48109-2122, USA

ABSTRACT

The current status and the future needs of image-guided ultrasound phased array systems for noninvasive surgery are addressed. Preliminary results from an integrated image-guided therapeutic phased array system for noninvasive surgical applications currently being developed at our laboratory are shown. The therapeutic array utilizes piezo-composite transducer technology and operates (therapeutically) at 1 and 2 MHz. It consists of 64 elements on a spherical shell with a geometric center at 100 mm from its apex. The array was shown to be capable of producing well defined thermal lesions in tissue media at depths from 40 to 60 mm and to scan therapeutic foci up to +/- 15 mm from its geometric center. Image guidance is provided by a modified diagnostic ultrasound scanner which, in addition to providing standard B-scan images of the target region, provides real-time images of the temperature rise due to the therapeutic beam. The temperature information is obtained using a correlation based algorithm for echo displacement estimation, which can be directly related to local variation in tissue temperature due to the therapeutic beam. A complete description of the combined imaging/therapy system is given. Furthermore, illustrative examples of noninvasive real-time image-guided tissue ablation, temperature estimation, and temperature control are presented and discussed.

Keywords: Thermal surgery, tissue ablation, temperature imaging, focusing

1. INTRODUCTION

1.1. Image Guided Surgery

The use of three dimensional (3D) MRI and/or CT has become routine practice in recent years for planning surgeries. Surface and volume rendering techniques for visualization are currently well developed and allow for unprecedented views of patient anatomy. Moreover, contemporary computer workstations are currently capable of interactive manipulation of these 3D data sets. It has therefore become possible for surgeons to plan their procedures based on accurate mapping of the treatment volume. More recently, techniques for multimodal image guidance for neurosurgery have been proposed.[1–3] These techniques will allow surgeons to bring their pre-treatment plans to the operating room (OR). Such advances will undoubtedly help minimize patient risk in delicate surgical procedures. They could also prove beneficial in eliminating unnecessary procedures and reduce side effects of certain surgical procedures. The increasing power and falling cost of computer and visualization technology will probably be an important factor in helping image-guided surgery gain widespread acceptance in the foreseeable future. While neurosurgery is currently the major application area, it is expected that image guidance will be utilized in other surgical applications, e.g., image guided biopsy and focused therapeutic procedures applied in tumor ablation.[3] The latter is the main focus of this paper and is described in the following subsection.

1.2. High-Intensity Focused Ultrasound: Background

High-intensity focused ultrasound (HIFU), in the frequency range of 500 kHz to 10 MHz, has been used in a wide range of therapeutic applications. For example, HIFU has considerable potential for deep localized hyperthermia,[45,43,47] primarily in conjunction with other cancer treatment modalities, e.g., radiation therapy.[54,61,44] This is due to the fact that ultrasound can be easily focused (with mm-size heating spots at the focus) at considerable depths (1 cm - 15 cm) depending on the frequency. The (typically) small heating spot at the focus can be scanned mechanically

Other author information: (Send correspondence to E.S.E)
E.S.E.: E-mail: emad@eecs.umich.edu
P.V.B.: E-mail: phillipv@eecs.umich.edu
C.S.: claudio@eecs.umich.edu

SPIE Vol. 3249 • 0277-786X/98/$10.00

or electronically to produce the desired heating pattern tailored to the tumor geometry. Clinical or pre-clinical hyperthermia systems utilizing HIFU have been used by a number of groups and they continue to demonstrate the promise of this technology.[58,47]

Another application where HIFU was demonstrated to have significant promise is in noninvasive tissue ablation for cancer treatment and in surgery. As early as the 1950s, Fry and coworkers[31] at the University of Illinois have shown that very precise ablation patterns in cat brains *in-vivo* is feasible. A system was developed and numerous experiments were performed further supporting the feasibility of this approach. Similar results were obtained by Lele at MIT[45,60] and most recently by Hynynen at the University of Arizona and Harvard[40] and Sanghvi et al at ICFAR.[37] It has been demonstrated by these investigators and by our group that thermal coagulation of tissue results from short (1-10 seconds) exposure to intense (1-3 kW/cm^2) acoustic fields. Furthermore, at these exposure levels and time durations, the ablated tissue volumes are largely defined by the specific absorption rate (SAR) of the focused ultrasonic field, i.e., the focal spot. For most practical ultrasound focusing systems, the ablated tissue is cigar-shaped at the focal spot with a diameter on the order of 1 mm and length on the order of 3 to 4 mm*. Even higher definition of the ablated region can be achieved by the appropriate choice of the operating frequency and the applicator design. For example Lizzi and coworkers[39] use 10 MHz HIFU system in the treatment of the eye.

Most HIFU systems in clinical use today employ (spherical) shell focused transducers operating in the range of 1 MHz through 4 MHz. These transducers are capable of producing very well-defined tissue necrosis in homogeneous tissue where no significant aberrations occur. More recently, however, phased array applicators were developed for hyperthermia and other HIFU applications. Phased arrays offer significantly improved control features that will be needed for precision lesion formation at depth in the presence of tissue inhomogeneity and patient/applicator movement. This is due to the electronic focusing capability of these applicators which can be performed dynamically at electronic speed to track the target (e.g., tumor) in real-time for the duration of the treatment. Effects of tissue inhomogeneities can be compensated for simply by the proper choice of the phases of the array elements. A number of optimal phasing schemes were developed[9,6,10,7,42] to refocus any array in the presence of tissue inhomogeneity based on minimally-invasive acoustic feedback using miniature probes.[18] In addition to finding the proper phase and amplitude distribution for refocusing the array, the algorithms described in[18] identify and deactivate any elements shadowed from the target by the presence of an acoustic obstacle (e.g., bone or air spaces). Therefore, the availability of this kind of feedback will allow for the use of arbitrary array geometries with multiple acoustical windows to maximize the power deposition to the target region. Another important feature unique to phased array system is their ability to dynamically synthesize optimal multiple-focus patterns.[5,7,9] Multiple-focus pattern can be used to simultaneously heat multiple target points without the need for scanning. They could prove essential for the reduction of the treatment time for HIFU procedures.

Despite the obvious advantages of HIFU for noninvasive therapeutic application and the availability of advanced phased-array applicator systems capable of precision lesion formation at depth, HIFU is not yet a widely accepted modality in the clinic either for normal hyperthermia or for surgery. Some of the main reasons behind this lack of progress in clinical utilization of HIFU are as follows:

1. Incomplete understanding of the limits on the use of HIFU to adequately heat specified volumes (e.g., tumors) at depth in the presence of tissue inhomoigeneities and/or shadowing bone structures.
2. Lack of clinical real-time non-invasive high-resolution temperature feedback throughout the treatment volume.
3. Lack of quantitative non-invasive measurement of tissue response to HIFU fields (especially important for tissue ablation). That is, we still do not have a noninvasive measurement for determining if a desired therapeutic end-point has been reached, nor do we have a noninvasive means for measuring thresholds for irreversible tissue thermal damage *in-vivo*.
4. Lack of realistic treatment planning software based on patient-specific 3D data sets to help in the optimization of the applicator and the treatment strategy.

The availability of high power piezocomposite transducer technology will certainly be the answer to the first problem. It is safe to say that phased arrays will be utilized in precision lesion formation even in the presence of strongly scattering obstacles, e.g., the rib cage.[13] Solving the second and third problems will lead to a guidance and visualization mechanism for the therapeutic beams based on a well established imaging modality. This may be

*The biological and experimental basis of this statement is given in Section 2 below.

considered the "enabling technology" that will finally help HIFU surgery gain widespread acceptance by the medical community. This fact has been recognized by a number of investigators with significant clinical support.[40,37] At this point, MRI[22] and B-scan ultrasound[17] are being used. These two methods (especially MRI) clearly illustrate that guidance visualization of the effects of therapeutic beams can be achieved.

2. PHYSIOLOGICAL BASIS FOR THERMAL SURGERY WITH HIFU

It has been verified experimentally[16] that the lesion size and shape is well predicted by the thermal dose parameter of *equivalent minutes at* 43°C, defined as

$$T_{43}(\vec{r},t) = \int_0^t R^{T(\vec{r},\tau)-43} d\tau, \tag{1}$$

where T is temperature in °C, t is time in minutes, $\vec{r}$ is a vector representing the 3D coordinate system of the region of interest, and R is an empirically determined constant. Equation 1 is derived from cell survival rates at different temperatures.[4] The concept of thermal dose, while not completely developed, has been accepted by most hyperthermia practitioners. An obvious implication of (1) is that the same therapeutic end-point (e.g., thermal coagulation) can be reached by maintaining tissue temperature of 43°C for 120 minutes or, alternatively, maintaining tissue temperature of 65°C for 2 seconds. While the two alternatives mentioned are equivalent for nonlocalized heating of non-perfused tissue, they differ greatly when localized heating of perfused tissue is considered. In the case of long-duration heating, heterogeneous blood perfusion and thermal conductivity of tissue complicate the requirements of temperature control algorithms, even with the most advanced applicators. On the other hand, the short-duration heating causes thermal coagulation before blood perfusion and conduction begin to affect the heating pattern. In the latter case, the temperature control problem is reduced to a pattern synthesis problem. Thus significantly simplifying the therapeutic procedure to achieve the desired end-point. This conclusion, which is made on theoretical analysis of the BHTE, is supported by a significant volume of research that has been performed on the determination of both thermal and cavitational thresholds for damage. This work, which was performed on exposed organs of small animals, indicate that thermal coagulation of tissue occurs according to a well-defined intensity-exposure relationship

$$IT_e^{0.5} = K, \tag{2}$$

where I is the intensity in W/cm^2 and T_e is the exposure (time duration) in seconds, and K is a constant depending on tissue type.[60,33,36,34,35,40] Interestingly enough, our thermal simulations based on the transient bioheat transfer equation[46,5] indicate that there is a general agreement between Equations (1) and (2) for exposure durations between 1 and 10 seconds. Therefore, current knowledge on thermal coagulation of tissue using HIFU allows us to state the following:

> *If one is able to control the ultrasonic power deposition for a specified time duration at a given site deep into the tissue, then thermal necrosis will occur at all points within the volume reaching the ultrasonic threshold given by (2). Equivalently, tissue damage will occur at all points within the volume reaching a thermal dose threshold given by (1).*

This statement provides the basis for localized thermal surgery with HIFU. It also provides a valuable treatment planning tool for the optimization of the power deposition to the target tissue.

3. TEMPERATURE FEEDBACK AND CONTROL

Current clinical practice relies heavily on the use of (invasive) thermocouple measurements for feedback control of tissue temperature in thermotherapies. Due to well known clinical limitations, these measurements are extremely sparse leaving large portions of the treatment volume without direct measurent of temperature. This lack of feedback is probably the single most important limitation of clinical application of most thermotherapies, especially hyperthermia. Several attempts to estimate tissue 2D and 3D temperature profiles from sparse measurements have been made,[64,53] but it is not clear whether these attempts will lead to a practical clinical application.

Recently, several groups have attempted to exploit temperature dependence of different image modalities to produce 2D maps of tissue temperature during heating. Early reports on using X-ray CT,[21] MRI[24] and even ultrasound[27] for noninvasive temperature estimation showed promise. Briefly, the CT method measures changes in

temperature-dependent density as reflected in thermal expansion of the tissue which appears in the imaging equation for the (non-dimensional) Hounsfield Unit (HU).[20] For MRI, several temperature sensitive parameters can be measured. However, the temperature-dependent proton resonant frequency shift is typically used.[23] Diagnostic pulse-echo ultrasound can be used for non-invasive temperature estimation by measuring changes in the mean scatterer spacing[19] or echo displacements.[30] Both of these effects have been shown to depend on local changes of temperature dependent speed of sound and the linear coefficient of thermal expansion. A complete description of a 2D temperature imaging algorithm based on echo displacement estimation is described in Ref. 28. Recent reports on the use of impedance tomography[25] and microwave imaging[26] for noninvasive temperature imaging have demonstrated the feasibility of these methods in phantoms and *in vivo*.

It should be mentioned, however, that clinical demonstration of these noninvasive procedures have not yet been made. Calibration issues as well as sources of artifacts are currently the limiting factors preventing quantitative temperature imaging based on the three modalities described. However, experimental demonstration of the feasibility of monitoring the effects of HIFU beams have been made for the three systems. This is significant in the important areas of guidance and monitoring of HIFU beams as discussed in the following two sections.

4. IMAGE GUIDANCE

All three systems described above can be used in image guidance due to the temperature sensitivity of the measured parameters. For all three imaging modalities, the HIFU beam can be initially applied to produce a small detectable, but non-destructive temperature change at the desired target. The resulting temperature profile is estimated by the imaging system. If the therapeutic beam is determined to be focused properly at the target, the therapeutic beam is applied with sufficiently high intensity to cause tissue damage. Otherwise, it is refocused until the focal spot size and location are properly adjusted within the desired target region.

In the area of image guidance, ultrasound holds an edge on the other two modalities in terms of both temporal and spatial resolutions which allows for excellent characterization of the heating spots due to the therapeutic beams in realtime.

5. DAMAGE ASSESSMENT

Both X-ray CT and MRI are quantitative imaging methods that can (and do) measure changes in tissue state due to the therapeutic beams. Both methods, therefore, hold great potential in the area of damage assessment, which is absolutely essential to the success of noninvasive surgical procedures. Pulse-echo ultrasound, on the other hand, is not quantitative without further processing. This may be the main limitation of ultrasound in this area. However, work is currently underway to develop signal processing methods for extracting quantitative tissue parameters that can be utilized for damage assessment. It is likely that several features (e.g., attenuation, mean scatterer spacing, reflection coefficients, etc.) will be needed to characterize damage with the help of adaptive learning algorithms such as neural networks or hidden Markov models.

6. ACTIVE RESEARCH PROGRAMS

The advent of diagnostic imaging technology over the past decade encouraged a number of groups to investigate image-guided HIFU in noninvasive surgery. Currently, two groups in the U.S. are pursuing clinical implementation of image-guided HIFU systems. K. Hynynen is developing an MRI-guided HIFU system at Harvard. His work indicates unequivocally that HIFU treatments can be monitored and guided using MRI. Another group currently developing an image-guided HIFU is working at the Indiana Center for Advanced Research (ICFAR). They are developing an ultrasound-guided HIFU system for prostate removal using intracavitary applicators with ultrasound imaging built into the applicator head.

Both systems at ICFAR and Harvard are approved for clinical trials. In addition to the two groups operating in the U.S., a number of active research groups in Europe investigating the use of HIFU in tissue ablation: C. R. Hill and G. ter Haar[32] (Basic biophysics of HIFU; Royal Marsden Hospital, Surrey, UK) and J.Y. Chapelon and coworkers[36] (Biophysics, transducer development; INSERM, Lyon, France). The work of all of the above mentioned groups (and experimental and simulation results obtained by our group) indicate that a number of key advances have to occur before image-guided HIFU surgery becomes a reality. Published work by the mentioned research teams generally agree that the challenges to full clinical implementation of HIFU are primarily those stated in Sect. 1

above. There is also general agreement that visualization and guidance will play very important role in the success of HIFU thermal surgery.

7. A PROTOTYPE PHASED ARRAY SYSTEM FOR HIFU

7.1. System description

A combined imaging/therapy system utilizing a HIFU-capable phased array and a realtime ultrasound imaging system for noninvasive temperature estimation. A description of the two main components of this system is given herein.

7.1.1. HIFU system

A piezocomposite spherical shape 64-element 1D array transducer (Imasonic, France) was used (Fig. 7). A Pentium computer was used to control the electronic circuitry responsible for driving the array elements. This circuitry provides individual control of amplitude (15 selectable values at 1MHz) and phase ($\pi/15$ resolution at 1MHz) for each of the array elements. The experimental data described below were obtained using the experiment setup shown in Figure 2.

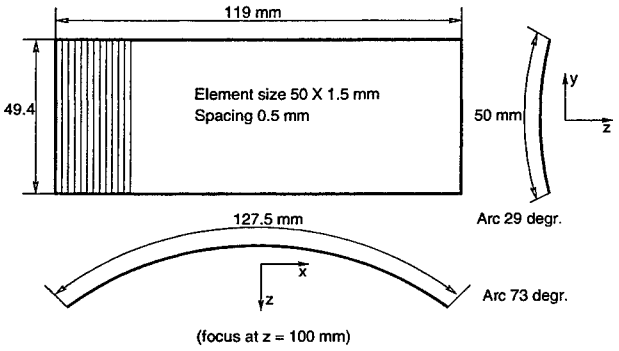

Figure 1. HIFU array.

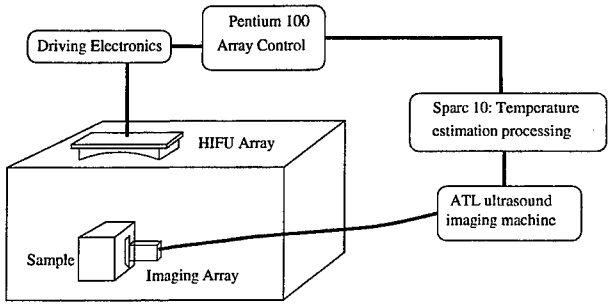

Figure 2. Prototype system setup.

7.1.2. Imaging system

From an ATL Ultramark 9 imaging system connected to a SUN Sparc 10, beamformed RF-data was collected in real time through a custom made VXI-compatible interface. The data was processed in real-time in the Sparc 10 to provide temperature estimates on a rectangular grid of 64 × 50 samples (38 × 75 mm^2). The temperature data was displayed using a color-coded overlay on the conventional gray-scale B-scan image and were updated on the Pentium monitor every 1.7 seconds. To avoid interference between the HIFU and imaging devices, the image data was acquired during a 200 ms interruption of the HIFU system.

7.2. Experiments and Results

7.2.1. Lesion Formation

To characterize our phased-array HIFU system, lesions were created in beef muscle *in vitro* using varied pulse durations. Eleven single focus pulses were delivered 30 mm deep within the tissue, and laterally spaced by 5 mm, distributed from -25 mm to +25 mm from the geometric focus of the transducer. The total acoustical power was fixed at 200 W (2000 W/cm^2 spatial peak intensity in water) and the duration time of each pulse was varied linearly between 0.25 sec and 2.75 sec. A long time delay (3 minutes) was given between successive pulses to allow the tissue to cool down, thereby avoiding temperature buildup from one shot to the next. The tissue sample was then cut along the scanned plane and lesions were observed for pulses with duration higher than 1.25 sec (Fig. 3). It should be noted here that the array was focused electronically at the various lesion locations and no physical movement of the array or the sample was needed to form the observed lesions. It is interesting to note that the shapes of the observed lesions reflected the shape of the focal spot size and the intensity thresholds for lesion formation were consistent with the thresholds predicted by Equations 1 & 2 above. A simulation result showing the general agreement between the two equations for the 1 - 10 second exposures is shown in Figure 4. This experiment is very important to our work as it demonstrates the ability of our prototype system to cause tissue ablation at depth. Furthermore, it appears to validate the mathematical model for thermal dose which will serve as a basis for our treatment planning algorithms.

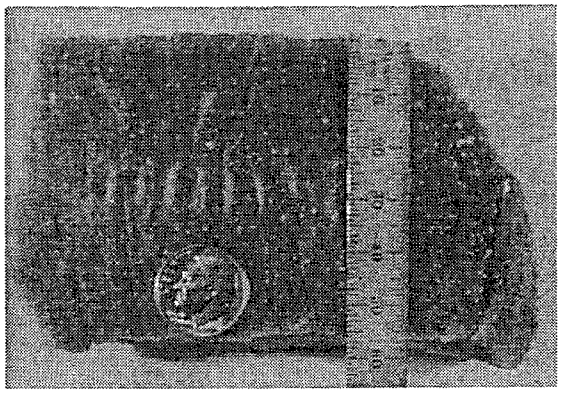

Figure 3. Lesions formed in beef muscle during HIFU system preliminary characterization experiment.

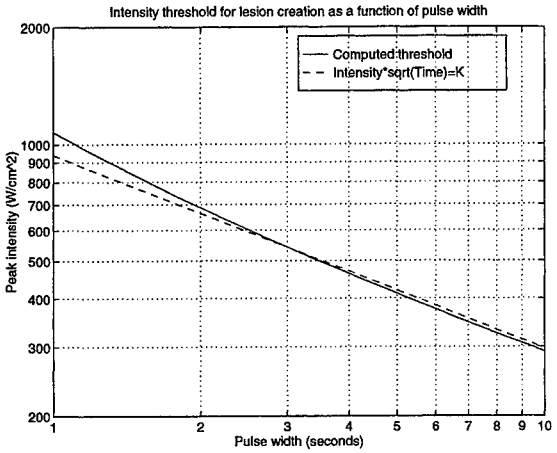

Figure 4. Intensity threshold for lesion formation (Solid: BHTE and Equation 1. Dashed: Equation 2).

7.2.2. Image Guidance

An *in vitro* beef muscle experiment was performed to characterize the realtime guidance of the therapeutic beam based on temperature imaging. The setup was the same as the previous experiment. The HIFU system was driven at low power, using a single focal point at range=27 mm, lateral=16 mm. The system was then switched to a double focus configuration, at range=27 mm, lateral=6 mm and 26 mm. The HIFU was then switched off, allowing the tissue sample to cool down. The temperature estimates are shown in Fig. 5

To create a lesion, a short-duration (3 sec), high-power (170 W acoustical) therapy pulse was delivered using the single focal pattern at lateral=16mm. The sample was cut and a lesion was observed at the expected location (35 mm deep within the tissue as shown in Figure 6).

7.2.3. Damage Assessment

At the time of writing this report, an experiment was performed where *in vitro* bovine muscle was electrically heated to ablate a spherical volume (18 mm diameter). Ultrasound RF frames were collected before, during, and after the heating. Figures 7 & 8 show the ultrasound image of the treated region before and after lesion formation, respectively. Clearly, there is significant change in the B-scan image due to the lesion formation where the top end of the lesion (closest to the imaging transducer) is clearly visible. Unfortunately, however, the extent of the lesion cannot be determined from the B-scan alone. We are currently investigating algorithms for extracting relevant tissue parameters that might be correlated with damage. Results of this investigation will be reported in a future report.

8. DISCUSSION AND CONCLUSIONS

An overview of the current status and future directions of some of the outstanding research problems relevant to interactive image-guided noninvasive HIFU surgey with phased arrays was given. While the physiological basis for thermal tissue damage by HIFU is fairly well understood, mechanical effects are not as well understood.[48,49] Nevertheless, there is general agreement that thermal surgery with HIFU can be performed noninvasively in several important sites, e.g., prostate. Phased array systems will make it possible to treat tumor sites previously inaccessible for therapeutic ultrasound, e.g., liver tumors. Treatment planning based on the BHTE and thermal dose concept appear to be valid based on experience in animal models.[16] The availability of 3D MRI and/or CT patient data sets will allow for patient specific treatment planning and optimization of the transducer array as well as the surgical procedure, e.g., scan trajectory, single- or multiple-focus patterns, etc.

The main challenge remains in developing accurate multidimensional temperature feedback for guidance and monitoring of the effects of the HIFU therapeutic beams. While early results on two-dimensional temperature imaging based on several imaging modalities are quite encouraging, several limitations still need to be overcome before these techniques are fully developed. However, there has never been a time when the promise of this "enabling technology"

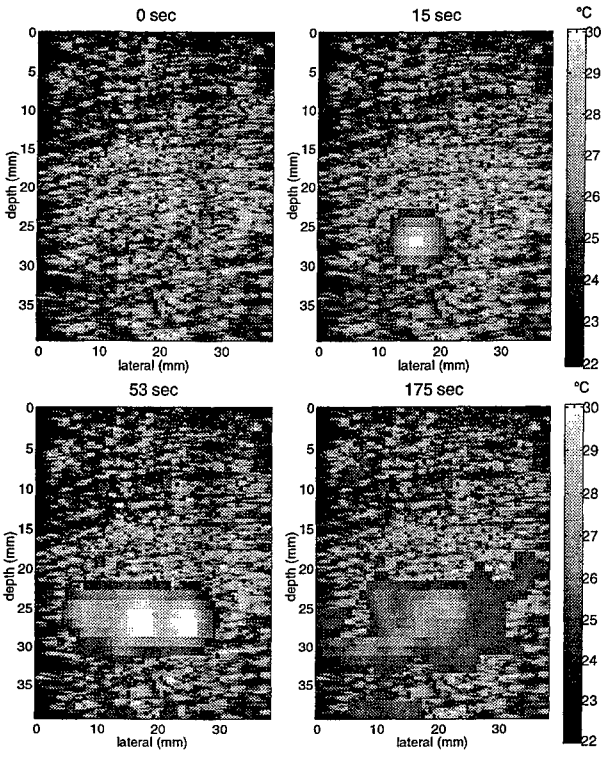

Figure 5. Sequence of temperature estimates *in vitro* bovine muscle experiment

Important Note:
In Figure 5 at 15 sec the heating from the single focus is evident at range=27 mm, lateral=16 mm. The frame at 53 sec shows the lingering heat of the first focal point and the initial heating of the double focus pattern. The frame at 175 sec shows the spread of heat due to conduction as the tissue cooled down. The entire sequence of frames can be seen at our web site (http://bul.eecs.umich.edu/research/phillipv/uss96.shtml).

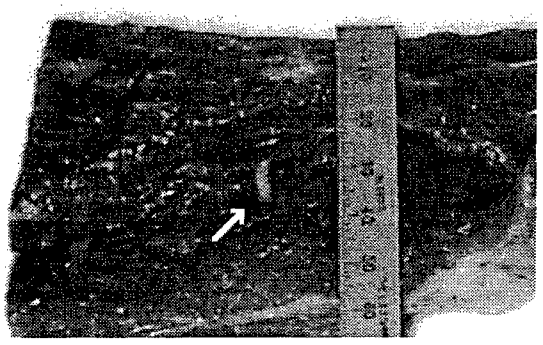

Figure 6. Lesion found at pre-specified location in beef muscle experiment.

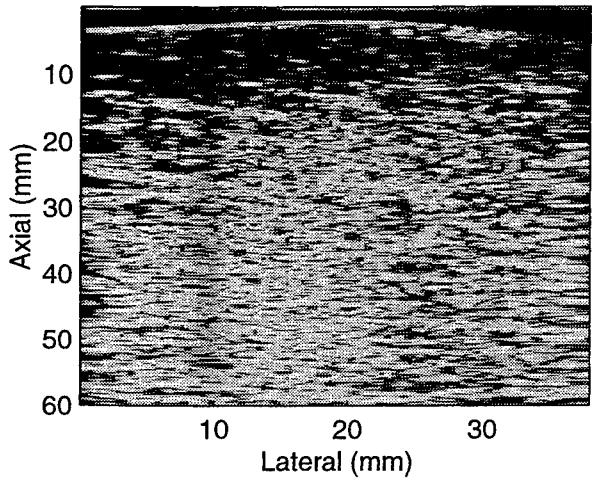

Figure 7. Ultrasound B-scan image before start of heating.

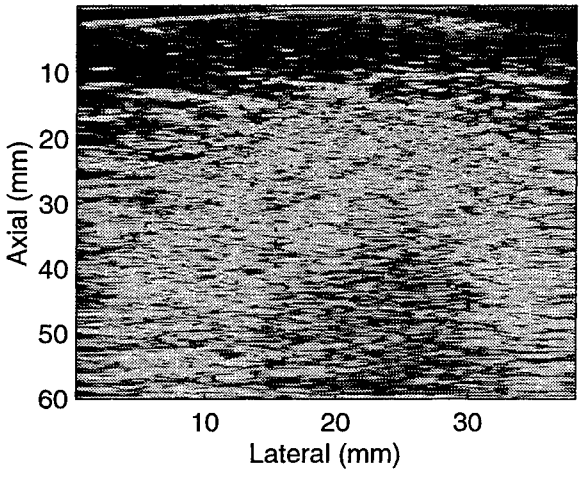

Figure 8. Ultrasound B-scan image after lesion formation.

has been larger. We have presented some results from our experience with our ultrasound-guided HIFU system for tissue ablation. Other groups have shown that MRI and X-ray CT can be used in a similar manner.

Finally, the issue of noninvasive damage assessment will become more and more important as HIFU-based noninvasive surgery systems continue to develop. In this area, it is almost certain that X-ray CT and MRI will be immensely useful, even though the cost of using them clinically for long-term assessment might be prohibitive. Ultrasound RF data with appropriate signal processing for extracting tissue parameters that may reflect change in

tissue state might prove useful in this regard. Work is currently underway to investigate a neural network model for damage detection based on diagnostic ultrasound pulse-echo data.

ACKNOWLEDGMENTS

This work is funded in part by the NIH Grant CA66602 and in part by NSF Grant ECS 9358301 (NSF Young Investigator). ATL provided the HDI Ultramark-9 scanner. The therapeutic array was acquired using funds from the Office of Vice President for Research at the University of Michigan.

REFERENCES

1. R. Maciunas, Editor *Interactive Image-Guided Neurosurgey* American Association of Neurological Surgeons, 1993.
2. T. Peters *et al* "Three-dimensional multimodal image guidance for neurosurgery," *IEEE Trans. Medical Imaging*, vol. 15, no. 2, pp. 121-128, 1996.
3. W. E. L. Grimson *et al* "An automatic registration method for frameless stereotaxy, image guided surgery, and enhanced reality visualization," *IEEE Trans. Medical Imaging*, vol. 15, no. 2, pp. 129-140, 1996.
4. S. Saparato and W. Dewey, "Thermal dose determination in cancer therapy," *Int. J. Rad. Onc. Biol. Phys.*, 10, pp. 787-800, 1984.
5. E. S. Ebbini, "*Deep Localized Hyperthermia with Ultrasound Phased Arrays Using the Pseudoinverse Pattern Synthesis Method* PhD Thesis, University of Illinois, Urbana- Champaign, 1990.
6. Ebbini E. S. & C. A. Cain, "A spherical-section ultrasound phased array applicator for deep localized hyperthermia", *IEEE Trans.Biomed. Eng.*, vol. 38, pp. 634 - 643, 1991.
7. Ebbini E. S. & C. A. Cain, "Multiple-focus ultrasound phased-array pattern synthesis: optimal driving-signal distributions for hyperthermia",*IEEE Trans. Ultrasonics, Ferroel. & Freq. Control*, vol. 36, pp. 540 - 548, 1989.
8. Ebbini E. S. & C. A. Cain, "Experimental evaluation of a prototype phased array applicator ",*IEEE Trans. Ultrasonics, Ferroel. & Freq. Control*, vol. 38, no. 5, pp. 510 - 520, 1991.
9. Ebbini E. S. & C. A. Cain, 'Optimization of the intensity gain of multiple-focus phased-array heating patterns",*Int. J. Hyperthermia*, vol. 7, no. 6, pp. 953-973, 1991.
10. Ebbini E. S., S-I Umemura, M. Ibbini & C. A. Cain, "A cylindrical-section ultrasound phased array applicator for hyperthermia cancer therapy", *IEEE Trans. Ultrasonics, Ferroel. & Freq. Control*, vol. 35, pp. 561 - 572, 1988.
11. H. Wang, E. Ebbini, M. O'Donnell, R. Seip and C. Cain, "Adaptive 2-D Cylindrical Section Phased Array System for Ultrasonic Hyperthermia," *Ultrasonics Symposium Proceedings*, Vol. 2, 1992, pp. 1261-1264.
12. R. Seip, E. S. Ebbini, J. H. Mo and A. L. Robinson, "Characterization of a Needle Hydrophone Array for Acoustic Feedback during Ultrasound Hyperthermia Treatments," *Ultrasonics Symposium Proceedings*, Vol. 2, 1992, pp. 1265-1269.
13. Y. Botros, J. Volakis, P. VanBaren, and E. Ebbini, "A hybrid computational model for ultrasound phased array heating in the presence of strongly scattering obstacles," *IEEE Trans. BME*, vol. 44, no. 11, pp. , 1997.
14. P. VanBaren, R. Seip, and E. S. Ebbini, "A New Algorithm for Dynamic Focusing of Phased-Array Hyperthermia Applicators through Tissue Inhomogeneities," *Ultrasonics Symposium Proceedings*, Vol. 2, 1993, pp. 1221-1224.
15. R. Seip, E.S. Ebbini, M. O'Donnell, and C.A. Cain, "Non-Invasive Detection of Thermal Effects due to Highly Focused Ultrasonic Fields," *Ultrasonics Symposium Proceedings*, Vol. 2 , 1993, pp. 1229-1232.
16. C.A. Damianou, K. Hynynen, and X. Fan, "Evaluation of accuracy of a theoretical model for predicting necrosed tissue volume during focused ultrasound surgery," *IEEE Trans. UFFC*, vol. 42, no. 2, pp. 182-187, 1995.
17. N. Sanghvi *et al*, "Noninvasive surgery of prostate tissue by high-intensity focused ultrasound," *IEEE Trans. UFFC*, vol. 43, no. 6, pp. 1099-1110, 1996.
18. R. Seip, P. VanBaren, and E. S. Ebbini, "Dynamic Focusing in Ultrasound Hyperthermia Treatments Using Implantable Hydrophone Arrays," *IEEE Transactions on Ultrasound, Ferroelectrics, and Frequency Control*, Vol. 41, No. 5, Sept. 1994, pp. 706-713.
19. R. Seip and E.S. Ebbini, "Non-invasive Estimation of Tissue Temperature Response to Heating Fields using Diagnostic Ultrasound," *IEEE Trans. on BME*, vol. 42, no. 8, pp. 828-839, 1995.

20. J. Jenne *et al*, "CT on-line Monitoring of HIFU therapy," to appear in the Proceedings of the 1997 IEEE International Ultrasonics Symposium.
21. B. Fallone *et al*, "Noninvasive thermometry with a clinical x-ray scanner," Medical Physics, vol. 9, no. 5, pp. 715-721, 1982.
22. K. Hynynen *et al*, "Feasibility of using ultrasound phased arrays for MRI monitored noninvasive surgery," *IEEE Trans. UFFC*, vol. 43, no. 6, pp. 1043-1053, 1996.
23. J. De Poorter *et al*, "Noninvasive MRI thermometry with the proton resonance frequency (PRF) method: *In vivo* results in human muscle," *Mag. Res. Med.*, vol. 33, pp. 74-81, 1995.
24. D. Parker, "Applications of NMR imaging in hyperthetmia: An evaluation of the potential for localized tissue heating and noninvasive temperature monitoring," *IEEE Trans. BME*, vol. 31, no. 1, pp. 161-167, 1984.
25. K. Paulsen *et al*, "Initial *in vivo* experience with EIT as a thermal estimator during hyperthermia," *Int. J. Hyperthermia*, vol. 12, no. 5, pp. 573-591, 1996.
26. P. Meaney *et al*, "Microwave imaging for tissue assessment: Initial evaluation in multitarget tissue-equivalent phantoms," *IEEE Trans. BME*, vol. 43, no. 9, pp. 878-890, 1996.
27. T. Bowen *et al*, "Measurement of the temperature dependence of the velocity of ultrasound in soft tissues," *Ultrasonic Tissue Characterization II*, M. Linzer, ed., NBS Spec. Publ. 525, pp. 57-61, 1979.
28. C. Simon, P. VanBaren, and E. Ebbini, "Two-dimensional temperature estimation for ultrasound thermotherapy using diagnostic ultrasound," *IEEE Trans. UFFC*, accepted.
29. P. VanBaren and E. Ebbini "Multi-point temperature control during hyperthermia treatments: Theory and Simulation," *IEEE Trans. on BME*, vol. 42, no. 8, pp. 828-839, 1995.
30. R. Seip, P. VanBaren, C. Cain, and E. Ebbini, "Noninvasive realtime multipoint temperature control for ultrasound phased array treatments," *IEEE TRans UFFC*, vol. 43, no. 6, pp. 1063-1073, 1996.
31. W.J. Fry, J.W. Barnard, F.J. Fry, R.F. Krumins, and J.F. Brennan, "Ultrasonic lesions in the mammalian central nervous system," *Science*, vol. 122, pp. 517-518, 1955.
32. G. ter Haar, D. Sinnett, and I. Rivvens, "High intensity focused ultrasound – a surgical technique for the treatment of discrete liver tumors," *Physics in Medicine and Biology*, vol. 34, pp. 1743-1750, 1989.
33. L. A. Frizzell, "Threshold dosages for damage to mammalian liver by high-intensity focused ultrasound," *IEEE Trans. UFFC*, vol. 35, no. 5, 1988.
34. F.J. Fry, G. Kossof, and R.C. Eggleton, "Threshold ultrasonic dosages for structural changes in mammalian brain, *J. Acous. Soc. Amer.*, vol 48, pp. 1413-1417, 1970.
35. F. Dunn and F.J. Fry, "Ultrasonic threshold dosages for the mammalian central nervous system," *IEEE Trans. BME*, vol. 18, pp. 253-256, 1971.
36. J.Y. Chapelon, J. Margonari, D. Cathinol, A. Gelet, C. Guers, Y. Theillere, "Threshlods for tissue ablation by focused ultrasound," *Proc. 1990 IEEE Ultrasonic Symposium*, vol. 2, pp. 1653-1656, 1990.
37. N.T. Sanghvi, F.J. Fry, R. Foster, R. Chua, G. Chua "System design Considerations for high intensity focused ultrasound device for the treatment of tissue *in-vivo*," *Med. Biol. Eng. Comp.*, vol. 29, Supp., p. 748, 1991.
38. A. Malcom and G. ter Haar, "A study of the formation of arrays of focused ultrasound lesions and measurements of their acoustic properties," Proceedings of the Workshop on Surgical Applications of Energy Sources, May 17 - 19, 1996, Estes Park, CO.
39. J. Driller and F. L. Lizzi, "Therapeutic applications of ultrasound: A review," *IEEE EMB Magazine*, vol. 6, no. 4, pp. 33-40, 1987.
40. H. Cline, K. Hynynen, R. Watkins, S. Souza, and F. Jolesz, "MRI-guided focused ultrasound surgery," *J. Computer Assisted tomography*, vol. 16, no. 6, 1992.
41. G. Vallancien, E. Chartier-Kastler, D. Chopin, B. Veillon, J.M. Brisset, and J. Andre-Bougaran, "Focused ultrasound extracorporeal piezoelectric pyrotherapy," *Technical report submitted to CERA - Fondation du l'Avenir- Paris, France, on the first two years of experimentation*, August 1991.
42. Wang H., E. S. Ebbini & C. A. Cain, "Computationally efficient algorithms for control of ultrasound phased-array hyperthermia applicators based on a pseudoinverse method", *IEEE Ultrasonics, Ferroel. & Freq. Control*, vol. 37, pp. 274 - 277, 1990.
43. G. Hahn,"Hyperthermia for the engineer: A short biological primer," IEEE Trans. BME, vol. BME-31, no. 1, pp. 3-8, 1984.

44. T. Samulski, E. Lee, and G. Hahn,"Hyperthermia as a clinical treatment modality," Cancer Treatment Reports, vol. 68, no. 1, pp 309-316, 1984.
45. P. Lele,"Physical aspects and clinical studies with ultrasonic hyperthermia," in *Hyperthermia in Cancer Therapy.* F. Storm, Ed., G. K. Hall Medical Publishers, Boston, Ma, 1983.
46. H.H. Pennes, "Analysis of tissue and arterial blood temperature in the resting human forearm," *J. Appl. Physiol.*, 1:93, 1948.
47. K. Hynynen, R. Roemer, D. Anhalt, C. Johnson, Z. Xu, W.Swindell, and T. Cetas," A scanned, focused, multiple transducer ultrasonic system for localized hyperthermia treatments," Int. J. Hyperthermia, vol. 3, no. 1, pp. 21-35, 1987.
48. E. Carstensen, W. Law, and D. McKay," Demonstration of nonlinear acoustical effects at biomedical frequencies and intensities," Ultrasound in Med. and Biology, vol. 6, pp. 359-368, 1980.
49. W. Swindell," A theoretical study of nonlinear effects with focused ultrasound in tissues: An acoustic Bragg peak," Ultrasound in Med. and Biology, vol. 11, no. 1, pp. 121-130, 1985.
50. K. Ocheltree, "Analysis of power deposition patterns and ultrasonic phased arrays for localized hyperthermia," Ph. D. Thesis, Univ. of Illinois at Urbana-Champaign, 1987.
51. T. Cavvichi and W. O'Brien, Jr., "Heat generated by ultrasound in an absorbing medium," J. Acous. Soc. Am. 76(4), Oct. 1984.
52. P. Corry, K. Jabboury, E. Armour, and J. Kong, "Human cancer treatment with ultrasound," IEEE Trans. Sonics. Ultrason., vol. SU-31, no. 5, pp. 444-456, 1984.
53. S. Clegg and R. Roemer, "Toward the estimation of three-dimensional temperature fields from noisy temperature measurements during hyperthermia," Int. Jour. Hyperthermia, vol. 5, no. 4, pp. 467-484, 1989.
54. C. Perez, "Rationale for clinical application of hyperthermia: Alone or combined with irradiation or cytotoxic drugs in cancer therapy," in *Physical aspects of hyperthermia.* G. Nausbaum, Ed., AAPM, New York, 1982.
55. G. Nausbaum, "Conceptual outline of hyperthermia physics," in *Physical aspects of hyperthermia.* G. Nausbaum, Ed., AAPM, New York, 1982.
56. E. Burdette, "Electromagnatic and acoustic properties of tissues," in *Physical aspects of hyperthermia.* G. Nausbaum, Ed., AAPM, New York, 1982.
57. F. Barber and C. Griffice, "Power deposition for ultrasound hyperthermia," in *Physical aspects of hyperthermia.* G. Nausbaum, Ed., AAPM, New York, 1982.
58. P. Lele, "Local hyperthermia by ultrasound," in *Physical aspects of hyperthermia.* G. Nausbaum, Ed., AAPM, New York, 1982.
59. S. Goss and F. Fry, "High intensity ultrasonic treatment of tumors," Proc. IEEE 1982 Ultrason. Symp., 1982.
60. P. Lele, "Effect of ultrasound on solid mammalian tissues and tumors in vivo," in *Ultrasound.* M. Rapacholi, M. Grandolfo, and A. Rindi Ed., Plenum Publishing Corp., 1987.
61. F. Storm, "Background, principles, and practice," in *Hyperthermia in Cancer Therapy.* F. Storm Ed., G. K. Hall Medical Publishers, Boston, Ma, 1983.
62. W. Nyborg *et al. Biological effects of ultrasound: mechanisms and clinical implications.* NCRP Report no. 74, 1983.
63. K. Ocheltree and L. Frizzel, "Sound field calculation for rectangular sources," IEEE Trans. Ultrason. Ferroelect. Freq. Contr., vol. 36, no. 2, pp. 242-248, 1989.
64. L. Edelstein-Keshet, M. Dewhirst, J. Oleson and T. Samulski, "Characterization of tumour temperature distributions in hyperthermia based on assumed mathematical forms," Int. J. Hyperthermia, vol. 5, no. 6, pp. 757-777, 1989.
65. R. Jain, "Bioheat Transfer: Mathematical Models of Thermal Systems," Ch. 2 in *Hyperthermia in Cancer Therapy.* F. Storm Ed., Massachusetts: G. K. Hall Medical Publishers, 1983.
66. S. Goss, R. Johnston and F. Dunn, "Compilation of empirical ultrasonic properties of mammalian tissues: II," J. Acoust. Soc. Am., vol 68, p93, 1980.

SESSION 8

Focused Ultrasound for Tissue Therapy II

Influence of acoustic power on parietal thermometry during extracorporeal high intensity focused ultrasound treatments

François Lacoste [b], Benoît Feuillu [a], Jacques Schlosser [a], and Guy Vallancien [c]

[a] Department of Urology, CHU Nancy-Brabois, Nancy 54511
[b] Edap-Technomed, Engineering Department, Vaulx en Velin 69120
[c] Department of Urology and Research (CERA), Institut Montsouris, Paris 75013
France

ABSTRACT

Objectives: Compare the muscular parietal heating during high intensity focused ultrasound (HIFU) at different acoustic power levels.
Methods: 3 series of 100 acoustic pulses of same energy but variable power were applied in vivo on the muscular lumbar and abdominal walls in 4 pigs. The target volume was located 47 to 94 mm behind the skin. Two thermocouples were inserted into the muscular wall facing the focal point 10-15 mm and 25-30 mm from the skin. The position of the treatment head was the same for the 3 series of acoustic pulses. The temperatures in the muscular wall were recorded during the HIFU treatment.
Results: The lumbar muscular wall heating were: at low acoustic power (53 to 67W) 1.5 to 4.0°C, at medium acoustic power (532 to 654W) 2.3 to 6.5°C and at high acoustic power (1895 to 2372W) 1.2 to 5.0°C. The abdominal muscular wall heating were: at low acoustic power (128 to 163W) 0.5 to 6.5°C, at medium acoustic power (451 to 574W) 2.7 to 8.4°C and at high acoustic power (1213 and 1545W) 3.3 to 8.5°C.
Conclusion: During extracorporeal HIFU treatments, the muscular parietal heating is variable among individuals and increases with the acoustic power.

Key words: High Intensity Focused Ultrasound, Acoustic Power, Parietal Thermometry.

1. INTRODUCTION

High Intensity Focused Ultrasound (HIFU) destroys tissues by means of a local thermal effect and an acoustic cavitation mechanism [1,2]. Clinical trials of transrectal treatment of prostate cancer are currently underway [3]. To treat deep tumors, such as bladder tumors, renal cancer and liver cancer, the ultrasound beam must cross the muscle wall, causing heating of the muscle wall [1]. This heating is poorly defined at the present time, as the authors [2,4,5,6,7] have been mainly concerned with the temperatures in the target organ. However, it is essential to evaluate this effect in order to prevent the development of harmful thermal effects on the muscle wall while maintaining a real effect at the target site. It has been suggested that a low intensity acoustic beam would create less cavitation in the intervening tissues than a high intensity one and hence would traverse those with less absorption. This study in pigs was designed to determine the influence of the acoustic power of HIFU on heating of the muscle wall.

2. MATERIAL AND METHOD

2.1 Material

2.1.1 The transducer

The Pyrotech is a transducer equipped with 160 piezoelectric ceramics, mounted on a spherical cap, which emit focused ultrasound at a frequency of 1 MHz and an adjustable acoustic power ranging from 50 to 6000 Watts. Its treatment head can be displaced in 3 dimensions with millimetric precision. The head contains a coupling liquid maintained at a

SPIE Vol. 3249 • 0277-786X/98/$10.00

constant temperature of 15 °C. A removable ultrasound transducer is situated in the center. It emits ultrasound at a frequency of 3.5 MHz and is used to locate the target organ.

2.1.2 The animal

The study was conducted in 4 Large White pigs with a mean weight of 60±5 kg. Before performing ultrasound detection of the target organ, acoustic gel was applied onto the previously shaved skin in contact with the treatment head to ensure good acoustic conduction.

2.1.3 Thermocouples

Model IT18 implantable tissue thermocouples were used (Physitemp Inc., Clifton, USA).

2.2 Method

Extracorporeal pyrotherapy was performed on the pigs under general anaesthesia and consisted of:
- Premedication by IM injection of 15 mg of carazolol and 0.5 mg of atropine sulphate.
- Induction by IM injection of 10 mg/kg of ketamine, then IV infusion of 10 mg/kg of thiopental sodium and 12 mg of vecuronium bromide into a vein of the ear.
- General anaesthesia was maintained by IV injection of thiopental sodium as required and ketamine via an electrical syringe (5 mg/min).

Endotracheal intubation was performed after induction.

Three successive series of 100 pulses with different acoustic powers but with the same firing energy were tested on the lumbar wall (facing the kidney) and the abdominal wall (facing the liver) of the pigs. The acoustic energy of each pulse was 71 J and 83 J to the lumbar wall, 250 J and 300 J to the abdominal wall. The firing energy was chosen as the maximal value tolerated by the skin at high intensity. The test was repeated on 4 pigs. The acoustic beams were focused at a depth of 47 to 94 mm below the skin. The acoustic powers were: 53 to 67 W, 532 to 654 W and 1895 to 2372 W over the lumbar wall and 128 to 163 W, 451 to 574 W and 1213 to 1545 W over the abdominal wall. Two thermocouples connected to a graphic recorder were placed in the muscle wall over the target site and centered on the acoustic beam: one superficial, 10-15 mm below the skin, and the other deep, 25-30 mm below the skin. The 3 series of pulses were consecutively applied with a sufficient time interval to let the tissue cool and return to the initial muscle wall temperature. The target volume was 1 cm^3 with a 1 mm displacement of the treatment head and 5 seconds waiting time between each of the 100 pulses. The target site was identical for the 3 acoustic powers tested over each lumbar and abdominal wall. The duration of treatment was 8 minutes 30 seconds for each series of pulses. The first series was repeated on 2 lumbar walls and 2 abdominal walls. The muscle walls were biopsied 3 days after treatment and were examined macroscopically.

3. RESULTS

The initial muscle wall temperature, T0, was always 1 to 6 °C lower on the surface (30.8±4.8 °C) that in the deeper tissues (34±3.1 °C). An example of thermal recording is presented in Figure 1. The recorded temperatures are presented in Table 1.

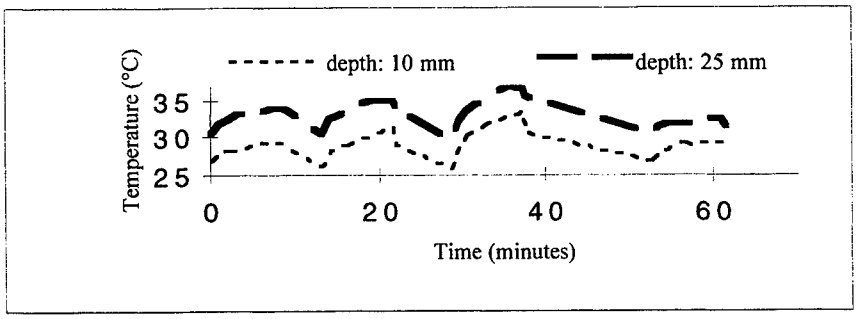

Figure 1: thermal recording for abdominal wall No 3.

No Wall	FE	Pf	To	Tf	Tf-To	To	Tf	Tf-To
			15 mm			25 mm		
	83	53	35.5	39.5	4	36.4	39.7	3.3
1	83	654	35.5	42	6.5	36.4	42.5	6.1
	83	1895	35.5	40.4	4.9	36.4	40.5	4.1
			15 mm			30 mm		
	71	61	29.5	31.3	1.8	36	39.5	3.5
2	71	532	26.5	30.5	4	36	39.5	3.5
	71	2176	26	31	5	36	39	3
	71	61	26	29.5	3.5	36	38.5	2.5
			15 mm			30 mm		
	71	67	32.5	36.3	3.8	37.1	39	1.9
3	71	580	33.5	37	3.5	37.1	39	2.3
	71	2372	33.5	35.6	2.1	37	38.2	1.2
	71	67	33.7	37	3.3	37	38.5	1.5

Table 1a: temperature recordings in the lumbar wall

No Wall	FE	Pf	To	Tf	Tf-To	To	Tf	Tf-To
			15 mm			30 mm		
	300	128	29.2	31.5	2.3	34.8	36.5	1.7
1	300	451	29.2	32.4	3.2	34.8	37.5	2.7
	300	1213	29.5	34.5	5	34.8	39.4	4.6
			15 mm			30 mm		
	250	163	31.5	32	0.5	36	37.5	1.5
2	250	574	30	36.5	6.5	36	41.7	5.7
	250	1545	30	35.5	5.5	36	39.3	3.3
	250	163	30	33.5	3.5	36	38.5	2.5
			10 mm			25 mm		
	250	163	27	29.5	2.5	30.5	34	3.5
3	250	574	26.5	31.5	5	30.5	35	4.5
	250	1545	26	33.5	7.5	29.8	36.8	7
	250	163	27	29.5	2.5	30.6	32.6	2
			15 mm			30 mm		
	250	163	32.5	39	6.5	35.5	40.5	5
4	250	574	32.5	40.9	8.4	35.5	42.5	7
	250	1545	32.5	41	8.5	35.5	41.8	6.3

Table 1b: temperature recordings in the abdominal wall

Table 1: temperature recordings in the walls
FE: firing energy, in Joules.
Pf: power at the focal point, in Watts, corrected for tissue absorption.
T0: initial wall temperature
Tf: final wall temperature
Tf-T0: heating of the wall in degrees Celsius between the start and end of treatment
... mm: depth of the thermocouple in the wall, in millimeters.

4. DISCUSSION

Focused ultrasound induces heating of the muscle wall in the path of the ultrasound beam. The temperatures measured in the muscle wall depended on the depth. The surface of the muscle wall was more effectively cooled by the conduction liquid, by an average of 7.2±4.8 °C. The temperatures observed in the deeper layer (34±3.1 °C) were close to the pig's physiological body temperature of 38 °C. Individual variations of temperature T0 at the same depth of the muscle wall depended on contact time of the treatment head on the skin. This time corresponded to identification of the target site, i.e. 10 to 30 minutes.

Heating of the muscle wall varied by 0.5 to 8.5 °C from one pig to another. This heating did not exclusively depend on the acoustic power, as different degrees of heating were recorded at identical firing energies and acoustic powers (for example compare the heating in abdominal walls No. 2 and No. 4)

These differences can be explained by individual variations in tissue echostructure and the energy delivered to the muscle wall. Foster and Hunt [8] reported that tissue heterogeneity could defocus the ultrasound beam. This risk of defocusing is amplified when treating deep organs, such as the kidney, liver and bladder, because of the greater number of tissue interfaces. The temperature of the muscle wall depends on the heat generated by absorption of acoustic energy and losses due to thermal diffusion at the skin-treatment head interface and tissue perfusion. The architecture, blood supply of the muscle wall, and the state of the skin influence thermal diffusion and provide a likely explanation for the individual variations in muscle wall heating . It has been shown that the role of blood perfusion at the target site is negligible for firing times less than two seconds [6]. However it does play a role in regulating the temperature of the wall, as acoustic heating of the wall takes place during the whole treatment.

The absence of burns of the muscle wall is due to the short treatment durations of less than 10 min. Longer treatments, lasting more than 30 min, could induce unacceptable heating of the muscle wall to a temperature greater than 45 °C. This thermal data must be taken into account when determining the duration of treatment with focused ultrasound.

At high acoustic power, the acoustic heating of the wall is not significantly higher than at low acoustic power. This contrasts with the findings of Chapelon [9] who showed that at high intensity, less energy was necessary to obliterate tissue than at low intensity. The present data suggests that high intensity pulses may be more efficient than low intensity pulses for extracorporeal treatment with HIFU.

5. CONCLUSION

Heating of the muscle wall increased with the focal acoustic power and varied considerably from one pig to another.

6. ACKNOWLEDGMENTS

We want to thank the engineers and technicians of the EDAP-TECHNOMED company and all members of the laboratory of research (CERA - Fondation de l'Avenir) for their technical assistance in this research.

7. REFERENCES

1. F.J. Fry, "Intense Focused Ultrasound in Medicine: Some Practical Guiding Physical Principles from Sound Source to Focal Site in Tissue", Eur Urol, 23(suppl 1), pp. 2-7, 1993.
2. G. Vallancien, E. Chartier-Kastler, D. Chopin, B. Veillon, JM. Brisset, and J. André-Bougaran, "Focused Extracorporeal Pyrotherapy: Experimental Results", Eur Urol, 20, pp. 211-219, 1991.
3. A. Gelet, J.Y. Chapelon, R. Bouvier, R. Souchon, C. Pangaud, A.F. Abdelrahim, D. Cathignol, and J.M. Dubernard, "Treatment of prostate cancer with transrectal focused ultrasound: Early clinical experience", Eur Urol, 29, pp.174-183, 1996.
4. K. Hynynen, A. Darkazanli, C.A. Damianou, E. Unger, and J.F. Schenck, "Tissue thermometry during ultrasound exposure", Eur Urol, 23(suppl1), pp. 12-16, 1993.
5. B.E. Billard, K. Hynynen, and R.B. Roemer, "Effects of physical parameters on high temperature ultrasound hyperthermia", Ultrasound Med Biol, 16, pp. 409-420, 1990.
6. K. Hynynen, D. DeYoung, M. Kundrat, and E. Moros "The effect of blood perfusion rate on the temperature distributions induced by multiple, scanned and focused ultrasonic beams in dogs' kydneys in vivo", Int J Hyperthermia, 5, pp. 485-97, 1989.
7. K. Hynynen, D. Schimm, D. Anhalt, B. Stea, H. Sykes, J.R. Cassady, and R.B. Roemer, "Temperature distributions during clinical scanned, focused ultrasound hyperthermia treatments", Int J Hyperthermia, 6, pp. 891-908, 1990.
8. F.S. Foster and J.W. Hunt, "The focusing of ultrasonic beams through human tissue", Acoustic Imaging, 8, pp. 709-718, 1980.
9. J.Y. Chapelon, J. Margonari, D. Cathignol, A. Gelet, C. Guers, Y. Theillère, "Threshlolds for tissue ablation by focused ultrasound", IEEE Ultrasonics Symposium Proceedings, pp. 1653-1656, 1990.

The intensity dependence of Focused Ultrasound lesion position.

Paul Meaney[#], Mark D. Cahill[+], Gail ter Haar[*]

[#]Thayer School of Engineering, Dartmouth College, Hanover, NH, USA
[+]Medical Physics Department, St Thomas' Hospital, London SE1, UK
[*]Joint Department of Physics, Royal Marsden Hospital, Sutton, Surrey SM2 5PT, UK

ABSTRACT

Knowledge of the spatial distribution of intensity loss from an ultrasonic beam is critical to predicting lesion formation in focused ultrasound surgery. To date most models have used linear propagation models to predict the intensity profiles needed to compute the temporally varying temperature distributions. These can be used to compute thermal dose contours that can in turn be used to predict the extent of thermal damage. However, these simulations fail to adequately describe the abnormal lesion formation behaviour observed for *in vitro* experiments in cases where the transducer drive levels are varied over a wide range. For these experiments, the extent of thermal damage has been observed to move significantly closer to the transducer with increasing transducer drive levels than would be predicted using linear propagation models. The simulations described herein, utilise the KZK (Khokhlov-Zabolotskaya-Kuznetsov) nonlinear propagation model with the parabolic approximation for highly focused ultrasound waves, to demonstrate that the positions of the peak intensity and the lesion do indeed move closer to the transducer. This illustrates that for accurate modelling of heating during FUS, nonlinear effects must be considered.

1. INTRODUCTION

Significant past work has been performed in modeling the formation of lesions created by high intensity focused ultrasound surgery (FUS) exposures in tissue. These efforts have generally involved the derivation of a relatively simple form of the intensity profile - either in the form of a finite cylinder or a Gaussian distribution[1-11] and the incorporation of this distribution into either an analytical or an axially symmetric numerical solution of the bioheat equation[12]. For well behaved single lesions, these techniques have worked well. However, it has been demonstrated by Watkin, et al.[13], that as transducer drive levels are increased, lesions formed in excised liver tissue move significantly closer to the transducer than would be expected from present models. These results also show that the part of the lesion closest to the transducer (the lesion head) becomes much wider than the back section (the lesion tail), giving the overall lesion a "tadpole-like" appearance. Finally, above a certain transducer drive level, the tail of the lesion remains relatively the same length. While it is probable that cavitation and tissue boiling, (for which there is not presently an adequate model for representing the resultant wave scattering), play a role in these aberrantly shaped lesions it is essential to understand the contribution of nonlinear wave propagation to this.

In general nonlinear propagation involves the deformation of a wave due to nonlinearities in the medium. This can be viewed as the generation of harmonics of the original fundamental frequency. Non-linear effects can lead to significant alteration in the effective attenuation of the medium[14], and movement of the position at which power dissipation by the beam is a maximum[14,15]. For the higher harmonics, the acoustic absorption coefficient is greater than at the fundamental, and there is therefore an overall loss of beam intensity compared to that which would be predicted from linear propagation models. Attempts have been made by Carstensen, et al.[1], Dalecki, et al.[3], Hynynen, et al.[6,16], Swindell[17], and Watkin, et al.[13] to incorporate nonlinear effects into their numerical models.

Baker[18], has used the KZK (Khokhlov-Zabolotskaya-Kuznetsov) equation to demonstrate that for both plane circular and lightly focused circular transducers, the axial peak intensity position shifts significantly towards the transducer with increasing drive levels. For these simulations, the Bergen code[19], which assumes the parabolic approximation, was applied using an axisymmetric geometry. However, the validity of this solution deteriorates in the highly focused configurations that

SPIE Vol. 3249 • 0277-786X/98/$10.00

are used in FUS. Criteria developed by Tjotta, et al.[20] define the domain of validity for the parabolic equation in these cases. For the FUS transducer used in this model, the critical parameters are at the limit of the domain of validity. It is critical to understand by how much this computation can differ from the exact solution because the most significant manifestation of this type of computational error is a shift in the peak intensity position towards the transducer. This is precisely part of the phenomena we are examining. We have therefore first performed these simulations at a very low drive level for comparison with the known results from a linear propagation model.

The energy deposition profiles created from this simulation at several transducer drive levels have been used as inputs to the 3D finite element thermal diffusion model[21] to allow computation of the time varying temperature profiles. The thermal dose has been computed for each node, and a threshold applied in an attempt to predict the extent of thermal damage. These results have been examined in light of the observations from the *in vitro* experiments at increasing drive levels.

2. METHODS

2.1 Experimental configuration

Figure 1 shows the configuration described in the *in vitro* experiments performed by Watkin, et al[13]. A focused bowl transducer with a diameter of 8.4cm and a radius of curvature of 15cm operating at 1.7 MHz was used. Individual lesions were formed with the geometric focus of the transducer positioned 2.7 cm below the bovine liver tissue surface. A range of transducer drive levels was chosen with a fixed exposure time of 2 seconds. The experiments were performed at 21° C. All samples were degassed as standard procedure. At each transducer drive level several lesions were created. The shape and size of the discoloured region corresponding to the FUS lesion was recorded. An "average geometry" was then derived.

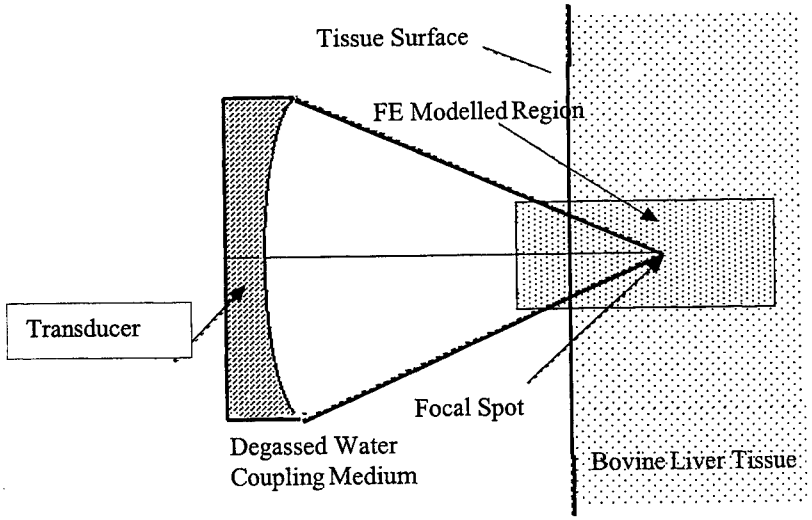

Figure 1 - Schematic Diagram of the region modeled in these simulations in relation to the Watkin et al. [1996] *in vitro* experiments (not to scale).

2.2 Nonlinear propagation model

2.2.1 Pressure Field Computation

The Khokhlov-Zabolotskaya-Kuznetsov (KZK) equation[22] in a given medium (with index i) can be written as

$$\frac{2}{c_i}\frac{\partial^2 p}{\partial z \partial t_i} - \frac{2\alpha}{c_i \omega^2}\frac{\partial^3 p}{\partial t_i^3} - \nabla_{\perp x}^2 p = \frac{\beta_i}{\rho_i c_i^4}\frac{\partial^2 p^2}{\partial t_i^2} \qquad (1)$$

and describes the propagation of sound of finite amplitude, in the "parabolic" approximation, that is, the limit in which the variation of the instantaneous pressure in one direction (taken to be the z-direction) is far more rapid than that in the perpendicular direction. Here p is the over pressure, ($p = P - p_o$ where P is the acoustic pressure and p_o is the ambient pressure). c_i is the speed of sound, α_i is the attenuation coefficient of a wave with frequency f and angular frequency ω,

given by $\alpha_i = \alpha_{0i} f^2$, β_i is the coefficient of nonlinearity, and ρ_i is the ambient density of the medium. t_i is a retarded time

$$t_i = t - z / c_i - t_{0i} \tag{2}$$

where t_{0i} is a constant chosen to make t_i continuous at the boundary between the media, and

$$\nabla^2_{\perp x} = \left(\frac{\partial^2}{\partial x^2} + \frac{\partial^2}{\partial y^2} \right) \tag{3}$$

Imposing the coordinate transformations

$$\tau_i = \left(t_i - \frac{\gamma}{2c_i} \frac{\mathbf{x}^2}{r_0 + \gamma z} \right) \omega \tag{4}$$

$$\sigma = \frac{z}{r_0} \tag{5}$$

$$\mathbf{u} = \frac{\mathbf{x}/a}{1 + \gamma z / r_0} \tag{6}$$

$$p' = (1 + \gamma z / r_0) p \tag{7}$$

where $\mathbf{x}$ and $\mathbf{u}$ are coordinates in the plane orthogonal to the z-axis, a is a characteristic transverse measure of the source, γ is a parameter of the co-ordinate transformation and r_0 the corresponding Rayleigh distance in a reference medium, such as water, the transformed beam equation (TBE)[20,23] can be derived :

$$\frac{\partial^2 p'}{\partial \tau_i \partial \sigma} = \alpha_i r_o \frac{\partial^3 p'}{\partial \tau_i^3} + \frac{c_i}{4 c_0 (1 + \gamma \sigma)^2} \nabla^2_u p' + \frac{r_0}{2 l_{di} P_0 (1 + \gamma \sigma)} \frac{\partial^2 p'^2}{\partial \tau_i^2} \tag{8}$$

Here c_0 is the speed of sound in the reference medium, P_0 is a characteristic pressure of the system, and

$$l_{di} = \frac{\rho_i c_i^3}{\beta_i \omega P_0} \tag{9}$$

is the discontinuity length in the medium of a plane wave with pressure amplitude P_0. The advantage of this transformation is that it is then possible to increase the definition of the model in the region of the focus, within limits indicated by Ystad and Bernsten[23] by taking a negative value for γ, or to model a diverging beam by using a positive value for γ.

When solving equation (8) in the temporal frequency domain, it is possible to modify the frequency dependence of the attenuation to obey the fractional power laws commonly used for biological media. Specific values used were[24], for water:

$c_w = 1486 \text{ ms}^{-1}$

$\rho_w = 1000 \text{ kg m}^{-3}$

$\beta_w = 3.5$

$\alpha_w = \alpha_{0,w} f^2$ with $\alpha_{0,w} = 2.5 \times 10^{-2} \text{ Np m}^{-1} \text{MHz}^{-2}$

for liver:

$c_l = 1614 \text{ ms}^{-1}$

$\rho_l = 1214 \text{ kg m}^{-3}$

$\beta_l = 4.775$

$\alpha_l = \alpha_{0,l} f^{1.266}$ with $\alpha_{0,l} = 4.3 \text{Np m}^{-1} \text{MHz}^{-1.266}$

The initial conditions for the pressure field were derived by evaluating the Rayleigh integral for the source transducer in a plane 1 cm from the back of the transducer numerically, and equation (8) was then solved with γ chosen to be negative to produce a coordinate singularity 180 mm from the back of the transducer in order to improve transverse accuracy in the region of the focus. For this implementation the non-axisymmetric Bergen code[19] which had already been modified to calculate the nonlinear term in the time-domain[15] was used to solve equation (8) in a two-layer system.

It has been shown mathematically for focused ultrasound configurations that the parabolic approximation is valid within the focal region when the following conditions are met[20]:

$$d/a >> 1$$

$$(ka)^{2/3}(2G)^{1/3} \geq 1 \qquad (10)$$

For the applications being considered here, both ka ($k = 2\pi/\lambda$) and G (the focal gain) are generally large. Thus, the first of these two criteria dominates. Simulations have been performed to explore the range of d/a (d is the focal length) for which the approximation is valid. Good agreement was found between this solution at a low drive level and that for the linear case using the Rayleigh integral for values of d/a as low as 3.5. Quite coincidentally, the d/a value for the transducer used in these experiments is 3.57 which is quite close to this limit. Thus, as noted in the introduction, the solution was examined for this configuration to see how much of a distortion could be expected.

2.2.2 Heating Term

In order to obtain the heat input to the thermal model, it was assumed that most of the energy lost by the sound beam was deposited locally in the medium, an assumption which appears justified for liver[24]. In order to obtain this loss we take the plane-wave approximation for intensity, which is valid in the parabolic approximation[29], and write

$$I_z = \frac{1}{2\rho_0 c}\sum_{n=1}^{N}|p_n|^2 \qquad (11)$$

where p_n is the pressure amplitude of the n^{th} harmonic of the beam, and

$$\frac{\partial p_{n,a}}{\partial z} = -\alpha_1 n^{1.266} b_n p_n \qquad (12)$$

where $\frac{\partial p_{n,a}}{\partial z}$ is the variation in p_n due to attenuation by the liver. The taper function (b_n), used in propagating the beam, artificially increases the attenuation of the highest 15 harmonics and represents attenuation due to the generation of frequencies with harmonic number greater than the largest N included in the model[25]. The model was run with varying numbers of harmonics, to ensure that this use of the taper function did indeed promote convergence and did not distort the calculation. We then have for the rate of loss of intensity due to attenuation:

$$\frac{\partial I_{z,a}}{\partial z} = \frac{1}{\rho_0 c}\sum_{n=1}^{N}\alpha_1 n^{1.266} b_n |p_n|^2 \qquad (13)$$

2.3 Thermal Model

The time dependent temperature profiles were computed usng a 3D finite element solution of the bioheat equation[12] which can be expressed as:

$$\rho C\frac{\partial T}{\partial t} = K\nabla^2 T - W_b C_b T + p_d + p_m \qquad (14)$$

where ρ, C, and K are the density, specific heat and thermal conductivity of the tissue, respectively. p_d is the power absorbed due to the ultrasound exposure from equation (13). Note that this model assumes that the majority of the attenuation is due to absorption[7,11]. T(x,y,z,t) is the spatially and temporally varying temperature distribution. The initial environmental condition was a uniform ambient temperature distribution achieved by allowing the excised bovine liver tissue

samples to equilibrate to room temperature (21° C). In the absence of perfusion and any metabolic processes, the terms of equation (14) which include W_b, the blood perfusion rate, C_b, the specific heat of the blood, and p_m, the power generated through metabolic processes could be ignored. Here the solution to equation (14) is produced using a 3D finite element model. For these simulations, the modeled region is initially divided into identical, right-angled hexahedrons each of which are subsequently subdivided into 6 equal-volume tetrahedrons. This geometry is ideal for use in the finite element method in that the solutions to the required integrations over each volume (required in forming the weighted residual statement) can be computed analytically[21,26].

The concept of the thermal dose developed by Sapareto et al.[27] to provide a quantitative relationship between temperature and time for the heating of tissue and the extent of cell killing produced is also applied here. For temperatures achieved in focused ultrasound surgery (generally above 50 ° C), the expression for thermal dose (TD) can be written as:

$$TD = \sum_{t_0}^{t_{end}} 2^{(T(t)-43)} \Delta t \qquad (13)$$

where $T(t)$ is the time-dependent temperature for an arbitrary tissue coordinate (dose contributions for temperatures below 43 ° C were ignored given their insignificant contribution in comparison with those from the much higher temperatures achieved in these simulations). Using this formulation, the thermal dose resulting from heating to 43 ° C for 120 minutes is roughly equivalent to that achieved by heating to 56 ° C for 1 second.

3. RESULTS

3.1 Pressure amplitude for low drive levels in water

Figure 2 compares the results of this model run for a low pressure amplitude in water with the same transducer geometry as that used by Watkin et al.[13] (without attenuation) with numerical evaluations of the Rayleigh integral (which does not involve the parabolic approximation). Figure 2a shows the axial variation of the pressure amplitude with the model predictions translated 3 mm to the left in order to compensate for the error in the focal position caused by the parabolic approximation. Similarly, Figure 2b shows the radial variation of the pressure amplitude 150 mm from the transducer in the case of the Rayleigh integral, and 153 mm in the case of the model run. Apart from the necessity for this shift of 3 mm the results agree well especially within the focal region. We therefore feel confident in modeling the beams used in the experiments with the Bergen code.

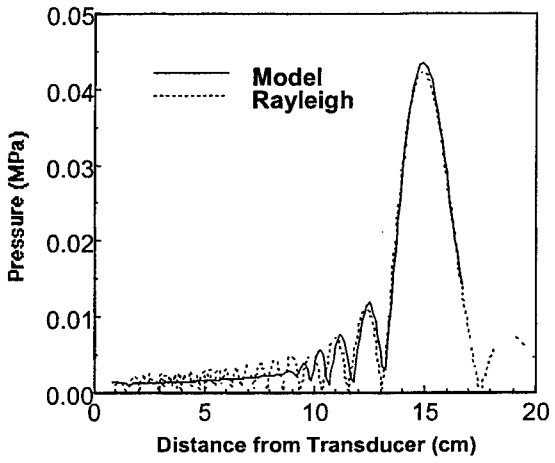

Figure 2a

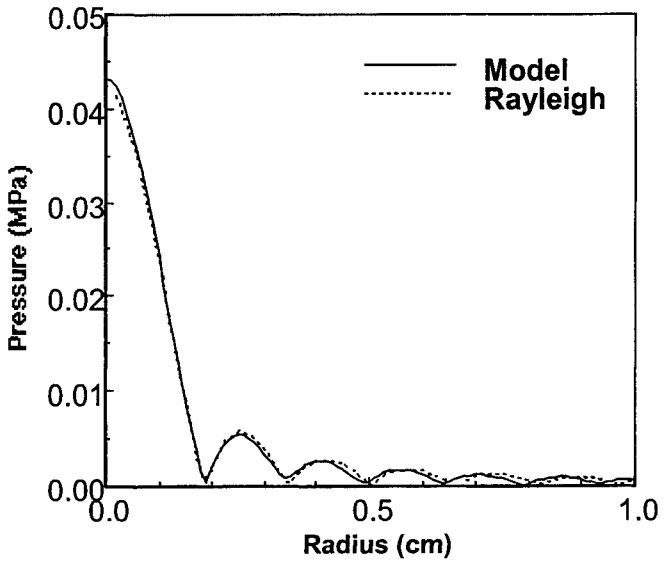

Figure 2b

Figure 2 - Comparisons of the pressure field profiles between the KZK nonlinear model and Rayleigh integral at low drive levels - (a) axial profile, (b) radial profile at the axial peaks. For clarity, the transmission medium is simply water for this comparison

3.2 Total power loss distribution in bovine liver tissue

The axial profiles of the total power loss (for all harmonics) are shown in Figure 3a for transducer drive levels of 0.668, 1.011, 1.642, and 2.274 MPa over the face of the transducer. For these simulations the geometric focal plane was positioned 2.7cm below the tissue surface. The peak positions for power loss for increasing drive levels were 24.4, 24.9, 24.1, and 23.4 cm below the tissue surface. This demonstrates an initial slight shift away from the transducer and then a movement back towards it. This is consistent with those observations of Baker[18]. It is interesting to note that the

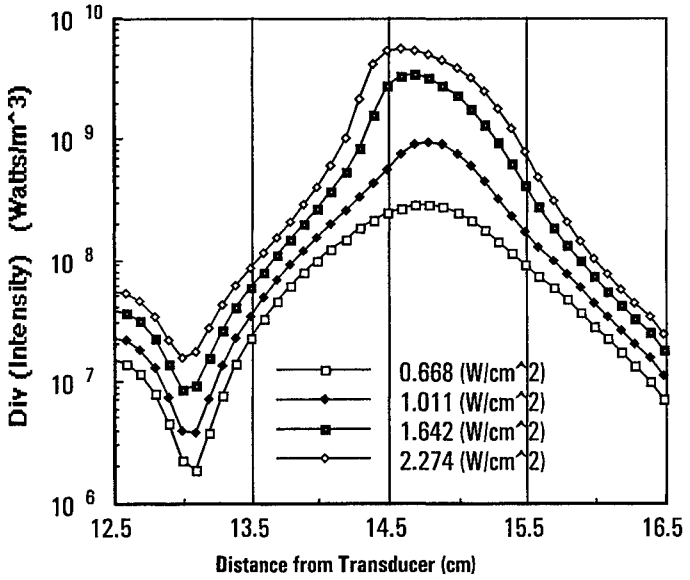

Figure 3a

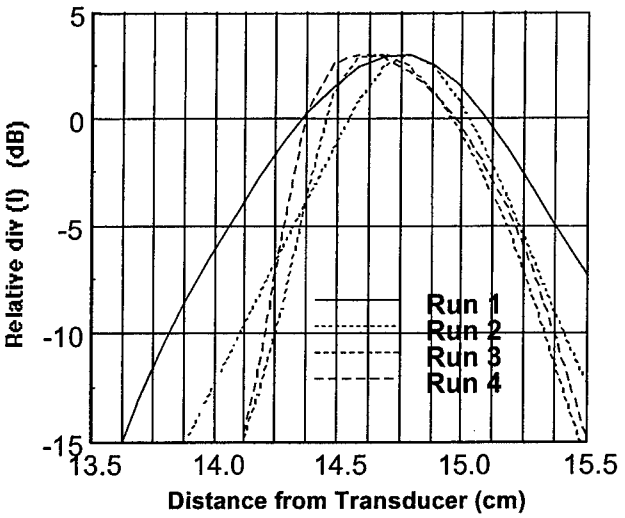

Figure 3b

Figure 3 - (a) Axial plots of the total power loss profiles for the four transducer drive levels. (b) Relative decibel plot of each total power loss profile - all profiles are normalized to their respective peak values which are set to +3 dB for easy comparison of the 3 dB beamwidth.

corresponding 3 dB axial beam widths are 7.4, 4.8, 5.1, and 6.0 mm. It would generally be expected that this axial profile will become narrower as nonlinear effects become more pronounced[17]. A detailed view of the relative power loss profile is shown in Figure 3b. In going from the 0.668 to 1.011 MPa drive, the 3 dB beam width narrows significantly as expected. However, at the two higher drive levels, the beam profile no longer appears Gaussian in nature and the 3 dB beam width actually increases to 5.1 and 6.0 mm, respectively.

3.3 Temperature modeling and thermal damage

The total power loss profiles were used as the source input in the 3D finite element thermal diffusion model. The finite element model used 15625 nodes (25 nodes in each axis) and 82944 tetrahedral elements. The dimensions of the modelled region in the two axes perpendicular to the direction of propagation were 8.4mm with nodal spacings of 0.35mm. The total dimension in the direction of propagation was 6.0cm (with a nodal spacing of 0.25mm) of which the first 0.5cm of the mesh closest to the transducer was modelled as water with the remainder modelled as excised bovine liver tissue. For all of these simulations, the exposure time was 2.0 seconds. The tissue thermal properties used were[28,24]:

Bovine Liver Tissue:		
	Thermal Conductivity, K :	0.508 W/m/° C
	density*heat capacity, ρC :	3.81×10^6 W sec/m^3/° C
Water:		
	Thermal Conductivity, K :	0.603 W/m/° C
	density*heat capacity, ρC :	4.31×10^6 W sec/m^3/° C

These were assumed to remain constant for the full experiment duration. Convection in the water was neglected in all simulations. A Dirichlet condition, setting the boundary temperatures to the initial ambient temperature (21 ° C), was used. This was shown to have no significant impact on the lesion shape formation.

Figure 4 illustrates the lesion shapes predicted for the four drive levels with the 2 second exposure times. In general the lesions grow in all directions as the drive level increases, with the exception that the growth of the lesion tail slows considerably from the third to fourth exposure level. Additionally, beginning with the third exposure level, the diameter of the front of the lesion is enlarged with comparison to the tail, possibly contributing to the "tadpole-like" appearance of the lesions observed by Watkin, et al.[13]. However, while the front of the lesions do move forward considerably with drive level, the extent of this movement is not sufficient to fully explain that observed in Watkin, et al.[13].

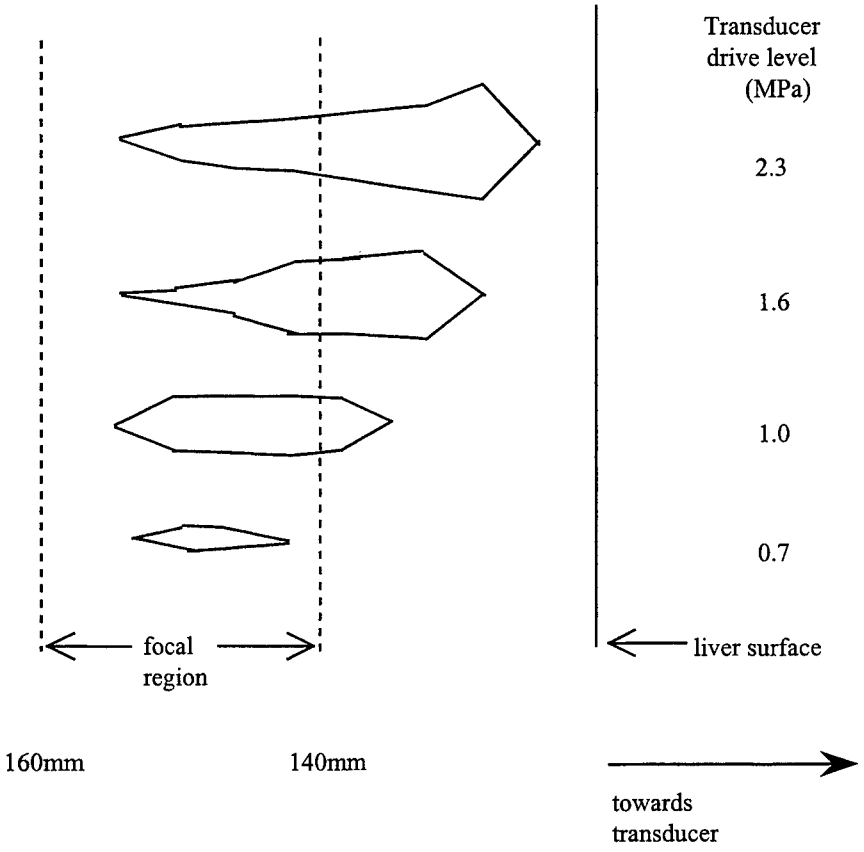

Figure 4 - Side-by-side comparison of the single lesions formed from the four transducer drive levels using 2 second exposures.

Figure 5 summarizes the peak temperatures predicted on axis for all four drive levels. It is clear that for the three highest drive levels at a minimum tissue boiling, and probably cavitation effects would occur with such high temperatures being achieved within the lesion areas. Especially for the two highest levels, temperatures above 100 ° C were achieved within the first 0.4 seconds, allowing for significant ultrasound scattering from newly produced vapour bubbles during the remaining 1.6 seconds of the exposure.

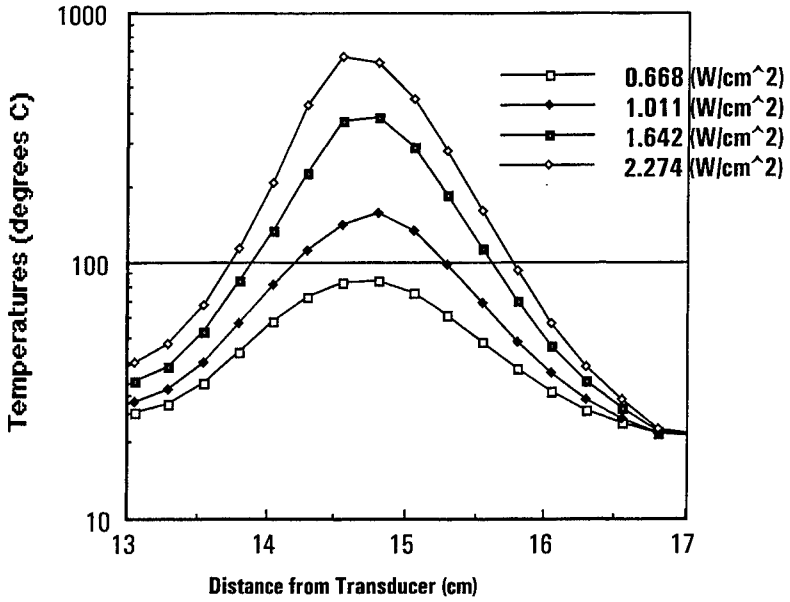

Figure 5 - Axial plots of the maximum tissue temperatures achieved for all four transducer drive levels.

4. DISCUSSION AND CONCLUSIONS

Application of the parabolic approximation for the prediction of pressure profiles in a highly focused configuration at low ultrasonic drive levels yields good agreement with the linear model apart from a nominal shift of the position of the peak pressure. The KZK equation was used to compute the spatial distribution of energy deposition which is needed to predict the time varying temperature distributions and iso-thermal dose contours.

For the transducer drive levels and exposure times examined here, the nonlinear model produces lesion shapes that are more realistic than the "cigar" shaped lesions predicted using the linear propagation models. However, these results still fall short of what is seen by Watkin, et al.[13]. It is important to note from the maximum temperatures achieved (shown in Figure 5), that boiling would have started well before the end of the exposure duration. As the exposure continues after vapour bubbles have been formed, the ultrasonic wave will be scattered in all directions about the site of the first ultrasound encounter with air bubbles with the bulk of the associated energy being deposited within a small radius. As the point of increased scattering is most likely to be at a boiling point close to the transducer, the scattered wave's energy will be deposited in the lesion "head", thus tending to increase the energy deposition within this region. This will enlarge the lesion head size while simultaneously decreasing the energy deposited near the lesion tail, thus reducing its size.

In conclusion therefore, we have shown that, in attempting to model the shape and position of FUS lesions induced by different exposures, it is necessary to include non-linear effects. However, a complete description of the observed behaviour has not been achieved.

5. ACKNOWLEDGEMENTS

The authors are grateful to Professors J. Bernsten, S. Tjotta and J. Naze Tjotta for the use of the Bergen code. Paul Meaney was funded by an NSF-NATO fellowship. M.D. Cahill was funded by MRC grant G9618910.

6. REFERENCES

1. Carstensen EL, Law WK, McKay ND, "Demonstration of nonlinear acoustical effects at biomedical frequencies and intensities," *Ultraound in Medicine and Biology*, vol. **6**, pp. 359-368, 1980.
2. Carstensen EL, Becroft SA, Law WK, Barbee DB, "Finite amplitude effects on the thresholds for lesion production in tissues by unfocused ultrasound," *Journal of the Acoustical Society of America*, vol. **70**, no. 2, pp. 302-312, 1981.
3. Dalecki D, Carstensen EL, Parker KJ, Bacon DR, "Absorption of finite amplitude focused ultrasound," *Journal of the Acoustical Society America*, vol. **89**, no. 5, pp. 2435-2447, 1991.
4. Wu J & Du G, "Temperature elevation generated by a focused Gaussian beam of ultrasound", *Ultrasound in Med. & Biol.*, **16**, pp 489-498
5. Hill CR, Rivens I, Vaughan MG, ter Haar GR, "Lesion development in focused ultrasound surgery : a general model", *Ultrasound in Med. & Biol.*, **20**, pp259-269, 1994
6. Hynynen K, Edwards DK, "Temperature measurements during ultrasound hyperthermia," *Medical Physics*, vol. **16**, no. 4, pp. 618-626, 1989
7. Kolios MC, Sherar MD, Hunt JW, "Blood flow cooling and ultrasonic lesion formation," *Med. Phys.*, vol. 23, no. 7, pp. 1287-1298, 1996.
8. Lizzi FL, Driller J, Ostramagilsky M, "Thermal model for ultrasound treatment of glaucoma", *Ultrasound in Med. & Biol.*, **10**, pp 289-298, 1984
9. Lizzi FL & Ostramagilsky M, "Analytical modelling of ultrasonically induced tissue heating", *Ultrasound in Med. & Biol.*, **13**, pp 607-618, 1987
10. Lizzi FL, Driller J, Lunzer B, Kalisz A, Coleman DJ, "Computer model of ultrasonic hyperthermia and ablation for ocular tumours using B-mode data", *Ultrasound in Med. & Biol.*, **18**, pp 59-73, 1992
11. Robinson TC, Lele PP, "An analysis of lesion development in the brain and in plastics by high-intensity focused ultrasound at low-megahertz frequencies," *The Journal of the Acoustical Society of America*, vol. **51**, no. 4, pp. 1333-1351, 1972.
12. Pennes HH, "Analysis of tissue and arterial blood temperatures in the resting human forearm," *Journal of Applied Physiology*, vol. 1, no. 2, pp. 93-122, 1948.
13. Watkin NA, ter Haar GR, Rivens I, "The intensity dependence of the site of maximal energy deposition in focused ultrasound surgery", *Ultrasound in Med. & Biol.*, **22**, pp 483-491,1996
14. Verma PK, Humphrey VF, Starritt HC, "Enhanced absorption due to nonlinear propagation in diagnostic ultrasound," Proceedings of the 13th ISNA, H. Hobaek (ed.) *World Scientific*, pp. 297-302, 1993.
15. Cahill MD, Baker AC, "Increased off-axis energy deposition due to diffraction and nonlinear propagation of ultrasound from rectangular sources," *Journal of the Acoustical Society America*, 1997 (submitted).
16. Hynynen K, Chung A, Jolesz FA, "In vivo detection of ultrasound induced cavitation using MRI," *Proc. Int. Soc. Magnetic Reson. In Medicine*, p. 525, 1997.
17. Swindell W, "A theoretical study of nonlinear effects with focused ultrasound in tissues : an "acoustic Bragg peak", *Ultrasound in Med. & Biol.*, **11**, pp 121-130.
18. Baker AC, "A numerical study of the effect of drive level on the intensity loss from an ultrasonic beam," *Ultrasound in Medicine and Biology*, 1997 (submitted).
19. Bernsten J, "Numerical calculation of finite amplitude sound beams," in Frontiers of nonlinear acoustics: Proceedings of the 12th ISNA, Hamilton MF and Blackstock DT (eds.), *Elsevier Science Publications*, pp. 191-196, 1990.
20. Tjotta JN, Tjotta S, Vefring EH, "Effects of focusing on the nonlinear interaction between two collinear finite amplitude sound beams," *Journal of the Acoustical Society America*, vol. **89**, no. 3, pp. 1017-1027, 1991.
21. Meaney PM, Clarke RL, ter Haar GR, Rivens IH, "A 3D finite element model for computation of temperature profiles and regions of thermal damage during focused ultrasound surgery exposures," *Ultrasound in Medicine and Biology*, 1997 (submitted).
22. Kuznetsov VP, "Equations of Nonlinear Acoustics," *Sov. Phys.-Acoust.*, vol. **16**, pp. 467-470, 1971.
23. Ystad B, Bernsten J, "Numerical solution of the KZK equation for focusing sources," *Acta Acustica*, vol. **3**, pp. 323-330, 1995.
24. Duck, FA, Physical Properties of Tissue, *Academic Press*, 1990.
25. Christopher PT, Parker KJ, "New approaches to nonlinear diffractive field propagation," *Journal of the Acoustical Society America*, vol. **90**, no. 1, pp. 488-499, 1991.
26. Reddy JN, An introduction to the finite element method, *McGraw-Hill, Inc.* (2nd Edition), 1993.

27. Sapareto SA, Dewey WC, "Thermal dose determination in cancer therapy", *Int. J. Radiation Oncology Biol. Physics*, **10**, pp 787-800, 1984.
28. Paulsen KD, Strohbehn JW, Lynch DR, "Theoretical temperature distributions produced by an annular phased array-type system in CT-based patient models", *Radiation Research*, **100**, pp 536-552, 1984.
29. Naze Tjøtta J., Tjøtta S., "Non-linear equations of acoustics", in Frontiers of NOnlinear Acoustics : Proceedings of the 12th ISNA edited by M.F. Hamilton & D.T. Blackstock, Elsevier Science Pubs. Pp 80-97, 1990

Treatment of in vivo bladder tissue with electronically scanned high intensity focused ultrasound

Benoît Feuillu[a], François Lacoste[b], Jacques Schlosser[a], and Guy Vallancien[c]

[a] Department of Urology, CHU Nancy-Brabois, Nancy 54511
[b] Engineering Department, Edap-Technomed, Vaulx en Velin 69120
[c] Department of Urology and Research (CERA), Institut Montsouris, Paris 75013 France

ABSTRACT

Introduction: The efficacy of extracorporeal High Intensity Focused Ultrasound (HIFU) on bladder wall has been demonstrated. However, the treatment is still slow, needing about 15 min to treat 1 cm^2.
Objectives: Demonstrate the feasibility of HIFU with electronic scanning and reduce the duration of HIFU treatments.
Methods: The HIFU machine was a modified Pyrotech (Edap-Technomed; France) allowing fast electronic scanning of the focal point. Each ultrasonic pulse could scan an adjustable square area ranging from 4x4 mm to 7x7 mm. On 16 anaesthetized pigs, 26 areas of the posterior bladder wall were treated with this technique. Target areas were 1.4 to 4.4 cm^2 large. Delays between ultrasonic pulses were ranging from 30 to 65 sec. The treatment durations were 5 to 10 min. Focal intensity between 7000 and 11000 W/cm^2. The bladder, the rectal wall and the abdominal wall were removed 3 days after HIFU treatments and histology was performed.
Results: 22 lesions were obtained on posterior bladder walls. Necrotic areas were surrounded by a 2 mm edematous rim. The sizes of necrotic areas were equal to the target sizes. Depth of lesions extended either over mucosa alone or mucosa and deep muscle. 7 superficial rectal lesions were noticed but none in the abdominal walls or on the skin.
Conclusions: Necrotic lesions on bladder posterior wall can be obtained with HIFU treatments using electronic scanning of the focal point. Average treatment duration with electronic scanning is reduced to 3 min 30 sec / cm^2.

Key Words : High intensity focused ultrasound, phased array, non invasive therapy, experimental, pig, bladder.

1. INTRODUCTION

High Intensity Focused Ultrasound (HIFU) can produce tissues necrosis in depth by a thermal effect and a mechanical effect: cavitation [1]. Their efficacy on bladder wall has been demonstrated [2-4]. Superficial bladder tumors visible with echography have been treated successfully [5,6]. However, these treatments were slow. Because of the small size of the focal point, 15 to 20 minutes were necessary to treat a 1 cm^3 tissue volume [4-6]. The purpose of this study was to demonstrate HIFU feasibility with electronic scanning on bladder wall, while reducing HIFU treatments duration.

2. MATERIAL AND METHOD

2.1 Material

The ultrasound source was the Pyrotech. The treatment head contained 160 flat round ceramics. The ultrasonic frequency was 1 MHz and the acoustic power was adjustable between 50 and 6000 Watts. The treatment head was mobile with a millimetric precision. In the treatment head, the coupling liquid was maintained at a constant 15°C temperature. An ultrasound probe placed in the center of the treatment head allowed to locate the bladder wall. During an acoustic pulse, the treated surface was chosen between 4x4 and 7x7 mm.

16 female Large White-Land Race pigs (body weight: 50 to 70 kg) were used for this experience.

2.2 Methods

During HIFU treatments, pigs were anaesthetized. The premedication was a carazol (0.15 mg) and atropine (0.5 mg) intramuscular injection. After perfusion of an ear's vein, the induction was the addition of an intravenous injection of thiopental (10 mg/kg) and vecuronium bromide (12 mg). The animals were intubated under direct vision with an endotracheal tube. Anaesthesia was maintained with intravenous thiopental.

The skin in front of the bladder was shaved. The coupling between the skin and the treatment head was ensured by an acoustic gel. 26 areas on the posterior bladder wall have been treated in 16 pigs. The target was located 33 to 62 mm in depth. During each impulsion, the treated surface was chosen between 4x4 mm to 7x7 mm. Nine contiguous pulses were used to treat areas ranging from 1.4 to 4.4 cm^2. Delays between ultrasonic pulses were ranging from 30 to 65 sec. Treatments duration were 4.5 to 10 min long. Focal intensities were chosen between 7000 à 11000 W/ cm^2. HIFU treatments parameters are summarized in table 1.

Focal depth (mm)	33-62
Volume (cm^3)	1.4-4.4
Focal spacing (mm)	4-7
Time delay (s)	30-65
Pulse duration (s)	0.7-3.9
Treatment time (min)	4.5-10
Focal intensity (W/cm^2)	7000-11000
Focal energy (kJ/cm^2)	2.6-7.7

Table 1: HIFU parameters for bladder treatment.

The bladder, the rectal wall and abdominal wall were removed 3 days after HIFU treatment. They were fixed with a 10% formalin solution and a microscopic examination was then performed if a macroscopic lesion was noticed.

3. RESULTS

22 lesions (84 %) were obtained on posterior bladder walls. Necrotic areas on the bladder were surrounded by a 2 mm edematous rim. The sizes of necrotic areas were equal to the target sizes. 7 rectal ulceration's were noticed (27 %), but no perforation or peritonitis. Microscopic examination showed constant edema in the submucosa and bladder mucosa, while deep muscle was inconstantly necrosed (15%). Histological examination of the rectal ulceration showed constant necrosis of the mucosa and inconstant necrosis of the muscular. We didn't notice any skin or abdominal burns.

4. DISCUSSION

This study has shown the feasibility of electronically scanned HIFU for bladder wall destruction in vivo. The success rate for bladder destruction was 81%. Failures were due to lack of energy at the focus or wrong targeting. The small thickness of the abdominal wall and the presence of urine in front of the target point is favorable for localization and tissue destruction.

Moreover, electronic scanning reduced significantly treatments duration. 10 to 15 minutes were necessary to treat a 1 cm^3 volume with mechanical scanning [4,5], whereas 2 or 5 minutes with electronic scanning in pigs. This confirms Fan's studies and the interest of phased arrays [7].

Histological destruction's were similar to those previously described [4,5]: mucosal necrosis, muscular edema or necrosis. Muscular destruction depend on focal energy, position of the focal point and importance of the cavitation which also depends on focal intensity.

HIFU treatments have limited side effects. Rectal burns (26%) have several explanations. The focal point could have been positioned to deeply in the bladder wall which is very thin: 5 to 10 mm. Its position may vary with focal intensity [8]. Watkin recommended not to place focal point to deeply in bladder wall [4]. Nevertheless, we didn't observe severe digestive complications. In humans, the bladder's thickness and the superposition of the focal point with the tumor basis will reduce the risk of rectal burns.

5. CONCLUSION

Necrosis can be created on the bladder wall through a HIFU treatment using focal scanning. Average time for such treatment is reduced to 3 min 30 sec / cm^2. Electronic scanning should reduce treatments duration for superficial bladder tumors imaged by echography.

6. ACKNOWLEDGMENTS

We want to thank the engineers and technicians of the EDAP-TECHNOMED company, all members of the laboratory of research (CERA - Fondation de l'Avenir), the doctors François Laborde, Emmanuel Chartier-Kastler, Nathalie Bataille, Mohamed Harouni and the professor Dominique Chopin (Henri Mondor Hospital) for their financial and technical assistance in this research.

7. REFERENCES

1. F.J. Fry, "Intense Focused Ultrasound in Medicine: Some Practical Guiding Physical Principles from Sound Source to Focal Site in Tissue", Eur Urol, 23(suppl 1), pp. 2-7, 1993.
2. G. Vallancien, E. Chartier-Kastler, D. Chopin, B. Veillon, JM. Brisset, and J. André-Bougaran, "Focused Extracorporeal Pyrotherapy: Experimental Results", Eur Urol, 20, pp. 211-219, 1991.
3. G. Vallancien, E. Chartier-Kastler, N. Bataille, D. Chopin, M. Harouni, and J. Bougaran, "Focused Extracorporeal Pyrotherapy", Eur Urol, 23, pp. 48-52, 1993.
4. N.A. Watkin, S.B. Morris, I.H. Rivens, C.R.J. Woodhouse and G.R. ter Haar, "A feasibility study for the non-invasive treatment of superficial bladder tumours with focused ultrasound", Br J Urol, 78, pp. 715-721, 1996.
5. G. Vallancien, M. Harouni, B. Guillonneau, B. Veillon, and J. Bougaran, "Ablation of superficial bladder tumors with focused extracorporeal pyroterapy", Urology, 47, pp. 204-207, 1996.
6. J. Schlosser and G. Vallancien, "High intensity focused ultrasound ablative surgery for bladder cancer", *Atlas of the Urologic Clinics of North America,* J.E. Montie, M.I. Resnick, and J. Kowalak, 5, pp. 125-141, W.B. Saunders Company, Philadelphia, 1997.
7. X. Fan and K. Hynynen, "Ultrasound surgery using multiple sonications - treatment time considerations", Ultrasound Med Biol, 22, pp. 471-482, 1996.
8. N.A. Watkin, G.R. ter Haar, and I. Rivens, "The intensity dependence of the site of maximal energy deposition in focused ultrasound surgery", Ultrasound Med Biol, 22, pp. 483-491, 1996.

Focused Ultrasound Surgery Induced Vascular Occlusion In Fetal Medicine

Ian Rivens[a], Ian Rowland[b], Mark Denbow[c], Nicholas Fisk[c], Martin Leach[b], Gail ter Haar [a].

[a]Joint Dept. of Physics, Institute of Cancer Research & Royal Marsden Hospital, Sutton, Surrey, UK
[b]CRC Clinical Magnetic Resonance Research Group & Joint Dept. of Physics, Royal Marsden Hospital, Sutton, Surrey, UK
[c]Centre for Fetal Care, Queen Charlottes Hospital, Goldhawk Road, London, UK

ABSTRACT

Aim: This study investigates whether it is possible to occlude blood flow *in vivo* using high intensity focused ultrasound surgery (FUS). Such an effect could be used in the non-invasive treatment of fetal dysfunctions.
Methods: A high power 1.7 MHz, 150 mm focal length, piezoelectric ultrasound transducer was used to expose femoral vessels to an array of exposures (free field Isp 4660 Wcm^{-2} for 2s) under terminal anaesthetic. Before and after FUS exposure, magnetic resonance (MR) FISP 3D angiograms and FLASH 3D images, with sub-millimetre in-plane spatial resolution, were acquired using a Siemens Vision MR System (1.5T) and extremity coil. Post FUS, images were acquired before and after contrast agent administration.
Results: In n=10 studies, MRA showed reduced blood flow in the treated region and distal to this. In occluded cases, FLASH images showed negligible contrast agent distal to the treated region.
Conclusion: Our ability to curtail blood flow using FUS allows the possibility of non-invasively treating feto-fetal transfusion syndrome by occluding the placental shunt vessels responsible for the vascular imbalance in twins sharing a placenta. This would have advantages over currently available interventional treatments (surgery or intrauterine lasers), which have significant related mortality and morbidity.

Keywords: focused ultrasound surgery, vascular occlusion, fetal medicine, magnetic resonance imaging

1. INTRODUCTION

Focused ultrasound surgery (FUS) has been used since the early 1940's to create soft tissue damage at depth, via heating or cavitation, without damage to overlying tissues[1,2,3,4]. This provides the basis from which FUS has been used as a non-invasive treatment for a variety of conditions[5] in neurology[6], oncology[7,8], ophthalmology[9], and urology[10,11].

The interaction between FUS and blood flow has been studied by various groups. The reduction of damage around large well perfused vessels has been demonstrated[12,13,14], as has the perfusion independence of the extent of FUS damage for exposures less than 2 seconds in duration[13,15]. In studies of soft tissue exposure, damage to large blood vessels was initially only reported at ultrasonic exposures above the acoustic cavitation threshold[16,17]. Exposures below this threshold have been shown to damage vessels less than 200 μm in diameter[18]. Recently, the potential adverse effects of blood vessel damage caused by intensities believed to be above the cavitation threshold (5800 Wcm^{-2} at 1.49 MHz) have been highlighted[19]. Vascular occlusion of veins was first studied by Delon-Martin *et al*[20] using 7 MHz FUS, at a spatial peak intensity 167 Wcm^{-2} for 3 seconds to induce thrombosis as an experimental model for the study of the FUS treatment of varicose veins. More recently, using magnetic resonance (MR) imaging to target the renal artery of rabbits non-invasively, Hynynen *et al*[19] showed that vessels up to 0.7 mm diameter could be blocked using a spatial array of exposures at two FUS intensities. Firstly, exposures at a spatial peak intensity of 6500 Wcm^{-2} for 1s were targeted at and around a renal artery. Once temporary occlusion was achieved, a second series of exposures at 2800 Wcm^{-2} for 10 seconds were applied to the same area. Each exposure was separated by 0.7 mm. Computed tomographic (CT) angiography was used to show vessel blockage and MR imaging demonstrated infarction damage to the kidney up to 7 days after exposure. This multiple exposure

SPIE Vol. 3249 • 0277-786X/98/$10.00

technique using two different intensity levels was thought to be effective because the high power exposures stemmed the blood flow and the lower power exposures produced thermal coagulation. CT angiograms showed constriction of the renal artery, but the underlying reason for this is unclear. Compression due to oedema in the surrounding tissue cannot be excluded as the cause. Hence, the mechanism(s) by which occlusion was achieved are not understood.

Our intended application for FUS occlusion is in the treatment of vascular malformations in fetal medicine. Thus, prior to this *in vivo* investigation, tissue characterisation measurements, using the method of Bamber and Bush[21], were performed on *ex vivo* human placental tissue. The results showed that the attenuation coefficient of placenta, which is highly vascular, is close to one third that of *ex vivo* ox liver. Thus, in these experiments, an *in situ* spatial peak intensity of 4660 Wcm^{-2} was used. This is three times that currently used in a phase I clinical trial at the Royal Marsden Hospital to create lesions in soft tissue tumours (1490 Wcm^{-2}).

The model selected for the study of vascular occlusion was the rat femoral vessels because they are the most appropriately sized rodent vessels which are easily accessible to ultrasound. This choice is considered further in the discussion.

In this paper, an occluding effect of FUS at 1.7 MHz is shown. An array of eight exposures at a single intensity level (4660 Wcm^{-2}) was used to demonstrate the technique. A subsequent study is currently in progress to determine the minimum `single shot` intensity and exposure duration capable of producing predictable occlusion.

The FUS system employed in this study has the potential for use in the investigation of vascular occlusion for the treatment of fetal vascular malformations, for the occlusion of major supply vessels in tumours, and possibly for the treatment of internal bleeding. The ability of the MR techniques in the assessment of blood flow and soft tissue damage is discussed, along with the benefits of using a contrast agent.

2. METHODS

The focused ultrasound surgery (FUS) equipment used for this work has been described fully elsewhere[4]. Briefly, the ultrasound source used was a spherically shaped piezoelectric ceramic (PZT4) crystal with a radius of curvature of 15 cm and diameter of 10 cm (Channel Industries, Santa Barbara, USA). The fundamental frequency of the transducer is 0.56 MHz and it was driven at its third harmonic to give an operating frequency of 1.69 MHz. A signal generator (Hewlett Packard Model 33120A) provided a continuous sine wave drive voltage at a peak-to-peak value of 1V. A digital oscilloscope (Fluke PM3380B) and digital frequency meter (Thandar TF 600) monitored the voltage, current and frequency of the signal applied to the transducer. A variable attenuator (Hatfield Instruments Type 2105) allowed the power of the drive signal to be reduced in 1dB steps. The resulting signal was transmitted via a radiofrequency power amplifier (ENI A300, amplification +55 dB) and coupled from the 50W drive circuit to the 12W transducer by a matching transformer. A perspex cone attached to the ultrasound transducer was used to support a bag of degassed water to allow acoustic transmission. Radiation force balance and acoustic hydrophone measurements demonstrated that the addition of the cone did not measurably alter the ultrasonic field.

All intensities quoted in this paper are free field spatial peak values determined using radiation force balance measurements and hydrophone measured beam profiles according to the method described by Hill[22]. The errors in their measurement are within 10%.

All experiments were carried out in accordance with Home Office regulations. Animals were anaesthetised using an intraperitoneally administered aqueous solution containing hypnorm (1.25 mg/ml midazolam.HCl) and hypnovel (0.079 mg/ml fentanyl citrate & 2.5 mg/ml fluanisone) at an initial dose of 2.8 ml/kg. Additional doses were given to maintain anaesthesia, for a maximum duration of 2 hours. The animals were not allowed to recover. Immediately after induction of anaesthesia, a small incision was made in the skin covering each thigh, revealing the superficial femoral vessels. This was performed firstly because the highly absorbing skin lies too close to the

target vessels to allow application of FUS without producing a skin burn, and secondly to allow visualisation of the vessels for targeting.

The femoral artery and vein in one thigh of CBH/CBI rats (196 ± 35 g, male & female) were exposed. Both rear limbs were submerged in a small tank of degassed water (25-30°C). The transducer was attached to a gantry which allowed full 3D positioning[4], and was located such that the focal depth was set 5mm beneath the tissue surface to minimise the risk of the mechanical forces associated with the ultrasound perforating the exposed vessel walls. The small tank of degassed water was filled so as to ensure that the cone water path was in good acoustic contact. This arrangement was used to avoid applying pressure to the femoral vessels during FUS exposure. The focal depth was set using a mechanical pointer.

In a preliminary study, six animals were used to refine the FUS application technique and to determine the optimum MR sequences for blood flow and tissue damage assessment. Data from these studies are not reported. A further ten animals were then treated and assessed identically, as a pilot study of FUS vascular occlusion.

Eight exposures were placed in two rows of four at a spatial separation of 2 mm, along the femoral vessels, in the order and position demonstrated in Figure 1. The exposures used were free field spatial peak intensities of 4660 Wcm^{-2} for 2s, with a 15-20 second delay between shots.

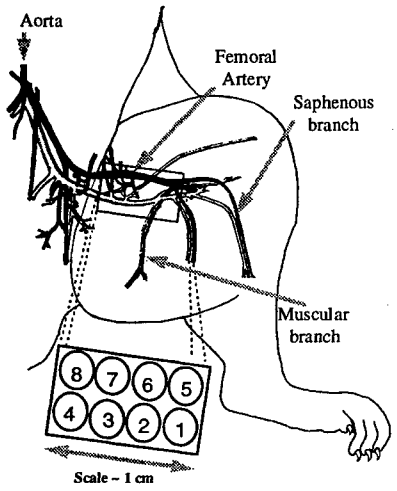

Figure 1. Schematic diagram demonstrating the approximate location of vessels in the rat thigh, and the positions in which ultrasound exposures were placed when an array of exposures was produced.

Magnetic resonance images were obtained before and after ultrasound treatment to allow assessment of the FUS induced changes. For each animal the unexposed contralateral thigh served as an additional experimental control. The animals were imaged with a Siemens Vision MR System (1.5T) using a Siemens extremity coil. FISP-3D magnitude contrast angiograms (TR=50ms, TE=14ms, Fl=15°, FOV=100x200mm, Ma=128x256, NEX=2) with an in-plane spatial resolution of 0.78x0.78mm and 1.0mm slice thickness were used to measure signals only from flowing blood. Fat suppressed FLASH-3D images (TR=33.8ms, TE=5ms, Fl=20°, FOV=100x200mm, Ma=128x256, NEX=2) with the same resolution were also acquired.

After FUS exposure, MR data were obtained both before and after the intravenous administration of 0.05 mmol/kg of polylysine-Gd-DTPA (48.7 kD molecular weight) blood pool contrast agent (Schering AG, Berlin). The contrast agent in the blood reduces the longitudinal relaxation time and subsequently enhances the signal ratio in images. The MRA data were used to assess vascular patency by comparing the FUS exposed thigh with both the contra-lateral thigh and the appearance of the vessels in the treated thigh before exposure. Subtraction of the 3D FLASH image datasets obtained pre-contrast from those obtained post-contrast yields information about the vasculature because only perfused regions appear hyperintense, due to the presence of contrast agent. The relatively large molecular weight of Gd-DTPA-PL means that the agent remains predominantly intravascular prior to renal excretion.

Maximum intensity projection (MIP) post processing was used to yield 2D representations of the full 3D datasets for analysis. Both the MR images shown in this paper are of this nature.

3. RESULTS

In this study, using arrays of lesions (I_{sp} = 4660 Wcm^{-2}), ultrasound damage was visible immediately after FUS exposure in all 10 animals. Damage was characterised by pallor in the vessels, and was usually associated with the inability to observe pulsatile flow in the femoral artery. Also there was a whitening of the surrounding muscle where it had been exposed to FUS. In 8/10 cases vessel rupture resulted in a local haemorrhage during exposure. In all cases, the bleeding had ceased before the final exposure.

The post-ultrasound MR angiogram (MRA) suggested significantly reduced blood flow in the exposed thigh compared with both the pre-ultrasound MRA and the contralateral (unexposed) thigh in 9/10 animals. The MRA sequence obtained after contrast agent administration yielded an improved signal to noise ratio, but did not significantly enhance the sensitivity of blood flow detection. One animal exhibited no signs of occlusion. In this case, visual inspection showed that the vessels had been mistargeted.

Figure 2 shows a typical contrast enhanced MRA post-FUS, suggesting total cessation of flow in the exposed left thigh (arrowed). The unexposed side shows the typical appearance of a normal limb, with much smaller vessels visible distal to the femoral vessels. The corresponding FLASH 3D subtraction image showed some localised enhancement in the FUS exposed area (arrowed in Figure 3) with negligible enhancement observed within the rest of the thigh. Further sets of images acquired over a 30 minute period (not shown) suggest that this region of hyperintensity was caused by the slow diffusion of contrast from the haemorrhagic region into interstitial spaces. Again the unexposed side of the image has the typical appearance of a normal limb. Despite the slight contrast leakage, the result of this study was deemed to be that of total occlusion since the blood flow had been completely curtailed. In total 4/10 thighs were observed to be similarly occluded.

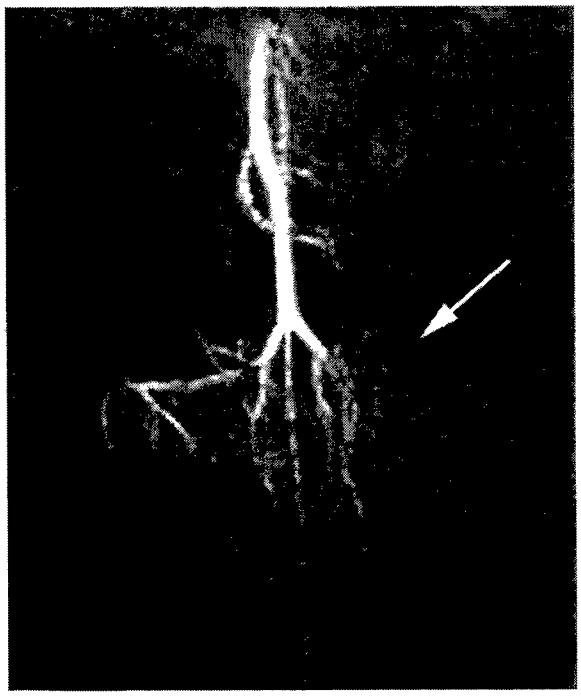

Figure 2 shows a typical contrast enhanced MRA image post-FUS exposure, suggesting total cessation of flow in the exposed left thigh (arrowed).

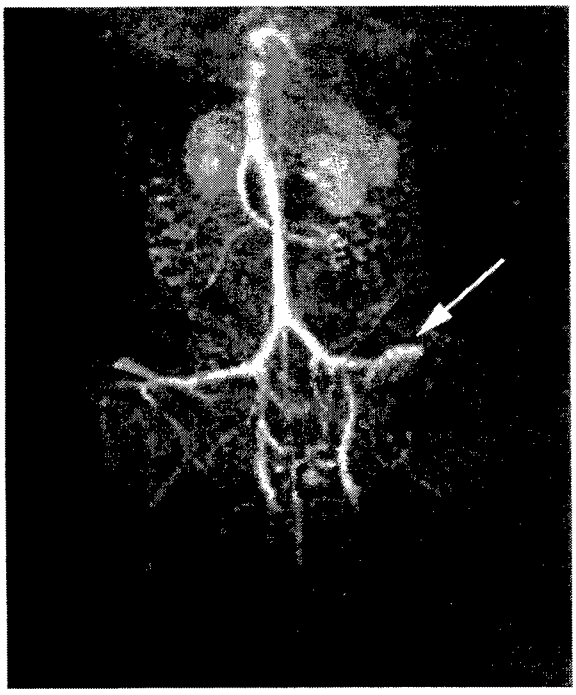

Figure 3 A subtracted FLASH image (post- minus pre-contrast) from the same study as in Figure 2. Contrast agent can be seen in the FUS exposed area (arrowed).

In contrast to this total occlusion, 5/10 studies yielded MRA images which detected no flow distal to the FUS exposure region. However, the corresponding subtracted FLASH images showed the presence of contrast agent within vessels immediately distal to the exposed region. These studies were assessed to have produced only partial occlusion.

In summary, no occluding effect was observed in one animal, visual inspection revealed that this had been mistargeted, sparing both femoral vessels. In 9/10 studies total or partial occlusion was achieved. Thus, the potential for ultrasound to occlude the femoral vessels has been demonstrated.

4. DISCUSSION & CONCLUSIONS

The ability to occlude blood flow in large vessels using non-invasive focused ultrasound surgery allows the possible treatment of conditions caused by abnormal blood flow. Many applications can be foreseen, including the treatment of tumours via vascular disruption; the treatment of internal bleeding in the brain, abdominal organs, and deep within muscle (e.g. for the treatment of varicose veins); and the treatment of disorders common in fetal medicine. In particular, we are interested in the treatment of feto-fetal transfusion syndrome (FFTS), a condition arising in the mid-term of multiple pregnancies which results in the death of both fetuses in >90% of cases, if left untreated. Presently, the only available treatments are serial amnio-reduction (survival rate 64%) under general anaesthetic or more recently intrauterine laser surgery under local anaesthetic (survival rate ~53%)[23], both of which have significant related mortality and morbidity. Recent studies, which show a single placental shunt vessel up to 3 mm in diameter to be responsible for the abnormal blood flow which causes FFTS[24], lead us to be optimistic that diagnostic ultrasound guided FUS may offer a non-invasive treatment, probably without the need for anaesthetic.

This study was designed to investigate the effect of FUS *in vivo*. The rat femoral vessels were chosen as the blood flow model because they are the most appropriately sized vessels (the artery is ~0.5mm and the vein is around 1.5mm) for the study of placental blood flow. These vessels are easily accessible to ultrasound and to visual inspection and targetting, requiring only a minor skin incision to externalise them. Also, the thigh should invoke a collateral circulation in response to FUS occlusion of the femoral vessels. The limb should dilate other blood vessels to compensate for the lost supply in order to ensure the limb remains perfused and viable, thus allowing a series of survival experiments to be performed.

The ability to occlude blood vessels *in vivo* with an array of multiple spatially separated FUS exposures at a single intensity, has been demonstrated in 9/10 rat femoral vessels. This is in general agreement with the results obtained in rabbit renal arteries by Hynynen *et al*[19] using dual intensity arrays. Our results show that arrays of multiple exposures at 4660 Wcm^{-2} were relatively effective, producing total occlusion in four and partial occlusion in five out of ten rats. However, the high incidence of haemorrhage (8/10) suggests that the power level used may have been excessive. Haemorrhage is likely to have been responsible for the diffusion of contrast agent into the treated area as shown in Figure 3. In cases where only partial occlusion has been observed (5/10), as a result of the presence of contrast agent in vessels distal to the FUS exposed region, it is possible that collateral blood supply from unexposed regions of the limb contributed the observed contrast enhancements. This warrants further investigation.

We have demonstrated that MR imaging can be used to assess the efficacy of FUS occlusion using sequences to detect flow and the presence of contrast agent. The use of such a blood borne contrast agent may be essential to acquire information about the continuity of vasculature. We have demonstrated that the subtracted FLASH 3D images, which are sensitive only to the effects of contrast agent, may not be relied upon in isolation because contrast agent can appear in vessels distal to the FUS exposed region due to what is believed to be collateral blood flow. Combining these with FISP 3D MRA data, which is a measure of blood flow only, appears to be a reliable method of assessing vascular occlusion. CT angiography is not available for experimental use.

A more refined approach to FUS induced vascular occlusion would be to use a single exposure. Experiments to determine the minimum intensity and exposure time which can predictably cause occlusion in both the femoral

artery and vein are currently underway. Furthermore, if FUS is to be a viable treatment for FFTS, the abnormal blood flow must remain occluded from mid-term to as close to full term as possible (~25 weeks). It is hoped that our current survival experiments using the rat femoral vessel model will lead to clinical application of the technique.

It is not clear whether the highest intensity used in this study (4660 Wcm^{-2}) is below the cavitation threshold and therefore we are developing methods for the non-invasive detection of cavitation to help elucidate the mechanism by which FUS can produce occlusion.

In conclusion, we have demonstrated an occluding effect of FUS *in vivo* at a frequency used to treat tumours at depths up to 12 cm within the body. We believe this effect can be exploited to treat conditions where alternative invasive treatments have high associated risks of mortality and morbidity.

5. ACKNOWLEDGEMENTS

We wish thank the Medical Research Council, the Cancer Research Campaign, the Fetal Medicine Department of Queen Charlottes' and Chelsea Hospital and the Wiseman Trust for their support. We also thank Schering AG, Berlin for supplying the polylysine-Gd-DTPA contrast agent.

6. REFERENCES

1. Lynn JG, Zwemer RL, Chick AJ, Miller AE. A new method for the generation and use of focused ultrasound in experimental biology. J Gen Physiol 1942;26:179-92.
2. Fry WJ, Barnard JW, Fry FJ, Krumins RF, Brennan JF. Ultrasonic lesions in the mammalian central nervous system. Science 1955;122:517-8.
3. Basauri L, Lele PP. A simple method of producing trackless focal lesions with ultrasound: Statistical evaluation of the effects of irradiation on the central nervous system of the cat. J Physiol 1962;160:513-34.
4. ter Haar GR, Clarke RL, Vaughan MG, Hill CR. Trackless surgery using focussed ultrasound: Technique and case report. Min Inv Ther 1991;1:13-9.
5. ter Haar GR. Ultrasound focal beam surgery. Ultrasound in Med & Biol 1995;21(9):1089-100.
6. Fry FJ. Intense focused ultrasound in medicine. Eur Urol 1993;23 (Suppl 1):2-7.
7. Hill CR, ter Haar GR. Review article: High intensity focused ultrasound - potential for cancer treatment. Br J Radiol 1995;68:1296-303.
8. Crum LA, Hynynen K. Sound therapy. Physics World 1996;Aug:28-33.
9. Driller J, Lizzi FL. Therapeutic applications of ultrasound: A Review. IEEE Eng in Med & Biol 1987;Dec:33-9.
10. Madersbacher S, Marberger M. Urological applications of high intensity focused ultrasound. Curr Op Urol 1995;5:147-9.
11. Watkin NA, Morris SB, Rivens I, Woodhouse CRJ, ter Haar GR. A feasibility study of the non-invasive treatment of superficial bladder tumours with focused ultrasound. B J Urol 1996;78:715-21.
12. Linke CA, Carstensen EL, Frizzell LA. Localized tissue destruction by high intensity focused ultrasound. Arch Surg 1973;107:887-91.
13. Chen L, ter Haar GR, Hill CR, Dworkin M, Carnochan P, Young H, Bensted JPM. Effect of blood perfusion on the ablation of liver parenchyma with high-intensity focused ultrasound. Phys Med Biol 1993;38:1661-73.
14. Yang R, Reilly CR, Rescorla FJ, Sanghvi NT, Fry FJ, Franklin TD, Lumeng L, Grosfeld JL. High intensity focused ultrasound in the treatment of experimental liver cancer. Arch Surg 1991;126:1002-9.
15. Billard BE, Hynynen K, Roemer RB. Effects of physical parameters on high temperature ultrasound hyperthermia. Ultrasound in Med & Biol 1990;16:409-20.
16. Fry FJ, Kossoff G, Eggleton RC, Dunn F. Threshold ultrasound dosages for structural changes in the mammalian brain. J Acoust Soc Am 1970;48:1413-7.

17. Lele PP. Hazzard DG, Litz ML, eds. Symposium on biological effects and characterisation of ultrasound sources. Rockville: DHEW (FDA) 78-8084; 1977;Thresholds and mechanisms of ultrasonic damage to `organized' animal tissues. p. 224-39.
18. Yang R, Griffith SL, Rescorla FJ, et al. Feasibility of using high intensity focused ultrasound for the treatment of unresectable retroperitoneal malignancies. [Abstract] J Ultrasound Med 1992;11:s37
19. Hynynen K, Colucci V, Chung A, Jolesz F. Noninvasive arterial-occlusion using mri-guided focused ultrasound. Ultrasound In Medicine And Biology 1996;22:1071-7.
20. Delon-Martin C, Vogt C, Chignier E, Guers C, Chapelon JY, Cathignol D. Venous thrombosis generation by means of high intensity focused ultrasound. Ultrasound in Med & Biol 1995;21(1):113-9.
21. Bush NL, Rivens I, ter Haar GR, Bamber JC. Acoustic properties of lesions generated with an ultrasound therapy system. Ultrasound in Med & Biol 1993;19:789-801.
22. Hill CR. Optimum Acoustic Frequency for focused ultrasound surgery. Ultrasound in Med & Biol 1994;20 (3):271-7.
23. Ville Y, et al. Preliminary experience with endoscopic laser surgery for severe twin-twin transfusion syndrome. New England Journal of Medicine 1995;332:224-7.
24. Denbow ML, Cox P, Talbert D, Fisk NM Association of arterio-arterial anastomoses in vivo with the feto-fetal transfusion syndrome. 6th World Congress of Ultrasound in Obstetrics and Gynecology. Ultrasound Obstet Gynecol. 1996; 8: Supp 1, 88.

Further author information -
I.Rivens (correspondence): E-mail: ian@icr.ac.uk WWW: http://www.icr.ac.uk/physics/phys5.html
Telephone: 0181 642 6011 ext. 3708 FAX: 0181 643 3812
Gail ter Haar: E-mail: Gail@icr.ac.uk; Ian Rowland: E-mail: IJR@icr.ac.uk

Focused ultrasound surgery on kidney

Jacques Schlosser [a], Benoît Feuillu [a], François Lacoste [b],
Joelle André-Bougaran [c], and Guy Vallancien [c]

[a] Department of Urology, CHU Nancy-Brabois, Nancy 54511
[b] Edap-Technomed, Engineering Department, Vaulx en Velin 69120
[c] Department of Urology and Research (CERA), Institut Montsouris, Paris 75013
France

ABSTRACT

Introduction: High Intensity Focused Ultrasound (HIFU) is a minimally invasive therapy which can produce tissues necrosis in depth by a local thermal effect.
Objectives: Evaluate the effect of extracorporeal HIFU with electronic scanning in the treatment of pig kidney.
Material and method: The kidney of 12 pigs were treated in vivo under general anaesthesia by extracorporeal HIFU. The HIFU machine was a Pyrotech (Edap-Technomed; France) modified with a fast electronic scanning of the focal point. Each ultrasonic pulse thus scans a square area of adjustable dimensions from 3x3 mm to 5x5 mm. An ultrasound probe inserted in the treatment head, allowed the localization of the target into the kidney. The volume treated in the kidney was 1.4 to 2.6 cm^3. The delay between the ultrasound pulses were 40 to 60 s. The treatments duration varied between 9 to 16 min. The kidneys were removed 3 days after the HIFU treatment and analyzed in histology.
Results: 7 kidneys had homogeneous necrotic lesions. The volume of the lesions corresponded to the treated volume. 3 kidneys had partial necrotic lesions, with non treated inclusions. In 2 kidneys, no lesions were found. Skin burns were observed on 2 pigs.
Conclusion: Extracorporeal HIFU with electronic scanning can produce tissue necrosis into pig's kidneys. This treatment could be used in human as a non invasive therapy of small kidney's tumors less than 30 cm^3 of volume.

Keywords: High intensity focused ultrasound, phased array, non invasive therapy, experimental, pig, kidney.

1. INTRODUCTION

High Intensity Focused Ultrasound (HIFU) can produce tissue necrosis in depth by a local thermal effect. If focal intensity is high enough, mechanical damages due to boiling and/or cavitation can appear [1]. Bladder, renal and hepatic tumors imaged with ultrasonography, have been treated with extracorporeal HIFU [2,3]. But these treatments were slow because of the small necrosed tissue volume induced by each pulse [4,5,6,7,8]. 15 to 45 minutes were necessary to treat a 1 cm^3 tissue volume [3,4,8]. Treatment simulations have shown that increasing the focal volume and reducing the number of pulses could theoretically offer significantly shorter treatment time [5,6]. Necrosed tissue volume can be enlarge by electronic scanning of the focused beam. The purpose of this experimentation was to show the feasibility and interest of this technique in vivo.

2. MATERIAL AND METHOD

2.1 Material

12 female Large White-Land Race pigs (body weight between 50 and 70 kg) were used for this study.

The ultrasound source was a modified Pyrotech (Edap-Technomed, France). Its treatment head contained 160 flat round piezoelectric ceramics, operating at a frequency of 1 MHz. The acoustic power was adjustable between 50 and 6000 Watts. The treatment head was mobile with a millimetric precision. Inside, the coupling liquid was maintained at a constant 15°C temperature. The target volume could be imaged with an ultrasound probe inserted in the center of the treatment head.

During each pulse, the scanned tissue volume could be chosen between 3x3x10 mm and 15x15x10 mm. Treatment of a larger volume required multiple exposures with movement of the treatment head.

2.2 Method

During HIFU treatments, pigs were anaesthetized. The premedication associated a carazol (0.15 mg) and an atropine (0.5 mg) intramuscular injection. After catheterism of an ear vein, the anaesthesia was induced with intravenous thiopental (10 mg/kg) and vecuronium bromide (12 mg). The animals were intubated under direct vision with an endotracheal tube. Anaesthesia was maintained with intravenous thiopental.

The pigs were placed on the right side to treat the left kidney. Before locating, the skin over the kidney was cleaned and shaved. The acoustic coupling between the treatment head and the skin was ensured by an acoustic gel (KY Lubrificating Jelly / Johnson & Johnson).

The ultrasound exposure parameters are summarized in table 1. The scanned volume during each pulse was 3x3x10 mm, 4x4x10 mm or 5x5x10 mm. Focal intensity have varied from 9000 to 11000 W/ cm^2. 9 to 16 pulses were applied contiguously in a square array to treat the target volume. Delay time between each pulse, depending of acoustical power, depth of the kidney and scanning size, varied between 40 and 60 seconds. Treated volumes varied from 1.4 to 2.6 cm^3. Treatments were 9 to 16 minutes long.

Focal depth (mm)	49-57
Treated volume (cm^3)	1.4-2.6
Focal spacing (mm)	3-5
Delay time (s)	40-60
Pulse duration (s)	0.6-1.4
Treatment time (min)	9-16
Focal intensity (W/cm^2)	9000-11000
Focal energy (kJ/cm^2)	4-6

Table 1. Acoustic parameters for HIFU treatment on kidney.

Kidneys were removed 3 days after treatment according to a surgical procedure. The animals were then sacrificed by barbiturate overdose. Spleen, bowels, lung and abdominal wall were systematically examined for macroscopic injury. The samples were fixed in a 10% formalin solution. Hematoxylin-eosin-saffron stain was used for microscopic examination.

3. RESULTS

Tissue damages were obtained in 10 kidneys (83%). The tissue necrosis was homogeneous in 7 cases (58%) and corresponded to the theoretical treated volume. In 3 kidneys (25%), necrosis was heterogeneous with areas of edematous congestion between small necrosis volumes. Around well delimited necrosis, renal fibrosis was often seen. Renal destruction's have been created with the 3 tested scanning sizes.

In 2 kidneys (16%), no damage was seen. 2 skin burns of first degree (16%) were noticed during this study. Around the kidney, no organ has been damaged.

4. DISCUSSION

This study has shown that HIFU with electronic scanning can produce renal necrosis in vivo. As demonstrated by Fan [5,6], enlarging the focus size can decrease treatments duration. 25 to 100 pulses were necessary for mechanical scanning of the a 1 cm^3 target [2,3,8,9], whereas 4 pulses can now be used to treat the same volume with electronic scanning. The treatment of a 1 cm^3 renal tissue volume is then 4 min 30 s to 8 min long. These treatment time variations depend on the scanning size, focal intensity and depth of the target.

The partial tissue necrosis can have two explanations: a loss of energy when the acoustic beam pass through the abdominal wall and the destruction mechanism. When high focal intensities are used, cavitation at the focus is important and can be an obstacle to the homogeneity of the lesion [10]. Skin burns were the consequence of too short time delay between two pulses, when compared with focal intensity and energy. The repetition of ultrasonic pulses can also lead to a temperature elevation of the abdominal wall with irreversible damage of the deep muscle. Delay time between each pulse have to be optimized.

5. CONCLUSION

Extracorporeal HIFU with electronic scanning can produce tissue necrosis into pig's kidneys. Treatments duration are significantly reduced. Electronically scanned high intensity focused ultrasound could be used in human for non invasive therapy of small kidney's tumors less than 30 cm^3.

6. ACKNOWLEDGMENTS

We want to thank the engineers and technicians of the EDAP-TECHNOMED company, all members of the laboratory of research (CERA - Fondation de l'Avenir), the doctors François Laborde, Emmanuel Chartier-Kastler, Nathalie Bataille, Mohamed Harouni and the professor Dominique Chopin (Henri Mondor Hospital) for their financial and technical assistance in this research.

7. REFERENCES

1. F.J. Fry, "Intense Focused Ultrasound in Medicine: Some Practical Guiding Physical Principles from Sound Source to Focal Site in Tissue", Eur Urol, 23(suppl 1), pp. 2-7, 1993.
2. G. Vallancien, E. Chartier-Kastler, N. Bataille, D. Chopin, M. Harouni, and J. Bougaran, "Focused Extracorporeal Pyrotherapy", Eur Urol, 23, pp. 48-52, 1993.
3. G. Vallancien, M. Harouni, B. Guillonneau, B. Veillon, and J. Bougaran, "Ablation of superficial bladder tumors with focused extracorporeal pyroterapy", Urology, 47, pp. 204-207, 1996.
4. G. Vallancien, E. Chartier-Kastler, D. Chopin, B. Veillon, JM. Brisset, and J. André-Bougaran, "Focused Extracorporeal Pyrotherapy: Experimental Results", Eur Urol, 20, pp. 211-219, 1991.
5. X. Fan and K. Hynynen, "Ultrasound surgery using multiple sonications - treatment time considerations", Ultrasound Med Biol, 22, pp. 471-482, 1996.
6. X. Fan and K. Hynynen, "Control of the necrosed tissue volume during noninvasive ultrasound surgery using a 16-element phased array", Med Phys, 22, pp. 297-306, 1995
7. C. Damianou and K. Hynynen, "Focal spacing and near-field heating during pulsed high temperature ultrasound therapy", Ultrasound Med Biol, 19, pp. 777-787, 1993.
8. J. Schlosser and G. Vallancien, "High intensity focused ultrasound ablative surgery for bladder cancer", *Atlas of the Urologic Clinics of North America,* J.E. Montie, M.I. Resnick, and J. Kowalak, 5, pp. 125-141, W.B. Saunders Company, Philadelphia, 1997.
9. N.A. Watkin, S.B. Morris, I.H. Rivens, C.R.J. Woodhouse and G.R. ter Haar, "A feasibility study for the non-invasive treatment of superficial bladder tumours with focused ultrasound", Br J Urol, 78, pp. 715-721, 1996.
10. J.Y. Chapelon, J. Margorani, R. Bouvier, D. Cathignol, F. Gorry, and A. Gelet, "Ablation tissulaire par ultrasons focalisés", Prog Urol, 1, pp. 231-243, 1991.

Phase 1 clinical trial of the use of focused ultrasound surgery for the treatment of soft tissue tumours.

Gail R ter Haar, Ian H Rivens, Eleanor Moskovic[#], Robert Huddart[*] Andrew G Visioli

Joint Department of Physics, Royal Marsden Hospital, Sutton, Surrey SM2 5PT, UK
[#]Radiology Department, Royal Marsden Hospital, [*]Radiotherapy Department, Royal Marsden Hospital

ABSTRACT

A prototype extra-corporeal focused ultrasound surgery device has been built and tested extensively in model systems both *in vivo* and *ex vivo*. A phase 1, normal tissue toxicity trial is now underway. Patients with soft tissue tumours lying 4 - 12 cm below the skin surface are being treated using a dose escalation technique. An *in situ* "ablative intensity" (AI) has been established from preclinical studies. This was found to be 1500 Wcm^{-2} for up to 3 seconds at 1.7 MHz. Groups of three patients are being treated at doses rising from 25% AI through 50%, 63%, 80%, 100% to 125%AI for 1 second. Finally, 2 and 3 second exposures will be used for the two highest doses. Patients receive no sedation or anaesthetic. Target sites include all soft tissue tumours, especially those of the prostate, kidney and liver. Patients are examined for skin erythema, and are asked to complete pain and symptom questionnaires prior to treatment, immediately after treatment, one week and one month later. Patients receive a diagnostic ultrasound scan before and immediately after exposure, and after 1 week. Those at the highest dose levels are also offered a magnetic resonance scan.

Keywords : ultrasound therapy, hyperthermia, cancer therapy

1. INTRODUCTION

The typical millimetre wavelength of Megahertz ultrasound in tissue allows high intensity ultrasonic beams to be brought to a tight focus close to their source[1]. It is therefore possible to arrange for the focus from an extra-corporeal transducer to lie at depth within the body. If the intensity at the focus is sufficiently high, the cells within this volume are killed, whilst cells lying elsewhere in the beam survive. The mechanism for cell killing is primarily thermal, temperatures in excess of 60°C being reached rapidly during the 1-3 second exposure. The principle of this technique, known variously as focussed ultrasound surgery (FUS) or high intensity focussed ultrasound (HIFU), is shown in fig. 1.

At a frequency of 1.7 MHz, typical dimensions of the approximately elliptically shaped damaged tissue volume are 15 mm in length, and 1.5 mm in diameter.

FUS was first developed in the 1940's, the original application being the selective destruction of targets in the brain to aid behavioural studies in animals[2,3]. Since that time, its application has been investigated in a number of clinical sites. Despite early reported promise for FUS treatment of Parkinson's disease[4,5] this was not widely taken up because of the simultaneous development of L-dopa therapy for this condition. Ophthalmological applications of FUS, which include treatment of glaucoma and sealing of retinal tears[6,7] have suffered a similar fate with the advent of medical lasers providing alternative techniques.

There has been a resurgence of interest in the clinical usage of FUS. This is due in part to improvements in imaging techniques which now allow accurate targetting and monitoring of the tissue volume of interest. Apart from the ophthalmology applications in FUS[8] recent clinical interest has been predominantly in the treatment of benign prostate hyperplasia (BPH). Trans-rectal applicators have been designed for prostate treatments, and these have been used in early clinical trials. Two commercial devices have been used. In one, a 4 MHz transducer was used for both imaging and therapy[9]. The whole 30 x 22 mm crystal was used for therapy with only the central portion (diameter 12 mm) being used for imaging. Single shots of 4s duration were placed side by side in the prostate, 12 seconds being left between adjacent shots.

SPIE Vol. 3249 • 0277-786X/98/$10.00

The second device[10] consists of a 2.25 MHz therapy transducer and a retractable 7.5 MHz imaging probe. In clinical treatments using this device, 4s shots are separated by 10 second intervals.

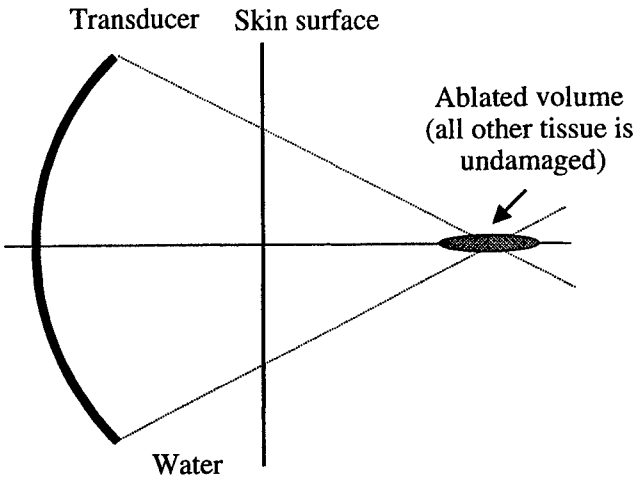

Figure 1. Schematic diagram showing principle of the extracorporeal FUS technique.

Early results for clinical trials of the efficacy of these trans-rectal devices in the treatment of BPH[9,11,12] showed initial improvement in symptom scores, maximum flow rates and post-void residual volumes (PVR), with these regressing slightly over two years, but with some improvement being maintained. In one study (13 patients)[11] the average symptom score dropped from 23 to 5 at one year, and was 7 after 2 years, mean flow rates increased from 9.9 ml/s to 14.2 ml/s at 6 months, 15.8 at 1 year and 10.6 after 2 years. The mean PVR was 86.1 ml before treatment and 18.1 ml at 2 years.

All these studies employed either spinal or general anaesthesia. Acute retention was encountered in all three trials, with the incidence varying from 8%[11] to 92%[12]. Other adverse reactions seen included haematospermia[9,12], gross haematuria[9,12], dysuria[9], microhaematuria[9], urinary tract infection[12].and epidyidymitis[12].

Trans-rectal devices have also been used for the treatment of prostate cancer. Madersbacher *et al*[12] treated 10 patients with 4 MHz ultrasound at intensities in the range 1260 – 1680 Wcm^{-2}. "Total cure" was reported in 3 patients, and "partial cure" in 7. Gelet *et al*[14] report an early study of the treatment of prostate cancer in 14 patients. They reported satisfactory local control in 50% of cases.

Some sites that can not easily be reached by a trans-rectal route may be treated using an extra-corporeal approach. A number of clinical devices have been described[15,16,17]. Vallancien *et al.*[15] have described the treatment of superficial bladder tumours using such a 1 MHz device. They reported that 67% of patients (n=20) with primary tumours treated with FUS had no recurrence after a year. Of patients with recurrent tumours (n=10) only 33% had no recurrence at one year. The source used in this study employs a firing head with 16 transducers. Shots lasting 0.015 – 1 second were used, with intensities in excess of 10 kW cm^{-2}.

Hynynen *et al.*[16] have shown a magnetic resonance (MR) image of a breast fibroadenoma following FUS treatment. The system used by this group employs a single spherical 1.5 MHz transducer (100mm diameter, 80 mm focal length) mounted in an MR scanner. Tumour targetting and treatment monitoring are carried out using MR imaging. Contrast agent studies have shown that treated tumours no longer take up the contrast medium.

The clinical study that is the subject of this paper is a phase I toxicity and tolerance trial for the treatment of soft tissue tumours. It differs from all previous studies in that the patients are fully conscious during treatment and receive no analgesia. Tumour targetting is carried out using diagnostic ultrasound, and treatments are followed up using diagnostic ultrasound, MR imaging and clinical assessment.

2. METHODS

2.1 Ultrasonic exposures

The FUS treatment was given using the clinical prototype device built at the Institute of Cancer Research. This has been described in detail elsewhere[17] and is shown in Figure 2. Briefly, a 10 cm diameter PZT4 focussed bowl transducer with focal length 15 cm operating at a frequency of 1.7 MHz is mounted on a gantry that is capable of movement in each of three orthogonal directions. The ultrasonic beam is coupled to the patient through a bag of degassed water. The tissue volume to be treated is identified using a 3.5 MHz imaging transducer which is mounted on the gantry in such a way that it has the same beam axis as the therapy transducer. Once the co-ordinates of the treatment volume have been established using this diagnostic system, the imaging probe is replaced by the therapy transducer, and the treatment of the pre-determined tissue volume carried out. During treatment, the patient's skin surface is inspected visually for signs of erythema.

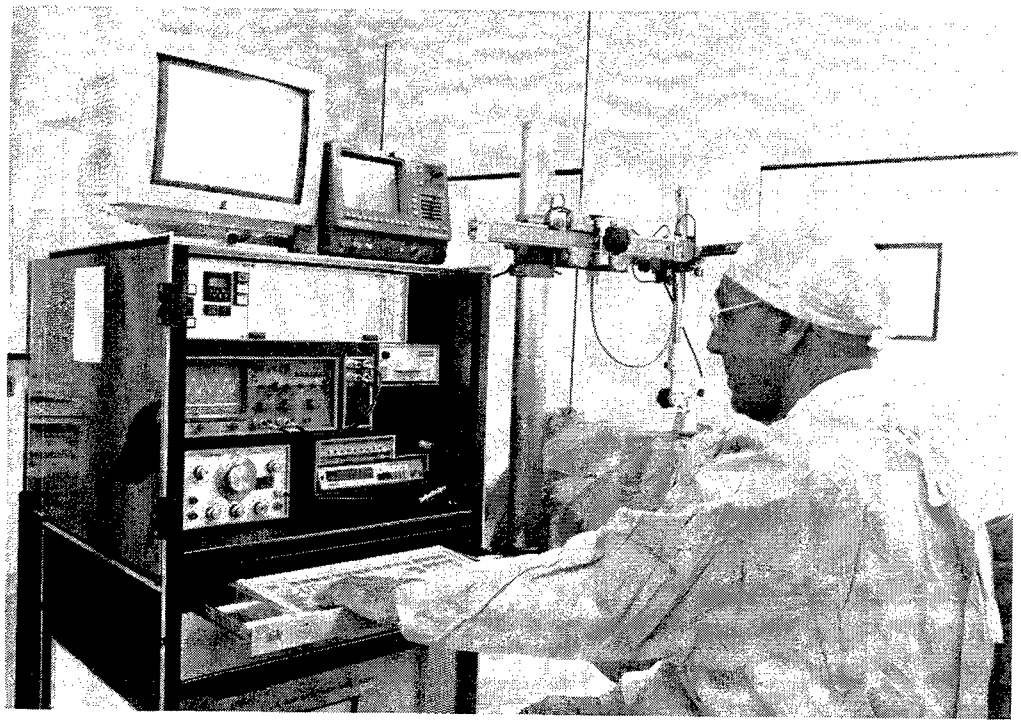

Figure 2. Photograph showing the clinical prototype device.

Ex vivo tissue experiments have determined that an *in situ* spatial peak intensity (I_{SP}[18]) of 1490 W cm^{-2} gives a lesion in tissue that is predictable both in terms of shape and position. We have therefore termed this our "ablative intensity" (AI). Transducer calibrations are carried out using a radiation pressure balance[19] to determine total power, and a PVDF membrane hydrophone[20] to give acoustic pressure distributions. The full width half maximum of the pressure distribution in the ellipsoidal focal volume is found to be 18mm along the beam direction, and 2mm perpendicular to this axis.

2.2 Clinical trial design

Eligible patients had soft tissue tumours lying 4 – 12 cm below the skin surface which could be seen on diagnostic ultrasound. It was necessary to have a suitable acoustic window on the skin surface, no bone or gas overlying the tumour, and no more than 6 cm of solid tissue path between the skin surface and the target site. Thus, for example, prostate tumours lying 12 cm deep could be treated if there was a significant beam path through the urine filled bladder. All patients had distant metastases. All primary lesions had been confirmed on histology. Treated metastases had not always been biopsied. All patients were attending the Royal Marsden Hospital for treatment.

All FUS planning, treatments and monitoring could be given as outpatient procedures, without sedation or anaesthesia. After signing a consent form, patients were given an ultrasonic planning scan in the Radiology department. The trial is a classic phase I descriptive toxicity and dose escalation study with the aim of determining any acute or delayed toxicity resulting from FUS given in increasing doses to a level capable of damaging tumour cells, while avoiding normal tissue complications.

The patient was asked to lie on a couch. Where necessary the skin area that would serve as the acoustic window was shaved. A bag containing degassed water was lowered on to the skin and was coupled to the surface using acoustic gel. The *in situ* intensity was increased from 0.25 AI through 0.5 AI, 0.63 AI, 0.8 AI to AI. 3 patients were exposed at each intensity level. Ablation was carried out as an array of individual FUS exposures, each lasting 1 second, with their centres separated by 2 mm. 60 seconds was left between exposures to allow for tissue cooling. The arrays varied from 4 x 4 (8mm x 8mm x 15mm) to 6 x 6 (12mm x 12mm x 15mm). When organs subject to significant respiratory movement (e.g. liver) were treated, the patient was asked hold their breath at end expiration. This was found to give the best reproducibility of organ position.

Patients were asked to fill in a questionnaire documenting pain and other symptoms before, immediately, one week and one month after treatment. Ablative effects in the target organ were monitored using diagnostic ultrasound. Patients receiving the 80-100% of the ablative dose were also offered an MR scan.

This paper reports the preliminary results for 14 patients, 3 treated at each intensity up to 0.8 AI, and two treated at AI.

3. RESULTS

14 patients have been treated to date. Table 1 summarises details of these patients and their treatment. Tumours treated include 5 recurrences of prostatic adenocarcinoma, 6 liver metastases, 2 renal cell carcinomas and one metastasis to acetabulum from a bladder transitional cell carcinoma.. The average age of these patients was 67.6 years. Table 2 shows the treatment details. The average time taken to set up was 49.1 minutes.

TABLE 1 Tumours treated

No	Sex	Age (Yrs)	Primary Tumour	Tumour treated	Dose
1	M	84	Adenocarcinoma prostate	Prostate	0.25 AI
2	M	71	Renal cell carcinoma	Kidney	0.25 AI
3	M	72	Renal cell carcinoma	Kidney	0.25 AI
4	M	66	Renal cell carcinoma	Liver	0.50 AI
5	M	67	Adenocarcinoma prostate	Prostate	0.50AI
6	M	76	Adenocarcinoma prostate	Prostate	0.50 AI
7	M	59	Bladder TCC	Hip bone	0.63 AI
8	M	72	Adenocarcinoma prostate	Prostate	0.63 AI
9	M	62	Melanoma	Liver	0.63 AI
10	F	75	Breast	Liver	0.80 AI
11	F	53	Abdominal leiomyosarcoma	Liver	0.80 AI
12	M	75	Adenocarcinoma prostate	Prostate	0.80 AI
13	F	55	Melanoma	Liver	AI
14	M	60	Rectal adenocarcinoma	Liver	AI

Table 3 details any side effects recorded and the patients' comments. No significant adverse effect has been recorded, and the treatment was well tolerated by all patients. Two patients reported a tingling sensation in their prostates during treatment. Patient #4 developed a liver cyst associated with a small amount of blood that was visible on the 1 week ultrasound scan, but was thought to be spontaneous in origin given the low ultrasound intensity to which this patient was exposed. Patient #9 developed an asymptomatic blister on the skin that resolved without causing problems.

Patients 12 and 13 both showed cystic regions at the treatment site on the ultrasound scan 1 week after FUS treatment. Patient #12 agreed to an MR scan which also showed signs of damage at this site dynamic contrast agent uptake study showed a region of hypoechogenicity in the volume of the prostate that had been targetted.

4. DISCUSSION

This trial represents the first reported study in which patients are treated with FUS without having received a general anaesthetic or any other form of sedation. This preliminary report shows that the procedure has been well tolerated, and that no significant normal tissue toxicity has been encountered. Patients who were experiencing bone pain found it slightly uncomfortable to lie still for an extended period, but this did not limit any treatment. In one patient, (#4), a small cyst with blood was observed in the liver one week after treatment, but this was thought to have arisen spontaneously. The intensity at the target in this case was half that known to induce damage in unperfused livers. It is possible that the tingling sensation experienced by 2 prostate patients may be due to some non-thermal interaction of the ultrasound beam with nerve endings. The first patient to report this, (#1), received a very low level of ultrasound exposure (0.25 AI).

Patients 12 and 13 showed signs of tissue damage at the target site at the one week ultrasound scan. There was also an indication of target tissue damage on the MR scan of patient #12 at 2 weeks.

This trial represents the first reported study in which patients are treated with FUS without having received a general anaesthetic or any other form of sedation. This preliminary report shows that the procedure has been well tolerated, and that no significant normal tissue toxicity has been encountered. Patients who were experiencing bone pain found it slightly uncomfortable to lie still for an extended period, but this did not limit any treatment. In one patient, (#4), a small cyst with blood was observed in the liver one week after treatment, but this was thought to have arisen spontaneously. The intensity at the target in this case was half that known to induce damage in unperfused livers. It is possible that the tingling sensation experienced by 2 prostate patients may be due to some non-thermal interaction of the ultrasound beam with nerve endings. The first patient to report this, (#1), received a very low level of ultrasound exposure (0.25 AI).

Patients 12 and 13 showed signs of tissue damage at the target site at the one week ultrasound scan. There was also an indication of target tissue damage on the MR scan of patient #12 at 2 weeks.

All patients recruited for this study had distant metastases, with an ECOG performance status of 3 or less. They all had lesions that were visualisable on ultrasound and which lay 4 – 12 cm below the skin surface. Only a small part of the tumour volume was treated in this trial, and thus no attempt has been made at cure. FUS given in this way can only have a palliative effect in these patients. This has not been an endpoint of the study so far.

This is an ongoing trial, for which this serves as a preliminary report of the findings. Further escalation of "dose" to patients is planned, first by increasing the time of each exposure at the Ablative Intensity (AI) to 2 and 3 seconds, and then by using 1.25 AI for 1 second. In this way, it should be possible to establish safe and effective exposures for these treatments. In all cases, it is expected that the limiting organ for safety will be the skin.

5 CONCLUSIONS

The technical requirements of FUS treatment have been adequately met, although there is much in the way of equipment development still possible. Preliminary results from this Phase I study show that the targetting and treatment of soft tissue tumours is possible, and that the procedure is well tolerated by conscious patients.

TABLE 2 Treatment parameters

No.	Tumour treated	Dose	Focal depth (cm)	Tissue Path (cm)	I_{SP} (water) (W cm^{-2})	I_{SP} (target) (W cm^{-2})	Set up time (mins)	Treatment time (mins)	No. of exposures
1	Prostate	0.25 AI	10.0	5.2	1490	372.5	50	30	4 x 4
2	Kidney	0.25 AI	4.0	4.0	960	372.5	38	32	4 x 4
3	Kidney	0.25 AI	4.0	4.0	600	372.5	30	29	5 x 3
4	Liver	0.50 AI	9.5	9.5	5700	745.0	-	-	4 x 4
5	Prostate	0.50 AI	10.5	5.5	3030	745.0	50	30	4 x 4
6	Prostate	0.50 AI	11.0	7.5	3430	745.0	50	25	4 x 4
7	Hip bone	0.63 AI	7.0	7.0	3430	940.0	33	30	5 x 5
8	Prostate	0.63 AI	11.0	5.5	3430	940.0	60	45	5 x 6
9	Liver	0.63 AI	4.0	4.0	2500	940.0	40	45	6 x 6
10	Liver	0.80 AI	5.0	5.0	3030	1220.0	65	-	6 x 6
11	Liver	0.80 AI	6.0	6.0	4200	1220.0	45	40	6 x 5
12	Prostate	0.80 AI	12.0	5.0	3430	1220.0	60	35	5 x 5
13	Liver	AI	5.0	5.0	4200	1490.0	50	40	6 x 6
14	Liver	AI	5.0	5.0	4200	1490.0	70	40	5 x 6

6. ACKNOWLEDGEMENTS

The authors would like to thank the NHS Executive – South Thames for funding this project. They would also like to thank Professors Horwich and Ott for their help and support, Dr. Judith Bliss for her help with the trial design, and Professor Clarke for his invaluable advice

TABLE 3 Toxicity results

No	Tumour treated	I_{SP} (target) W cm^{-2}	Side effects / Patient comments
1	Prostate	372.5	During treatment : slight tingling in prostate After treatment : micturition improved (subjective)
2	Kidney	372.5	None
3	Kidney	372.5	One week post-treatment – moderate local pain
4	Liver	745	One week post-treatment –bout of moderate pain Cyst observed with some blood
5	Prostate	745	None
6	Prostate	745	None
7	Hip Bone	940	Deceased before one week assessment
8	Prostate	940	None
9	Liver	940	Asymptomatic blister on skin for 5 days
10	Liver	1220	None
11	Liver	1220	None
12	Prostate	1220	Tingling in prostate, sensation of warmth on skin Micturation improved with reduced noctural frequency (subjective)
13	Liver	1490	None
14	Liver	1490	None

7. REFERENCES

1. G.R. ter Haar, "Ultrasound Focal Beam Intensity", *Ultrasound in Med. & Biol.* **21**, pp 1089-1100, 1995.
2. J.G. Lynn, R.L.Zwemmer, A.J. Chick, A.F. Miller, "A new method for the generation and use of focused ultrasound in experimental biology", *J. Gen. Physiol.* **26**, pp 179-193, 1942.
3. W.J. Fry, J.W. Barnard, F.J. Fr selective lesions in the central nervous system y, J.F. Brennan, "Ultrasonically produced localised selective lesions in the central nervous system", *Am. J. Phys. Med.* **34**, pp 413-423, 1955.
4. R. Meyers, F.J. Fry, W.J. Fry, R.C. Eggleton, D.F. Schultz, " Determination of topological hunman brain representations ans modifications of signs and symptoms of some neurological disorders by the use of high level ultrasound", *Neurology* **10**, pp 271-277, 1960.
5. W.J. Fry & F.J. Fry, "Fundamental neurological research and human neurosurgery using intense ultrasound", *IRE Trans. Med. Electron.* **ME-7**, pp 166-181, 1960.
6. D.J.Coleman, F.L. Lizzi, J. Driller *et al.*, "Therapeutic ultrasound in the treatment of glaucoma II. Clinical applications", *Ophthalmology* **92**, pp 347-353, 1985.
7. L.R. Rosecan, T. Iwamoto., A Rosado, *et al.*, "Therapeutic ultrasound in the treatment of retinal detachment : clinical observation and light and electron microscopy", *Retina* **5**, pp 115-122, 1985.
8. R.H. Silverman, B. Vogelsang, M.J. Rondeau, D.J. Coleman, " Therapeutic ultrasound for the treatment of glaucoma", *Am. J. Ophthalmol.*, **111**, pp 327-337, 1991.
9. R. Bihrle, R.S. Foster, N.T. Sanghvi, J.P. Donohue, P.J. Hood, "High intensity focused ultrasound for the treatment of benign prostatic hyperplasia : early United States clinical experience" *J. Urol.* **151**, pp 1271-1275, 1994.
10. A. Gelet, J.Y. Chapelon, J. Margonari *et al*, "High intensity focused ultrasound experimentation on human benign prostatic hypertrophy", *Eur. Urol.*, **23(Suppl. 1)**, pp44-47, 1993.
11. E.D. Mulligan, T.H. Lynch, D. Mulvin, J.M. Greene, J.M. Smith, J.M. Fitzpatrick, "High intensity focused ultrasound in the treatment of benign prostatic hyperplasia", *Brit. J. Urol.* **79**, pp 177-180, 1997.
12. S. Madersbacher, C. Kratzik, M. Susani, M. Marberger, " Tissue ablation in benign prostatic hyperplasia with high intensity focused ultrasound", *J. Urol.* **152**, pp 1956-1961, 1994.
13. S. Madersbacher, M. Pedevilla, L. Vingers *et al.*, "Effect of high intensity focused ultrasound on human prostate cancer *in vivo*", *Cancer Research* **55**, pp 3346-3351, 1995.
14. A. Gelet, J.Y. Chapelon, R. Bouvier *et al.*, "Treatment of prostate cancer with transrectal focused ultrasound : early clinical experience", *Eur. Urol.* **29**, pp 174-183, 1996.
15. G. Vallancien, M. Harouni, B. Guillonneau *et al.*, "Ablation of superficial bladder tumours with focused extracorporeal pyrotherapy", *Urology* **47**, pp 204-207. 1996.
16. K. Hynynen, W.R. Freund, H.E. Cline *et al.*, "A clinical, noninvasive, MR imaging-monitored ultrasound surgery method", *Radiographics* **16**, pp 185-195, 1996.
17. G.R. ter Haar, R.L. Clarke, M. Vaughan, C.R. Hill, "Trackless surgery using focused ultrasound : technique and case report", *Minimal. Invas. Ther.* **1**, pp 13-19, 1991.
18. N.A.Watkin, G.R. ter Haar, I. Rivens, , "The intensity dependence of the site of maximum energy deposition in focused ultrasound surgery" *Ultrasound in Med. & Biol.* **22**, pp 483-491, 1996.
19. C.R. Hill, "Calibration of ultrasonic beams for biomedical applications", *Phys. Med. Biol.* **15**, pp 241-248, 1970
20. R.C. Preston, D. Bacon, A.J. Livett, K. Rajendran, "PVdF membrane hydrophone performance properties and their relevance to the measurement of acoustic output of medical ultrasonic equipment", *J. Phys. E. Sci. Instrument.* **16**, pp 786-796, 1983.

Addendum

The following papers were announced for publication in this proceedings but have been withdrawn or are unavailable.

[3249-01] **Ultrasound technology for interstitial and intracavitary thermal therapy: a review**
C. J. Diederich, Univ. of California/San Francisco

[3249-11] **Clinical laser therapy on injury of skull by intravascular irradiation He-Ne laser: results analysis**
Y. Zhang, Y. Gao, S. Liu, C. Liao, South China Normal Univ.

[3249-21] **Issues in developing and validating computational models of electromagnetic heating of tissues**
K. D. Paulsen, Dartmouth College

[3249-25] **Ultrasound-guided interstitial high-frequency thermotherapy (HFTT) of liver metastases/tumors**
W. Müller, Berchtold Medizin-Elektronik GmbH & Co. (FRG)

Author Index

Albrecht, Dirk, 85
André-Bougaran, Joelle, 267
Bérubé, Dany, 61
Brassell, James, 142
Burdette, Everette C., 2
Buysse, Steve, 125
Cahill, Mark D., 246
Chandler, James, 125
Chang, John T., 171
Deardorff, Dana L., 2, 13
Denbow, Mark, 260
Desinger, Kai, 94, 147
Diederich, Chris J., Addendum, 2, 13
Dubuc, Marc, 31
Ebbini, Emad S., 182, 230
Eggleston, Jeff, 125
Fanning, Margaret, 171
Feuillu, Benoît, 242, 257, 267
Fisk, Nicholas M., 260
Gao, Yunqing, Addendum
Garza-Leal, Jose, 115
Gazelle, G. Scott, 104
Germer, Christoph T., 85
Goldberg, S. Nahum, 104, 130
Grimbergen, Matthijs G. M., 68, 72
Hartov, Alex, 193
Helfmann, Juergen, 94
Hoopes, P. Jack, 50
Huddart, Robert, 270
Humphries, Stanley, 206
Jarosz, Boguslaw J., 20
Jolesz, Ferenc A., 162
Kacher, Daniel F., 162
Kennedy, Jenifer S., 125
Kerner, Todd, 193
Kettenbach, Joachim, 162
Khalil-Bustany, Ismail S., 2
Knappe, Verena, 85
Kniep, F., 85
Kuk-Nagle, Karen, 115
Lacoste, François, 242, 257, 267
Lawes, Kate, 130
Leach, Martin O., 260
Lewis, James W., 31
Liao, Changjun, Addendum
Liebold, K., 94
Liem, L. Bing, 61
Liu, Shong-hao, Addendum
Mack, Martin G., 85, 147
Manganiello, Paul D., 50
Mazzarese, Rob, 193
Meaney, Paul M., 171, 246
Miller, Scott A. III, 142
Morrison, Paul R., 162
Moskovic, Eleanor, 270
Müller, Gerhard J., 85, 94, 147
Müller, Wolfgang, Addendum
Nau, William H., 2, 13
Osterman, Kendra S., 193
Paulsen, Keith D., Addendum, 171, 193
Pearce, John A., 217
Platt, Robert C., 206
Priem, Gert, 72
Ritz, Joerg-Peter, 85
Rivens, Ian H., 260, 270
Roggan, Andre, 85
Rondinone, David M., 142
Rondinone, Joseph, 142
Rowland, Ian, 260
Ryan, Thomas P., 115, 130, 206
Safabash, Jason, 142
Schlosser, Jacques, 242, 257, 267
Schwartz, Richard B., 162
Silverman, Stuart G., 162
Simon, Claudio, 182, 230
Soto, Cindi, 115
Stauffer, Paul R., 2, 13, 38
Stein, T., 94, 147
Taylor, Kenneth D., 125
ter Haar, Gail R., 246, 260, 270
Thomsen, Sharon L., 115, 125, 217
Thorne, Jonathan O., 142
Trembly, B. Stuart, 50
Vallancien, Guy, 242, 257, 267
van Swol, Christiaan F. P., 68, 72
van Vliet, Remco J., 68
VanBaren, Philip D., 182, 230
Vancaillie, Thierry G., 115
Vega, Felix, 142
Verdaasdonk, Rudolf M., 68, 72
Visioli, Andrew G., 270
Vogl, Thomas J., 85, 147
Wong, Terence Z., 162
Wu, Max, 2
Zhang, You, Addendum